COMPUTED TOMOGRAPHY BASED BIOMECHANICS

EDITED BY: Asa Barber, Gianluca Tozzi and Martino Pani
PUBLISHED IN: Frontiers in Materials

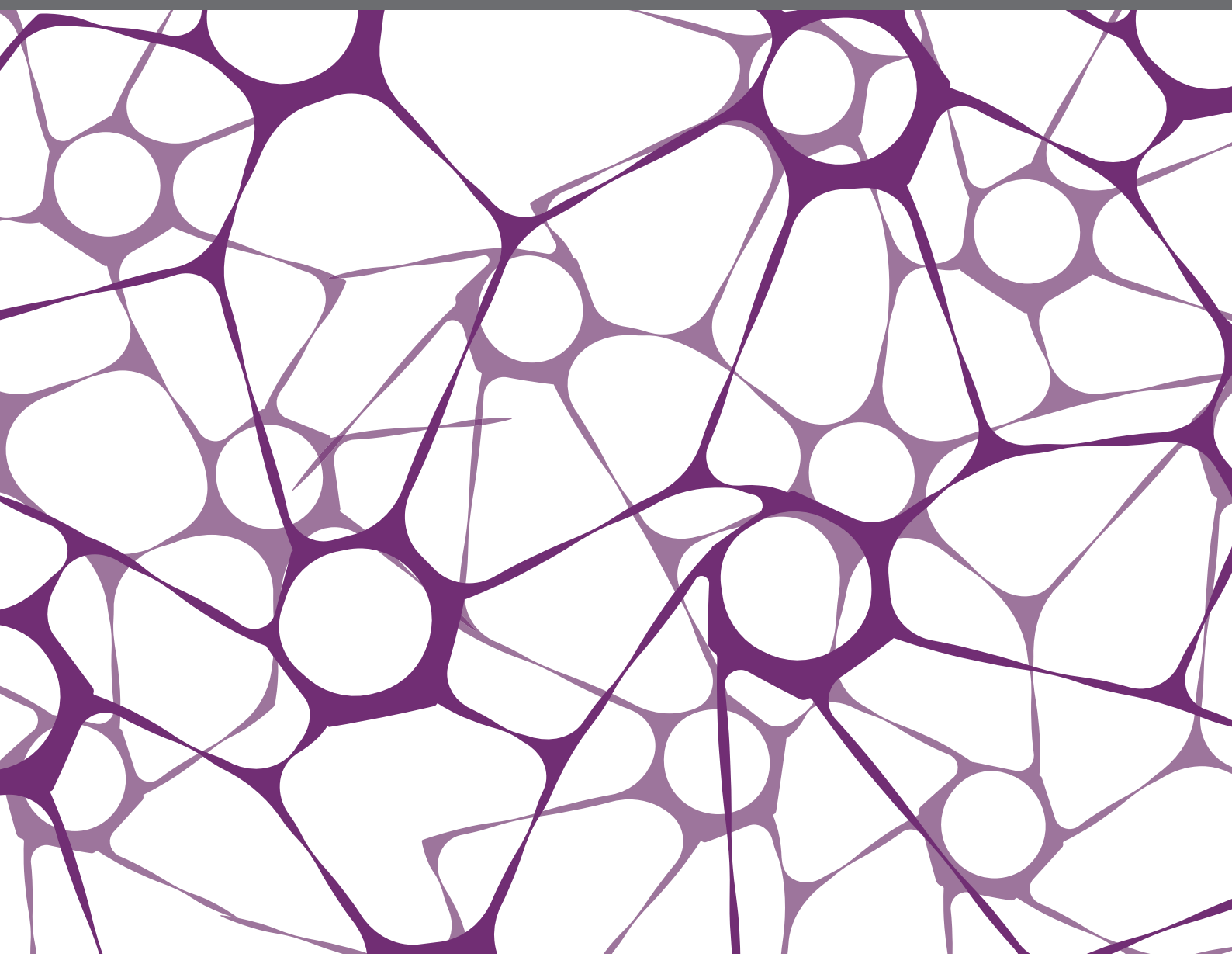

frontiers Research Topics

ISSN 1664-8714
ISBN 978-2-88945-780-9
DOI 10.3389/978-2-88945-780-9

About Frontiers

Frontiers is more than just an open-access publisher of scholarly articles: it is a pioneering approach to the world of academia, radically improving the way scholarly research is managed. The grand vision of Frontiers is a world where all people have an equal opportunity to seek, share and generate knowledge. Frontiers provides immediate and permanent online open access to all its publications, but this alone is not enough to realize our grand goals.

Frontiers Journal Series

The Frontiers Journal Series is a multi-tier and interdisciplinary set of open-access, online journals, promising a paradigm shift from the current review, selection and dissemination processes in academic publishing. All Frontiers journals are driven by researchers for researchers; therefore, they constitute a service to the scholarly community. At the same time, the Frontiers Journal Series operates on a revolutionary invention, the tiered publishing system, initially addressing specific communities of scholars, and gradually climbing up to broader public understanding, thus serving the interests of the lay society, too.

Dedication to Quality

Each Frontiers article is a landmark of the highest quality, thanks to genuinely collaborative interactions between authors and review editors, who include some of the world's best academicians. Research must be certified by peers before entering a stream of knowledge that may eventually reach the public - and shape society; therefore, Frontiers only applies the most rigorous and unbiased reviews.
Frontiers revolutionizes research publishing by freely delivering the most outstanding research, evaluated with no bias from both the academic and social point of view. By applying the most advanced information technologies, Frontiers is catapulting scholarly publishing into a new generation.

What are Frontiers Research Topics?

Frontiers Research Topics are very popular trademarks of the Frontiers Journals Series: they are collections of at least ten articles, all centered on a particular subject. With their unique mix of varied contributions from Original Research to Review Articles, Frontiers Research Topics unify the most influential researchers, the latest key findings and historical advances in a hot research area! Find out more on how to host your own Frontiers Research Topic or contribute to one as an author by contacting the Frontiers Editorial Office: researchtopics@frontiersin.org

COMPUTED TOMOGRAPHY BASED BIOMECHANICS

Topic Editors:
Asa Barber, London South Bank University, United Kingdom
Gianluca Tozzi, University of Portsmouth, United Kingdom
Martino Pani, University of Portsmouth, United Kingdom

Citation: Barber, A., Tozzi, G., Pani, M., eds. (2019). Computed Tomography Based Biomechanics. Lausanne: Frontiers Media. doi: 10.3389/978-2-88945-780-9

Table of Contents

frontiers in Mechanical Engineering

ORIGINAL RESEARCH
published: 27 September 2018
doi: 10.3389/fmech.2018.00012

Abrasion Induced Volume Loss in Porcine Teeth Measured Using X-Ray Microtomography

Alexander P. Kao[1], *Shaz Khan*[2] *and Asa H. Barber*[1,3]*

[1] School of Mechanical and Design Engineering, University of Portsmouth, Portsmouth, United Kingdom, [2] Glaxosmithkline Consumer Healthcare, Oral Health Innovation, Brentford, United Kingdom, [3] School of Engineering, London South Bank University, London, United Kingdom

Teeth are complex biological structures consisting primarily of enamel and dentin. The mechanical loading of teeth due to the action of brushing provides a complex interaction between applied forces and the biological structure, resulting in volume loss of dental tissue. The volume loss as a resulting of using an *ex situ* brushing of teeth was measured using x-ray microcomputed tomography (XCT) and corresponding image analyses. Three-dimension reconstructions of teeth reveal a considerably loss of dentin at a rate of over 30 times that of enamel during brushing, as would be expected by the consideration of the corresponding structures. The approach here is flexible and can be applied to a range of brushing, teeth, and environmental conditions.

Keywords: X-ray microtomography, tooth, mechanical processes, structural biology, abrasion

OPEN ACCESS

Edited by:
Federico Bosia,
Università degli Studi di Torino, Italy

Reviewed by:
Victor E. Arana-Chavez,
Universidade de São Paulo, Brazil
Urszula Stachewicz,
AGH University of Science and Technology, Poland

***Correspondence:**
Asa H. Barber
barbera8@lsbu.ac.uk

Specialty section:
This article was submitted to Mechanics of Materials, a section of the journal Frontiers in Mechanical Engineering

Received: *08 January 2018*
Accepted: *06 September 2018*
Published: *27 September 2018*

Citation:
Kao AP, Khan S and Barber AH (2018) Abrasion Induced Volume Loss in Porcine Teeth Measured Using X-Ray Microtomography. Front. Mech. Eng. 4:12. doi: 10.3389/fmech.2018.00012

INTRODUCTION

Teeth are a complex biological structure composed primarily of enamel and dentin. The enamel forms the outermost layer of the tooth and is formed of highly ordered apatite prisms (Fincham et al., 1999). These prisms are combined to form enamel rods, which provides a high degree of mechanical performance (Imbeni et al., 2005). Dentin is a collagen and mineral based biocomposite that forms the second major component and comprises the bulk of the tooth volume (Fratzl, 2008). Dentin has a pronounced tubular structure, where the tubules run from the tooth pulp chamber to the dentin-enamel junction. The tubules have a diameter on the order of several micrometers, narrowing in diameter as they approach the surface of the dentin or the dentin-enamel junction (Fratzl, 2008). The primary component of dentin is the intertubular dentin that is a dense fibrillar structure of mainly mineralized collagen (Zaslansky et al., 2006). The intertubular dentin surrounds the highly mineralized peritubular dentin, which in turn surrounds the dentin tubules (Jud et al., 2015). Peritubular dentin is reported to contain no collagen and is composed of highly developed hydroxyapatite crystals (Fratzl, 2008). The main function of dentin is to provide mechanical support for the enamel layer in order to facilitate the translation of the forces from the enamel through to the jaw bone (Zaslansky et al., 2006). The enamel and dentin are designed to work in conjunction, and be resistant to the repeated forces experienced within the oral cavity mainly from mastication (Montoya et al., 2016). The surface of the dentin is covered by a mineralised layer known as the cementum. The cementum generally covers the dentin surface up to the gum line where it meets the enamel (Nanci, 2014). The cementum serves as the binding point between the tooth and the periodontal ligament, which anchors the tooth to the alveolar bone (Bosshardt and Selvig, 1997). The interface between the cementum and enamel is known as the cementoenamel

junction. Generally at this junction the cementum will directly interface with the enamel, slightly overlap or in some cases leave a gap of exposed root surface (Arambawatta et al., 2009).

The inherent resistance to mechanical stresses of the enamel is highlighted by the mechanical properties. Enamel has significantly higher mechanical properties when compared to dentin. The elastic modulus of human dental enamel is in the range of 63 to 98 GPa, whereas the dentin has an elastic modulus between 19 and 24 GPa (Fong et al., 2000; Habelitz et al., 2001; Marshall et al., 2001, 2003; Kinney et al., 2003; Inoue et al., 2009; Bertassoni et al., 2011; Yilmaz and Schneider, 2016). The trend is similar when examining the reported hardness values of enamel (2.7 to 4.8 GPa) and dentin (0.55 to 0.81 GPa) (Habelitz et al., 2001; Marshall et al., 2001; Cuy et al., 2002; Low, 2004; Inoue et al., 2009; Sui et al., 2014). Compared to both the enamel and dentin, the cementum has reduced mechanical properties. The elastic modulus of the cementum present in human teeth has been reported to range from 2.3 to 16 GPa (Ho et al., 2004, 2009; Srivicharnkul et al., 2005).

Unlike many biological structures, teeth do not undergo major remodeling following damage or tissue loss (Fratzl, 2008), which means that understanding their wear behavior is important for maintaining healthy teeth. Tooth brushing is widely considered the most common method for routine dental cleaning to maintain healthy teeth (Addy and Hunter, 2003). Brushing of the teeth with the addition of a tooth paste is performed to mechanically remove dental plaque (Dyer et al., 2000). Dental plaques contribute to the development of caries and lesions on the teeth (Hicks et al., 2003). Brushing with a toothpaste has been identified as a contributor to the wear of teeth through abrasion of the tooth surface (Tellefsen et al., 2011). Low mechanical loading of the tooth from brushing, considered as a "normal" brushing condition, is advantageous as little abrasive damage occurs to the enamel such that damage is repaired by the remineralization process of the enamel that occurs within the oral cavity (Wiegand et al., 2007). Understanding damage within the tooth from brushing conditions is therefore important in providing routes to limit this damage and provide repair from remineralization.

A wide range of abrasive forces are applied to the tooth during brushing that are highly dependent on the user and the type of toothbrush, which are grouped into manual or powered, that are used. Studies quantifying the brushing mechanism are limited but some works have measured the brushing force applied by patients using strain gauges attached directly to the toothbrush. Specifically, Ganss et al. reported that patients with a manual tooth brush apply a mean force of 2.4 ± 0.8 N with a maximum force of 5.5 ± 1.9 N (Ganss et al., 2009). Wiegand et al. indicated patients with a manual toothbrush applied a mean force of 1.6 N and mean force of 0.9 N with a powered toothbrush (Wiegand et al., 2013). In both studies the patients were uninstructed regarding brushing force or technique. These studies show that the brushing forces applied to the tooth are varied but can be relatively high, which can lead to abrasion of the tooth surface when combined with a toothpaste (Kielbassa et al., 2005).

Many studies have investigated the effects of tooth brushing on the wear of dental tissue in conjunction with the effects of erosion (Attin et al., 1997; Hooper et al., 2003; Wiegand et al., 2007; Lima et al., 2013; Bizhang et al., 2016). The erosion is included in these studies to replicate the effects of acid mediated softening of the dental tissue, as sound dental tissue is considered as not susceptible to abrasive wear alone (Kielbassa et al., 2005). The softening by acidic substances or foods increases the susceptibility of the dental tissue to abrasive damage. In addition to the erosive damage leading to increased wear, gingival recession is one route that can lead to exposure of the underlying dentin (Bizhang et al., 2016). Dentin has reduced mechanical resistance to abrasion when compared to enamel, and has been shown to be susceptible to significant abrasive damage following an erosive attack (Bizhang et al., 2016).

To study the wear characteristics of enamel and dentin, the abrasive wear is conducted over a period repeated brushing cycles on polished sections of dental material. These abrasive wear studies often exclude the presence of the cementoenamel junction and cementum on the surface of the dentin or completely remove the layer prior to beginning the study. The total wear is often assessed using profilometry over a specific region of the brushed area to measure the mean change or peak change in the height of the sample within the brushed region, which provides a one dimension characterization of the damage (Dyer et al., 2000; Hooper et al., 2003; Kielbassa et al., 2005; Wiegand et al., 2013; Arnold et al., 2016; Bizhang et al., 2016). The one dimensional analysis of the wear provides a convenient method of drawing comparisons between varying conditions applied between the brush and the tooth surface, but provides less information about the overall changes occurring within the tooth structure during the wear process.

Extending the analysis to three dimensions would provide extensive information on changes in tooth volume due to the applied brushing forces. X-ray microcomputed tomography (XCT) is a powerful technique to acquire images of an entire volume at the micrometer length scale. The ability of XCT to accurately evaluate volume changes in teeth due to brushing forces has not been fully explored and evidence within the literature of quantifying small, micrometer scale, volume loss in teeth using XCT is lacking. X-ray tomography techniques have been exploited to investigate large scale abrasion wear in teeth (Kofmehl et al., 2010) but does not consider loading from a contacting toothbrush. We believe state-of-the-art x-ray microscopy techniques are not fully realized as a potential method for exploring volumetric wear in dental materials. The aim of this work is therefore to investigate the abrasive wear of tooth brushing on teeth using XCT. A particular emphasis is on quantifying the total volume loss within the enamel and dentin as a result of *ex situ* brushing using only the movement applied by a (powered) sonic toothbrush.

METHODS

Porcine teeth were extracted from the lower jaw of a pig and cleaned under running water to remove any excess soft tissue. The individual teeth were then mounted to aluminum tubing using epoxy resin (Devcon 5 minute epoxy, ITW Devcon, IE)

in order to secure the teeth in the sample holders for the XCT. Aluminum phantoms, ∼0.2 mm in diameter, were adhered to the surface of the tooth adjacent to the region of interest using epoxy resin. The phantoms provide a reference point on the sample during image processing.

Tooth brushing was performed using a powered sonic toothbrush (Philips Sonicare Easyclean, Philips, USA) and a toothpaste slurry with a ratio of 1:3 toothpaste (Sensodyne Daily Care, GSK, UK) to water. The toothbrush was secured on a ring stand and static weights were attached to the main handle of the toothbrush. The force applied to the tooth through the toothbrush head was 2.8 N. The toothbrush head was immersed in the toothpaste slurry then attached to the toothbrush prior to brushing. Brushing consisted of contacting the long length of the tooth approximately at the gum-line position and activating the toothbrush. The experimental setup for tooth brushing is shown in **Figure 1**. Using this region of interested ensured that both enamel, present at the surface of the tooth above the gum-line, and dentin, present at the surface of the tooth below the gum-line, were examined in this work to explore differences in their response to the brushing. Each tooth was brushed at 2 min time intervals for up to 20 min, with the tooth rinsed using deionized water, dried using laboratory wipes and imaged prior to the subsequent brushing interval. A total of three teeth were imaged and exposed to the tooth brushing cycles.

XCT was conducted using an x-ray microscope (Versa 510, Carl Zeiss, USA/EU) operating at a voltage of 50 kV with a power of 4 W and a Zeiss LE2 filter positioned directly after the x-ray source to filter the x-ray spectrum. One thousand and six hundred and one projections were collected over 360°at an interval of 0.22° with an isotropic voxel size of 3 μm for each tomography reconstruction. An exposure time of 5–6 s was used for each projection. The exposure time was selected individually for each sample and maintained throughout the study. Two initial scans were conducted for each sample; between the initial scans no changes were made to the experimental equipment or the position of the sample. The projections were reconstructed

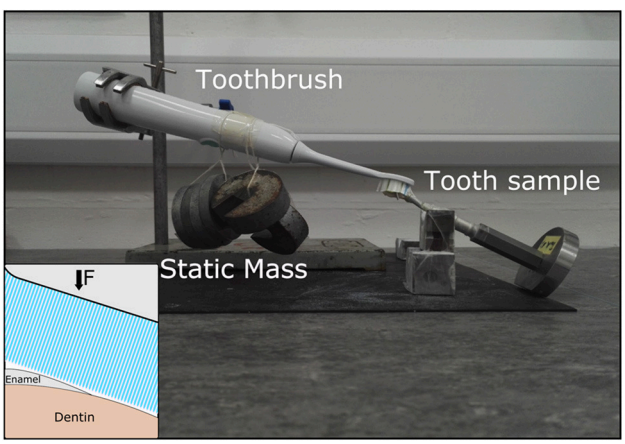

FIGURE 1 | Optical image of the *ex situ* brushing set up. Static weights are applied to the central portion of the electric toothbrush. The tooth sample is mounted in the XCT sample holder and stabilized by a steel v-block. A schematic of the brushing location is shown in the bottom left hand corner of the image.

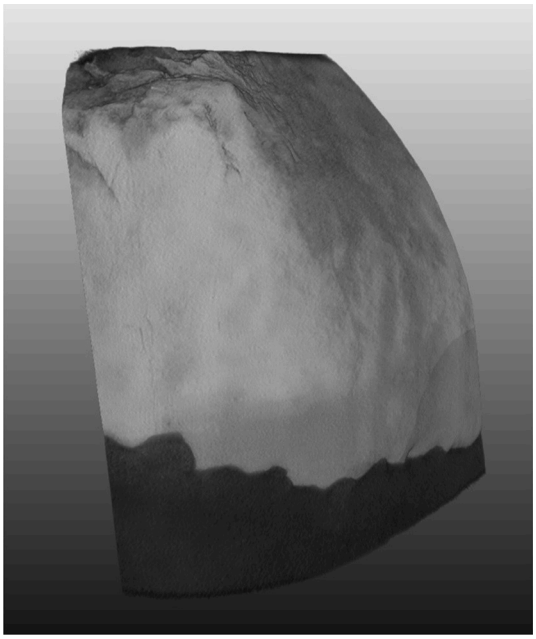

FIGURE 2 | 3D volume rendering of the scanned region of the tooth. A greyscale lookup table is applied to the rendering, showing the enamel in the lighter coloration and the dentin the darker coloration.

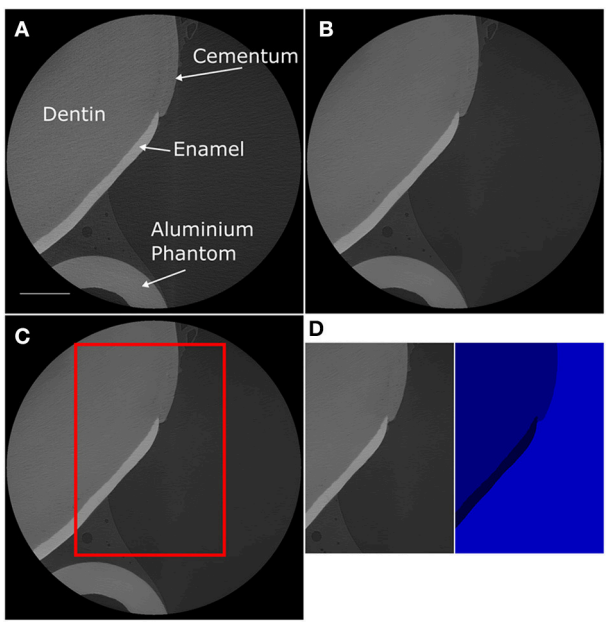

FIGURE 3 | 2D virtual slices of the 3D tomography data captured via XCT. **(A)** Initial reconstructed slice. **(B)** Reconstructed slice following application of a NLM denoising filter. **(C)** The red box highlights the ROI selected for calculating the volume of enamel and dentin. **(D)** The selected region of interest and the resulting segmented data.

using software incorporating a filtered back projection algorithm (Scout and Scan, Carl Zeiss, USA/EU). For each dataset the center shift was manually found, the standard beam hardening correction was applied with a value of 0.2–0.7 depending on the specific sample and a smoothing correction of 0.5–0.7 used. The beam hardening and smoothing corrections were kept constant for each individual sample.

The reconstructed datasets were filtered using a non-local means denoising filter in ImageJ (NIST, USA) (Darbon et al., 2008; Buades et al., 2011). The filtered datasets were registered to the initial scans using the manual rigid registration module in MeVisLab (MeVis Medical Solutions AG, DE). The aluminum phantoms were used as key features for the registration process. Registration of the datasets ensured that the center of each scan was aligned and a consistent region of interest (ROI) could be selected from each dataset.

The specific ROI from each dataset were segmented through pixel classification using the ilastik software (Sommer et al., 2011). Pixel classification was carried out using 15 features: Gaussian Smoothing ($\sigma = 0.3$ px-3.5 px), Laplacian of Gaussian ($\sigma = 0.7$ px-5.0 px), Structure Tensor Eigenvalues ($\sigma = 0.7$ px-5.0 px). Each dataset was segmented individually using three labels. The labels were selected to represent the enamel, dentin, and air present in the images. Each label is represented by a single color value within the segmented data, resulting in a dataset containing only three pixel color values. The volume

TABLE 1 | List of the volumetric data calculated from the XCT images captured for each tooth sample over 10 brushing time points.

ROI volume (μm^3)		Enamel			Cementum/Dentin		
		Measured volume (μm^3)	Difference in volume (μm^3)	Normalized volume change	Measured volume (μm^3)	Difference in volume (μm^3)	Normalized volume change
TOOTH 1							
4.51E+09							
	Initial Scan 1	306979362			2421110331		
	Initial Scan 2	307444059	464697	0.000103	2435130783	14020452	0.003108
Cumulative brushing time	2 min	308825676	1846314	0.0004093	2481981615	60871284	0.013495
	4 min	308805615	1826253	0.0004049	2377530333	−4.4E + 07	−0.00966
	6 min	310667373	3688011	0.0008176	2393336754	−2.8E + 07	−0.00616
	8 min	315229644	8250282	0.0018291	2385672966	−3.5E + 07	−0.00786
	10 min	307217502	238140	5.279E−05	2396889441	−2.4E + 07	−0.00537
	14 min	305646561	−1332801	−0.000295	2351522961	−7E + 07	−0.01543
	20 min	305596908	−1382454	−0.000306	2333317104	−8.8E + 07	−0.01946
TOOTH 2							
2.8E+09							
	Initial Scan 1	107233713			1078093422		
	Initial Scan 2	108846234	1612521	0.0005759	1080123147	2029725	0.000725
Cumulative brushing time	2 min	105393798	−1839915	−0.000657	1078893108	799686	0.000286
	4 min	106819560	−414153	−0.000148	1081021086	2927664	0.001046
	6 min	106619112	−614601	−0.000219	1077492132	−601290	−0.00021
	8 min	106163676	−1070037	−0.000382	1060871580	−1.7E + 07	−0.00615
	10 min	107536059	302346	0.000108	1063602441	−1.4E + 07	−0.00517
	14 min	105769989	−1463724	−0.000523	1043337699	−3.5E + 07	−0.01241
	20 min	106732134	−501579	−0.000179	1039972338	−3.8E + 07	−0.01361
TOOTH 3							
1.23E+09							
	Initial Scan 1	67284702			569502549		
	Initial Scan 2	67524327	239625	0.0001942	570971349	1468800	0.001191
Cumulative brushing time	2 min	67395834	111132	9.008*E*-05	566421471	−3081078	−0.0025
	4 min	67446675	161973	0.0001313	567022788	−2479761	−0.00201
	6 min	66814065	−470637	−0.000381	560944764	−8557785	−0.00694
	8 min	66461310	−823392	−0.000667	559115568	−1E + 07	−0.00842
	10 min	66894903	−389799	−0.000316	558533475	−1.1E + 07	−0.00889
	14 min	66791817	−492885	−0.0004	557282754	−1.2E + 07	−0.0099
	20 min	66694806	−589896	−0.000478	554612157	−1.5E + 07	−0.01207

The corresponding difference in volume is calculated as the volume measured in the initial scan 1 subtracted from the measured volume of the time step.

of each label was calculated by counting the number of pixels for each specific color within each slice of the ROI. The total number of pixels for each color within a dataset were counted using a custom python script. The volume was then calculated by multiplying the number of pixels by the voxel size of the images.

RESULTS

Porcine teeth were successfully imaged using XCT, focusing mainly on the region of the tooth surface that transitions from enamel to dentin. **Figure 2** shows the 3D rendered volume of an imaged tooth and highlights the presence of both the enamel and the dentin within the imaged volume. A plane section of the imaged volume is shown in **Figure 3**, where the enamel and dentin can be distinguished clearly. **Figure 3A** also highlights the cementum at the surface of the tooth, which is indicated by the change in the image morphology. The interface between the cementum and dentin is not clear from the XCT images, but was confirmed using light microscopy (**Supplementary Figure 1**). The light microscopy images indicated that the cementum in these samples connects directly to the enamel and there is no overlap of the two layers. The artifacts present within **Figure 3** are likely caused by the presence of the aluminum phantom adhered to the tooth surface. **Figure 3** shows the plane section that has been produced using a non-local means denoising filter and indicates that the filter has reduced the overall noise while maintaining the features of the sample.

The filtered image datasets were segmented to accurately distinguish between the enamel, dentin and air in order to quantify the volume of each phase present. The volume of the enamel and dentin present within each sample at each time point is recorded in **Table 1**. The table also displays the volume data for the initial repeat scans. **Table 1** shows the change in volume at each time point against the initial reference scan, labeled initial scan 1, which shows an increase in the volume lost in both the enamel and dentin over the course of the total brushing time. The size of the ROI varies for each sample, therefore to draw comparisons between each samples the data is normalized against the total measured volume of the ROI in the initial scan. The total volume of the ROI and the normalized volume at each time point are displayed in **Table 1**. The average change in the volume of each phase as a function of the applied brushing time can therefore be observed and is plotted in **Figure 4**. A linear regression fit to the data to describe the rate of volume loss within each phase was made.

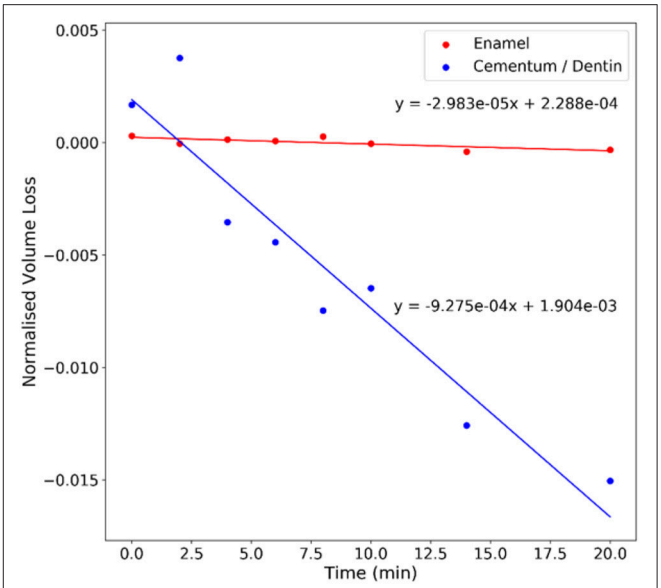

FIGURE 4 | Plot of the average normalized changes in volume for the enamel and cementum/dentin vs. the cumulative brushing time (in minutes).

DISCUSSION

In the XCT images the cementum at the surface of the tooth can be identified but the interface between the cementum and the dentin cannot be consistently differentiated. The lack of contrast between the cementum and dentin is likely due to the similiarity of mineral concentration for each material. Dentin has ∼60% hydroxyapatite, where cementum has between 45 and 50% (Ho et al., 2004; Srivicharnkul et al., 2005; Goldberg, 2011; Yamaguchi et al., 2016) The high mineral content of the enamel, over 90% (Habelitz et al., 2001; Goldberg et al., 2014; Yilmaz and Schneider, 2016), results in significant contrast to the cementum and dentin. Therefore, it is not possible to indicate when the abrasive behavior of the tooth brushing has completely removed the cementum and then begun to remove the underlying dentin. The removal of the cementum from the tooth surface exposes the dentin and the openings of the dentin tubules, which has been shown to lead to hypersensitivity (Addy and Hunter, 2003; Arnold et al., 2016). As a result of this, the discussion here considers the dentin and cementum as one material component of the tooth and the enamel as another.

The plots in **Figure 4** indicate a substantial increase in the volume of the cementum/dentin lost when compared to the enamel. This difference in rate of volume loss was expected as the enamel has greater mechanical properties and is a biological structure that is designed to withstand long term exposure to wear forces. An initial increase in the normalized volume changes in both the enamel and dentin is noted and is expected to be due to initial deposition of material or redeposition of loose material within the ROI, which is absent as removal of the tooth material becomes active.

The increased wear resistance observed in the enamel is consistent with the literature, where brushing of enamel produces minimal volume loss when compared to the dentin and also holds for acid softened/eroded dentin and enamel (Wiegand et al., 2007, 2013). The consistency with previous work can be evaluated by comparing the ratio of the rate of dentin volume loss to rate of enamel volume loss. Wiegand et al. showed, using profilometry, that brushing of enamel and dentin with powered sonic toothbrushes resulted in an average dentin to enamel volume loss ratio of 12.6:1 (Wiegand et al., 2013). The data we

present here indicates an average cementum/dentin to enamel volume loss ratio of 35.48:1, which indicates a more rapid volume loss compared to the literature. The ratio was calculated using the slope from the linear regression of the volume loss vs. time data for each sample. This increase in the ratio appears to be related to the applied force during brushing, where increasing the applied force by a factor of three increased the ratio of volume loss by a similar factor. The force applied in this work was ∼2.8 N, while Wiegand et al. applied 0.9 N with the sonic toothbrush (Wiegand et al., 2013). The increase of the ratio with force indicates that the increase in cementum/dentin volume loss observed here is not dependent on the material properties, and is potentially related to the experimental methodology. The work presented by Wiegand et al. used controlled sample geometry, whereas in this work a geometry more representative of *in vivo* brushing was employed to take advantage of the XCT imaging capabilities. The irregular geometry used in this work may lead to increased contact stresses arising at the surface during brushing that may not be observed using polished blocks used for profilometric studies. In addition, the sample preparation techniques employed in other works, namely mechanical surface polishing, may preferentially remove weakly bound or damaged material prior to the wear testing. Specifically, the polishing in Wiegand et al. removed 200 μm from the surface of the enamel and dentin block faces (Wiegand et al., 2013), thus potentially removing weaker material, and the cementum, that could be lost more easily due to brushing. Polishing is also expected to defects from the surface that act as initiation sites for damage or volume removal. Future work should therefore examine the interaction of the toothbrush head with the dentin and enamel surfaces using *in situ* XCT to provide better insight into how the contact stresses are being applied to an irregular tooth surface.

SUMMARY

The volume change of teeth following *ex situ* tooth brushing was successfully measured using XCT to observe the wear characteristics of teeth. The rate of volume loss for enamel was observed to be lower than that of the cementum/dentin within these teeth samples, consistent with the literature of brushing performed on dental material. Specifically, the rate of volume loss of cementum/dentin was found to be over 30 times higher than for enamel. The methodology for experimentally measuring the volume loss using x-ray imaging and corresponding image analyses provide robust approaches for assessing a wide range of brushing interactions with teeth in relevant 3-dimensional space.

ETHICS STATEMENT

All porcine material was obtained from a local butcher. Ethics approval was not required as per the University of Portsmouth's guidelines and national regulations.

AUTHOR CONTRIBUTIONS

AK, AB, and SK devised the experiments. AK carried out the experimental work. Data analysis was carried out by AK, AB, and SK. All authors contributed to the writing of the manuscript.

FUNDING

The work was supported by the GSK grant Multiscale imaging and mechanical evaluation of biomaterials in the oral cavity.

SUPPLEMENTARY MATERIAL

The Supplementary Material for this article can be found online at: https://www.frontiersin.org/articles/10.3389/fmech.2018.00012/full#supplementary-material

Supplementary Figure 1 | Light microscopy image of the cross section of a porcine tooth used in this study. The image shows the presence of the enamel, dentin, cementum and cementoenamel junction. Scale bar is 0.1 mm.

REFERENCES

Addy, M., and Hunter, M. L. (2003). Can tooth brushing damage your health? Effects on oral and dental tissues. *Int. Dent. J.* 53, 177–186. doi: 10.1111/j.1875-595X.2003.tb00768.x

Arambawatta, K., Peiris, R., and Nanayakkara, D. (2009). Morphology of the cemento-enamel junction in premolar teeth. *J. Oral Sci.* 51, 623–627. doi: 10.2334/josnusd.51.623

Arnold, W. H., Gröger, C., Bizhang, M., and Naumova, E. A. (2016). Dentin abrasivity of various desensitizing toothpastes. *Head Face Med.* 12:16. doi: 10.1186/s13005-016-0113-1

Attin, T., Koidl, U., Buchalla, W., Schaller, H. G., Kielbassa, A. M., and Hellwig, E. (1997). Correlation of microhardness and wear in differently eroded bovine dental enamel. *Arch. Oral Biol.* 42, 243–250. doi: 10.1016/0003-9969(06)00073-2

Bertassoni, L. E., Habelitz, S., Pugach, M., Soares, P. C., Marshall, J., William, G., et al. (2011). Following remineralization of dentin. *Scanning* 32, 312–319. doi: 10.1002/sca.20199

Bizhang, M., Riemer, K., Arnold, W. H., Domin, J., and Zimmer, S. (2016). Influence of bristle stiffness of manual toothbrushes on eroded and sound human dentin - an *in vitro* study. *PLoS ONE* 11:e0153250. doi: 10.1371/journal.pone.0153250

Bosshardt, D. D., and Selvig, K. A. (1997). Dental cementum: the dynamic tissue covering of the root. *Periodontol. 2000* 13, 41–75. doi: 10.1111/j.1600-0757.1997.tb00095.x

Buades, A., Coll, B., and Morel, J. (2011). Non-local means denoising. *Image Process. Line* 1, 208–212. doi: 10.5201/ipol.2011.bcm_nlm

Cuy, J. L., Mann, A. B., Livi, K. J., Teaford, M. F., and Weihs, T. P. (2002). Nanoindentation mapping of the mechanical properties of human molar tooth enamel. *Arch. Oral Biol.* 47, 281–291. doi: 10.1016/S0003-9969(02)00006-7

Darbon, J., Cunha, A., Chan, T. F., Osher, S., and Jensen, G. J. (2008). "Fast nonlocal filtering applied to electron cryomicroscopy," in *2008 5th IEEE International Symposium on Biomedical Imaging: From Nano to Macro, Proceedings, ISBI* (Paris), 1331–1334. doi: 10.1109/ISBI.2008.4541250

Dyer, D., Addy, M., and Newcombe, R. G. (2000). Studies *in vitro* of abrasion by different manual toothbrush heads and a standard toothpaste. *J. Clin. Periodontol.* 27, 99–103. doi: 10.1034/j.1600-051x.2000.027002099.x

Fincham, A. G., Moradian-Oldak, J., and Simmer, J. P. (1999). The structural biology of the developing dental enamel matrix. *J. Struct. Biol.* 126, 270–299. doi: 10.1006/jsbi.1999.4130

Fong, H., Sarikaya, M., White, S. N., and Snead, M. L. (2000). Nano-mechanical properties profiles across dentin–enamel junction of human incisor teeth. *Mater. Sci. Eng. C* 7, 119–128. doi: 10.1016/S0928-4931(99)00133-2

Fratzl, P. (ed.) (2008). *Collagen: Structure and Mechanics*. Boston, MA: Springer US. doi: 10.1007/978-0-387-73906-9

Ganss, C., Schlueter, N., Preiss, S., and Klimek, J. (2009). Tooth brushing habits in uninstructed adults - Frequency, technique, duration and force. *Clin. Oral Investig.* 13, 203–208. doi: 10.1007/s00784-008-0230-8

Goldberg, M. (2011). Dentin structure composition and mineralization. *Front. Biosci.* E3:281. doi: 10.2741/e281

Goldberg, M., Kellermann, O., Dimitrova-Nakov, S., Harichane, Y., and Baudry, A. (2014). Comparative studies between mice molars and incisors are required to draw an overview of enamel structural complexity. *Front. Physiol.* 5:359. doi: 10.3389/fphys.2014.00359

Habelitz, S., Marshall, S., Marshall, G., and Balooch, M. (2001). Mechanical properties of human dental enamel on the nanometre scale. *Arch. Oral Biol.* 46, 173–183. doi: 10.1016/S0003-9969(00)00089-3

Hicks, J., Garcia-Godoy, F., and Flaitz, C. (2003). Biological factors in dental caries: role of saliva and dental plaque in the dynamic process of demineralization and remineralization (part 1). *J. Clin. Pediatr. Dent.* 28, 47–52. doi: 10.17796/jcpd.28.1.yg6m443046k50u20

Ho, S. P., Balooch, M., Goodis, H. E., Marshall, G. W., and Marshall, S. J. (2004). Ultrastructure and nanomechanical properties of cementum dentin junction. *J. Biomed. Mater. Res.* 68A, 343–351. doi: 10.1002/jbm.a.20061

Ho, S. P., Senkyrikova, P., Marshall, G. W., Yun, W., Wang, Y., Karan, K., et al. (2009). Structure, chemical composition and mechanical properties of coronal cementum in human deciduous molars. *Dent. Mater.* 25, 1195–1204. doi: 10.1016/j.dental.2009.04.005

Hooper, S., West, N. X., Pickles, M. J., Joiner, A., Newcombe, R. G., and Addy, M. (2003). Investigation of erosion and abrasion on enamel and dentine: a model *in situ* using toothpastes of different abrasivity. *J. Clin. Periodontol.* 30, 802–808. doi: 10.1034/j.1600-051X.2003.00367.x

Imbeni, V., Kruzic, J. J., Marshall, G. W., Marshall, S. J., and Ritchie, R. O. (2005). The dentin-enamel junction and the fracture of human teeth. *Nat. Mater.* 4, 229–232. doi: 10.1038/0nmat1323

Inoue, T., Saito, M., Yamamoto, M., Debari, K., Kou, K., and Nishimura, F. (2009). Comparison of nanohardness between coronal and radicular intertubular dentin *Dent. Mater. J.* 28, 295–300. doi: 10.4012/dmj.28.295

Jud, C., Schaff, F., Zanette, I., Wolf, J., Fehringer, A., and Pfeiffer, F. (2015). Dentinal tubules revealed with X-ray tensor tomography. *Dent. Mater.* 32, 1189–1195. doi: 10.1016/j.dental.2016.06.021

Kielbassa, A. M., Gillmann, L., Zantner, C., Meyer-Lueckel, H., Hellwig, E., and Schulte-Mönting, J. (2005). Profilometric and microradiographic studies on the effects of toothpaste and acidic gel abrasivity on sound and demineralized bovine dental enamel. *Caries Res.* 39, 380–386. doi: 10.1159/000086844

Kinney, J. H., Marshall, S. J., and Marshall, G. W. (2003). The mechanical properties of human dentin: a critical review and re-evaluation of the dental literature. *Crit. Rev. Oral Biol. Med.* 14, 13–29. doi: 10.1177/154411130301400103

Kofmehl, L., Schulz, G., Deyhle, H., Filippi, A., Hotz, G., Berndt-Dagassan, D., et al. (2010). Computed tomography to quantify tooth abrasion. *Proc. SPIE* 7804, 1–10. doi: 10.1117/12.859278

Lima, J. P. M., Melo, M. A. S., Passos, V. F., Braga, C. L. N., Rodrigues, L. K. A., and Santiago, S. L. (2013). Dentin erosion by whitening mouthwash associated to toothbrushing abrasion: a focus variation 3D scanning microscopy study. *Microsc. Res. Tech.* 76, 904–908. doi: 10.1002/jemt.22246

Low, I. M. (2004). Depth-profiling of crystal structure, texture, and microhardness in a functionally graded tooth enamel. *J. Am. Ceram. Soc.* 87, 2125–2131. doi: 10.1111/j.1151-2916.2004.tb06369.x

Marshall, G. W., Balooch, M., Gallagher, R. R., Gansky, S. A., and Marshall, S. J. (2001). Mechanical properties of the dentinoenamel junction: AFM studies of nanohardness, elastic modulus, and fracture. *J. Biomed. Mater. Res.* 54, 87–95. doi: 10.1002/1097-4636(200101)54:1<87::AID-JBM10>3.0.CO;2-Z

Marshall, S. J., Balooch, M., Habelitz, S., Balooch, G., Gallagher, R., and Marshall, G. W. (2003). The dentin - enamel junction - a natural, multilevel interface. *J. Eur. Ceram. Soc.* 23, 2897–2904. doi: 10.1016/S0955-2219(03)00301-7

Montoya, C., Arola, D., and Ossa, E. A. (2016). Importance of tubule density to the fracture toughness of dentin. *Arch. Oral Biol.* 67, 9–14. doi: 10.1016/j.archoralbio.2016.03.003

Nanci, A. (2014). *Ten Cate's Oral Histology - E-Book: Development, Structure, and Function*. Elsevier Health Sciences. Available online at: https://books.google.co.uk/books?id=I8fsAwAAQBAJ

Sommer, C., Straehle, C., Kothe, U., and Hamprecht, F. A. (2011). "Ilastik: interactive learning and segmentation toolkit," in *Proceedings - IEEE International Symposium on Biomedical Imaging* (Chicago, IL), 230–233. doi: 10.1109/ISBI.2011.5872394

Srivicharnkul, P., Kharbanda, O. P., Swain, M. V., Petocz, P., and Darendeliler, M. A. (2005). Physical properties of root cementum: part 3. Hardness and elastic modulus after application of light and heavy forces. *Am. J. Orthod. Dentofac. Orthop.* 127, 168–176. doi: 10.1016/j.ajodo.2003.12.021

Sui, T., Sandholzer, M. A., Le Bourhis, E., Baimpas, N., Landini, G., and Korsunsky, A. M. (2014). Structure-mechanical function relations at nano-scale in heat-affected human dental tissue. *J. Mech. Behav. Biomed. Mater.* 32, 112–124. doi: 10.1016/j.jmbbm.2013.12.014

Tellefsen, G., Liljeborg, A., Johannsen, A., and Johannsen, G. (2011). The role of the toothbrush in the abrasion process. *Int. J. Dent. Hyg.* 9, 284–290. doi: 10.1111/j.1601-5037.2011.00505.x

Wiegand, A., Burkhard, J. P. M., Eggmann, F., and Attin, T. (2013). Brushing force of manual and sonic toothbrushes affects dental hard tissue abrasion. *Clin. Oral Investig.* 17, 815–822. doi: 10.1007/s00784-012-0788-z

Wiegand, A., Köwing, L., and Attin, T. (2007). Impact of brushing force on abrasion of acid-softened and sound enamel. *Arch. Oral Biol.* 52, 1043–1047. doi: 10.1016/j.archoralbio.2007.06.004

Yamaguchi, M., Yao-Umezawa, E., Tanimoto, Y., Shimizu, M., Kikuta, J., Hikida, T., et al. (2016). Individual variations in the hardness and elastic modulus of the human cementum. *J. Hard Tissue Biol.* 25, 345–350. doi: 10.2485/jhtb.25.345

Yilmaz, E. D., and Schneider, G. A. (2016). Mechanical behavior of enamel rods under micro-compression. *J. Mech. Behav. Biomed. Mater.* 63, 183–194. doi: 10.1016/j.jmbbm.2016.06.017

Zaslansky, P., Friesem, A. A., and Weiner, S. (2006). Structure and mechanical properties of the soft zone separating bulk dentin and enamel in crowns of human teeth: insight into tooth function. *J. Struct. Biol.* 153, 188–199. doi: 10.1016/j.jsb.2005.10.010

Conflict of Interest Statement: The authors declare that the research was conducted in the absence of any commercial or financial relationships that could be construed as a potential conflict of interest.

frontiers in Materials

ORIGINAL RESEARCH
published: 05 June 2018
doi: 10.3389/fmats.2018.00032

An Automated Step-Wise Micro-Compression Device for 3D Dynamic Image-Guided Failure Assessment of Bone Tissue on a Microstructural Level Using Time-Lapsed Tomography

*Alina Levchuk, Philipp Schneider, Matias Meier, Peter Vogel, Finn Donaldson and Ralph Müller**

Department of Health Sciences and Technology, Institute for Biomechanics, ETH Zürich, Zürich, Switzerland

OPEN ACCESS

Edited by:
Gianluca Tozzi,
University of Portsmouth,
United Kingdom

Reviewed by:
Andrew Anthony Pitsillides,
Royal Veterinary College,
United Kingdom
Andrew J. Bodey,
Diamond Light Source,
United Kingdom

***Correspondence:**
Ralph Müller
ram@ethz.ch

Specialty section:
This article was submitted to Mechanics of Materials, a section of the journal Frontiers in Materials

Received: *09 November 2017*
Accepted: *15 May 2018*
Published: *05 June 2018*

Citation:
Levchuk A, Schneider P, Meier M, Vogel P, Donaldson F and Müller R (2018) An Automated Step-Wise Micro-Compression Device for 3D Dynamic Image-Guided Failure Assessment of Bone Tissue on a Microstructural Level Using Time-Lapsed Tomography. Front. Mater. 5:32. doi: 10.3389/fmats.2018.00032

Microstructural bone phenotypes, such as the intracortical canal network, could be directly linked to the mechanical failure behavior of cortical bone tissue. In addition, high accumulation of microdamage can significantly increase bone brittleness and thus, is a precursor of mechanical failure. Here, we discuss the development and validation of an automated step-wise micro-compression device (MCD) for dynamic image-guided failure assessment (DIGFA) of intracortical bone microstructure and bone microdamage. The device was found to be highly accurate and precise with positioning errors of less than 1 μm and force errors of less than 1.25 N. In addition, the results of a first biological study using DIGFA and time-lapsed computed tomography are presented. In short, whole mouse femora from mature C57BL/6 (B6) and C3H/He (C3H) mice with mid-diaphyseal notches were tested in step-wise compression and concomitantly imaged until failure. DIGFA was performed at the TOMCAT beamline of the Swiss Light Source (SLS) using synchrotron radiation-based computed tomography (SR CT). Following the experiment, intracortical porosity was separated into the canal network, osteocyte lacunae, and microcracks for subsequent morphometric evaluation. The thicker cortex of C3H was penetrated by a dense canal network, whereas in B6 only a few scattered canals were observed. For B6, the first occurrence of crack was noted at 1.45% local strain, while for C3H, crack initiation took place only at 2.66% local strain. In addition, we were able to relate whole bone mechanics to local failure events by deriving correlations between microstructural porosity and microdamage propagation. In conclusion, initiation and accumulation of microcracks were investigated for two mouse phenotypes demonstrating that DIGFA in combination with SR CT is a suitable technique for time-lapsed three-dimensional assessment of bone morphology and bone fracture behavior down to the cellular level.

Keywords: bone, microstructure, synchrotron radiation-based computed tomography, dynamic image-guided failure assessment, step-wise micro-compression, microdamage

INTRODUCTION

Bone is a hierarchical composite material whose mechanical properties highly depend on the structural and material organization (Cowin, 2001). The material properties of bone can be largely attributed to its composition, and define the types of loading it experiences (Carter and Spengler, 1978). On the other hand, structural properties of the tissue stem directly from the architectural arrangement of the material, and differ across bone types, species, and hierarchical level under investigation (Goulet et al., 1994; Rho et al., 1998). These properties define the amount of loading bone can withstand before fracture (Turner, 2006; Currey, 2012).

Regarding the bone structure on the tissue level, it is the trabecular and cortical bone which deserve attention. Trabecular bone consists of an intertwined network of rod- and strut-shaped trabeculae, and provides large porous spaces for marrow encapsulation (Wehrli, 2007). Cortical bone is a major load-bearing and protective structure of the body. It is particularly resistive to compressive deformations, while it remains relatively weak in tension (Reilly and Burstein, 1975). Furthermore, the influence of microstructural porosity on the mechanical properties of bone has been widely established (Currey, 1988; Mccalden et al., 1993). Intracortical canals and osteocyte lacunae have been shown to play an important role in the mechanical properties of cortical bone (Schneider et al., 2013) and therefore its ability to resist fracture. With respect to the material properties, microdamage has been identified to be an important determinant for bone mechanics (Donahue and Galley, 2006). Several studies attempted to describe and quantify the relationship between bone microstructure and the behavior of microdamage in bone (Voide et al., 2009, 2011). Small amounts of microdamage in bone were shown to lead to large reductions in bone strength and stiffness (Hernandez et al., 2014). However, so far we still lack information about the location of accumulated microdamage and the specific future fracture of bones. Until recently, this link between bone structure and function was lacking temporal resolution, which is necessary for the investigation of the dynamic process of bone fracture.

The visualization of bone microdamage initiation and propagation has been steadily advancing from two dimensional (2D) imaging methods, such as histology and microscopy (Burr et al., 1985, 1998; Choi and Goldstein, 1992; Diab and Vashishth, 2005), to three-dimensional (3D) techniques, such as confocal microscopy (Fazzalari et al., 1998; Reilly, 2000) and micro-computed tomography (μCT) (Nalla et al., 2004; Voide et al., 2008a; Larrue et al., 2011; Palanca et al., 2017). For high-resolution 3D imaging in the sub-micrometer domain synchrotron radiation-based computed tomography (SR CT) has been gaining popularity (Schneider et al., 2007; Cooper et al., 2011; Pacureanu et al., 2012; Tommasini et al., 2012; Dong et al., 2014). SR CT provides isotropic spatial resolution of 1 μm or better (Stampanoni et al., 2007), which allows differentiation of separate components of intracortical bone microstructure. Combined with mechanical testing, this method can facilitate the assessment of the role of bone porosity in the failure behavior of the tissue. This application, also referred to as functional or biomechanical imaging (Voide et al., 2008d), enables tomographic visualization of the sample following each loading step, and provides direct time-lapsed imaging of the bone tissue's load response. Several *in situ* testing systems of various degrees of automation and sophistication have been introduced to facilitate image-guided failure assessment (IGFA) in conjunction with μCT and SR CT (Müller et al., 1998; Bleuet et al., 2004; Nazarian and Müller, 2004; Thurner et al., 2006; Voide et al., 2009; Jang et al., 2014; Evans et al., 2017). However, so far the loading devices have either required manual operation (Voide et al., 2009), or were limited by their geometric arrangements (Bleuet et al., 2004; Thurner et al., 2006) or mechanical capabilities (Müller et al., 1998; Nazarian and Müller, 2004). In addition, only one of the loading devices listed above has been validated for precision and accuracy (Nazarian and Müller, 2004).

Therefore, taking into account the potential of IGFA to assess the dynamic failure process, the first goal of this study was to design and build an automated and thus, user-independent step-wise micro-compression device (MCD), which would allow functional imaging of the dynamic processes in bone, i.e., dynamic IGFA (DIGFA). The second goal was to perform a verification study for the precision and accuracy of the mechanical components, which provides a protocol for calibration of the MCD. Finally, as a third goal, the device was tested for sensitivity within a first biological study, in which microdamage initiation and propagation within cortical bone of a mouse model was examined by DIGFA using the new MCD.

MATERIALS AND METHODS

Design and Construction of the Micro-Compression Device (MCD)

The first objective of this study was to design and build a MCD for DIGFA (Schneider and Müller, 2010) for whole rodent bones and sections of human trabecular or cortical bone, which is compatible with SR CT imaging setups. Consequently, as the primary use of the MCD is as *in situ* rig at beamlines of SR facilities that offer experimental stations for tomographic imaging, it must be compact and mobile as well as easy and quick to build up and disassemble for transport. Therefore, the design requirements identified were low weight and height, simplicity of installation, and ease of individual component replacement. Low weight and height are important factors to guarantee proper operation of the motors driving the rotation stage for high-resolution CT and to avoid precession of the rotation axis, respectively. Thus, the weight limit for the MCD excluding the control system was set to 5 kg, and the height had to be kept to the minimum. The requirements for the motor and load cell were based on the mechanical properties of the expected specimens (whole rodent bones and sections of human trabecular or cortical bone). The components had to be able to both exert and detect forces of at least 500 N, and the motor and load cell selection had to favor highest resolution and accuracy for biomechanical imaging of bone tissue failure at a microstructural level. In order to facilitate (absorption-based) SR CT imaging, the design at the

sample height had to be X-ray transparent and small in diameter for minimal sample-to-detector distance, to reduce absorption by the MCD and to minimize the influence of edge enhancement due to the coherent nature of SR light, respectively. The control system of the designed MCD had to be digitally synchronized with the controls for SR CT imaging at the TOMCAT beamline (Stampanoni et al., 2007) of the Swiss Light Source (SLS) to allow step-wise and user-independent loading and intermittent tomographic scanning of the dynamic failure process within the bone tissue. Finally, the system had to facilitate real-time output of the mechanical data for experimental monitoring, as well as produce comprehensive log files upon the completion of the experiment.

The key element of the developed MCD (**Figure 1**) is a compact linear stepper motor, which serves as linear actuator (NA23C60; Zaber Technologies Inc., Vancouver, Canada), with a travel range of 60 mm, maximum force of 800 N, and spatial resolution of 0.2 μm. Attached to the motor shaft is a subminiature load cell (Model 11; Honeywell Sensing & Control, Columbus, OH, USA), which operates both in tension and compression, sustaining forces up to 1,250 N with a reproducibility of 99.9% or a precision of 1.25 N as reported by the manufacturer. The top part of the MCD ends with a stainless steel ball-point tip attached to the motor plunger, which is put into contact with a stainless steel loading plate on top of the tested sample. The ball bearing between the plunger and the sample ensures axial loading (no shearing). The sample holder base of the bottom part of the MCD was manufactured out of polyoxymethylene (POM), whereas the smaller inner cylinder of the sample holder (inner Ø = 7 mm, wall thickness = 0.5 mm, height = 30 mm) and the larger load-bearing outer cylinder (inner Ø = 36 mm, wall thickness = 1 mm, height = 190 mm) were manufactured out of custom-made glass-free carbon fiber reinforced plastic (CFRP) (Suter Kunststoffe AG, Fraubrunnen, Switzerland). POM was chosen for its low mass, low friction, and wear resistance, as well as high stiffness, and very good dimensional stability. CFRP has been given preference because it is a light, but very strong composite material (stiffness > 100 GPa in the longitudinal direction, both in compression and tension). In addition, compared to mineralized bone tissue, both POM and glass-free CFRP are practically X-ray translucent at the X-ray energies used for (absorption-based) SR CT. This is an important factor for the quality of the CT reconstructions as it reduces typical cupping artifacts due to the local tomographic setup (Schneider et al., 2009), where the X-ray projection of the sample and the sample holder (specifically the outer CFRP cylinder) exceeds the field of view of the detector. Other off-the-shelf CFRPs have been tested, containing glass components, which are detrimental for X-ray imaging as they significantly absorb X-rays and are thus cannot be considered X-ray translucent. The exchangeable inner CFRP cylinder is designed to hold the sample, retain moisture, and any liquid required for the experiment. The outer CFRP cylinder counteracts the forces exerted by the actuator onto the sample stage, while mechanically protecting the load cell and the plunger during experimental testing. The dimension of the MCD is 65 × 65 × 335 mm and the overall weight is less than 2 kg. During experimental testing and imaging, the outer cylinder must be attached to the sample stage and the whole device has to be firmly fixed to the rotation stage of the CT setup at TOMCAT (**Figure 2**), also controlling sample alignment.

Data acquisition and system control have been managed using LabVIEW 8.1 (National Instruments, Austin, TX, USA), which allowed direct communication between the MCD and the beamline EPICS control channels via TCP/IP. In addition, an intuitive graphical user interface (GUI) was designed to guide users step-by-step during DIGFA.

A typical experimental protocol would begin with the initiation of the linear actuator and resetting of the load cell. A contact point with the sample will then be detected either manually by tracking X-ray projections on the CCD camera during plunger movement toward the sample, or by setting a predefined force limit during plunger approach. At the beginning of the test, a static pre-load step for sample stabilization or a cyclic pre-load for samples requiring pre-conditioning are available. Free parameters for an actual mechanical test is the force for pre-loading, rate of strain increase, sample size (for the strain calculation), number of total loading steps, as well as the relaxation time after each loading step. Once the DIGFA experiment is started, loading and CT scanning will be performed user-independently, in an automatic manner. The scan is initiated immediately after relaxation time. The experiment can be halted at any point, but will automatically terminate once the desired number of loading steps is carried out. The position and force data remain available through the entire test, starting with the initiation of the motor, where the sampling frequency for the mechanical data recording can be defined by the user. Finally, settings for mechanical tests and CT measurement are logged for use in future experiments.

Verification and Calibration of the Micro-Compression Device (MCD)

In the second aim, the functionality of the MCD for DIGFA was verified in its final assembly state. Due to possible non-linearities and setup-induced performance deviations, the load cell and the linear stepper motor were identified as critical components of the MCD. The following experimental and statistical measures were designed to verify and calibrate these mechanical constituents of the MCD.

All experiments were carried out on a Zwick/Roell material testing system (1456; Zwick/Roell AG, Ulm, Germany). The method of using servo-hydraulic devices for compression experiments and for calibration of external load cells has been previously established in several studies (Thurner et al., 2006; Voide et al., 2008d). Importantly, although the calibration protocols are similar across all devices, the non-continuous nature of previous experiments (Thurner et al., 2006; Voide et al., 2008d) introduces a delay of several minutes between the application of the load and the initiation of the scan, which in turn could allow for further stress propagation and consequent structural damage. At the same time, continuous load monitoring could provide valuable insights into tissue responses that occur between the load application and scanning, suggesting that

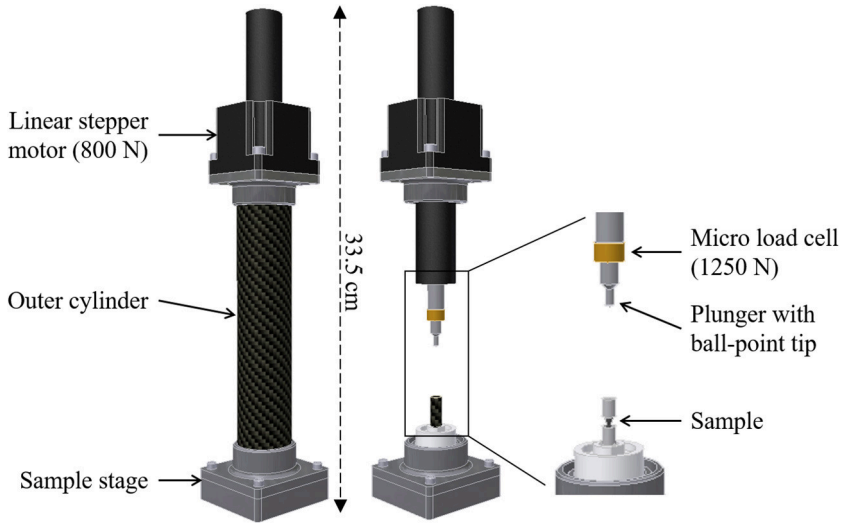

FIGURE 1 | Design of the micro-compression device (MCD) for dynamic image-guided failure assessment (DIGFA). **(Left)** Fully assembled state of the MCD. **(Right)** MCD view showing component assembly.

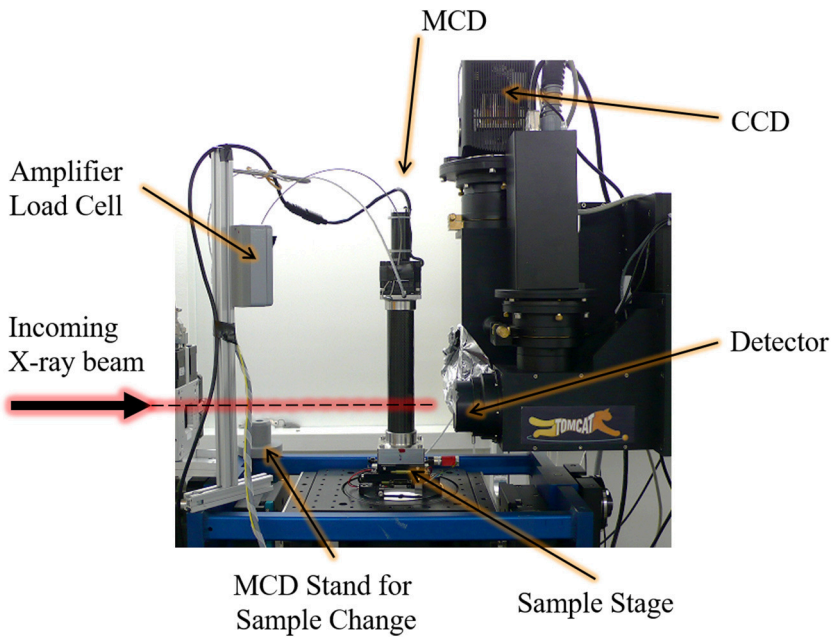

FIGURE 2 | Micro-compression device (MCD) for dynamic image-guided failure assessment (DIGFA) mounted at the TOMCAT beamline of the Swiss Light Source (SLS).

validated load cell function is of utmost importance in these types of experiments. In general, load cells of servo-hydraulic machines undergo routine calibrations by the manufacturer, thus guaranteeing the reliability of the measurement. Since the experiments with the MCD were planned for a wide range of loads, the calibration of the MCD was done on both macro and micro scales using two different calibrating load cells of the Zwick/Roell material testing system with a maximal load of 5 kN and 10 N, respectively. Calibration tests were done in compression, where a plastic stopper (FIBROFLEX® -Rundfeder, 80 Shore A (outer diameter = 20 mm, height = 16 mm); Brütsch/Rüegger Holding AG, Urdorf, Switzerland) was used to separate the MCD load cell from the compression plate, thus preventing damage to either component. An additional metal holder was manufactured to prevent slipping and sliding between the components of the setup. All tests ran according to a step-wise compression protocol provided in the Zwick/Roell software package. The number of steps, force increase per step, and

upper force limit varied depending on the range of the planned compression tests. The hold time was considered as an additional variable in the experiment. A single run was started with the pre-load application followed by gradual loading. After the test the setup was returned to the initial position, and reassembled prior to the next test. All tests were done by a single experimenter, and repeated five times for each loading protocol.

The MCD has been designed for small rodent and human bone samples with maximal dimensions of 20 mm in length and 6 mm in cross-section. Therefore, based on the size and estimated mechanical properties of the samples and the maximum attainable displacement resolution of the motor, the desired level of precision for the measurement was set to be 1 μm. A Mercury 2000 (MicroE systems, Bedford, MA, USA) smart encoder system using 18 mm long linear scale was chosen as a suitable measurement tool for the verification of plunger displacement, which also fitted the set precision requirement of 1 μm. The signal interpolation factor for the verification test using the smart encoder system was set to 200 steps, at which the system performs measurements with the precision of 0.10 μm, and with an interpolation accuracy of 0.12 μm or better. The encoder of the system was integrated into the MCD control software, where a separate graphical user interface for the calibration experiment was designed in Labview 8.1. The acquisition of the signals from the linear encoder and the load cell were triggered at the same time with the motor displacement, thus fully synchronizing the three measurement systems (stepper motor, MCD load cell, smart encoder system). In the calibration experiment, the MCD plunger was advanced against the stationary compressing plate of the Zwick/Roell machine, where the two systems were separated by the plastic stopper, as described beforehand. For the calibration tests, different factors influencing motor operation have been identified, including the amplitude of the reaction force, speed of displacement, level of plunger extension, and the direction of motion. The influence of the magnitude of the reaction force was simulated by applying and maintaining a pre-defined force with the Zwick/Roell compression plate, while advancing the MCD plunger to counteract the force. The other factors could be assessed by varying the settings in the control system of the MCD. Data acquisition was done in Labview 8.1, via a standalone program. The step number along with the voltage read-out from the MCD load cell were monitored continuously, at a sampling frequency of 1,000 Hz. All test runs were performed five times by a single investigator, and average values were used for the statistical evaluation.

Dynamic Image-Guided Failure Assessment (DIGFA) of Bone Tissue on Microstructural Level

The final objective of the study was to test the sensitivity of the MCD for biomechanical imaging, regarding visualization and quantification of intracortical microdamage initiation and propagation in a mouse model.

For DIGFA based on SR CT imaging, two different mouse strains have been used, C57BL/6 (B6) and C3H/He (C3H), representing low and high bone mass, respectively (Beamer et al., 1996; Turner et al., 2000). Femora from 16-week old mice were prepared as previously described (Voide et al., 2008b). In short, left femora were extracted and stored in 70% ethanol. The bones were embedded in polymethyl methacrylate cement (PMMA), leaving only 4 mm of the central femoral shaft exposed. POM cylinders (6 mm in diameter) were used to provide stability at the ends. In the next step, all samples were aligned similarly to a previously developed procedure (Voide et al., 2008c). A transverse notch, measuring 0.76 mm in depth and 0.89 mm in width was introduced in the mid-diaphyseal region to create an area of reduced strength, and to induce microdamage formation in this region (**Figure 3**). Cortical thickness in the mid-diaphysis was significantly different ($p < 0.001$) between B6 (Ct.Th = 0.17 ± 0.1 mm) and C3H (Ct.Th = 0.34 ± 0.1 mm). Nevertheless, the relative average cross sectional area removed by the defect was comparable in both mouse strains and accounted for 40 ± 5% in average cross-sectional area reduction (Voide et al., 2011). The defect created a weakened region in the cortical bone. A micro-finite element analysis of this loading model showed that, around the reduced cross-section, the strains were parallel to the loading direction and ranged between 0.11 and −1.56% when 1% overall compressive strain was applied (Voide et al., 2009). Before mechanical testing, all samples were rehydrated in phosphate buffered saline (PBS) for 24 h prior to the time-lapsed biomechanical imaging experiments at TOMCAT. During experimental testing and imaging, the samples were immersed in PBS to ensure proper hydration of the tissue. This study was carried out in accordance with the recommendations of and approved by the Kantonales Veterinäramt Zürich (Cantonal Veterinary Office, Zürich, Switzerland).

Axial compression tests of the embedded samples were carried out using the MCD. The apparent strains in the experiment are given with respect to the full length of the mouse femurs, typically 16–18 mm. All tests were performed until failure, at an interval of 0.05% strain/step and at a rate of 0.001% strain/second. Each compression step was followed by 5 min relaxation time at constant displacement, providing CT images without any visible movement artifacts. Subsequently, a tomographic scan was acquired within the femoral cortex at the height of the notch (**Figure 3**) using a 20X objective for optical magnification and including 2X binning on the detector to increase the signal-to-noise ratio, resulting in a voxel size of 740 nm. A total of 1501 projections at an individual exposure time of 150 ms were taken over a range of 180° in a step-and-go mode and at a photon energy of 17.5 keV. The projections have been flat field-corrected using five dark images (X-rays off) and five flat images (sample outside of X-ray beam) taken at the beginning of each experiment and five additional flat images acquired at the end of each run. While the imaging time accounted for less than 1 min per scan, a single cycle of compression, relaxation time, and scanning took on average 7 min. CT reconstruction was performed using standard filtered back-projection including an automated ring removal procedure, where fine-tuning of the CT reconstruction center has been optimized visually. The cylindrical reconstructed volume of interest (VOI), which comprises a segment of the bone mid-diaphysis (see **Figure 3**), had a diameter and height of 1,024 × 1,024 pixels or 0.76 μm × 0.76 μm. A radial polynomial

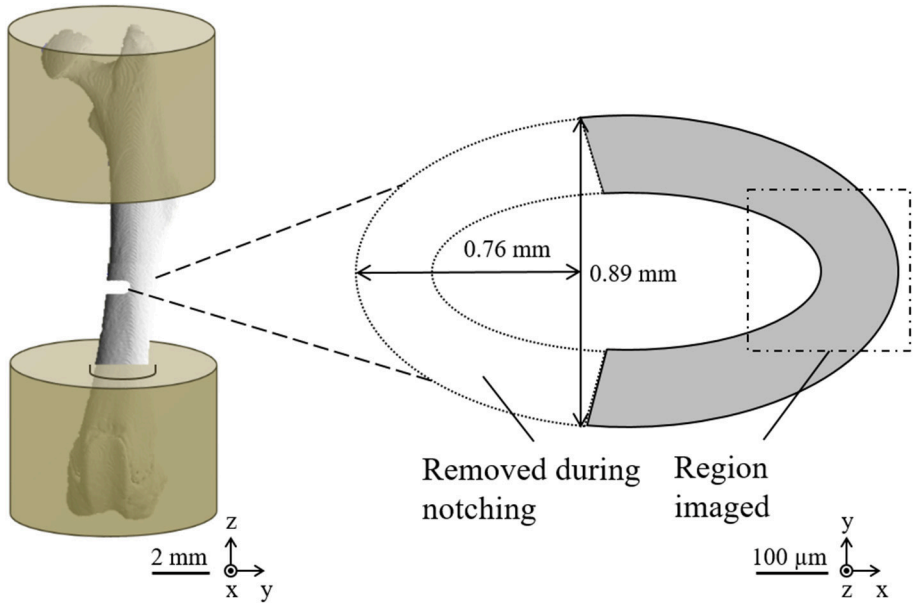

FIGURE 3 | Sample preparation for image-guided failure assessment based on a combination of micro-compression and SR CT imaging. **(Left)** Schematic drawing of mouse femora embedded in PMMA and notched at the mid-diaphysis. **(Right)** A cross-sectional sketch, showing the volume of interest for SR CT imaging.

gradient correction was then applied on the reconstructed data to correct for radial gradients due to the local tomographic setup (Schneider et al., 2009). One of the C3H samples was damaged during sample exchange, while another one was eliminated from the evaluation due to ultimate failure after only two loading steps. Consequently, the total number of successfully assessed samples was four and six for B6 and C3H mice, respectively. Since local mechanical strains are different for regions of varying cross-sectional areas, a normalization of the overall strain for notched and full cross-section regions was performed to provide apparent local mechanical strains. For the normalization, we assumed that the force over each section was equal and that the sum of sectional displacements corresponded to the total displacement. Known variables were cross-sectional areas in the sample (A_1 and A_2, notched and un-notched), as well as total longitudinal strain (ε_t), while the two variables to be determined were corresponding strains in each of the cross sections (ε_1 and ε_2). The total strain ε_t was first expressed as a function of the applied displacement (D) and the length of two cross-sections (L_1 and L_2):

$$\varepsilon_t = \frac{D}{(L_1 + L_2)} \tag{1}$$

Since D itself can be expressed as a sum of the change of length in each section ($D = \Delta L_1 + \Delta L_2 = \varepsilon_1 L_1 + \varepsilon_2 L_2$), Equation (1) could be written as:

$$\varepsilon_t = \frac{(\varepsilon_1 L_1 + \varepsilon_2 L_2)}{(L_1 + L_2)} \tag{2}$$

By equating the force (F_1 and F_2) in each section one can solve for ε_1 and ε_2. From Young's law a solution for the relationship between ε_1 and ε_2 can be obtained.

$$\begin{aligned} F_1 &= F_2 \\ \varepsilon_1 A_1 E &= \varepsilon_2 A_2 E \\ \varepsilon_1 \frac{A_1}{A_2} &= \varepsilon_2 \end{aligned} \tag{3}$$

Further combination of Equations (2) and (3) resulted in the following relationship:

$$\varepsilon_t = \frac{(\varepsilon_1 L_1 + \varepsilon_1 L_2 \frac{A_1}{A_2})}{(L_1 + L_2)} \tag{4}$$

Using Equations (3) and (4) the final expressions for ε_1 and ε_2 can be derived:

$$\varepsilon_1 = \varepsilon_t \frac{(L_1 + L_2)}{(L_1 + L_2 \frac{A_1}{A_2})} \tag{5}$$

$$\varepsilon_2 = \varepsilon_t \frac{(L_1 + L_2)}{(L_1 \frac{A_2}{A_1} + L_2)} \tag{6}$$

Whole-sample apparent strains were used in the context of mechanical testing, while normalized local strains were referred to in the context of bone microstructure and microdamage analysis.

All samples were evaluated for quantitative morphometry according to the following protocol: A previously described method for negative imaging was used to extract the intracortical bone microstructure, in which the mineralized bone matrix was segmented by global thresholding and inverted (Schneider et al., 2007). Pre-processing steps that were applied in this

method included Levenberg-Marquardt polynomial gradient correction of ring artifacts, iterative thresholding to produce binary images, generation of the full mask of the bone tissue, inversion of the mask to extract voids within the tissue, and removal of single-voxel artifacts. Extraction of the canal network, osteocyte lacunae, and microcracks was achieved through a combination of different image processing procedures (IPL; Scanco Medical AG, Brüttisellen, Switzerland), including component labeling and morphological operators, namely erosion and dilation. Morphological operators were mainly applied to close the intracortical porosity, providing a solid mask for the cortical bone, needed to segment the different intracortical microstructures from the negative imprint of the mineralized bone tissue and to calculate the cortical bone volume (Ct.BV). All porous elements where then separated into the distinct microstructural phases (canal network, osteocyte lacunae, and microcracks) based on their size and morphology. Thus, pores smaller than 175 μm^3 were excluded, elements ranging from 175 to 593 μm^3 were classified as osteocyte lacunae, and the ones larger than $1.4{\cdot}10^3$ μm^3 were grouped as canal network, based on the previously reported values (Schneider et al., 2007). Subsequently, pores of the intermediate sizes ranging from 0.5 to $1.4{\cdot}10^3$ μm^3, as well as those grouped as canal network were initially examined visually to refine their morphological classification. In the automated segmentation process, pores morphologically defined as planar surfaces were classified as microcracks.

For each one of the microstructural phases, a set of morphometric indices including number, volume, and volume density was defined similar to Schneider et al. (2007) and Voide et al. (2009) and in line with standard nomenclature for bone morphometry (Parfitt et al., 1987; Bouxsein et al., 2010). Explicitly, we have evaluated cortical bone volume (Ct.BV) in the VOI, as well as numbers of disconnected canals (N.Ca), osteocyte lacunae (N.Lc), and microcracks (N.Cr). Furthermore, volumes of canal network (Ca.V), osteocyte lacunae (Lc.V), and microcracks (Cr.V) have also been assessed. To compensate for the differences in bone size between the two mouse strains, we have normalized microstructural volume parameters (Ca.V, Lc.V, and Cr.V) by Ct.BV, which provides canal volume density (Ca.V/Ct.BV), lacuna volume density (Lc.V/Ct.BV), and crack volume density (Cr.V/Ct.BV). Finally, in an attempt to establish a correlation between the interplay of microstructural elements as a function of the applied mechanical strains, we introduced a parameter for the normalization of crack volume by the volume of canal network (Cr.V/Ca.V), motivated by the reported importance of the canal network for microcrack initiation and propagation (Voide et al., 2011).

Statistical Analysis

Statistical analysis was performed using the GNU statistical package R (version 2.4.1, http://www.r-project.org) unless stated otherwise, including the additional SFSMISC package (version 1.0, http://cran.r-project.org/web/packages/sfsmisc) for residual analysis.

For the assessment of the load cell data a single predictor variable linear regression model was applied. The measurements obtained from the Zwick load cell were taken as the predictor variable, while those from the MCD load cell represented the response variable. The one-to-one linear relation of the variables was taken as the null hypothesis. Rejection of the null hypothesis was based on the F-statistic for the $r^2 > 0.95$, and corresponding residual analysis, where r is Pearson's correlation coefficient used to assess the strength of linear relationship between the two variables. For the satisfactory results of the model fit, a very high value of the F-statistic, as well as the minimal value of the p-value were expected (Christensen, 2002). Mean values of five repeated tests for each test run were used for data fitting. The residuals were checked using graphical methods. The assumptions to be verified were that the mean of errors was 0, that all errors had the same theoretical variance, that the errors were normally distributed, and that all errors were independent. To test those assumptions a scale-location plot, Tukey-Anscombe plots, a histogram and Q-Q plots were applied, respectively. Significance of the model was given by the p-value for the calculated F-statistic, where models with $p < 0.05$ were considered statistically significant. Eventually, the new calibration coefficient for the MCD load cell was determined based on the linear model.

For the verification of the linear stepper motor operation, assessment of the previously identified factors influencing motor operation (amplitude of the reaction force, speed of displacement, level of plunger extension, and the direction of motion) was performed in a crossed block design (Faraway, 2004, 2005), in which the initial interaction model was constructed using 16 terms. The model was then reduced through the analysis of significance of any given predictor variables, including quadruple interactions of several variables. The final model describing motor displacement included only statistically significant factors for which the p-value was < 0.05 in the analysis.

Relationships between microcracks and canal network were analyzed using linear regression analysis, where p-values < 0.01 were considered statistically significant. Microdamage propagation in terms of Cr.V was studied as a function of normalized local mechanical strains using Excel 2010 (Microsoft, Redmond, OR, USA). In the final part of the analysis, data for the B6 and C3H samples were combined together to establish group-wise trends for microdamage buildup. Increase in the microcrack volume (Cr.V) normalized with one other morphometric parameter at the time was then correlated with the increase in the local mechanical strain. Trend line fitting and statistical evaluation was then further conducted using Excel 2010 (Microsoft, Redmond, OR, USA) to detect any meaningful interactions.

RESULTS

Validation and Calibration of the Micro-Compression Device (MCD)

Validation and calibration of the MCD focused on two integral components of the device, the linear stepper motor and the load cell, which are potentially prone to performance disruption within the integrated construction. For the validation

and calibration of the micro load cell, we hypothesized that the performance of the MCD and the calibrating load cells are linearly related, as would be expected by the technical descriptions of both instruments. Consequently, the minimum value of the correlation coefficient of 0.95 was specified as the decision factor for the rejection of the null hypothesis. The correlation coefficients that were actually obtained for the test with the 10 N load cell were equal to 1.00, and those for the 5 kN load cell were greater than 0.99. The F-statistic, calculated from the ratio of sample variances to verify for possible lack of fit in the linear model, was greater than 2.57×10^5 for all tests, and the corresponding p-values were < 0.001 across all tests. The final step in the model validation was the analysis of residuals and consequent hypothesis decision. The graphical results confirmed the assumptions across all tests, and the null hypothesis for the experiment was thus accepted based on the values of the F-statistic and the residual analysis. These results supported the assumption that the micro load cell incorporated into the MCD and the load cells used in the material testing Zwick/Roell system show linear performances. In addition, a new calibration factor was calculated for the micro load cell. Ideally, such calibrations should be performed prior to each high-resolution imaging experiment.

For the verification of the linear stepper motor, the discrepancies in plunger displacement have been investigated as a function of amplitude of the reaction force, speed of displacement, level of plunger extension, and the direction of motion. Statistical analysis compared the experimental data collected by the reference smart encoder system during repeated test runs against the displacements set by the control of the stepper motor. Both individual and combined effects of the experimental variables have been calculated and analyzed. The results showed that the speed of the plunger displacement or its extension level at the beginning of the experiment had no significant influence on the precision of the system. On the other hand, it was noted that high

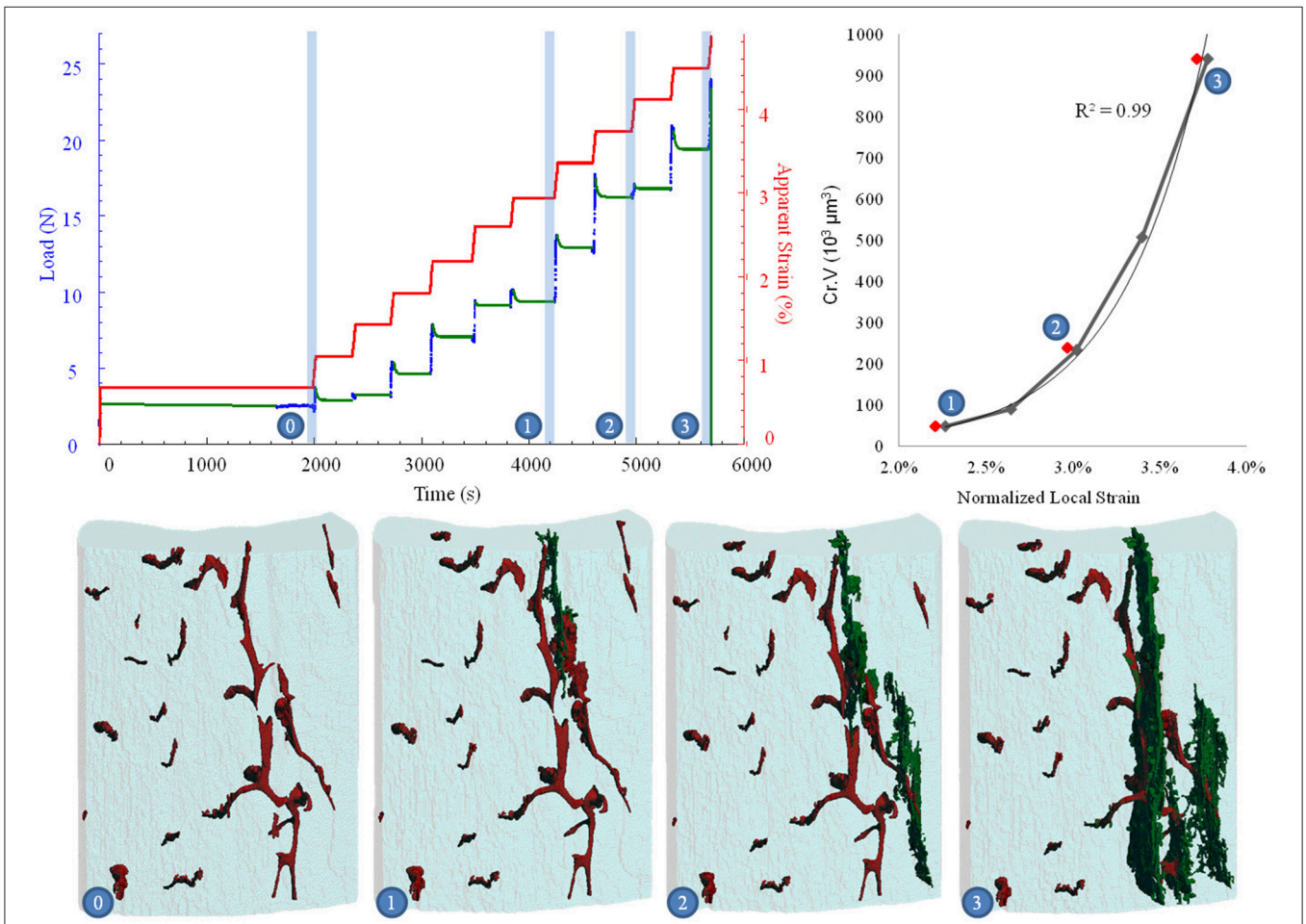

FIGURE 4 | Biomechanical imaging combining bone mechanics **(top left)** and image-guided failure assessment (**bottom** and **top right**). **(Top left)** Blue and red plots show applied loads and corresponding apparent strains in the sample as a function of time. Time slots of stress relaxation and failure are shown in green. **(Top right)** Microcrack growth with the increase in applied strains, showing the equation of the fitted exponential function and the corresponding coefficient of determination. **(Bottom)** Visualized bone microstructure, where canal network is shown in red, microcracks in green, and cortical bone outline in light blue. (0–3) denote matching time points in all images.

reaction forces before the start of the experiment can both introduce small offsets and influence the precision of the motor displacements. However, statistical analysis did not identify reaction force as a significant factor for the precision of the device. Alternatively, the direction of plunger movement was identified as a significant factor, with $p < 0.001$, and errors in displacements of 0.9%. The analysis of the quadruple interactions in the full model produced meaningful results; however, none of the evaluated combinations were statistically significant. Thus, from the analysis of the complete interaction model, it can be concluded that the errors in measurement were random and the overall system precision from the full factorial design model verified an accuracy of 1 μm in 99% of the tests.

Biomechanical Imaging

In the current study, dynamic biomechanical imaging has proven to be a powerful tool for tracking microdamage initiation and propagation in cortical bone all the way through complete mechanical failure. A total of 10 samples were tested in a quasi-continuous way for subsequent visualization and morphometric analysis. The microstructural phases (canal network, osteocyte lacunae, and microcracks) of each sample were visualized, classified, and morphometrically analyzed. In addition, for specimens that sustained more than three compression steps until ultimate failure, the rate of microcrack propagation was fitted with exponential functions.

The stepwise nature of the biomechanical imaging approach allowed comparison between whole bone fracture mechanics and the accumulation of local damage on the micro scale (**Figure 4**, **Supplementary Presentation 1**). This allowed investigation of the linear, as well as post-yield phases of bone loading and overloading. For B6 mice, ultimate load ranged between 14 and 25 N with corresponding maximal apparent mechanical strains in the range of 3.0–3.7%. In the C3H group, maximum sustained load levels were between 22 and 26 N with equivalent apparent mechanical strains of 3.6–5.5%. The normalized local strain, where microdamage initiation started at the height of the notched region, were 1.45 and 2.66% for B6 and C3H, respectively. In addition, the recorded stress-strain curves (**Figure 4**, top left) during biomechanical imaging allowed correlation of fracture events (microcrack initiation and propagation shown in **Figure 4**, bottom)—indicated by stress drops (**Figure 4**, top left) and microcrack morphometry (**Figure 4**, top right)—with local tissue deformation (**Figure 4**, top right). Interestingly, for all B6 samples a sharp decrease in stress levels (at constant apparent strain levels during the relaxation stage) was always observed one or two steps prior to the visualized crack formation and one compression step prior to ultimate failure. For C3H mice, all samples showed stress drops occurring earlier, usually within three compression steps before microcrack detection in the VOI of the SR CT data. Furthermore, multiple succeeding stress drops were noted previous to ultimate bone failure for C3H mice. For each DIGFA experiment the relationship between normalized local strain and microdamage build-up was analyzed and fitted with exponential functions. Regardless of the mouse strain,

TABLE 1 | Normalized local strains and morphometric measures describing the intracortical microstructures for B6 and C3H mice.

Mouse strain		Initiation strain (%)	Ultimate strain (%)	Ct.BV (10^6 μm^3)	N.Ca(1)	N.Lc(1)	N.Cr(1)	Ca.V (10^6 μm^3)	Lc.V (10^6 μm^3)	Cr.V (10^6 μm^3)	Ca.V/Ct.BV (%)	Lc.V/Ct.BV (%)	Cr.V/Ct.BV (%)
B6 ($n = 6$)	Mean	1.45	3.15	63	20	4,264	2	0.85	1.20	0.55	0.41	1.89	0.86
	Std. Dev.	0.34	0.44	4	7	361	1	1.38	0.14	0.26	0.19	0.13	0.42
C3H ($n = 4$)	Mean	2.66	4.22	139	16	8,251	4	3.64	2.95	0.91	2.62	2.11	0.63
	Std. Dev.	0.32	0.86	15	7	774	2	0.94	0.47	0.44	0.56	0.14	0.25
	Group difference	**$p < 0.01$**	$p = 0.05$	**$p < 0.01$**	$p = 0.45$	**$p < 0.01$**	$p = 0.11$	**$p < 0.05$**	**$p < 0.01$**	$p = 0.18$	**$p < 0.01$**	$p = 0.05$	$p = 0.40$

Initiation and ultimate normalized local mechanical strains indicate mechanical states where first microcracks were observed using SR CT, and where complete failure of the bones occurred, respectively. P-values from a two-tailed Student's t-test quantify mouse strain differences, where statistically significant results ($p < 0.05$) are shown in bold.

microcrack propagation could be described with R^2-values ranging from 0.58-0.99.

Following visualization and classification of the microstructural phases in 3D, a full morphometric evaluation was performed for all samples (**Table 1**). Cortical bone volume (Ct.BV) was significantly different and twice as high in C3H compared to B6. The number of disconnected canals (N.Ca) showed no statistically significant differences between mouse strains. However, the canal volume (Ca.V) and corresponding canal volume density (Ca.V/Ct.BV) varied significantly. A different trend was observed in lacunar statistics. While number of lacunae (N.Lc) and lacuna volume (Lc.V) were significantly higher in C3H animals compared to B6, lacuna volume density (Lc.V/Ct.BV) showed no significant differences between mouse strains. Finally, number of microcracks (N.Cr) and microcrack volume (Cr.V) were higher in C3H compared to B6 mice, while microcrack volume density (Cr.V/Ct.BV) was found to be higher in B6 mice. Yet, neither of the crack-related morphometric dissimilarities between groups was significant.

As a final part of the microstructural evaluation, microcrack volume was correlated with morphometric descriptors of the canal network. The only statistically significant result was observed for Cr.V/Ca.V (**Figure 5**). The normalized local mechanical strain could explain almost 90% of the variation observed in microcrack to canal volume relationship in C3H mice, but only 36% in B6 mice.

DISCUSSION

When studying bone it is important to look at the hierarchical order of events in the range from macroscopic to microscopic scales (Fratzl and Weinkamer, 2007; Müller, 2009). While constant improvements in visualization and analytical techniques make assessment on each level feasible, it is impossible to subject a single sample to the full range of the available mechanical testing techniques, mainly due to their destructive nature. It is a common approach therefore to combine mechanical assessment with visualization techniques, usually referred to as biomechanical imaging. In this study, we brought together micro-compression experiments and image-guide failure assessment (IGFA) for the visualization and monitoring of microdamage initiation and propagation on macroscopic and microscopic levels. For this purpose, a MCD was constructed and incorporated at a high-resolution 3D imaging station, namely the TOMCAT beamline of the SLS, where the synchrotron radiation-based computed tomography (SR CT) experiments were performed.

Other studies introduced similar devices (Müller et al., 1998; Bleuet et al., 2004; Nazarian and Müller, 2004; Thurner et al., 2006; Voide et al., 2009) combining mechanical compression and CT imaging of bone failure. However, those devices always had a set of constraints, such as bulky size and restricting shape, limited range of motion or accuracy, or lack of validation. For DIGFA studies of either small animal bones or human bone biopsies, we recommend a device with a weight of maximally 2 kg and inner diameters of at least 7 mm in diameter and 30 mm in length with a travel range of the stepper motor of minimally 20 mm and a step resolution of 0.2 μm. The accuracy precision should be 1 μm or better for overall displacement and 1 N or better for the force with a maximum of at least 500 N. In order to reach highest possible resolution, the outer diameters should be not more than 36 mm in diameter with a wall thickness of the radiolucent material of 1 mm or less to allow submicron resolutions without significant local tomography artifacts. A number of commercially available devices have been introduced lately (Jang et al., 2014; Evans et al., 2017). Although these devices promise similar performance, they have not be thoroughly tested and validated yet for applications in bone.

With respect to this objective, the MCD was designed to be versatile, and fully integrated within the experimental CT setup at TOMCAT. The total weight of the machine is less than 2 kg, and the installation at the beamline involves a simple fixation of the device base with four screws. Sample change can be carried out by a single investigator within a few minutes. The fact that the experimental course is fully automated and interlinked with the scanning triggers of the beamline, not only drastically reduces the possibility of human errors, but also allows to cut down the time between scans, better adapting to the dynamic mechanical processes in the sample. It is important to note though that dynamic does not mean real-time as we still have step-wise compression that is both terminal and discontinuous in its image data collection of the bone structure.

In the second objective, we planned and carried out the validation of the key parts of the MCD, and thus confirmed the reliability and accuracy of its mechanical parts, and its robustness within the full range of performance. In addition, the ball-point plunger, originally combined with a stainless steel plunger disk for even distribution of contact pressure in the compressive experiments (Dhillon et al., 2011), can also be substituted with a clipping mechanism attached to the specimen to enable experiments in tensile mode as well (Bergomi et al., 2010).

Finally, the third goal comprised a sensitivity study, in which we performed a multiscale evaluation and high-resolution visualization of microdamage dynamics in murine cortical bone with the newly constructed MCD. To this end, microstructure and microdamage growth within cortical bone of a mouse model was visualized in a quasi-continuous manner in 3D. Similarly to the previous reports for both human and rodent bones (Schaffler et al., 1995; Voide et al., 2009), we have seen that ultimate bone failure is the result of progressive damage accumulation in the bone tissue. In addition, we have also observed numerous events of stress drops, likely associated with stress redistribution and energy dissipation, prior to bone failure. This phenomenon was more frequently observed in C3H compared to the B6 samples, however was commonly seen in both phenotypes preceding the appearance of detectable microcracks in the 3D images, as well as immediately before failure. In several cases, stress-strain curves indicated redistribution of stress in the sample; however, no microcracks were detected in the imaged VOI. Nevertheless, since we only observe a very small VOI, our ability to detect microdamage in the imaged volume represents a limitation of

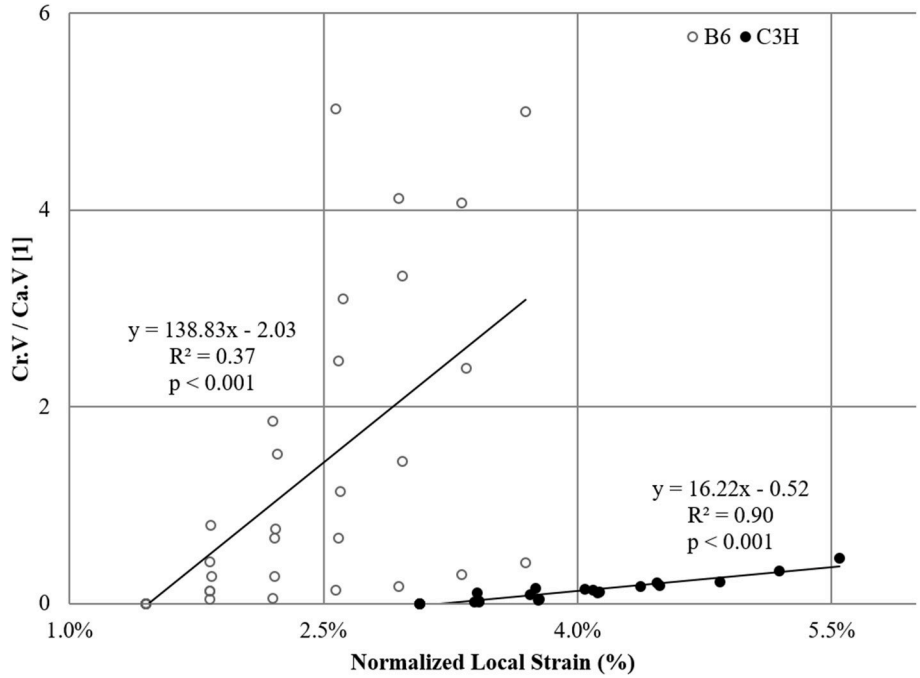

FIGURE 5 | Correlation between microcracks and canal network. Plotted is the volume ratio Cr.V/Ca.V (normalized crack volume) as a function of normalized local mechanical strains for B6 ($R^2 = 0.37$, $p < 0.001$) and C3H ($R^2 = 0.90$, $p < 0.001$).

the current biomechanical imaging approach. This also explains the apparent rapid failure in some samples as a consequence of undetected microcrack build-up, as in the case of the eliminated specimen, which failed within two compression steps. While the measurement of overall mechanical strains is a function of the load cell operation, and is therefore subject to the range of errors within the confidence interval of the load cell performance, we believe that the readout from the device is accurate and meaningful. It has to be mentioned though that calculation and normalization of the local mechanical strains relies of a number of assumptions that we have deemed reasonable—namely, that the force over each section is equal and that the sum of sectional displacements correspond to the total displacement. We are aware that the inter-sample variability and human error in the preparation process has an impact on the individual local strains; however, we believe that the proposed method is based on sound underlying mechanical principles, and therefore provides meaningful and relevant calculations of the local mechanical strains.

Both mechanical testing and visual evidence suggest that femoral cortical bone of C3H mice is more resistant to microcracking and can sustain higher strains until ultimate failure than that of B6 mice. Similar results have been reported in the studies employing different assessment methods (Voide et al., 2008b; Courtland et al., 2009), and can be attributed to both structural and architectural differences in bone. Nevertheless, it must be considered that the suitability of the SR CT visualization for the mechanical testing has been disputed due to the adverse effects of X-ray irradiation on the tissue (Barth et al., 2011). In a previous study (Voide et al., 2011) we conducted mechanical testing on femoral specimens of 19-week-old B6 mice under similar SR CT experimental conditions as reported here, to investigate the influence of X-ray irradiation on bone mechanics. We observed a decrease in ultimate load due to X-ray irradiation (49%, $p < 0.05$) and stiffness (36%, $p = 0.09$), which was lower than expected (>90%) from model calculations for *in situ* SR X-ray scattering and CT experiments (Barth et al., 2011). Nevertheless, it is important to note that although SR imaging does negatively affect the mechanical bone properties, it does not affect the microstructure itself. A recent study found high reproducibility and inter-class correlations of microstructural bone parameters (Hemmatian et al., 2017) indicating that there are no significant microstructural changes at this level of resolution even after multiple image acquisitions. Additionally, it should be mentioned that our studies used whole femurs that were notched in the mid-diaphysis of the bones. As the notching is destructive, it may also have changed the bone structure just adjacent of the notch, which is our region of interest to observe microstructure and microcrack initiation and progression. Nevertheless, no changes or damage was observed in our baseline images indicating that possible changes associated with the notching were not detectable in our setting.

The results of the morphometric assessment have shown that the average cortical bone volume for B6 strain is less than half that of C3H samples, similar to the average volume of the accumulated microdamage, initiation strains, and the rate of microcrack propagation (1:2). Average microcrack volume density (Cr.V/Ct.BV) albeit larger in B6 was not significantly

different between the two mouse strains, which can be attributed partly to the low number of cracks found in the VOI and the resulting high standard deviation associated with both N.Cr and Cr.V. Nevertheless, the observed microdamage build-up can in part be explained by increased bone mass and density, along with different tissue material properties, such as higher mineral-to-matrix ratio, and corresponding higher stiffness in C3H in contrast to B6 mice (Courtland et al., 2009). Additionally, the influence of bone microstructure has to be equally accounted for. To this end, while a more recent hypothesis suggest that it is the canaliculi, i.e., the tubular connections between different osteocyte lacunae, that are directly involved in the initiation of microcracks (Ebacher et al., 2012), it has previously been shown that osteocytes can play an active role, both as stress concentrating elements and contributors to crack blunting (Peterlik et al., 2006; Christen et al., 2012). Nevertheless, when we look only at the differences in the number of osteocyte lacunae, we were not able to show a significant effect of osteocyte number on microcrack development. It may well be though that osteocyte lacunae are more important for crack progression than initiation as suggested by these authors. Conversely, canal volume density (Ca.V/Ct.BV) was significantly different for the two mouse strains, and was more than six times greater in C3H than in B6 mice. Several studies comment on the significance of the canal network in the initiation and propagation of microdamage (Voide et al., 2009, 2011). In our assessment, we have found that while microcracks always ran parallel to the direction of loading, they were aligned with the canal network only if it was also parallel to the loading axis, which was common in C3H samples, but rarely observed in the B6 strain in this work. A recent study has shown that microcracks orientation is also dependent on the type of mechanical loading applied (Wolfram et al., 2016). Where compression resulted in microcracks parallel to the loading axis, tension provoked microcracks to align perpendicular to the loading axis. In our study, the applied strain was a significant factor in almost 90% of the interactions between microcrack and canal volumes in C3H samples, but only in 36% for the B6 mouse strain (**Figure 5**). The lower correlation can be explained by the almost complete absence of canals in the B6 mice, where microcracks initiate on the endocortical side of the bone and propagate outwards to the periosteal cortex rather than along the internal canals as seen in C3H mice.

An important benefit of the proposed dynamic image-guide failure assessment (DIGFA) technique is quasi-continuous visualization and quantification of microdamage in 3D. This approach enabled creation of dynamic animations of crack propagation and to establish relationships for the post-yield phase of bone overloading. For both mouse strains the relationship between strain and microdamage build-up could be described as an exponential function (R^2-values ranged from 0.58 to 0.99). The coefficients of the exponent varied from as low as 34 to as high as 315, with no obvious inter-phenotype differences. When juxtaposed with visualized microdamage this analysis yielded a correlation in which lowest coefficients corresponded to the samples that failed due to the propagation of the planar microcracks, which aligned well with canals, a process typically seen in brittle materials (Peterlik et al., 2006). In the samples with highest exponential coefficients visualized microdamage contained multiple disconnected and frequently out-of-plane cracks, which could be categorized as quasiductile failure mechanism. Previously, the distinction between brittle and quasiductile failure in bone has been attributed to the collagen fiber orientation (Peterlik et al., 2006) and can be further supported by findings of more complex interactions between microstructure and material properties in murine bone tissue (Courtland et al., 2009; Kerschnitzki et al., 2011). Consequently, performing similar kinds of DIGFA experiments on human bone samples will further elucidate the interactions between material properties and architecture of bone tissue and their role in the initiation and propagation of bone microdamage.

Because of the non-lamellar structure of rodent bones the biological results of this study cannot be directly exploited for a better understanding of failure in human bones. However, having established and validated the MCD at hand for 3D visualization and quantification of dynamic bone failure, this biomechanical imaging approach is now ready to be used for studies of human bone. In the long run, better understanding of failure mechanisms in cortical bone can lead to more successful ways of prediction and prevention of both age- and injury-related bone fractures.

AUTHOR CONTRIBUTIONS

PS, AL, and RM designed the experiment. AL, PS, MM, PV, and FD performed the study. All authors were involved in drafting the work and approved it for publication.

ACKNOWLEDGMENTS

The authors thank Marco Hitz and Peter Schwilch for help with the device design and construction. This study was supported by a fellowship from the Whitaker Foundation (AL).

SUPPLEMENTARY MATERIAL

The Supplementary Material for this article can be found online at: https://www.frontiersin.org/articles/10.3389/fmats.2018.00032/full#supplementary-material

Supplementary Presentation 1 | Image-guided failure assessment of time-lapsed cortical bone failure in B6 and C3H mice. Visualized bone microstructure, where canal network is shown in red, microcracks in green, and cortical bone outline in light blue.

REFERENCES

Barth, H. D., Zimmermann, E. A., Schaible, E., Tang, S. Y., Alliston, T., and Ritchie, R. O. (2011). Characterization of the effects of x-ray irradiation on the hierarchical structure and mechanical properties of human cortical bone. *Biomaterials* 32, 8892–8904. doi: 10.1016/j.biomaterials.2011.08.013

Beamer, W. G., Donahue, L. R., Rosen, C. J., and Baylink, D. J. (1996). Genetic variability in adult bone density among inbred strains of mice. *Bone* 18, 397–403. doi: 10.1016/8756-3282(96)00047-6

Bergomi, M., Cugnoni, J., Wiskott, H. W. A., Schneider, P., Stampanoni, M., Botsis, J., et al. (2010). Three-dimensional morphometry of strained bovine periodontal ligament using synchrotron radiation-based tomography. *J. Anat.* 217, 126–134. doi: 10.1111/j.1469-7580.2010.01250.x

Bleuet, P., Roux, J. P., Dabin, Y., and Boivin, G. (2004). *In-situ* microtomography study of human bones under strain with synchrotron radiation. *Dev. X-Ray Tomogr. Iv* 5535, 129–136. doi: 10.1117/12.555670

Bouxsein, M. L., Boyd, S. K., Christiansen, B. A., Guldberg, R. E., Jepsen, K. J., and Müller, R. (2010). Guidelines for assessment of bone microstructure in rodents using micro-computed tomography. *J. Bone Miner. Res.* 25, 1468–1486. doi: 10.1002/jbmr.141

Burr, D. B., Martin, R. B., Schaffler, M. B., and Radin, E. L. (1985). Bone remodeling in response to *in vivo* fatigue microdamage. *J. Biomech.* 18, 189–200. doi: 10.1016/0021-9290(85)90204-0

Burr, D. B., Turner, C. H., Naick, P., Forwood, M. R., Ambrosius, W., Hasan, M. S., et al. (1998). Does microdamage accumulation affect the mechanical properties of bone? *J. Biomech.* 31, 337–345. doi: 10.1016/S0021-9290(98)00016-5

Carter, D. R., and Spengler, D. M. (1978). Mechanical properties and composition of cortical bone. *Clin. Orthop. Relat. Res.* 135, 192–217. doi: 10.1097/00003086-197809000-00041

Choi, K., and Goldstein, S. A. (1992). A comparison of the fatigue behavior of human trabecular and cortical bone tissue. *J. Biomech.* 25, 1371–1381. doi: 10.1016/0021-9290(92)90051-2

Christen, D., Levchuk, A., Schori, S., Schneider, P., Boyd, S. K., and Müller, R. (2012). Deformable image registration and 3D strain mapping for the quantitative assessment of cortical bone microdamage. *J. Mech. Behav. Biomed. Mater.* 8, 184–193. doi: 10.1016/j.jmbbm.2011.12.009

Christensen, R. (2002). *Plane Answers of Linear Models*: *The Theory of Linear Models*. New York, NY: Springer.

Cooper, D. M. L., Erickson, B., Peele, A. G., Hannah, K., Thomas, C. D. L., and Clement, J. G. (2011). Visualization of 3D osteon morphology by synchrotron radiation micro-CT. *J. Anat.* 219, 481–489. doi: 10.1111/j.1469-7580.2011.01398.x

Courtland, H. W., Spevak, M., Boskey, A. L., and Jepsen, K. J. (2009). Genetic variation in mouse femoral tissue-level mineral content underlies differences in whole bone mechanical properties. *Cells Tissues Organs* 189, 237–240. doi: 10.1159/000151381

Cowin, S. C. (2001). *Bone Mechanics Handbook*. BocaRaton, FL: CRC Press.

Currey, J. D. (1988). The effect of porosity and mineral-content on the youngs modulus of elasticity of compact-bone. *J. Biomech.* 21, 131–139. doi: 10.1016/0021-9290(88)90006-1

Currey, J. D. (2012). The structure and mechanics of bone. *J. Mat. Sci.* 47, 41–54. doi: 10.1007/s10853-011-5914-9

Dhillon, A., Schneider, P., Kuhn, G., Reinwald, Y., White, L. J., Levchuk, A., et al. (2011). Analysis of sintered polymer scaffolds using concomitant synchrotron computed tomography and *in situ* mechanical testing. *J. Mat. Sci. Mat. Med.* 22, 2599–2605. doi: 10.1007/s10856-011-4443-z

Diab, T., and Vashishth, D. (2005). Effects of damage morphology on cortical bone fragility. *Bone* 37, 96–102. doi: 10.1016/j.bone.2005.03.014

Donahue, S. W., and Galley, S. A. (2006). Microdamage in bone: implications for fracture, repair, remodeling, and adaptation. *Crit. Rev. Biomed. Eng.* 34, 215–271. doi: 10.1615/CritRevBiomedEng.v34.i3.20

Dong, P., Haupert, S., Hesse, B., Langer, M., Gouttenoire, P. J., Bousson, V., et al. (2014). 3D osteocyte lacunar morphometric properties and distributions in human femoral cortical bone using synchrotron radiation micro-CT images. *Bone* 60, 172–185. doi: 10.1016/j.bone.2013.12.008

Ebacher, V., Guy, P., Oxland, T., and Wang, R. (2012). Sub-lamellar microcracking and roles of canaliculi in human cortical bone. *Acta Biomater.* 8, 1093–1100. doi: 10.1016/j.actbio.2011.11.013

Evans, N. T., Torstrick, F. B., Safranski, D. L., Guldberg, R. E., and Gall, K. (2017). Local deformation behavior of surface porous polyether-ether-ketone. *J. Mech. Behav. Biomed. Mater.* 65, 522–532. doi: 10.1016/j.jmbbm.2016.09.006

Faraway, J. J. (2004). "Linear models with R," in *Chapman and Hall/CRC Texts in Statistical Science*, eds B. P. Carlin, C. Chatfield, M. Tanner, and J. Zidek (Boca Raton, FL: CRC Press), 200–210.

Faraway, J. J. (2005). "Extending the linear model with r: generalized linear, mixed effects and nonparametric regression models," in *Chapman & Hall/CRC Texts in Statistical Sciences*, eds B. P. Carlin, C. Chatfield, M. Tanner, and J. Zidek (Boca Raton, FL: CRC Press), 153–174.

Fazzalari, N. L., Forwood, M. R., Manthey, B. A., Smith, K., and Kolesik, P. (1998). Three-dimensional confocal images of microdamage in cancellous bone. *Bone* 23, 373–378. doi: 10.1016/S8756-3282(98)00111-2

Fratzl, P., and Weinkamer, R. (2007). Nature's hierarchical materials. *Prog. Mater. Sci.* 52, 1263–1334. doi: 10.1016/j.pmatsci.2007.06.001

Goulet, R. W., Goldstein, S. A., Ciarelli, M. J., Kuhn, J. L., Brown, M. B., and Feldkamp, L. A. (1994). The relationship between the structural and orthogonal compressive properties of trabecular bone. *J. Biomech.* 27, 375–389. doi: 10.1016/0021-9290(94)90014-0

Hemmatian, H., Laurent, M. R., Ghazanfari, S., Vanderschueren, D., Bakker, A. D., Klein-Nulend, J., et al. (2017). Accuracy and reproducibility of mouse cortical bone microporosity as quantified by desktop microcomputed tomography. *PLoS ONE* 12:e0182996. doi: 10.1371/journal.pone.0182996

Hernandez, C. J., Lambers, F. M., Widjaja, J., Chapa, C., and Rimnac, C. M. (2014). Quantitative relationships between microdamage and cancellous bone strength and stiffness. *Bone* 66, 205–213. doi: 10.1016/j.bone.2014.05.023

Jang, A. T., Lin, J. D., Seo, Y., Etchin, S., Merkle, A., Fahey, K., et al. (2014). *In situ* compressive loading and correlative noninvasive imaging of the bone-periodontal ligament-tooth fibrous joint. *J. Vis. Exp.* 85:51147. doi: 10.3791/51147

Kerschnitzki, M., Wagermaier, W., Roschger, P., Seto, J., Shahar, R., Duda, G. N., et al. (2011). The organization of the osteocyte network mirrors the extracellular matrix orientation in bone. *J. Struct. Biol.* 173, 303–311. doi: 10.1016/j.jsb.2010.11.014

Larrue, A., Rattner, A., Peter, Z. A., Olivier, C., Laroche, N., Vico, L., et al. (2011). Synchrotron radiation micro-CT at the micrometer scale for the analysis of the three-dimensional morphology of microcracks in human trabecular bone. *PLoS ONE* 6:e21297. doi: 10.1371/journal.pone.0021297

Mccalden, R. W., Mcgeough, J. A., Barker, M. B., and Courtbrown, C. M. (1993). Age-related-changes in the tensile properties of cortical bone - the relative importance of changes in porosity, mineralization, and microstructure. *J. Bone Joint Surg. Am.* 75, 1193–1205. doi: 10.2106/00004623-199308000-00009

Müller, R. (2009). Hierarchical microimaging of bone structure and function. *Nat. Rev. Rheumatol.* 5, 373–381. doi: 10.1038/nrrheum.2009.107

Müller, R., Gerber, S. C., and Hayes, W. C. (1998). Micro-compression: a novel technique for the nondestructive assessment of local bone failure. *Technol. Health Care* 6, 433–444.

Nalla, R. K., Kruzic, J. J., Kinney, J. H., and Ritchie, R. O. (2004). Effect of aging on the toughness of human cortical bone: evaluation by R-curves. *Bone* 35, 1240–1246. doi: 10.1016/j.bone.2004.07.016

Nazarian, A., and Müller, R. (2004). Time-lapsed microstructural imaging of bone failure behavior. *J. Biomech.* 37, 55–65. doi: 10.1016/S0021-9290(03)00254-9

Pacureanu, A., Langer, M., Boller, E., Tafforeau, P., and Peyrin, F. (2012). Nanoscale imaging of the bone cell network with synchrotron X-ray tomography: optimization of acquisition setup. *Med. Phys.* 39, 2229–2238. doi: 10.1118/1.3697525

Palanca, M., Bodey, A. J., Giorgi, M., Viceconti, M., Lacroix, D., Cristofolini, L., et al. (2017). Local displacement and strain uncertainties in different bone types by digital volume correlation of synchrotron microtomograms. *J. Biomech.* 58, 27–36. doi: 10.1016/j.jbiomech.2017.04.007

Parfitt, A. M., Drezner, M. K., Glorieux, F. H., Kanis, J. A., Malluche, H., Meunier, P. J., et al. (1987). Bone histomorphometry: standardization of nomenclature, symbols, and units. report of the ASBMR histomorphometry nomenclature committee. *J. Bone Miner. Res.* 2, 595–610. doi: 10.1002/jbmr.5650020617

Peterlik, H., Roschger, P., Klaushofer, K., and Fratzl, P. (2006). From brittle to ductile fracture of bone. *Nat. Mater.* 5, 52–55. doi: 10.1038/nmat1545

Reilly, D. T., and Burstein, A. H. (1975). The elastic and ultimate properties of compact bone tissue. *J. Biomech.* 8, 393–405. doi: 10.1016/0021-9290(75)90075-5

Reilly, G. C. (2000). Observations of microdamage around osteocyte lacunae in bone. *J. Biomech.* 33, 1131–1134. doi: 10.1016/S0021-9290(00)00090-7

Rho, J. Y., Kuhn-Spearing, L., and Zioupos, P. (1998). Mechanical properties and the hierarchical structure of bone. *Med. Eng. Phys.* 20, 92–102. doi: 10.1016/S1350-4533(98)00007-1

Schaffler, M. B., Choi, K., and Milgrom, C. (1995). Aging and matrix microdamage accumulation in human compact bone. *Bone* 17, 521–525. doi: 10.1016/8756-3282(95)00370-3

Schneider, P., and Müller, R. (2010). Automated micro-compression device for dynamic image-guided failure assessment of bone ultrastructure and bone microdamage. *Biomed. Eng.* 55, 8–10. doi: 10.1515/BMT.2010.703

Schneider, P., Stauber, M., Voide, R., Stampanoni, M., Donahue, L. R., and Müller, R. (2007). Ultrastructural properties in cortical bone vary greatly in two inbred strains of mice as assessed by synchrotron light based micro- and nano-CT. *J. Bone Miner. Res.* 22, 1557–1570. doi: 10.1359/jbmr.070703

Schneider, P., Voide, R., Stampanoni, M., Donahue, L. R., and Muller, R. (2013). The importance of the intracortical canal network for murine bone mechanics. *Bone* 53, 120–128. doi: 10.1016/j.bone.2012.11.024

Schneider, P., Voide, R., Stampanoni, M., and Müller, R. (2009). Post-processing technique for improved assessment of hard tissues in the submicrometer domain using local synchrotron radiation-based computed tomography. *Biomed. Tech. Biomed. Eng.* 54, 48–54. doi: 10.1515/BMT.2009.007

Stampanoni, M., Groso, A., Isenegger, A., Mikuljan, G., Chen, Q., Meister, D., et al. (2007). TOMCAT: a beamline for tomographic microscopy and coherent radiology experiments. *Sync. Radiat. Instrument.* 879, 848–851. doi: 10.1063/1.2436193

Thurner, P. J., Wyss, P., Voide, R., Stauber, M., Stampanoni, M., Sennhauser, U., et al. (2006). Time-lapsed investigation of three-dimensional failure and damage accumulation in trabecular bone using synchrotron light. *Bone* 39, 289–299. doi: 10.1016/j.bone.2006.01.147

Tommasini, S. M., Trinward, A., Acerbo, A. S., De Carlo, F., Miller, L. M., and Judex, S. (2012). Changes in intracortical microporosities induced by pharmaceutical treatment of osteoporosis as detected by high resolution micro-CT. *Bone* 50, 596–604. doi: 10.1016/j.bone.2011.12.012

Turner, C. H. (2006). Bone strength: current concepts. *Skelet. Dev. Remodel. Health Dis. Aging* 1068, 429–446. doi: 10.1196/annals.1346.039

Turner, C. H., Hsieh, Y. F., Müller, R., Bouxsein, M. L., Baylink, D. J., Rosen, C. J., et al. (2000). Genetic regulation of cortical and trabecular bone strength and microstructure in inbred strains of mice. *J. Bone Miner. Res.* 15, 1126–1131. doi: 10.1359/jbmr.2000.15.6.1126

Voide, R., Schneider, P., Stauber, M., Van Lenthe, G. H., Stampanoni, M., and Müller, R. (2011). The importance of murine cortical bone microstructure for microcrack initiation and propagation. *Bone* 49, 1186–1193. doi: 10.1016/j.bone.2011.08.011

Voide, R., Schneider, P., Stauber, M., Wyss, R., Stampanoni, M., Sennhauser, U., et al. (2009). Time-lapsed assessment of microcrack initiation and propagation in murine cortical bone at submicrometer resolution. *Bone* 45, 164–173. doi: 10.1016/j.bone.2009.04.248

Voide, R., Van Lenthe, G. H., and Müller, R. (2008a). Bone morphometry strongly predicts cortical bone stiffness and strength, but not toughness, in inbred mouse models of high and low bone mass. *J. Bone Miner. Res.* 23, 1194–1203. doi: 10.1359/jbmr.080311

Voide, R., Van Lenthe, G. H., and Müller, R. (2008b). Differential effects of bone structural and material properties on bone competence in C57BL/6 and C3H/He inbred strains of mice. *Calcif. Tissue Int.* 83, 61–69. doi: 10.1007/s00223-008-9120-y

Voide, R., Van Lenthe, G. H., and Müller, R. (2008c). Femoral stiffness and strength critically depend on loading angle: a parametric study in a mouse-inbred strain. *Biomed. Tech. Biomed. Eng.* 53, 122–129. doi: 10.1515/BMT.2008.019

Voide, R., Van Lenthe, G. H., Stauber, M., Schneider, P., Thurner, P. J., Wyss, P., et al. (2008d). Functional microimaging: a hierarchical investigation of bone failure behavior. *J. Jpn. Soc. Bone Morphometry* 18, 9–21. Available Online at: https://ci.nii.ac.jp/naid/10024127139

Wehrli, F. W. (2007). Structural and functional assessment of trabecular and cortical bone by micro magnetic resonance imaging. *J. Magn. Reson. Imaging* 25, 390–409. doi: 10.1002/jmri.20807

Wolfram, U., Schwiedrzik, J. J., Mirzaali, M. J., Burki, A., Varga, P., Olivier, C., et al. (2016). Characterizing microcrack orientation distribution functions in osteonal bone samples. *J. Microsc.* 264, 268–281. doi: 10.1111/jmi.12440

Conflict of Interest Statement: The authors declare that the research was conducted in the absence of any commercial or financial relationships that could be construed as a potential conflict of interest.

frontiers in Mechanical Engineering

ORIGINAL RESEARCH
published: 05 March 2018
doi: 10.3389/fmech.2018.00003

Three-Dimensional Full-Field Strain Measurements across a Whole Porcine Aorta Subjected to Tensile Loading Using Optical Coherence Tomography–Digital Volume Correlation

Víctor A. Acosta Santamaría[1,2,3], María Flechas García[1,2,3], Jérôme Molimard[1,2,3] and Stephane Avril[1,2,3]*

[1] SaInBioSE, INSERM, U1059, Saint Etienne, France, [2] Mines Saint-Etienne, Saint Etienne, France, [3] Université de Lyon, Saint Etienne, France

OPEN ACCESS

Edited by:
Gianluca Tozzi,
University of Portsmouth,
United Kingdom

Reviewed by:
Hari Arora,
Imperial College London,
United Kingdom
Brian Bay,
Oregon State University,
United States
Pablo Daniel Ruiz,
Loughborough University,
United Kingdom

***Correspondence:**
Víctor A. Acosta Santamaría
victor.acosta@emse.fr

Specialty section:
This article was submitted to Mechanics of Materials, a section of the journal Frontiers in Mechanical Engineering

Received: 28 August 2017
Accepted: 02 February 2018
Published: 05 March 2018

Citation:
Acosta Santamaría VA, Flechas García M, Molimard J and Avril S (2018) Three-Dimensional Full-Field Strain Measurements across a Whole Porcine Aorta Subjected to Tensile Loading Using Optical Coherence Tomography–Digital Volume Correlation. Front. Mech. Eng. 4:3. doi: 10.3389/fmech.2018.00003

Optical coherence tomography (OCT) combined with digital volume correlation (DVC) is a suitable technique to investigate the biomechanical behavior of biological tissues at the microscale. However, to characterize the whole thickness of large human or porcine arteries, the use of osmotic tissue clearing agents, such as propylene glycol (PG), is unavoidable due to intrinsic tissue scattering of light. The mechanical response of biological tissues immersed in tissue clearing agents has been poorly investigated so far. Nevertheless, understanding the mechanisms of tissue clearing could be helpful for developing safe optical-clearing methods for possible *in vivo* applications. The goal of the present work is to combine OCT and DVC to measure displacement and strain fields in porcine aortic tissues immersed in PG and subjected to stress-relaxation uniaxial tension. Displacement and strain fields are measured across the whole thickness of the porcine aortic wall for the first time. Measurement uncertainties and optimal OCT-DVC parameters are determined to define useful technical recommendations for future similar analyses. It is known that the main effect of PG is a significant increase in collagen fibril packing density due to important loss of water (dehydration). It results in a pronounced stiffening of the aortic tensile response when compared to the response of the same tissue immersed in phosphate buffered saline (PBS). This effect is reversible when the aortic tissue is removed from PG polypropylene glycol and immersed again in PBS. Another effect is a dramatic reduction in the Poisson's effect during tensile loading. But the OCT-DVC-measured strain fields also reveal heterogeneities of this effect among the different layers of the aorta. It appears that the reduced Poisson's effect is concentrated in the media layer, whereas the adventitia and intima layer keep a usual Poisson's effect of nearly incompressible tissues. It is concluded that further work should be conducted on how the smooth muscle cells highly present in the media layer are affected by PG polypropylene glycol immersion for a better understanding of these effects.

Keywords: aortic wall, optical coherence tomography, digital volume correlation, tissue clearing technique, uniaxial tensile test

INTRODUCTION

Optical coherence tomography (OCT) is an imaging modality of micrometric scale permitting the visualization of tissue microstructure at different sub-surface levels (high-resolution and cross-sectional images acquisition with a near-infrared light) (Yang et al., 2006; Huang et al., 2009; Tucker-Schwartz and Skala, 2012; Real et al., 2013; Ling et al., 2016; Mahdian et al., 2016). It is continuously under development, with for instance recent real time acquisitions (Schmitt et al., 1994; Boppart et al., 1999; Yabushita et al., 2002; Yang et al., 2006; Tucker-Schwartz and Skala, 2012).

As an optical imaging technique, OCT has been used for medical application studies (*in vivo*) and for biomedical and bioengineering research (*in vitro*). OCT was applied to characterize soft and hard human tissues such as vessels (aorta and coronary arteries), respiratory tract, gastrointestinal tissues (stomach and esophagus), cartilage, skin, nervous systems, cornea and retinal tissues, fatty tissue, cancellous and cortical bone, human enamel, etc. For medical applications, this technique has been employed to detect and characterize the morphological alterations of microstructure and structure of human tissues undergoing pathologic changes such as: atherosclerotic plaques, thoracic aortic aneurysms, airways dysfunctions (asthma and bronchiectasis), gastrointestinal tumor tissue, articular cartilage degenerative changes, retinal vascular diseases, microfractures and inflammations in oral tissues, etc. It has also been used on biomaterials such as dental implants, three-dimensional (3D) porous scaffolds applied in tissue engineering and hydrogels, among others (Brezinski et al., 1996; Wang, 2002; Wang and Elder, 2002; Yabushita et al., 2002; Yang et al., 2006, 2007; Huang et al., 2009; Prati et al., 2010; Williamson et al., 2011; Li et al., 2012; Real et al., 2013; Jia et al., 2015; Liba et al., 2016; Mahdian et al., 2016; Nebelung et al., 2016; Alibhai et al., 2017).

Additionally, the OCT technique can be applied to evaluate and determine the mechanical properties of biological tissues (Rogowska et al., 2004; Palanca et al., 2016). For experimental biomechanics, mechanical characterization may be achieved by a full-field measurement of displacements and strains (Fu et al., 2013; Palanca et al., 2016). Due to the complex anisotropic structure and non-linear response of biological tissues, the strain gradients can fluctuate significantly through the thickness of the tissue. In this context, a 3D full-field deformation measurement is required (Fu et al., 2013; Palanca et al., 2016). The digital volume correlation (DVC) is a 3D extension of the 2D digital image correlation (DIC) method. For DIC, the strain measurements are limited to evaluate the specimen's surface. However, the DVC method provides 3D full-field measurements across the specimen microstructure (Rogowska et al., 2004; Liu and Morgan, 2007; Fu et al., 2013; Hild et al., 2013; Bouterf et al., 2014; Gillard et al., 2014). To achieve a correct correlation between the reconstructed volumes, it is necessary to define an adequate speckle contrast. Additionally, parameters such as the uncertainty of the measured displacements and the spatial resolution depend on the texture of the analyzed images and should be adjusted for each study (Leclerc et al., 2011; Fu et al., 2013).

Different studies have been conducted so far using DIC to characterize the mechanical and structural properties on aortic tissue. Zhang et al. (2002) used a tensile test and measured displacement and strain fields on bovine aorta (intima and media layers). Genovese and Humphrey (2015) applied a pressure test to assess the full-field surface deformations and regional wall thickness on a porcine aortic arch. In a previous study of our group, Trabelsi et al. (2015) applied a bulge inflation test to characterize stress and strain distributions and estimate the rupture stresses of human ascending thoracic aortic aneurysms. Additionally, and regarding the characterization of aortas, few studies have applied the OCT technique (Real et al., 2013). Fu et al. (2013) applied a tensile test in conjunction with the OCT and DVC methods to obtain measurements of depth-resolved deformations on silicone gels. Real et al. (2013) studied human aorta aneurysms (*in vitro*), in order to define structure abnormalities. However, no reference of a combined OCT/DVC approach could be found on aortic tissue.

This lack of study on aortic tissue can be explained by the main limitations of OCT, which are its penetration depth and image contrast. The penetration depth across aortic tissue is usually less than 500 μm, whereas human or porcine aortas have a thickness of about 2 mm. These limitations of OCT are related to the scattering properties of biological tissues, defined as the spectral and angular characteristics of light interacting with the heterogeneous features of the tissue. Additionally, the refractive index is affected by the structural composition of the tissue (intra and extracellular fluids, cell organelles, and fiber structures) (Boppart et al., 1999; Welzel, 2001; Wang, 2002; Pancrazio et al., 2007; Sudheendran et al., 2011; Larin et al., 2012; Tucker-Schwartz and Skala, 2012; Puhakka et al., 2015; Dao Luong et al., 2016).

To overcome these intrinsic limitations, different ways have been investigated. *In vivo*, OCT, and large gold nanorods were combined in a non-invasive method to acquire images at high spatial resolution, containing both rich anatomical structure and insight into functional biology (Liba et al., 2016). Photothermal OCT is another non-invasive technique that uses an amplitude-modulated laser to achieve spatial resolution and imaging depth with minimal effects on the tissue properties (Tucker-Schwartz and Skala, 2012; Tucker-Schwartz et al., 2012). In several *in vitro* studies, the tissues were immersed in different types of media in order to keep the sample hydrated and/or to maximize light penetration and minimize refraction during OCT measurements. Media such as PBS, normal saline, pure water, or distilled water have been applied in numerous cases (Brezinski et al., 1996; Yabushita et al., 2002; Yang et al., 2006, 2007; Shimamura et al., 2011; Mahdian et al., 2016; Nebelung et al., 2016). Wang et al. (2002) applied a tissue clearing technique to increase the OCT imaging contrast and depth capability on human stomach and esophagus tissues. To improve the optical scattering properties, the authors compared two optical clearing agents (OCAs): glycerol and propylene glycol PG. Glycerol replaces the interstitial extracellular fluid *via* osmotic forces. As a highly hyperosmotic agent, PG induces tissue dehydration. The result is a more homogeneous refractive index. Moreover, OCAs reduce the scattering coefficient. Other OCAs have been applied in different studies (glucose, mannitol, dextrose, fructose, and polyethylene glycol) (Welzel, 2001; Wang, 2002; Wang and Elder, 2002; Khan et al., 2004; Proskurin and Meglinski, 2007; Larina et al., 2008; Sudheendran et al., 2011; Larin et al., 2012).

The mechanical response of biological tissues immersed in tissue clearing agents has been poorly investigated so far. Nevertheless, understanding the mechanisms of tissue clearing could be helpful for developing safe optical-clearing methods for possible *in vivo* applications.

The goal of the present work is to combine OCT and DVC to measure displacement and strain fields in porcine aortic tissues immersed in a tissue clearing agent (PG) and subjected to stress-relaxation uniaxial tension. We first introduce the experimental protocol, delivering useful technical recommendations for measuring displacement and strain fields across the whole thickness of porcine aortic walls. The obtained OCT–DVC strain fields show interesting inhomogeneities across the different layers of the aorta. Results are discussed in the light of how immersion in PG can modify the biomechanical response of the aorta.

MATERIALS AND METHODS

Sample Preparation

Two longitudinal samples of a descending thoracic aorta were collected from a healthy female pig (Large White × Landrace breed weighing 80–90 kg). The Veterinary School of Lyon (Institut Claude Bourgelat) supplied the aortic tissue in accordance with the recommendations of the ethics committee of VetAgro Sup (C2EA No 18), and following the animal testing regulation – Directive 2010/63/EU. The study and the protocol were reviewed and approved by the ethics committee of VetAgro Sup (project approved under No 1546). The samples were stored frozen at −20°C until the measurements were performed. About the freezing effects in porcine thoracic aorta samples, Matsumoto et al. (2009) showed that the mechanical properties were similar for samples stored at −23°C in comparison to fresh specimens at 37°C. Before the OCT acquisition, the tissue was placed into an osmotically active solution of 85% (v/v) PG in PBS, at 37°C for 2 h (Lomas et al., 2003). The sample was located and immersed in a chamber with the osmotic solution during OCT measurements (**Figure 1**). This hydrophilic agent dehydrates the tissue, extracting the interstitial and intracellular water content. This effect decreases the volume fraction of the scattering centers. The tissue becomes translucent, and the light penetration through the sublayers increases, improving the optical scattering properties, contrast and depth capability acquisition. In the vessel walls, the scattering origin is attributed to the long collagen and elastin fibers and the extracellular medium which have a different refractive index than interstitial and intracellular water and lipidic cell membranes (Wang, 2002; Wang and Elder, 2002; Larin et al., 2012). For the 3D images acquisition, the OCT lens was focused on the outer surface of the intima layer (corresponding to OCT B-scans) (Real et al., 2013). The sample geometries must present an intermediate flat zone (**Table 1**).

Experimental Protocols

For the mechanical characterization of the aortic tissue, an OCT experimental setup was developed to apply two different experimental protocols: a rigid body translation (RB) test and a stress-relaxation uniaxial tensile (UT) test (**Figure 1**). The objective for the RB test was to calibrate the optical scattering parameters that allow full-field measurements in the aortic wall

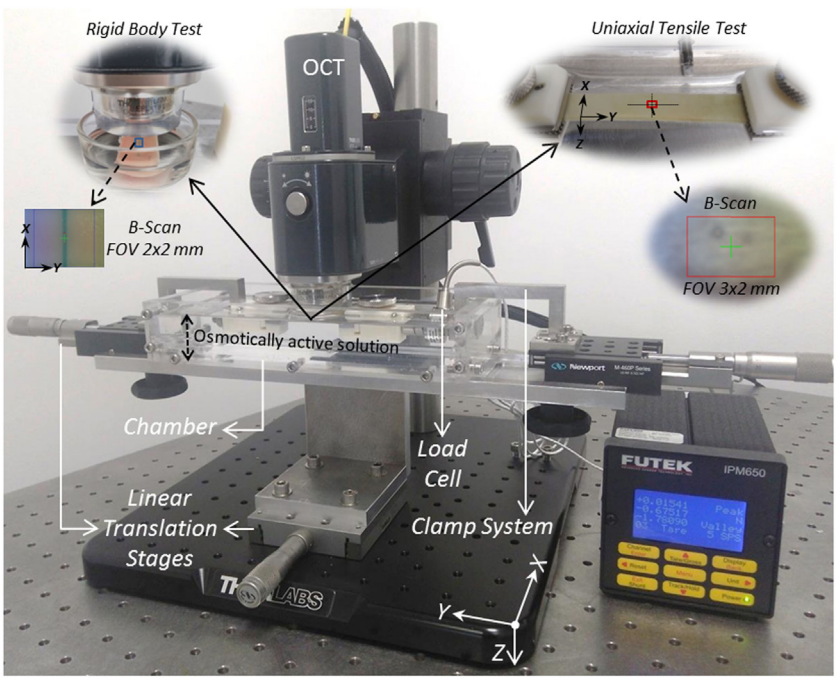

FIGURE 1 | Experimental setup used for the rigid body translation test and for the stress-relaxation uniaxial tensile test.

tissue, applying the OCT technique in conjunction with the DVC method. In order to define the optimal field of view (FOV), a full thickness measurement was considered (corresponding to OCT A-scans) (**Table 1**). To determine the necessary spatial resolution and achieve the full-field displacement measurement through the tissue, OCT acquisitions were performed with different pixel sizes (3, 4, 5, and 6 μm) (**Table 2**). For each pixel size three displacement increments were applied (20, 40, and 60 μm), with a linear translation stage (**Figure 1**). The displacements were defined only on the *X*-axis (corresponding to OCT B-scans), and a free boundary condition was maintained during the test (**Figure 1**). Four OCT acquisitions were performed for each pixel size.

Once the optical scattering properties and the correlation parameters were defined, the UT test was performed (**Figure 1**). The experiment started with a preconditioning of 5% of deformation (with respect to the unloaded length of the sample), followed by 40 min of relaxation. The purpose of preconditioning was to activate the tissue fibers and ensure a flat and taut sample for the OCT acquisitions (Fu et al., 2013). After that, a stepwise stress-relaxation ramp was applied with nine controlled displacements and a relaxation period between increments of 30 min (required time to achieve the equilibrium of the swelling effect). The criterion for a complete equilibrium was a relaxation rate of <100 Pa/min (Korhonen et al., 2002). The displacement ramp was defined on the longitudinal direction of the tissue (*Y*-axis, corresponding to OCT B-scans) and was applied in two directions simultaneously (±*Y*-axis), in such a way as the zone of interest deforms without significant rigid body motion (**Figure 1**). The displacement range of the pulling translation stages was defined between 0 and 6.3 mm and each increment was 0.7 mm (0.35 mm in each direction). A final deformation of 16.5% was approximately reached. The load history generated during the experiment was monitored with a load cell of 22 N (rated output ±1.57 mV/V) conditioned with a Futek IPM650 panel mount display (input range up to ±500 mV/V) (**Figure 2**). An OCT acquisition was performed for each displacement increment. The experiment lasted 6 h.

TABLE 1 | Details of the aortic tissue samples and tests.

	Rigid body translation test			Stress-relaxation uniaxial tensile test		
	x	***y***	***z***	***x***	***y***	***z***
Sample dimensions (mm)	20.0	37.5	1.15 ± 0.04	10.0	41.4	1.44 ± 0.02
Field of view (mm)	2.0	2.0	1.15	2.0	3.0	2.31

OCT – Acquisition System

For the 3D volume image sequence acquisition, the aortic wall reflectivity measurements were obtained with an OCT system (Thorlabs OCT- TEL220C1) (**Figure 1**). The system features were as follows: a center wavelength of 1,300 nm, lateral resolution 7 μm, focal length 18 mm, maximum sensitivity range 111 dB (at 5.5 kHz), imaging depth 2.6 mm (in water), axial resolution 4.2 μm in water and 5.5 μm in air, and 5 for A-scan averaging. The PG refractive index is 1.432. Additionally, and during the experiments, the OCT illumination tube was in full-contact with the osmotic solution. About the RB test, the OCT parameters were different for each experiment (**Table 2**). The OCT acquisition data were saved as TIFF format. The TIFF virtual stack was imported using ImageJ® software. The data were rescaled and converted to eight bits for intensity levels digitalization (Real et al., 2013; Keyes et al., 2016). Finally, the data were exported as RAW image format. With the RAW data, and applying the DVC method, the full-field displacements were measured.

DVC – Assessment of Measurement Performance

The correlation quality (between the reference and deformed configurations) determines the displacement measurements reliability. Moreover, a sufficient contrast is required in order to determine a displacement vector and reduce the measurements uncertainties (Fu et al., 2013; Madi et al., 2013). The full-field measurements of displacement were obtained using DaVis® (LaVision). The software applied the local correlation algorithm (LA-DVC) (Fu et al., 2013; Hild et al., 2013; Keyes et al., 2016). The measurements were acquired with a direct correlation. A sub-volume discretization and multi-pass approach were used to achieve the maximum cross-correlation coefficient and considering the gray-level distributions (Hussein et al., 2012; Fu et al., 2013; Hild et al., 2013; Madi et al., 2013). The reference configuration (f) can be represented by the gray-level function $f(x,y,z)$, and the deformed state (g) as $g(x+u, y+v, z+w)$, where (x,y,z) represents the coordinates and (u,v,w) the offset in each direction. Considering (u,v,w) as the displacement mapping, the continuity of the gray-level can be assumed as $f(x,y,z) = g(x+u, y+v, z+w)$ (Gillard et al., 2014; Keyes et al., 2016). More details about

TABLE 2 | Definition of optical coherence tomography (OCT) parameters for the rigid body translation test.

OCT parameters	**Rigid body translation test**											
	Case 1			**Case 2**			**Case 3**			**Case 4**		
	x	***y***	***z***	***x***	***y***	***z***	***x***	***y***	***z***	***x***	***y***	***z***
Size (pixels)	666	666	470	499	499	470	399	399	470	333	333	470
Pixel size (μm)	3.0	3.0	2.45	4.0	4.0	2.45	5.0	5.0	2.45	6.0	6.0	2.45
A-scan – reference intensity (%)	71.75			71.85			71.84			71.80		
Acquisition time (min)	7.02			4.0			2.36			1.50		

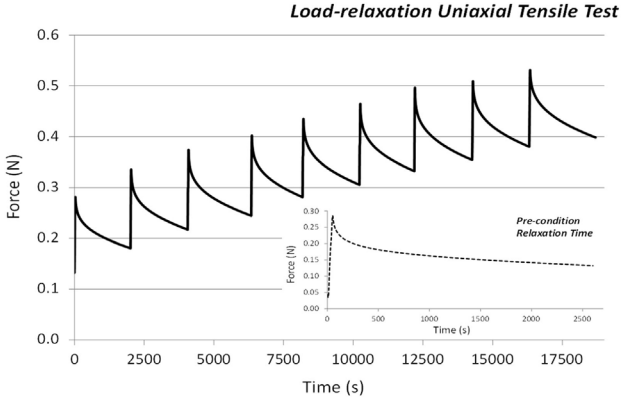

FIGURE 2 | Stepwise stress-relaxation as a function of time and typical behavior of aortic wall in a uniaxial tensile test.

LA-DVC are exposed in the studies by Fu et al. (2013), Madi et al. (2013), and Gillard et al. (2014).

For the RB test, the defined correlation parameters were as follows: a required valid voxel per subset of 40%. Initially, a double-pass approach was defined for various subset sizes (96, 76, 48, 24, and 12 voxels). In the last pass, the final subset size was eight voxels with 75% overlap, and eight passes were applied. For each evaluated subset size and the four increments of displacement (including the reference configuration), three correlations were obtained. About the UT test, the subset size was the only parameter that was modified (128, 96, 64, 32, 16, and 8 voxels). A total of nine correlations were obtained, taking into account the reference configuration (precondition) and the nine defined displacement increments. Moreover, in order to define the different criteria in the reference and deformed states, a sum of differential operation was considered for both experiments. Finally, for each displacement step, the full-field measurements of displacement and strain were obtained. The displacement mean values (MVs), SDs, and the components of the Green–Lagrange strain tensor were calculated with MatLab® after fitting the displacement fields with tricubic functions. The SD defined the measurements of uncertainties of the proposed method.

RESULTS

Optical Effect of Propylene Glycol

Two additional OCT acquisitions were performed in different types of media (air and water). The optical scattering parameters applied were the maximum frequency – and therefore sensitivity – (5.5 kHz) (Choma et al., 2003), the related refractive index per media (1.0 and 1.33, respectively), an FOV of 2 mm × 2 mm × 1.6 mm and a pixel size of 3 μm × 3 μm × 2.64 μm. In comparison with these media, PG obviously improved the contrast, depth capability acquisition, and permitted a full thickness measurement for the aortic wall tissue (**Figure 3**).

With the tissue clearing technique, a gray level pattern across the aortic wall at different sub-surface levels was obtained. However, a specific attention had to be paid to the voxel size as the spatial resolution worsens when the voxel size increases. We tested voxel sizes from 3 to 6 μm, showing significant effects on the gray-level distributions. **Figure 3D** shows an example of the obtained images for the same FOV but with voxel size ranging from 3 to 6 μm. Images with voxel size of 3 or 4 μm show highly visible diffraction patterns, whereas the diffraction patterns disappear for larger pixel size. The airy disk radius commonly gives a theoretical limit of the optical resolution, which is inversely proportional to the numerical aperture and proportional to the light wavelength. In the particular case of this OCT set-up, the light wavelength is higher than in classical visible optics and explains this unusual value.

Optimal Settings of OCT-DVC

Subsequently, for each voxel size we performed full-field measurements for the different displacements assigned to the sample during the RB experiment. For the following displacement values: 0.02, 0.04, and 0.06 mm, an error estimate is reported in **Table 3**. Regarding *u* displacement (along the *X*-axis in the OCT B-scans), the difference increased with respect to the experimental values when the displacement increased. These trends were reported by the MV ± SD (**Table 3**). Case 3 (5 μm voxel size) showed the maximum difference with a relative error of 17% for the first target, 34.5 and 25% for the second and third targets, respectively. The highest correlation was obtained for 6 μm voxel size with relative errors of 8.5% for the first and second targets and 9% for the third one (**Figure 4**). However, with the lowest SD, the smallest errors were obtained for case 1 (3 μm pixel size) (**Table 3**).

In the RB test, a translation was applied only along the *X*-axis; thus, the displacement fields should be zero for *v* (corresponding to the *Y*-axis for the OCT B-scans). As for the *u* displacement correlations, the difference increases (MV ± SD data) (**Table 3**). The highest difference was reported for 3 μm voxel size, with relative errors of 0.18, 0.35, and 0.45% (corresponding target displacements). Moreover, the maximum correlation and the minor uncertainties were achieved for 6 μm voxel size, with relative errors of 0.018, 0.040, and 0.045%, respectively (**Figure 4**). For the aortic wall tissue, and taking into account the full-field displacement measurements, the optimal correlation was enhanced with the 6 μm voxel size.

Additionally, the Green–Lagrange strain components (E_{xx},E_{yy},E_{xy}) were calculated for all cases (**Table 3**). A null strain was expected across the FOV, as it is the case for a RB test (Fu et al., 2013). The smallest root mean square values were obtained for case 4 (6 μm voxel size).

Uniaxial Tensile Response of a Porcine Aortic Sample Immersed in Propylene Glycol

After determining the optimal acquisition and correlation settings with the RB test, the optical properties and correlation parameters were fixed, and the UT test was carried out (**Table 4**). In order to involve more information in the 3D image sequence acquisition by tracking constitutive patterns, the FOV size was increased (2 × 3 × 2.31) (**Figure 5**). According to the experimental setup,

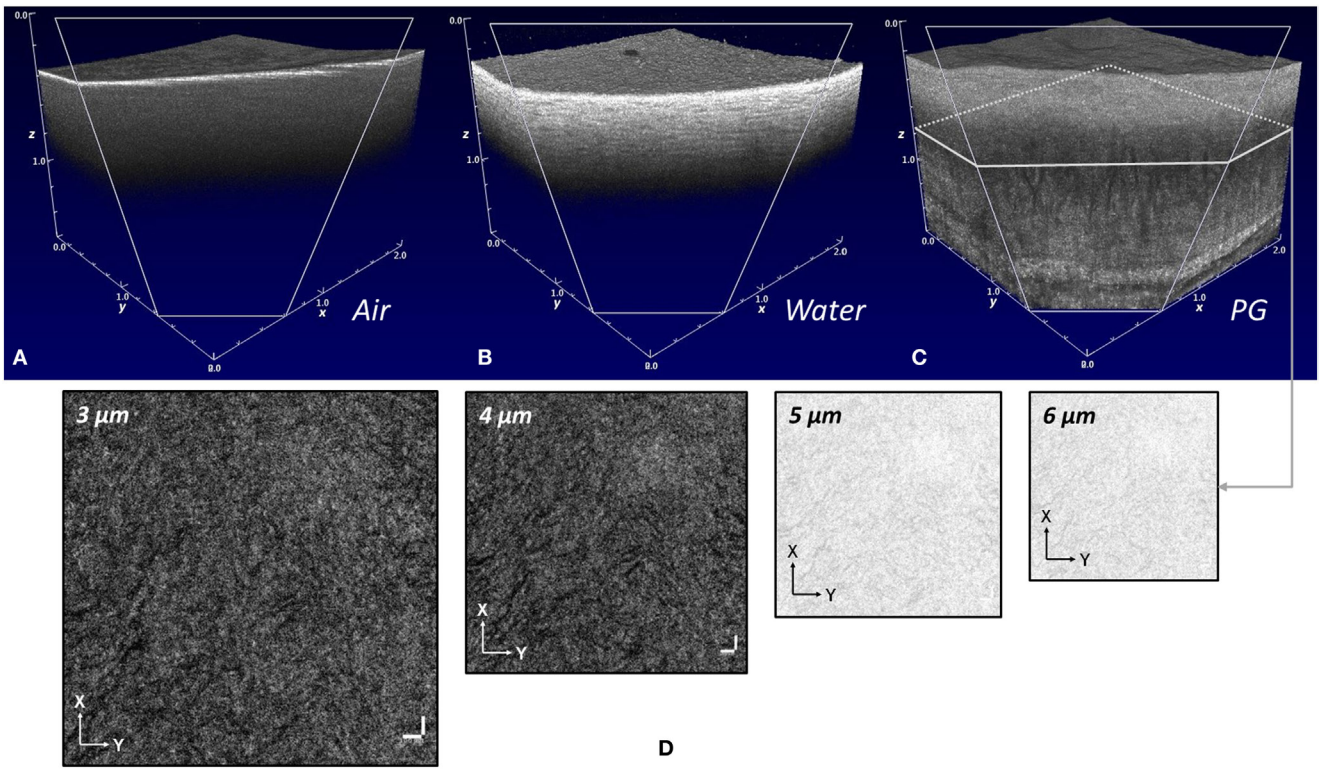

FIGURE 3 | Optical coherence tomography (OCT) measurements on porcine aortic tissue with different types of contrast media. **(A)** Using air as contrast media. **(B)** Water as contrast media. **(C)** Osmotically active solution – propylene glycol. **(D)** Definition of the spatial resolution with different pixel sizes (e.g., OCT image corresponding to the aortic media layer).

TABLE 3 | Average values derived from full-field measurements for the rigid body translation test.

Optical coherence tomography pixel size study cases (μm)	Target displacement (mm)	Full-field measurements						
		Displacements (mm)				Strain components (%)		
		u	±SD	v	±SD	E_{xx}	E_{yy}	E_{xy}
3	0.02	0.023	±0.003	0.002	±0.002	−0.005	0.085	0.001
	0.04	0.049	±0.005	0.004	±0.002	0.099	0.189	0.007
	0.06	0.073	±0.006	0.005	±0.003	0.206	0.260	0.039
4	0.02	0.024	±0.003	0.001	±0.001	0.157	0.038	0.034
	0.04	0.047	±0.005	0.002	±0.002	0.096	0.055	0.024
	0.06	0.072	±0.007	0.002	±0.002	0.120	0.105	0.023
5	0.02	0.023	±0.004	0.002	±0.002	−0.095	0.132	0.006
	0.04	0.054	±0.008	0.004	±0.003	−0.159	0.200	−0.008
	0.06	0.075	±0.012	0.004	±0.004	−0.418	0.242	0.009
6	0.02	0.022	±0.003	0.0002	±0.001	−0.053	0.013	0.002
	0.04	0.043	±0.005	0.0004	±0.002	−0.140	0.022	−0.001
	0.06	0.065	±0.008	0.0005	±0.002	−0.323	0.020	−0.001

the displacement was applied along the *Y*-axis. For all the loading stages, displacement maps were evaluated using the Davis® software (**Figure 6**). The vector directions and the displacement gradients showed trends that are characteristics of uniaxial tension. The vector magnitude increased with the loading stages. Artifacts appeared close to the right and to the bottom edges of the FOV; they were caused by a mismatch between the initial FOV and the successive current FOV at each loading stage. These artifacts were filtered out for the further strain reconstructions.

The six components of the Green-Lagrange strain fields are shown in **Figure 7** for the largest deformation (12.64%). The strain fields were reconstructed independently for each layer (intima, media, and adventitia) for comparing their potentially different responses.

As expected, the shear strain components (E_{xy},E_{xz},E_{yz}) were significantly lower than their normal counterparts, see average values in **Table 5**. Regarding the normal strain components (E_{xx},E_{yy},E_{zz}) and the global behavior of the tissue, the reported data were consistent with strain fields commonly expected in uniaxial tension, see **Figure 8**. The E_{yy} values, along the tensile axis, showed a consistent trend with the assigned deformation (**Table 5**). Regarding the Poisson's effects, E_{xx} and E_{zz} reached average absolute strain values of 1.91 and 2.13%, respectively (**Table 5**). The trace of the strain matrix $E_{xx} + E_{yy} + E_{zz}$, which can be related to the volume change in infinitesimal deformations, constantly increases with the tensile loading and reaches 8% for the final stage. This indicates a significant volume increase, which is not characteristic of the incompressible behavior of soft biological tissue. This must be a consequence of dehydration induced by the immersion in PG.

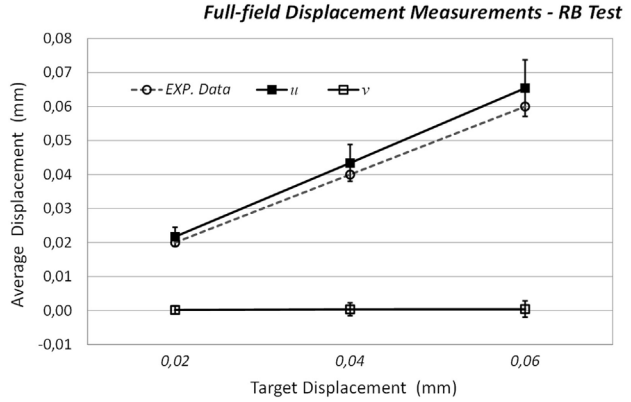

FIGURE 4 | Full-field displacement measurements defined for the rigid body translation test.

TABLE 4 | Definition of optical coherence tomography (OCT) parameters for the stress-relaxation uniaxial tensile test.

OCT parameters	Stress-relaxation uniaxial tensile test		
	x	*y*	*z*
Size (pixel)	333	500	940
Pixel size (μm)	6.0	6.0	2.45
A-scan – reference intensity (%)		76.45	
Acquisition time (min)		2.46	

The OCT-DVC measured strain fields also revealed major heterogeneities among the different layers of the aorta. Whereas E_{yy} was rather uniform, E_{xx} and E_{zz} showed a complex behavior with large compressive values close to the borders (intima and adventitia), see **Figure 8**. The intima and the adventitia showed the major Poisson's effect on the mechanical behavior in E_{zz} with corresponding strains of 4.58 and 3.80%, respectively (which are values expected for a nearly incompressible material). Conversely, the media layer reported a very small Poisson's effect (strain value of 1.28%) (**Table 5**). We hypothesize that the swelling effect of the tissue and the osmotic stress generated by the OCAs have a major effect to account for the heterogeneities in the strain distribution.

DISCUSSION

OCT-DVC Is a Suitable Technique to Characterize the Biomechanical Behavior of Porcine Aortas *In Vitro*

To characterize the uniaxial tensile response across the whole thickness of a porcine aorta, an OCT high-contrast acquisition was required. With the tissue clearing technique, and using the PG as OCA, the scattering properties were improved. The depth

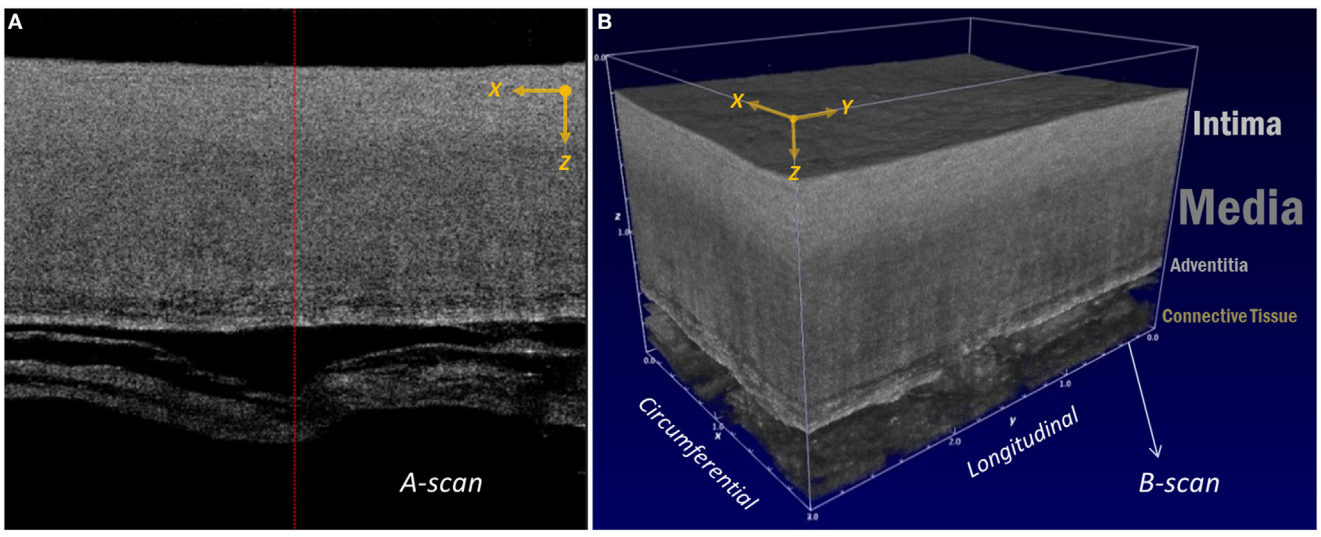

FIGURE 5 | Whole-thickness measurement using the tissue clearing technique and the stress-relaxation uniaxial tensile test. **(A)** Typical A-scan. **(B)** three-dimensional image sequence acquisition.

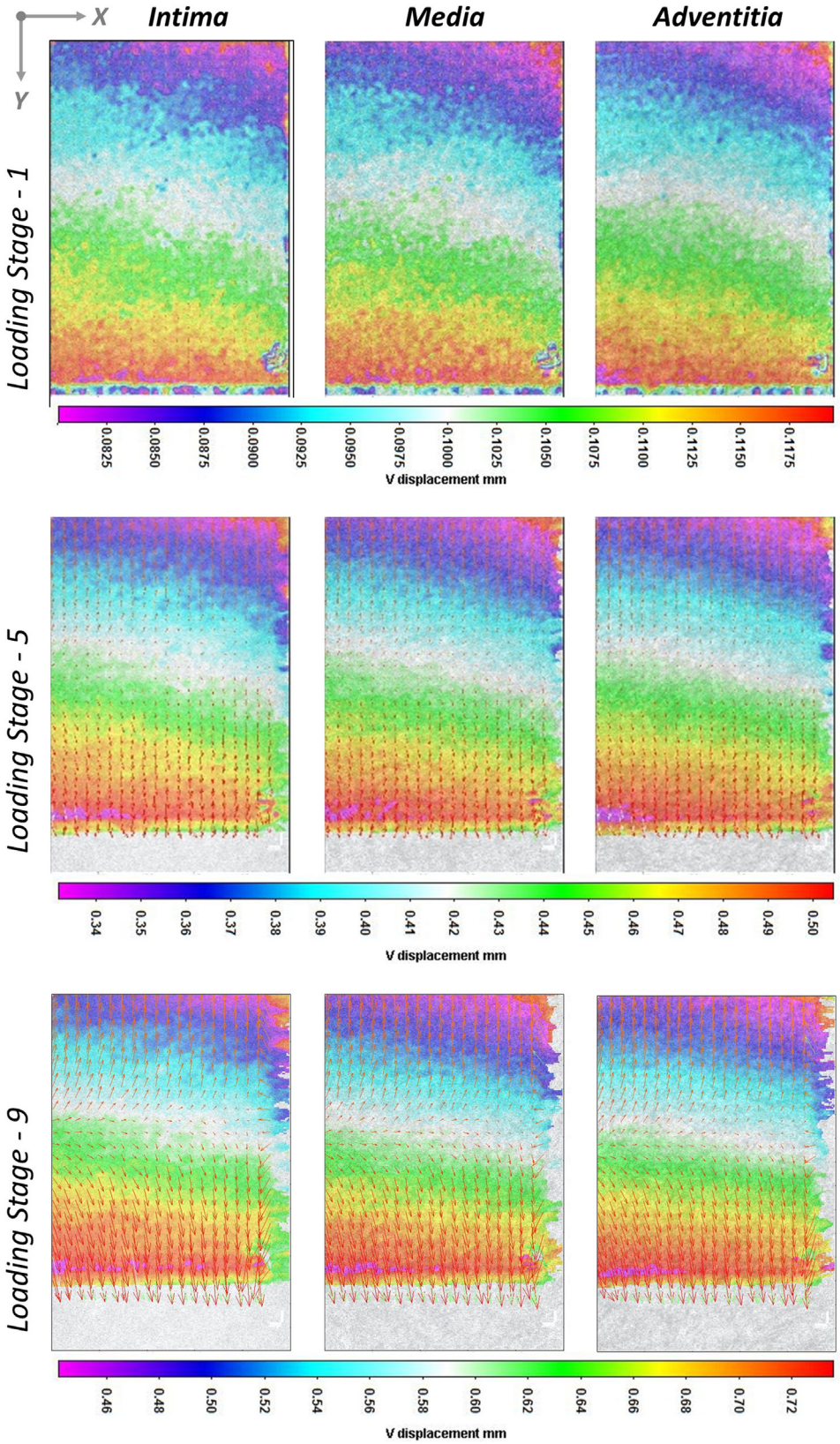

FIGURE 6 | Displacement maps obtained at different aortic layers (intima, media, and adventitia) and for different loading stages. The backgrounds represent the displacement measurements and the vectors display the displacements relative to average.

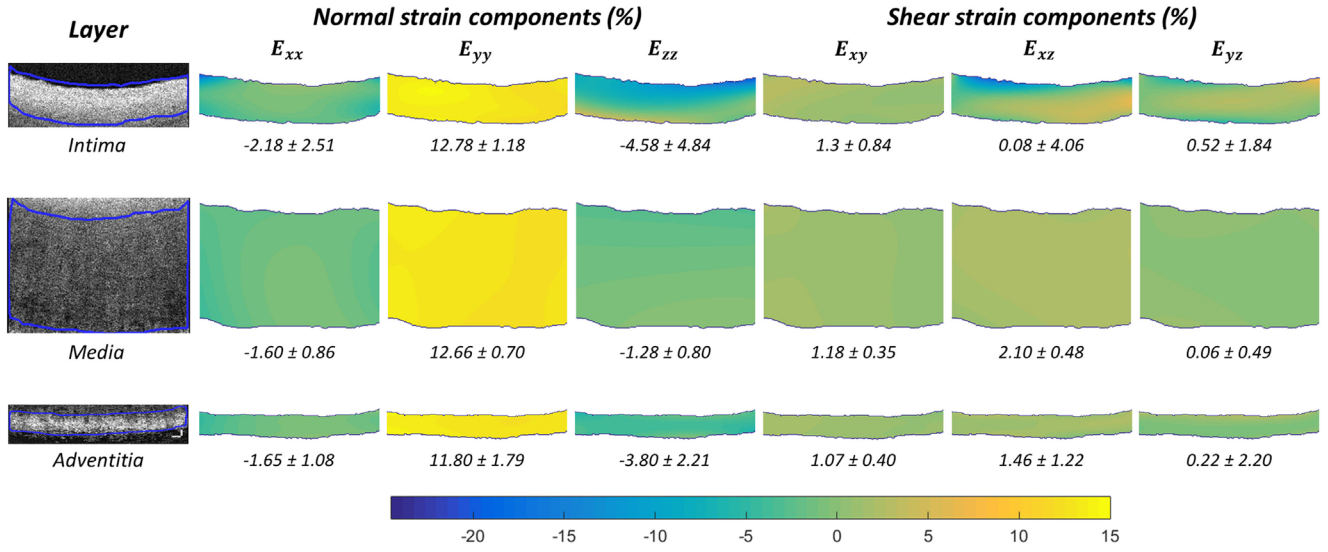

FIGURE 7 | Measured fields of Green-Lagrange strain components for the maximum load in the uniaxial tensile test. The slice corresponds to the field of view middle zone, respect to the *Y*-axis (optical coherence tomography B-scans).

capability and the contrast of the images allowed measurements across the full thickness.

Considering the large number of acquisition and processing parameters, the OCT-DVC method must be preliminarily optimized according to the optical properties (contrast and spatial resolution), and the correlation parameters (optimal sub-volume voxel size). Fu et al. applied a stationary and RB test to characterize the OCT-DVC method. The authors defined four different subset sizes to evaluate the spatial resolution and the uncertainties variation. The analysis focused on determining the minimum strain and its corresponding deviation (Fu et al., 2013). However, in the present work, subset size is minimized with a multiscale correlation approach; consequently the spatial resolution – in voxels – is optimized (eight voxels). Ideal correlation conditions were reached directly in the 3D OCT image sequence acquisition (different voxel sizes) and using a RB test. The voxel size was used as a key parameter to reduce the uncertainties of the full-field measurements. The 6 μm voxel size showed the best compromise. A speckle-like noise due to diffraction is visible with high optical resolution: this noise being unstable during loading, it increases the noise on displacement. Increasing the pixel size averages this noise and makes it disappear. Of course, this operation should not average the tissue structure that provides the optical contrast necessary to correlation. Additionally, the OCT acquisitions can be affected by pool surfaces and misalignments (Real et al., 2013).

To study the aortic tissue microstructure at different subsurface levels, the spatial resolution needed small voxel sizes (OCT acquisition). The correlation can be validated with histological studies (Wang et al., 2001; Wang, 2002; Wang and Elder, 2002). However, for the mechanical characterization of the aortic tissue it was necessary to increase the voxel size to achieve the full-field measurements with the DVC method. Finally, maximum correlation coefficients (CI), which yield the most reliable measures, are obtained for highest degree of similarity in the gray-level distribution (Fu et al., 2013). For the applied loading stages and the aortic layers, CI was reported between 0.7 and 0.9. As the displacement increases, CI became closer to 0.9.

Global Mechanical Effects of Tissue Clearing

It was known that OCAs can change reversibly the light scattering properties of biological tissues (Larin et al., 2012). Nevertheless, the incidence on the mechanical properties needed is still a topic of important research. Lomas et al. (2003) preserved cadaveric skin allografts with these osmotic solutions. The authors observed that a high glycerol concentration did not generate significant detrimental effects on the structure and the biocompatibility properties of the tissue. However, the use of PG as a preservation agent requires further development (Lomas et al., 2003). Ling et al. (2016) studied the effects on elastic properties in tissues fixed and preserved with a proposed Thiel embalming method (fixed between 0 and 6 months). The elastic modulus remained constant during the first month and small fluctuations only appeared after this period. Water, glycol, and salts are the main components of Thiel embalming fluid (Ling et al., 2016). Yeh and Hirshburg (2006) analyzed the molecular interactions for different OCAs. Nonreactive chemical agents, as glycerol, induced a dissociation of collagen fibrils into microfibrils (collagen Type I). However, the effects were reversible structurally and mechanically. The effects on the mechanical properties have been characterized using stress–strain measurements (Yeh and Hirshburg, 2006). Furthermore, Wells et al. (2006) demonstrated that glycerol is also an effective means for optical clearing (immersed condition). This medium protects cleared tissue by increasing its thermal stability and minimizing the mechanical properties alterations. The

TABLE 5 | Average values derived from full-field measurements for the stress-relaxation uniaxial tensile test.

Force (*N*)	Layer	Full-field strains measurements											
		Normal strain components (%)						Shear strain components (%)					
		E_{xx}	±SD	E_{yy}	±SD	E_{zz}	±SD	E_{xy}	±SD	E_{xz}	±SD	E_{yz}	±SD
0.18	AW	0.25	0.39	1.35	0.23	−0.18	0.20	0.13	0.19	0.24	0.11	−0.01	0.09
	I	0.12	0.55	1.38	0.27	−0.13	0.54	0.15	0.24	0.00	0.62	−0.02	0.35
	M	0.28	0.38	1.35	0.23	−0.23	0.38	0.13	0.16	0.24	0.12	−0.05	0.06
	A	0.25	0.43	1.34	0.20	−0.20	0.38	0.11	0.18	0.20	0.23	0.07	0.28
0.22	AW	0.24	0.43	2.70	0.38	−0.45	0.31	0.25	0.20	0.42	0.22	−0.01	0.14
	I	0.08	0.76	2.75	0.47	−0.51	0.85	0.28	0.29	−0.07	1.07	0.00	0.56
	M	0.26	0.37	2.70	0.37	−0.43	0.58	0.23	0.17	0.46	0.22	−0.07	0.12
	A	0.22	0.47	2.68	0.36	−0.55	0.67	0.22	0.17	0.38	0.29	0.08	0.46
0.24	AW	0.07	0.58	4.04	0.47	−0.74	0.41	0.35	0.22	0.68	0.33	0.01	0.19
	I	−0.13	1.02	4.11	0.56	−0.89	1.37	0.40	0.38	−0.08	1.55	0.05	0.75
	M	0.13	0.45	4.04	0.45	−0.68	0.73	0.33	0.17	0.75	0.29	−0.06	0.17
	A	0.06	0.54	4.02	0.46	−0.89	0.89	0.31	0.18	0.57	0.36	0.10	0.60
0.28	AW	−0.28	0.67	5.43	0.52	−0.99	0.47	0.49	0.28	0.92	0.41	0.02	0.24
	I	−0.52	1.28	5.52	0.69	−1.32	1.90	0.57	0.47	−0.12	2.12	0.17	0.86
	M	−0.23	0.53	5.44	0.49	−0.85	0.84	0.49	0.20	1.05	0.34	−0.04	0.22
	A	−0.25	0.61	5.40	0.51	−1.29	0.97	0.44	0.19	0.82	0.48	0.03	0.74
0.31	AW	−0.65	0.80	6.84	0.59	−1.23	0.53	0.62	0.32	1.10	0.50	0.03	0.28
	I	−0.85	1.33	6.94	0.83	−1.90	2.41	0.69	0.56	−0.03	2.30	0.23	1.17
	M	−0.58	0.61	6.84	0.54	−1.00	0.86	0.61	0.23	1.27	0.37	−0.04	0.27
	A	−0.66	0.79	6.06	1.60	−1.63	1.76	0.57	0.31	0.92	0.76	−0.01	1.31
0.33	AW	−0.88	0.95	8.26	0.66	−1.49	0.65	0.74	0.39	1.31	0.60	0.02	0.32
	I	−1.12	1.66	8.36	0.94	−2.41	2.95	0.86	0.62	0.00	2.74	0.28	1.38
	M	−0.77	0.68	8.25	0.58	−1.13	0.88	0.73	0.25	1.48	0.41	−0.02	0.32
	A	−0.88	0.89	7.41	1.76	−2.20	1.86	0.68	0.38	1.10	1.09	−0.05	1.43
0.35	AW	−1.20	1.14	9.68	0.70	−1.72	0.82	0.86	0.42	1.52	0.71	0.03	0.38
	I	−1.53	2.00	9.78	0.97	−3.14	3.55	0.94	0.69	−0.02	3.36	0.32	1.50
	M	−1.05	0.76	9.69	0.59	−1.20	0.86	0.85	0.28	1.69	0.44	0.00	0.39
	A	−1.16	0.99	8.84	1.78	−2.77	2.16	0.80	0.38	1.28	1.21	−0.11	1.60
0.38	AW	−1.64	1.45	11.16	0.75	−1.95	1.03	1.05	0.43	1.69	0.90	0.05	0.43
	I	−1.92	2.26	11.31	1.06	−3.83	4.13	1.14	0.79	0.19	3.65	0.42	1.68
	M	−1.40	0.77	11.17	0.64	−1.27	0.83	1.02	0.31	1.89	0.46	0.04	0.44
	A	−1.48	1.02	10.33	1.77	−3.22	2.23	0.94	0.38	1.26	1.13	0.07	1.74
0.40	AW	−1.91	1.73	12.64	0.84	−2.13	1.26	1.20	0.49	1.90	1.05	0.06	0.49
	I	−2.18	2.51	12.78	1.18	−4.58	4.84	1.30	0.84	0.08	4.06	0.52	1.84
	M	−1.60	0.86	12.66	0.70	−1.28	0.80	1.18	0.35	2.10	0.48	0.06	0.49
	A	−1.65	1.08	11.80	1.79	−3.80	2.21	1.07	0.40	1.46	1.22	0.22	2.20

AW, aortic wall; I, intima; M, media; A, adventitia.

mechanical changes induced by the glycerol are fully reversible (Wells et al., 2006).

These previous studies needed to be completed by a characterization of the effect of PG effect on the mechanical properties of arteries. For the purpose of the present study, additional experimental tests were considered (immersed stress-relaxation uniaxial tensile tests). Four porcine aortic wall samples were evaluated (41.4 mm × 10 mm × 1.92 ± 0.19 mm). A preconditioning of 5% of deformation was applied followed by 40 min of relaxation. A stress-relaxation ramp was defined with four controlled displacement of 1.4 mm and 30 min of relaxation between each displacement increment. Approximately, 0.18 strain was reached during the test. One sample was tested with the immersion protocol defined in the present work [osmotically active solution of 85% (v/v) PG in PBS]. Once the experiment was completed, the sample was relaxed in PBS (1 h) to recover and preserve the physiological conditions of the tissue (Acosta Santamaría et al., 2013). After that, to evaluate the structurally and mechanically reversible effect of the OCA, an additional test was carried out using the same sample but a different immersion media (PBS). The immersion order was inverted for the second sample, first PBS and subsequently the PG (PBS-PG). Finally, two control samples were tested on air (without immersion media). To avoid tissue dehydration during these tests, an ultrasonic humidifier was used (Peña et al., 2015). For each experiment, the reported forces at the maximum relaxation periods were used to define the stress–strain values (**Figure 9**).

For the control samples, the linear elastic moduli were 0.03 and 0.02 MPa (control 1 and control 2, respectively). Considering the exposed immersion cases, and with respect

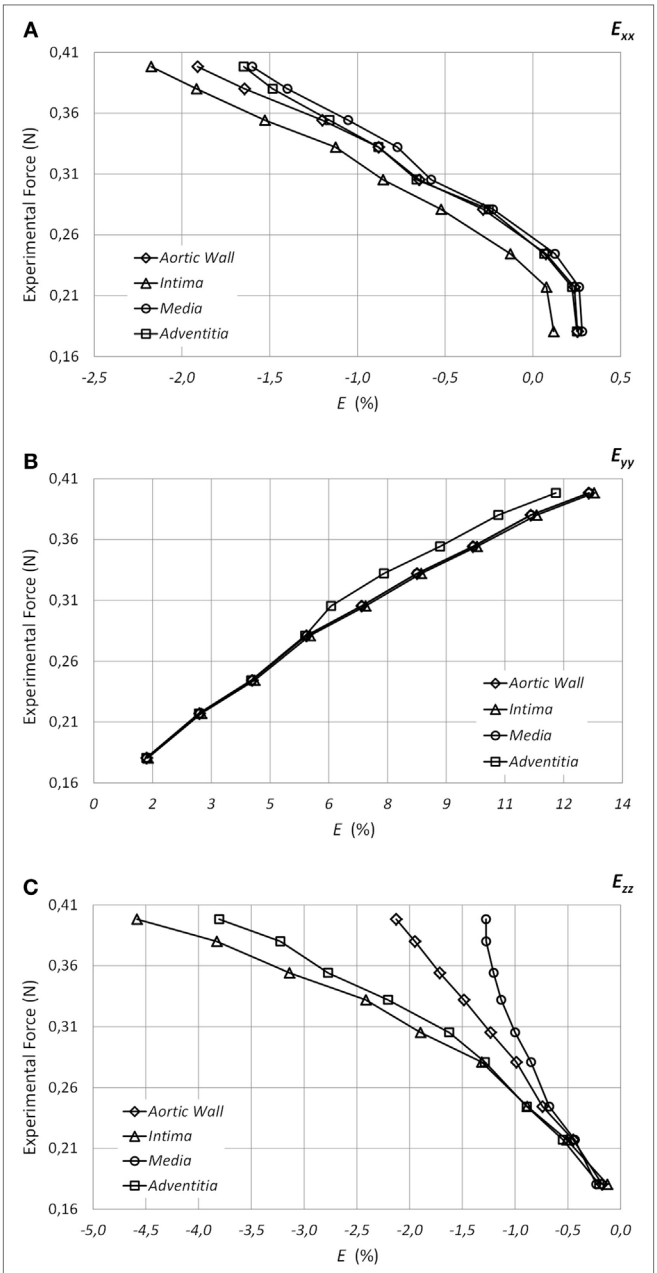

FIGURE 8 | Evolution of the average values of each normal strain components [**(A)** E_{xx}, **(B)** E_{yy}, and **(C)** E_{zz}] across the whole aorta and across each aortic layer (intima, media, and adventitia).

to the control samples, the PG increases the elastic modulus of the tissue. The elastic modulus MV was increased by a factor of 0.13 (PG = 0.183 MPa). Also, the modulus was increased by 28.70%, using the PBS as an immersion media (PBS = 0.032 MPa). The reversible effect was demonstrated by evaluating the mechanical behavior of the tissue immersed in different media (PG and PBS) (**Figure 9**). In addition, the stress-relaxation test was applied to evaluate the viscoelastic behavior of the tissue. Wang et al. (2016) reported for the aortic tissue the dynamic elastic modulus (0.039 ± 0.01 MPa). This result validates the reported data for the controls and the samples immersed in PBS.

The obtained results open a discussion on the incidence of the hyperosmotic agents in the mechanical properties of the evaluated tissue. For collagen-based tissues, the relationship between the OCAs and the tissue swelling effect could involve a change in the supramolecular structure. Additionally, due to the induction of osmotic stress, a high concentration of the hyperosmotic agents can induce cell apoptosis, local hemostasis, and/or tissue necrosis (Larin et al., 2012). Therefore, it is relevant to define an appropriate OCA concentration to minimize its impact on the tissue structure and define optical scattering properties (Sudheendran et al., 2011).

Local Mechanical Effects of Tissue Clearing Revealed by OCT-DVC

The full-field measurements performed on the aortic wall immersed in PG highlight the complexity of the different effects induced by tissue clearing. The biomechanical behavior of arterial walls is known to be complex and anisotropic due to its fibrous nature (elastin and collagen) and due to its layered structure (intima, media, and adventitia). An original aspect of the local mechanical behavior revealed by OCT-DVC was the heterogeneity of Poisson's effects across the thickness. The intima and the adventitia showed the major Poisson's effect on the mechanical behavior in E_{zz} with corresponding strains of 4.58 and 3.80%, respectively (which are values expected for a nearly incompressible material). Conversely, the media layer reported a very small Poisson's effect (strain value of 1.28%).

Measuring strains in the through-thickness direction is something completely original for arteries tested *in vitro*. Peña et al. (2015) reported the thickness ratios (layer thickness to total wall thickness) for the adventitia, media, and intima layers (0.33, 0.50, and 0.15, respectively) of distal porcine aorta. With the clearing technique used in the present work, we could track the thickness variations of each layer under tensile conditions (**Figure 10**). However, tracking thickness variations does not permit to evaluate the transverse strains with enough accuracy, showing that strain measurements obtained with OCT-DVC, as reported in **Table 5**, have a strong potential for characterizing through-thickness deformations in arteries.

Limitations and Future Work

Numerous improvements can still be considered to the proposed methodology and to the characterization of mechanical effects of PG. The FOV may be increased to involve more information of the tissue structure (tracking patterns). Lesions could also be artificially induced in the tissue with enzymes such as collagenase or elastase to study how PG affects independently collagen and/or elastin fibers. Lomas et al. (2003) have already established that PG was compatible with collagenase digestion. Finally, we observed that the effect of PG induced dehydration had a stringer impact on the Poisson's effect of the media layer. Further work should be conducted on how the smooth muscle cells highly present in

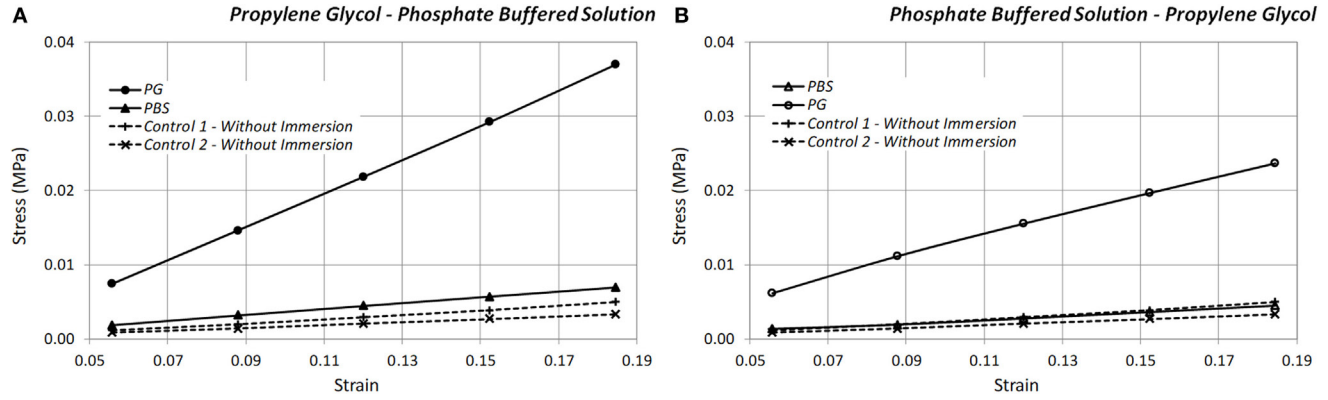

FIGURE 9 | Stress–strain curves under two different immersion protocols and for stress-relaxation uniaxial tensile tests. **(A)** First protocol: immersion in propylene glycol (PG) and a subsequent immersion in phosphate buffered saline (PBS). **(B)** Second protocol: immersion in PBS and a subsequent immersion in PG.

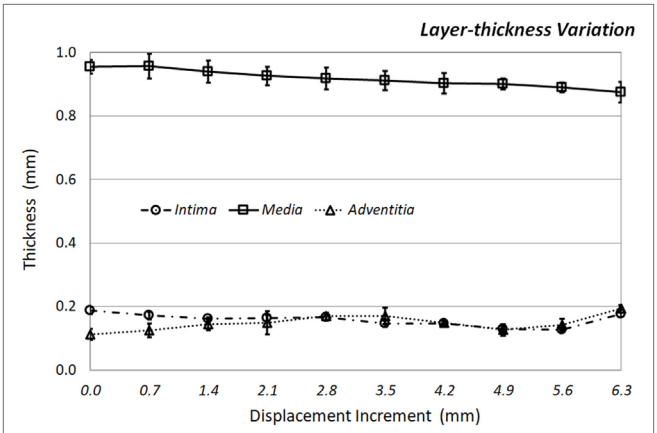

FIGURE 10 | Aortic layer-thickness variation during the uniaxial tensile test immersed in propylene glycol.

the media layer are affected by PG immersion for a better understanding of these effects.

CONCLUSION

In this paper, we have developed and evaluated a novel methodology to characterize the mechanical response of porcine or human aortas *in vitro* at different sub-surface levels and with a sub-millimeter spatial resolution. The technique relies on OCT-DVC and requires the use of a tissue clearing agent, namely propylene glycol. Tissue dehydration caused by immersion in propylene glycol induced interesting mechanical effects revealed by OCT-DVC, such as a heterogeneous Poisson's effect across the layers of the aorta. It is still necessary to understand the effect of the immersion on the mechanical behavior of major components of the tissue such as elastin, collagen, and smooth muscle cells for potential future applications of the methodology.

ETHICS STATEMENT

The present study used animal tissue supplied by the Veterinary School of Lyon (Institut Claude Bourgelat – Investigation Pré-Clinique, Biomedicale et Analytique – http://icbl.vetagro-sup.fr/) which performed the excision. The animals were sacrificed for the purpose of other studies, and the porcine aortic wall was donated for the goal of the present work.

AUTHOR CONTRIBUTIONS

All the authors were fully involved in the study and preparation of the manuscript. All the authors have made substantial contributions to all of the following: (1) the conception and design of the study, acquisition of data, analysis, and interpretation of data, (2) revising the article critically for important intellectual content, and (3) final approval of the version to be submitted.

ACKNOWLEDGMENTS

The authors are grateful to the European Research Council for grant ERC-2014-CoG BIOLOCHANICS.

REFERENCES

Acosta Santamaría, V. A., García Aznar, J. M., Ochoa, I., and Doblare, M. (2013). Effect of sample pre-contact on the experimental evaluation of cartilage mechanical properties. *Exp. Mech.* 53, 911–917. doi:10.1007/s11340-012-9698-x

Alibhai,A.Y.,Moult,E.M.,Shahzad,R.,Rebhun,C.B.,Moreira-Neto,C.,McGowan,M., et al. (2017). Quantifying microvascular changes using OCT angiography in diabetic eyes without clinical evidence of retinopathy. *Ophthalmol. Retin.* doi:10.1016/j.oret.2017.09.011

Boppart, S. A., Herrmann, J., Pitris, C., Stamper, D. L., Brezinski, M. E., and Fujimoto, J. G. (1999). High-resolution optical coherence tomography-guided laser ablation of surgical tissue. *J. Surg. Res.* 82, 275–284. doi:10.1006/jsre.1998.5555

Bouterf, A., Roux, S., Hild, F., Adrien, J., Maire, E., and Meille, S. (2014). Digital volume correlation applied to X-ray tomography images from spherical

indentation tests on lightweight gypsum. *Strain* 50, 444–453. doi:10.1111/str.12101

Brezinski, M. E., Tearney, G. J., Bouma, B. E., Izatt, J. A., Hee, M. R., Swanson, E. A., et al. (1996). Optical coherence tomography for optical biopsy. *Circulation* 93, 1206–1213. doi:10.1161/01.CIR.93.6.1206

Choma, M. A., Sarunic, M. V., Yang, C., and Izatt, J. (2003). Sensitivity advantage of swept source and Fourier domain optical coherence tomography. *Opt. Express* 11, 2183–2189. doi:10.1364/OE.11.002183

Dao Luong, M. N., Shimada, Y., Turkistani, A., Tagami, J., Sumi, Y., and Sadr, A. (2016). Fractography of interface after microtensile bond strength test using swept-source optical coherence tomography. *Dent. Mater.* 32, 862–869. doi:10.1016/j.dental.2016.03.019

Fu, J., Pierron, F., and Ruiz, P. D. (2013). Elastic stiffness characterization using three-dimensional full-field deformation obtained with optical coherence tomography and digital volume correlation. *J. Biomed. Opt.* 18, 121512. doi:10.1117/1.JBO.18.12.121512

Genovese, K., and Humphrey, J. D. (2015). Multimodal optical measurement in vitro of surface deformations and wall thickness of the pressurized aortic arch. *J. Biomed. Opt.* 20, 046005. doi:10.1117/1.JBO.20.4.046005

Gillard, F., Boardman, R., Mavrogordato, M., Hollis, D., Sinclair, I., Pierron, F., et al. (2014). The application of digital volume correlation (DVC) to study the microstructural behaviour of trabecular bone during compression. *J. Mech. Behav. Biomed. Mater.* 29, 480–499. doi:10.1016/j.jmbbm.2013.09.014

Hild, F., Roux, S., Bernard, D., Hauss, G., and Rebai, M. (2013). "On the use of 3D images and 3D displacement measurements for the analysis of damage mechanisms in concrete-like materials," in *8th International Conference on Fracture Mechanics of Concrete and Concrete Structures*, Toledo.

Huang, Y.-P., Zheng, Y.-P., Wang, S.-Z., Chen, Z.-P., Huang, Q.-H., and He, Y.-H. (2009). An optical coherence tomography (OCT)-based air jet indentation system for measuring the mechanical properties of soft tissues. *Meas. Sci. Technol.* 20, 1–11. doi:10.1088/0957-0233/20/1/015805

Hussein, A. I., Barbone, P. E., and Morgan, E. F. (2012). Digital volume correlation for study of the mechanics of whole bones. *Procedia IUTAM* 4, 116–125. doi:10.1016/j.piutam.2012.05.013

Jia, Y., Bailey, S. T., Hwang, T. S., McClintic, S. M., Gao, S. S., Pennesi, M. E., et al. (2015). Quantitative optical coherence tomography angiography of vascular abnormalities in the living human eye. *Proc. Natl. Acad. Sci. U.S.A.* 112, E2395–E2402. doi:10.1073/pnas.1500185112

Keyes, S. D., Gillard, F., Soper, N., Mavrogordato, M. N., Sinclair, I., and Roose, T. (2016). Mapping soil deformation around plant roots using in vivo 4D X-ray computed tomography and digital volume correlation. *J. Biomech.* 49, 1802–1811. doi:10.1016/j.jbiomech.2016.04.023

Khan, M. H., Choi, B., Chess, S., Kelly, K. M., McCullough, J., and Nelson, J. S. (2004). Optical clearing of in vivo human skin: implications for light-based diagnostic imaging and therapeutics. *Lasers Surg. Med.* 34, 83–85. doi:10.1002/lsm.20014

Korhonen, R. K., Laasanen, M. S., Töyräs, J., Rieppo, J., Hirvonen, J., Helminen, H. J., et al. (2002). Comparison of the equilibrium response of articular cartilage in unconfined compression, confined compression and indentation. *J. Biomech.* 35, 903–909. doi:10.1016/S0021-9290(02)00052-0

Larin, K. V., Ghosn, M. G., Bashkatov, A. N., Genina, E. A., Trunina, N. A., and Tuchin, V. V. (2012). Optical clearing for OCT image enhancement and in-depth monitoring of molecular diffusion. *IEEE J. Sel. Top. Quantum Electron.* 18, 1244–1259. doi:10.1109/JSTQE.2011.2181991

Larina, I. V., Carbajal, E. F., Tuchin, V. V., Dickinson, M. E., and Larin, K. V. (2008). Enhanced OCT imaging of embryonic tissue with optical clearing. *Laser Phys. Lett.* 5, 476–479. doi:10.1002/lapl.200810019

Leclerc, H., Périé, J.-N., Roux, S., and Hild, F. (2011). Voxel-scale digital volume correlation. *Soc. Exp. Mech.* 51, 479–490. doi:10.1007/s11340-010-9407-6

Li, C., Guan, G., Reif, R., Huang, Z., and Wang, R. K. (2012). Determining elastic properties of skin by measuring surface waves from an impulse mechanical stimulus using phase-sensitive optical coherence tomography. *J. R. Soc. Interface* 9, 831–841. doi:10.1098/rsif.2011.0583

Liba, O., SoRelle, E. D., Sen, D., and de la Zerda, A. (2016). Contrast-enhanced optical coherence tomography with picomolar sensitivity for functional in vivo imaging. *Sci. Rep.* 6, 23337. doi:10.1038/srep23337

Ling, Y., Li, C., Feng, K., Duncan, R., Eisma, R., Huang, Z., et al. (2016). Effects of fixation and preservation on tissue elastic properties measured by quantitative optical coherence elastography (OCE). *J. Biomech.* 49, 1009–1015. doi:10.1016/j.jbiomech.2016.02.013

Liu, L., and Morgan, E. F. (2007). Accuracy and precision of digital volume correlation in quantifying displacements and strains in trabecular bone. *J. Biomech.* 40, 3516–3520. doi:10.1016/j.jbiomech.2007.04.019

Lomas, R. J., Cruse-Sawyer, J. E., Simpson, C., Ingham, E., Bojar, R., and Kearney, J. N. (2003). Assessment of the biological properties of human split skin allografts disinfected with peracetic acid and preserved in glycerol. *Burns* 29, 515–525. doi:10.1016/S0305-4179(03)00137-2

Madi, K., Tozzi, G., Zhang, Q. H., Tong, J., Cossey, A., Au, A., et al. (2013). Computation of full-field displacements in a scaffold implant using digital volume correlation and finite element analysis. *Med. Eng. Phys.* 35, 1298–1312. doi:10.1016/j.medengphy.2013.02.001

Mahdian, M., Salehi, H. S., Lurie, A. G., Yadav, S., and Tadinada, A. (2016). Tissue characterization using optical coherence tomography and cone beam computed tomography: a comparative pilot study. *Oral Surg. Oral Med. Oral Pathol. Oral Radiol.* 122, 98–103. doi:10.1016/j.oooo.2016.03.021

Matsumoto, T., Fukui, T., Tanaka, T., Ikuta, N., Ohashi, T., Kumagai, K., et al. (2009). Biaxial tensile properties of thoracic aortic aneurysm tissues. *J. Biomech. Sci. Eng.* 4, 518–529. doi:10.1299/jbse.4.518

Nebelung, S., Brill, N., Müller, F., Tingart, M., Pufe, T., Merhof, D., et al. (2016). Towards optical coherence tomography-based elastographic evaluation of human cartilage. *J. Mech. Behav. Biomed. Mater.* 56, 106–119. doi:10.1016/j.jmbbm.2015.11.025

Palanca, M., Tozzi, G., and Cristofolini, L. (2016). The use of digital image correlation in the biomechanical area: a review. *Int. Biomech.* 3, 1–21. doi:10.1080/23335432.2015.1117395

Pancrazio, J. J., Wang, F., and Kelley, C. A. (2007). Enabling tools for tissue engineering. *Biosens. Bioelectron.* 22, 2803–2811. doi:10.1016/j.bios.2006.12.023

Peña, J. A., Martínez, M. A., and Peña, E. (2015). Layer-specific residual deformations and uniaxial and biaxial mechanical properties of thoracic porcine aorta. *J. Mech. Behav. Biomed. Mater.* 50, 55–69. doi:10.1016/j.jmbbm.2015.05.024

Prati, F., Regar, E., Mintz, G. S., Arbustini, E., Di Mario, C., Jang, I. K., et al. (2010). Expert review document on methodology, terminology, and clinical applications of optical coherence tomography: physical principles, methodology of image acquisition, and clinical application for assessment of coronary arteries and atherosclerosis. *Eur. Heart J.* 31, 401–415. doi:10.1093/eurheartj/ehp433

Proskurin, S. G., and Meglinski, I. V. (2007). Optical coherence tomography imaging depth enhancement by superficial skin optical clearing. *Laser Phys. Lett.* 4, 824–826. doi:10.1002/lapl.200710056

Puhakka, P. H., te Moller, N. C. R., Afara, I. O., Mäkelä, J. T. A., Tiitu, V., Korhonen, R. K., et al. (2015). Estimation of articular cartilage properties using multivariate analysis of optical coherence tomography signal. *Osteoarthr. Cartil.* 23, 2206–2213. doi:10.1016/j.joca.2015.05.034

Real, E., Eguizabal, A., Pontón, A., Díez, M. C., Fernando Val-Bernal, J., Mayorga, M., et al. (2013). Optical coherence tomography assessment of vessel wall degradation in thoracic aortic aneurysms. *J. Biomed. Opt.* 18, 126003. doi:10.1117/1.JBO.18.12.126003

Rogowska, J., Patel, N. A., Fujimoto, J. G., and Brezinski, M. E. (2004). Optical coherence tomographic elastography technique for measuring deformation and strain of atherosclerotic tissues. *Heart* 90, 556–562. doi:10.1136/hrt.2003.016956

Schmitt, J. M., Knüttel, A., Yadlowsky, M., and Eckhaus, M. A. (1994). Optical-coherence tomography of a dense tissue: statistics of attenuation and backscattering. *Phys. Med. Biol.* 39, 1705–1720. doi:10.1088/0031-9155/39/10/013

Shimamura, Y., Murayama, R., Kurokawa, H., Miyazaki, M., Mihata, Y., and Kmaguchi, S. (2011). Influence of tooth-surface hydration conditions on optical coherence-tomography imaging. *J. Dent.* 39, 572–577. doi:10.1016/j.jdent.2011.06.004

Sudheendran, N., Mohamed, M., Ghosn, M. G., Tuchin, V. V., and Larin, K. V. (2011). Assessment of tissue optical clearing as a function of glucose concentration using optical coherence tomography. *J. Innov. Opt. Health Sci.* 3, 169–176. doi:10.1142/S1793545810001039

Trabelsi, O., Davis, F. M., Rodriguez-Matas, J. F., Duprey, A., and Avril, S. (2015). Patient specific stress and rupture analysis of ascending thoracic aneurysms. *J. Biomech.* 48, 1836–1843. doi:10.1016/j.jbiomech.2015.04.035

Tucker-Schwartz, J., and Skala, M. (2012). *Contrast Enhancement in Optical Coherence Tomography*. SPIE Newsroom Biomedical Optics & Medical Imaging, 2–4. doi:10.1117/2.1201212.004626

Tucker-Schwartz, J. M., Meyer, T. A., Patil, C. A., Duvall, C. L., and Skala, M. C. (2012). In vivo photothermal optical coherence tomography of gold nanorod contrast agents. *Biomed. Opt. Exp.* 3, 2881. doi:10.1364/BOE.3.002881

Wang, R. K. (2002). "Tissue clearing as a tool to enhance imaging capability for optical coherence tomography", in *Proc. SPIE 4619, Coherence Domain Optical Methods in Biomedical Science and Clinical Applications VI*. doi:10.1117/12.470494

Wang, R. K., and Elder, J. B. (2002). Propylene glycol as a contrasting agent for optical coherence tomography to image gastrointestinal tissues. *Lasers Surg. Med.* 30, 201–208. doi:10.1002/lsm.10013

Wang, R. K., Xiangqun, X., Tuchin, V. V., Elder, J. B., Xu, X., Tuchin, V. V., et al. (2001). Concurrent enhancement of imaging depth and contrast for optical coherence tomography by hyperosmotic agents. *J. Opt. Soc. Am. B* 18, 948–953. doi:10.1364/JOSAB.18.000948

Wang, Z., Golob, M. J., and Chesler, N. C. (2016). "Viscoelastic properties of cardiovascular tissues," in *Viscoelastic and Viscoplastic Materials* (InTech). doi:10.5772/64169

Wells, P. B., Yeh, A. T., and Humphrey, J. D. (2006). Influence of glycerol on the mechanical reversibility and thermal damage susceptibility of collagenous tissues. *IEEE Trans. Biomed. Eng.* 53, 747–753. doi:10.1109/TBME.2006.870232

Welzel, J. (2001). Optical coherence tomography in dermatology: a review. *Skin Res. Technol.* 7, 1–9. doi:10.1034/j.1600-0846.2001.007001001.x

Williamson, J. P., McLaughlin, R. A., Noffsinger, W. J., James, A. L., Baker, V. A., Curatolo, A., et al. (2011). Elastic properties of the central airways in obstructive lung diseases measured using anatomical optical coherence tomography. *Am. J. Respir. Crit. Care Med.* 183, 612–619. doi:10.1164/rccm.201002-0178OC

Yabushita, H., Bouma, B. E., Houser, S. L., Aretz, H. T., Jang, I. K., Schlendorf, K. H., et al. (2002). Characterization of human atherosclerosis by optical coherence tomography. *Circulation* 106, 1640–1645. doi:10.1161/01.CIR.0000029927.92825.F6

Yang, Y., Bagnaninchi, P. O., Ahearne, M., Wang, R. K., and Liu, K.-K. (2007). A novel optical coherence tomography-based micro-indentation technique for mechanical characterization of hydrogels. *J. R. Soc. Interface* 4, 1169–1173. doi:10.1098/rsif.2007.1044

Yang, Y., Dubois, A., Qin, X., Li, J., El Haj, A., and Wang, R. K. (2006). Investigation of optical coherence tomography as an imaging modality in tissue engineering. *Phys. Med. Biol.* 51, 1649–1659. doi:10.1088/0031-9155/51/7/001

Yeh, A. T., and Hirshburg, J. (2006). Molecular interactions of exogenous chemical agents with collagen – implications for tissue optical clearing. *J. Biomed. Opt.* 11, 14003. doi:10.1117/1.2166381

Zhang, D., Eggleton, C. D., and Arola, D. D. (2002). Evaluating the mechanical behavior of arterial tissue using digital image correlation. *Exp. Mech.* 42, 409–416. doi:10.1007/BF02412146

Conflict of Interest Statement: The authors declare that the research was conducted in the absence of any commercial or financial relationships that could be construed as a potential conflict of interest.

frontiers in Materials

ORIGINAL RESEARCH
published: 16 February 2018
doi: 10.3389/fmats.2018.00006

Trabecular Fracture Zone Might Not Be the Higher Strain Region of the Trabecular Framework

Simone Tassani[1], Martino Pani[2], Jerome Noailly[1] and Miguel Angel Gonzalez Ballester[1,3]*

[1] Barcelona Centre for New Medical Technologies (BCN MedTech), Pompeu Fabra University, Barcelona, Spain, [2] School of Engineering, University of Portsmouth, Portsmouth, United Kingdom, [3] Institució Catalana de Recerca i Estudis Avançats (ICREA), Barcelona, Spain

Trabecular bone fracture is a traumatic and localized event studied worldwide in order to predict it. During the years, researchers focused over the mechanical characterization of the trabecular tissue to understand its mechanics. Several studies pointed out the very local nature of the trabecular failure, finally identifying the fracture zone with the aim to study it separately. The complexity of the three-dimensional trabecular framework and the local nature of the fracture event do not allow the direct evaluation of a single trabecula's behavior within its natural environment. For this reason, micro-Finite Element Modeling has been seen as the best way to investigate this biomechanical issue. Mechanical strain analysis is adopted in the literature for the identification of micro fracture using criteria based on principal strains. However, it was never verified if the fracture zone is actually the zone where principal strains are concentrated. Here, we show how the maximum strain of the tissue might not be directly correlated to the fracture. In the present work, a previously validated technique was used to identify the fracture zone of 10 trabecular specimen mechanically tested in compression and scanned in micro-CT before and after the mechanical test. Before-compression datasets were used to develop 10 micro-FE models were the same boundary conditions of the mechanical test were reproduced. Our results show how the known linear behavior of the trabecular framework might not be directly related to the development of the fracture suggesting other non-linear phenomenon, like buckling or microdamage, as actual cause of the traumatic event. This result might have several implications both in micro-modeling and in clinical applications for the study of fracture related pathology, like osteoporosis.

Keywords: micro-CT, micro-FEM, trabecular bone, fractures, bone, micro strain

OPEN ACCESS

Edited by:
Alberto Corigliano, Politecnico di Milano, Italy

Reviewed by:
Stefano Vidoli, Sapienza Università di Roma, Italy
Enrico Radi, University of Modena and Reggio Emilia, Italy

****Correspondence:***
Simone Tassani
simone.tassani@upf.edu

Specialty section:
This article was submitted to Mechanics of Materials, a section of the journal Frontiers in Materials

Received: *31 August 2017*
Accepted: *25 January 2018*
Published: *16 February 2018*

Citation:
Tassani S, Pani M, Noailly J and Gonzalez Ballester MA (2018) Trabecular Fracture Zone Might Not Be the Higher Strain Region of the Trabecular Framework. Front. Mater. 5:6. doi: 10.3389/fmats.2018.00006

INTRODUCTION

Mechanical characterization of trabecular bone is an issue studied since several years due to its relationship with several musculo-skeletal pathologies (Crane et al., 1990; Aerssens et al., 1997; Silva and Gibson, 1997; Goldring, 2009; Kijowski et al., 2012; Milovanovic et al., 2012; Djuric et al., 2013).

The principal way to investigate trabecular bone biomechanics is the mechanical testing of tissue specimens (Helgason et al., 2008). The most common procedure includes the extraction of the specimens from different anatomical sites, embedment in endcaps to avoid toe-artifacts during the measurement, and finally mechanical test in compression using an axial testing machine. Even if

this introduced procedure is still today considered the golden standard for mechanical studies of trabecular bone behavior, it clearly presents several limitations.

First of all, the test described is a destructive one; therefore, it can only be applied once for each specimen. This limits also the number of measurements that can be taken for each specimen; typically, Young modulus, yield, and ultimate stress. Moreover, these values can be related only to global characteristics of the specimen without any insight of the internal and local behavior of the tissue. This is a strong limitation since the trabecular framework is a complex structure, and its failure passes through local damage of the structure followed by the development of the fracture. In this process, the local morphology of the bone plays a relevant role.

The 3-dimensional morphology of trabecular microstructure can nowadays be investigated by means of micro-tomography (micro-CT). Micro-CT allows visualizing and studying the trabecular framework performing non-destructive analysis. Following this procedure, correlation studies of the framework morphology with the mechanical behavior can be carried out (Ohman et al., 2007; Nazarian et al., 2009). The combination of the two techniques soon showed the importance of trabecular framework heterogeneity in the evaluation of the mechanical behavior of bone. Local analyses were suggested by several authors with different methodologies in order to take into consideration the variability of the structure in analysis (Nazarian et al., 2006; Perilli et al., 2008; Tassani et al., 2010). The study of local morphology leads to the study of the trabecular fracture zone itself, aiming to investigate the specific morphology that could explain the development of the trabecular framework failure. A method for the identification of the trabecular fracture zone was proposed (Tassani et al., 2012) and validated (Tassani and Matsopoulos, 2014). Results again underlined the local and three-dimensional nature of the fracture event identifying full 3D fracture zone having a volumetric broken fraction of about 9% (average). The morphometry identified with this procedure allowed to successfully describe (*a posteriori* classification, 95.5% accuracy) (Tassani and Matsopoulos, 2014) and predict (*a priori* classification, 91.8% AUC) (Korfiatis et al., 2017) the fracture zone of each trabecular specimen.

In this scenario, micro-Finite Element Modeling (micro-FEM) has the potentiality to play an important role to study the local and internal behavior of the trabecular bone. Several works were already presented suggesting different approaches (Pistoia et al., 2002; Nagaraja et al., 2005; Verhulp et al., 2008a; Sidorenko et al., 2011; Zysset et al., 2013).

The most common approach of micro-FEM simulation is probably the linear one. Even if this is clearly valid only in the elastic stress-strain zone and cannot describe the fractures themselves, the resulting values are often used as predictive value of the bone strength as reaction to external loads. Using this technique strain and stresses of the 3D framework can be plotted and used as estimator of the fracture initiation.

Micro-FEM models have been widely used to study the mechanical behavior of trabecular bone at tissue level. Most of the studies reported in the literature adopted linear elastic constitutive law (Hara et al., 2002; Verhulp et al., 2006; Kim et al., 2007; Bevill and Keaveny, 2009; Wolfram et al., 2010; Vilayphiou et al., 2011; Torcasio et al., 2012; Gross et al., 2013; Harrison et al., 2013; Bauer et al., 2014) to assess elastic modulus at tissue level, to retrieve overall mechanical behavior at apparent level or finally to study the strain distribution. A number of non-linear models are reported in the literature, adopting both different constitutive law and failure criteria to try to replicate the force–displacement curve as experimentally measured at apparent level (Niebur et al., 2000; Bayraktar and Keaveny, 2004; Verhulp et al., 2008b; Sanyal et al., 2012; Wolfram et al., 2012; Harrison et al., 2013; Bauer et al., 2014; Baumann et al., 2016). However, there is lack of a clear consensus of the literature over which non-linear approach is the most suitable and reliable in identifying the overall failure in terms of both ultimate strain and loading curve. On the other hand, models based on purely linear elastic constitutive laws have been successfully proposed at both organ level [homogenized CT based models (Schileo et al., 2008; Falcinelli et al., 2014)] and tissue level [micro-CT based models (Pistoia et al., 2002; Hosseini et al., 2017)]: these models adopted a principal strain based failure criteria and identified the failure load by simply scaling the linear model in order to reach the yielding condition in a given portion of the model volume. The idea behind this approach is that fracture is a strain driven mechanical event that can be modeled adopting a maximum principal strain criterion.

Aim of non-linear models was mainly the identification of the mechanical behavior of the bone tissue rather than the prediction of the sites of fracture. It is worth here to mention that for the purposes of the latter aim, an independent method to identify the fracture is required. In many studies, fracture zones are identified by visual inspection over the complex three-dimensional trabecular framework. Consequently, the whole procedure is time-consuming and operator-dependent, possibly inducing a considerable bias in the analysis and, therefore, not applicable to large scale analysis. Damage localization has been proposed by Nagaraja et al. (2005) who studied the occurrence of microdamage events in quasi-static uniaxial compression of trabecular bone using linear elastic micro-CT finite element models and registered histological sections. On the other hand, Hambli (2013) proposed an isotropic micro-FEM coupled to a damage law to predict apparent failure properties of human trabecular bone under quasi-static uniaxial compression. The results were visually validated against the micro-CT images of the same specimen mechanically tested showing good correspondence. The work presented an interesting tool for the description of the fracture propagation leaving an open question: are linear micro-FEM good tools for the identification of fracture regions?

It is clear that micro-FEM cannot describe the propagation of trabecular fracture without the aid of the damage law; nonetheless, the identification of a good correlation between stiffness and bone strength can be considered a reasonable basis to predict the mechanical behavior of the trabecular framework and to identify the initiation of the fracture event.

Aim of the present study is to check whether a correspondence exists between the regions where fracture has been identified and regions where principal strains values are higher in linear finite element models. This correspondence will be validated using a full3D and user-independent automatic technique. In other

words, aim of the study is to verify the consistency of the basic assumption (i.e., principal strain concentration as indicator of bone failure initiation) made by many studies that identified bone fracture by means of principal strain analysis based on linear elastic models.

MATERIALS AND METHODS

This study is partially based on the analysis of data previously collected during the European projects Living Human Digital Library (LHDL; IST-2004-026932) and MOSAIC (PIEF-GA-2009-253924), and none of the authors had access to identifiable patient information. For this reason, an ethics approval for the present study was not required as per institutional and national guidelines and regulations. Micro-CT images were produced by Laboratorio di Tecnologia Medica, Istituto Ortopedico Rizzoli, Bologna, Italy, with the financial support of the EU project LHDL (IST-2004-026932). The authors only had access to anonymized images.

The whole data collection procedure is here briefly summarized. Four femora and four tibiae were obtained from two female cadavers (72 and 78 years old) without skeletal disorders by means of a donor program during the LHDL European project. The samples had been embalmed using the modified Dankmeyer's method (Van Sint Jan and Rooze, 1992; Ohman et al., 2008). Tibiae and femora were cut into slices perpendicular to the longitudinal axis of the bone. The epiphyses were cut into 26-mm slices. A number of cylindrical trabecular specimens, with a diameter of 10 mm, were then extracted (Tassani et al., 2011). All specimens were scanned by means of a micro-CT (model Skyscan 1072, Bruker microCT, Kontich, Belgium) with an isotropic voxel size of 19.5 μm, using a previously published protocol (Perilli et al., 2007a,b). All specimens were loaded to failure (displacement control, strain rate 0.01 s^{-1}, model Mini bionix 858, MTS Systems Corp., Minneapolis, MN, USA). Each specimen was cemented directly onto the testing machine. The free length of each specimen was 20 mm (Ohman et al., 2007; Perilli et al., 2008; Tassani et al., 2010). The same acquisition procedure was performed both before (pre-failure dataset) and after the mechanical testing (post-failure dataset). In each set, the final analyzed volume of interest (VOI) was a cylinder of 991 micro-CT cross sections (slices) equal to 19.3 mm height and 9 mm in diameter (Perilli et al., 2008). A fixed threshold was used for the segmentation of trabecular structure from marrow [GV = 143, established in a previous comparison between segmented dataset analyses and histological sections, on trabecular bone specimens adopting the same micro-CT settings (Ohman et al., 2007; Perilli et al., 2007b)]. The fracture zone was identified using a two-step registration method already described in the literature (Tassani et al., 2012; Tassani and Matsopoulos, 2014). The trabecular fracture zone was defined as the region presenting brittle fracture or plastic deformation of at least one trabecula. Briefly, the two steps 3D registration was implemented with the aim to highlight differences between the pre- and post-failure datasets due to mechanical testing. For each slice, each disconnected trabecula lying on the slice in the pre-failure dataset is compared to the same trabecula in the post-failure dataset. Each trabecula of each slice of each dataset was classified as broken if the trabecula of the pre- and post-failure datasets had an overlap inferior of a threshold of 30% [the value of the threshold was identified during the validation study reported in Tassani et al. (2012)]. In order to identify a "full 3D" fracture zone, a morphological 3D dilation procedure was used to calculate a VOI around each broken trabecula. Each VOI was dilated in every direction by 25 px [about 0.50 mm in radius, according to Nazarian et al. (2006)]; thus, an ellipsoidal VOI centered on the broken trabecula was obtained. When trabeculae were closer than 50 px in any direction (25 for each ROI), the VOIs fused creating a single VOI.

In the present study, 10 specimens were selected and for each of them a micro-FEM was developed. The specimens were selected based on the dimension of the identified fracture zone to explore its relation to the deformation of the trabecular framework. Specifically, five specimens with a fracture zone larger than 10% and five with a fracture zone smaller than 1% of total specimen volume were selected.

Micro-FEM Development

A voxel-based Finite Element model was built from segmented micro-CT datasets by direct conversion of voxels in hexahedral Finite Elements. Fixed global threshold was adopted.

Boundary conditions were imposed to replicate the uniaxial compression test: all the nodes lying on the lower surface were fully constrained; all the nodes belongings to the top slices were imposed vertical displacement corresponding to 0.5% of apparent axial strain for the whole specimen and no transverse displacement were allowed.

The material of the trabecular structure was assumed homogeneous and isotropic with a linear elastic constitutive law. Thanks to the linearity of the model and to the purely cinematic nature of the studied problem (essential boundary conditions imposed studying the output strains), a conventional value for the Young's modulus (1 GPa) was considered. Poisson's ratio was assumed 0.3.

The solution of each model was obtained using the fully parallel micro-FE linear solver based on octree ParOSol (Flaig and Arbenz, 2012) using 20 parallel processes on Sciama HPC cluster of the Institute of Cosmology and Gravitation of the University of Portsmouth. Compression and tension principal strains were then computed at the centroid of each voxel.

Principal Strains Analysis: Maximum Strain Identification

To remove artifacts related to single high-strain voxels and in the boundary elements of the rough voxel-based surfaces, an erosion procedure (1 px), followed by a 3D median filter (kernel 3 px × 3 px × 3 px) were applied to all the generated datasets (ImageJ 15.1n Wayne Rasband National Institutes of Health, USA). The new datasets were mapped back on a 256 gray values colormap of a typical 8-bit micro-CT dataset reconstruction.

Maximum strains were identified in both compression and tension datasets as the maximum 5% of strain range in each specimen (95% to maximum strain). For each dataset, all the voxels included in the maximum strain criteria were labeled. Starting from these voxels, a procedure similar to the one described for

the identification of the full 3D fracture zone, was applied for the identification of the maximum strain zone (CtAn, Bruker microCT, Kontich, Belgium).

For each slice, each disconnected trabecula lying on the slice was analyzed. The whole trabecula including the maximum strain pixel was identified as "maximum strain tissue." In order to identify a "full 3D" max strain zone, a morphological 3D dilation procedure was used to calculate a VOI around each max strain trabecula. Each VOI was dilated in every direction by 25 px [about 0.50 mm in radius, according to Nazarian et al. (2006)]; thus an ellipsoidal VOI centered on the broken trabecular was obtained. When trabeculae were closer than 50 px in any direction (25 for each ROI), the VOIs fused creating a single VOI.

Finally, three zones were identified and compared to each other, in each specimen: whole specimen, fracture zone, and maximum strain. The analysis was performed over both compression and tension strains. However, while fracture zone was a constant region, independent of the kind of strain, maximum compression and maximum tension led to the identification of two different regions. Once identified, the maximum strain zones were visually compared to the fracture zone.

Principal Strains Analysis: Comparison of Strains

A two-way ANOVA for repeated measurements was implemented to test the influence of both "within" and "between" factors over the strain distribution. The identified *region* was defined as within factor to analyze since each specimen was compared against itself. The *region* factor presented three categorical levels; whole specimen, fracture zone, and maximum strain zone. The "between" factor was the *kind of stress* generated with two levels defined; compression and tension. *Kind of stress* was not a within factor since the regions of tension and compression were different in each specimen. A *post hoc* test with Bonferroni correction for multiple testing was used to evaluate the statistical differences among the three levels of the *region* factor.

The whole statistical model was used to evaluate the effect of the two defined factors and their interaction on the absolute values of the strains.

RESULTS

Global strains showed to be generally homogenous with fluctuations given by the complexity of the trabecular framework (**Figure 1**). Fracture regions and maximum strain regions, both compression and tension, are shown in **Figure 2** for low fracture volume specimen and in **Figure 3** for high fracture volume specimens. The location of the maximum strain regions show no direct relation to the fracture zone.

The strain distributions in the whole specimen and in the fracture region shown to be statistically different from the strain in the maximum strain region. Strain in the fracture region was also found higher than the average strain of the whole specimen but lower than the ones in the maximum strain region. Average compression and tension values for each region and kind of strain are shown in **Figure 4**. No interaction between region and type of strain was detected (p-value = 0.056, Greenhouse–Geisser sphericity correction).

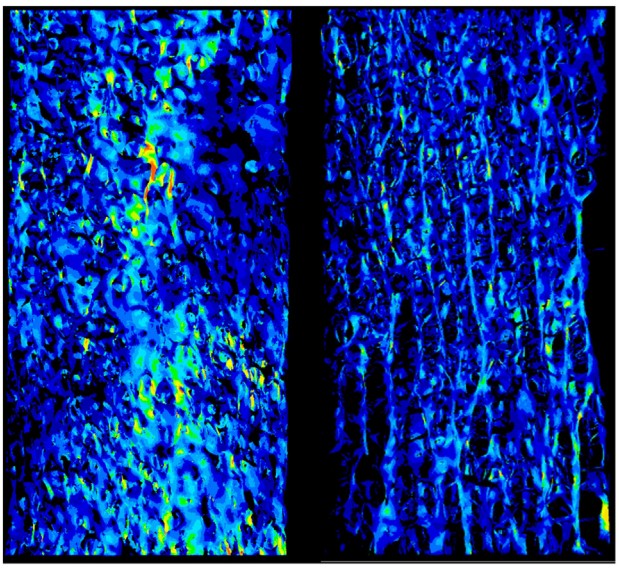

FIGURE 1 | The strain field of two specimens is shown. It appears to be essentially homogeneous with punctual strain variations related to the complexity to the geometry.

There seems to be no relation between the dimension of the fracture zone and the dimension and distribution of the maximum strain regions.

DISCUSSION

The presented work led to two main results. First, the visual analysis underlined the local nature of maximum strain. **Figure 1** shows how the distribution of the strain is essentially homogeneous. Since the numerical model assumes the material to be homogeneous (a strong assumption widely adopted in the high majority of such kind of models), strain fluctuations are uniquely related to the complexity to the geometry. **Figures 2** and **3** are collecting fracture and maximum strain zones for all the specimens. It is easy to see how the maximum strain regions identified by the proposed criterion, both in compression and in tension, are extremely localized, very often related to few, or even one single trabecula. In the same figures, the detail of the strain distribution underline that often the trabecula showing maximum strain is isolated. This result could support the hypothesis that maximum strain can identify the specific point in which the fracture can start and propagate. However, the same visual results allow to compare maximum strain zones to the fracture zone of the same specimen. The identification of the fracture zone was automatic and completely described the 3D framework. This approach allowed to fully compare the distribution of the strain to the fracture zone of several specimens, without the limitation of visual identification. The reported relation appears to be poor. In more than half of the cases, the maximum strain zones appeared unrelated to the identified fracture zone, therefore, rejecting the

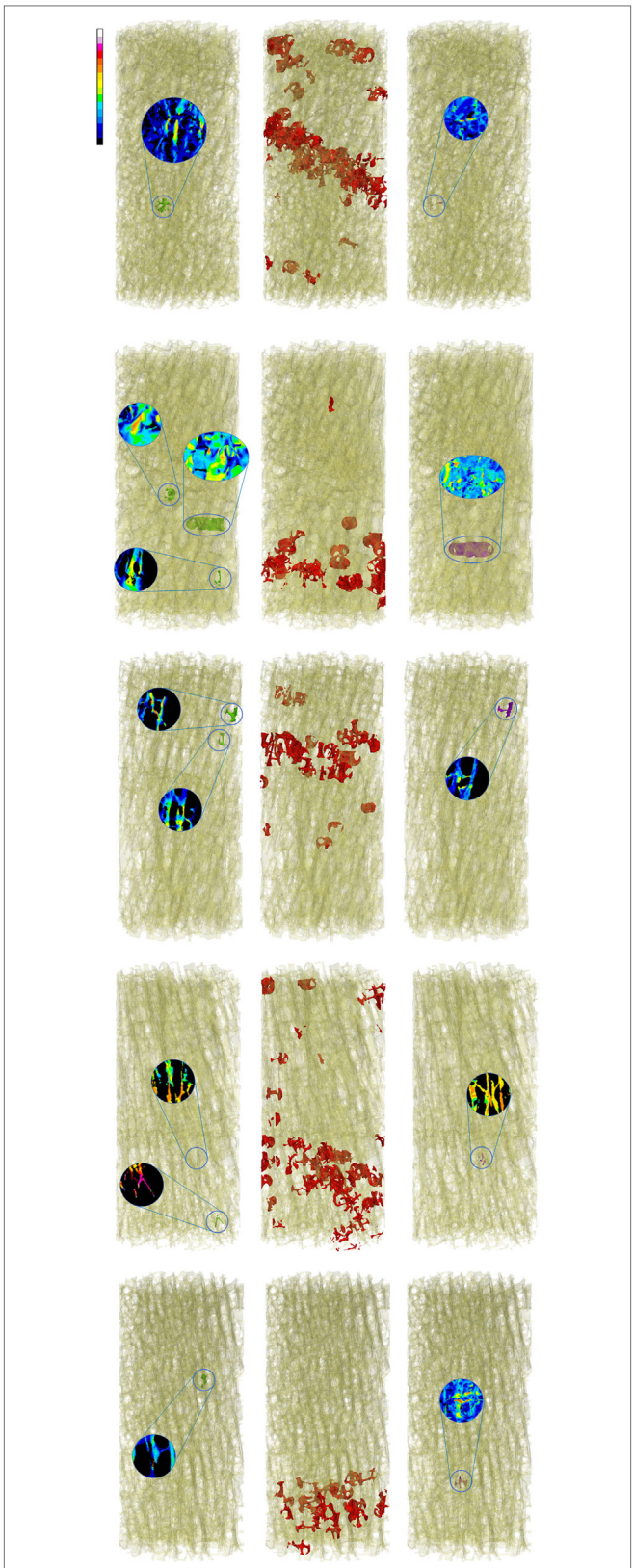

FIGURE 2 | Zones of maximum compression (left) and maximum tension (right), are reported in comparison to the fracture zone (center) for the five low fracture volume specimens.

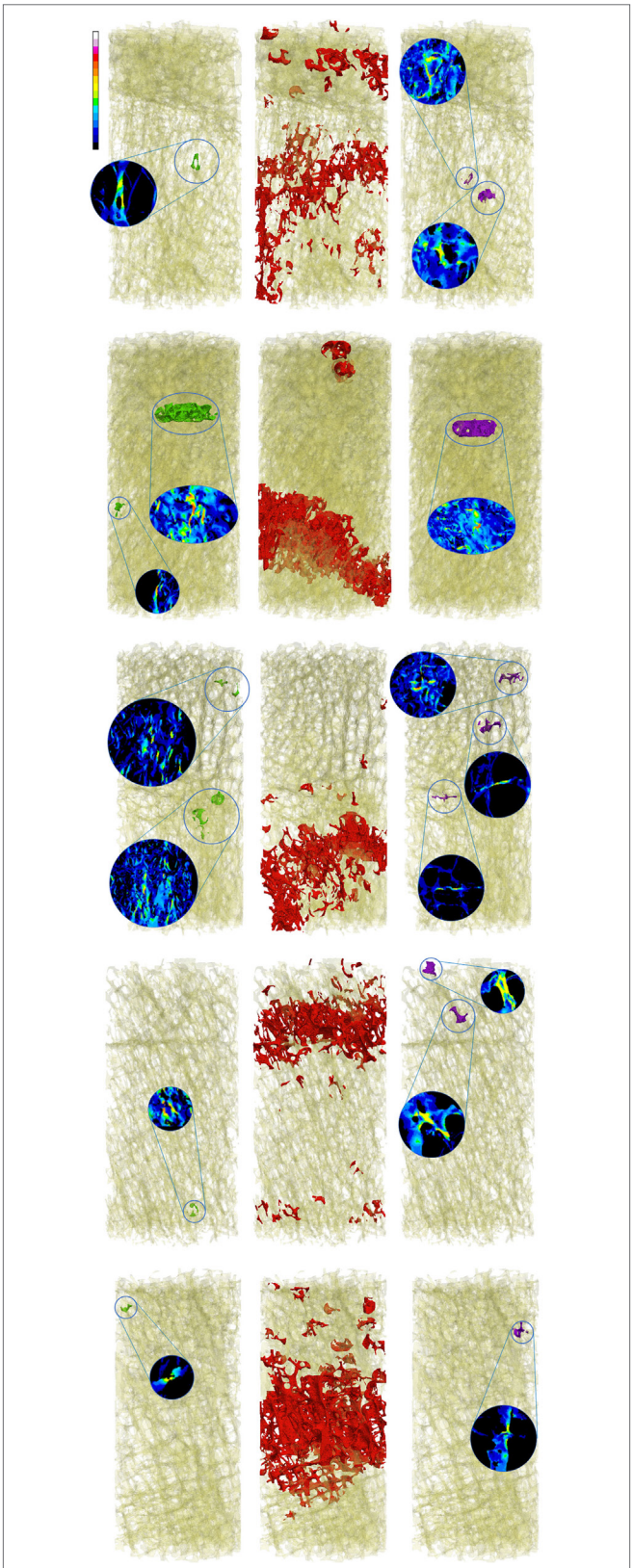

FIGURE 3 | Zones of maximum compression (left), fracture (center), and maximum tension (right) are reported in comparison to the fracture zone (center) for the five high fracture volume specimens.

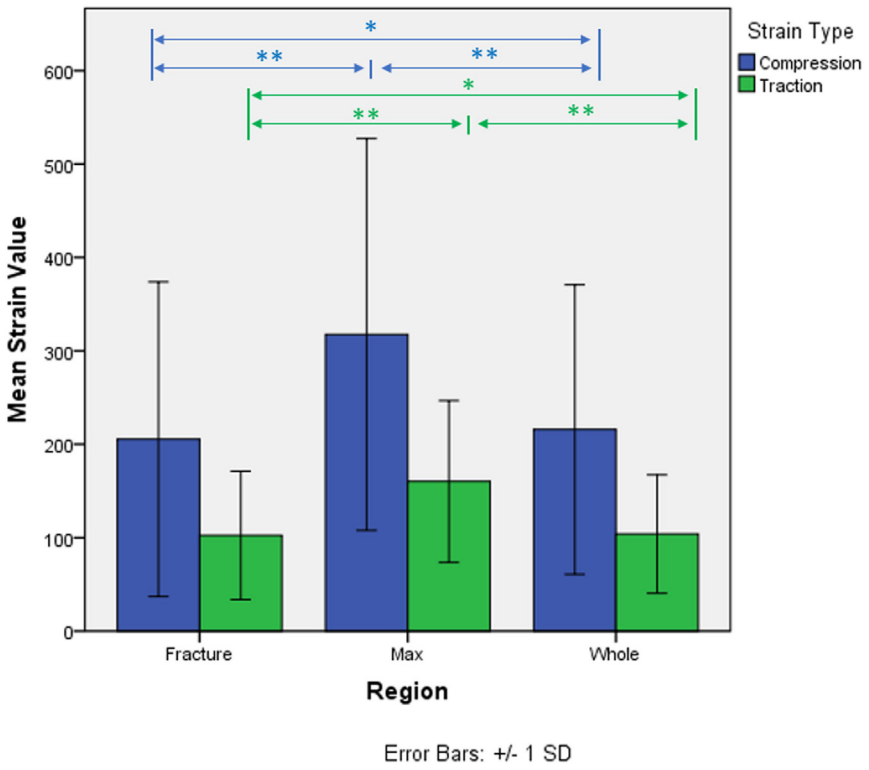

FIGURE 4 | Micro-strains in compression and traction in the three identified regions of analysis. *p-value < 0.05. **p-value < 0.005.

hypothesis that maximum strain can identify the initiation point of the fracture. Maximum strain regions seem also unrelated to the final dimension of the fracture.

Second, the paired analysis showed how in each specimen the maximum strain region, both in compression and in tension, consisted of statistically higher strain, compared to both the fracture region and the average of the whole specimen. Particularly, the strains of the maximum strain region showed to be almost double the ones of the fracture region; 413 ± 211 μstrain max strain region and 256 ± 131 μstrain fracture region in compression, 179 ± 53 μstrain max strain region and 120 ± 50 μstrain fracture region in tension. Again, this result suggests how the whole fracture zone might not develop simply following the laws of higher strain, since the strains localized in the fracture are much lower. On the other hand, fracture regions also showed slightly higher strain compared to the average of the whole specimen (209 ± 83 μstrain compression and 98 ± 29 μstrain tension) letting open the possibility that strain can actually play a role in the development of the fracture. The interaction between the two factors was rejected; however, the p-value was very close to the threshold of 5% (p-value = 0.056). Considering the fact that only 10 specimens were analyzed, the possibility that the structure might behave differently in compression and tension, in relation to the fracture and max strain zone, should be further explored.

After the failure of the first trabecula the work of the whole trabecular framework is far from over. Loads can be redistributed and let the structure strong enough to sustain the global load. If not, compaction of the trabecular bone creates a new shape of the structure that can again sustain the load. Following the concept that the biggest amount of bone can ensure a stronger tissue, bone volume fraction has been used for several years for bone strength prediction (Helgason et al., 2008). Nonetheless, BV/TV was recently suggested to be a poor descriptor (Tassani and Matsopoulos, 2014) and predictor (Korfiatis et al., 2017) of the trabecular fracture zone. The trabecular tissue seems to behave following the distribution of the bone in the elastic region; however, this does not describe the event of the fracture where non-linear events might play an important role. In the same way, maximum strain can describe the elastic behavior of the structure; however, failure of the framework, or even of a single trabecula, cannot be explained by this feature.

From Kopperdahl and Keaveny (1998), non-linear behavior in compression in slender trabeculae is dominated by buckling instead of yielding. At least for lower bone volume fraction, failure seems to be related to buckling occurring in regions of trabeculae aligned with the applied load. On the other hand, Snyder et al. (1991) demonstrated how trabecular slenderness is negatively correlated with bone volume fraction. Müller et al. (1998) observed as in a rod-like architecture failure was initiate by buckling of trabeculae followed by the collapse of the overloaded structure. It is worth to highlight as this collapse can results in a ductile apparent behavior due to individual response of individual trabeculae to buckling in wet condition (Townsend et al., 1975). On the theoretical side, Ramtani and Abdi (2005)

formalized the framework to experimentally assess buckling in plate-like trabeculae, focusing the relevance of this instability also in wider structural elements. These assumptions are supported by the results showed in the literature (Tassani and Matsopoulos, 2014), where BV/TV was shown to be lower and structure model index higher, indicating more rod-like trabeculae, in the fracture zone.

According to Stölken and Gibson (Gibson, 1985; Stölken and Kinney, 2003), buckling might occur in individual trabeculae that are not necessarily the most highly strained ones (especially if highly slender). What is more, Eswaran et al. (2007) highlighted how in trabecular bone initial failure may occur in regions that result different from the regions where subsequent failure is located.

Clearly, non-linear behavior of the trabecular framework can also be related to the heterogeneity of the extracellular matrix (Fantner et al., 2004; Gao, 2006; Viguet-Carrin et al., 2006). Microdamage could accumulate and lead to structure failure. According to Blanchard et al. (2013), plasticity prior to fracture may involve nanoscale processes that in terms depend on the nano-to-micro composition and ultrastructure of bone. In this sense, considering homogeneous elastic modulus might limit the here presented results. However, in previous works the tissue mineral density was proved to be fairly constant in trabecular bone (Tassani et al., 2011), reducing the effect of extracellular matrix heterogeneity, and in more recent studies morphometrical characteristics alone were enough to correctly describe (Tassani and Matsopoulos, 2014) and predict (Korfiatis et al., 2017) in more than 90% of the cases, the trabecular fracture zone. These results suggest that the key to understand the mechanics of trabecular fracture might be more related to the micro-level of the structure than to the nanoscale of the tissue.

Moreover, in a recently published paper, Goff et al. (2015) studied the correlation between microdamage localization and local strains as identified by linear micro-FE models. Even though microdamage appears more likely to occur at the greatest tissue level, they did not identify principal strains as a reliable predictor of microdamage occurrence. What is more, the locations with the greatest tissue strains appeared rarely near site of microdamage. Once again, even if heterogeneity of the nano-structure might play a relevant role in the definition of trabecular failure, principal strains seems to be unrelated even at that scale.

Some limitations must be taken into consideration before to conclude this discussion. First of all, the study takes into consideration only 10 specimens from two donors. Even if the specimens were selected in order to study the variety of the trabecular fracture zone, more specimens might be required in order to have a more complete description. Moreover, the definition of the maximum strain region might be considered somehow arbitrary, even if it was chosen to be consistent with the process for the identification of the fracture region. For convenience of the analysis, a single value per voxel was computed at the centroid instead of using and averaging the values at the integration points. The imposed apparent strain was fixed at only 0.5%. Nonetheless, thanks to the linearity of the model, even if the absolute values of the strains would change, the relative distribution of strain is independent from the imposed apparent strain, and therefore, the identification of the maximum strain region would not change. Because of the proposed linearity, the model lacks the capability to capture geometric and constitutive non-linearities that might alter the strain evolution pattern. Buckling it is an example of non-linearity and is exactly what we pointed out as the most probable origin of collapse mechanism that occurred in all the studied specimens. Non-linear constitutive law might be the key to the description of the trabecular fracture zone. Finally, even though nobody seems to be worried about this point, we acknowledge that results might exhibit some sort of dependency on the segmentation technique implemented, since smaller and slender trabeculae might be reduced or completely disappear if the wrong segmentation is applied.

In conclusion, the present study shows not direct correspondence between the regions where fracture have been identified and regions where strains values are higher. Not only the identified maximum strain regions are extremely small but also often not related to the fracture zone, therefore, excluding the possibility to be directly associated to the initiation zone of the fracture. This output does not corroborate the assumption on which some work reported in the literature based their analyses (i.e., the consistency between strain concentration and fracture initiation, particularly for those models that assumed a linear elastic constitutive law). This "negative" result does not provide further insight to the comprehension of bone mechanic while consolidate the claim that a modeling procedure more complex must be considered when approaching the fracture identification on bony structures. Authors consider their outcomes to be significant mostly for their meaning of stressing open questions, in the belief of the importance of negative results, which are more and more difficult to find in modern literature while they should be much more present (Knight, 2003; Ioannidis, 2005; Fanelli, 2012).

AUTHOR CONTRIBUTIONS

ST and MP were principal investigators and conceived together the main study's aim. ST and JN designed and performed measurements, while MP developed all the micro-FEM models. JN and MB supervised the study. All authors discussed the results and implications, performed the data analysis, and reviewed the manuscript at all stages.

ACKNOWLEDGMENTS

The micro-CT datasets were produced by Laboratorio di Tecnologia Medica, Istituto Ortopedico Rizzoli, Bologna, Italy, with the financial support of the EU project LHDL (IST-2004-026932). This work was partially supported by the Spanish Government (project number RYC—2015-18888) and by Chair QUAES-UPF Computational Technologies for Healthcare.

SUPPLEMENTARY MATERIAL

The Supplementary Material for this article can be found online at http://www.frontiersin.org/articles/10.3389/fmats.2018.00006/full#supplementary-material.

REFERENCES

Aerssens, J., Boonen, S., Joly, J., and Dequeker, J. (1997). Variations in trabecular bone composition with anatomical site and age: potential implications for bone quality assessment. *J. Endocrinol.* 155, 411–421. doi:10.1677/joe.0.1550411

Bauer, J. S., Sidorenko, I., Mueller, D., Baum, T., Issever, A. S., Eckstein, F., et al. (2014). Prediction of bone strength by micro-CT and MDCT-based finite-element-models: how much spatial resolution is needed? *Eur. J. Radiol.* 83, e36–e42. doi:10.1016/j.ejrad.2013.10.024

Baumann, A. P., Shi, X., Roeder, R. K., and Niebur, G. L. (2016). The sensitivity of nonlinear computational models of trabecular bone to tissue level constitutive model. *Comput. Methods Biomech. Biomed. Engin.* 19, 465–473. doi:10.1080/10255842.2015.1041022

Bayraktar, H. H., and Keaveny, T. M. (2004). Mechanisms of uniformity of yield strains for trabecular bone. *J. Biomech.* 37, 1671–1678. doi:10.1016/j.jbiomech.2004.02.045

Bevill, G., and Keaveny, T. M. (2009). Trabecular bone strength predictions using finite element analysis of micro-scale images at limited spatial resolution. *Bone* 44, 579–584. doi:10.1016/j.bone.2008.11.020

Blanchard, R., Dejaco, A., Bongaers, E., and Hellmich, C. (2013). Intravoxel bone micromechanics for microCT-based finite element simulations. *J. Biomech.* 46, 2710–2721. doi:10.1016/j.jbiomech.2013.06.036

Crane, G. J., Fazzalari, N. L., Parkinson, I. H., and Vernon-Roberts, B. (1990). Age-related changes in femoral trabecular bone in arthrosis. *Acta Orthop. Scand.* 61, 421–426. doi:10.3109/17453679008993554

Djuric, M., Zagorac, S., Milovanovic, P., Djonic, D., Nikolic, S., Hahn, M., et al. (2013). Enhanced trabecular micro-architecture of the femoral neck in hip osteoarthritis vs. healthy controls: a micro-computer tomography study in post-menopausal women. *Int. Orthop.* 37, 21–26. doi:10.1007/s00264-012-1713-4

Eswaran, S. K., Gupta, A., and Keaveny, T. M. (2007). Locations of bone tissue at high risk of initial failure during compressive loading of the human vertebral body. *Bone* 41, 733–739. doi:10.1016/j.bone.2007.05.017

Falcinelli, C., Schileo, E., Balistreri, L., Baruffaldi, F., Bordini, B., Viceconti, M., et al. (2014). Multiple loading conditions analysis can improve the association between finite element bone strength estimates and proximal femur fractures: a preliminary study in elderly women. *Bone* 67, 71–80. doi:10.1016/j.bone.2014.06.038

Fanelli, D. (2012). Negative results are disappearing from most disciplines and countries. *Scientometrics* 90, 891–904. doi:10.1007/s11192-011-0494-7

Fantner, G. E., Birkedal, H., Kindt, J. H., Hassenkam, T., Weaver, J. C., Cutroni, J. A., et al. (2004). Influence of the degradation of the organic matrix on the microscopic fracture behavior of trabecular bone. *Bone* 35, 1013–1022. doi:10.1016/j.bone.2004.05.027

Flaig, C., and Arbenz, P. (2012). "A highly scalable matrix-free multigrid solver for μFE analysis based on a pointer-less octree," in *Lecture Notes in Computer Science (Including Subseries Lecture Notes in Artificial Intelligence and Lecture Notes in Bioinformatics)*, Vol. 7116, 498–506. doi:10.1007/978-3-642-29843-1_56

Gao, H. (2006). Application of fracture mechanics concepts to hierarchical biomechanics of bone and bone-like materials. *Int. J. Fract.* 138, 101–137. doi:10.1007/s10704-006-7156-4

Gibson, L. J. (1985). The mechanical behaviour of cancellous bone. *J. Biomech.* 18, 317–328. doi:10.1016/0021-9290(85)90287-8

Goff, M. G., Lambers, F. M., Sorna, R. M., Keaveny, T. M., and Hernandez, C. J. (2015). Finite element models predict the location of microdamage in cancellous bone following uniaxial loading. *J. Biomech.* 48, 4142–4148. doi:10.1016/j.jbiomech.2015.10.023

Goldring, S. R. (2009). Role of bone in osteoarthritis pathogenesis. *Med. Clin. North Am.* 93, 25–35,xv. doi:10.1016/j.mcna.2008.09.006

Gross, T., Pahr, D. H., and Zysset, P. K. (2013). Morphology-elasticity relationships using decreasing fabric information of human trabecular bone from three major anatomical locations. *Biomech. Model. Mechanobiol.* 12, 793–800. doi:10.1007/s10237-012-0443-2

Hambli, R. (2013). Micro-CT finite element model and experimental validation of trabecular bone damage and fracture. *Bone* 56, 363–374. doi:10.1016/j.bone.2013.06.028

Hara, T., Tanck, E., Homminga, J., and Huiskes, R. (2002). The influence of micro-computed tomography threshold variations on the assessment of structural and mechanical trabecular bone properties. *Bone* 31, 107–109. doi:10.1016/S8756-3282(02)00782-2

Harrison, N. M., McDonnell, P., Mullins, L., Wilson, N., O'Mahoney, D., and McHugh, P. E. (2013). Failure modelling of trabecular bone using a non-linear combined damage and fracture voxel finite element approach. *Biomech. Model. Mechanobiol.* 12, 225–241. doi:10.1007/s10237-012-0394-7

Helgason, B., Perilli, E., Schileo, E., Taddei, F., Brynjólfsson, S., and Viceconti, M. (2008). Mathematical relationships between bone density and mechanical properties: a literature review. *Clin. Biomech. (Bristol, Avon)* 23, 135–146. doi:10.1016/j.clinbiomech.2007.08.024

Hosseini, H. S., Dünki, A., Fabech, J., Stauber, M., Vilayphiou, N., Pahr, D., et al. (2017). Fast estimation of Colles' fracture load of the distal section of the radius by homogenized finite element analysis based on HR-pQCT. *Bone* 97, 65–75. doi:10.1016/j.bone.2017.01.003

Ioannidis, J. P. (2005). Why most published research findings are false. *PLoS Med.* 2:e124. doi:10.1371/journal.pmed.0020124

Kijowski, R., Tuite, M., Kruger, D., Munoz Del Rio, A., Kleerekoper, M., and Binkley, N. (2012). Evaluation of trabecular microarchitecture in nonosteoporotic postmenopausal women with and without fracture. *J. Bone Miner. Res.* 27, 1494–1500. doi:10.1002/jbmr.1595

Kim, C. H., Zhang, H., Mikhail, G., von Stechow, D., Müller, R., Kim, H. S., et al. (2007). Effects of thresholding techniques on microCT-based finite element models of trabecular bone. *J. Biomech. Eng.* 129, 481–486. doi:10.1115/1.2746368

Knight, J. (2003). Negative results: null and void. *Nature* 422, 554–555. doi:10.1038/422554a

Kopperdahl, D. L., and Keaveny, T. M. (1998). Yield strain behavior of trabecular bone. *J. Biomech.* 31, 601–608. doi:10.1016/S0021-9290(98)00057-8

Korfiatis, V. C., Tassani, S., and Matsopoulos, G. K. (2017). A new Ensemble Classification System for fracture zone prediction using imbalanced micro-CT bone morphometrical data. *IEEE J. Biomed. Health Inform.* doi:10.1109/JBHI.2017.2723463

Milovanovic, P., Djonic, D., Marshall, R. P., Hahn, M., Nikolic, S., Zivkovic, V., et al. (2012). Micro-structural basis for particular vulnerability of the superolateral neck trabecular bone in the postmenopausal women with hip fractures. *Bone* 50, 63–68. doi:10.1016/j.bone.2011.09.044

Müller, R., Gerber, S. C., and Hayes, W. C. (1998). Micro-compression: a novel technique for the nondestructive assessment of local bone failure. *Technol. Health Care* 6, 433–444. doi:10.1016/S0021-9290(98)80302-3

Nagaraja, S., Couse, T. L., and Guldberg, R. E. (2005). Trabecular bone microdamage and microstructural stresses under uniaxial compression. *J. Biomech.* 38, 707–716. doi:10.1016/j.jbiomech.2004.05.013

Nazarian, A., Meier, D., Müller, R., and Snyder, B. D. (2009). Functional dependence of cancellous bone shear properties on trabecular microstructure evaluated using time-lapsed micro-computed tomographic imaging and torsion testing. *J. Orthop. Res.* 27, 1667–1674. doi:10.1002/jor.20931

Nazarian, A., Stauber, M., Zurakowski, D., Snyder, B. D., and Müller, R. (2006). The interaction of microstructure and volume fraction in predicting failure in cancellous bone. *Bone* 39, 1196–1202. doi:10.1016/j.bone.2006.06.013

Niebur, G. L., Feldstein, M. J., Yuen, J. C., Chen, T. J., and Keaveny, T. M. (2000). High-resolution finite element models with tissue strength asymmetry accurately predict failure of trabecular bone. *J. Biomech.* 33, 1575–1583. doi:10.1016/S0021-9290(00)00149-4

Ohman, C., Baleani, M., Perilli, E., Dall'Ara, E., Tassani, S., Baruffaldi, F., et al. (2007). Mechanical testing of cancellous bone from the femoral head: experimental errors due to off-axis measurements. *J. Biomech.* 40, 2426–2433. doi:10.1016/j.jbiomech.2006.11.020

Ohman, C., Dall'Ara, E., Baleani, M., Van Sint Jan, S., and Viceconti, M. (2008). The effects of embalming using a 4% formalin solution on the compressive mechanical properties of human cortical bone. *Clin. Biomech. (Bristol, Avon)* 23, 1294–1298. doi:10.1016/j.clinbiomech.2008.07.007

Perilli, E., Baleani, M., Ohman, C., Baruffaldi, F., and Viceconti, M. (2007a). Structural parameters and mechanical strength of cancellous bone in the femoral head in osteoarthritis do not depend on age. *Bone* 41, 760–768. doi:10.1016/j.bone.2007.07.014

Perilli, E., Baruffaldi, F., Visentin, M., Bordini, B., Traina, F., Cappello, A., et al. (2007b). MicroCT examination of human bone specimens: effects of polymethylmethacrylate embedding on structural parameters. *J. Microsc.* 225, 192–200. doi:10.1111/j.1365-2818.2007.01731.x

Perilli, E., Baleani, M., Ohman, C., Fognani, R., Baruffaldi, F., and Viceconti, M. (2008). Dependence of mechanical compressive strength on local variations in microarchitecture in cancellous bone of proximal human femur. *J. Biomech.* 41, 438–446. doi:10.1016/j.jbiomech.2007.08.003

Pistoia, W., van Rietbergen, B., Lochmüller, E.-M., Lill, C. A., Eckstein, F., and Rüegsegger, P. (2002). Estimation of distal radius failure load with micro-finite element analysis models based on three-dimensional peripheral quantitative computed tomography images. *Bone* 30, 842–848. doi:10.1016/S8756-3282(02)00736-6

Ramtani, S., and Abdi, M. (2005). Buckling of adaptive elastic bone-plate: theoretical and numerical investigation. *Biomech. Model. Mechanobiol.* 3, 200–208. doi:10.1007/s10237-004-0056-5

Sanyal, A., Gupta, A., Bayraktar, H. H., Kwon, R. Y., and Keaveny, T. M. (2012). Shear strength behavior of human trabecular bone. *J. Biomech.* 45, 2513–2519. doi:10.1016/j.jbiomech.2012.07.023

Schileo, E., Taddei, F., Cristofolini, L., and Viceconti, M. (2008). Subject-specific finite element models implementing a maximum principal strain criterion are able to estimate failure risk and fracture location on human femurs tested in vitro. *J. Biomech.* 41, 356–367. doi:10.1016/j.jbiomech.2007.09.009

Sidorenko, I., Monetti, R., Bauer, J., Mueller, D., Rummeny, E., Eckstein, F., et al. (2011). Assessing methods for characterising local and global structural and biomechanical properties of the trabecular bone network. *Curr. Med. Chem.* 18, 3402–3409. doi:10.2174/092986711796504754

Silva, M., and Gibson, L. (1997). Modeling the mechanical behavior of vertebral trabecular bone: effects of age-related changes in microstructure. *Bone* 21, 191–199. doi:10.1016/S8756-3282(97)00100-2

Snyder, B. D., Piazza, S. J., and Hayes, W. C. (1991). "Mechanisms of trabecular bone failure in the osteoporotic lumbar vertebral body," in *Transactions of the Orthopaedic Research Society*, Vol. 16 (Anaheim, CA), 132.

Stölken, J. S., and Kinney, J. H. (2003). On the importance of geometric nonlinearity in finite-element simulations of trabecular bone failure. *Bone* 33, 494–504. doi:10.1016/S8756-3282(03)00214-X

Tassani, S., Matsopoulos, G., and Baruffaldi, F. (2012). 3D identification of trabecular bone fracture zone using an automatic image registration scheme: a validation study. *J. Biomech.* 45, 2035–2040. doi:10.1016/j.jbiomech.2012.05.019

Tassani, S., and Matsopoulos, G. K. (2014). The micro-structure of bone trabecular fracture: an inter-site study. *Bone* 60, 78–86. doi:10.1016/j.bone.2013.12.007

Tassani, S., Ohman, C., Baleani, M., Baruffaldi, F., and Viceconti, M. (2010). Anisotropy and inhomogeneity of the trabecular structure can describe the mechanical strength of osteoarthritic cancellous bone. *J. Biomech.* 43, 1160–1166. doi:10.1016/j.jbiomech.2009.11.034

Tassani, S., Ohman, C., Baruffaldi, F., Baleani, M., and Viceconti, M. (2011). Volume to density relation in adult human bone tissue. *J. Biomech.* 44, 103–108. doi:10.1016/j.jbiomech.2010.08.032

Torcasio, A., Zhang, X., Duyck, J., and Van Lenthe, G. H. (2012). 3D characterization of bone strains in the rat tibia loading model. *Biomech. Model. Mechanobiol.* 11, 403–410. doi:10.1007/s10237-011-0320-4

Townsend, P. R., Rose, R. M., and Radin, E. L. (1975). Buckling studies of single human trabeculae. *J. Biomech.* 8, 199–200. doi:10.1016/0021-9290(75)90025-1

Van Sint Jan, S., and Rooze, M. (1992). The thenar muscles – new findings. *Surg. Radiol. Anat.* 14, 325–329. doi:10.1007/BF01794759

Verhulp, E., van Rietbergen, B., and Huiskes, R. (2006). Comparison of micro-level and continuum-level voxel models of the proximal femur. *J. Biomech.* 39, 2951–2957. doi:10.1016/j.jbiomech.2005.10.027

Verhulp, E., Van Rietbergen, B., Muller, R., and Huiskes, R. (2008a). Micro-finite element simulation of trabecular-bone post-yield behaviour – effects of material model, element size and type. *Comput. Methods Biomech. Biomed. Engin.* 11, 389–395. doi:10.1080/10255840701848756

Verhulp, E., van Rietbergen, B., Müller, R., and Huiskes, R. (2008b). Indirect determination of trabecular bone effective tissue failure properties using micro-finite element simulations. *J. Biomech.* 41, 1479–1485. doi:10.1016/j.jbiomech.2008.02.032

Viguet-Carrin, S., Garnero, P., and Delmas, P. D. (2006). The role of collagen in bone strength. *Osteoporos. Int.* 17, 319–336. doi:10.1007/s00198-005-2035-9

Vilayphiou, N., Boutroy, S., Szulc, P., Van Rietbergen, B., Munoz, F., Delmas, P. D., et al. (2011). Finite element analysis performed on radius and tibia HR-pQCT images and fragility fractures at all sites in men. *J. Bone Miner. Res.* 26, 965–973. doi:10.1002/jbmr.297

Wolfram, U., Gross, T., Pahr, D. H., Schwiedrzik, J., Wilke, H. J., and Zysset, P. K. (2012). Fabric-based Tsai-Wu yield criteria for vertebral trabecular bone in stress and strain space. *J. Mech. Behav. Biomed. Mater.* 15, 218–228. doi:10.1016/j.jmbbm.2012.07.005

Wolfram, U., Wilke, H. J., and Zysset, P. K. (2010). Valid micro finite element models of vertebral trabecular bone can be obtained using tissue properties measured with nanoindentation under wet conditions. *J. Biomech.* 43, 1731–1737. doi:10.1016/j.jbiomech.2010.02.026

Zysset, P. K., Dall'ara, E., Varga, P., and Pahr, D. H. (2013). Finite element analysis for prediction of bone strength. *Bonekey Rep.* 2, 386. doi:10.1038/bonekey.2013.120

Conflict of Interest Statement: The authors declare that the research was conducted in the absence of any commercial or financial relationships that could be construed as a potential conflict of interest.

frontiers in Mechanical Engineering

ORIGINAL RESEARCH
published: 05 February 2018
doi: 10.3389/fmech.2017.00023

Bone Apparent and Material Densities Examined by Cone Beam Computed Tomography and the Archimedes Technique: Comparison of the Two Methods and Their Results

*George J. Adams[1], Richard B. Cook[2], John R. Hutchinson[3] and Peter Zioupos[1]**

[1] Cranfield Forensic Institute, Cranfield University, Defence Academy of the United Kingdom, Shrivenham, United Kingdom, [2] National Centre for Advanced Tribology at Southampton (nCATS), Faculty of Engineering and the Environment, University of Southampton, Southampton, United Kingdom, [3] Structure and Motion Laboratory, Department of Comparative Biomedical Sciences, Royal Veterinary College, University of London, Hatfield, United Kingdom

OPEN ACCESS

Edited by:
Gianluca Tozzi, University of Portsmouth, United Kingdom

Reviewed by:
Alexandre Terrier, École Polytechnique Fédérale de Lausanne, Switzerland
Katherine A. Staines, Edinburgh Napier University, United Kingdom

***Correspondence:**
Peter Zioupos
p.zioupos@cranfield.ac.uk

Specialty section:
This article was submitted to Mechanics of Materials, a section of the journal Frontiers in Mechanical Engineering

Received: *03 October 2017*
Accepted: *21 December 2017*
Published: *05 February 2018*

Citation:
Adams GJ, Cook RB, Hutchinson JR and Zioupos P (2018) Bone Apparent and Material Densities Examined by Cone Beam Computed Tomography and the Archimedes Technique: Comparison of the Two Methods and Their Results. Front. Mech. Eng. 3:23. doi: 10.3389/fmech.2017.00023

An understanding of bone apparent and material densities and how they vary within bone at the organ level is of great interest in the understanding of degenerative bone conditions and for biomedical engineering applications. The densities of bone tissue have been shown to appreciably influence the mechanical competency of bone tissue. In order to assess the density of bone in the body, it is important to ensure that the parameters being measured *in vivo* are truly representative of the real values that have been measured *in vitro*. To assess the densities of bone across the entire spectrum of available porosities, 112 samples from an elephant femur were assessed using the Archimedes method (water displacement) and by micro-computed tomography (μ-CT). Comparisons were drawn between the two methods to determine if the densities calculated by μ-CT were representative of physically measured densities. The results showed that the apparent densities measured over the entire spectrum were very similar but varied in the intermediate regions of bone tissue, probably due to an increased presence of osteoid, increased remodeling, or experimental error as these type of bone is known for the presence of regions of closed cell geometry in the cancellous architecture. It could be argued that the measurements taken by μ-CT are more reliable of bone density values for the mineralized regions of bone as the threshold is defined with respect to the absorption of X-rays by the mineral. In contrast, the Archimedes method thresholds everything with a density value above that of the surrounding medium, 1 (g cm^{-3}) for water, and hence it is more sensitive to the presence of osteoid, soft collagenous matrix, and epithelial cell layers. Further research is required to optimize the parameters of scanning methods for the structural properties of different bone tissue porosities, which hopefully in turn will be able to provide a basis for the development of predictive remodeling models.

Keywords: bone, cancellous, cortical, density, porosity, BV/TV, micro-computed tomography

INTRODUCTION

Bone, the material, exists at the organ level as whole bones. Whilst bone may seem relatively inert compared with other structures in the bone it is in fact an adaptive material which responds to its environment. The fundamental results of Wolff's Law hold true but his explanation and understanding of the underlying mechanisms were misunderstood (Currey, 2002). The nature of the biological and micro-mechanical mechanisms that drive bone remodeling is still not fully understood. At its material level, bone is a multiphase composite material formed of both organic and inorganic constituents. It has a hierarchical structure that ranges from the sub-nano level of the collagen-mineral composite through to the macro-structure of cortical and cancellous bone.

The density and structure of bone are important characteristics that determine its mechanical behavior in everyday life. An understanding of these underpinning properties is crucial in the investigation of bone as a structural material. Density can be defined in a number of ways ranging from the micro- to the macro- or organ level. The two generally accepted versions of density are the "apparent" and "material" ones. Apparent density (D_{app}) is the mass of the mineralized tissue over the total volume occupied by the tissue with the inclusion of its voids. The most common representation of D_{app} used in respect to bone is bone mineral density (BMD_a) which, when measured by dual energy X-ray diffraction (DEXA), is an area assessment of this characteristic. Material density (D_{mat}) is defined as the same mass as for apparent density divided by the volume the solid mineralized tissue occupies with the exclusion of any voids that may exist within the structure. The most popular use of this is often referred to as tissue mineral density. These definitions highlight that the difference between these properties is the consideration of mass with respect to the micro-structure of the tissue, such as: voids, osteocyte lacunae, osteonal canals, and analogous non-mineralized architectural features:

$$D_{app} = \text{Bone mass/Total Volume} \quad (1)$$

$$D_{mat} = \text{Bone mass/Bone Volume} \quad (2)$$

$$\text{BV/TV} = D_{app}/D_{mat} \quad (3)$$

where BV is the bone volume and TV is the total volume. The assessment of densities within bone tissue is considered to be important as it will impact upon the resultant mechanical properties and remodeling characteristics of bone (Martin, 1984; Fyhrie et al., 1993; Zioupos et al., 2008). The derivation of D_{app} is not contested because it is simply the wet bone mass of a sample over the Cartesian geometric volume occupied by the same bone sample. Different methods for material density, however, have caused some debate (Schileo et al., 2008; Zioupos et al., 2008). The most conventional technique employed for this assessment relies on the Archimedes principle (usually *via* water displacement). Application of this method relies critically on ensuring that pores must be fully flushed and refilled (Zou et al., 1997). This flushing and refilling are particularly difficult in cases where there are cells of closed geometry within the trabecular architecture (Rho et al., 1995). Comparisons of DEXA and the Archimedes technique have previously reported substantial differences (Keenan et al., 1997) whilst fractional quantitative and cone beam computed tomography has been shown to be in closer agreement with Archimedes (Lee et al., 2004; Ahlowalia et al., 2013). When investigating D_{app} and D_{mat}, consideration must be given to the volume of bone or BV/TV (dimensionless ratio of actual bone volume to the total volume of the sample). This can be calculated with the Archimedes principle using Eq. 3. Calculating BV/TV with the Archimedes method depends therefore in ensuring that the displaced suspending medium (water, a solution of known density, or a gas) infiltrates all the pores and thus derives the true BV for the sample. BV/TV has also been calculated/measured by using a series of histological slices (Martin, 1984). This technique can also carry an inherent error due to the limitation of physical slice thickness which requires interpolation between each slice; in the addition to sample destruction.

The D_{app} is often considered to be one of the primary characteristics of bone that influence its mechanical properties at the macro-mechanical level and has been shown to influence not

TABLE 1 | Properties of QRM calibration phantom.

Sample	Mean gray[a]	Density[b] (g cm^{-3})	Mineral %[c]
Standard 1	36.1 ± 6.4	1.13 ± 0.02	0.000
Standard 2	48.6 ± 9.4	1.18 ± 0.02	0.424
Standard 3	112.2 ± 12.6	1.26 ± 0.02	15.889
Standard 4	337.2 ± 33.7	1.64 ± 0.02	48.293
Standard 5	478.5 ± 42.0	1.90 ± 0.02	63.168

[a]*Measured in test.*
[b]*Provided by calibration certificate for QRM standard.*
[c]*Calculated for resin density = 1.13 g cm^{-3} and HAp density = 3.3 g cm^{-3}.*

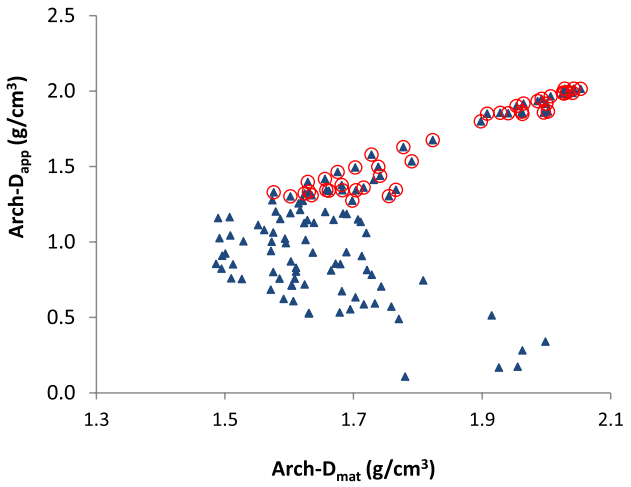

FIGURE 1 | Apparent (D_{app}) vs. material density (D_{mat}) for all samples (triangles) produced from the same femur in both cortical and cancellous regions, adapted from Zioupos et al. (2008). The samples having D_{app} > 1.3, which on visual inspection would be identified as cortical bone regions, are encircled and the same notation is used in the following figures to allow visual comparisons to be made between figures. Material density (D_{mat}) showed lower values for intermediate BV/TV values in the range of 0.4–0.7. "Arch" denotes the measurements were obtained in a study using the Archimedes method.

only the compressive but also the fracture toughness properties of bone (Rice et al., 1988; Cook and Zioupos, 2009). D_{mat} determines material behavior primarily at the trabecular level. However, due to the fact that D_{app} is the product of $D_{mat} \times$ BV/TV, it determines properties at the structural level too. A previous study has shown, in elephant bone samples, that the relationship between D_{app} and D_{mat} are interdependent and that D_{mat} is at its highest (~2.3g cm^{-3}) value at the extremes of porosity, as BV/TV tends toward 1 and 0, and exhibits minimum values at intermediate levels of BV/TV of 0.4–0.7 (Zioupos et al., 2008).

This relationship has, however, been brought into question when it was suggested that the actual shape of it may be due to limitations of the Archimedes method in the assessment of bone tissue material density (Schileo et al., 2009) because, as commented earlier, the method depends on ensuring that the displaced suspending medium infiltrates all the pores and thus derives the true BV of a sample. To overcome this limitation, μ-CT can be used as it gives information on the internal structure, it is non-destructive and it can penetrate throughout the material so that marrow-filled spaces and more enclosed cells are accessible and thus these will not affect the results. Some previous work has looked at the density relationship applied at cortical and cancellous regions using μ-CT (Schileo et al., 2008), but it has not considered bone densities throughout the entire range with particular attention to the intermediate range of densities. The present study, therefore, aims to test the hypothesis that, when applied to the same bone tissue samples, Archimedes and μ-CT can produce effectively the same results and also to explore the implications of μ-CT derived data in mechanobiology studies.

MATERIALS AND METHODS

Specimens

In this study, 112 samples were taken from the right femur of an adult Asian elephant (3,432 kg, 24 years old). The specimen was collected shortly after the animal's euthanasia (for reasons unrelated to this study) at Whipsnade Zoo (Bedfordshire, UK) and frozen (−20°C) until sample testing. Whilst use of elephant tissue is not ideal for human applications, is does have certain advantages as it is mammalian with the shape and properties at the bone matrix level (confirmed by nano-indentation tests in our laboratories; unpublished data) similar to those of a human femur, the only major difference, therefore, being one of size. This large size enabled extraction of extensive volumes of cortical and cancellous bone which allowed structural effects similar to human tissue to be observed on a scale in tens of millimeters; additionally, it enabled production of all cortical and cancellous samples from the same sections throughout the same bone (no intra- or inter-individual variability), and obtained from a sample from an animal known to have previously been healthy. The samples had been characterized in a previous study (Zioupos et al., 2008), where full details of sample extraction can be found.

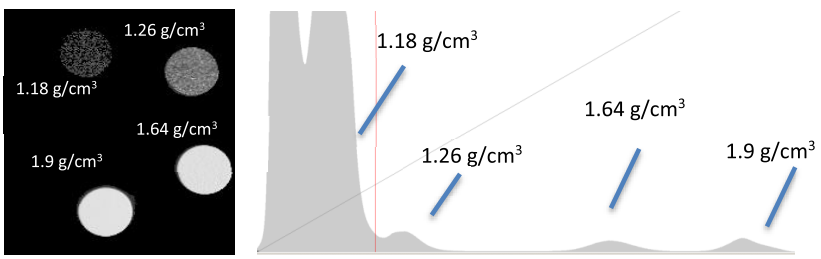

FIGURE 2 | QRM calibration phantom images and histogram; the average density, gray, and mineral % are given in **Table 1**.

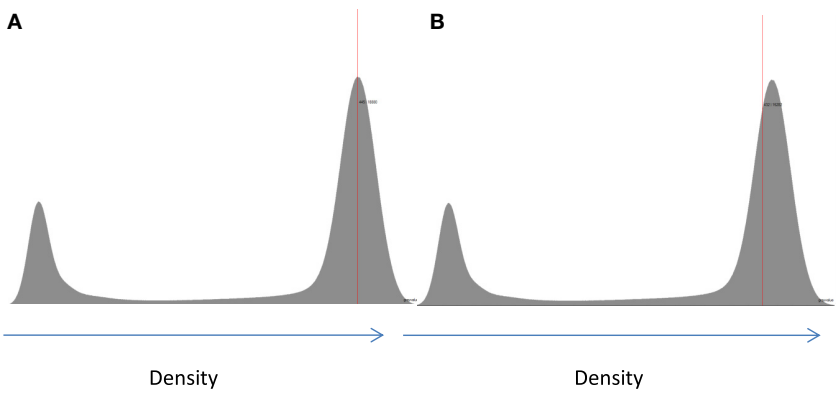

FIGURE 3 | Example of two possible ways to determining the material density from the histogram for a cortical bone sample: **(A)** taking a measurement of the peak value (mode) and **(B)** taking the mean value above the determined threshold.

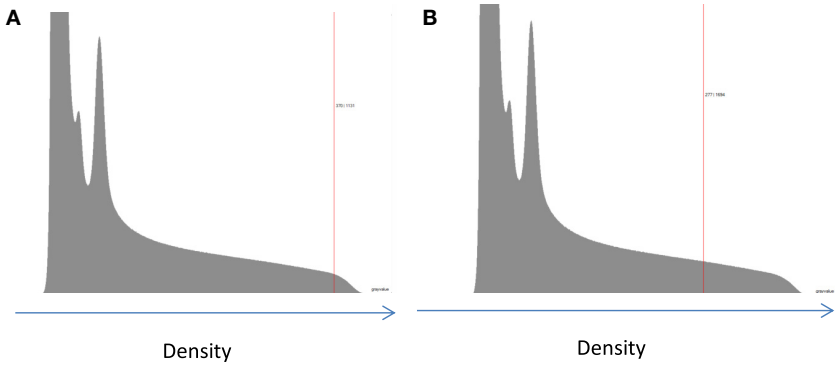

FIGURE 4 | Example of two possible ways to determining the material density from the histogram for an extremely porous cancellous bone sample: **(A)** taking a measurement of the peak value; the location of the peak value is approximated due to the lack of a resolved peak in the low-BV/TV samples; **(B)** taking the mean value above the determined threshold. There is a high score for low-density voxels on the left-hand side of the histogram which correspond to water, fat, marrow, remnants of blood clots, and other such contaminants in the samples.

μ-CT Imaging

All samples were imaged using a cone beam μ-CT scanner, XTEK CT H 225 (Nikon Metrology, Nottingham, UK). The samples were imaged in ABS plastic sample holders (~1-mm thick) at 50 kV, 65 μA with a 500 ms exposure time. The resultant voxel size was ~16 μm, making them suitable to accurately determine the samples' morphology (Yan et al., 2011). Each sample was imaged twice. First they were imaged fully submerged in deionized water. The samples were then imaged again in air. All image data were manually reconstructed using CT Pro 3D. With CT Pro the beam hardening and noise reduction filters were applied to provide an optimal image; this image setting was then standardized across the data set to ensure that the data collected were comparable.

Image Analysis

Image analysis was carried out using VG Studio Max 2.2. Regions of interest were taken from the center of each sample ~9 mm^3 to exclude any external surfaces from the calculations. A surface determination was performed using the gray level of an internal void as the background and the largest void-less section of bone as the sample gray value, as per the manufacturers' recommendations. After the surface determination, an automatic morphometric report was exported which contained: BV/TV, specific surface, mean trabecular thickness, mean trabecular number, and mean trabecular spacing.

From the histogram, the mean, mode, minimum, and maximum gray levels were recorded to be used in calculation of the material density. A QRM-MicroCT-HA calibration phantom was scanned and reconstructed under the same conditions in order to determine D_{mat}. Determination of material density is more favorable than deriving Hounsfield units (HU) in this context as HU provides a relative density based on the attenuation coefficients of the material that cannot be measured by traditional densitometry. However, density as mass per unit volume can easily be compared with physical densitometry techniques.

Density Calibration

A histogram of the QRM HA calibration phantom alongside the 3D image of the scan is shown in **Figure 2**. Both the histogram and image were obtained using VG Studio Max software. Within the software, each density was isolated and the average gray scale was determined and plotted against the density provided by the supplier. This provided a calibration curve [a least squares regression equation: density (g cm^{-3}) = 1.099 + (0.0015 + gray value)] from which the density of the elephant samples could be determined. The average gray value of each sample was measured, and using the calibration curve, D_{mat} was determined for each sample.

The D_{app} was determined from the product of the BV/TV and D_{mat} by rearranging Eq. 3. In the present study, to distinguish between measurements taken from CT and measurements taken using the Archimedes technique, the prefixes CT- and Arch- are used, respectively.

A comparison of two possible methods for determination of density is shown in **Figure 3**. Density can either be taken from the average gray value in the sample or from the center of the peak on the histogram, which represented the modal gray value for the sample. Each method has advantages and disadvantages. Measuring the mean gives the average gray value; however, it inevitably includes voxels that are only partially filled with bone caused by the partial voxel effect, which can skew the mean to be less than the true mean. Taking the center of the peak avoids this issue related to partial volumes but only takes the most common density in the scan and has the potential to ignore a non-uniform distribution of densities around the mode.

Inevitably, and as shown in **Figure 3**, the mode value taken will always be higher than the mean value due to the non-zero regions between the background, in this case water, and the bone peak. As such, taking the measurement from the mode value is unaffected by the background, which would suggest that it is the best method to use. However, this cannot be applied uniformly across the whole range of porosities. For extremely porous cancellous bone, there is very little bone from which to quantify the gray level (density) and then taking a measurement from the center of the bone peak

is extremely difficult. In these few cases, using the mean value is the most suitable option so that a reliable density variable can be obtained across the entire cohort (**Figure 4**). The examples in **Figures 3** and **4** serve to illustrate the considerable difficulties in obtaining reliable density values from gray levels in the CT across the whole BV/TV range in bone. Similar to Archimedes, the CT method is not, therefore, without its own limitations. Indeed, another argument could be that the integrated pixel values should be used to quantify density, which would take into account any partial voxels (i.e., only partly occupied by bone) that otherwise cannot fully be taken into account with the prior two methods. We focus here on those other two methods but a future study using the integrated pixel values would be interesting.

RESULTS

The full results of the way densities compare with each other, when measured by the mode or the mean value of gray levels (after appropriate and specific thresholding of the voxels), are in **Figure 5**. The material density calculated by the mean underestimates the value produced by the mode, as expected, but the two are very well linearly correlated with each other (**Figure 5**). There are also very few outliers where the two values deviate considerably for some difficult samples, but these do not spoil the overall pattern nor do they cast a strong shadow of doubt on the very principle of measuring bone densities across the complete range of porosities. The symbols encircled in red are, as is our practice, those for the cortical bone samples. Once again, as in the original paper using the Archimedes method (Zioupos et al., 2008), there is an underlying regressive behavior of the sample density, which goes down and up as bone goes from dense cortical to porous cancellous between these two extremes and which is can be appreciated by the arrows added manually on the graph.

A comparison of the CT-D_{app} measured from the mean and Arch-D_{app} by the laboratory method of Zioupos et al. (2008) is shown in **Figure 6**. The plot has a slight inflection in the intermediate bone density values. If we consider that Arch-D_{app} is a more reliable method because it is simply the wet weight over the bone sample volume, then it appears that CT-D_{app} underestimates apparent bone density in these intermediate value regions as it is based on the absorption of X-rays from mineralized tissue alone. Data for Arch-D_{app} are produced empirically using a microbalance to measure wet weight of the bone and Vernier calipers to measure volume. Arch-D_{app} is in essence the method for apparent density that is used in every biomechanical lab

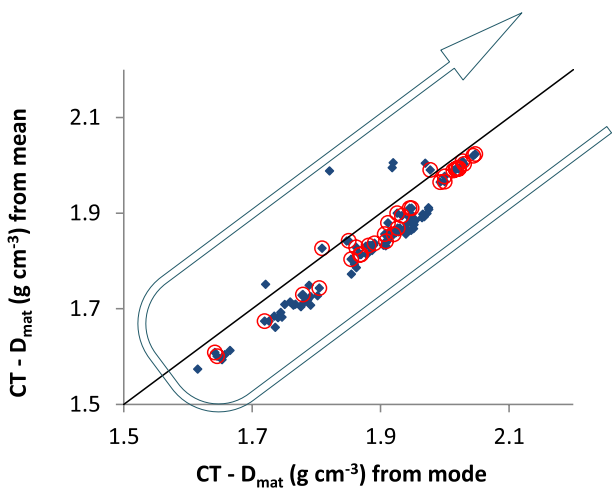

FIGURE 5 | Comparison of estimating material density by the "mean" and "mode" gray levels of the bone samples. The line shown represents a slope of one and goes through zero, for illustrative purposes. Some outliers exist where there is little bone in the scan so the "mode value" does not lie near the center of the "mean value." The arrow points to the underlying regressive behavior of the sample material density, which goes down and up as bone goes from dense cortical to porous cancellous between the two extremes of BV/TV.

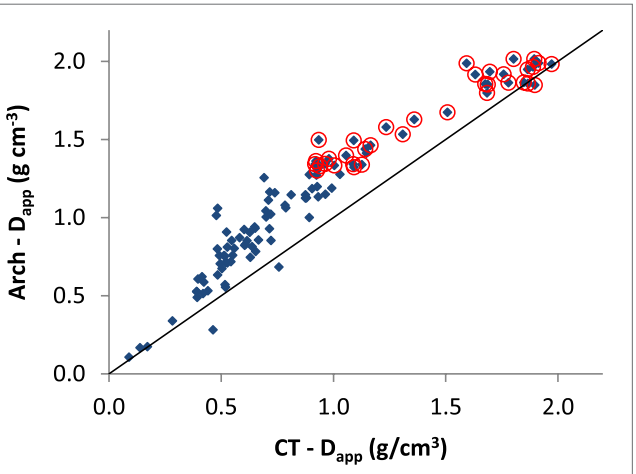

FIGURE 6 | Comparison of D_{app} from Zioupos et al. (2008) vs. D_{app} measured by CT in the present study (on the same samples). Otherwise, the description in **Figure 5**'s caption applies.

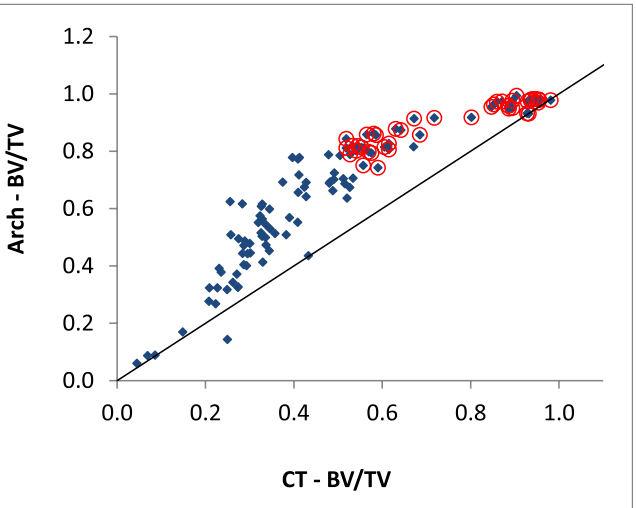

FIGURE 7 | Comparison of the BV/TV ratio measured by μ-CT with previous reported BV/TV values measured by Zioupos et al. (2008) ("Arch-BV/TV") for the same samples. Otherwise, the description in **Figure 5**'s caption applies.

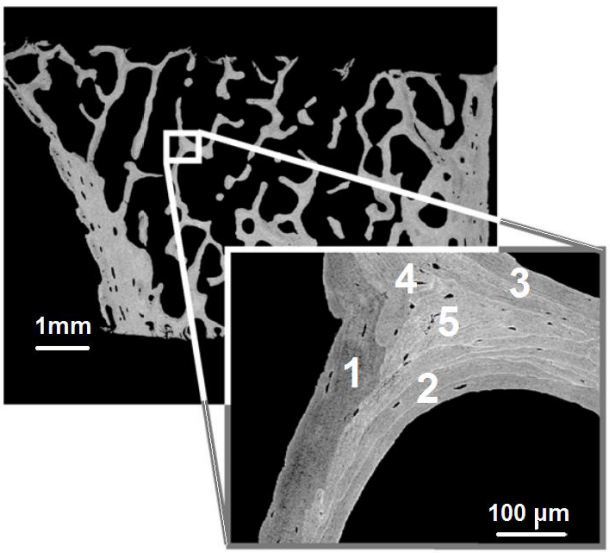

FIGURE 8 | Microscope images showing the mosaic of different layers of bone tissue with progressively denser mineralization levels (adapted and modified from original in Ruffoni et al., 2007). Based on gray level alone, one would have numbered the various tissue compartments as 1 being the more recent, toward 5 being the older one.

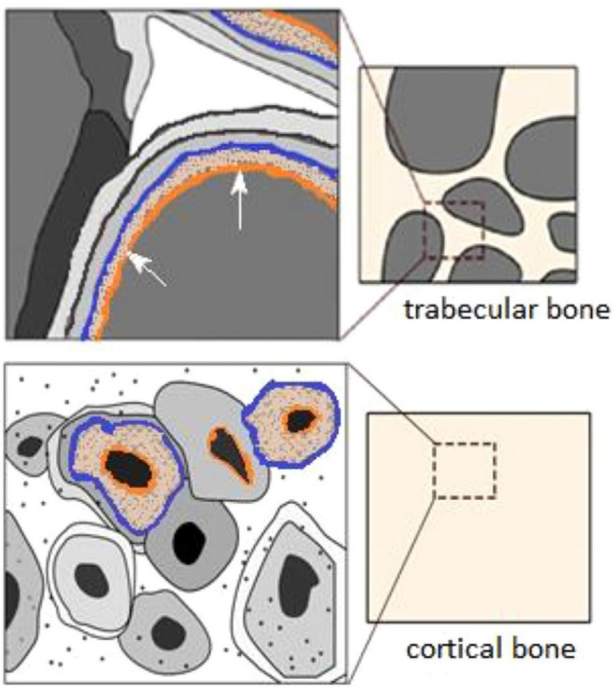

FIGURE 9 | Graphic displaying the remodeling regions of bone tissue in cancellous and cortical bone adapted from Berli et al. (2017) with proposed possible thresholds which have been added to image for the Archimedes (1.0 g cm^{-3}) (orange) and µ-CT thresholds (1.3 g cm^{-3}) (blue), for the soft collagenous boundary and osteoid tissue, respectively.

globally to produce Modulus of Elasticity = *f*(Apparent Density) relationships. The data show that there is "bone" matter which is not captured or quantified by the CT-D_{app} variable, and this matter is most likely be the lower density non-mineralized portions of the bone samples in remodeled areas, practically regions of osteoid tissue in its various stages toward full skeletal maturity.

The comparison of BV/TV measurements shown in **Figure 7** demonstrates that the Arch-BV/TV measured in the laboratory is higher in the intermediate regions, most likely due the fact that the Archimedes measurements consider all tissue including the un-mineralized layers on the surface of the tissue. It is most apparent in the intermediate region as it is a surface effect, and in the intermediate regions there is the greatest amount of specific surface available (Martin, 1984; Berli et al., 2017) for the volume of bone.

The results of **Figures 6** and **7** are in agreement with each other as to what disparities exist between the methods. These low-density regions on the surfaces of bone are due to the remodeling of bone where the "younger" bone regions are less mineralized. Microscope images displaying localized structural properties of bone are shown in **Figure 8** and are widespread in the literature. **Figure 9** depicts graphically the "mosaic" of tissue compartments that bone is at any point in time. These compartments are regions of varying mineral contents at various temporal points in the development of the mineralization process that leads from osteoid formation to mature, fully mineralized bone.

Figure 10 shows the "boomerang"-like pattern previously shown by Zioupos et al. (2008) is now apparent in both Archimedes-based and µ-CT-produced data. The µ-CT-produced curves do, however, have shallower inflection points: the lowest Arch-D_{mat} is ~1.48 g cm^{-3} as opposed to 1.60 g cm^{-3} for CT-D_{app}. The shallower inflection point is due to higher values for measured D_{mat} in the intermediate bone porosities when µ-CT is used. In views of the previous arguments and graphs, these higher values for D_{mat} most likely exist for two possible reasons: (i) the density measured by the Archimedes method is skewed by the presence of approximately closed voids in the cancellous bone matrix, which would overestimate the volume to bone if they are not fully flushed for the marrow they contain (in the calculation of D_{mat} = weight/volume a higher volume will lead to a reduced D_{mat} whereas in µ-CT these voids do not impact on the data) and/or (ii) the surface of cancellous bone in Archimedes measurements is thresholded at a density of 1 g cm^{-3} (because it displaces water in the Archimedes tests), thus including low-density epithelial layers and newly forming osteoid, but this same soft organic material does not possess a density high enough to register in the µ-CT measured density. The disparity between the measurements most likely exists due to a combination of these factors. The differences between the measurements are also apparent in **Figures 6** and **7**, which shows a clear inflection in the intermediate range of bone densities. The apparent density measured *via* Archimedes is undisputed and seems to carry less error than any other physical method—a statement that is open to interpretation (measurement of actual weight and of physical dimensions with calipers). However, we conclude that it is the

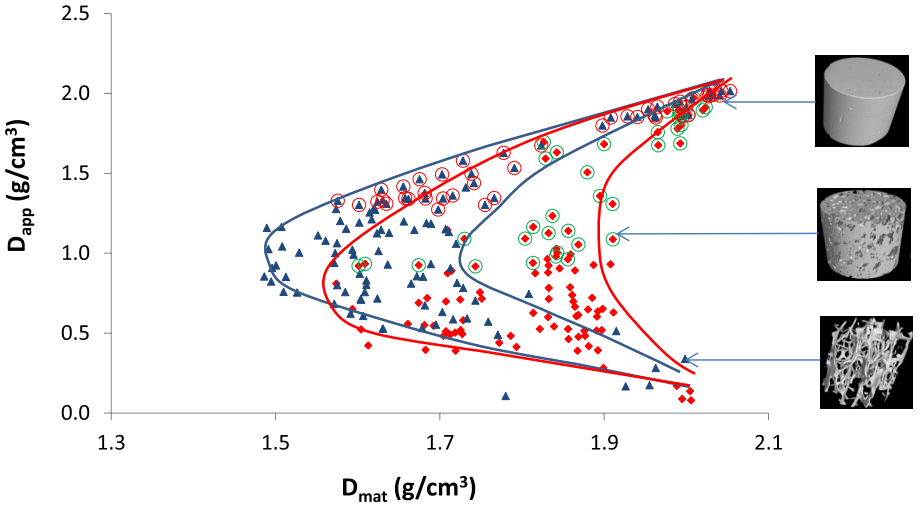

FIGURE 10 | Apparent vs. material density for all samples throughout the whole range from cortical to cancellous bone. Blue triangles are produced by the Archimedes method (Zioupos et al., 2008), the red diamonds are from μ-CT, and the lines showing the envelopes were manually added around the two data sets. 3D reconstructed images of samples are shown on the right at their respective densities.

μ-CT method, not so much the Archimedes method, that needs particularly cautious attention for potentially misleading technical errors. In both ways for both methods, the "boomerang"-like pattern is strongly evident.

DISCUSSION

Here, we have furthered the investigation into the basic relationships that exist between apparent and material density values within bone in both its cortical and cancellous forms, and throughout its whole porosity range. Bone densities directly impact upon the mechanical competency of the tissue (Rho et al., 1995; Zioupos et al., 2008). Understanding the behavior of bone density across the full range of porosity values is vitally important for the comprehensive understanding of remodeling behavior and remodeling rates at specific sites within the human body (Martin, 1984; Fyhrie et al., 1993). Such density data will contribute to future development of patient-specific finite element modeling, which depends on accurate assessment of the material properties of the tissue and its structure (Chevalier et al., 2007; Schileo et al., 2008). Conflicting reports have been made on the nature of the density variations across the full porosity range (Schileo et al., 2008, 2009; Zioupos et al., 2008), which, however, used different methods to assess the same property and on different samples. Assessing these bone properties has typically been carried out by means of histological measurements (sectioning) and traditional densitometry techniques such as the Archimedes technique (Martin, 1984; Rho et al., 1995; Zou et al., 1997; Zioupos et al., 2008). These methods are destructive and can be criticized for their limitations in reproducibility, which is most likely due to their inability to guarantee full penetration of the sample using various solvents, which has led some studies to use a gas pycnometer (helium displacement method; Zou et al., 1997).

μ-CT imaging has its own limitations which interfere with density measurements, too. In μ-CT imaging, it is important to ensure that image resolution is suitable for the size and structures being assessed. In this study, the imaging resolution was sufficient for determination of cancellous micro-architecture but not for further assessment of the vascular nano-micro-architecture, which is at a range <1 μm (Yan et al., 2011). This is an important consideration when looking at the specific surface of bone, because when looking at cellular sites for bone remodeling the cortical bone may be more porous than the results here would suggest and consequently the reported remodeling rates would be also affected. Additionally, the densities presented in this work were calculated in grams per cubic centimeter to provide comparison between the two methods. In contrast, for clinical relevance HU would be of greater value, which have been shown to be suitable when using cone beam micro-computed tomography (Mah et al., 2010). Moreover, in μ-CT imaging consideration must also be given to the methods of density determination; be it by the "mean" or "mode" values of the gray value distribution (or other approaches as noted above in Section "Materials and Methods"); as in highly porous samples determination of both can be problematic, and as shown by **Figure 4** there is a deviation in the produced values in such cases of very porous bone material.

This study's findings have confirmed the trend of data from experiments on the same collection of samples used by Zioupos et al. (2008). These samples when using the Archimedes density determination method showed a highly non-linear relationship between D_{mat} and D_{app} for bone across all porosities and showed an inflection in the data in the intermediate regions between cortical and cancellous bone (**Figure 1**). The results from both methods (**Figure 10**) agree in the shape of the curve but differ in the magnitude of the non-linearity. The difference is understandable in that the two methods (one mechanical; one physical) use different physical principles and measure bone density differently. The limitation of a μ-CT scan is that it assesses density indirectly through the absorption of X-rays by the hard matter of bone (Schileo et al., 2008; Mah et al., 2010) and thus it

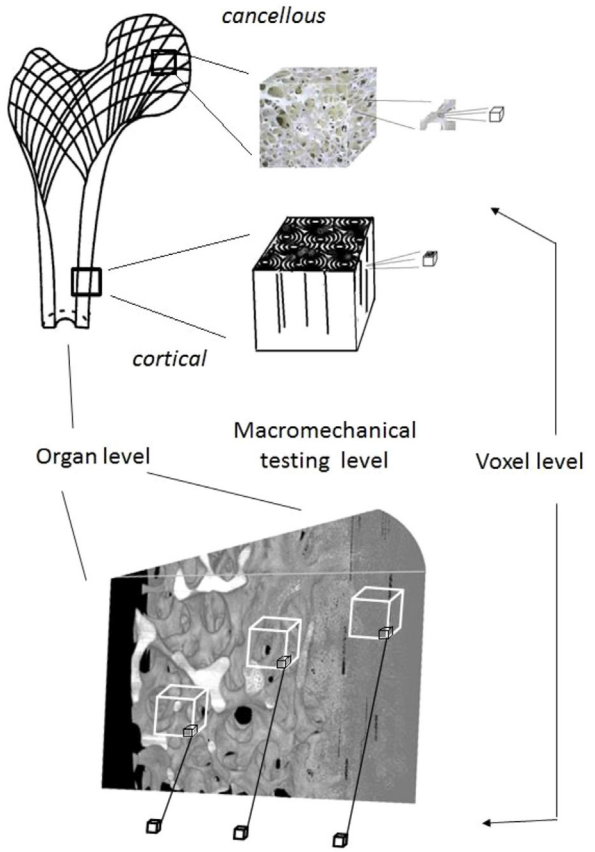

FIGURE 11 | Material property assignment is performed on relationships produced by mechanical testing at the macro-mechanical level. However, at voxel scales the relationship is one of (E) = f(mineral level) instead and as the present study has demonstrated this level is dependent on the level of BV/TV too. Consequently, in micro-FEA studies the assignment of $E = f$[gray level = f(%mineral)] should be made *via* appropriately conducted studies for tests (by using nano-indentation, for instance, Wolfram et al., 2010) at this magnification level.

certainly ignores the soft organic matrix. The limitations of the Archimedes method is that it requires repeated measurements and very careful preparation for cancellous samples with more closed cell architecture where the suspending medium (usually water) does not penetrates fully the entire space. In spite of these differences, both data sets are in agreement of a "boomerang" like effect which is prominent (density variation between high and low values of at least 37%) and is certainly not a constant value for D_{mat} across the whole range as claimed by Schileo et al. (2008, 2009).

In bone histology, less dense regions of bone are typically considered to be younger bone which in turn suggests that the intermediate porosity regions, which here are shown to contain bone of lower material density, do so because they experience higher rates of remodeling. The work of Berli et al. (2017) has attributed this to a process which is a surface-moderated effect, whereby the greater the specific surface area available, the higher the remodeling rate and the lower the mineral density due to the increased formation and presence of osteoid. The results also confirm that μ-CT based measurements of density, which are pursued for the purpose of scanning bones for micro-FEA, ought to use relationships between gray level/density/modulus of elasticity that are produced by micro-mechanics (e.g., nano-indentation tests) at the same magnification level and not the commonly provided ones produced at a macro-mechanical level (Morgan et al., 2003). Micro-mechanical tests are needed for micro-mechanical level data for micro-FEA because the bone material density fluctuates with porosity and does not maintain a constant value as has been assumed in past studies. This is shown by **Figure 11**. Erroneous material data values can be assigned if elastic modulus vs. density relationships from the literature [$E = f(D)$], which have been produced at a macro-mechanical level, are assigned to bone at the voxel size level for micro-FEA. When the voxel size is smaller than the bone pore size, for instance, if the voxel is at a void the E value is zero, if it is where bone mass is, the modulus value should be a function of the bone mineralization level and of only this.

CONCLUSION

This study has shown that bone material density varies non-linearly with bone apparent density across the full spectrum of bone porosities. We have provided further evidence in favor of density-dependent material models for the future development of patient-specific finite element models. Additional care must be taken when setting thresholds and sampling the material density—it is recommended that further work be carried out into the impact of setting μ-CT sampling thresholds on the material data. More investigation is needed into the source of the disparity, where it exists, between data obtained from the Archimedes and μ-CT methods. Additionally, the micro-architectural properties of bone across all porosities should be investigated more carefully because this may allow more profound inferences into the development of remodeling models.

ETHICS STATEMENT

The study was approved by institutional Cranfield University Research & Ethics committee.

AUTHOR CONTRIBUTIONS

GA, JH, RC, and PZ design the study. GA performed the study. GA, RC, and PZ analyzed the results. GA and PZ wrote the manuscript. GA, RC, JH, and PZ had equal contribution to the paper.

FUNDING

The tests were carried out in the Biomechanics laboratories of the Cranfield Forensic Institute of Cranfield University in Shrivenham, UK. The authors are thankful to Professor Michael Fagan for supplying the QRM HA calibration standard, Dr. Michael Doube for helpful comments on an earlier draft of this paper, the EPSRC (GR/N33225; GR/N33102; GR/M59167), the BBSRC (BB/C516844/1), the Department of Comparative Biomedical Sciences (RVC) for financial support and ZSL Whipsnade Zoo for provision of the specimen.

REFERENCES

Ahlowalia, M. S., Patel, S., Anwar, H. M., Cama, G., Austin, R. S., Wilson, R., et al. (2013). Accuracy of CBCT for volumetric measurement of simulated periapical lesions. *Int. Endod. J.* 46, 538–546. doi:10.1111/iej.12023

Berli, M., Borau, C., Decco, O., Adams, G., Cook, R. B., García Aznar, J. M., et al. (2017). Localized tissue mineralization regulated by bone remodelling: a computational approach. *PLoS ONE* 12:e0173228. doi:10.1371/journal.pone.0173228

Chevalier, Y., Pahr, D., Allmer, H., Charlebois, M., and Zysset, P. (2007). Validation of a voxel-based FE method for prediction of the uniaxial apparent modulus of human trabecular bone using macroscopic mechanical tests and nanoindentation. *J. Biomech.* 40, 3333–3340. doi:10.1016/j.jbiomech.2007.05.004

Cook, R. B., and Zioupos, P. (2009). The fracture toughness of cancellous bone. *J. Biomech.* 42, 2054–2060. doi:10.1016/j.jbiomech.2009.06.001

Currey, J. D. (2002). *Bones: Structure and Mechanics*. Woodstock, Oxon: Princeton University Press.

Fyhrie, D. P., Fazzalari, N. L., Goulet, R., and Goldstein, S. A. (1993). Direct calculation of the surface-to-volume ratio for human cancellous bone. *J. Biomech.* 26, 955–967. doi:10.1016/0021-9290(93)90057-L

Keenan, M. J., Hegsted, M., Jones, K. L., Delany, J. P., Kime, J. C., Melancon, L. E., et al. (1997). Comparison of bone density measurement techniques: DXA and Archimedes' principle. *J. Bone Min. Res.* 12, 1903–1907. doi:10.1359/jbmr.1997.12.11.1903

Lee, J., Shin, H. I., and Kim, S. Y. (2004). Fractional quantitative computed tomography for bone mineral density evaluation: accuracy, precision, and comparison to quantitative computed tomography. *J. Comput. Assist. Tomogr.* 28, 566–571. doi:10.1097/00004728-200407000-00022

Mah, P., Reeves, T. E., and McDavid, W. D. (2010). Deriving Hounsfield units using grey levels in cone beam computed tomography. *Dentomaxillofac. Radiol.* 39, 323–335. doi:10.1259/dmfr/19603304

Martin, R. B. (1984). Porosity and specific surface of bone. *Crit. Rev. Biomed. Eng.* 10, 179–222.

Morgan, E. F., Bayraktar, H. H., Tony, M., and Keaveny, T. M. (2003). Trabecular bone modulus–density relationships depend on anatomic site. *J Biomech.* 36, 897–904. doi:10.1016/S0021-9290(03)00071-X

Rho, J. Y., Hobatho, M. C., and Ashman, R. B. (1995). Relations of mechanical properties to density and CT numbers in human bone. *Med. Eng. Phys.* 17, 347–355. doi:10.1016/1350-4533(95)97314-F

Rice, J. C., Cowin, S. C., and Bowman, J. A. (1988). On the dependence of the elasticity and strength of cancellous bone on apparent density. *J. Biomech.* 21, 155–168. doi:10.1016/0021-9290(88)90008-5

Ruffoni, D., Fratzl, P., Roschger, P., Klaushofer, K., and Weinkamer, R. (2007). The bone mineralization density distribution as a fingerprint of the mineralization process. *Bone* 40, 1308–1319. doi:10.1016/j.bone.2007.01.012

Schileo, E., Dall'ara, E., Taddei, F., Malandrino, A., Schotkamp, T., Baleani, M., et al. (2008). An accurate estimation of bone density improves the accuracy of subject-specific finite element models. *J. Biomech.* 41, 2483–2491. doi:10.1016/j.jbiomech.2008.05.017

Schileo, E., Taddei, F., and Baleani, M. (2009). Letter to the Editor referring to the article "Some basic relationship between density values in cancellous bone and cortical bone" published on Journal of Biomechanics (volume 41, Issue 9, Pages 1961–8). *J. Biomech.* 42, 793. doi:10.1016/j.jbiomech.2009.01.013

Wolfram, U., Wilke, H. J., and Zysset, P. K. (2010). Valid micro finite element models of vertebral trabecular bone can be obtained using tissue properties measured with nanoindentation under wet conditions. *J. Biomech.* 43, 1731–1737. doi:10.1016/j.jbiomech.2010.02.026

Yan, Y. B., Qi, W., Wang, J., Liu, L. F., Teo, E. C., Tianxia, Q., et al. (2011). Relationship between architectural parameters and sample volume of human cancellous bone in micro-CT scanning. *Med. Eng. Phys.* 33, 764–769. doi:10.1016/j.medengphy.2011.01.014

Zioupos, P., Cook, R. B., and Hutchinson, J. R. (2008). Some basic relationships between density values in cancellous and cortical bone. *J. Biomech.* 41, 1961–1968. doi:10.1016/j.jbiomech.2008.03.025

Zou, L., Bloebaum, R. D., and Bachus, K. N. (1997). Reproducibility of techniques using Archimedes' principle in measuring cancellous bone volume. *Med. Eng. Phys.* 19, 63–68. doi:10.1016/S1350-4533(96)00045-8

Conflict of Interest Statement: The authors have no commercial or any other financial relationship or any conflict of interest to declare in conjunction with the work presented in this paper.

frontiers in Materials

ORIGINAL RESEARCH
published: 23 January 2018
doi: 10.3389/fmats.2017.00048

A Computed Microtomography Method for Understanding Epiphyseal Growth Plate Fusion

Katherine A. Staines[1]†, Kamel Madi[2†], Behzad Javaheri[3], Peter D. Lee[2‡] and Andrew A. Pitsillides[3‡]*

[1] School of Applied Sciences, Edinburgh Napier University, Edinburgh, United Kingdom, [2] School of Materials, The University of Manchester, Manchester, United Kingdom, [3] Comparative Biomedical Sciences, Royal Veterinary College, London, United Kingdom

The epiphyseal growth plate is a developmental region responsible for linear bone growth, in which chondrocytes undertake a tightly regulated series of biological processes. Concomitant with the cessation of growth and sexual maturation, the human growth plate undergoes progressive narrowing, and ultimately disappears. Despite the crucial role of this growth plate fusion "bridging" event, the precise mechanisms by which it is governed are complex and yet to be established. Progress is hindered by the current methods for growth plate visualization; these are invasive and largely rely on histological procedures. Here, we describe our non-invasive method utilizing synchrotron X-ray computed microtomography for the examination of growth plate bridging, which ultimately leads to its closure coincident with termination of further longitudinal bone growth. We then apply this method to a dataset obtained from a benchtop micro computed tomography scanner to highlight its potential for wide usage. Furthermore, we conduct finite element modeling at the micron-scale to reveal the effects of growth plate bridging on local tissue mechanics. Employment of these 3D analyses of growth plate bone bridging is likely to advance our understanding of the physiological mechanisms that control growth plate fusion.

Keywords: growth plate, mouse, bone, synchrotron, computed tomography, fusion

OPEN ACCESS

Edited by:
Gianluca Tozzi, University of Portsmouth, United Kingdom

Reviewed by:
Ralph Mueller, ETH Zurich, Switzerland
Brian Metscher, University of Vienna, Austria

****Correspondence:***
Katherine A. Staines
k.staines@napier.ac.uk

†Joint first authorship.

‡Joint senior authorship.

Specialty section:
This article was submitted to Mechanics of Materials, a section of the journal Frontiers in Materials

Received: *27 July 2017*
Accepted: *22 December 2017*
Published: *23 January 2018*

Citation:
Staines KA, Madi K, Javaheri B, Lee PD and Pitsillides AA (2018) A Computed Microtomography Method for Understanding Epiphyseal Growth Plate Fusion. Front. Mater. 4:48. doi: 10.3389/fmats.2017.00048

INTRODUCTION

Endochondral ossification is a tightly regulated process responsible for the formation and postnatal linear growth of the long bones, including the tibia and femur. Endochondral ossification is carefully orchestrated to involve the replacement of a cartilage scaffold by mineralized bone, and integral to this is the epiphyseal growth plate, a developmental region located in the metaphysis of the long bones (Staines et al., 2012).

The growth plate consists of chondrocytes arranged in columns. These chondrocytes are surrounded by their extracellular matrix, consisting of specific collagens, namely Collagen types II and X, as well as proteoglycans such as aggrecan and other non-collagenous matrix proteins including the SIBLING family of proteins (Ballock and O'Keefe, 2003; Mackie et al., 2011). Chondrocytes undergo distinct maturation stages of proliferation, differentiation, and hypertrophy, while maintaining their spatially fixed location (Hunziker et al., 1987). It is the terminally differentiated hypertrophic chondrocyte, which mineralizes its surrounding extracellular matrix (Castagnola et al., 1988). This

process, thought to involve membrane-limited matrix vesicles, is biphasic and tightly regulated by a number of enzymes and factors including alkaline phosphatase (Alpl), PHOSPHO1, the ankylosis protein (Ank), ecto-nucleotide pyrophosphatase/phosphodiesterase-1 (Enpp1) (Terkeltaub et al., 1994; Anderson, 1995; Roberts et al., 2007). Mineralization of the cartilage extracellular matrix facilitates vascular invasion allowing the infiltration of bone resorbing osteoclasts and bone forming osteoblasts (Zelzer et al., 2002). This is a key step in endochondral ossification and enables the replacement of the cartilaginous scaffold by bone.

Throughout the majority of embryonic and postnatal longitudinal bone growth, the processes of mineralized cartilage production and replacement by bone are coupled. However, as growth slows, the human growth plate undergoes progressive narrowing as bony bridges form and span its width. This ultimately leads to complete growth plate closure and the cessation of human growth. These bone bridges are also known to form upon growth plate injury, thought to be through an intramembranous ossification mechanism (Xian et al., 2004). Despite this, the molecular mechanisms underpinning their formation are unknown. It is well established though that growth plate closure in humans coincides with sexual maturation with estrogen playing a pivotal role, although the precise mechanisms are complex and are also yet to be fully established. Indeed, in two genetic mutations resulting in estrogen deficiency (in the estrogen-receptor gene, and in the CYP19 gene), the growth plate fails to fuse and growth persists, albeit rather slowly, into adulthood (Smith et al., 1994; Morishima et al., 1995; Grumbach and Auchus, 1999; Grumbach, 2000).

Whether growth plate fusion occurs prior to or after the cessation of growth is of significant controversy in the field and has been somewhat overlooked (Parfitt, 2002). Evidence from studies in both humans and rats revealed the cessation of growth long before any histological evidence of growth plate fusion, suggesting that epiphyseal fusion is a marker of growth cessation and not its cause (Becks et al., 1948; Moss and Noback, 1958; Weise et al., 2001). This goes against the current state of knowledge and it is essential that the exact temporal and spatial relationship between growth cessation and growth plate fusion is delineated before the complexities of epiphyseal growth plate function can be fully understood.

Research into growth plate fusion mechanisms may have been hindered somewhat by the limitation in current methods available for its visualization, which are invasive and largely reliant upon histological procedures. While nano-scale imaging is now possible *via* many approaches, the high flux and superior detectors in synchrotron (SR) micro-computed tomography (CT) enable excellent spatial resolution and high speed imaging, ideal for the rapid collection of multiple image volumes. Furthermore, computational mechanobiology is recognized as powerful tool for predicting tissue growth and adaptation (Prendergast et al., 1997). The relationship between macroscopic mechanical loads and the local stresses and strains that influence tissue formation can now be calculated using computational models (Carter and Wong, 1988; Lacroix and Prendergast, 2002a,b; Lacroix et al., 2002; Shefelbine and Carter, 2004; Stokes et al., 2006; Garzón-Alvarado et al., 2009; Gerhard et al., 2009; Lin et al., 2009; Reina-Romo et al., 2010; Schulte et al., 2013; Betts and Müller, 2014; Giorgi et al., 2015). To the best of our knowledge, due to the lack of information on the undulating internal structure, the 3D morphology of the growth plate has not yet been included in models of endochondral ossification or its complex fusion mechanisms (Gao et al., 2014). It seems likely that the local mechanical stresses, which may contribute to such fusion will be better predicted by the addition of 3D morphology of the growth plate. Therefore, we have developed a readily accessible method that could be useful in discriminating between normal and abnormal growth plate dynamics.

Here, we describe a non-invasive method for the 3-dimensational (3D) quantification of growth plate bridging using gold standard SR microCT, which we have then also applied to images acquired using a standard, more widely accessible benchtop microCT scanner. We have then used these images to conduct finite element (FE) modeling to assess currently unexplored associations between growth plate bridging and local strain distributions. Exploitation of these new methods is likely to advance understanding of the physiological mechanisms, which lead to growth plate closure and the effects of this on local tissue mechanics.

MATERIALS AND METHODS

Animal Model

Wild-type mice (C57/BL6 and CBA) were housed up to four per cage in polypropylene cages with wood chip and paper bedding and provided standard mouse chow and water *ad libitum* throughout the study. Weaners up to 8 weeks of age were fed a standard rodent breeding diet and thereafter a standard rodent maintenance diet (Special Diet Services, South Witham, UK). All procedures complied with the UK Animals (Scientific Procedures) Act 1986 and were reviewed and approved by the ethics committee of the Royal Veterinary College (London, UK).

Imaging

Tissue Imaging by Benchtop MicroCT

The tibia from a 20-month-old female C57/BL6 mouse (Charles River, UK) was fixed in 70% EtOH and stored until scanning using the Skyscan 1172 (Skyscan, Kontich, Belgium), with X-ray tube operated at 50 kV and 200 μA, 1,600 ms exposure time with a 0.5 mm aluminum filter and an acquisition pixel size of 5 μm. The slices were then reconstructed using NRecon 1.6.9.4 with a pixel matrix of 2,000 × 2,000 (Skyscan, Kontich, Belgium) (Javaheri et al., 2015).

Tissue Imaging by SR MicroCT

Tibiae from an 8- and 40-week old CBA mouse were dissected and frozen at −20°C until scanning. The SR microCT was performed at Diamond Light Source on the Diamond-Manchester Branchline I13-2 using 19 keV (based on an energy sensitivity study for optimum image contrast) monochromatic X-ray (Rau et al., 2011). 1,800 projections on 180° were collected using a 4× magnification lens by a PCO 4000 CCD imaging camera with 4,008 × 2,672 pixels, giving an effective pixel size of 1.1 μm. The projections were normalized and reconstruction was performed

with the tomography reconstruction module of the software Data Analysis WorkbeNch (Dawn) 1.7 (Basham et al., 2015), using Diamond's computing cluster to produce 3D volumes of the X-ray attenuation (Atwood et al., 2010; Titarenko et al., 2010). The images were filtered using a 3D median filter with a small kernel size of 2 to remove the "shot noise" common with tomography with minimal blurring effect on image texture.

Development of a 3D Quantification Method for Growth Plate Bridging

Tibiae scans from both benchtop microCT or SR microCT were used to identify growth plate bridges observed as indicated in **Figure 1**. Scans were segmented using Avizo® software (V8.0, VSG, Burlington, VT, USA), using a region-growing algorithm within the software. This algorithm starts from a seed point and selects all connected voxels with a gray value in a given tolerance interval. The volume images were aligned manually along the metaphyseal tibial shaft (defined as the *z*-axis; **Figure 2A**) and the central points of each individual bony bridge crossing the entire growth plate width were examined from slices cut in multiple orientations, and individually identified by an observer (**Figure 2B**). To reduce uncertainties due to partial volume effects, all the bridges smaller than about 125 voxels in volume were not considered. Once all the bridges were selected, each was quantified and rendered a separate color to confirm correct manual identification.

To quantify the bone bridge local number density, a method for projecting them onto the joint surface was developed. The center of all bridges (blue circles) were extracted using a skeletonization (**Figure 2C**) and each bridge was orthogonally projected onto the tibial joint surface using an in-house line intercept method implemented in Matlab (Mathworks, USA). The method consists of (1) generating straight lines along the (*z*) direction passing through the bridges (**Figure 2D**), (2) determining the intersection between the straight lines and the tibial plateau (segmented using a region growing algorithm, **Figure 2E**), and (3) detecting the endpoints of the lines that intercept the joint surface (**Figure 2F**). From this, the areal number density, *N*, is defined as the number of bridges per 256 μm × 256 μm window (**Figure 2G**). The distribution of the areal number density of bridges is then superimposed on the tibial joint surface (each bridge has a color that represents the areal number density at the bridge location, **Figure 2H**) (Staines et al., 2016).

FE Modeling

The SR microCT images from the 8- and 40-week old mice were imported into the Avizo software (Avizo Fire, 9.2.0, VSG) to generate unstructured linear tetrahedral meshes using the methodology described by Madi et al. (2007). FE computations were carried out to simulate static compressive tests (sustained loading). The nodes at the bottom of the tibia have their vertical displacements fixed and certain rotations have been restrained to block rigid body motion. To restrain the rotations, one node is blocked in the three directions, one node is blocked along *X* and one node is blocked along *Y*. At the top, loads equal to three times body weight (~1 N) were applied as nodal forces (Cook et al., 1983) in the medial and lateral aspects of the tibia (**Figure 3**). Bone and growth plate cartilage tissues were treated as isotropic linear elastic materials (see **Table 1**) (Piszczatowski, 2012; Poulet et al., 2013). Following a mesh sensitivity study, the number of elements was fixed to about 2,500,000. The mesh density was approximately 250 voxels/element (the images were binned,

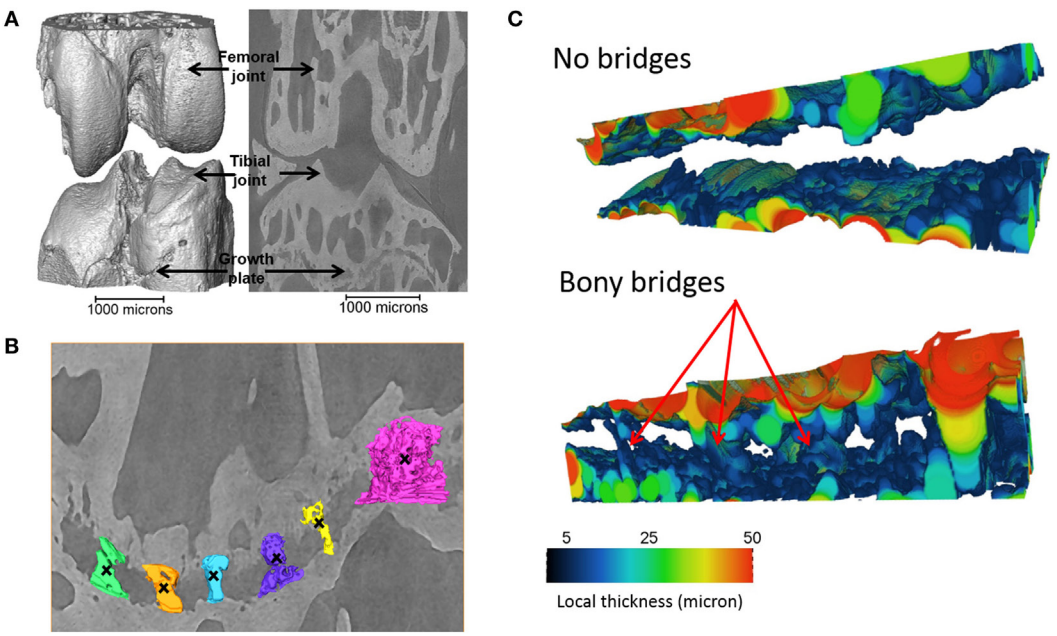

FIGURE 1 | Identification of the bridges crossing the growth plate **(A)** 3D representation of the whole joint, **(B)** bridges crossing the growth plate, in an ROI (black crosses indicate bony bridges identified by an observer). **(C)** 3D representation of the growth plate with no bridges and multiple bridges observed. Adapted from Staines et al. (2016).

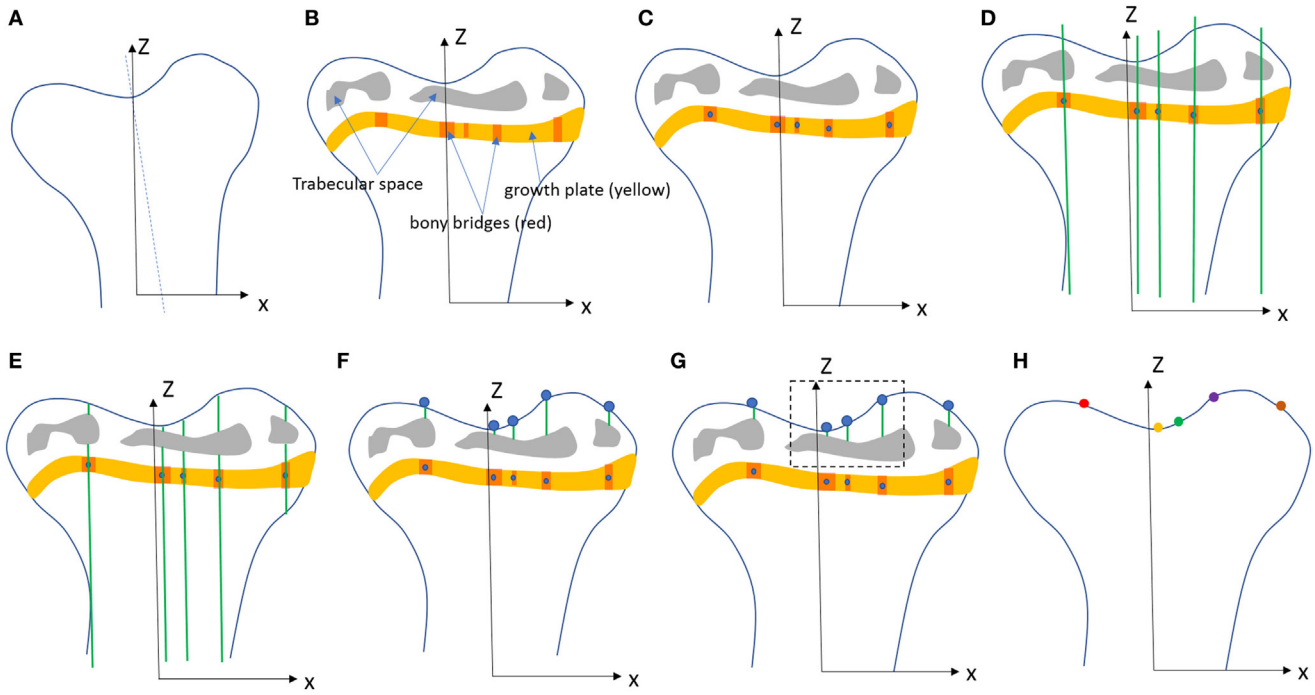

FIGURE 2 | Procedure developed to project the bridges and their areal number density onto the tibial joint surface: **(A)** the volume images were aligned along the metaphyseal tibial shaft (*z*-axis), **(B)** the central point of all bony bridges crossing the growth plate were examined from slices cut in multiple orientations, and identified by an observer who highlighted them individually with the cursor, **(C)** the center of all bridges (blue circles) were extracted using a skeletonization, **(D)** generation of straight lines along the (*z*) direction passing through the bridges, **(E)** intersection between the straight lines and the tibia (segmented using a region growing algorithm), **(F)** detection of endpoints of the lines that intercept the joint surface, **(G)** the areal number density, N_A, is calculated as the number of bridges per 256 μm × 256 μm window, **(H)** the distribution of the areal number density of bridges is superimposed on the tibial joint surface (each bridge has a color that represents the areal number density at the bridge location).

i.e., 2.2 μm voxel size), and was based on average and local (line profiles) axial stresses plotted against number of elements (error criterion: 5% of asymptotic value).

RESULTS

Herein, we used our method for the visualization and quantification of growth plate bridging, and our FE model to examine the effects of bridging on local tissue mechanics.

Application of Novel Method to Benchtop MicroCT Scans

We have previously shown that the above developed method is a valuable model for examining growth plate bridging during healthy and pathological aging (Staines et al., 2016). However, the use of SR microCT is not readily available for most laboratories due to high costs and availability of beamtime. Therefore we sought to examine whether our method could be applied to benchtop microCT at a pixel size of 5 μm. As detailed in our methods, the tibia from a C57/BL6 20-month-old female mouse was scanned using the SkyScan 1172 scanner. Images were reconstructed and our method for growth plate bridging 3D quantification method was applied (**Figures 1** and **2**). We were able to clearly identify growth plate bridges at 5 μm and once all the bridges were selected, we were able to superimpose the distribution of the areal number density onto the tibial joint surface (**Figure 4**). Spatial evaluation of growth plate bridges indicates that thicker bridges are not randomly distributed but rather that these are preferentially enriched in peripheral growth plate locations, consistent with our previous results (Staines et al., 2016) (**Figure 4**).

Application of 3D Quantification of Growth Plate Bridging in FE Models of the Loaded Tibia

We reveal that in young (8 weeks old) CBA wild-type mice, growth plate bridging is associated with locations that contain high local von Mises stresses (**Figures 5A,B**). Moreover, we reveal that with aging an increased number and density of growth plate bridges is observed (**Figure 5B**), indicative of growth plate closure (Staines et al., 2016). Our FE modeling indicates that this increase in growth plate bridging with aging is translated into greater stresses in the growth plate (**Figure 5C**). This, therefore, offers insights into the biomechanical functionality of growth plate fusion.

DISCUSSION

The results presented in this study report a method for the 3D quantification of growth plate bridging in murine bones. Although

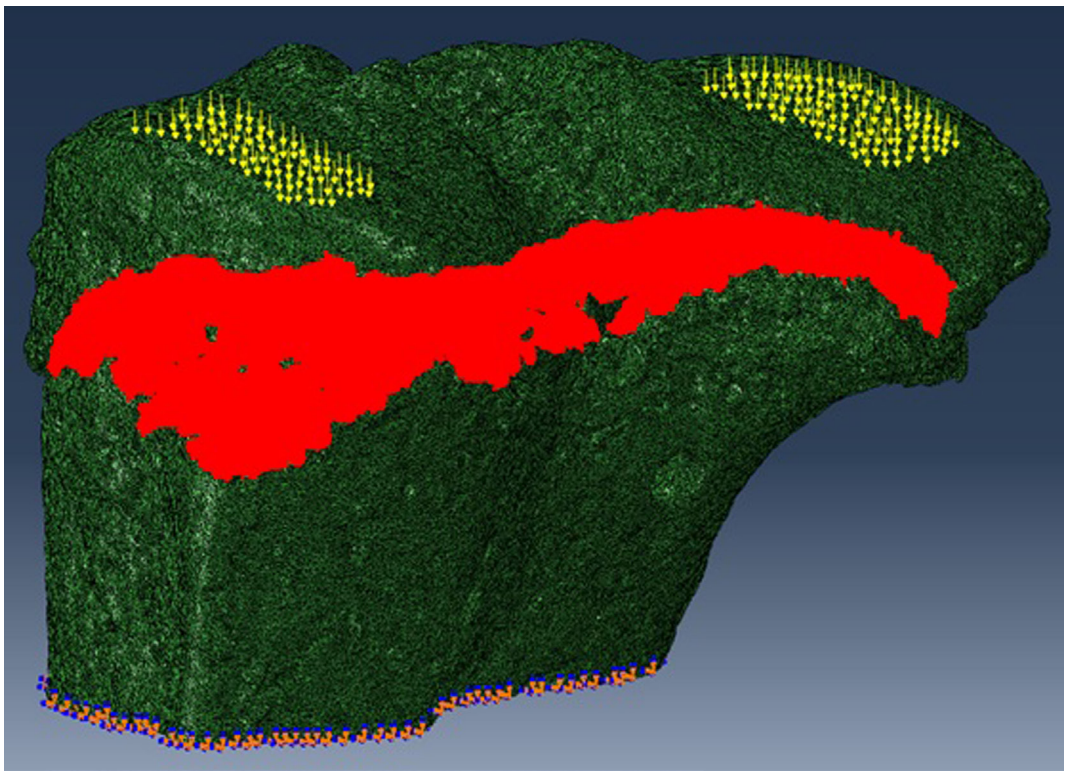

FIGURE 3 | For finite element (FE) modeling, FE computations were carried out to simulate static compressive tests (sustained loading). The nodes at the bottom of the tibia have their vertical displacements fixed and certain rotations are restrained to block rigid body motion. At the top, equal loads of three times body weight (~1 N) were applied in the medial and lateral aspects of the tibia.

TABLE 1 | Material properties of bone and cartilage.

Material properties	Bone	Growth plate
E (MPa)	17,000	6
Poisson coefficient	0.3	0.49

initially developed for SR microCT, we demonstrate that this method can also be applied to benchtop microCT scans collected at high resolutions. Furthermore, we reveal that this model can then be combined with FE modeling to understand local tissue mechanics. The relationship between mechanical loads and the local stresses and strains that influence tissue formation can be calculated using computational models for macro-, meso-, and nano-scales (Webster et al., 2008; Schulte et al., 2013). This method described herein will contribute to future advances in the development of hierarchical models for understanding bone development and adaptation.

We show that, in wild-type mice, increased growth plate bridging translates into increased stresses in the bone directly beneath the growth plate. At 8 weeks (**Figure 5B**), few bridges are detected and overall the growth plate is squeezed in a "sandwich" configuration. This suggests that compressive hydrostatic stresses are engendered across major volumes and that higher shear stresses are generated only at the peripheral edges of the growth plate. Yet, the results of numerous mechanobiological

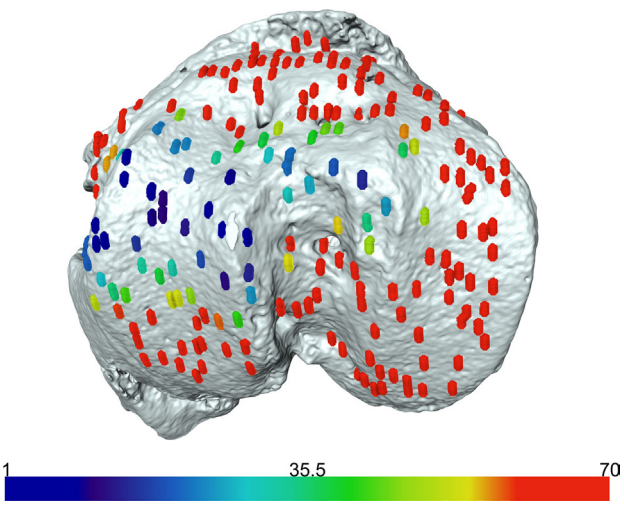

FIGURE 4 | Laboratory-based computed tomography image of the tibial joint surface from a 20-month-old C57BL6 female mouse. The distribution of the areal number density of bridges is superimposed on the tibial joint surface and each bridge has a color that represents the areal number density at the bridge location.

models support that growth and ossification is accelerated by tensile strain (or shear stresses) and that cartilage tends to be maintained by hydrostatic compressive stress (Carter and Wong,

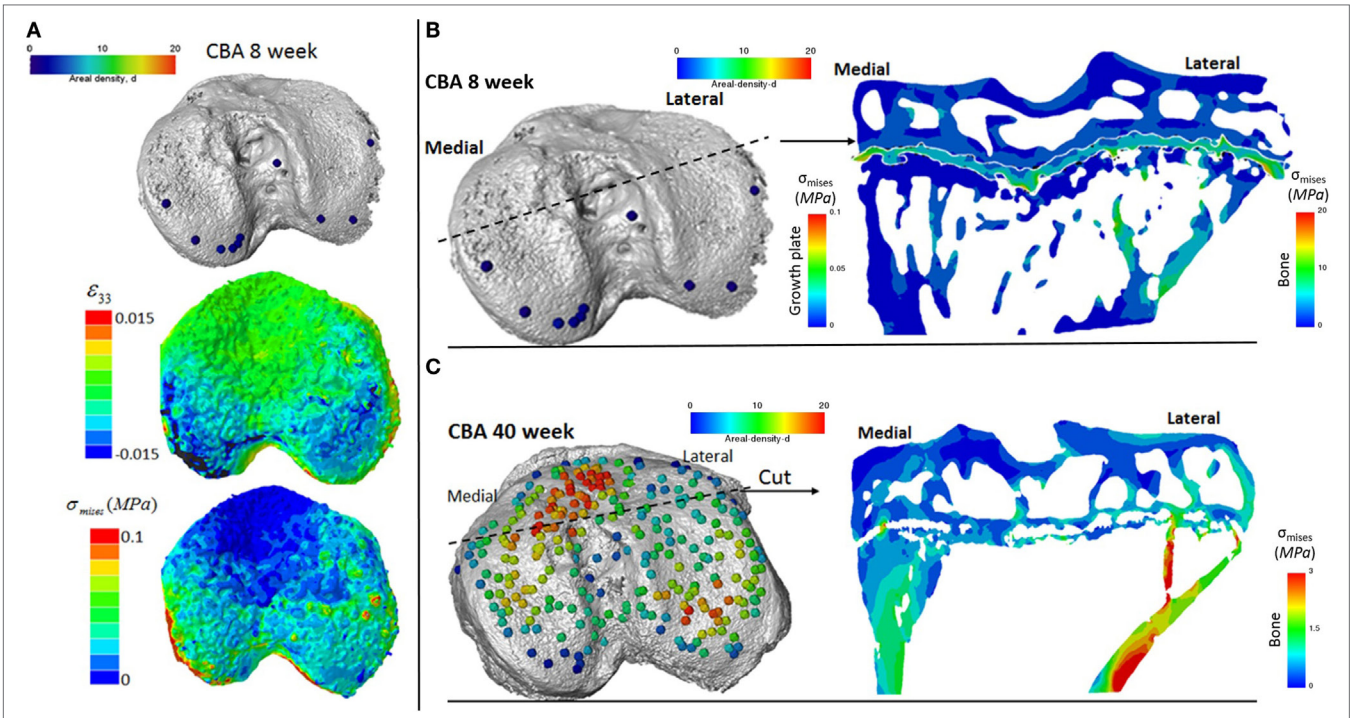

FIGURE 5 | Finite element models of the loaded tibia in CBA wild-type mice **(A)** visualization of von Mises stresses on the tibial joint plateau. Visualization of the stresses associated with growth plate bridging in a coronal section of the tibia for a **(B)** young (8 week) and **(C)** mature (40 week) mouse joint.

2003; Stokes et al., 2007; Villemure and Stokes, 2009). This would be consistent with our observations and may offer an explanation for why the bridges start growing first at the edges. At 40 weeks (**Figure 5C**), the mechanical environment of the growth plate is more complex; the thicker bridges act as stress concentrators. This appears to increase the likelihood that growth plate bridges in older animals will fracture under loading and/or achieve the redistribution of stresses to within their particular vicinities of the growth plate cartilage. Reciprocally, during endochondral ossification, growth-related strain in the mice may generate stresses that are contained by the bony bridges, accelerating growth arrest at these vicinities. More time points (between 8 and 40 weeks) and modeling are needed to support this hypothesis, but this work has provided novel insights into the use of CT, advanced image processing, and FE modeling in understanding biomechanics in health and disease. Our methodology offers a unique mode for visualizing these events and the potential to address questions that have hitherto remained elusive in this field.

There are a number of unanswered questions in our pursuit of understanding growth plate closure such as; in which direction does growth plate bridging occur? Does bridging follow a conserved pattern across all growth plates? What is the trajectory of individual bridge expansion during growth cessation? And does genetics or mechanics define the initiation and progression of growth plate bridging? Such questions may now be addressable with the development of our novel non-invasive method for 3D quantification of bony bridging linked to FE models, and this will likely advance understanding of mechanisms involved in growth plate closure, which have hitherto been hindered somewhat by reliance upon invasive, largely histological methods.

The growth plate is responsible for the development and growth of long bones, up until puberty at which point it begins to close. During this closure, bone bridges form and span the width of the growth plate, eventually leading to the replacement of the entire growth plate cartilage anlagen by mineralized bone. Histological studies have identified this to be an early event involving several pre-osteoblastic molecules such as osteoprotegerin, interleukin-6, bone morphogenetic protein, and Collagen type X (Pichler et al., 2013). Similarly, trauma to the growth plate, e.g., in fractures, can also provoke abnormal growth plate bridging and the impairment of longitudinal growth.

Biomechanically, the growth plate is subject to a number of different loads placed upon it and previous studies have identified regional variations in the mechanical properties of the growth plate and surrounding tissues by confocal and atomic force microscopies (Bachrach et al., 1995; Radhakrishnan et al., 2004; Villemure et al., 2007). It is known that different compressive mechanical strains are found throughout the different zones of the growth plate, with the proliferative zone of chondrocytes exhibiting lower compressive strains than that of the resting and hypertrophic zones (Villemure et al., 2007). Similarly, compressive differences are also observed spatially throughout the growth plate with interior samples from bovine femoral growth plates being 40% more rigid than samples taken from the periphery of the growth plate (Cohen et al., 1994). Here, we reveal an association between growth plate bridging and increased stress

dissipation distal to the growth plate, by applying FE modeling to our method. Future investigations will improve FE models to include more realistic boundary conditions, material properties, and cartilage mechanobiological principles. Our final aim is to examine the combined effects of hydrostatic pressure and shear stress (in the form of an osteogenix index) on the development of the skeleton and articular cartilage.

We have previously used SR microCT to study growth plate bridging in the context of a murine model of spontaneous osteoarthritis (Staines et al., 2016). Herein, we have also employed benchtop microCT to image the tibia of wild-type mice and confirm suitability of using benchtop microCT-based imaging for bridging analysis. Despite imaging at a lower resolution (5 instead of 1.1 μm voxel size), we were able to replicate our method and confirm that in both imaging modalities, similar data can be obtained. Further, the data obtained from the benchtop microCT are analogous to the gold-standard SR imaging. Of course, there are disadvantages related to the use of dose radiation. This may have an impact on the mechanical properties of bone and cartilage and limit the validity of 4D *in situ* mechanical experiments as showed by Barth et al. (2010), but to our knowledge, exert little effect on the 3D morphology. The missing link in current mechanobiological models is the 3D real morphology of the growth plate which is very complex and cannot be captured correctly by 2D approaches. Herein, we have aimed to address this by describing and then utilizing our 3D non-destructive imaging methodology for the quantification of growth plate bridging. Employment of these 3D analyses of growth plate bone bridging is likely to advance our understanding of the physiological mechanisms, which lead to growth plate closure and subsequent FE modeling allows investigations into the associated biomechanical functionality. This will ultimately enable investigators to study the role of local tissue mechanics on endochondral ossification patterns, skeletal morphology, and articular cartilage function.

ETHICS STATEMENT

This study was carried out in accordance with the recommendations of the UK Animals (Scientific Procedures) Act 1986 and were reviewed and approved by the ethics committee of the Royal Veterinary College (London, UK).

AUTHOR CONTRIBUTIONS

Conception and design of work: KS, KM, PL, and AP. Acquisition of data: KM and BJ. Interpretation of data, revising the manuscript and final approval, and agreement to be accountable for all aspects of the work: KS, KM, BJ, PL, and AP. Drafting the manuscript: KS.

FUNDING

This work was funded by Arthritis Research UK (18768 and 20581) and by the EPSRC (EP/I02249X/1). Facilities and research support were provided by the Diamond-Manchester Branchline (I13-2) at Diamond Light Source (Beamtimes MT13237-1, MT11076-1, MT5003-1). The datasets generated during and/or analysed during this study are not publicly available due to their large size but are available from the corresponding author on reasonable request.

REFERENCES

Anderson, H. C. (1995). Molecular biology of matrix vesicles. *Clin. Orthop. Relat. Res.* 314, 266–280.

Atwood, R. C., Lee, P. D., Konerding, M. A., Rockett, P., and Mitchell, C. A. (2010). Quantitation of microcomputed tomography-imaged ocular microvasculature. *Microcirculation* 17, 59–68. doi:10.1111/j.1549-8719.2009.00009.x

Bachrach, N. M., Valhmu, W. B., Stazzone, E., Ratcliffe, A., Lai, W. M., and Mow, V. C. (1995). Changes in proteoglycan synthesis of chondrocytes in articular cartilage are associated with the time-dependent changes in their mechanical environment. *J. Biomech.* 28, 1561–1569. doi:10.1016/0021-9290(95)00103-4

Ballock, R. T., and O'Keefe, R. J. (2003). Physiology and pathophysiology of the growth plate. *Birth Defects Res. C Embryo Today* 69, 123–143. doi:10.1002/bdrc.10014

Barth, H. D., Zimmermann, E. A., Schaible, E., Tang, S. Y., Alliston, T., and Ritchie, R. O. (2010). Characterization of the effects of x-ray irradiation on the hierarchical structure and mechanical properties of human cortical bone. *Biomaterials* 32, 8892–8904. doi:10.1016/j.biomaterials.2011.08.013

Basham, M., Filik, J., Wharmby, M. T., Chang, P. C., El Kassaby, B., Gerring, M., et al. (2015). Data Analysis WorkbeNch (DAWN). *J Synchrotron Radiat* 22, 853–858. doi:10.1107/S1600577515002283

Becks, H., Asling, C. W., Collins, D. A., Simpson, M. E., and Evans, H. M. (1948). Changes with increasing age in the ossification of the third metacarpal of the female rat. *Anat. Rec.* 100, 577–591. doi:10.1002/ar.1091000407

Betts, D. C., and Müller, R. (2014). Mechanical regulation of bone regeneration: theories, models, and experiments. *Front. Endocrinol.* 2014:5. doi:10.3389/fendo.2014.00211

Carter, D. R., and Wong, M. (1988). Mechanical stresses and endochondral ossification in the chondroepiphysis. *J. Orthop. Res.* 6, 148–154. doi:10.1002/jor.1100060120

Carter, D. R., and Wong, M. (2003). Modelling cartilage mechanobiology. *Philos. Trans. R. Soc. Lond. B Biol. Sci.* 358. Available at: http://rstb.royalsocietypublishing.org/content/358/1437/1461

Castagnola, P., Dozin, B., Moro, G., and Cancedda, R. (1988). Changes in the expression of collagen genes show two stages in chondrocyte differentiation in vitro. *J. Cell Biol.* 106, 461–467. doi:10.1083/jcb.106.2.461

Cohen, B., Chorney, G. S., Phillips, D. P., Dick, H. M., and Mow, V. C. (1994). Compressive stress-relaxation behavior of bovine growth plate may be described by the nonlinear biphasic theory. *J. Orthop. Res.* 12, 804–813. doi:10.1002/jor.1100120608

Cook, S. D., Lavernia, C. J., Burke, S. W., Skinner, H. B., and Haddad, R. J. Jr. (1983). A biomechanical analysis of the etiology of the tibia vara. *J. Pediatr. Orthop.* 3, 449–454. doi:10.1097/01241398-198309000-00006

Gao, J., Williams, J. L., and Roan, E. (2014). On the state of stress in the growth plate under physiologic compressive loading. *Open J. Biophys.* 4, 41661–41670. doi:10.4236/ojbiphy.2014.41003

Garzón-Alvarado, D. A., García-Aznar, J. M., and Doblaré, M. (2009). A reaction-diffusion model for long bones growth. *Biomech. Model. Mechanobiol.* 8, 381–395. doi:10.1007/s10237-008-0144-z

Gerhard, F. A., Webster, D. J., van Lenthe, G. H., and Müller, R. (2009). In silico biology of bone modelling and remodelling: adaptation. *Philos. Trans. A Math. Phys. Eng. Sci.* 367, 2011–2030. doi:10.1098/rsta.2008.0297

Giorgi, M., Carriero, A., Shefelbine, S. J., and Nowlan, N. C. (2015). Effects of normal and abnormal loading conditions on morphogenesis of the prenatal hip joint: application to hip dysplasia. *J. Biomech.* 2015, 3390–3397. doi:10.1016/j.jbiomech.2015.06.002

Grumbach, M. M. (2000). Estrogen, bone, growth and sex: a sea change in conventional wisdom. *J. Pediatr. Endocrinol. Metab.* 13(Suppl. 6), 1439–1455. doi:10.1515/jpem-2000-s619

Grumbach, M. M., and Auchus, R. J. (1999). Estrogen: consequences and implications of human mutations in synthesis and action. *J. Clin. Endocrinol. Metab.* 84, 4677–4694. doi:10.1210/jcem.84.12.6290

Hunziker, E. B., Schenk, R. K., and Cruz-Orive, L. M. (1987). Quantitation of chondrocyte performance in growth-plate cartilage during longitudinal bone growth. *J. Bone Joint Surg. Am.* 69, 162–173. doi:10.2106/00004623-198769020-00002

Javaheri, B., Carriero, A., Staines, K. A., Chang, Y. M., Houston, D. A., Oldknow, K. J., et al. (2015). Phospho1 deficiency transiently modifies bone architecture yet produces consistent modification in osteocyte differentiation and vascular porosity with ageing. *Bone* 81, 277–291. doi:10.1016/j.bone.2015.07.035

Lacroix, D., and Prendergast, P. J. (2002a). A mechano-regulation model for tissue differentiation during fracture healing: analysis of gap size and loading. *J. Biomech.* 35, 1163–1171. doi:10.1016/S0021-9290(02)00086-6

Lacroix, D., and Prendergast, P. J. (2002b). Three-dimensional simulation of fracture repair in the human tibia. *Comput. Methods Biomech. Biomed. Engin.* 2002, 369–376. doi:10.1080/1025584021000025014

Lacroix, D., Prendergast, P. J., Li, G., and Marsh, D. (2002). Biomechanical model to simulate tissue differentiation and bone regeneration: application to fracture healing. *Med. Biol. Eng. Comput.* 2002, 14–21. doi:10.1007/BF02347690

Lin, H., Aubin, C. E., Parent, S., and Villemure, I. (2009). Mechanobiological bone growth: comparative analysis of two biomechanical modeling approaches. *Med. Biol. Eng. Comput.* 47, 357–366. doi:10.1007/s11517-008-0425-9

Mackie, E. J., Tatarczuch, L., and Mirams, M. (2011). The skeleton: a multi-functional complex organ: the growth plate chondrocyte and endochondral ossification. *J. Endocrinol.* 211, 109–121. doi:10.1530/JOE-11-0048

Madi, K., Forest, S., Boussuge, M., Gailliègue, S., Lataste, E., Buffière, J., et al. (2007). Finite element simulations of the deformation of fused-cast refractories based on X-ray computed tomography. *Comput. Mater. Sci.* 39, 224–229. doi:10.1016/j.commatsci.2006.01.033

Morishima, A., Grumbach, M. M., Simpson, E. R., Fisher, C., and Qin, K. (1995). Aromatase deficiency in male and female siblings caused by a novel mutation and the physiological role of estrogens. *J. Clin. Endocrinol. Metab.* 80, 3689–3698. doi:10.1210/jcem.80.12.8530621

Moss, M. L., and Noback, C. R. (1958). A longitudinal study of digital epiphyseal fusion in adolescence. *Anat. Rec.* 131, 19–32. doi:10.1002/ar.1091310103

Parfitt, A. M. (2002). Misconceptions (1): epiphyseal fusion causes cessation of growth. *Bone* 30, 337–339. doi:10.1016/S8756-3282(01)00668-8

Pichler, K., Musumeci, G., Vielgut, I., Martinelli, E., Sadoghi, P., Loreto, C., et al. (2013). Towards a better understanding of bone bridge formation in the growth plate? An immunohistochemical approach. *Connect. Tissue Res.* 54, 408–415. doi:10.3109/03008207.2013.828715

Piszczatowski, S. (2012). Geometrical aspects of growth plate modelling using Carters and Stokess approaches. *Acta Bioeng. Biomech.* 14, 93–106.

Poulet, B., Westerhof, T. A., Hamilton, R. W., Shefelbine, S. J., and Pitsillides, A. A. (2013). Spontaneous osteoarthritis in Str/ort mice is unlikely due to greater vulnerability to mechanical trauma. *Osteoarthr. Cartil.* 21, 756–763. doi:10.1016/j.joca.2013.02.652

Prendergast, P. J., Huiskes, R., and Søballe, K. (1997). Biophysical stimuli on cells during tissue differentiation at implant interfaces. *J. Biomech.* 30, 539–548. doi:10.1016/S0021-9290(96)00140-6

Radhakrishnan, P., Lewis, N. T., and Mao, J. J. (2004). Zone-specific micromechanical properties of the extracellular matrices of growth plate cartilage. *Ann. Biomed. Eng.* 32, 284–291. doi:10.1023/B:ABME.0000012748.41851.b4

Rau, C., Wagner, U., Pesic, Z., and De Fanis, A. (2011). Coherent imaging at the diamond beamline I13. *Phys. Status Solidi* 208, 2522–2525. doi:10.1002/pssa.201184272

Reina-Romo, E., Gómez-Benito, M. J., García-Aznar, J. M., Domínguez, J., and Doblaré, M. (2010). Growth mixture model of distraction osteogenesis: effect of pre-traction stresses. *Biomech. Model. Mechanobiol.* 2010, 103–115. doi:10.1007/s10237-009-0162-5

Roberts, S., Narisawa, S., Harmey, D., Millán, J. L., and Farquharson, C. (2007). Functional involvement of PHOSPHO1 in matrix vesicle-mediated skeletal mineralization. *J. Bone Miner. Res.* 22, 617–627. doi:10.1359/jbmr.070108

Schulte, F. A., Ruffoni, D., Lambers, F. M., Christen, D., Webster, D. J., Kuhn, G., et al. (2013). Local mechanical stimuli regulate bone formation and resorption in mice at the tissue level. *PLoS ONE* 2013:e62172. doi:10.1371/journal.pone.0062172

Shefelbine, S. J., and Carter, D. R. (2004). Mechanobiological predictions of growth front morphology in developmental hip dysplasia. *J. Orthop. Res.* 22, 346–352. doi:10.1016/j.orthres.2003.08.004

Smith, E. P., Boyd, J., Frank, G. R., Takahashi, H., Cohen, R. M., Specker, B., et al. (1994). Estrogen resistance caused by a mutation in the estrogen-receptor gene in a man. *N. Engl. J. Med.* 331, 1056–1061. doi:10.1056/NEJM199410203311604

Staines, K. A., Macrae, V. E., and Farquharson, C. (2012). The importance of the SIBLING family of proteins on skeletal mineralisation and bone remodelling. *J. Endocrinol.* 214, 241–255. doi:10.1530/JOE-12-0143

Staines, K. A., Madi, K., Mirczuk, S. M., Parker, S., Burleigh, A., Poulet, B., et al. (2016). Endochondral growth defect and deployment of transient chondrocyte behaviors underlie osteoarthritis onset in a natural murine model. *Arthritis Rheumatol.* 68, 880–891. doi:10.1002/art.39508

Stokes, I. A., Aronsson, D. D., Dimock, A. N., Cortright, V., and Beck, S. (2006). Endochondral growth in growth plates of three species at two anatomical locations modulated by mechanical compression and tension. *J. Orthop. Res.* 24, 1327–1334. doi:10.1002/jor.20189

Stokes, I. A., Clark, K. C., Farnum, C. E., and Aronsson, D. D. (2007). Alterations in the growth plate associated with growth modulation by sustained compression or distraction. *Bone* 41, 197–205. doi:10.1016/j.bone.2007.04.180

Terkeltaub, R., Rosenbach, M., Fong, F., and Goding, J. (1994). Causal link between nucleotide pyrophosphohydrolase overactivity and increased intracellular inorganic pyrophosphate generation demonstrated by transfection of cultured fibroblasts and osteoblasts with plasma cell membrane glycoprotein-1. Relevance to cal. *Arthritis Rheum.* 37, 934–941. doi:10.1002/art.1780370624

Titarenko, V., Titarenko, S., Withers, P. J., De Carlo, F., and Xiao, X. (2010). Improved tomographic reconstructions using adaptive time-dependent intensity normalization. *J. Synchrotron Radiat.* 17, 689–699. doi:10.1107/S0909049510024908

Villemure, I., Cloutier, L., Matyas, J. R., and Duncan, N. A. (2007). Non-uniform strain distribution within rat cartilaginous growth plate under uniaxial compression. *J. Biomech.* 40, 149–156. doi:10.1016/j.jbiomech.2005.11.008

Villemure, I., and Stokes, I. A. F. (2009). Growth plate mechanics and mechanobiology. A survey of present understanding. *J. Biomech.* 45, 1793–1803. doi:10.1016/j.jbiomech.2009.05.021

Webster, D. J., Morley, P. L., van Lenthe, G. H., and Müller, R. (2008). A novel *in vivo* mouse model for mechanically stimulated bone adaptaion – a combined experimental and compulational validation study. *Comput. Methods Biomech. Biomed. Eng.* 11, 435–441. doi:10.1080/10255840802078014

Weise, M., De-Levi, S., Barnes, K. M., Gafni, R. I., Abad, V., and Baron, J. (2001). Effects of estrogen on growth plate senescence and epiphyseal fusion. *Proc. Natl. Acad. Sci. U.S.A.* 98, 6871–6876. doi:10.1073/pnas.121180498

Xian, C. J., Zhou, F. H., McCarty, R. C., and Foster, B. K. (2004). Intramembranous ossification mechanism for bone bridge formation at the growth plate cartilage injury site. *J. Orthop. Res.* 22, 417–426. doi:10.1016/j.orthres.2003.08.003

Zelzer, E., McLean, W., Ng, Y. S., Fukai, N., Reginato, A. M., Lovejoy, S., et al. (2002). Skeletal defects in VEGF(120/120) mice reveal multiple roles for VEGF in skeletogenesis. *Development* 129, 1893–1904.

Conflict of Interest Statement: The authors declare that the research was conducted in the absence of any commercial or financial relationships that could be construed as a potential conflict of interest.

frontiers in Materials

ORIGINAL RESEARCH
published: 21 December 2017
doi: 10.3389/fmats.2017.00043

X-ray Tomographic Imaging of Tensile Deformation Modes of Electrospun Biodegradable Polyester Fibers

Jekaterina Maksimcuka[1], Akiko Obata[2], William W. Sampson[1], Remi Blanc[3], Chunxia Gao[2], Philip J. Withers[1,4,5], Olga Tsigkou[1], Toshihiro Kasuga[2], Peter D. Lee[1,5] and Gowsihan Poologasundarampillai[1,5]**

[1] School of Materials, University of Manchester, Manchester, United Kingdom, [2] Division of Advanced Ceramics, Nagoya Institute of Technology, Nagoya, Japan, [3] Thermo Fisher Scientific, Bordeaux, France, [4] Manchester X-ray Imaging Facility, University of Manchester, Manchester, United Kingdom, [5] Research Complex at Harwell, Rutherford Appleton Laboratory, Harwell, United Kingdom

OPEN ACCESS

Edited by:
Gianluca Tozzi, University of Portsmouth, United Kingdom

Reviewed by:
Maria Letizia Focarete, Università di Bologna, Italy
Kheng Lim Goh, Newcastle University, United Kingdom

***Correspondence:**
Akiko Obata
obata.akiko@nitech.ac.jp;
Gowsihan Poologasundarampillai
g.poolo@manchester.ac.uk

Specialty section:
This article was submitted to Mechanics of Materials, a section of the journal Frontiers in Materials

Received: *11 September 2017*
Accepted: *04 December 2017*
Published: *21 December 2017*

Citation:
Maksimcuka J, Obata A, Sampson WW, Blanc R, Gao C, Withers PJ, Tsigkou O, Kasuga T, Lee PD and Poologasundarampillai G (2017) X-ray Tomographic Imaging of Tensile Deformation Modes of Electrospun Biodegradable Polyester Fibers. Front. Mater. 4:43. doi: 10.3389/fmats.2017.00043

Electrospinning allows the production of fibrous networks for tissue engineering, drug delivery, and wound healing in health care. It enables the production of constructs with large surface area and a fibrous morphology that closely resembles the extracellular matrix of many tissues. A fibrous structure not only promotes cell attachment and tissue formation but could also lead to very interesting mechanical properties. Poly(3-hydroxybutyrate-co-4-hydroxybutyrate) (P(3HB-co-4HB)) is a biodegradable polyester that exhibits a large (>400%) elongation before failure. In this study, synchrotron X-ray phase contrast imaging was performed during tensile deformation to failure on a non-woven fiber mat of P(3HB-co-4HB) fibers. Significant reorientation of the fibers in the straining direction was observed, followed by localized necking and eventual failure. From an original average fiber diameter of 4.3 μm, a bimodal distribution of fiber diameter (modal diameters of 1.9 and 3.7 μm) formed after tensile deformation. Extensive localized necking (thinning) of fibers between (thicker) fiber–fiber contacts was found to be the cause for non-uniform thinning of the fibers, a phenomenon that is expected but has not been observed in 3D previously. The data presented here have implications not only in tissue regeneration but for fibrous materials in general.

Keywords: scaffolds, *in situ*, fiber necking, tissue regeneration, synchrotron X-ray

INTRODUCTION

Electrospun constructs for the repair of load-bearing tissues are required to have adequate mechanical properties. However, the failure mechanisms of electrospun fibrous materials are not well understood. Existing literature focuses on failure modes of individual fibers and/or on bulk mechanical properties of whole fiber mats. In this manuscript, we investigate the tensile deformation of a biodegradable polyester, P(3HB-co-4HB), that undergoes large elongation to failure using a bespoke tensile tester (P2R) and synchrotron X-ray tomography to shed light on structure–property relationships.

Biodegradable and biocompatible polymers are in use to produce implant materials for tissue regeneration. Polyesters such as poly(L-lactic acid) (PLLA) and poly(L-glycolic acid) (PLGA) are used in several FDA-approved medical devices (Jamshidian et al., 2010; Makadia and Siegel, 2011). Poly (3-hydroxybutyrate-co-4-hydroxybutyrate) (P(3HB-co-4HB)) is a type of polyester in the family of polyhydroxyalkanoates (PHA) and is produced by microorganisms under unbalanced growth conditions (Türesin et al., 2001). PHAs are of significant interest to the biomedical community due to their biodegradability, biocompatibility, and mechanical properties (Anjum et al., 2016; Li and Loh, 2017). Physical properties of microbial polyesters can be regulated by varying the proportions of the copolymers. In the case of P(3HB-co-4HB), enzymatic degradation and mechanical properties, such as elongation and tensile strength, can be regulated by varying the 4HB content. One of the remarkable properties of P(3HB-co-4HB) is its large elongation before failure. Saito and Doi (1994) showed that the P(3HB-co-4HB) films with 82 mol% 4HB exhibit 1320% elongation before failure. These remarkable mechanical properties of P(3HB-co-4HB) are a result of a unique 4HB fraction that reduces the crystallinity of the polymer which in turn influences the mechanical properties (Saito and Doi, 1994; Türesin et al., 2001). Thus, P(3HB-co-4HB) has considerable potential for use as a biodegradable material in implants requiring large elongation.

Electrospun fibers of biodegradable polymers are excellent candidate materials for use in tissue engineering, drug delivery, and wound healing (Greiner and Wendorff, 2007; Sill and von Recum, 2008; Poologasundarampillai et al., 2011; Vigneswari et al., 2016). Electrospinning is a versatile technique to produce fibrous materials with structures ranging from randomly oriented fiber mats and aligned fiber conduits to spun knitted or twisted yarns (Teo and Ramakrishna, 2006) or cotton-wool-like structures (Poologasundarampillai et al., 2014). Continuous fibers with diameters ranging from 10s of nanometers to a few microns can be produced (Badami et al., 2006; Jose et al., 2009). The continuous ultrathin fibers have unique properties when compared to bulk materials. Interesting observations of higher elastic modulus and tensile strength compared to bulk films have been observed, although with controversy on the specific fiber diameter at which the increase starts to occur (Tan and Lim, 2004; Liu et al., 2011). Several types of electrospun P(3HB-co-4HB) fibres have been developed for use in tissue regeneration applications. Vigneswari et al. (2016) prepared electrospun P(3HB-co-4HB)/collagen peptides for wound healing and reported that cell compatibility (*in vitro*) and wound healing (*in vivo*) were improved by adding collagen peptides to P(3HB-co-4HB). Zhijiang et al. (2017) controlled mechanical properties of electrospun P(3HB-co-4HB) by blending zein, natural protein obtained from corn, and confirmed the electrospun P(3HB-co-4HB)/zein was biocompatibile *in vitro*. Nishizuka et al. (2014) focused on the excellent elongation property of P(3HB-co-4HB) to develop a novel fracture fixation device, intramedullary-fixation with biodegradable materials, for weakened long bones using electrospun P(3HB-co-4HB) as a bone-cement bag. All the aforementioned and future developments of electrospun P(3HB-co-4HB) materials for tissue regeneration heavily depends on an in-depth knowledge of their mechanical behavior under tensile loading and their failure modes. In this study, X-ray tomography was employed to investigate the mechanical deformation of electrospun P(3HB-co-4HB) networks over large tensile strains, and the correlation of mechanical properties to structure is investigated.

Tensile properties of electrospun fiber mats depend on several factors: the microstructure of individual fibers and macroscopic organization of the fibers, including alignment, their length, porosity, the number of fiber-fiber contacts, and the joint strength at these regions of contact (Pedicini and Farris, 2003; Rizvi et al., 2012). Further, many of the techniques for conventionally studying the micromechanics of materials are not well suited to the study of 3D fiber mats, and so their behavior is not yet well understood. Such electrospun materials have submicron features which are not easily resolved using optical techniques. Fiber mats up to 1 mm in thickness are often produced for use as membranes in tissue engineering, EM, and optical measurements which have short depth of focus are not able to capture, simultaneously, the deformation of the entire 3D fiber mats. Despite these limitations, these techniques have been successfully applied to assess the deformation of single fibers and their mechanical properties. Several authors have employed SEM in combination with AFM or optical microscopy in combination with AFM- or MEMS-based device to investigate the structure of nanofibers following tensile deformation (Yu et al., 2000; Zussman et al., 2006; Naraghi et al., 2007; Baker et al., 2016). Such investigations have revealed that the deformation of electrospun fibers is *via* multiple neck formation (also described as ripples) and crazing followed by rupture of multiple thin fibrils. Literature on the failure mechanisms of whole fiber mats is sparse. It is known that in the case of non-woven fiber mats the fibers first reorientate to the direction of the applied force, and this is then followed by fiber thinning and failure of individual fibers and hence the network (Lee et al., 2002; Pedicini and Farris, 2003; Kim et al., 2004; Lu et al., 2008; Cheng et al., 2011). The complex micro and macro-structures formed by electrospinning makes it a difficult task to explain failure mechanisms of entire fiber mats and then to compare it to individual fibers and bulk materials. Bulk elastomeric materials fail at high strains; molecular realignment at lower stresses leads to accommodation of large elongation and concurrent strain hardening, bulk materials therefore fracture at higher stresses and large strain (Pedicini and Farris, 2003). While, electrospun materials fail at considerably lower strains compared to their bulk counterparts. Attempts have been made in the past to explain these disparities in the failure of electrospun fiber mats to bulk materials through their differences in molecular alignments and fiber mat structure (Pedicini and Farris, 2003). Although these insights are useful, the structural correlation to deformation are derived from *ex situ* tensile testing and post-SEM imaging, where the fibers were allowed to relax between loads, leading to an incomplete picture of the failure mechanism. Mathematical models of random fiber mats on the other hand have come a long way in describing the micro and macro structural changes with tensile testing (Xiaofan et al., 2009; Rizvi et al., 2012; Rizvi and Pal, 2014; Mohammadzadehmoghadam

et al., 2016; Zundel et al., 2017). In particular, elastic moduli, tensile strength, fiber realignment, and fiber elongation (stretch) with network connectivity can be modeled with good accuracy. However, models assume a homogeneous intra-fiber structure and hence are unable to reproduce changes in fiber diameter with strain. The assumptions of idealized inter–fiber interactions and network characteristics also produce an idealistic prediction of the structural changes.

In this study, we perform *in situ* 3D high resolution X-ray computed tomography (CT) measurements on tensile testing of P(3HB-co-4HB) fiber mats using synchrotron based X-rays available at the Diamond Light Source Diamond-Manchester (I13-2) beamline. We then apply sophisticated segmentation and quantification of the data to provide novel insights into the failure of P(3HB-co-4HB) non-woven fiber mats.

MATERIALS AND METHODS

Preparation of P(3HB-co-4HB) Fiber Mats

Poly(3-hydroxybutyrate-co-4-hydroxybutyrate), G5, Japan) with a molecular weight of 660 kDa and containing 18 mol% 4-hydroxybutyrate (4HB) was dissolved in a mixture of chloroform and acetone (Wako Pure Chemicals Industries Ltd., Japan) with 100/0, 75/25, 65/35, 50/50, and 0/100 of the chroloform/acetone weight ratio and P(3HB-co-4HB) concentration of 8 wt%. P(3HB-co-4HB) fiber mats were fabricated with a Nanofibre Electrospinning Unit (Kato Tech Co., Japan) run at 8 kV applied to a metallic needle placed 150 mm from a grounded rotating drum collector rotating at a speed of 0.08 m s^{-1} (**Figure 1**). A solution flow rate of 1.5 µl s^{-1} was used.

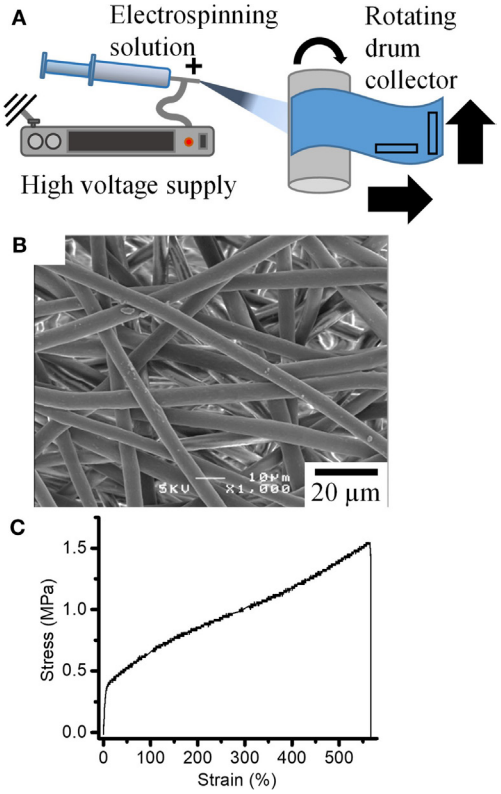

FIGURE 1 | **(A)** Schematic of electrospinning setup used to produce fiber mats. **(B)** SEM image of the fiber mats obtained. **(C)** Typical stress–strain curves for the tensile deformation of the fiber mats.

Microstructural Characterization

The surface morphology and fiber diameter of the fiber mats were analyzed by scanning electron microscopy (JSM-6301F, JEOL, Japan). Prior to the SEM observation, all of the samples were coated with amorphous osmium (Neoc, Meiwafosis, Japan). The average fiber diameter was determined from 100 measurements using ImageJ software.

Tensile Tests

Rectangular P(3HB-co-4HB) fiber mats (n = 8) measuring 20 mm length, 5 mm width, and 0.1 mm thickness were cut from as-prepared samples with the longest side (20 mm) in the direction parallel or perpendicular to the spinning direction, as shown in **Figure 1**. Sample cross sectional area was calculated as 5 mm × 0.1 mm. Cut samples were then tested in tension along this side using Autograph (AGS-G, Shimadzu, Japan) at a rate of 0.1 mm s^{-1}.

In Situ Synchrotron Imaging and Tensile Deformation

Tensile Testing on the P2R

Dog bone shaped fiber mats (**Figure 2**) were laser cut using an FB series laser cutter with a power of 5 W and 100 mm s^{-1} travel speed. Samples were clamped between a set of purpose-built grips and loaded onto a bespoke micro-mechanical tester (P2R) (Puncreobutr et al., 2012). Tensile deformation was performed at a rate of 0.1 mm s^{-1} until failure.

Synchrotron Imaging

Radiographic imaging and CT were performed with tensile deformation of the P(3HB-co-4HB) fiber mats at the Diamond Manchester Branchline (I13-2) (Rau et al., 2011) Diamond Light Source. Polychromatic X-rays with energy in the range of 8–35 kV filtered with C, Al, and stainless steel were used. Radiographs of the deformation and failure of the fiber mats were captured at a rate of 67 Hz using a PCO edge camera with 2,560 × 2,160 detector array giving an effective pixel size of 0.81 µm. Radiographs centered in the middle of the dog bone sample was obtained. As the sample was strained at 0.1 mm s^{-1}, the testing rig was lowered at half the strain rate to keep the same region of fiber mat in view.

Due to the X-ray induced damage on the samples, tomography was performed post-tensile deformation to various strains on different samples. 1,500 projections were collected from 0 to 180° with a step size of 0.12° and exposure ranging from 0.075 to 0.15 ms from the center of the dog-bone sample where maximum strain is expected. Filtered back projection was applied to reconstruct the projections using codes developed at Diamond Light Source (Atwood et al., 2015). The resulting tomographs each comprise 2,560 × 2,560 × 2,160 voxels with an effective voxel size of 0.33 µm.

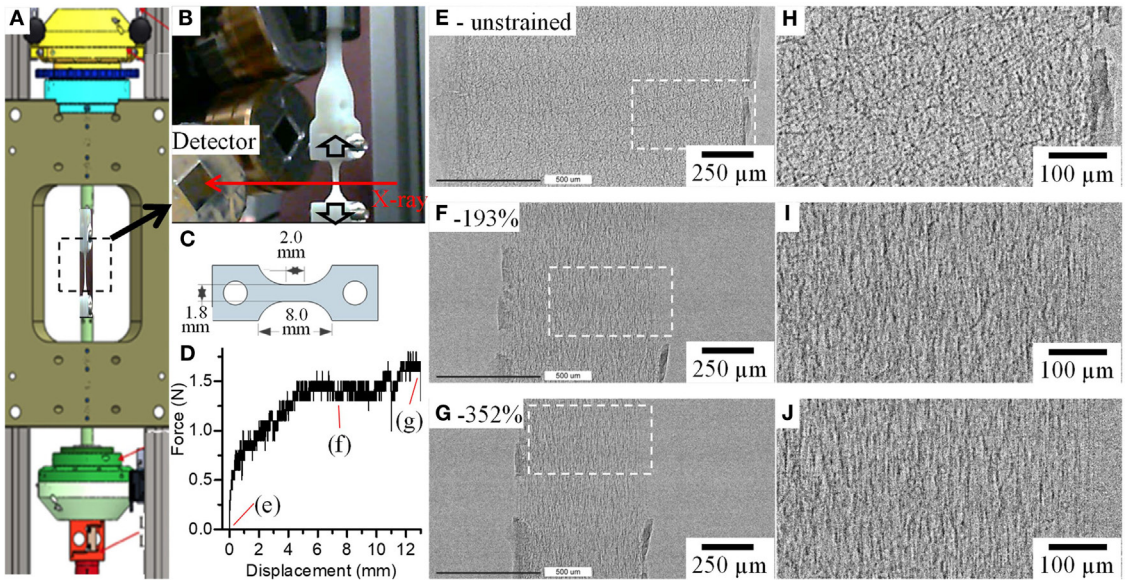

FIGURE 2 | **(A)** P2R tensile tester with **(B)** fiber mat held together between bespoke grips on the Diamond Manchester Beamline (I13-2) at Diamond Light Source. **(C)** Dog-bone-shaped samples used for the tests and **(D)** a force vs displacement curve obtained for the P(3HB-co-4HB) fiber mat. **(E–J)** show radiographs and magnified images of boxed areas on **(E–G)**, respectively, of the fiber mats before (e-unstrained), after 7 mm (f-193%) and 13 mm (g-352%) displacements.

Image Segmentation and Analysis

Avizo® (Thermo Fisher Scientific) and Fiji were used for data processing and visualization. Fiji was used to quantify the fiber diameter. From each dataset a 540 × 600 × 600 voxel volume was extracted and used. Images were then converted to 8 bit and smoothed using a median filter with a 10 pixel radius. Thresholding was performed using the ISO data method. Any remaining noise was removed by using the following features: despeckle, remove dark outliers with radius 4 pixels. Connected fibers were separated using an adjustable watershed plugin. To measure the diameter of fibers in 2D, ellipses were fitted onto fiber cross-sections and analyzed by "analyze particles" feature. Minor axes of ellipses were taken to represent fiber diameter which allowed accurate measure of fibers oriented at an angle to the xy plane. Mathematica (Wolfram Research, Inc., IL, USA) was used to fit Gaussian distributions and estimate mean (μ), SD (σ), and coefficient of variation (CV).

Avizo, a commercially available software package, was used for all the visualization and image analysis performed in this study and described below. The process involves readily available modules from the software, and a few custom tools developed using its python scripting interface.

Fiber Segmentation

First, an anisotropic diffusion filter was applied to all the scans. A binary mask was obtained by a simple threshold operation to segment all fibers (Figure S1B in Supplementary Material). While a simple threshold was sufficient to obtain a fairly accurate binary mask of the fibers, it was very challenging to separate and label individual fibers, due to extensive surface contact. Accordingly, a template matching stage was performed, by correlating cylindrical templates oriented along various directions sampling the orientation sphere, and various radii covering the range of values observed in the dataset. As an output of this first stage, the correlation score of the best matching template, and the corresponding orientation and radius were collected.

A fiber centerline tracing algorithm was then employed (Figure S1C in Supplementary Material), which starts by sorting the pixels by decreasing correlation values into a buffer (up to a minimum correlation value). The first pixel in the buffer was used to initiate the tracing of a fiber. This tracing was performed by iteratively searching for the next point with high correlation within a search cone oriented along the template matching orientation. Once a fiber was fully traced, all points near its centerline were removed from the buffer, and the process was repeated until the buffer emptied. The template matching and tracing algorithm are described in Weber et al. (2012) and Rigort et al. (2012). By construction, no branching can occur between the fibers.

Finally, in order to segment and label each fiber individually, a watershed algorithm was employed to grow centerlines of the markers within the bounds of the binary mask, and to make them join at low intensity regions (Figure S1D in Supplementary Material). This appeared as a reliable marker for identifying the contact areas between neighboring objects.

Fiber Thickness/Local Diameter

In order to estimate the local fiber diameter, a thickness map was computed for each fiber that reports for each voxel, the radius of the largest sphere containing the voxel and fully inside the corresponding fiber, following the definition of Hildebrand and Rüegsegger (1997). This corresponds to the shortest radius of the cross section. This value was reported on the graph representing the fiber centerlines obtained in the tracing stage (Figure S1E in Supplementary Material).

Pair Correlation Function and Aggregation of Thick Fiber Segments

In order to quantify the spatial distribution of thick segments, and their apparent tendency to remain aggregated together at higher strains, we used the pair correlation function. The pair correlation function, $g(r)$, indicates the probability of finding a particle at a distance r from a given reference particle, normalized by the corresponding probability for a purely random (Poisson) distribution. Definition and estimators for this function can be found in Ripley (1976) and Nagel (1995). When $g(r)$ takes values less than 1, this indicates a tendency to repulsion between particles, whereas values larger than 1 indicate aggregation. Since this function characterizes a distribution of points, we first select fiber segments that are thicker than 3.7 μm and evaluate the pair correlation function on the barycenter of these thick fiber segments.

RESULTS AND DISCUSSION

Morphology and Tensile Properties of P(3HB-co-4HB) Fiber Mats

Fiber mats with homogenous fiber morphology were obtained for P(3HB-co-4HB) solutions prepared with chloroform/acetone ratio of 100/0, 75/25, 65/35, and 50/50 (**Figure 1B**; Figure S2 in Supplementary Material). The mean fiber diameter of the resulting P(3HB-co-4HB) fibers decreased from 5.4 to 1.3 μm with increasing amounts of acetone in the P(3HB-co-4HB) solution. The relative permittivity (dielectric constant) of solvents is known to have significant influence on fiber morphology, in particular on fiber diameter Sill and von Recum, 2008; Guarino et al., 2011). The relative permittivity of chloroform and acetone are 4.8 and 19.5, respectively. Increased relative permittivity of the electrospinning solution with addition of acetone increases the amount of positive charge the solution can accommodate. Thus, this solution, once electrospun will experience higher force from the electric potential present between the nozzle and collector hence its fiber diameter is observed to decrease. For 100% acetone, a fibrous structure could not be obtained using our system, which may be attributable to poor solubility of P(3HB-co-4HB) in 100% acetone. Fiber mats produced using 100% chloroform solution were chosen for further studies due to its large and homogeneous fiber diameter, to aid faithful imaging.

Figure 1C shows a typical stress-strain curve of a tensile test of P(3HB-co-4HB) fiber mat. Initial elastic response is followed by a large deformation (> 500%) before failure. This is around half the strain reported for bulk materials of similar composition (Saito and Doi, 1994; Anjum et al., 2016). This is in agreement with literature which suggests that the electrospinning leads to reduced strain before failure from a combination of lower density of the material, pre-existing molecular alignment, and higher stresses experienced by the fibers from stress concentrations and early strain hardening (Pedicini and Farris, 2003; Zussman et al., 2003).

The tensile strength of the P(3HB-co-4HB) fiber mat is three times larger than yield stress suggesting that the P(3HB-co-4HB) fiber mats also strain hardened on deformation. Rotating drum collectors are known to induce fiber alignment in the fiber mats along the spinning direction, although at extremely high velocities (> 5 m s^{-1}) (Zussman et al., 2006). Here, a relatively slow speed of 0.08 m s^{-1} was used. To investigate the effect of such alignment on mechanical properties, tensile tests were performed in parallel and perpendicular directions to the electrospinning direction (**Figure 1A**). Results for the tensile tests on P(3HB-co-4HB) fiber mats prepared using 100% chloroform are summarized in Figure S3 in Supplementary Material. Although elongation is similar in both directions, the tensile strength in the perpendicular direction is 1.5 times higher than in the parallel direction. The opposite would be expected if the rotating drum collector was inducing alignment in the parallel direction. Fiber alignment and its influence on mechanical deformation will be discussed in detail later. Another explanation for this difference could be found in an earlier work by Zussman et al. (2003), who demonstrated that fiber collection using a rotating drum could result in necking (fiber thinning) due to cold drawing of the fibers on the rotating wheel. It is possible that in this study the rotating drum had the effect of cold drawing the fibers producing necks in the fibers along the parallel direction therefore weakening the fiber mat along this direction. Samples for *in situ* synchrotron testing were laser cut in the perpendicular direction.

Deformation Mechanisms under Tensile Loading

Fiber Mat Deformation

Figure 2 shows an overview of the setup used (**Figures 2A–C**), a typical force vs displacement curve (**Figure 2D**) obtained for the P(3HB-co-4HB) samples using this setup and radiographs (**Figures 2E–J**) of a fiber mat that was strained to failure. The radiographs (**Figures 2E–J**) and Figures S4 and S5 in Supplementary Material show that the fiber mat narrows with increasing strain and at strain >350% ruptures. Magnified images in **Figures 2H–J** show that before any deformation the fibers are randomly oriented within the fiber mat (**Figure 2H**); however, once deformation starts, the fibers begin to reorient and align in the direction parallel to the applied force (**Figures 2I,J**). Rotation and realignment of fibers along direction of the strain has previously been shown in the literature (Lee et al., 2002; Pedicini and Farris, 2003; Kim et al., 2004; Lu et al., 2008; Cheng et al., 2011; Zundel et al., 2017). Closer investigation of P(3HB-co-4HB) fibers shows that majority of fiber reorientation is complete by strain of 100% and this is then followed by fiber thinning to accommodate the large strain the material displays. The macroscale deformation of fiber mat and fibers observed here is in agreement to other studies which report similar observations of fiber reorientation (Yano et al., 2012) and thinning (Lu et al., 2008).

Microscale Fiber Deformation

High resolution 3D tomographic imaging allowed microscale deformation of the fiber mats to be studied. **Figure 3** shows 3D rendering of a region of interest ($350 \times 550 \times 700$ pixels) extracted from the original CT scans after 0% strain (**Figures 3A–D**) and after 352% strain (**Figures 3E–H**). Individual fibers can be

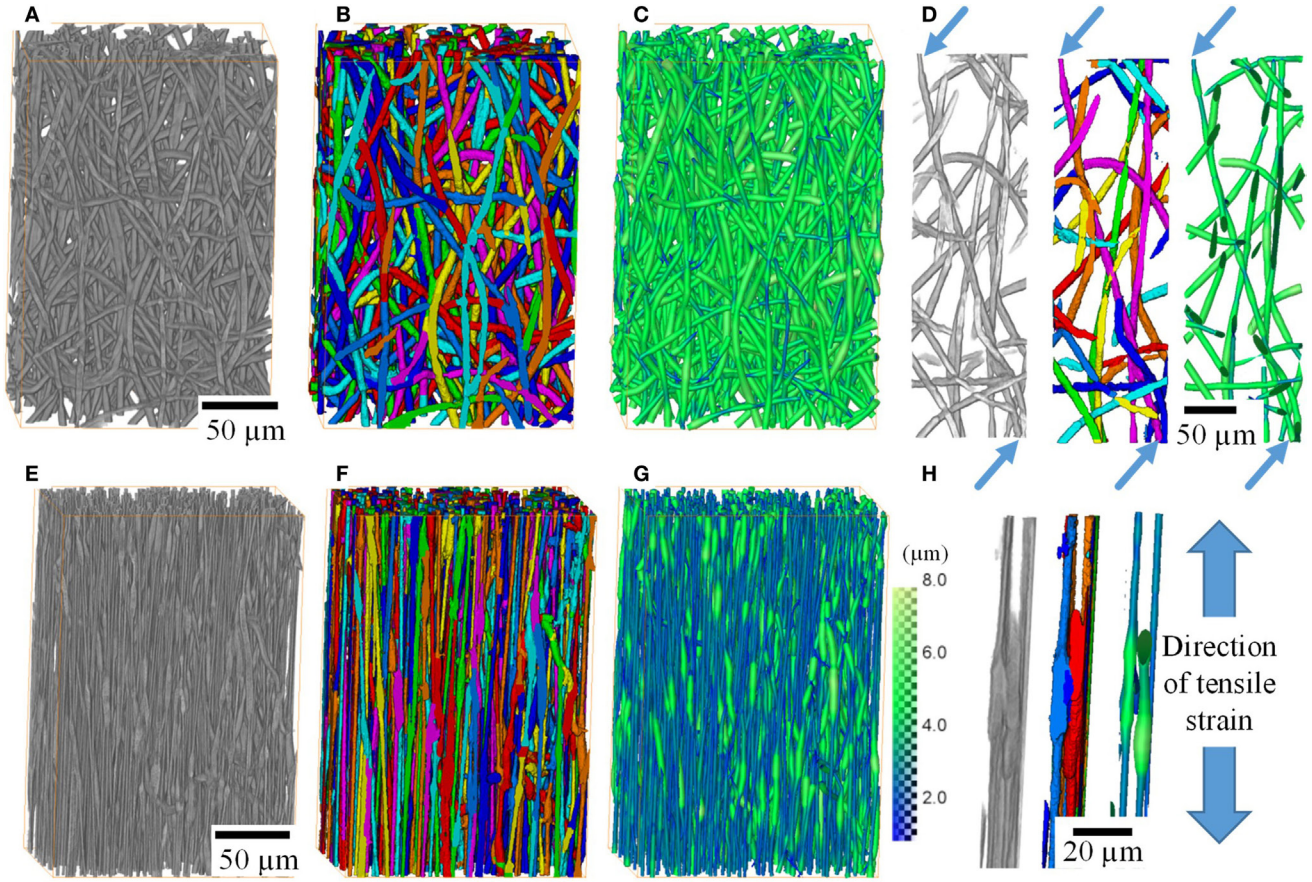

FIGURE 3 | 3D rendering of small volumes of the P(3HB-co-4HB) fiber mats before any deformation **(A—H)** after application of 352% strain. Images show 3D volume rendering after filtering **(A,E)**, segmentation of individual fibers **(B,F)** and with fiber thickness displayed as color intensity **(C,G)**. Fibers can be traced and segmented accurately, enabling identification of individual fibers **(D)** and contact points between these **(H)**. Scans of the fiber mats were performed unstrained and after loading. Loaded samples were left to stabilize for 5 min at constant strain before scanning in their loaded state.

identified, in the undeformed state; they exhibit an isotropic randomly aligned fiber orientation distribution with a narrow fiber diameter range. However, after straining to 352%, the fibers are well aligned in the tensile direction, and majority of the fibers have thinned. The figures also show that the segmentation pipeline used has successfully produced a good segmentation of individual fibers (**Figure 3D**). Segmentation has also accurately captured the changes in the fiber diameter along the fiber length, represented with a color map in **Figures 3C,G**. The segmentation pipeline not only works for the undeformed fiber mat but also after deformation where the fibers have thinned unevenly (**Figures 3E–G**). **Figure 3H** shows two fibers zoomed in after a strain of 352%. The figure demonstrates that the segmentation was successful in separating fibers even when fibers are bonded to each other.

Orientation of Fibers within Fiber Mat

Radiographic images and 3D rendering showed, qualitatively, fiber reorientation and alignment in the direction of the applied force. Segmentation of individual fibers on 3D tomographic data allowed orientation of each individual fiber to be quantified. **Figures 4A–D** show 3D images of small sections of the fiber mat with fibers colored according to their in-plane orientation (θ) from 0° (blue) to 90° (green-yellow) and scatter plot of fiber orientation on polar coordinates θ (in-plane, 0–90°) and Φ (out-of-plane, 0–360°). It is apparent that unstrained it exhibits an out-of-plane (Φ) orientation as shown in **Figures 4A–D** where the scatter is concentrated around 90° and 270°. This is expected as electrospinning results in continuous fibers being deposited on top of each other leading to an alignment in the out-of-plane direction, i.e., fibers lie flat on the surface of the collector therefore their long axis is aligned parallel to the surface of the collector. Although there is not a clear in-plane alignment, **Figure 4A** scatter plot shows that a large fraction of fibers are scattered within 45° suggesting that there is a higher number of fibers aligned in the direction perpendicular to electrospinning. This could explain the higher strength observed in the perpendicular direction compared to parallel direction (**Figure 1**). After 33% strain (**Figure 4B**), fibers do not show noticeable difference in alignment to unstrained. However, once strained to ~190% (**Figure 4C**) and ~350% (**Figure 4D**) the majority, if not all the fibers, are realigned in the 0°.

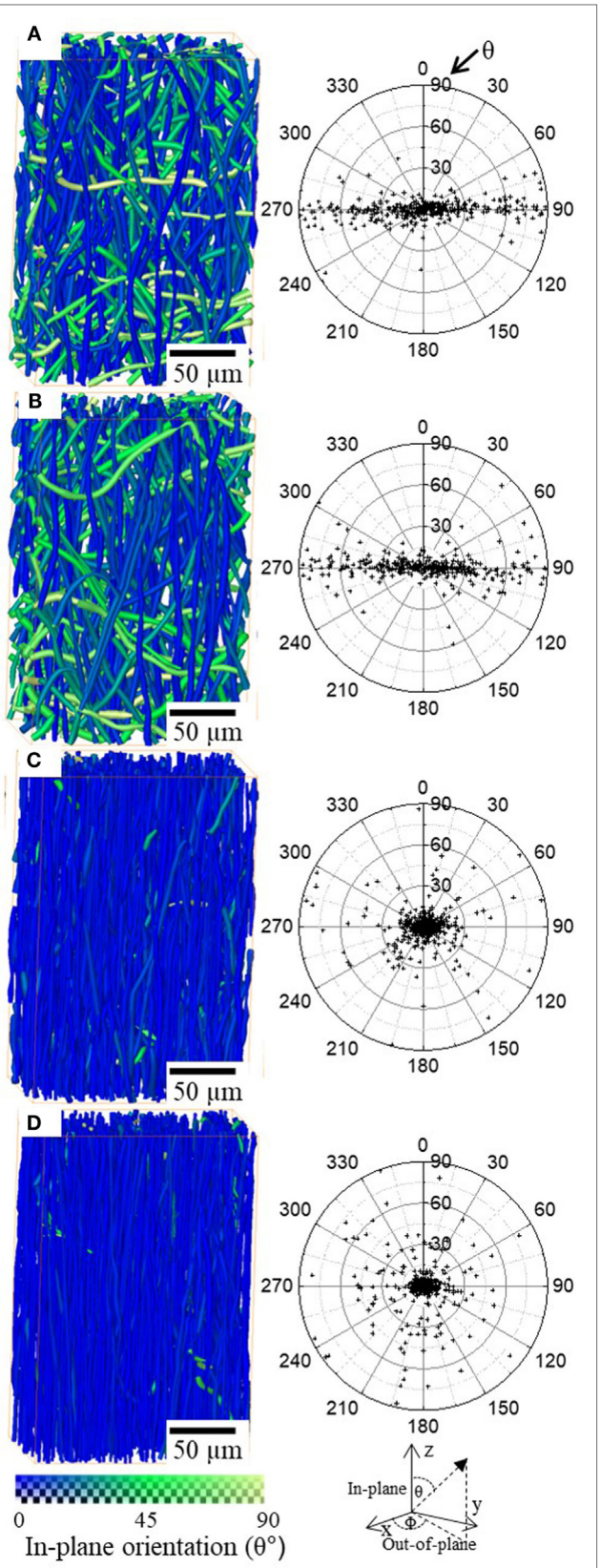

FIGURE 4 | Continued

FIGURE 4 | Continued
3D rendering of small volumes of the P(3HB-co-4HB) fiber mats unstrained **(A)** 33% strain **(B)**, 193% strain **(C)**, and 352% strain **(D)**. The color map at the bottom represent in-plane (θ) fiber orientation. Scatter plots of the fiber orientation is plotted with in-plane (θ) and out-of-plane (Φ) polar coordinates for all the fibers in the volumes.

Distributions of Fiber Diameter

Figures 5A–D shows a 3D rendering of the fiber mats strained to various extents. Fiber realignment and thinning are clearly visible. It also shows that all the fibers in the fiber mat thin after deformation, however, undeformed segments are still visible even at 352% deformation. Fiber diameter distributions are also plotted in **Figure 5E** and summarized in **Table 1**. Mathematica was used to fit mixed-Gaussian distributions to the fiber diameter distribution solving for Eq. 1

$$f(x) = \frac{e^{-(x-\mu_1)^2/(2\sigma_1^2)}\alpha}{\sigma_1\sqrt{2\pi}} + \frac{e^{-(x-\mu_2)^2/(2\sigma_2^2)}(1-\alpha)}{\sigma_2\sqrt{2\pi}} \quad (1)$$

where μ_1 and μ_2 the mean, σ_1 and σ_2 are the standard deviations for distributions 1 and 2, respectively, α is the fraction of distribution 1, (1-α) the fraction of distribution 2.

The overall mean fiber diameter decreases from 4.32 to 2.42 μm. At all the strains from 0 to 350%, the fiber diameter can be fitted with a bimodal distribution of "thin" segments and "thick" segments with a mode between $\mu_1 = 1.72$ to 1.86 μm and $\mu_2 = 3.71$ to 4.48 μm, respectively. The unstrained sample has 4% population of the fibers (α) which are "thin" with a mode of $\mu_1 = 1.74$ μm and the rest (1-α = 96%) are the thick segments with a mode of $\mu_2 = 4.43$ μm. It is clear from the images that these two populations, thin and thick segments, do not arise from two individual populations of fibers of different fiber diameters, but rather individual fibers exhibit thin and thick segments. The fact that the unstrained sample has a bimodal distribution suggests that the fibers, although homogenous, exhibit a small population of thin segments even before any deformation. These thin regions could have formed during the electrospinning process as demonstrated by Zussman et al. (2003). **Figure 5E** shows the changes in μ_1, μ_2, and overall fiber diameter as a function of total fraction of fiber diameters within distribution 1 (α). α increases with increasing strain, suggesting that the proportions of thin segments increase with strain. This is supported by the 3D rendered images in **Figure 5**. With increasing strain, the total fraction of fibers with fiber diameter in the 1st distribution, increases from 4 to 69% however its modal fiber diameter, μ_1, remains largely unchanged. On the other hand, the fraction of thick fibers (2nd distribution) decreases from 96 to 31% and its mode, μ_2, decreases from 4.43 to 3.71 μm. Interestingly, the coefficient of variation (CV = σ/μ) for the two distributions remain fairly constant with increasing strain, in comparison, the CV of the overall fiber diameter which is seen to increase significantly. This suggests that with increasing strain the fibers are simply being stretched, forming necks where these necks have a diameter that falls directly in the "thin" segment (1st distribution), i.e., a gradual decrease in

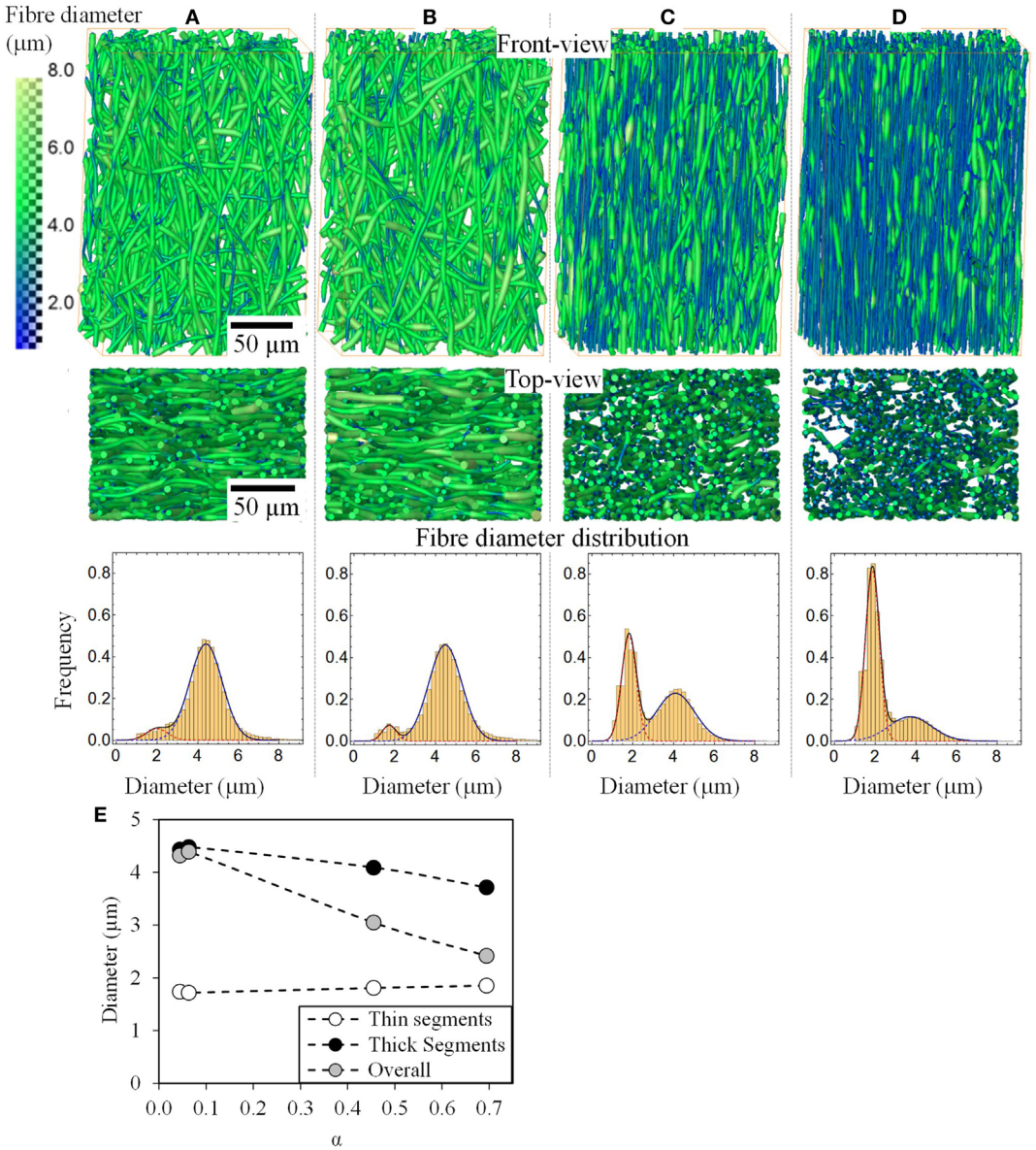

FIGURE 5 | Front and top view 3D rendering of small volumes of the P(3HB-co-4HB) fiber mats and fiber diameter distributions for the unstrained **(A)**, 33% **(B)**, 193% **(C)**, and 352% strained **(D)**. The color map on the left represents fiber diameter in micrometers. The fiber diameters could be fitted with a bimodal Gaussian distribution. The modes of the overall and the two distributions are also plotted in **(E)** as a function of their fraction (α).

TABLE 1 | Summary of modal fiber diameters (μ, μ_1, μ_2), standard deviations (σ, σ_1, σ_2), fraction (α), and coefficient of variation (CV) obtained from the fiber diameter distributions for the unstrained and samples strained to different deformations.

	Directly calculated				From fitting					
	Overall			α	Thin fiber segments			Thick fiber segments		
Strain (%)	μ (μm)	σ (μm)	CV		μ_1 (μm)	σ_1 (μm)	CV	μ_2 (μm)	σ_2 (μm)	CV
0	4.32	1.13	0.26	0.04	1.74	0.43	0.25	4.43	0.80	0.18
33	4.39	1.23	0.28	0.06	1.72	0.34	0.20	4.48	0.81	0.18
193	3.05	1.36	0.45	0.46	1.81	0.36	0.20	4.09	0.95	0.23
352	2.42	1.07	0.44	0.69	1.86	0.34	0.18	3.71	1.05	0.28

fiber diameter seen with conventional fibers that fail by necking was not observed here, rather a shift from "thick" unstrained fibers to necked "thin" fibers is found.

Fiber Deformation and Necking

Thin segments which are necks in the strained samples are also observed in the unstrained sample (**Figure 5A**). It is possible that these pre-existing thin segments could have acted as locations for stress concentration for deformation to initiate and propagate. Such thin sections could have formed during the fabrication process where during electrospinning large extensional forces are transmitted through a solidifying fiber which could lead to cold stretching and neck formation (Zussman et al., 2003; Richard-Lacroix and Pellerin, 2013). There is however controversy surrounding this. Reports have suggested that necking/thin segments only form when fibers are collected on rotating disk collectors that is spun as fast as 5 m s^{-1} and are not observed when spun on flat plate collectors (Richard-Lacroix and Pellerin, 2013). In this study, a rotating drum collector spun at a rate of 0.08 m s^{-1} was used. This is unlikely to induce any cold drawing on the depositing fibers. Further, cold drawing induced necking has mainly been observed in fibers <500 nm in diameter. This suggests that the fiber mats may have experienced mechanical deformation post-synthesis and during sample handling.

Thin sections are regions of stress concentration where deformation initiates and grows at the expense of the thick segments. It seems that the thin segments become strain hardened (Haward, 2007) and pull on the unstrained thicker regions at its ends leading to further deformation and eventual network failure. However, at the highest strain, just before failure, a large number of thick segments are present in the fiber mat. This suggests that these are regions of high strength. Closer investigation reveals that these remaining thick segments are regions where fibers are bonded to their neighbors (**Figure 3H**). Fusion of the fibers leads to enhanced load transfer between the fibers, increasing its tensile strength. It was shown in the literature that fusion of fibers enhances tensile strength and elastic modulus of the fiber mat (Xiaofan et al., 2009).

Figure 6 shows thick segment-Pair Correlation Functions, g(r) for the unstrained, 33, 193, and 352% strained samples. When g(r) has values less than 1, this indicates a tendency for repulsion between particles, whereas values larger than 1 indicate aggregation and 1 represents a random distribution. Correlation function for all the samples below distances of 5–7 μm is less than 1 as the diameter of two thick segments is of these lengths therefore they are seen to repel each other. However, at higher distances both, unstrained and 33% strained samples quickly approach 1 meaning that the thick segments exhibit no particular clustering patterns at this stage. However, in the case of fiber mats strained to 193 and 352% g(r) peaks at roughly 1.5 and 2, respectively, at distances of 5–10 μm, before returning to values close to 1, i.e., at large strains, the thick segments in the fiber mats are shown to be aggregated. This suggests that with increasing strain thick segments remaining unstrained are very close to each other and hence likely are mutually bonded at those regions therefore are stronger than the rest of the fibers. This therefore means that there is a degree of fiber–fiber coupling present within the fiber mat. However, since a large extent of fiber realignment and fiber stretching was observed in these fiber mats, it indicates that the fiber–fiber coupling (crosslinking density) is low (Zundel et al., 2017).

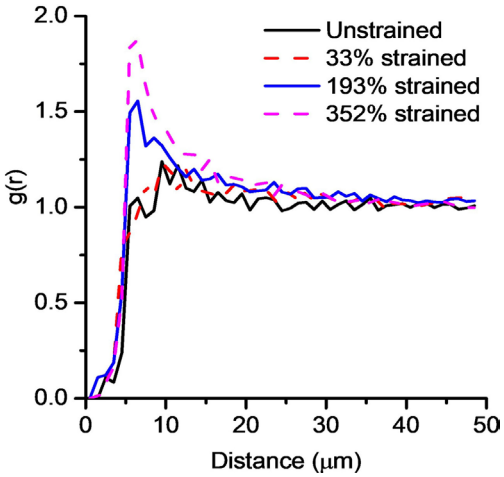

FIGURE 6 | Pair correlation function for thick segments (>3.7μm) for the unstrained fiber mat and fiber mats strained to 33, 193, and 352%.

CONCLUSION

Synchrotron X-ray phase contrast imaging of electrospun biodegradable polyester (P(3HB-co-4HB)) non-woven fiber mats has revealed that prior to failure, the fibers reorient significantly in the direction of the applied strain, followed by significant fiber thinning by a characteristic mode of localized necking and neck growth. Once strained, the fibers, with original diameter of 4.3 μm, thinned without a gradual reduction in fiber diameter, leading to a distinct bimodal distribution of fiber diameters with modes at 1.9 and 3.7 μm. As-made fiber mats were also observed to have fibers with thin regions, these regions may have acted as seeds for necks to form and grow. Results, here, also highlight that the bonded regions/contact points between fibers remained thick (largely unstrained) right up until failure thus suggesting that the fibers were strongly coupled to each other but that the degree of coupling (number of nodes) was low. This paper presents novel insights into the failure mechanism of electrospun fiber mats, the relationship between contact points and deformation behavior and highlights the value of performing 3D *in situ* X-ray CT measurements of entire electrospun fiber mats.

This study has demonstrated that it is important to study not only the deformation of individual fibers, but the entire fiber mat network to understand its failure mechanism in a holistic approach. Electron microscopy is required to resolve individual nanofibers and their deformation, optical microscopy is ideal to image the entire fiber mats, while, high resolution synchrotron CT as performed in this study complements these techniques

and sits well in the intermediate length scale in studying structure–property relationship of materials. The application of high resolution CT has shed light on novel mechanisms of fiber deformation though necking and neck growth of highly elastic P(3HB-co-4HB) polyester fiber mats. It has shown that the fibers realign and then thin between bonded regions which act as branches through which stress is distributed to the individual fibers. Further studies are planned where X-ray induced damage to samples is negligible such that a single sample could be strained to multiple strains at higher resolution. This will allow us to resolve structure–property relationships of the fiber mats in a truly 4D manner.

AUTHOR CONTRIBUTIONS

JM, OT, PL, and GP designed the experiments and participated in the beamtime where the tensile test and image acquisition were performed. AO, CG, and TK produced the fiber mats and performed all the initial characterization. RB created the segmentation pipeline and quantification of Pair correlation function, meanwhile JM and GP processed the CT data and produced images. WS analyzed distributions of fiber diameters in Mathematica and plotted figures. The draft of the paper was produced by GP, JM, AO, and RB. PW, WS, TK, and GP supervised the work and contributed to the final version of the manuscript.

ACKNOWLEDGMENTS

JM and GP would like to acknowledge facilities and support provided by the University of Manchester and Research Complex at Harwell (RCaH). Diamond Light Source and Diamond Manchester Collaboration for beamtime MT14367. We would like to thank Professor Andre Phillion and Dr. Loic Courtois for helping with tensile testing. Furthermore, we would like to thank Dr Andrew Bodey for helping to set up the scans and Dr Kazimir Wenelik for helping with image reconstruction scrips.

FUNDING

JM, GP, and PL would like to acknowledge EPSRC and MRC for funding (EP/L014904/1, EP/M023877/1, EP/I02249X/1, and EP/M009688/1). PW is grateful for a European Research Council for funding COREL-CT under grant No 695638. AO and TK would like to acknowledge JSPS for funding (JSPS KAKENHI #16K14403).

SUPPLEMENTARY MATERIAL

The Supplementary Material for this article can be found online at http://www.frontiersin.org/articles/10.3389/fmats.2017.00043/full#supplementary-material.

VIDEO S1 | Video showing tensile deformation of fiber mat.

REFERENCES

Anjum, A., Zuber, M., Zia, K. M., Noreen, A., Anjum, M. N., and Tabasum, S. (2016). Microbial production of polyhydroxyalkanoates (PHAs) and its copolymers: a review of recent advancements. *Int. J. Biol. Macromol.* 89, 161–174. doi:10.1016/j.ijbiomac.2016.04.069

Atwood, R. C., Bodey, A. J., Price, S. W. T., Basham, M., and Drakopoulos, M. (2015). A high-throughput system for high-quality tomographic reconstruction of large datasets at Diamond Light Source. *Philos. Trans. R. Soc. A Math. Phys. Eng. Sci.* 373, 20140398. doi:10.1098/rsta.2014.0398

Badami, A. S., Kreke, M. R., Thompson, M. S., Riffle, J. S., and Goldstein, A. S. (2006). Effect of fiber diameter on spreading, proliferation, and differentiation of osteoblastic cells on electrospun poly(lactic acid) substrates. *Biomaterials* 27, 596–606. doi:10.1016/j.biomaterials.2005.05.084

Baker, S. R., Banerjee, S., Bonin, K., and Guthold, M. (2016). Determining the mechanical properties of electrospun poly-ε-caprolactone (PCL) nanofibers using AFM and a novel fiber anchoring technique. *Mater. Sci. Eng. C* 59, 203–212. doi:10.1016/j.msec.2015.09.102

Cheng, M.-L., Chen, P.-Y., Lan, C.-H., and Sun, Y.-M. (2011). Structure, mechanical properties and degradation behaviors of the electrospun fibrous blends of PHBHHx/PDLLA. *Polymer* 52, 1391–1401. doi:10.1016/j.polymer.2011.01.039

Greiner, A., and Wendorff, J. H. (2007). Electrospinning: a fascinating method for the preparation of ultrathin fibers. *Angew. Chem. Int. Ed. Engl.* 46, 5670–5703. doi:10.1002/anie.200604646

Guarino, V., Cirillo, V., Taddei, P., Alvarez-Perez, M. A., and Ambrosio, L. (2011). Tuning size scale and crystallinity of PCL electrospun fibres via solvent permittivity to address hMSC response. *Macromol. Biosci.* 11, 1694–1705. doi:10.1002/mabi.201100204

Haward, R. N. (2007). Strain hardening of high density polyethylene. *J. Polym. Sci. B Polym. Phys.* 45, 1090–1099. doi:10.1002/polb.21123

Hildebrand, T., and Rüegsegger, P. (1997). A new method for the model-independent assessment of thickness in three-dimensional images. *J. Microsc.* 185, 67–75. doi:10.1046/j.1365-2818.1997.1340694.x

Jamshidian, M., Tehrany, E. A., Imran, M., Jacquot, M., and Desobry, S. (2010). Poly-lactic acid: production, applications, nanocomposites, and release studies. *Compr. Rev. Food Sci. Food Saf.* 9, 552–571. doi:10.1111/j.1541-4337.2010.00126.x

Jose, M. V., Thomas, V., Johnson, K. T., Dean, D. R., and Nyairo, E. (2009). Aligned PLGA/HA nanofibrous nanocomposite scaffolds for bone tissue engineering. *Acta Biomater.* 5, 305–315. doi:10.1016/j.actbio.2008.07.019

Kim, K. W., Lee, K. H., Khil, M. S., Ho, Y. S., and Kim, H. Y. (2004). The effect of molecular weight and the linear velocity of drum surface on the properties of electrospun poly(ethylene terephthalate) nonwovens. *Fibers Polym.* 5, 122–127. doi:10.1007/BF02902925

Lee, K. H., Kim, H. Y., La, Y. M., Lee, D. R., and Sung, N. H. (2002). Influence of a mixing solvent with tetrahydrofuran and N,N-dimethylformamide on electrospun poly(vinyl chloride) nonwoven mats. *J. Polym. Sci. B Polym. Phys.* 40, 2259–2268. doi:10.1002/polb.10293

Li, Z., and Loh, X. J. (2017). Recent advances of using polyhydroxyalkanoate-based nanovehicles as therapeutic delivery carriers. *Wiley Interdiscip. Rev. Nanomed. Nanobiotechnol.* 9, e1429. doi:10.1002/wnan.1429

Liu, Y., Chen, S., Zussman, E., Korach, C. S., Zhao, W., and Rafailovich, M. (2011). Diameter-dependent modulus and melting behavior in electrospun semicrystalline polymer fibers. *Macromolecules* 44, 4439–4444. doi:10.1021/ma200262z

Lu, J.-W., Zhang, Z.-P., Ren, X.-Z., Chen, Y.-Z., Yu, J., and Guo, Z.-X. (2008). High-elongation fiber mats by electrospinning of polyoxymethylene. *Macromolecules* 41, 3762–3764. doi:10.1021/ma702881k

Makadia, H. K., and Siegel, S. J. (2011). Poly lactic-co-glycolic acid (PLGA) as biodegradable controlled drug delivery carrier. *Polymers (Basel)* 3, 1377–1397. doi:10.3390/polym3031377

Mohammadzadehmoghadam, S., Dong, Y., and Davies, I. J. (2016). Modeling electrospun nanofibers: an overview from theoretical, empirical, and numerical approaches. *Int. J. Polym. Mater. Polym. Biomater.* 65, 901–915. doi:10.1080/00914037.2016.1180617

Nagel, W. (1995). Stoyan, D./Stoyan, H.: Fractals, Random Shapes and Point Fields. Methods of Geometrical Statistics. John Wiley & Sons, Chichester 1994, XIV, 389 pp. £39.95. *Biom. J.* 37, 978–978. doi:10.1002/bimj.4710370810

Naraghi, M., Chasiotis, I., Kahn, H., Wen, Y., and Dzenis, Y. (2007). Mechanical deformation and failure of electrospun polyacrylonitrile nanofibers as a function of strain rate. *Appl. Phys. Lett.* 91, 151901. doi:10.1063/1.2795799

Nishizuka, T., Kurahashi, T., Hara, T., Hirata, H., and Kasuga, T. (2014). Novel intramedullary-fixation technique for long bone fragility fractures using bioresorbable materials. *PLoS ONE* 9:e104603. doi:10.1371/journal.pone.0104603

Pedicini, A., and Farris, R. J. (2003). Mechanical behavior of electrospun polyurethane. *Polymer* 44, 6857–6862. doi:10.1016/j.polymer.2003.08.040

Poologasundarampillai, G., Wang, D., Li, S., Nakamura, J., Bradley, R., Lee, P. D., et al. (2014). Cotton-wool-like bioactive glasses for bone regeneration. *Acta Biomater.* 10, 3733–3746. doi:10.1016/j.actbio.2014.05.020

Poologasundarampillai, G., Yu, B., Jones, J. R., and Kasuga, T. (2011). Electrospun silica/PLLA hybrid materials for skeletal regeneration. *Soft Matter* 7, 10241–10251. doi:10.1039/c1sm06171b

Puncreobutr, C., Lee, P. D., Hamilton, R. W., and Phillion, A. B. (2012). Quantitative 3D characterization of solidification structure and defect evolution in Al alloys. *JOM* 64, 89–95. doi:10.1007/s11837-011-0217-9

Rau, C., Wagner, U., Pešić, Z., and De Fanis, A. (2011). Coherent imaging at the diamond beamline I13. *Phys. Status Solidi A* 208, 2522–2525. doi:10.1002/pssa.201184272

Richard-Lacroix, M., and Pellerin, C. (2013). Molecular orientation in electrospun fibers: from mats to single fibers. *Macromolecules* 46, 9473–9493. doi:10.1021/ma401681m

Rigort, A., Gunther, D., Hegerl, R., Baum, D., Weber, B., Prohaska, S., et al. (2012). Automated segmentation of electron tomograms for a quantitative description of actin filament networks. *J. Struct. Biol.* 177, 135–144. doi:10.1016/j.jsb.2011.08.012

Ripley, B. D. (1976). The second-order analysis of stationary point processes. *J. Appl. Probab.* 13, 255–266. doi:10.2307/3212829

Rizvi, M. S., Kumar, P., Katti, D. S., and Pal, A. (2012). Mathematical model of mechanical behavior of micro/nanofibrous materials designed for extracellular matrix substitutes. *Acta Biomater.* 8, 4111–4122. doi:10.1016/j.actbio.2012.07.025

Rizvi, M. S., and Pal, A. (2014). Statistical model for the mechanical behavior of the tissue engineering non-woven fibrous matrices under large deformation. *J. Mech. Behav. Biomed. Mater.* 37, 235–250. doi:10.1016/j.jmbbm.2014.05.026

Saito, Y., and Doi, Y. (1994). Microbial synthesis and properties of poly(3-hydroxybutyrate-co-4-hydroxybutyrate) in *Comamonas acidovorans*. *Int. J. Biol. Macromol.* 16, 99–104. doi:10.1016/0141-8130(94)90022-1

Sill, T. J., and von Recum, H. A. (2008). Electrospinning: applications in drug delivery and tissue engineering. *Biomaterials* 29, 1989–2006. doi:10.1016/j.biomaterials.2008.01.011

Tan, E. P. S., and Lim, C. T. (2004). Physical properties of a single polymeric nanofiber. *Appl. Phys. Lett.* 84, 1603–1605. doi:10.1063/1.1651643

Teo, W. E., and Ramakrishna, S. (2006). A review on electrospinning design and nanofibre assemblies. *Nanotechnology* 17, R89–R106. doi:10.1088/0957-4484/17/14/R01

Türesin, F., Gürsel, I., and Hasirci, V. (2001). Biodegradable polyhydroxyalkanoate implants for osteomyelitis therapy: in vitro antibiotic release. *J. Biomater. Sci. Polym. Ed.* 12, 195–207. doi:10.1163/156856201750180924

Vigneswari, S., Murugaiyah, V., Kaur, G., Abdul Khalil, H. P. S., and Amirul, A. A. (2016). Simultaneous dual syringe electrospinning system using benign solvent to fabricate nanofibrous P(3HB-co-4HB)/collagen peptides construct as potential leave-on wound dressing. *Mater. Sci. Eng. C Mater. Biol. Appl.* 66, 147–155. doi:10.1016/j.msec.2016.03.102

Weber, B., Greenan, G., Prohaska, S., Baum, D., Hege, H. C., Muller-Reichert, T., et al. (2012). Automated tracing of microtubules in electron tomograms of plastic embedded samples of *Caenorhabditis elegans* embryos. *J. Struct. Biol.* 178, 129–138. doi:10.1016/j.jsb.2011.12.004

Xiaofan, W., Zhenhai, X., Shing-Chung, W., and Avinash, B. (2009). Modelling of mechanical properties of electrospun nanofibre network. *Int. J. Exp. Comput. Biomech.* 1, 45–57. doi:10.1504/IJECB.2009.022858

Yano, T., Higaki, Y., Tao, D., Murakami, D., Kobayashi, M., Ohta, N., et al. (2012). Orientation of poly(vinyl alcohol) nanofiber and crystallites in non-woven electrospun nanofiber mats under uniaxial stretching. *Polymer* 53, 4702–4708. doi:10.1016/j.polymer.2012.07.067

Yu, M.-F., Files, B. S., Arepalli, S., and Ruoff, R. S. (2000). Tensile loading of ropes of single wall carbon nanotubes and their mechanical properties. *Phys. Rev. Lett.* 84, 5552–5555. doi:10.1103/PhysRevLett.84.5552

Zhijiang, C., Qin, Z., Xianyou, S., and Yuanpei, L. (2017). Zein/poly(3-hydroxybutyrate-co-4-hydroxybutyrate) electrospun blend fiber scaffolds: preparation, characterization and cytocompatibility. *Mater. Sci. Eng. C* 71, 797–806. doi:10.1016/j.msec.2016.10.053

Zundel, M., Mazza, E., and Ehret, A. E. (2017). A 2.5D approach to the mechanics of electrospun fibre mats. *Soft Matter* 13, 6407–6421. doi:10.1039/c7sm01241a

Zussman, E., Burman, M., Yarin, A. L., Khalfin, R., and Cohen, Y. (2006). Tensile deformation of electrospun nylon-6,6 nanofibers. *J. Polym. Sci. B Polym. Phys.* 44, 1482–1489. doi:10.1002/polb.20803

Zussman, E., Rittel, D., and Yarin, A. L. (2003). Failure modes of electrospun nanofibers. *Appl. Phys. Lett.* 82, 3958–3960. doi:10.1063/1.1579125

Conflict of Interest Statement: The authors declare that the research was conducted in the absence of any commercial or financial relationships that could be construed as a potential conflict of interest.

frontiers in Materials

ORIGINAL RESEARCH
published: 20 December 2017
doi: 10.3389/fmats.2017.00044

Combining Digital Image Correlation and Acoustic Emission for Monitoring of the Strain Distribution until Yielding during Compression of Bovine Cancellous Bone

*Athanasios Tsirigotis and Despoina D. Deligianni**

Laboratory of Biomechanics and Biomedical Engineering, Department of Mechanical Engineering and Aeronautics, University of Patras, Rio, Greece

In this work, the surface heterogeneity in mechanical compressive strain of cancellous bone was investigated with digital image correlation (DIC). Moreover, the onset and progression of failure was studied by acoustic emission (AE). Cubic cancellous bone specimens, with side of 15 mm, were obtained from bovine femur and kept frozen at −20°C until testing. Specimen strain was analyzed by measuring the change of distance between the platens (crosshead) and *via* an optical method, by following the strain evolution with a camera. Simultaneously, AE monitoring was performed. The experiments showed that compressive Young's modulus determined by crosshead strain is underestimated at 23% in comparison to optically determined strain. However, surface strain fields defined by DIC displayed steep strain gradients, which can be attributed to cancellous bone porosity and inhomogeneity. The cumulative number of events for the total AE activity recorded from the sensors showed that the activity started at a mean load level of 36% of the maximum load and indicated the initiation of micro-cracking phenomena. Further experiments, determining 3D strain with μCT apart from surface strain, are necessary to clarify the issue of strain inhomogeneity in cancellous bone.

Keywords: cancellous bone, acoustic emission, digital image correlation, microdamage, evolution

OPEN ACCESS

Edited by:
Gianluca Tozzi, University of Portsmouth, United Kingdom

Reviewed by:
Dongchan Jang, KAIST, South Korea
Christian Langton, Queensland University of Technology, Australia

***Correspondence:**
Despoina D. Deligianni
deliyian@upatras.gr

Specialty section:
This article was submitted to Mechanics of Materials, a section of the journal Frontiers in Materials

Received: *31 August 2017*
Accepted: *04 December 2017*
Published: *20 December 2017*

Citation:
Tsirigotis A and Deligianni DD (2017) Combining Digital Image Correlation and Acoustic Emission for Monitoring of the Strain Distribution until Yielding during Compression of Bovine Cancellous Bone. Front. Mater. 4:44. doi: 10.3389/fmats.2017.00044

INTRODUCTION

The determination of trabecular bone tissue elastic and failure properties is important from both biological and clinical aspect, as they influence significantly the pathophysiology of aging, disease, and its treatment. Much research has been also performed in predicting bone fractures with the purpose of optimal design of orthopedic implants (Maurer-Ertl et al., 2015). The mechanical properties are typically obtained from experimental testing (Carter and Hayes, 1977) of excised specimens of trabecular bone. The measured mechanical properties underestimate the *in vivo* behavior of cancellous bone. Measurements of strain with extensometers include the "side-artifact," as there is loss of connectivity at the outer surface of the machined specimen because of the interruption of the trabecular network during preparation (Un et al., 2006), which mechanistically depends on trabecular spacing (Onck et al., 2001; Un et al., 2006). This artifact can underestimate the elastic modulus up to 50% in human vertebral bone (Un et al., 2006). The accuracy of compressive strain measurements derived from the relative displacement of the platens is restricted by artifacts due to

loss of connectivity at the specimen ends and friction at the specimen–platens interface (Linde and Hvid, 1987, 1989; Odgaard et al., 1989; Odgaard and Linde, 1991; Linde et al., 1992a,b).

For this reason, different techniques, most of them non-contact, have emerged to overcome the aforementioned measurement inaccuracies. Strain mapping techniques have been applied to monitor local damage and measure local displacements during deformation. Optical technique allow contactless measurements that permit the determination of strain without intervention at the local structure and response of the material. Among optical non-destructive techniques, used for monitoring crack initiation and progress, are the electronic speckle pattern interferometry and the digital image correlation (DIC) (Hoult et al., 2013; Lionello and Cristofolini, 2014), which give two-dimensional (2D) strain mapping. Optical methods have also recently included measurements of strain of the 3D space (Roberts et al., 2014; Palanca et al., 2015). DIC is a promising optical technique, which depicts clearly and accurately the surface strain field, as well as the transient changes originated from stress redistribution after local fracture events occurrence (Sutton et al., 1983, 2009; Freddi et al., 2015).

The amount of tissue damage at the microscopic level in bone tissue is a determinant of bone quality, contributing to whole bone fragility. Activities of daily living or overloading events can cause microdamage in bone tissue of normal individuals. Accumulation of microdamage is considered a mechanism in the development of fatigue fractures, insufficiency, and atypical fractures (Hernandez et al., 2014). The development of bone local yielding or fracturing as a consequence of mechanical loading, is difficult to quantify, which limits the ability to define injury and develop injury criteria. Tissue material toughness and resistance to the formation of tissue microdamage play the main role in understanding failure mechanisms in bone (Goff et al., 2015). Very low amounts of microdamage, which occupy less than 2% of the tissue, result in much higher decreases in stiffness, strength, and fatigue of cancellous bone (Lambers et al., 2013; Hernandez et al., 2014), displaying that tissue microdamage can have significant influence to clinical fractures.

Acoustic emission (AE) by materials is sonic and ultrasonic wave generation during their deformation when fracture or microcracking processes start. AE technique permits determination of structural health non-destructively and with high sensitivity and is widely used throughout civil and mechanical engineering. AE is a well-established method for real-time damage monitoring and has found wide use to detect effects in different mechanical structures. Its application within the field of orthopedic surgery is of particular interest. The use of AE technology in orthopedics is wide ranging and is implemented in the study of the mechanical behavior of bone (Cardoso et al., 2003), especially in fracture behavior, aiming in determining failure mechanisms, which are connected with bone overloading or cemented implants, aiming in improving prosthetic design. The last years, its analysis has been applied to discern microcracks initiated with yield in bone and continued in the post-yield region until failure (Wright et al., 1981). The nature of AE signals from bone has been already suggested as a tool for measuring its quality. AE has been monitored from whole bones subject to torque (Jonsson et al., 1984) and bending (Hanagud et al., 1973) and has been proposed as a tool for monitoring the bone fracture healing process (Shrivastava and Prakash, 2009, 2011).

In this work, the macroscopic strain and the surface strain field, at which crack formation initiated and propagated until fracture, were investigated. For this reason, DIC and AE were simultaneously performed. These results provide new insights into the process of failure and a new level of detail in fracture characterization.

MATERIALS AND METHODS

Sample Preparation

Trabecular bone specimens were prepared from bovine femur resulting in $n = 20$ samples. All femurs were obtained from local butcheries. The specimens were cut along the longitudinal axis of the femur to produce 15 mm × 15 mm × 15 mm cubic specimens. They were kept frozen at a temperature of −20°C until testing. All tests were performed at room temperature. The cubic specimens were machined with a Struers Minitom Low-Speed Diamond Saw. Specimen dimensions were obtained with a micrometer before mechanical testing.

Strain Measurement

Specimens were loaded in compression, placed between two parallel steel platens, at a constant strain rate of 1/60 s^{-1} in a Monsanto tensometer testing machine (**Figure 1**). Each specimen was compressed along its axis. There were performed two independent measurements of deformation: a measurement by the conventional extensometer fixed to the platens as close to the specimen as possible, and an optical deformation measurement, described below in detail.

The optically measured strain was determined between two points lying one in each of two pairs of transverse planes, which divide the length of the specimen in three equal parts. The pairs of planes created on the specimen's surface two areas for strain measurement, the small and the large one (**Figure 2**). The small is the central part of the specimen, where usually macroscopic fractures occur. The large area represents the whole length of the specimen, with a certain length—approximately 1 mm from the platens—excluded. Thus, the surface strain was measured at a middle area of the specimen and simultaneously at a the whole length in order to examine the inhomogeneity of the strain along the length of the specimen. The strain in each of these areas was considered as homogeneous. The DIC set-up for measuring the displacement and strain at the frontal surface of the specimens was as the following: the specimen's surface was painted white and black landmarks were created along the transverse planes in order to make contrast. These landmarks were followed by a CCD video camera (Sony Exmor R) throughout the test (Resolution of Images 1,280 × 720) (**Figure 1**), which recorded the whole experiment. The system captures pictures every 10 N. By using an algorithm *via* MATLAB Image Analysis, the strain distribution at the surface was determined by depicting the exact position of the pixel corresponding to a specific landmark/speckle dot at each image. Each speckle dot has been displaced a few pixels

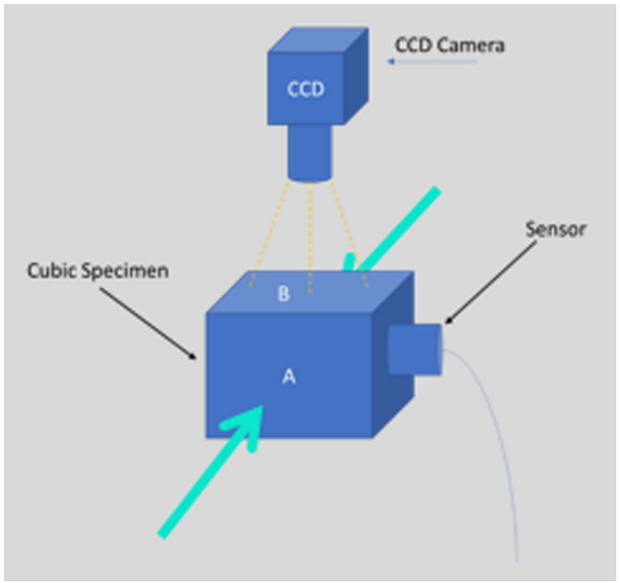

FIGURE 1 | CCD camera used to monitor the whole experiment and acoustic emission sensor detects the acoustic events. The green arrows indicate the loading direction (compression mode) of the specimen.

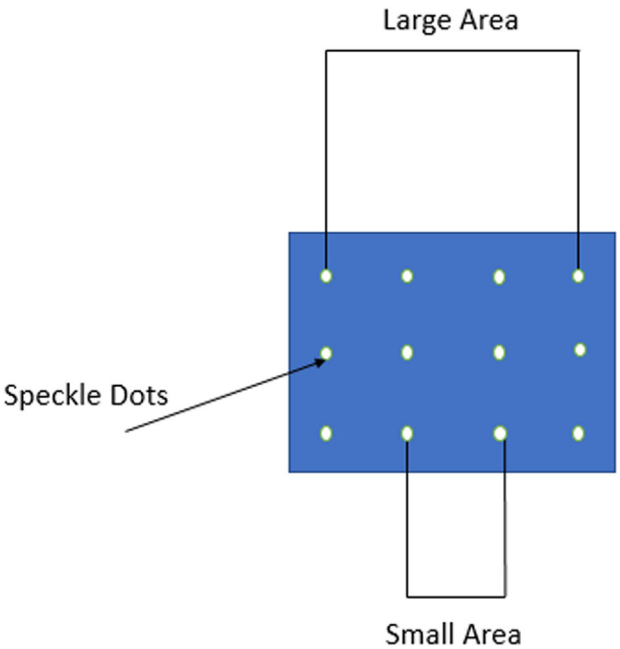

FIGURE 2 | The formed speckle dots on the front surface of the specimen. "Large" and "small" areas are shown in the figure.

at every image as the specimen was compressed and deformed. The exact position of each dot was recorded in a Matlab array for every image. When all the images were processed, the displacement between two dots was calculated and consequently the strain, since the original distance (undeformed image) between two dots was known. With the optically calculated strain and the strain measured by the extensometer, two kinds of elastic moduli were determined and compared. Conventional elastic modulus was obtained as the maximum slope of the stress–strain curves by a best-fit linear ($R^2 = 0.99$) straight line over a range of approximately 0.02 strain with varying origin.

Ncorr DIC Algorithm

Ncorr is a well-documented flexible code that can be adapted to suit each user's needs (http://www.ncorr.com/index.php). It is a freely available 2D subset-based DIC software package. The work flow of Ncorr is the following: 1-Set Reference Image; 2-Set Current Images; 3-Set Region of Interest (ROI); 4-Set DIC Parameters; 5-DIC Analysis; 6-Format Displacements; 7-Calculate Strains.

For the data analysis, the following elements were used: a group of neighboring pixels, which was compared in the reference and loaded images, consisting of 29 pixels (called subset size), a step size/subset spacing (the number of pixels the center point of this subset was moved in order to calculate the full displacement field) of 2 pixels, and a Strain Radius (suitable for the calculation of strains) of 29 pixels (equal to the number of the subset size). Additionally, the ROI was either a rectangle or an ellipse according to the geometry of the specimen and the needs of each experiment. The values of the above parameters were chosen as to minimize the computational cost without losing in the accuracy of the results.

Acoustic Emission

Acoustic signals emitted from the specimen during compression were monitored using a broadband sensor (R-15, Physical Acoustic Corporation) placed at the axis normal to the main compression direction (see **Figure 1**). The position of the sensor was chosen because the above surface of the specimen was monitored by the camera for the DIC method. One transducer was used for all the experiments. The specific sensor was selected due to their response because its diameter was suitable for the length (15 mm) of our specimens. Thus, its placement on the surface was easy. Furthermore, acoustic coupling was improved using sonic gel between the sensor and the contact point of it on the surface and tape was used to ensure the stability of the sensor during the experiment.

The signals were amplified at 35 dB and were continuously recorded using a two-channel acquisition system (Mistras micro-II board). A sampling rate of 10 MHz was implemented. The characteristics of the signal, which were recorded, were: AE amplitude (magnitude of the signal at the peak), AE energy, duration (time interval between the first and the last threshold crossing), and rise time (RT) (see **Figure 3**). The threshold was set at 35 dB (or 0.2 mV), while Gain and Pre-Ampl. was set at 0 dB. The peak and hit definition times (PDT and HDT) were 50 and 200 μs, respectively, whereas the hit lockout time was 500 μs.

Amplitude shows the intensity of the fracture incident. AE signal energy is determined by the area under the rectified waveform. Moreover, RT is the delay between the first threshold crossing and the peak amplitude (peak value). Another important parameter is the RT over amplitude (RA value). It is defined as RT

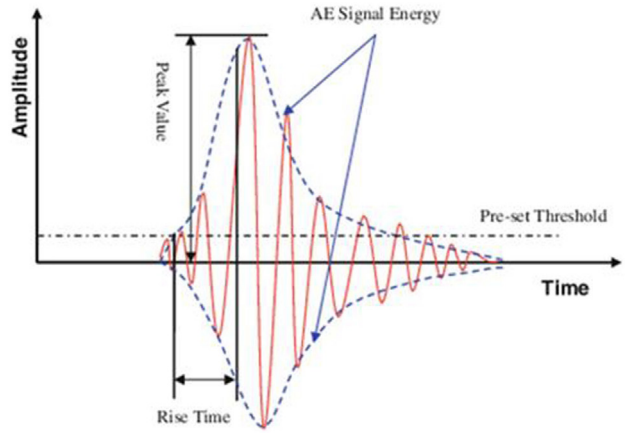

FIGURE 3 | Amplitude, acoustic emission (AE) signal energy, rise time, and threshold of the AE activity.

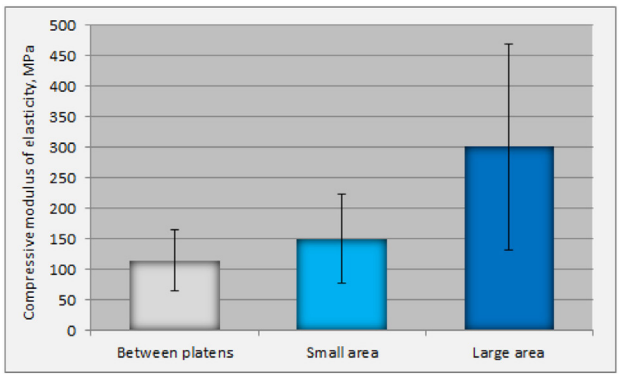

FIGURE 4 | Differences in the values of Young's Moduli as determined by platens displacements and by the optically calculated strain (in the small and large areas).

divided by the amplitude and its unit is microseconds per volts. The average frequency equals the number of threshold crossings over the whole duration of the signal and represents the frequency content of the waveform.

RESULTS

The experiments showed that compressive Young's modulus (E) determined by platens relative displacement is underestimated at 23% in comparison to optically determined surface strain at the "small" middle area (**Figure 4**). Statistically significant difference ($p < 0.001$) between the values of E determined in the middle area of the specimen and in the "large" area was also observed (**Figure 4**). The optical measurements of strain show that trabecular bone exhibits linear elastic behavior, without initial concave part, and yields at low strains (less than 1.8%).

Figure 5 depicts the longitudinal surface strain field (e_{xx}) evolution during compression of the specimen until yielding. In any level of loading, there was not observed increased strain at the periphery of the specimen or at the plane end surfaces. Increased strain occurs only in areas where the bone is weaker and consequently more compliant.

Figure 6A shows the load history and the cumulative AE activity for a specimen, which is typical for all specimens. **Figure 6B** focuses on cumulative AE activity at low loads. Acoustic signals start emitting before the peak of loading at a slow rate. The cumulative number of hits for the total AE activity recorded from the sensor showed that the activity started at a mean level of 36.6% of the maximum load. The time or the strain of the first initiation of the AE activity is the moment when micro-cracking phenomena were initiated within the specimens. Although there are differences among specimens and inhomogeneity is present, most of them exhibited the start of micro-cracking between 30 and 40% of the maximum load, and only a few exceptions were present.

The number of AEs released from the samples did not vary widely. The range of emissions was 200–700 events until macroscopic yielding. In the initial concave upwards part of the stress–strain curve, there are no AE events, which means that the trabeculae may buckle, deform under low loads, but not fracture. The strain at which AE activity initiates ranges between 3.5 and 5% (time 2.2–4.5 s), meaning that AE activity appears in the linear part of the σ–ε curve (**Figure 6**). The latency of the sharp change in strain relative to the onset of the AE was consistent across all experiments.

Amplitude, RT, and signal power were not correlated with any tissue material property. This result was attributed to the fact that some tests were destructive, while others were not and the number of AE events is very low. Steep strain gradients were observed when strain fields were calculated by DIC. They were attributed to bone inhomogeneity resulting in inhomogeneous strain distribution (**Figure 5**).

DISCUSSION

It has been stated that structural phenomena at the interface result in an underestimation of Young's modulus. On the other hand, the presence of frictional effects on the upper and bottom surfaces of the specimen, which contact the compression platens, may counteract this effect by increasing stiffness due to stress field altering by friction. The hypothesis that initiated the current experiments was whether the conventional compression test gives an accurate value of the compressive Young's modulus after the compromise between friction and loss of connectivity, by comparing it with the optically determined one.

The mechanical testing of cancellous bone and the results interpretation are generally difficult due to its porosity. The loss of connectivity during preparation of cored samples results in a greater compliance at the cut surfaces than in *in situ* areas. If the compliance increases at the upper and bottom ends of the specimen, the consequence is an underestimation of the whole sample's elastic modulus and strength (end effect). The trabeculae around the circumference of a sample loose also their connectivity during specimen preparation, resulting in reduced compliance (side artifact). In this way, the measured mechanical properties underestimate the *in vivo* behavior of cancellous

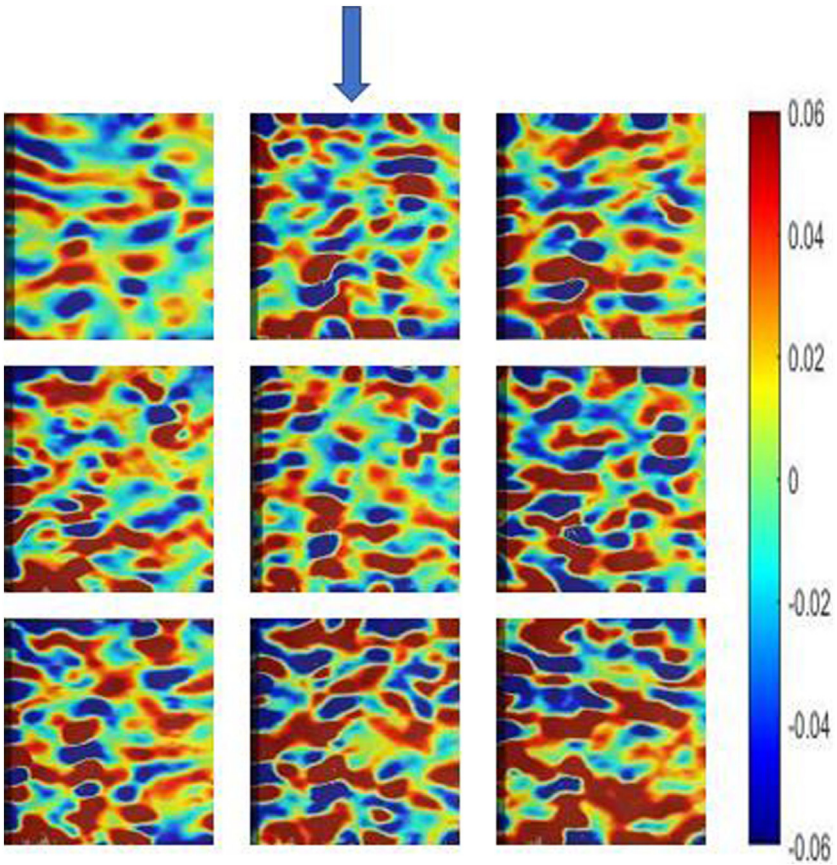

FIGURE 5 | Longitudinal surface strain field (e_{xx}) evolution during compression of a specimen at nine time points until yielding, as measured by digital image correlation (Ncorr algorithm). The sequence of the images is from left to right starting from the upper left image. The arrow indicates the compression direction.

bone, with intact trabecular network. Several published works confront this issue by correcting for side effects (Un et al., 2006). The hypothesis also tested in this work was whether surface strain, determined by DIC, was homogeneous throughout the surface of the specimen, or increased at the periphery, justifying underestimation of compressive Young's modulus. Moreover, the macroscopic strain and the surface strain field, at which first yielding phenomena appeared with crack formation initiation, were investigated. For this reason, DIC and AE were simultaneously performed.

The specimens, in this work, were not confined by endcaps, as it has been found by three-dimensional finite element models that confining leads to overestimation of modulus for specimens shorter than 10 mm (Lievers et al., 2010).

The specimens were not preconditioned, as preconditioning has controversial effects on stiffness measurements. Decrease of tensile and compressive moduli by preconditioning suggested that initial yielding involves microstructural damage of a number of trabeculae and indicated that the tensile and compressive yield strain of trabecular bone from bovine tibiae is less than 0.5% (Keaveny et al., 1994). However, the compressive modulus was decreased by preconditioning at 5.3% ($p < 0.01$). The decrease in tensile modulus was even larger (on average 8.83%, $p < 0.01$). These results support the hypotheses that local microfractures of osteopenic vertebral bodies are created, start propagating, and accumulate at lower strains than those of normal vertebrae.

The measurements of the current research displayed a large difference between the values of Young's modulus calculated in the "small" and "large" areas. This difference can be attributed to the fact that most specimens failed in the middle area, resulting in larger deformation of this specific area. In terms of strain, because the length of the middle area is smaller that that of the "large," the strain in this area is higher, resulting in is lower modulus of elasticity in the middle area. It was difficult to interpret the onset of very high values of SD in the "large" area: the high spreading of values of modulus of elasticity (66–536 MPa) could be attributed to the higher length f examination, which increased the possibility of inclusion in the calculation of areas with large variation in architecture. Data (not shown) from cylindrical trabecular bone specimens have shown no underestimation of Young's Modulus determined by platens relative displacement. Geometry of the specimen plays a significant role in mechanical properties of trabecular bone, as it has been recognized by several investigators (Linde et al., 1992a,b).

In the literature, average elastic modulus underestimation ranged from 22% for the human proximal tibia up to 38%

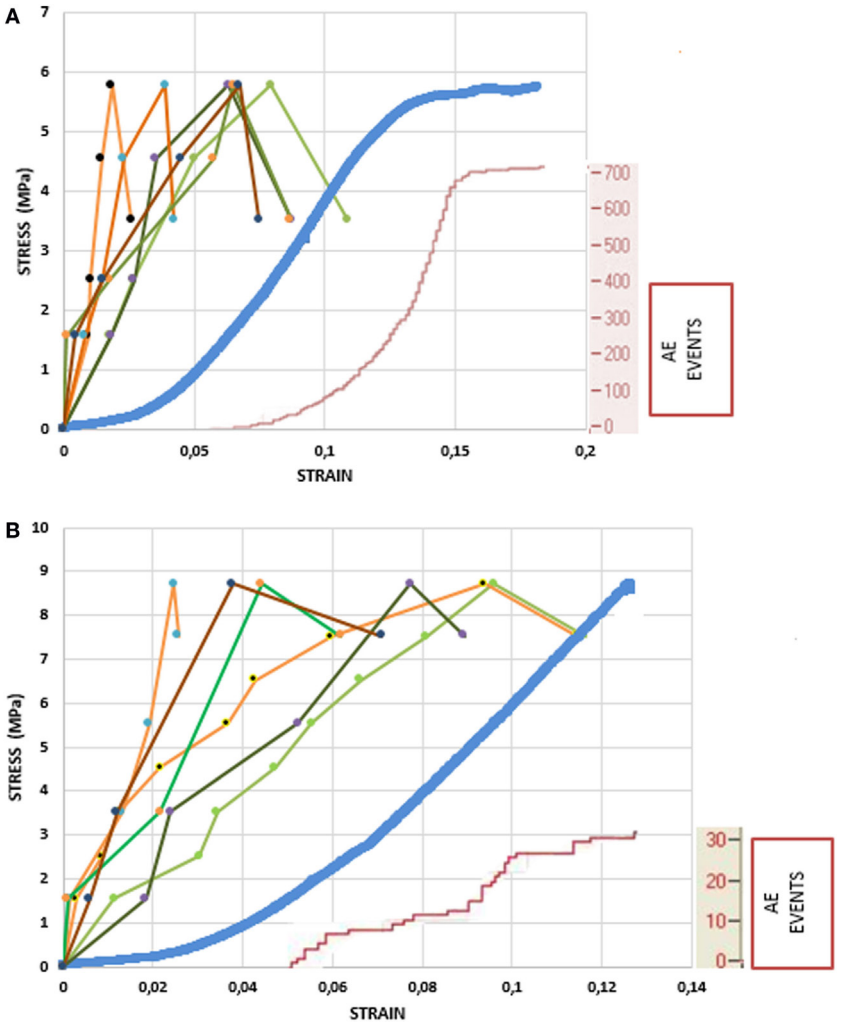

FIGURE 6 | Load history and cumulative acoustic emission (AE) activity for two different specimens (small area is shown with tints of green color, large area with tints of orange color, platens displacement with blue color, and AE events are shown with red color). **(A)** Loading until fracture. **(B)** Focus on the stress–strain curve at the low loads.

for the bovine proximal humerus (Odgaard and Linde, 1991; Keaveny et al., 1993). Our values of underestimation were comparable to those found in the literature using cubic specimens and measuring strain in the central area. Experimental and numerical results have shown that side effects can be ignored if tested specimens have a suitably large diameter, whose minimum dimension depends on the cancellous architecture. This is justified by the fact that a cancellous bone specimen has a "damaged" region of lost connectivity around its periphery, with a characteristic thickness, t, depending upon the underlying architecture. In a cylinder with diameter D, when D increases, there is a decrease of the relative volume of this outer region in the periphery in relation to the total volume V of the cylinder. Therefore, if the specimen has an adequately large diameter, the magnitude of the side artifacts can become negligible, and there exists some minimum diameter above which the side effects can be ignored (Lievers et al., 2010). However, this logical result is not supported by our data. Because of the heterogeneous nature of cancellous bone, there are areas with a different microarchitecture (Perilli et al., 2008). The depiction of the longitudinal surface strain field evolution during compression reflected the presence of stiffer or more compliant areas of trabecular bone throughout the specimen surface. The strain was not increased in a systematic way at the periphery of the specimen. Thus, the hypothesis of reduced compliance due to loss of connectivity of the trabeculae at the periphery of a sample was not supported by these experiments.

Acoustic emission in cancellous bone during compression loading to confirm the microdamage initiation and accumulation (Hasegawa et al., 1993) was measured in this study. A microdamage event, either bone microfracture or microcrack propagation, releases energy. Some of this energy is in the form of acoustic waves. Using optical measurements, it has been found that trabecular bone exhibits fully linear elastic behavior and

yields at low strains (less than 1.8%). It has been also suggested in the literature that minor structural changes may occur at a strain level as low as 0.8% (Linde et al., 1988; Madsen et al., 1988). AE activity revealed that microdamage initiated at about one-third of the maximum compressive strength. The surface yield strain in bone correlated with AE activity as in most homogeneous and non-porous materials (Alam and Loukili, 2010). On the contrary, initiation of AE activity occurred much earlier than the initiation of macroscopic yielding. The first detected microcracking probably concerned the thinner and most compliant trabeculae, which influenced the macroscopic stiffness in a smaller scale. The accumulation of these tiny microcracks led to macroscopic yielding, as it was revealed in the conventional stress–strain diagrams.

The number of AEs released from the trabecular bone samples did not vary widely. This behavior is totally different from that of compact bone where it has been noticed that a number of samples gave less than a dozen emissions until failure, whereas other samples generated hundreds of emissions (Agcaoglu and Akkus, 2013). These emission results imply that there are different patterns of compact bone failure: some samples failed with generation of few but large cracks whereas others failed by incremental growth of many small cracks. In trabecular bone, the failure mode is totally different. Fracture occurs after a sufficient number of trabeculae have been damaged. Moreover, the initiation of AEs of compact bone samples occurred at the time of the nonlinear increase in sample compliance and the cumulative number of AE events increased asymptotically in the prefailure period, whereas in cancellous bone AE events initiate in the macroscopic linear part of the σ–ε curve.

The detection of first AE of a significant amplitude would signal the initiation of failure. Thus, it is important to determine the time to failure at the first AE event. When these emissions are detected, they may provide an early warning in order to interrupt loading and prevent stress fracture, if AE is applied *in vivo* (Agcaoglu and Akkus, 2013). The AE is a function of bone material properties and the behavior of the bone microstructure during loading and failure procedure. More experiments are necessary to correlate the time of AE activity initiation with material properties in order to predict failure timely.

The measurement of the surface strain fields by DIC techniques have high resolution, enabling the determination of crack openings of microcracks present on the surface. However, this method is only limited to the surface of the specimen and cannot predict presence of cracks inside the specimen and inaccessible areas. Further experiments, determining 3D strain with digital volume correlation (DVC) apart from surface strain, are necessary to clarify the issue of strain inhomogeneity in cancellous bone (Gillard et al., 2014). Knowledge of the three-dimensional stress and strain distribution within bone tissue, MicroCT-imaging to assess the morphometric parameters and visualization of the failure region along with AE monitoring of released strain energy during bone mechanical testing will permit to understand the mechanism of bone failure, and may lead to an improved understanding of mechanisms of certain diseases' initiation, prevention, and treatment (Leichter et al., 1990).

CONCLUSION

In conclusion, compressive Young's modulus determined by platens relative displacement was underestimated in comparison to optically determined surface strain. There is also significant inhomogeneity in the strain distribution, resulting in large differences in the modulus, depending on the area over which it is calculated. Optical measurement of strain showed that compressive yielding occurs at low strains (less than 1.8%).

Strain at which microcracking initiates in cancellous bone and its relation to macroscopic yield strain has not been determined until now. Piezoelectric sensors on the specimens' surface monitor AE activity, which indicates the initiation of local fracturing, which occurs much earlier than macroscopic yielding and fracture. AE activity recorded simultaneously with strain field measurements can clarify issues relating to understanding of the macroscopic strain at which crack formation initiate and propagates until fracture, inhomogeneity of bone tissue mechanical behavior and mechanisms of bone failure for improved understanding of certain diseases' initiation, prevention, and treatment. Determination of 3D strain with DVC is necessary to clarify further the above issues.

AUTHOR CONTRIBUTIONS

DD, University of Patras, contributed to overall design of the experiments, results interpretation, and manuscript writing. AT contributed to performance of experiments, results interpretation, and manuscript writing.

FUNDING

Funding was provided from General Secretariat for Research and Technology (GSRT) and Hellenic Foundation for Research and Innovation (HFRI).

REFERENCES

Agcaoglu, S., and Akkus, O. (2013). Acoustic emission based monitoring of the microdamage evolution during fatigue of human cortical bone. *J. Biomech.* 135, 81005–81008. doi:10.1115/1.4024134

Alam, S. Y., and Loukili, A. (2010). "Application of digital image correlation to size effect tests of concrete," in *7th International Conference on Fracture Mechanics of Concrete and Concrete Structures*, North Korea, 91–97.

Cardoso, L., Teboul, F., Sedel, L., Oddou, C., and Meunier, A. (2003). In vitro acoustic waves propagation in human and bovine cancellous bone. *J. Bone Miner. Res.* 18, 1803–1812. doi:10.1359/jbmr.2003.18.10.1803

Carter, D. R., and Hayes, W. C. (1977). The compressive behavior of bone as a two-phase porous structure. *J. Bone Joint Surg.* 59, 954–962. doi:10.2106/00004623-197759070-00021

Freddi, A., Olmi, G., and Cristofolini, L. (2015). *Experimental Stress Analysis for Materials and Structures: Stress Analysis Models for Developing Design Methodologies*. Cham: Springer.

Gillard, F., Boardman, R., Mavrogordato, M., Hollis, D., Sinclair, I., Pierron, F., et al. (2014). The application of digital volume correlation (DVC) to study the microstructural behaviour of trabecular bone during compression. *J. Mech. Beh. Biomed. Mater.* 29, 480–499. doi:10.1016/j.jmbbm.2013.09.014

Goff, M. G., Lambers, F. M., Sorna, R. M., Keaveny, T. M., and Hernandez, C. J. (2015). Finite element models predict the location of microdamage in cancellous bone following uniaxial loading. *J. Biomech.* 48, 4142–4148. doi:10.1016/j.jbiomech.2015.10.023

Hanagud, S., Clinton, R. G., and Lopez, J. P. (1973). "Acoustic emission in bone substance," in *Proceedings of the ASME Symposium on Biomechanics*, New York, 79–81.

Hasegawa, K., Takahashi, H. E., Koga, Y., Kawashima, T., Hara, T., Tanabe, Y., et al. (1993). Mechanical properties of osteopenic vertebral bodies monitored by acoustic emission. *Bone* 14, 737–743. doi:10.1016/8756-3282(93)90205-O

Hernandez, C. J., Lambers, F. M., Widjaja, J., Chapa, C., and Rimnac, C. M. (2014). Quantitative relationships between microdamage and cancellous bone strength and stiffness. *Bone* 66, 205–213. doi:10.1016/j.bone.2014.05.023

Hoult, N., Take, A., Lee, C., and Dutton, M. (2013). Experimental accuracy of two-dimensional strain measurements using digital image correlation. *Eng. Struct.* 46, 718–726. doi:10.1016/j.engstruct.2012.08.018

Jonsson, U., and Eriksson, K. (1984). Microcracking in dog bone under load. A biomechanical study of bone visco-elasticity. *Acta Orthop. Scand.* 55, 441–445. doi:10.3109/17453678408992391

Keaveny, T. M., Borchers, R. E., Gibson, L. J., and Hayes, W. C. (1993). Theoretical analysis of the experimental artifact in trabecular bone compressive modulus. *J. Biomech.* 26, 599–607. doi:10.1016/0021-9290(93)90021-6

Keaveny, T. M., Guo, X., Wachtel, E., McMahon, T., and Hayes, W. (1994). Trabecular bone exhibits fully linear elastic behavior and yields at low strains. *J. Biomech.* 27, 1127–1136. doi:10.1016/0021-9290(94)90053-1

Lambers, F. M., Bouman, A. R., Rimnac, A. C., and Hernandez, C. J. (2013). Microdamage caused by fatique loading in human cancellous bone: relationship to reductions in bone biomechanical performance. *PLoS ONE* 8, e1562. doi:10.1371/journal.pone.0083662

Leichter, I., Bivas, A., Margulies, J. Y., Roman, I., and Simkin, A. (1990). Acoustic emission from trabecular bone during mechanical testing: the effect of osteoporosis and osteoarthritis. *Proc. Inst. Mech. Eng. H* 204, 123–127. doi:10.1243/PIME_PROC_1990_204_241_02

Lievers, W. B., Petryshyn, A. C., Poljsak, A. S., Waldman, S. D., and Pilkey, A. K. (2010). Specimen diameter and "side artifacts" in cancellous bone evaluated using end-constrained elastic tension. *Bone* 47, 371–377. doi:10.1016/j.bone.2010.03.024

Linde, F., and Hvid, I. (1987). Stiffness behaviour of trabecular bone specimens. *J. Biomech.* 20, 83–89. doi:10.1016/0021-9290(87)90270-3

Linde, F., Gothgen, C. B., Hvid, I., and Pongsoipetch, B. (1988). Mechanical properties of trabecular bone by a non-destructive testing approach. *Eng. Med.* 17, 23–29. doi:10.1243/EMED_JOUR_198017_008_02

Linde, F., and Hvid, I. (1989). The effect of constraint on the mechanical behaviour of trabecular bone specimens. *J. Biomech.* 22, 485–490. doi:10.1016/0021-9290(89)90209-1

Linde, F., Hvid, I., and Madsen, F. (1992a). The effect of specimen geometry on the mechanical behaviour of trabecular bone specimens. *J. Biomech.* 25, 359–368. doi:10.1016/0021-9290(92)90255-Y

Linde, F., Hvid, I., and Madsen, F. (1992b). The effect of specimen size and geometry on the mechanical behaviour of trabecular bone specimens. *J. Biomech.* 24, 454. doi:10.1016/0021-9290(91)90046-P

Lionello, G., and Cristofolini, L. (2014). A practical approach to optimizing the preparation of speckle patterns for digital-image correlation. *Meas. Sci. Technol.* 25, 1–9. doi:10.1088/0957-0233/25/10/107001

Madsen, F., Odgaard, A., and Linde, F. (1988). "The consequences of compression strain level on energy absorption in trabecular bone specimens performance," in *Proc 6th Mtg* (London: ESB London).

Maurer-Ertl, W., Friesenbichler, J., Svehlik, M., Holzer, L., Sadoghi, P., Ogris, K., et al. (2015). The effects of the surgical approach on the postoperative gait mechanics following total hip arthroplasty. *Ann. Orthop. Rheumatol.* 3, 1056.

Odgaard, A., Hvid, I., and Linde, F. (1989). Strain distributions in cancellous bone specimens. *J. Biomech.* 23, 367. doi:10.1016/0021-9290(90)90078-H

Odgaard, A., and Linde, F. (1991). The underestimation of Young's Modulus in compressive testing of cancellous bone specimens. *J. Biomech.* 24, 691–698. doi:10.1016/0021-9290(91)90333-I

Onck, P. R., Andrews, E., and Gibson, L. J. (2001). Size effects in ductile cellular solids. Part I: modeling. *Int. J. Mech. Sci.* 43, 681–699. doi:10.1016/S0020-7403(00)00042-4

Palanca, M., Tozzi, G., and Cristofolini, L. (2015). The use of digital image correlation in the biomechanical area: a review. *Int. Biomech.* 3, 1–21. doi:10.1080/23335432.2015.1117395

Perilli, E., Baleani, M., Ohman, C., Fognani, R., Baruffaldi, F., and Viceconti, M. (2008). Dependence of mechanical compressive strength on local variations in microarchitecture in cancellous bone of proximal human femur. *J. Biomech.* 41, 438–446. doi:10.1016/j.jbiomech.2007.08.003

Roberts, B., Perilli, E., and Reynolds, K. (2014). Application of the digital volume correlation technique for the measurement of displacement and strain fields in bone: a literature review. *J. Biomech.* 47, 923–934. doi:10.1016/j.jbiomech.2014.01.001

Shrivastava, S., and Prakash, R. (2009). Assessment of bone condition by acoustic emission technique: a review. *J. Biomed. Sci. Eng.* 2, 144–154. doi:10.4236/jbise.2009.23025

Shrivastava, S., and Prakash, R. (2011). In vitro study of bone condition using acousto-ultrasonic technique. *Int. J. Healthcare Manage.* 12, 168–178. doi:10.1504/IJHTM.2011.039627

Sutton, M., Wolters, W. J., Peters, W. H., Ranson, W. F., and McNeill, S. R. (1983). Determination of displacements using an improved digital correlation method. *Image Vis. Comput.* 1, 133–139. doi:10.1016/0262-8856(83)90064-1

Sutton, M. A., Orteu, J. J., and Schreier, H. W. (2009). *Image Correlation for Shape, Motion and Deformation Measurements*. New York: Springer Science.

Un, K., Bevill, G., and Keaveny, T. M. (2006). The effects of side-artifacts on the elastic modulus of trabecular bone. *J. Biomech.* 36, 1955–1963. doi:10.1016/j.jbiomech.2006.05.012

Wright, T. M., Vosburgh, F., and Burstein, A. H. (1981). Permanent deformation of compact bone monitored by acoustic emission. *J. Biomech.* 14, 405–409. doi:10.1016/0021-9290(81)90058-0

Conflict of Interest Statement: The authors declare that the research was conducted in the absence of any commercial or financial relationships that could be construed as a potential conflict of interest.

frontiers in Materials

ORIGINAL RESEARCH
published: 13 December 2017
doi: 10.3389/fmats.2017.00041

Microstructural Consequences of Blast Lung Injury Characterized with Digital Volume Correlation

Hari Arora[1,2], Alex Nila[3], Kalpani Vitharana[2], Joseph M. Sherwood[2], Thuy-Tien N. Nguyen[2], Angelo Karunaratne[4], Idris K. Mohammed[2], Andrew J. Bodey[5], Peter J. Hellyer[2], Darryl R. Overby[2], Robert C. Schroter[2] and Dave Hollis[3]*

[1] Swansea University, Swansea, United Kingdom, [2] Imperial College London, London, United Kingdom, [3] LaVisionUK Ltd., Oxford, United Kingdom, [4] University of Moratuwa, Moratuwa, Sri Lanka, [5] Diamond Light Source, Didcot, United Kingdom

This study focuses on microstructural changes that occur within the mammalian lung when subject to blast and how these changes influence strain distributions within the tissue. Shock tube experiments were performed to generate the blast injured specimens (cadaveric Sprague-Dawley rats). Blast overpressures of 100 and 180 kPa were studied. Synchrotron tomography imaging was used to capture volumetric image data of lungs. Specimens were ventilated using a custom-built system to study multiple inflation pressures during each tomography scan. These data enabled the first digital volume correlation (DVC) measurements in lung tissue to be performed. Quantitative analysis was performed to describe the damaged architecture of the lung. No clear changes in the microstructure of the tissue morphology were observed due to controlled low- to moderate-level blast exposure. However, significant focal sites of injury were observed using DVC, which allowed the detection of bias and concentration in the patterns of strain level. Morphological analysis corroborated the findings, illustrating that the focal damage caused by a blast can give rise to diffuse influence across the tissue. It is important to characterize the non-instantly fatal doses of blast, given the transient nature of blast lung in the clinical setting. This research has highlighted the need for better understanding of focal injury and its zone of influence (alveolar interdependency and neighboring tissue burden as a result of focal injury). DVC techniques show great promise as a tool to advance this endeavor, providing a new perspective on lung mechanics after blast.

Keywords: digital volume correlation, blast lung injury, synchrotron tomography, lung microstructure, shock tube, lung biomechanics

OPEN ACCESS

Edited by:
Gianluca Tozzi, University of Portsmouth, United Kingdom

Reviewed by:
Stephane Avril, Centre Ingénierie et Santé, Ecole des Mines de Saint-Étienne, France
Sourav Chatterjee, Facebook, United States

****Correspondence:***
Hari Arora
hari.arora@swansea.ac.uk

Specialty section:
This article was submitted to Mechanics of Materials, a section of the journal Frontiers in Materials

Received: *27 August 2017*
Accepted: *20 November 2017*
Published: *13 December 2017*

Citation:
Arora H, Nila A, Vitharana K, Sherwood JM, Nguyen T-TN, Karunaratne A, Mohammed IK, Bodey AJ, Hellyer PJ, Overby DR, Schroter RC and Hollis D (2017) Microstructural Consequences of Blast Lung Injury Characterized with Digital Volume Correlation. Front. Mater. 4:41. doi: 10.3389/fmats.2017.00041

INTRODUCTION

Trauma research is a vast and rapidly growing field and blast injuries represent the most extreme level of trauma. Nowadays, blast injuries present a concern, not only for military personnel in the context of combat but also civilians. This is due to a host of explosive threats that injure unprotected civilians in everyday life, such as industrial accidents, legacies from war (landmines), and terrorism. The importance of blast injury research is further heightened by the fact that blast injuries are far more complex and severe than conventional civilian trauma, such as road traffic accidents. The nature of the blast threat (blast loading) is constantly evolving, meaning the nature

and mechanisms of the injuries will differ, depending on a range of variables associated with the explosive event. The chasm in knowledge surrounding blast injuries is created by the sheer number of variables present in a blast event (weight/type/shape of explosive, the position relative to the victim, the surrounding environment, etc.). Hence, new approaches are required to identify the underlying mechanism and effects of injury associated with blast lung trauma.

Clinical and postmortem data collected during the recent conflict in Afghanistan revealed that blast lung injury (BLI) was found in 6–11% of survivors, increasing to 80% in non-survivors (17% dying from BLI alone) (Scott, 2016). BLI incidence increases to more than 90% in terrorist attacks occurring in enclosed spaces such as trains. However, BLI is not thoroughly understood with some casualties being undiagnosed, leading to complications with treatment or even, preventable and avoidable, death. Models exist in the literature, with many more being proposed each year to tackle or address new aspects of the pathology (CR Bass et al., 2008; Garner et al., 2010; Kohsuke et al., 2016). One study presents 2,550 large animal (sheep, pig, monkey, goat, dog, and burro) experiments on blast lethality (CR Bass et al., 2008). This collection of work is not the norm in terms of experimental numbers, which typically range from 20 to 200 per study; animal models range from pigs (large) (Garner et al., 2010) down to mice (small) (Kohsuke et al., 2016). While much research focuses on global effects of trauma, which contributes significantly to knowledge of patient outcome, lung injuries actually range from diffuse and sparse regions of visible tissue damage to non-detectable damage (by conventional imaging techniques) (Scott et al., 2017).

The lung is a dynamic, hierarchical organ with strain- and strain-rate-sensitive mechanical properties. The microarchitecture resembles that of foam, built from constituents, including collagen, elastin, extracellular matrix, and endothelial and epithelial cells, in varying proportions throughout the lung and across species (Hoppin et al., 1975; Matsuda et al., 1987; Mercer et al., 1994; Yuan et al., 1997; Black et al., 2005; Suki et al., 2005; Andrikakou et al., 2016). Alveoli form tightly packed networks that expand and contract during respiration, influencing each other while stretching, compressing and straining with their neighbors. Tethering stresses that exist between neighboring groups of alveoli promote non-uniformity in deformation during respiration (Sera et al., 2004; Denny and Schroter, 2006). This study uses high-resolution synchrotron imaging to facilitate improved understanding of micro-scale lung mechanics in trauma.

Digital volume correlation (DVC) is a powerful technique used to explore true three-dimensional strain fields within a given deforming object. It is achieved in conjunction with various powerful volumetric imaging techniques and obeys the principles of all image correlation or tracking methods (Schreier et al., 2009). DVC has been performed in structural biomaterials such as bone (Bay et al., 1999; Gillard et al., 2014; Roberts et al., 2014; Palanca et al., 2015), characterizing microstructural mechanics and the accuracy of the technique itself. This study aims to explore microstructural deformation in lung tissue using DVC, specifically showing how differing levels of blast loading can affect the behavior of lung tissue during respiration. This is to determine whether the observed loss of lung function is a time-related mechanical effect, e.g., plasticity causing abnormal wall characteristics, leading to possible fatigue in the long term.

The interdependency of healthy tissue on neighboring damaged tissue units is also considered in this study. Local defects can develop into larger injury sites over a period of time. Scans were performed for different volumetric pre-strain (i.e., levels of inflation) to calculate wall strain during respiration. Damaged and injured lung tissue mechanics are characterized in a greater depth than previously reported.

MATERIALS AND METHODS

An overview of the experiment is given in **Figure 1**, showing the three key elements of this study. The specimen is ventilated, subject to blast, and then excised and prepared for imaging. Airway pressure is set to 10 cmH_2O prior to the first scan and then increased to 20 cmH_2O for the second scan. Based on the local deformations between the two pressure states, strains can be resolved using DVC algorithms. Details of these procedures are provided in the following sections.

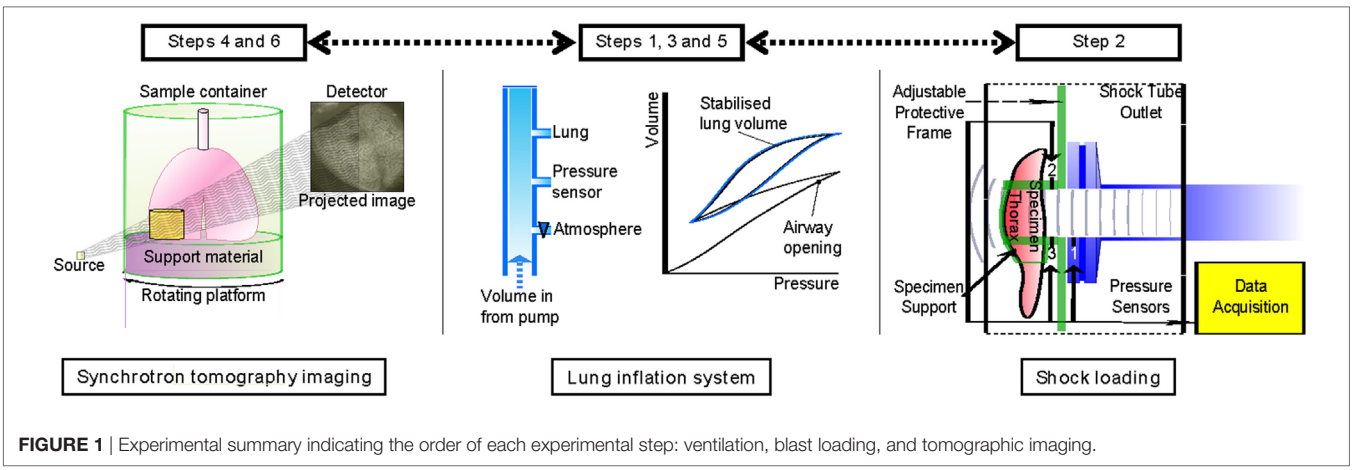

FIGURE 1 | Experimental summary indicating the order of each experimental step: ventilation, blast loading, and tomographic imaging.

Sample Preparation and Handling

Female cadaveric Sprague-Dawley rats (200–280 g), purchased from Charles River, Kent, UK, were delivered within 4–6 hours of sacrifice during this study. No live animals or human subjects were tested in this study. Cadaveric tissue was obtained from animals from a registered animal supplier. Procedures were approved by the Imperial College London ethical review process and strictly conformed to the Animals (Scientific Procedures) Act 1986 UK Home Office guidelines, which also fulfill the US NIH Guide for the Care and Use of Laboratory Animals. Previous research within the group established the *in vivo* model (Barnett-Vanes et al., 2016) and found it exhibited comparable physical behavior to freshly harvested tissue. Therefore, it was deemed appropriate to proceed with cadaveric tissue for the experimental program to establish the feasibility of this strain measurement technique.

Specimens were weighed before and after each procedure to monitor superficially any major water loss during the experiment. Pre-experimentation, a tracheostomy was performed to enable the lungs to be ventilated. A series of ventilation cycles were performed to minimize airway closure and degradation, which is commonly reported to occur rapidly after death in unventilated lungs. A Harvard PHD Ultra syringe pump was used to deliver a controlled volume of air, while tracheal pressure was monitored *via* a sensor (Omegadyne PX309) mounted in the circuit (between pump and lung). Compliance of the air in the ventilation system was corrected for to enable representative pressure-volume characteristics of the lung to be captured. The setup was controlled using LabVIEW, and pressure-volume data were visualized and monitored during each experiment. Ventilation was performed under pressure control (0–20 cmH_2O) to ensure open airways were not overpressurized, while promoting airway reopening of any collapsed airways *via* cyclic loading. Once the monitored pressure-volume loops of the lungs stabilized, i.e., no further progressive volume changes recorded, the samples were ready for blast experimentation.

Samples were held at a predetermined lung volume, equating to the peak pressure 20 cmH_2O, prior to single blast wave loading. Relaxation from this initial set-point condition was expected, monitored, and accounted for during the timings of each test. There was typically a 10% drift in reduced pressure during the relaxation phase. All other organs were shielded from the blast (head, abdomen and limbs). The efficiency of blast wave isolation to a target region of the specimen has been established previously (Eftaxiopoulou et al., 2015; Barnett-Vanes et al., 2016). The high lung volume was used to replicate the pre-tension of breathing lung tissue during a blast event. Controls did not receive a blast wave but were otherwise treated identically, undergoing all procedures including being mounted on the shock tube for the equivalent period of time.

After the procedure, rats were re-mounted on the ventilation system for the assessment of injury and to restore any collapsed airways. Once stabilized, the thorax of the specimen was dissected and the lung was isolated, while lung volume was maintained by the ventilator. The lung was then mounted within a sealable polymer tube, which contained ballast for stability during imaging and phosphate buffer solution to maintain surface moisture of the specimen.

Specimen Loading Device: Shock Tube

A shock tube was employed to generate blast wave pressure pulses of controlled intensity and duration. This shock tube is formed of sections of stainless steel tube (3.8 m total length), with an internal diameter of 59 ± 1 mm. Compressed air is used to pressurize the driver section. The driven section remains at atmospheric pressure. For this study, the minimum driver volume was used, equivalent to 2.2×10^{-4} m^3 of air per test shot. The system was operated in a single-diaphragm configuration, using thin film polymer (Mylar) diaphragms of varying thickness (50–100 μm). Blast waves with magnitudes up to 180 kPa were produced during this study. The setup used here promoted the formation of blast waves that approximate the Friedlander waveform due to the small driver volumes and open-loading configuration.

Three pressure gauges were mounted along the shock tube and around the test specimen to monitor the loading experienced by the specimen during each blast test. Sensor 1 was mounted radially at the shock tube outlet to ensure that the incident wave produced is repeatable and consistent in single-diaphragm firing mode. Two further sensors were attached to the specimen mount. The specimen mount was designed to allow for near consistent loading conditions to be achieved for each specimen. The opening for the specimen is adaptable to account for the small variations in size from animal to animal. The blast wave is isolated to the thorax alone and shielded distal to the thorax, leading to a repeatable loading conditions (Barnett-Vanes et al., 2016). Sensors 2 and 3 were installed on the loading platform above and below the incident blast pressure loading site of the specimen. These sensors recorded the transient pressure state in front of the thorax. A combination of incident and reflected overpressure was recorded, due to the proximity of the sensors to the thorax. High-speed photography was employed to ensure the setup and desired loading condition was maintained throughout the duration of each test. A Phantom V210 camera (208×128 pixels at 53,000 fps) was used, positioned square-on to the sample and loading direction.

Two blast conditions were studied alongside the control case: (1) low-intensity blast (peak overpressure 100 kPa) and (2) a moderate-intensity blast (peak overpressure 180 kPa). This moderate case is known to approach the upper bound of survivability in live animals (Barnett-Vanes et al., 2016). Therefore, this case was included in this cadaveric study to highlight any tissue changes that may have occurred (tissue stiffness), which are not visibly shown to be damaging, i.e., no hemorrhage, but may cause structural changes potentially visible in the strain fields.

Tomographic Image Acquisition

Synchrotron X-ray microtomography experiments were conducted at the Diamond-Manchester Imaging Branchline I13-2 of Diamond Light Source (DLS), UK. Synchrotron light sources enable tomographic data sets to be collected with higher signal-to-noise ratio and higher spatial and temporal resolution more quickly than micro-focus tube sources ("laboratory CT") and also provide phase contrast more readily. Inflated lungs are very prone to tissue creep, and the high flux of X-rays at I13-2 enabled data of good signal-to-noise ratio to be collected

quickly enough for creep to be kept acceptably low. Total scan time to collect all projections was 30 s. A partially coherent, polychromatic "pink" beam (photon energy range: 5–35 keV) of parallel geometry was generated by an undulator from electrons in a storage ring of 3.0 GeV current. The undulator gap was set to 5 mm for data collection and, to limit sample damage, 11 mm for alignment. The beam was reflected from the Pt stripe of a grazing-incidence focusing mirror and, to limit sample damage, high-pass filtered with 1.3 mm pyrolytic graphite and 3.11 mm aluminum. Images were acquired at equally spaced angles over 180° of continuous rotation ("fly scan") by a ZnWO4 scintillator-coupled pco.edge 5.5 (PCO AG, Germany) detector, with a sCMOS sensor of 2,560 × 2,160 pixels. With 2.5× total magnification, this gave a field of view of 6.7 mm × 5.6 mm and an effective pixel size of 2.6 μm. Various propagation distances were studied to determine the optimal inline phase contrast, and 150 mm was chosen. Images recorded at 180° were compared to those recorded at 0° to check for (potentially subtle) experimental problems including sample deformation and damage (Atwood et al., 2015). To balance the signal-to-noise ratio and angular sampling with tissue damage and deformation *via* tissue creep, various exposure times and numbers of projections were trialed; data sets were then collected with 1,801 projection images of 30 ms exposure time. Prior to reconstruction *via* filtered back projection with DAWN 1.7 (Basham et al., 2015), projection images were flat- and dark-field corrected, and ring artifact suppression was performed (Titarenko, 2016).

Samples were scanned and then cycled again on the ventilator, prior to being scanned a second time. The pilot study (MT10583-1) concluded that to avoid excessive tissue dehydration, which could augment the tissue mechanics, samples should be kept in a fully humidified chamber. The lung was imaged intact to allow a fixed volume of air to be kept within the tissue during each scan. Imaging parameters were further optimized for the whole intact set of lungs. Lungs were subject to ventilation, and prior to each scan, they were stopped at mid- and low-lung volumes. Imaging biopsies would not allow for airway control in this manner. Care was taken to ensure minimal movement of the lung between original and second mounting position. The relatively large field of view meant correlation between sub-volumes in each scan was possible. An overview of the full experimental procedure is provided in **Figure 1**.

Image Processing

Image stacks were imported into the DaVis software for DVC to be performed. Rigid body translations were expected given the sample had been removed from the imaging platform between scans (to ventilate and set to the second lung pressure/volume). Rigid body motion was removed from the strain computation *via* a transformation matrix computed within the DaVis software. The DVC process is mapped out schematically in **Figure 2**, illustrating the use of sub-volume tracking of regions to compute the strain vector between neighbors. The computed strain result was produced by a final correlation sub-volume size pass of 32 × 32 × 32 voxels. The DVC software employs piecewise linear shape functions when matching sub-volume deformation between the reference and the deformed image. The number of "pieces" in that piecewise linear shape function is determined by the overlap percentage. Therefore, a higher overlap (75%) results in more (linear) pieces to describe the sub-volume deformation; the higher the percentage overlap, the closer the shape function gets to a second order approximation (compared to purely first order for zero overlap). With more overlap, the ability to detect discontinuities is enhanced, and the algorithm can more accurately describe the high-gradient displacement changes expected in lung tissue.

The correlation was performed between an image stack acquired at one pressure state and another image stack acquired at the second pressure state. This creates one set of strain data representing the deformation between the two pressure states. Maximum three-dimensional strain (maximum principal) was exported for further analysis in MATLAB. Analysis was performed on each result file to compare blast conditions in terms of visual differences and spatial variation. Subregions within each specimen were studied in relation to the global volume characteristics.

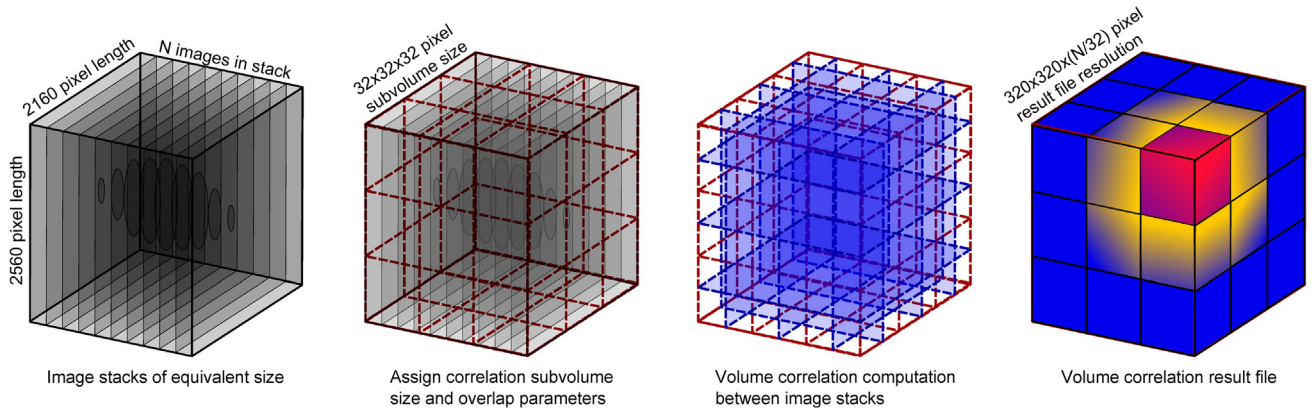

FIGURE 2 | Schematic of the volume correlation process, including details of the input volume size versus the result file size.

RESULTS AND ANALYSIS

Sample blast wave profiles from the two blast conditions are shown in **Figure 3**. Peak blast wave pressures of 100 kPa for the low-level blast and 180 kPa for the moderate-level blast were measured at the outlet of the shock tube. **Figure 3** illustrates the near instantaneous rise time and characteristic decay associated with a blast wave. When monitoring the local pressure history in front of the thorax of the specimen, local lateral pressures initially peaked at 50 and 100 kPa for the two test cases. To extend the analysis of the loading conditions on each specimen, studies have correlated lateral and head-on (reflected) pressures for this shock tube under both the open- and closed-tube configuration (Nguyen et al., 2014; Nguyen, 2016).[1] The closed-tube configuration can approximate the maximum pressure that the test specimens would observe. Therefore, in the case for a lateral pressure recorded at the outlet of 100 kPa, this results in a peak reflected pressure of 320 kPa. For an open-tube configuration, this peak reflected pressure reduction to 265 kPa. Similarly, for the moderate blast loading, the closed- and open-tube configurations would deliver peak reflected pressures of 575 and 480 kPa respectively. In reality, the peak loading on the sample lies within this range as the specimen is positioned at the outlet. There are local variations in the pressures measured at the top of the thorax compared to the base, due to differences in structural compliance along from the apex to the base of the thorax. This structural compliance of the system will result in a differing decay characteristic in the loading and therefore comments on the peak are presented here with reference to the open- and closed-tube configurations (Nguyen et al., 2014; Nguyen, 2016; see text footnote 1). The pressure values lie within the range of the commonly reported threshold for lung injury (CR Bass et al., 2008).

An example of the process to convert the tomography image to the computed strain field is shown for a control (un-blasted) sample in **Figure 4**. Here, a sub-volume of the acquired image stack and the resultant extracted strain contours is shown. This highlights the nature of strain banding aligned to the stretched alveolar walls. Although the strain overlay plots help to visualize how the lung volume has deformed, for interpretation of the strain fields, specific strain vectors were extracted for direct analysis seen in **Figure 4**. Color and gray plots are included to show the origins of the strain plots, analyzed later in the article.

To characterize the healthy lung, the entire volume of the control specimen was computed. **Figure 5** presents the central

[1] Nguyen, T.-T. N., Brown, K. A., and Proud, W. G. (in preparation). Part I: a highly versatile shock tube system for cell, tissue and whole animal models of damage and blast injury. *Appl. Phys. Lett. Bioeng.*

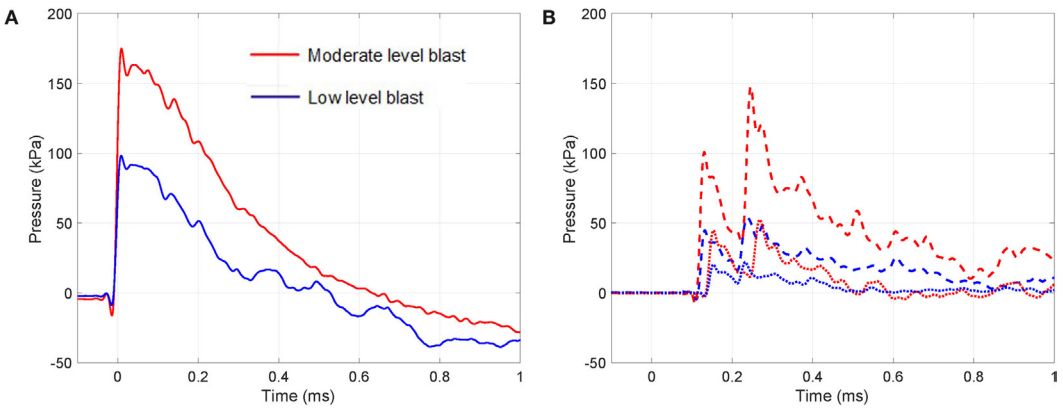

FIGURE 3 | Transient pressure measured during the moderate and low-intensity blasts: **(A)** at outlet of the shock tube (solid line) and **(B)** at the top (dashed line) and bottom (dotted line) regions in front of the thorax.

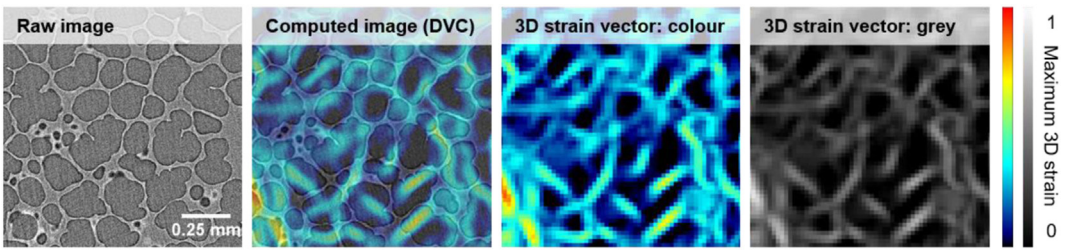

FIGURE 4 | Volume correlation process applied to a control sample. Images show the steps from a raw volume image to the extracted maximum three-dimensional strain field.

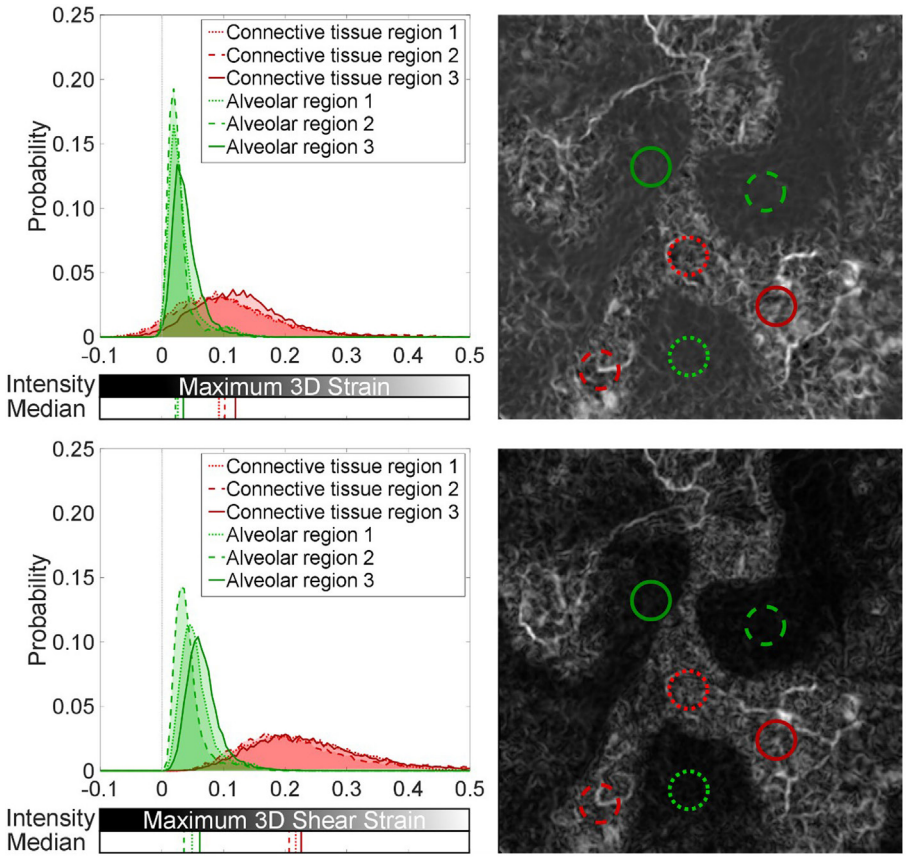

FIGURE 5 | Spatial analysis of strain field in the control: (top) maximum three-dimensional strain and (bottom) maximum three-dimensional shear strain. Sub-volumes (0.26-mm radius) within the control specimen were analyzed to highlight uniform low-level strains in alveolar regions (green) and a dense network of higher strains in connective tissue between lobular regions of alveoli (red). The median for each distribution is also plotted.

plane of the three-dimensional strain contour plot for maximum three-dimensional strain, the maximum three-dimensional shear strain, and the probability distribution functions relating to these two contour plots.

Maximum three-dimensional strain here equates to the maximum principal (normal) three-dimensional strain. Principal/normal strain are the Eigenvalues of the Matrix:

$$\begin{matrix} Exx & Exy & Exz \\ Eyx & Eyy & Eyz \\ Ezx & Ezy & Ezz \end{matrix}$$

To get the derivative *Ezz* you need a multi plane vector field (more than one *z*-planes). The Eigenvectors e_x, e_y, and e_z of that Matrix define the coordinate system where no shear is present, and the deformation can be described by using only strain along e_x, e_y, and e_z. The biggest Eigenvalue is called maximum (normal) three-dimensional strain. Maximum 3D shear strain is defined as the maximum Eigenvalue minus the minimum Eigenvalue of the strain tensor.

Subsections of the contour plots were analyzed in **Figure 5** for differences between alveolar and connective regions of the control lung. The probability distribution functions present a fair means of normalizing the distribution of strain components found within equivalent sized regions of the global volume. These distributions show how the volume is behaving, supporting the visual two-dimensional slice contour map, which was taken at the central plane of the three-dimensional data. Medians of their distributions are presented to highlight regional variation.

Figure 5 reveals local regions of strain uniformity within the alveolar-dense regions (airspaces) of ~2–5% in magnitude. However, there are also connective regions between lobular sections of airspace networks, which exhibit higher strains (~10%). Since regions (lobes) of the parenchyma are inflating next to each other, this causes relative movement between neighboring lobes. The ventilation of each region and the asymmetries present in the structure of these lobes will cause these lobular regions of airspaces to move relative to each other, i.e., not cohesively as one global unit, leading to higher strains between these independent clusters of alveoli (airspaces). The strains were discretized into component of normal and shear. The relative movement of the lobes within the parenchyma causes strain bands (white regions) within the tissue to be composed primarily of shear strains (~20%) within the connective tissue regions.

A Mann–Whitney *U*-test was performed on the distributions in the article. All alveolar regions were statistically significantly

different when compared to the connective regions for both the maximum three-dimensional shear and normal strain distributions ($p < 0.001$). The differences from the alveolar regions are indicated by the major shifts in the medians (~10% for maximum 3D strain and ~15% in maximum 3D shear) and spread of the distributions for the connective regions plotted in **Figure 5**.

Blast loaded specimens were then analyzed—a sample planar (or slice) view of the three-dimensional strain field is presented for each case in **Figure 6**. Comparing the control (un-blasted) specimen to the blast cases, there is a clear difference in global strain magnitude and the localization of high strain regions.

Both low- and moderate-blast cases observed in peak strains of ~100%. This localization of high strain indicates regions of overstrain, overdistension, during the ventilation procedure. To ensure the strains observed were independent of imaging artifact, one sample was imaged repeatedly on the beam line with a delay between scans greater than the length of a given experiment (5 min) to assess the maximum level of tissue creep that might be observed during imaging process. The lungs are viscoelastic in nature and therefore are susceptible to relaxation. This tissue creep assessment shows that, even after a 5-min delay between scans, strains barely peak over a few percent. Imaging for all specimens was conducted within a 30-s period to mitigate creep effects, keeping most likely well below the creep strain levels recorded during this exaggerated creep assessment. The color maps highlight the general network of strains seen in the tissue providing an overview of the entire sample and how it deforms. Strain localization occurred in regions inset from the boundary and along branch-way connections within the moderate-blast specimens. To obtain an improved perspective on the nature of tissue strain in health and injury, further analysis was performed on the distributions of strains.

Figure 7 analyzes the entire lung volumes and shows the probability distribution function for the strain content within each of the specimens shown in **Figure 6**. There are significant

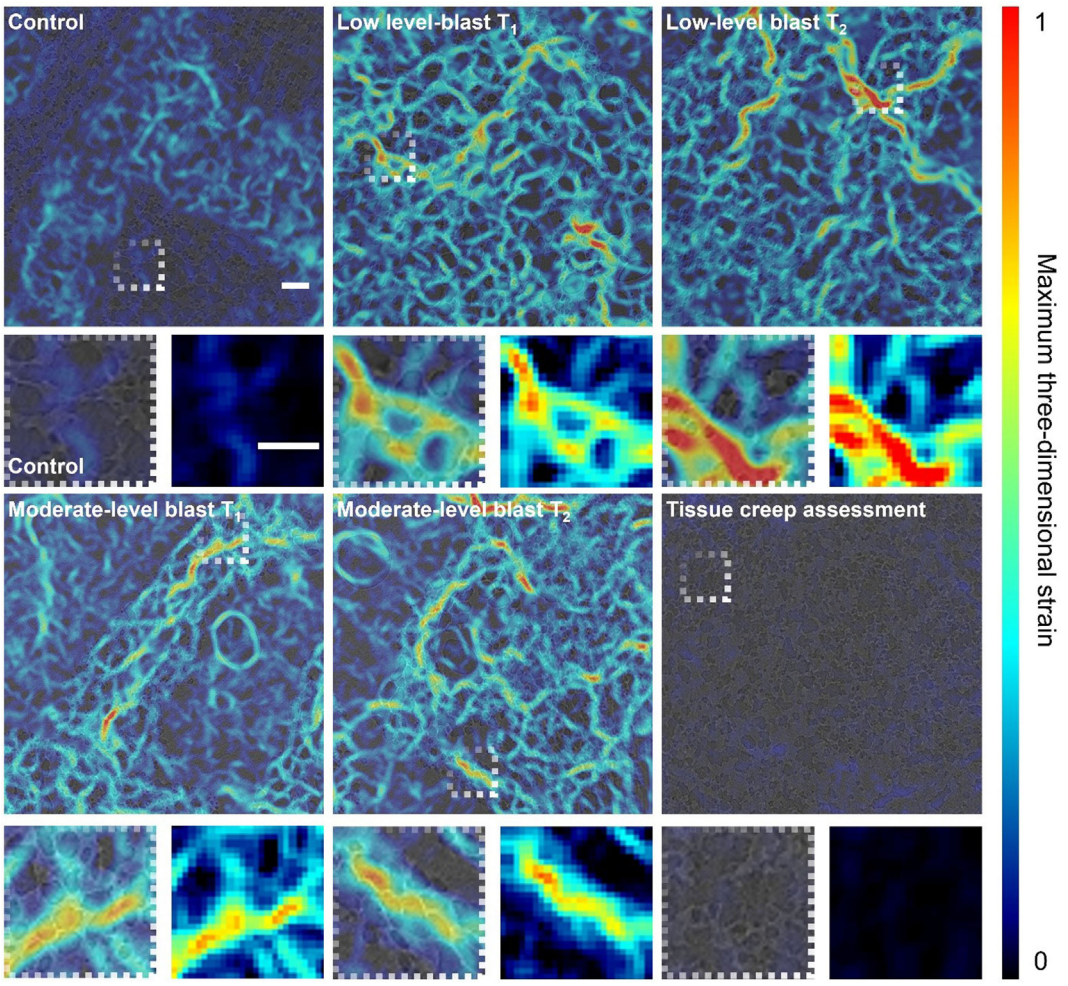

FIGURE 6 | Digital volume correlation results displaying the maximum three-dimensional strain at a given plane within the lung volume for each loading case: control, low-level blast and moderate-level blast. T_1 and T_2 denote repeat experiments. In addition, one blast specimen was scanned twice with a time delay between scans to highlight the maximum level of tissue creep during the imaging process as a proxy measure of noise and error in strain measurement. Scale bar indicates 200 μm.

differences in the distributions from the control to the blast injured specimens, as expected from the visual strain maps presented in **Figure 6** ($p < 0.001$). A shift of ~10% was observed in the median for all blast samples compared to the control. The spread of the distribution was seen to increase as well for each blast case, indicating that sites of higher tensile strain induce an effect on surrounding regions. There were no discernible differences overall between the two blast cases in terms of the global distribution, averaged over the whole specimen volume.

It is interesting to note the greater presence of negative strains in the blast cases. This is due to the net balance in strain within a given volume of tissue. Sites of damage may augment local mechanics. This can lead to some regions, healthy or injured, observing extra tension (overdistension), which may compress neighboring regions, which may also be damaged or occluded upstream and not ventilating well, causing a local compression. This is unlike healthy lungs, where alveoli are seen to expand more uniformly, stretching together, leading to small but generally tensile strains. To study these strain fields in detail, sub-volumes were explored within the global (entire) scan.

Figure 8 presents the same probability distribution analysis, this time applied to sub-volumes (zones) within the full volume image. Regions of high strain localization were targeted for the smallest sub-volume (Zone 1), which is a 0.26-mm radius sphere of the specimen/data. Larger shells surrounding Zone 1 and the focal strain site of interest were also computed. Distributions corresponding to those measured within Zone 1 (0–0.26 mm), Zone 2 (0.26–0.44 mm), Zone 3 (0.44–0.61 mm), and the full volume were processed and are presented in **Figure 8**.

Zones 1, 2, and 3 in each region studied in **Figure 8** exhibit significant differences in distributions compared to the full volume, or global behavior ($p < 0.001$). This supports the visual interpretation from **Figure 8** that these sites of observed different mechanical behavior are focal. There is an observable offset in the median in Zone 1 compared to the full volume across the three regions (~10–15%). However, there are no statistical differences among Zones 1, 2, and 3 in each image, implying that these regions are behaving in a similar fashion to each other (still different to the global behavior, i.e., full volume). This analysis enforces that these focal zones are composed of higher than usual strains in parts and are behaving differently to the global volume within that 0.61-mm radius zone.

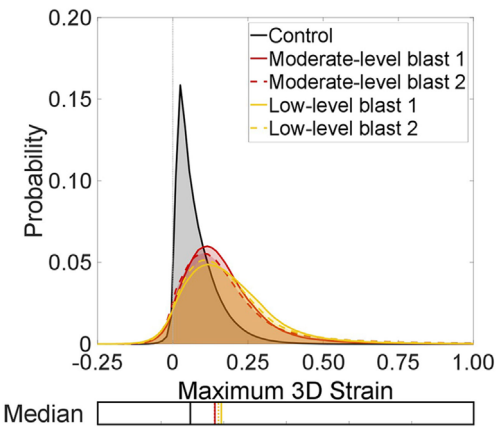

FIGURE 7 | Probability distributions for the strain content of each test case to show the global trends between each lung volume in terms of maximum three-dimensional strains. The median for each distribution is also plotted.

In each region of focus, the observable influence of the central defect region (Zone 1) begins to diminish, shown by the progressive shift of the median toward the control value for Zones 2 and 3. Where the defect is having an influence, Zones 2 and 3 have the tail of their distributions shifted away from the global. **Figure 8** and the zonal analysis indicate that the tissue is not uniformly damaged.

When studying the moderate-blast level, the sub-volumes showed similar deviation from the global average. A significant shift in the distributions was observed in Zones 1–3 in each region of focus in **Figure 9** ($p < 0.001$). However, the magnitude of influence on the surrounding tissue that each focal defect showed was in one case different to the rest (see the first region analyzed in **Figure 9**). Comparing Zones 1 and 3 ($p < 0.01$) and Zones 1 and 2 ($p < 0.05$) indicates local differences between Zone 1 and its immediate surroundings. This particular defect is perhaps more focal in nature to the others studied. There is not just a shift in the distribution, given the final region analyzed in **Figure 9** exhibits the largest difference in the medians (~25%). However, the tail was broadly composed of higher strained regions implying some subtle differences in strain or damage intensity. This zonal analysis is one way in which these regional effects on tissue mechanics can be quantified and analyzed.

This set of analysis implies no diffuse injury is present, but a localized event with a mild but significant effect on the neighboring tissue. Here, a focal zone (Zone 1 ~ 0.26-mm radius sphere) of blast injured tissue, indicated here by a region of high strains, can affect the surrounding region. This zone can modify the local strain distribution and shift it away from the global average, and even further away from the healthy conditions (referring to **Figure 7**). In real terms, this equates to a small region ~0.1 mm^3 (Zone 1) that may be obviously damaged by the blast, potentially compromising a region 10 times that size in terms of the mechanics. The fact this is not observed throughout the specimen nor affecting the greater surrounding region of this lung volume (100% or full volume) supports the fact that this is a moderate-blast condition and a non-lethal dose (Barnett-Vanes et al., 2016).

DISCUSSION

In this study, intact cadaveric rats were subjected to a range of blast exposures generated by a laboratory shock tube device. The specimens were preconditioned using a ventilator before and after blast to mitigate airway closure due to handling and inactivity. Lungs were excised ready for imaging and were ventilated between tomographic scans performed at DLS (I13-2 branch line). This allowed for the relative effects of any damage to be highlighted through use of DVC computation.

Studying the control (un-blasted) specimens, it was clear that the strain distributions were uniform for the most part in the air-filled regions. This experiment took advantage of the high-spatial

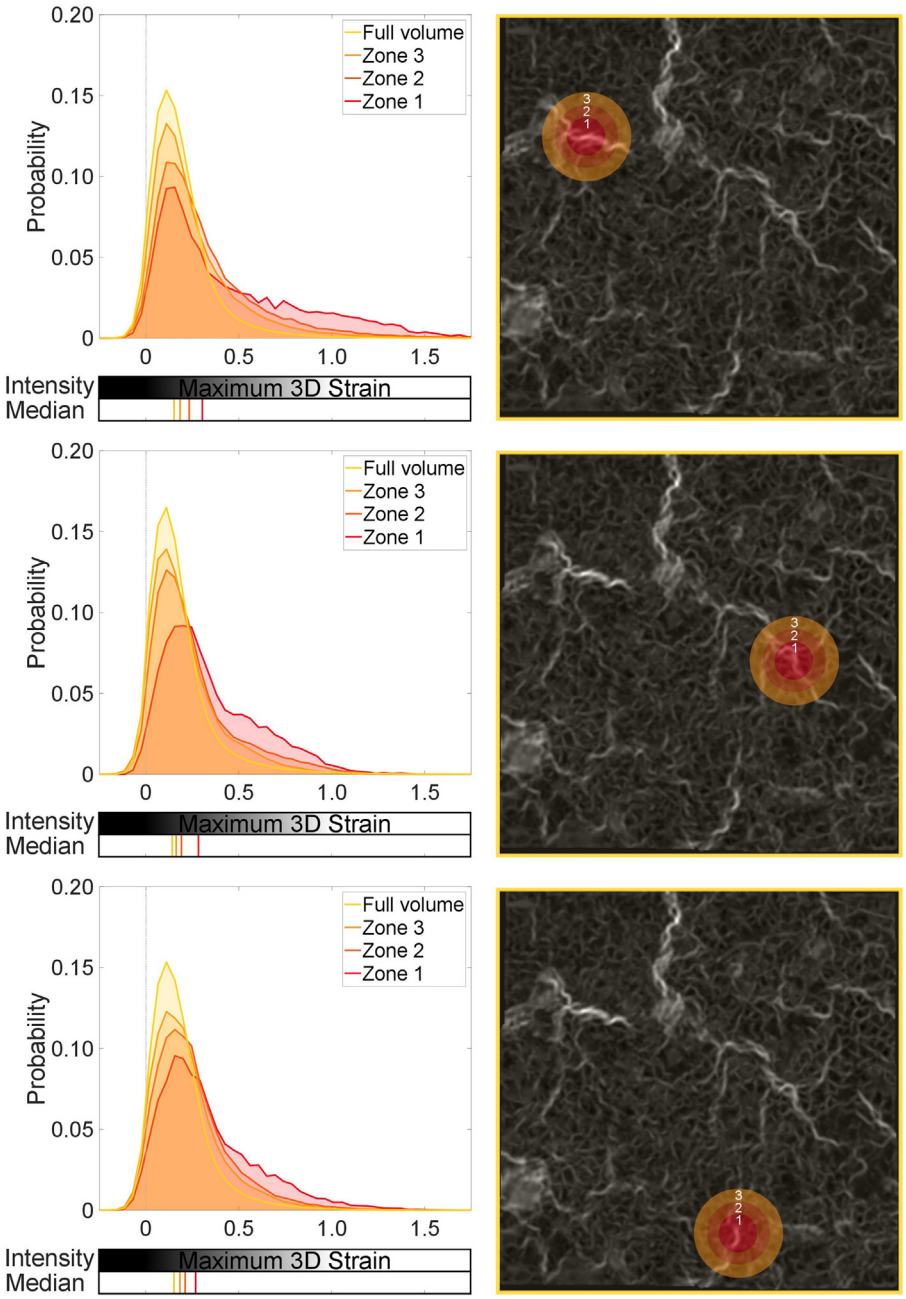

FIGURE 8 | Global and local strain distributions around a strain concentration: low-level blast. Three regions are selected, with sequential spherical shell volumes analyzed to show the effect of the local strain discontinuity on the surrounding tissue. Zone 1 is the central sphere focused on a given strain concentration. Zones 2 and 3 are shells leading from Zone 1. The median for each distribution is also plotted.

resolution and relatively large field of view when performing tomography imaging with synchrotron sources. A larger lung volume was imaged at much higher acquisition speeds, compared to that achievable with conventional micro-CT methods, and lobular regions of the parenchyma were identified and studied.

Digital volume correlation enabled the interactions not only of the alveoli to be visualized but also the bulk parenchyma, including interactions between lobular regions. On a local scale, **Figures 4** and **5** show the strains present in the microarchitecture. Here, the low levels of tension in the alveolar walls are visible. When expanding the field of view, interactions between lobes are also visible. **Figure 5** highlighted how these more macroscopic interactions occur during simulated respiration, recording lung microstructure at two instantaneous lung volumes. Ventilation of the airways is a heterogeneous process. For slow or normal respiration conditions, the expansion of airways overall is uniform. The pathways associated with the microarchitecture are asymmetrical, and each path may not see the same local flow

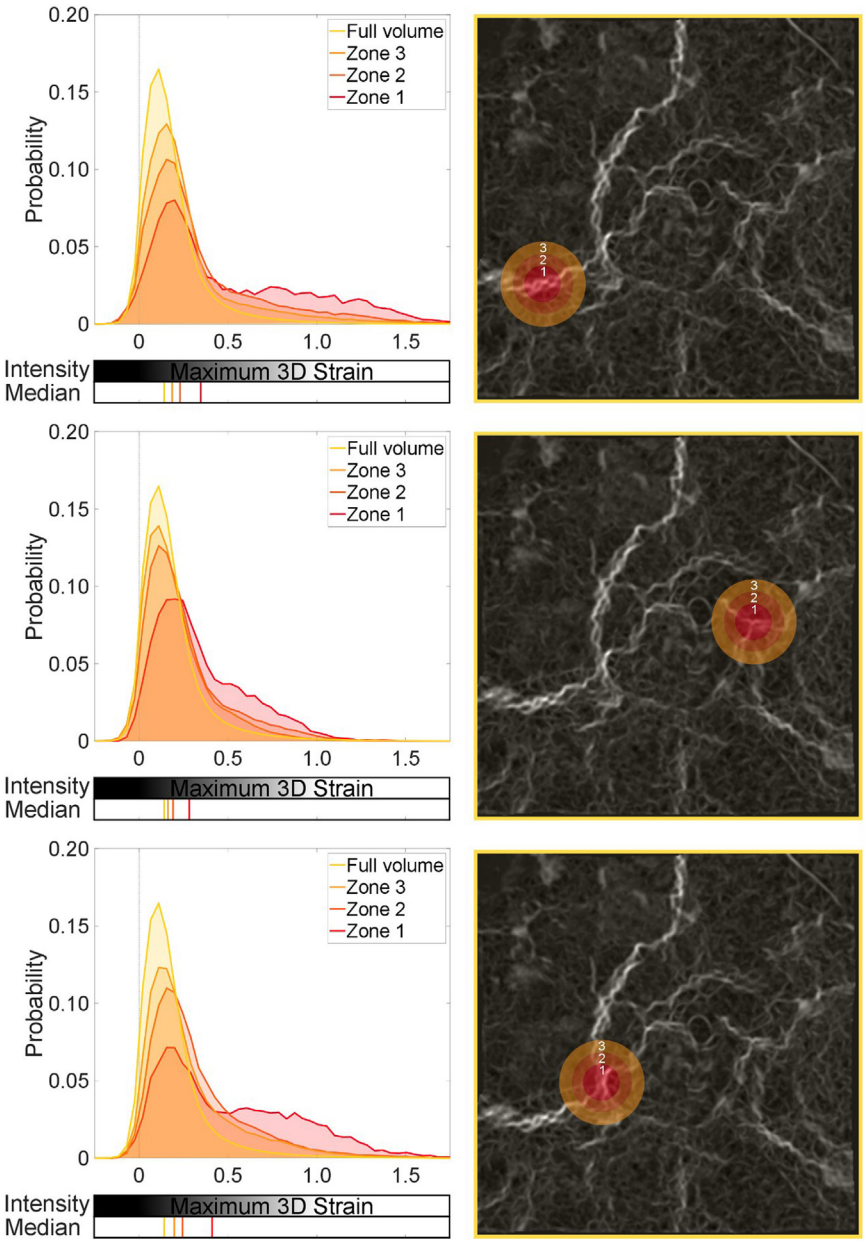

FIGURE 9 | Global and local strain distributions around a strain concentration: moderate-level blast. Three regions are selected, with sequential spherical shell volumes analyzed to show the effect of the local strain discontinuity on the surrounding tissue. Zone 1 is the central sphere focused on a given strain concentration. Zones 2 and 3 are shells leading from Zone 1. The median for each distribution is also plotted.

characteristics at a given instant. Therefore, it is very interesting to extract this level of detail about not only the alveoli on the microscale but also the surrounding interaction of airway structures on a macroscale.

The idealized model of uniform inflation within a given acinus, or group of alveoli, was confirmed by these low-level strain maps. However, where the tissue microstructure has been grossly affected by trauma, there was considerable strain concentration and an expansion in distribution of strains within the global tissue. Applied blast pressures (**Figure 3**) were in or below the level of the reported thresholds for lung injury (CR Bass et al., 2008). Previous research on BLI suggested the moderate blast case is survivable with no observable structural damage (Barnett-Vanes et al., 2016).

When lung is subject to blast, a large and dynamic pressure change is forced through the tissues and within the various airway paths. Each path has its own differing parallel pathway resistance. This would cause inhomogeneous loading (possible damage) and subsequent inflation between nearby alveolar ducts/acini. There are multiple interlinking processes in terms of solid

and fluid mechanics, which are being studied here in terms of the tissue mechanics after blast. The strain differentials highlighted, although local, could cause problems in the long term, if not immediately disruptive.

This experiment aimed to explore beyond the visible damage and focus on the structural mechanics, studying the residual tissue mechanics of the lung via DVC. It was clear from **Figure 6** how the structural organization and accommodation of the tissue changed in response to the same ventilation cycle, since regions of the blast injured lungs for both the low and moderate cases were hyperstrained. Signs from both blast cases indicated that there had not been any diffuse level of major damage. Spatial analysis of the strain fields highlighted the local zone of influence that these focal defects (high strained regions) had on the surrounding tissue. This reflects the usual experience that these are survivable injuries, since local tissue mechanics did not affect the surroundings to a major extent.

The strain concentrations observed could stabilize and remain constant. Alternatively, due to fatigue, it may cause deleterious effects, and this focal injury may spread within the lung. It is difficult to quantify at this stage how this focal injury may progress, but this process is certainly a possibility. BLI has been reported to exhibit non-visible lung damage soon after blast but, over a period of 24–48 hours, it may progress toward a critical and life-threatening injury (Scott et al., 2017). Potentially the augmentation of structural mechanics reported here plays a role in the degradation of the tissue, alongside the resulting physiological consequences.

CONCLUSION

This study has initiated a new fine resolution way to assess focal injury and novel methods for quantifying alveolar interdependency. Synchrotron tomography imaging was performed on blast injured lung tissue, and DVC was performed for the first time on these types of specimens. New insight on the subsequent effect of blast trauma on tissue mechanics at a microlevel was presented.

Three-dimensional strain maps within the lungs were analyzed to highlight alveolar interactions and how they differ in health and injury. The zone of influence of focal sites of hyperstraining tissue was quantified for blast loaded lung tissue. The effect of non-instantly fatal blast waves was explored and showed that the mechanical behavior of the lung has been significantly distorted in these cases. In the clinical context of BLI, this information provides new possible explanations as to why people may present delayed extreme symptoms of lung injury (combined with the known inflammatory pathway) or suffer exacerbated injury during treatment (mechanical ventilation).

This study was successful, and the data support the applicability of the technique to explore more blast conditions to further characterize the nature of BLI and identify potentially higher risk diffuse injury processes *via* this novel applied powerful imaging and image analysis method.

ETHICS STATEMENT

This study was performed on cadaveric tissue and is therefore exempt from approval required for *in vivo* experiments. However, all procedures were still approved by the Imperial College London ethical review process and strictly conformed to the Animals (Scientific Procedures) Act 1986 UK Home Office guidelines, which also fulfill the US NIH Guide for the Care and Use of Laboratory Animals.

AUTHOR CONTRIBUTIONS

Conception of study: HA. Beam time application: RS, AB, AK, and HA. Shock loading development: T-TN, KV, and HA. Ventilation system development: JS, DO, KV, and HA. Image acquisition: AB, IM, AK, T-TN, KV, and HA. Image processing: DH, RS, PH, AN, and HA. Data analysis; reviewing and editing the manuscript: all authors. Writing the manuscript: HA.

ACKNOWLEDGMENTS

The authors would like to thank Diamond Light Source for beamtime at I13-2 under proposal MT12864 and time at its associated data beamline (Bodey and Rau, 2016).

FUNDING

This work was conducted under the auspices of the Royal British Legion Centre for Blast Injury Studies at Imperial College London. The authors would like to acknowledge the financial support of the Royal British Legion. The authors would also like to acknowledge the Royal Society for their financial support of the image analysis portion of the study through their Research Grant Scheme.

REFERENCES

Andrikakou, P., Vikraman, K., and Arora, H. (2016). On the behaviour of lung tissue under tension and compression. *Sci. Rep.* 6, 36642. doi:10.1038/srep36642

Atwood, R. C., Bodey, A. J., Price, S. W. T., Basham, M., and Drakopoulos, M. (2015). A high-throughput system for high-quality tomographic reconstruction of large datasets at Diamond Light Source. *Phil. Trans. R. Soc. A* 373. doi:10.1098/rsta.2014.0398

Barnett-Vanes, A., Sharrock, A., Eftaxiopoulou, T., Arora, H., Macdonald, W., Bull, A. M. J., et al. (2016). CD43Lo classical monocytes participate in the cellular immune response to isolated primary blast lung injury. *J. Trauma Acute Care Surg.* 81, 500–511. doi:10.1097/TA.0000000000001116

Basham, M., Filik, J., Wharmby, M. T., Chang, P. C. Y., El Kassaby, B., Gerring, M., et al. (2015). Data Analysis WorkbeNch (DAWN). *J. Synchrotron Radiat.* 22, 853–858. doi:10.1107/S1600577515002283

Bay, B. K., Smith, T. S., Fyhrie, D. P., and Saad, M. (1999). Digital volume correlation: three-dimensional strain mapping using x-ray tomography. *Exp. Mech.* 39, 217–226. doi:10.1007/BF02323555

Black, L., Brewer, K. K., Morris, S. M., Schreiber, B. M., Toselli, P., Nugent, M. A., et al. (2005). Effects of elastase on the mechanical and failure properties of engineered elastin-rich matrices. *J. Appl. Physiol. (1985)* 98, 1434–1441. doi:10.1152/japplphysiol.00921.2004

Bodey, A. J., and Rau, C. (2016). Launch of the I13-2 data beamline at the Diamond Light Source synchrotron. *J. Phys. Conf. Ser.* 849. doi:10.1088/1742-6596/849/1/012038

CR Bass, K. A., Rafaels, K. A., and Salzar, R. S. (2008). Pulmonary injury risk assessment for short-duration blasts. *J. Trauma* 65, 604–615. doi:10.1097/TA.0b013e3181454ab4

Denny, E., and Schroter, R. C. (2006). A model of non-uniform lung parenchyma distortion. *J. Biomech.* 39, 652–663. doi:10.1016/j.jbiomech.2005.01.010

Eftaxiopoulou, T., Barnett-Vanes, A., Arora, H., Macdonald, W., Nguyen, T.-T. N., Sharrock, A. E., et al. (2015). Prolonged but not short-duration blast waves elicit acute inflammation in a rodent model of primary blast limb trauma. *Injury* 47, 625–632. doi:10.1016/j.injury.2016.01.017

Garner, J., Watts, S., Parry, C., Bird, J., Cooper, G., and Kirkman, E. (2010). Prolonged permissive hypotensive resuscitation is associated with poor outcome in primary blast injury with controlled hemorrhage. *Ann. Surg.* 251, 1131–1139. doi:10.1097/SLA.0b013e3181e00fcb

Gillard, F., Boardman, R., Mavrogordato, M., Hollis, D., Sinclair, I., Pierron, F., et al. (2014). The application of digital volume correlation (DVC) to study the microstructural behaviour of trabecular bone during compression. *J. Mech. Behav. Biomed. Mater.* 29, 480–499. doi:10.1016/j.jmbbm.2013.09.014

Hoppin, F. G. Jr., Lee, G. C., and Dawson, S. V. (1975). Properties of lung parenchyma in distortion. *J. Appl. Physiol. (1985)* 39, 742–751.

Kohsuke, H., Manabu, K., Hiroki, M., Shunichi, S., Hiromi, M., Shinji, T., et al. (2016). Fibrinogen γ-chain peptide-coated adenosine 5' diphosphate-encapsulated liposomes rescue mice from lethal blast lung injury via adenosine signaling. *Crit. Care Med.* 44, 827–837. doi:10.1097/CCM.0000000000001707

Matsuda, M., Fung, Y. C., and Sobin, S. S. (1987). Collagen and elastin fibers in human pulmonary alveolar mouths and ducts. *J. Appl. Physiol. (1985)* 63, 1185–1194.

Mercer, R. R., Russell, M. L., and Crapo, J. D. (1994). Alveolar septal structure in different species. *J. Appl. Physiol. (1985)* 77, 1060–1066.

Nguyen, T.-T. N. (2016). *The Characterisation of a Shock Tube System for Blast Injury Studies*. Doctoral Thesis, United Kingdom: Imperial College London.

Nguyen, T.-T. N., Wilgeroth, J. M., and Proud, W. G. (2014). Controlling blast wave generation in a shock tube for biological applications. *J. Phys. Conf. Ser.* 500, 142025. doi:10.1088/1742-6596/500/14/142025

Palanca, M., Tozzi, G., Cristofolini, L., Viceconti, M., and Dall'Ara, E. (2015). 3D local measurements of bone strain and displacement: comparison of three digital volume correlation approaches. *J. Biomech. Eng.* 137, 1–14. doi:10.1115/1.4030174

Roberts, B. C., Perilli, E., and Reynolds, K. J. (2014). Application of the digital volume correlation technique for the measurement of displacement and strain fields in bone: a literature review. *J. Biomech.* 47, 923–934. doi:10.1016/j.jbiomech.2014.01.001

Schreier, H., Orteu, J.-J., and Sutton, M. A. (2009). *Image Correlation for Shape, Motion and Deformation Measurements: Basic Concepts, Theory and Applications*. Springer.

Scott, T. E. (2016). *Primary Blast Lung Injury, Blast Injury Science and Engineering, a Guide for Clinicians and Researchers*. Birmingham: Springer.

Scott, T. E., Kirkman, E., Haque, M., Gibb, I. E., Mahony, P., and Hardman, J. G. (2017). Primary blast lung injury – a review. *Br. J. Anaesth.* 118, 311–316. doi:10.1093/bja/aew385

Sera, T., Fujioka, H., Yokota, H., Makinouchi, A., Himeno, R., Schroter, R. C., et al. (2004). Localized compliance of small airways in excised rat lungs using microfocal X-ray computed tomography. *J. Appl. Physiol. (1985)* 96, 1665–1673. doi:10.1152/japplphysiol.00624.2003

Suki, B., Ito, S., Stamenovic, D., Lutchen, K. R., and Ingenito, E. P. (2005). Biomechanics of the lung parenchyma: critical roles of collagen and mechanical forces. *J. Appl. Physiol. (1985)* 98, 1892–1899. doi:10.1152/japplphysiol.01087.2004

Titarenko, V. (2016). Analytical formula for two-dimensional ring artefact suppression. *J. Synchrotron Radiat.* 23, 1447–1461. doi:10.1107/S160057751601479X

Yuan, H., Ingenito, E. P., and Suki, B. (1997). Dynamic properties of lung parenchyma: mechanical contributions of fiber network and interstitial cells. *J. Appl. Physiol. (1985)* 83, 1420–1431.

Conflict of Interest Statement: The authors declare that the research was conducted in the absence of any commercial or financial relationships that could be construed as a potential conflict of interest.

frontiers in Materials

ORIGINAL RESEARCH
published: 29 November 2017
doi: 10.3389/fmats.2017.00040

Combining Ultrasound Pulse-Echo and Transmission Computed Tomography for Quantitative Imaging the Cortical Shell of Long-Bone Replicas

*Matthew P. Shortell[1], Marwan A. M. Althomali[1,2], Marie-Luise Wille[1] and Christian M. Langton[1,3]**

[1] Science and Engineering Faculty, Institute of Health and Biomedical Innovation, Queensland University of Technology, Brisbane, QLD, Australia, [2] University College in Al-Jamoum, Umm Al-Qura University, Mecca, Saudi Arabia, [3] Laboratory of Ultrasonic Electronics, Doshisha University, Kyotanabe, Japan

OPEN ACCESS

Edited by:
Gianluca Tozzi, University of Portsmouth, United Kingdom

Reviewed by:
Pasquale Vena, Politecnico di Milano, Italy
Marco Miniaci, UMR6294 Laboratoire Ondes et Milieux Complexes (LOMC), France

***Correspondence:**
Christian M. Langton
christian.langton@qut.edu.au

Specialty section:
This article was submitted to Mechanics of Materials, a section of the journal Frontiers in Materials

Received: *24 August 2017*
Accepted: *09 November 2017*
Published: *29 November 2017*

Citation:
Shortell MP, Althomali MAM, Wille M-L and Langton CM (2017) Combining Ultrasound Pulse-Echo and Transmission Computed Tomography for Quantitative Imaging the Cortical Shell of Long-Bone Replicas. Front. Mater. 4:40. doi: 10.3389/fmats.2017.00040

We demonstrate a simple technique for quantitative ultrasound imaging of the cortical shell of long-bone replicas. Traditional ultrasound computed tomography instruments use the transmitted or reflected waves for separate reconstructions but suffer from strong refraction artifacts in highly heterogeneous samples such as bones in soft tissue. The technique described here simplifies the long bone to a two-component composite and uses both the transmitted and reflected waves for reconstructions, allowing the speed of sound and thickness of the cortical shell to be calculated accurately. The technique is simple to implement, computationally inexpensive, and sample positioning errors are minimal.

Keywords: ultrasound, computed tomography, long bones, bone thickness, bone velocity

INTRODUCTION

X-ray-based modalities are currently used as the primary method to determine bone health (Genant et al., 1996; Barkmann and Glüer, 2011). Unfortunately, they are far from perfect at predicting the mechanical properties and regular testing of patients cannot be performed due to limits on X-ray exposure levels. Over the past three decades, quantitative ultrasound methods have been heavily investigated for quantifying bone health due to the inherent relationship between ultrasound waves and mechanical properties of materials (Langton et al., 1984; Laugier and Haïat, 2011; Raum et al., 2014).

One of the earliest demonstrations of a portable clinical quantitative ultrasound system to determine bone ultrasound properties was the CUBA system (Langton et al., 1990) which measured the broadband ultrasound attenuation (BUA) and speed of sound (SOS) through ultrasound transmission measurements. However, for long bones, most recent efforts have focused on single-sided pulse-echo techniques to determine the cortical shell thickness and SOS (Foldes et al., 1995; Sievänen et al., 2001; Chen et al., 2004). These instruments require a highly trained operator to make decisions on how and where to place the transducers on the skin, making them inherently operator dependent. A computed tomography (CT)-based quantitative ultrasound approach for

long bones would not require a highly trained operator, would be highly repeatable, and provide 3D detailed spatial information to the clinician as well.

There has been a plethora of research into quantitative ultrasound computed tomography (UCT) for soft tissues for applications such as detecting cancer risk in breast tissue (André et al., 2013). In these soft tissues, refraction artifacts have a small but significant effect on reconstructed images. Several image reconstruction methods have been developed to overcome this small perturbation from the straight ray approximation. Unfortunately, using these techniques in highly heterogeneous media such as bone in soft tissue is not possible (Lasaygues et al., 2010).

Typically, there are two types of UCT techniques: transmission UCT (T-UCT) and pulse-echo UCT (PE-UCT). T-UCT uses a similar principle to traditional X-ray CT by measuring the ultrasound pulse transmitted through the sample at different rotation angles and translational positions. In soft tissue, this can produce accurate high-resolution quantitative maps of BUA and SOS in the tissue. In samples containing bone, the images are not quantitative and produce a blurry image of the bone; the cortical thickness cannot be accurately measured.

Pulse-echo UCT methods are usually defined as non-quantitative; they usually cannot provide a SOS map of the bone. They can produce high-resolution images of the outer bone surface. To determine the structure of the inner cortical shell surface, a bone SOS value based on previous *ex vivo* ultrasound transmission measurements of a population is used. Since bone SOS is an indicator of bone health as well as cortical shell thickness, the reconstruction of the shell inner surface is unreliable using this technique.

The Lasaygues group has led the way in extending UCT to allow quantitative imaging of the long-bone cortical shell with two main methods developed. Compound Quantitative Ultrasonic Tomography (CQUT) is an iterative experimental method that compensates for refraction by adjusting the transmitting and receiving transducer locations and angles to sample the equivalent straight path through the bone (Lasaygues, 2007). Distorted Born Diffraction Tomography (DBDT) uses a single set of experiments but performs iterative simulations of the sample (Lasaygues et al., 2006). Although both CQUT and DBDT have resulted in good quantitative images of the cortical shell, they require either multiple experiments and heavy data processing requirements (CQUT) or are very computationally time expensive (DBDT). A fast and simple technique for quantitative UCT of long bones to output the key clinically relevant metrics has not been developed yet.

Here, we demonstrate a simple and fast UCT technique (PE-T-UCT) to extract an average bone SOS and a mean cortical shell thickness. The useful data in T-UCT are combined with the reconstructed PE image using a two-component model of the cortical shell. We then used this averaged SOS to accurately reconstruct each PE image, avoiding the use of a population averaged SOS.

THEORY

Measuring bone SOS and cortical shell thickness using transmitted and reflected pulses has been proposed by Zheng and Lasaygues (2013) using single-element transducers at a single angle. It is extended here using reconstructed PE-UCT and T-UCT data instead of the raw echo data. We also use multi-element transducers so that positioning errors are minimal and a better sample average is obtained. For a simple two-component model of cortical bone, the SOS in the bone cortical shell (v_b) is assumed to be a constant and all other volumes are assumed to have the SOS in water (v_w = 1,483 m/s). The apparent delay time (Δt) of an ultrasound wave travelling through the bone is measured directly in T-UCT. It is calculated as the time taken for the ultrasound wave to pass through the sample minus the time through a reference measurement (water only). It is related to v_b by

$$\Delta t = d\left(\frac{1}{v_b} - \frac{1}{v_w}\right). \tag{1}$$

Here, d is not the bone diameter, but rather the total length of bone that the ultrasound wave propagates through to be detected at the receiving transducer. If we only consider propagation through the middle of the bone, then d is given by the addition of the bone shell thickness on both sides (T_1, T_2) that the wave propagates through

$$d = T_1 + T_2 = (t_1 + t_2)v_b, \tag{2}$$

where t_1 and t_2 are the time taken for the wave to propagate through the first and second sides of the bone shell, respectively. These equations can be solved to find the SOS in bone as

$$v_b = v_w \frac{t_1 + t_2 - \Delta t}{t_1 + t_2}. \tag{3}$$

Although t_1 and t_2 can be measured directly in a PE sonogram, it is more intuitive to use the reconstructed PE-UCT image. This is particularly important in complex samples where different transducer positions are required to resolve the inner and outer interfaces. In the PE-UCT reconstruction, the SOS is assumed to be v_w everywhere, causing the shell thickness to appear thinner in a PE-UCT image. This reduced thickness (T_1' or T_2') can be converted back into a shell propagation time using

$$t = \frac{T'}{v_w}. \tag{4}$$

Combining Equations (3) and (4) allows the calculation of v_b for various angles of sample rotation. The true cortical shell thickness uses the calculated v_b values along with the measured apparent thickness values to calculate the corrected thickness values:

$$T = T'\frac{v_b}{v_w}. \tag{5}$$

EXPERIMENTAL METHODS

Data Acquisition

The samples were scanned using a lab-built UCT system (Althomali et al., 2017a,b). Two 2.25-MHz 128-element linear phased-array transducers (Olympus, Corporation, Shinjuku,

Tokyo, Japan) were used with an element width of 0.75 mm (*xy*-plane) and height of 12 mm (*z*-axis). The total transducer width was therefore $128 \times 0.75 = 96$ mm. One transducer acted as a transmitter and receiver (for PE-UCT), and the other as a receiver only (for T-UCT). They were coaxially aligned in a fixture 137 mm apart and immersed in a water tank with the sample placed roughly in the center between the two transducers. To obtain a 360° ultrasound scan (in 1° steps), the phased-array transducers were rotated around the *z*-axis using a user-programmed Motoman HP6 robotic arm (YASKAWA Electric Corporation, Japan). Each transducer was connected to an Omniscan MX device (Olympus, Corporation, Shinjuku, Tokyo, Japan), and controlled by the Olympus TomoView software (version 2.7, Olympus, Corporation, Shinjuku, Tokyo, Japan), to emit and receive the ultrasound signals. **Figure 1** shows a schematic representation of the UCT system.

TomoView was used to set all signal acquisition parameters as well as the beam profile. The transmitting transducer was set to fire five neighboring elements at a time (equivalent emitter size of 3.75 mm). These set of five elements were incremented by one for successive scans to give a total of 124 measurements per rotation angle per transducer. The transmitting transducer received data only on the central firing element. The receive-only transducer was set to receive on the same element number directly opposite. Ideally, this results in both transducers only sampling 124 straight paths perpendicular to the transducers. The electronic gain on each transducer was set dynamically depending on the sample to minimize saturation but still resolve all the sample features. The digitization frequency was 25 MHz and the pulse length was 300 ns.

Samples

A simple hollow cylinder structure was studied first to demonstrate the PE-T-UCT concept. Two hollow Perspex cylinders were used with outer diameters of 25 and 35 mm and labeled as P25 and P35, respectively. The holes were drilled as close as possible to the center and the thickness of the shell was approximately 7.5 mm. Although these do not represent real bones, they are simple test cases for demonstrating the PE-T-UCT concept and they have no variation in the *z*-direction, and hence there are minimal slice averaging effects.

To demonstrate the concept with long bone like shapes, a plastic femur bone from 3B Scientific was used. Three plastic-bone segments each approximately 30 mm long were cut. Holes were drilled through the center of each segment and allowed to fill with water in UCT experiments to mimic the medullary cavity. One sample (PB1) was taken from the Metaphysis and two (PB2 and PB3) were taken from the Diaphysis. **Figure 2** shows a photograph of the samples.

PE-UCT Reconstructions and Reduced Thickness Calculations

Pulse-echo UCT reconstructions were performed using the fully rectified data collected from the transmitting transducer. Time

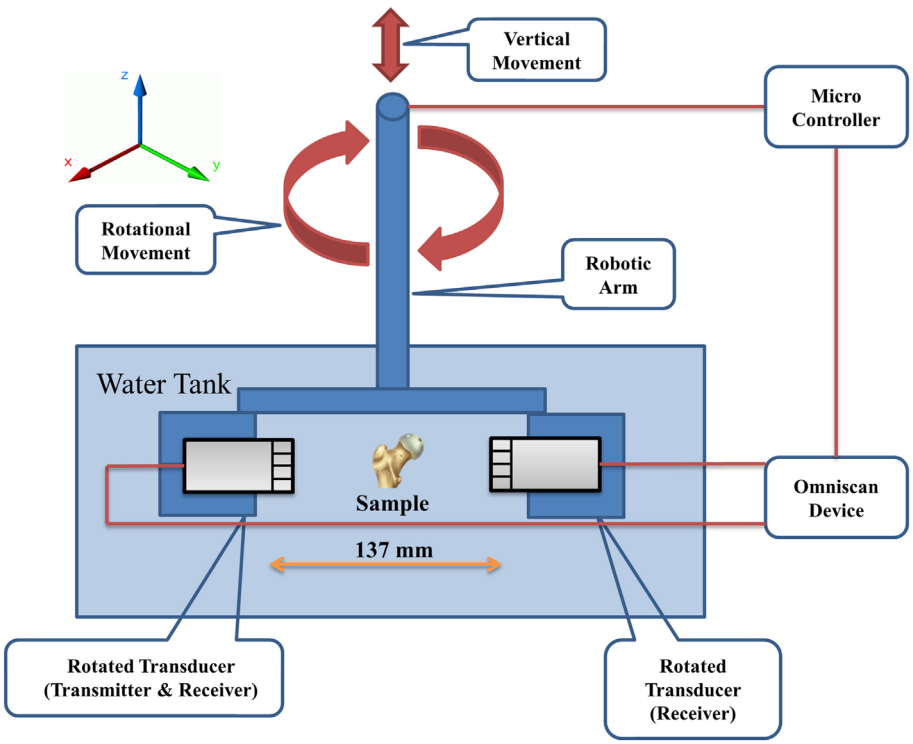

FIGURE 1 | Schematic representation of the UCT system. The robotic arm is used to position the transducers such that the sample is approximately centered between the transducers in the *xy*-plane and positioned at the correct *z*-position for imaging. The robotic arm also rotates the transducers during acquisition. UCT, ultrasound computed tomography.

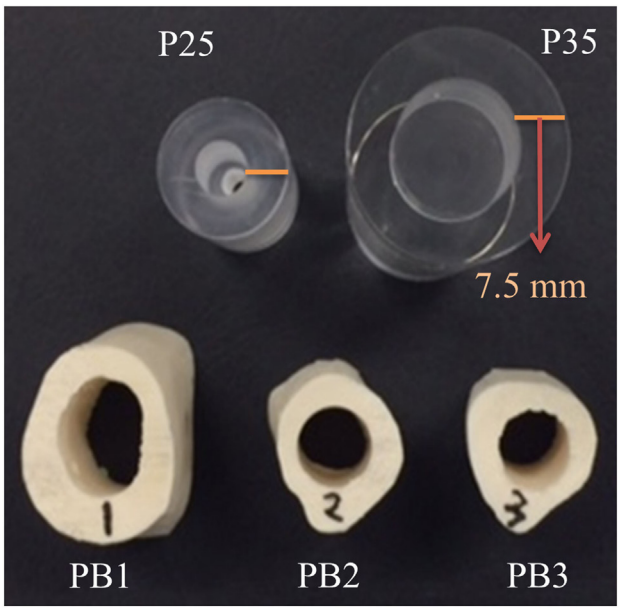

FIGURE 2 | Photograph of the Perspex cylinder samples: P25 and P35 with 25 and 35 mm diameters, respectively, and the plastic-bone samples: PB1, PB2, and PB3.

since transducer firing (τ) was converted into a distance perpendicular to the emitting transducer (y') using

$$y' = v_w \tau / 2. \quad (6)$$

Using the element position on the transducer (x') and the rotation angle, the location that the signal originated from can be calculated in the stationary frame (x, y). Each signal from a total of $124 \times 360 = 44{,}640$ scans were then binned onto a common xy grid (square pixel size of 0.375 mm) and summed.

ImageJ was used to remove reconstructed interfaces originating from reflections from the sample interfaces on the far side of the sample. These reflections appear much closer to the center of the samples due to the higher velocity experienced through the first side of the sample. They are easily identified by reconstructing only the first half of the data to give a one-sided view of the sample. For the Perspex samples, the inner and outer interfaces were identified using the "findpeaks" function in MATLAB (release 2016b, The MathWorks, Inc., Natick, MA, USA) in a fully automated fashion. For the plastic-bone samples, identification of the interfaces was required by manually drawing a polygon of the inner and outer interfaces over the reconstructed images and thresholding. The apparent shell thickness (T_1' or T_2') as a function of rotation angle (θ) was found by rotating the image by θ, finding the center of the bone on the x'-axis and taking the average thickness along the y'-direction over a width of 1.875 mm. Samples were taken over 360° in 1° steps to compare with the transmission data.

Calculating Apparent Delay Time from Transmission Data

The apparent delay time for each element at each θ is found as the difference in time of arrival (using the maximum of the fully rectified data) of the ultrasound pulse at the receiver compared with when there is no sample present (water only). For samples with an SOS higher than water, this results in a negative Δt if the path length of the received sample is equal to the path length in water. For each θ, only Δt that satisfy $-20 < \Delta t < -0.5$ µs are used. These bounds were chosen to remove physically unrealistic data that can occur when the signal strength is below the noise level. If there are no elements for an angle that satisfy these criteria, the angle is not used for further calculations and the corresponding T_1' and T_2' calculated earlier are also removed from further calculations. From the allowed Δt values, the middle (spatially along the transducer) third elements are used to calculate a mean value of Δt for each allowable angle.

SOS and Thickness Calculations

The set of calculated Δt, T_1' and T_2' values are then used to calculate a set of v_b values using Equations (3) and (4). If any of the v_b values are outside the bounds of $1{,}500 < v_b < 5{,}000$ m/s then they are excluded along with the corresponding T_2' and T_2' values. From these allowed v_b, T_1' and T_2' values, the corrected thickness values are then calculated from Equation (5). Average values of the bone SOS ($\overline{v}_b$) and shell thickness ($\overline{T}$) are then calculated. For visualization of the cortical shell in the PE-T-UCT image, $\overline{v}_b$ is used to reconstruct the inner interface of the cortical shell along with the existing outer shell from the PE-UCT reconstruction.

Reference Measurements

Speed of sound measurements of the bulk materials were taken with the same experimental apparatus except the transducers remained stationary. For Perspex SOS measurements, a large rectangular Perspex prism was positioned with its largest faces parallel to the transducers; the path length was 24 mm. For plastic bone, an 8 mm thick slice of the femur was cut and positioned with the cut sides parallel to the transducers. In both materials, an average Δt was taken over the middle half of the samples and the $\overline{v}_b$ was calculated using Equation 1.

To determine the actual shell thickness of the samples, optical images of the samples in the xy-plane from one side were taken using a desktop optical scanner. Thresholding in ImageJ was used to produce binary images of the sample cross-sections for comparison with UCT images and to calculate the average cortical shell thickness. For plastic bone 1, the side closest to the middle of the shaft was used. For the plastic-bone samples, there are slight changes in morphology across the length of the cut samples so the images and derived shell thickness are not as accurate as the Perspex samples.

T-UCT Bulk Attenuation Map Reconstruction

Bulk attenuation (β) maps were reconstructed from the fully rectified transmission data using MATLAB. The ultrasound pulse amplitude through the sample (I_s) for each element and angle is compared with the amplitude through water alone (I_0) to calculate β using

$$\beta = -20 \log\left(I_s / I_0 \right). \quad (7)$$

This produces a 124 × 360 element matrix representing the 124-transducer element locations in the rotating frame and 360 rotations. A 5-point image median filter was then applied to reduce the noise level using the "med2filt" function. Image reconstruction was then performed using the inverse radon transformation ("iradon" function) with linear interpolation and Ram-Lak filter. Finally, a 33% threshold was applied to the reconstructed image for clarity. Reconstructions using the metrics of BUA and SOS were also attempted. Unfortunately, the data were too noisy for BUA calculations and the SOS reconstruction was nonsensical in most samples.

RESULTS AND DISCUSSION

Strong refraction and reflection in the transition of ultrasound waves between soft tissue and bone have a detrimental effect in T-UCT. **Figure 3** shows the received ultrasound signal across the elements after propagating through the 35 mm hollow Perspex cylinder. Since the SOS in Perspex is higher than water, there should be a negative time delay seen at the receiving transducers in the absence of refraction. Through the center of the cylinder where the curvature is at a minimum this does occur and the delay time would be correctly calculated for image reconstruction. As we look further from the center, the delay time increases toward zero even though the bone projection should appear thicker away from the center. This is due to refraction; the path length is increasing and offsetting the higher SOS in the Perspex. Far from the center, there is a positive delay time due to the very high reflection of most the incident plane wave. The only part of the wave that is detected by the receiving transducer element has gone through such large refraction angles that the path length has increased greatly. This phenomenon makes it impossible to reconstruct high-resolution qualitative (let alone quantitative) reconstructions of bone in T-UCT without using more complicated methods (Lasaygues et al., 2010).

Figure 4 shows cross-sections of the samples studied and reconstructed UCT images. The PE-UCT images generally represent the outside of the samples quite well except for PB1 where the overall size looks the same but the surface shape looks different. This could be because we probed the middle of the sample in UCT but used the end of the sample for reference images. For the other samples, this is not as much a problem since their morphology does not change drastically over the sample height like PB1. The T-UCT images give a blurred image of the sample cross-sections. In general, the size appears contracted but also broadened resulting in smaller and denser images. The PE-T-UCT reconstructions improved the inner surface of the PE-UCT images greatly. This is most noticeable in PB2 and PB3 samples where the hole has almost returned to being perfectly circular.

To gain a quantitative understanding of how well the UCT system performed, **Table 1** shows the calculated bone outer diameter, SOS, and bone thickness, as well as the reference measurements values. First, we calculate the average sample outer diameter ($\bar{D}$) to see how well the PE-UCT system is working. The PE-UCT system performed quite well considering it is a lab-built system. The diameters measured for P25 and P35 suggest that there may be a slight center of rotation offset error in the system as they both have a positive error value. These values suggest that the best accuracy of the PE-UCT system is approximately 0.5 mm for measuring the bone diameter. Although this is a large value compared with the thickness of the samples, this error will have little effect on the bone thickness measurement and SOS since the same offset will apply to the inner diameter of the bone. In the P25 and P35 samples, the samples have a perfectly circular cross-section, and therefore the SD (σ) in the actual diameters is near 0. Therefore, the PE-UCT SD in P25 and P35 samples (~0.2 mm) indicates the precision of the PE-UCT system.

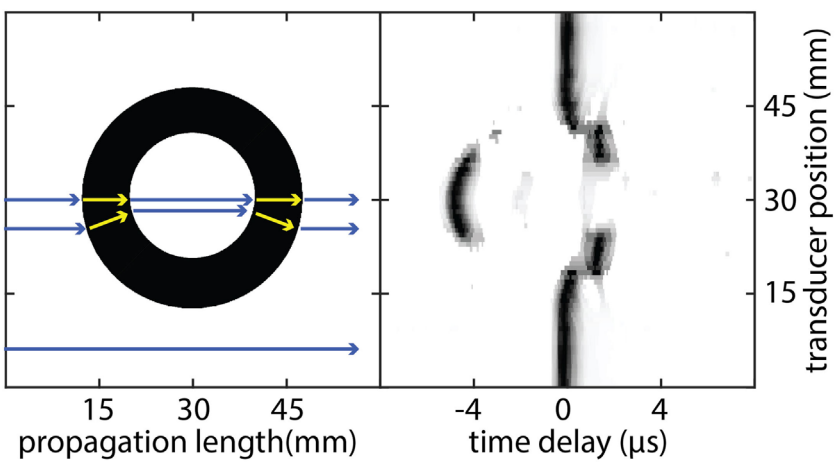

FIGURE 3 | Schematic representation of ultrasound propagation through a hollow 35 mm diameter Perspex cylinder (left) and the resulting ultrasound signal amplitude detected at the receiving transducer as a function of time (right). As each wave propagates from the transmitting transducer, it experiences different propagation speeds when it travels through different media. Each wave can also experience different path lengths if there is significant refraction occurring. The combination of both effects results in a time delay registered at the receiving transducer compared with propagation through water alone. Each transducer element signal is normalized to the maximum value separately for clarity.

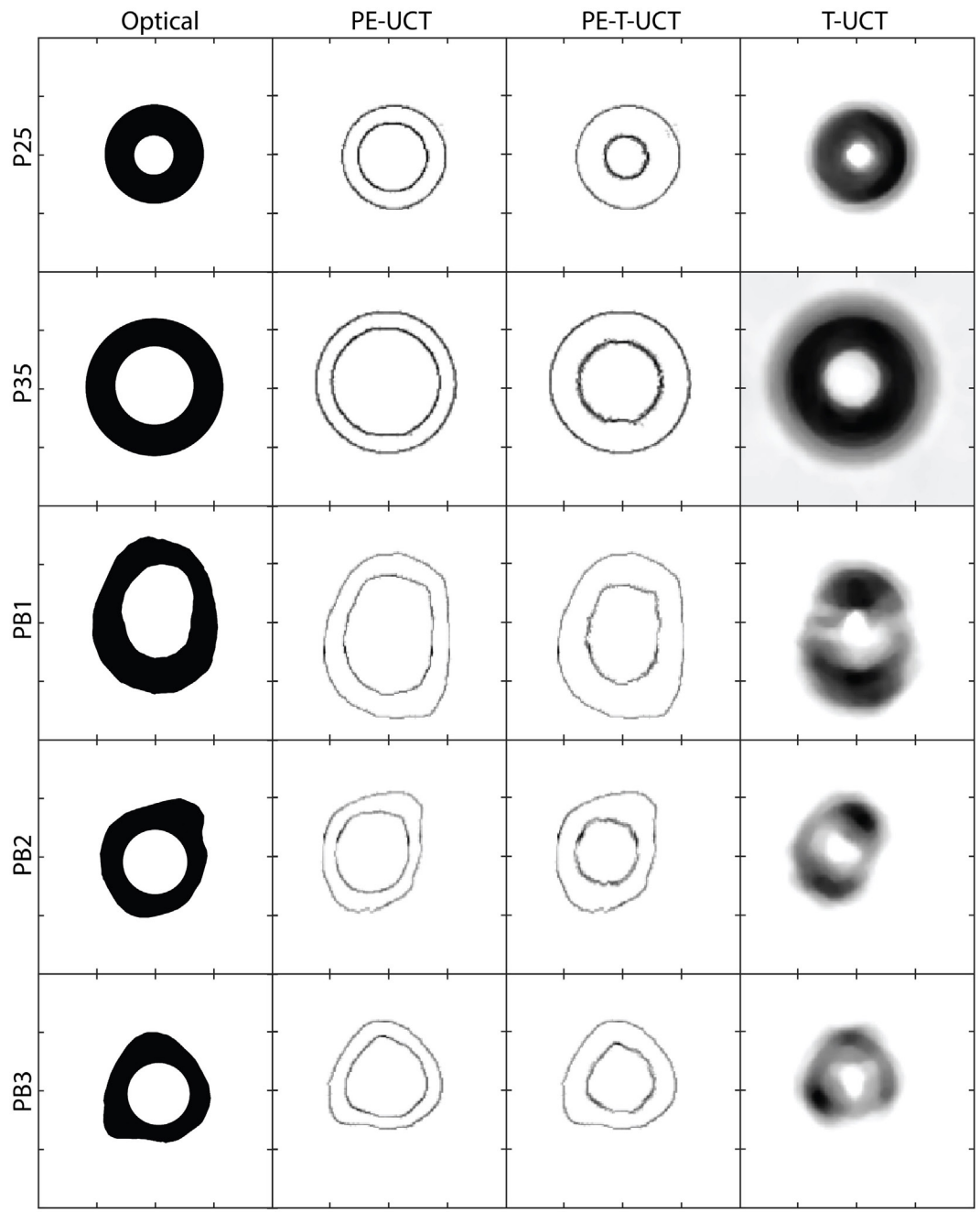

FIGURE 4 | From left to right: the sample dimensions from optical micrographs, PE-UCT reconstructions, PE-T-UCT reconstruction, and T-UCT reconstruction. From top to bottom: P25, P35, PB1, PB2, and PB3. The scale is the same for all images which are 60 mm × 60 mm in size and the tick marks are 15 mm apart. PE-UCT, pulse-echo ultrasound computed tomography; T-UCT, transmission ultrasound computed tomography.

The results for PB1-3 are, as expected, not as good as the ideal Perspex samples. This is in part due to the inaccuracy of the reference measurements, but also due to the increased noise in the rougher plastic-bone samples. Given the larger distribution of diameter sizes in the plastic bones, the largest error of less than 4% is still quite reasonable for a lab-built system.

The SOS measurements for the bulk materials compared with the mean SOS from PE-T-UCT reconstructions are shown next. The SOS is consistently slightly underestimated with a maximum error of <5%. The SD is not sufficiently high to suggest that it is a noise issue in the measurement technique. It is likely that the underestimation of the sample velocity is due to refraction in the samples causing, on average, a slightly longer path length and hence a slightly lower delay time in the transmission measurements.

Since both the Perspex and plastic-bone samples are made of a single homogeneous material, the SOS SD represents the

TABLE 1 | Tabulated results of the PE-UCT measured mean bone diameter and PE-T-UCT measured mean SOS and mean shell thickness.

	Bone diameter (mm)				SOS (m/s)			Shell thickness (mm)			
	Actual		PE-UCT		Actual	PE-T-UCT		Actual		PE-T-UCT	
	$\overline{D}$	σ	$\overline{D}$	σ	v_b	$\overline{v}_b$	σ	$\overline{T}$	σ	$\overline{T}$	σ
P25	25.44	0.01	26.21 +0.77	0.12 +0.11	2,740	2,640 −100	30	7.71	0.01	7.78 +0.07	0.08 +0.08
P35	35.33	0.01	35.61 +0.28	0.23 +0.22	2,740	2,710 −40	30	7.67	0.01	7.49 −0.18	0.14 +0.13
PB1	35.82	2.87	37.29 +1.47	3.83 +0.96	2,230	2,180 −50	60	7.61	0.49	7.90 +0.29	0.68 +0.19
PB2	28.84	1.87	27.84 −1.00	2.68 +0.81	2,230	2,170 −50	210	6.24	0.92	5.86 −0.38	0.94 +0.02
PB3	27.61	0.85	27.95 +0.33	0.79 −0.07	2,230	2,150 −70	80	5.93	0.47	5.55 −0.37	0.35 −0.12

Actual values refer to measurements from either optical micrographs or SOS measurements of bulk material. Bottom numbers in each cell are the measured values minus the reference values (if applicable). SD (σ) are also shown when appropriate.

PE-UCT, pulse-echo ultrasound computed tomography; SOS, speed of sound; PE-T-UCT, pulse-echo transmission ultrasound computed tomography.

precision of the method. For the simple Perspex samples the precision is very high at 30 m/s, while for the more complex bone samples it is closer to 100 m/s.

The average measured shell thickness is shown in **Table 1** with their SD for both optical micrograph and PE-T-UCT measurements. Despite the slight underestimation in SOS values from PE-T-UCT, there is no clear overestimation in the thickness values, although the sample size is limited. All the Perspex and plastic-bone samples are within 3 and 7% of the optical micrograph measurements, respectively. The Perspex samples have holes that are well centered, and hence the SD in the optical micrograph shell thickness is very small. The SD in the PE-T-UCT results suggests that the best possible precision for bone thickness is near 0.1 mm for the PE-T-UCT technique with the UCT setup used. The bone thickness varies considerably in the plastic-bone samples which is adequately represented in the PE-T-UCT results.

CONCLUSION AND FUTURE WORK

We have demonstrated a simple UCT method (PE-T-UCT) to measure the cortical shell thickness and the SOS in the cortical shell of long-bone replicas. Although it uses standard phased-array transducers, it can easily be implemented from standard B-scan ultrasound systems or from commercial UCT breast imaging systems using rotating phased-array transducers. The technique is computationally inexpensive and sample positioning errors are minimal since a trained operator is not required to position transducers.

This technique has several avenues for extension and improved accuracy. A more accurate estimate of the path length through the bone would help obtain more accurate SOS measurements. Given the simple two-component model considered, this could potentially be done through ray-tracing simulations to keep the post-processing time short. This would need to be an iterative procedure since the SOS in bone would be unknown. However, the number of iterations would be minimal given the start points are within 5% of the actual SOS and within 10% of the cortical shell thickness.

AUTHOR CONTRIBUTIONS

MS contributed to the design of the UCT system for PE-UCT and T-UCT, carried out the experiments, performed the data analysis, and wrote the manuscript. MA prepared all the samples and performed the experiments. M-L W wrote the manuscript. CL contributed to the design of the experiment and writing of the manuscript.

REFERENCES

Althomali, M. A., Wille, M.-L., Shortell, M. P., Epari, D. R., Koponen, J., Johnston, M., et al. (2017a). *Estimation of Mechanical Stiffness by Finite Element Analysis of Ultrasound Computed Tomography (UCT-FEA); A Comparison with Conventional FEA in Simplistic Structures*.

Althomali, M. A. M., Wille, M.-L., Shortell, M. P., and Langton, C. M. (2017b). *Estimation of Mechanical Stiffness by Finite Element Analysis of Ultrasound Computed Tomography (UCT-FEA); A Comparison with microCT Based FEA in Cancellous Bone Replica Models*.

André, M., Wiskin, J., and Borup, D. (2013). *Quantitative Ultrasound in Soft Tissues* (Dordrecht: Springer). doi:10.1007/978-94-007-6952-6

Barkmann, R., and Glüer, C.-C. (2011). "Clinical applications," in *Bone Quantitative Ultrasound*, eds P. Laugier and G. Haïat (Dordrecht: Springer Netherlands), 73–81.

Chen, T., Chen, P.-J., Fung, C.-S., Lin, C.-J., and Yao, W.-J. (2004). Quantitative assessment of osteoporosis from the tibia shaft by ultrasound techniques. *Med. Eng. Phys.* 26, 141–145. doi:10.1016/j.medengphy.2003.09.001

Foldes, A. J., Rimon, A., Keinan, D. D., and Popovtzer, M. M. (1995). Quantitative ultrasound of the tibia: a novel approach for assessment of bone status. *Bone* 17, 363–367. doi:10.1016/S8756-3282(95)00244-8

Genant, H. K., Engelke, K., Fuerst, T., Glüer, C.-C., Grampp, S., Harris, S. T., et al. (1996). Noninvasive assessment of bone mineral and structure: state of the art. *J. Bone Miner. Res.* 11, 707–730. doi:10.1002/jbmr.5650110602

Langton, C. M., Ali, A. V., Riggs, C. M., Evans, G. P., and Bonfield, W. (1990). A contact method for the assessment of ultrasonic velocity and broadband attenuation in cortical and cancellous bone. *Clin. Phys. Physiol. Meas.* 11, 243–249. doi:10.1088/0143-0815/11/3/007

Langton, C. M., Palmer, S. B., and Porter, R. W. (1984). The measurement of broadband ultrasonic attenuation in cancellous bone. *Eng. Med.* 13, 89–91. doi:10.1243/EMED_JOUR_1984_013_022_02

Lasaygues, P. (2007). Compound quantitative ultrasonic tomography of long bones using wavelets analysis. *Acoust. Imag.* 28, 223–229. doi:10.1007/1-4020-5721-0_24

Lasaygues, P., Guillermin, R., and Lefebvre, J.-P. (2006). Distorted born diffraction tomography applied to inverting ultrasonic field scattered by noncircular infinite elastic tube. *Ultrason. Imaging* 28, 211–229. doi:10.1177/016173460602800402

Lasaygues, P., Guillermin, R., and Lefebvre, J.-P. (2010). "Ultrasonic computed tomography," in *Bone Quantitative Ultrasound*, eds P. Laugier and G. Haïat (Dordrecht: Springer Netherlands), 441–459.

Laugier, P., and Haïat, G. (eds). (2011). "Introduction to the physics of ultrasound," in *Bone Quantitative Ultrasound* (Dordrecht: Springer Netherlands), 29–45.

Raum, K., Grimal, Q., Varga, P., Barkmann, R., Glüer, C. C., and Laugier, P. (2014). Ultrasound to assess bone quality. *Curr. Osteoporos. Rep.* 12, 154–162. doi:10.1007/s11914-014-0205-4

Sievänen, H., Cheng, S., Ollikainen, S., and Uusi-Rasi, K. (2001). Ultrasound velocity and cortical bone characteristics in vivo. *Osteoporos. Int.* 12, 399–405. doi:10.1007/s001980170109

Zheng, R., and Lasaygues, P. (2013). "Simultaneous assessment of bone thickness and velocity for ultrasonic computed tomography using transmission-echo method," in *IEEE Int Ultrason Symp IUS* (Prague: Czech Republic), 2084–2087. doi:10.1109/ULTSYM.2013.0532

Conflict of Interest Statement: The authors declare that the research was conducted in the absence of any commercial or financial relationships that could be construed as a potential conflict of interest.

frontiers in Materials

ORIGINAL RESEARCH
published: 27 November 2017
doi: 10.3389/fmats.2017.00037

Decrease in Local Volumetric Bone Mineral Density in Osteoarthritic Joints Is Associated with the Increase in Cartilage Damage: A Peripheral Quantitative CT Study

*Maryam Tamaddon[1], Shen Mao Chen[1], Leyre Vanaclocha[1], Alister Hart[1,2], Moataz El-Husseiny[2], Johann Henckel[2] and Chaozong Liu[1]**

[1] Division of Surgery and Interventional Science, Institute of Orthopaedic and Musculoskeletal Science, University College London, Royal National Orthopaedic Hospital, London, United Kingdom, [2] Royal National Orthopaedic Hospital, London, United Kingdom

Osteoarthritis (OA) is one of the most prevalent joint diseases, which causes pain and disability in the adult population. OA affects the osteochondral unit in the joints, which comprises both cartilage and subchondral bone. There has been some progress in understanding the changes in subchondral bone with progression of OA. However, local changes in subchondral bone such as microstructure or volumetric bone mineral density (vBMD) in connection with the defect in cartilage are relatively unexplored. To develop an effective treatment for progression of OA, it is important to understand how the physical environment provided by the subchondral bone affects the overlying cartilage. In this study, we examined the vBMD distribution in the OA joint tissues obtained from total hip replacement surgeries due to OA, using peripheral quantitative CT (pQCT). It was found that there is a significant decrease in vBMD, which co-localizes with the damage in the overlying cartilage. This was not limited to the subchondral bone immediately adjacent to the cartilage defect but continued in the layers below. Bone resorption and cyst formation in the OA tissues were also detected. We observed that the bone surrounding subchondral bone cysts exhibited much higher vBMD than that of the surrounding bones. pQCT was able to detect significant changes in vBMD between OA and non-OA samples, as well as between areas of different cartilage degeneration, which points to its potential as a technique for detection of early OA.

Keywords: volumetric bone mineral density, osteoarthritis, subchondral bone, cartilage degeneration, bone cyst, peripheral quantitative CT

OPEN ACCESS

Edited by:
Gianluca Tozzi, University of Portsmouth, United Kingdom

Reviewed by:
Simone Tassani, Pompeu Fabra University, Spain
Urszula Stachewicz, AGH University of Science and Technology, Poland

****Correspondence:***
Chaozong Liu
chaozong.liu@ucl.ac.uk

Specialty section:
This article was submitted to Mechanics of Materials, a section of the journal Frontiers in Materials

Received: *31 July 2017*
Accepted: *30 October 2017*
Published: *27 November 2017*

Citation:
Tamaddon M, Chen SM, Vanaclocha L, Hart A, El-Husseiny M, Henckel J and Liu C (2017) Decrease in Local Volumetric Bone Mineral Density in Osteoarthritic Joints Is Associated with the Increase in Cartilage Damage: A Peripheral Quantitative CT Study. Front. Mater. 4:37. doi: 10.3389/fmats.2017.00037

INTRODUCTION

Osteoarthritis (OA) is a degenerative joint disease, characterized by degradation of cartilage and changes in the subchondral bone. Patients with OA often suffer from pain, loss of mobility, and go on to require an end-stage total joint replacement. In 2015, 215,502 joint replacements were performed in England and Wales predominantly for OA (93%) (National Joint Registry for England, 2015). According to the World Health Organisation, 52% of people over 70 years old have OA. It affects around 400 million people's lives, and this number will increase with an increasing aging population (Goldring and Goldring, 2010, Litwic et al., 2013). It has been predicted that the

incidence of OA would be increased to 35% by 2030 (Thomas et al., 2014). OA affects both articular cartilage and subchondral bone. The degradation and loss of cartilage during OA stems from the decrease in the levels of proteoglycans and changes in biomechanics of the extracellular matrix, altering morphology and metabolic activity of chondrocytes (Martel-Pelletier et al., 2008, Maldonado and Nam, 2013). Radiologically, OA is characterized by the narrowing of joint space, osteophytes formation, subchondral sclerosis, and subchondral bone cysts are usually observed in advanced cases. In OA, thickness of subchondral bone comprising both subchondral bone plate and subarticular spongiosa is increased, mineral content is reduced, and trabecular structure is changed (Madry et al., 2016).

It has been shown that bone mineral density (BMD) changes are associated with the progression of OA (Sepriano et al., 2015). Reliable methods to assess BMD have been attracting an increasing interest. Currently, dual-energy x-ray absorptiometry (DXA) and magnetic resonance imaging (MRI) are used to measure the BMD. However, MRI techniques are only able to provide an indirect measurement of BMD (Bennell et al., 2008). Another technique used for BMD research is quantitative computerized tomography (QCT), which utilizes an X-ray based device to measure BMD in three dimensional space (Adams, 2013). One of the advantages of QCT over the conventional DXA is that the volumetric bone mineral density (vBMD, mg/cm^3) readings obtained from it, is independent of bone size (Bennell et al., 2008). Peripheral quantitative CT (pQCT) is a type of QCT that is increasingly used in measurements of BMD especially in peripheral regions of the body. Although BMD of the joint is positively associated with prevalence and incidence of OA, its relationship with the advancement of OA is not well understood (Lee et al., 2013). More so, scarcely data are available regarding the local changes in BMD with progressive degeneration of articular cartilage. The aim of this study was, therefore, to measure and compare the subchondral vBMD distribution in more advanced OA joints and correlate vBMD distribution with degeneration of overlying articular cartilage. The results would improve our understanding of the role of subchondral bone remodeling and resorption on the cartilage degeneration.

MATERIALS AND METHODS

Sample Collection

Femoral heads of nine patients undergoing total hip replacement were collected at Royal National Orthopedic Hospital, approved by UK Health Research Authority (REC reference: 15/LO/2052). Inclusion criteria consisted of femoral heads which had been removed during arthroplasty due to clinically diagnosed OA ($n = 7$) or due to developmental dysplasia of the hip (DDH) (non-OA, $n = 1$). The non-OA sample is used as a reference for comparison in cartilage grading only. Exclusion criteria included excessive joint damage or deformation that prevented a successful analysis. Age of the patients ranged between 25 and 78 (mean 61.14 ± 15.7). The characteristics of the patients such as height, body mass index, history of other disease, and medications were not disclosed and were not a concern in this study. Specimens were preserved in 10% neutral buffered formalin at 4°C until required.

Cartilage Grading

The cartilage on the femoral head was visually graded by two independent observers using modified Outerbridge classification (Wright, 2014) (**Table 1**). A map was designed containing 36 different regions of interests (ROIs) for analysis of cartilage degeneration of vBMD distribution, as shown in **Figure 1A**. A non-OA femoral head from a 25-year-old patient due DDH was used as reference for comparison. The reason for replacement was DDH but the head did not show any severe cartilage damage.

Measurements of vBMD

The femoral heads were introduced into a pQCT machine (Stratec XCT3000, Germany) to measure the vBMD (mg/cm^3). The samples were scanned through six groups which together gave information on all 36 ROIs (**Figure 1A**) on three different depth levels: outer (0–5 mm), mid (5–10 mm), and inner (10–15 mm), as illustrated in **Figure 1B**. In total, 108 ROIs per sample were examined. The pQCT scans were analyzed using XCT3000 software (version 6.20, Stratec, Germany), which provided direct data on *trabecular* vBMD (thereafter referred to as vBMD). The parameters for the pQCT scan were set to 10 slices of 0.1 mm, 0.2 mm voxel size, 180 mg/cm^3 threshold and trabecular area of 90%. Therefore, in total 1,080 ROIs per sample were obtained, and the vBMD of these 10 slices were averaged and the mean value was used for each of the 108 analyzed ROIs (**Figure 1B**). On those femoral head scanned where cysts existed, the cysts were excluded in the ROIs as they are filled with fluid, not bone, and would affect the true vBMD calculations (**Figure 2**).

Statistical Analysis

For cartilage grading, Kruskal–Wallis tests were used to determine any significant differences between OA and non-OA samples. For vBMD, effects of the two factors (cartilage grading and depth/level) and their interactions on vBMD were examined. Data were ranked and aligned as Schapiro–Wilk tests rejected normality and a nonparametric multifactorial test was required. Aligned rank transformation (ART) of data was performed using the ARTool software (Kay and Wobbrock, 2017) available at http://depts.washington.edu/madlab/proj/art/ (Wobbrock et al., 2011). Statistical analysis was then performed on ART data using the SPSS 22 (SPSS Inc., Chicago, IL, USA) full-factorial ANOVA. The data were plotted using OriginPro 2017 (OriginLab, Northampton, MA, USA).

TABLE 1 | Outerbridge classification for grading the degeneration of cartilage.

Grade	Visual finding
0	Normal articular cartilage
I	Swelling and softening of the articular cartilage
II	Fibrillation or superficial fissures of the cartilage
III	Deep fibrillation or fissures of the cartilage without exposed bone
IV	Exposure of subchondral bone

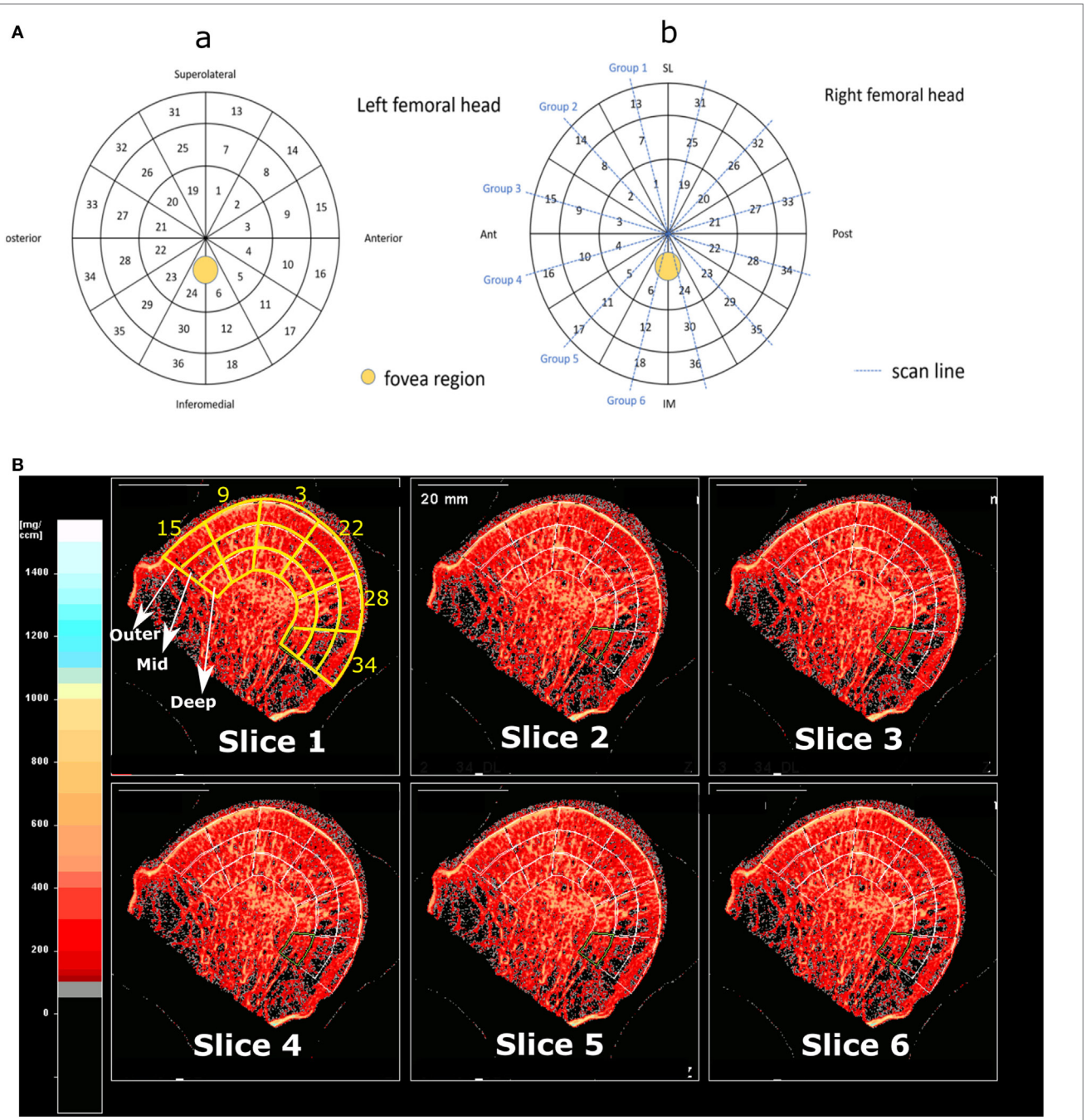

FIGURE 1 | **(A)** Panel (a) shows the different ROIs, birdview from a left femoral head, and panel (b) shows the scan lines on a right femoral head. **(B)** Shows the three different scan depths across 6 different regions in *group 3*, which according to panel (a) are regions 15, 9, 3, 22, 28, and 34. 6 out of 10 slices for this group are shown.

RESULTS

The Changes in Cartilage Grading and Subchondral vBMD with OA

Cartilage grading with Outerbridge classification were performed in all 36 ROIs of OA samples. It was observed that the remaining cartilage on the femoral heads are in varying degrees of degeneration (I–IV). Whereas in the non-OA control sample no severe (grade III or IV) cartilage degradation was observed. Overall scoring of the cartilage showed that the cartilage on OA femoral heads have significantly higher score than that of control sample ($p < 0.001$). Cartilage degeneration pattern in the OA samples are quite different from that of control DDH sample, as demonstrated in **Figure 3**.

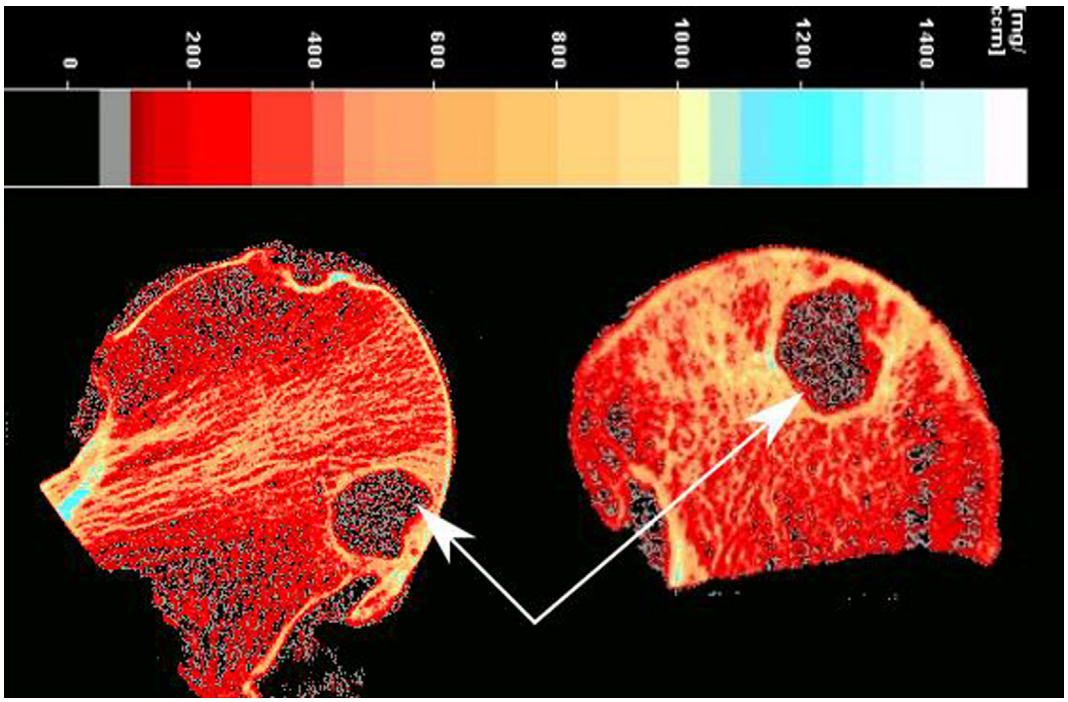

FIGURE 2 | Presence of a large cyst (white arrows) in an osteoarthritis sample.

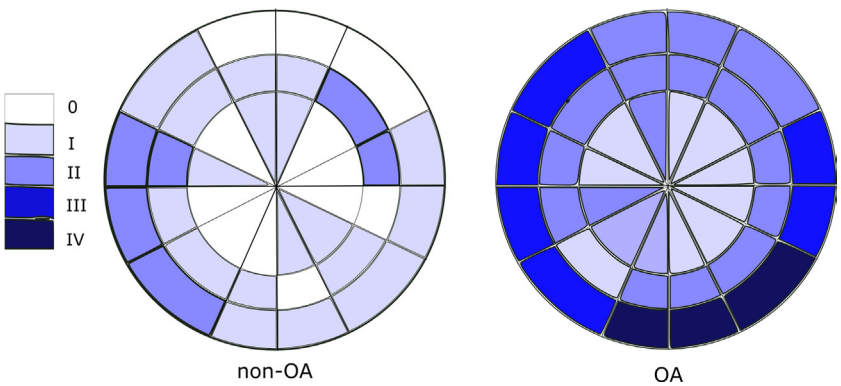

FIGURE 3 | Outerbridge scoring (median score) of OA and non-OA samples shows minimal cartilage degeneration in non-OA samples and severe cartilage degeneration in 25% of regions of interest in OA samples.

The Effects of Cartilage Degeneration and Depth on Subchondral vBMD

Both cartilage grading and depth had significant effects on vBMD in the OA group ($p < 0.001$). Within the OA group, there was an inverse relationship between the cartilage grading and vBMD (**Figure 4A**), meaning that the vBMD decreased with progressively damaged cartilage, which was shown by a weak ($r = -0.36$), but significant ($p < 0.001$) Pearson correlation between cartilage damage and vBMD. Statistical analysis confirmed a significant decrease in vBMD with cartilage damage ($p < 0.001$) with an exception between grade II and III cartilage.

In the outer levels, the subchondral bone adjacent to the grade I cartilage had a vBMD of 423 mg/cm^3 ($\pm$161); this decreased to 358 mg/cm^3 ($\pm$157) for the subchondral bone adjacent to the grade II cartilage, and 333 mg/cm^3 ($\pm$143) for the bone beneath grade III cartilage. Much lower vBMD values, 246 mg/cm^3 ($\pm$96), was observed for the subchondral bone adjacent to a more severely degraded grade IV cartilage.

Also, the depth from the cartilage surface significantly affected the vBMD measurements ($p < 0.001$), where mid levels showed significantly lower vBMD compared to outer and inner levels, as shown in **Figure 4B**.

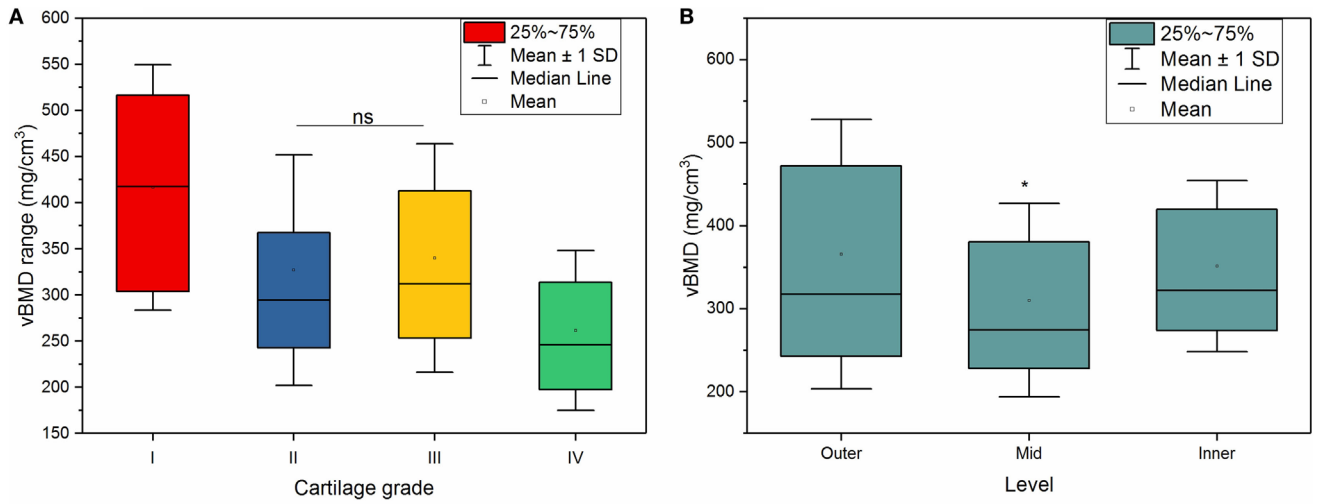

FIGURE 4 | **(A)** Volumetric bone mineral density (vBMD) of osteoarthritis samples according cartilage grading. A significant decrease in vBMD of subchondral bone with cartilage grading was observed at all grades ($p < 0.001$), except between grade II and III (ns, no significant difference). **(B)** vBMD according to depth. Mid levels showed significantly lower vBMD compared to outer and inner levels; $^*p < 0.001$.

The Combined Effects of Cartilage Degeneration and Depth on Subchondral vBMD

The decline in vBMD with cartilage grading was observed not only in the outer level, which is adjacent to the overlying cartilage, but also in mid and inner levels, which are distant to the degenerated cartilage as shown in **Figure 5**.

There was a significant interaction between cartilage degeneration and depth ($p = 0.003$), which means that cartilage degeneration affected vBMD in some levels more than others. In fact, the level with the most change was the outer level ($761.01 - 121.54 = 639.47$ mg/cm^3), followed by the middle level ($648.73 - 132.93 = 515.8$ mg/cm^3) and finally by the inner depth ($658.21 - 153.72 = 504.49$ mg/cm^3) (**Figure 6A**). This shows that the advanced cartilage damage (grade IV) affects outer levels significantly more than mid and inner layers.

Another interesting observation was related to the vBMD surrounding the subchondral bone cysts. These subchondral bone cysts were present in all of OA cases and areas surrounding the cysts showed a significantly higher vBMD (894.8 ± 64 mg/cm^3) compared to the neighboring sites (**Figure 2**).

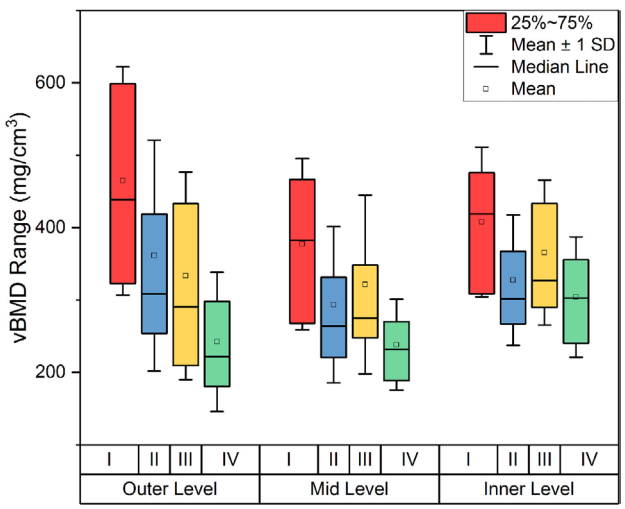

FIGURE 5 | Volumetric bone mineral density (vBMD) of OA samples according to both cartilage grading and depth.

DISCUSSION

We investigated the effects of cartilage degeneration in the OA joints on subchondral vBMD both locally and distantly to the overlying cartilage, as well as the association of vBMD in OA subchondral bone with the degree of damage in the articular cartilage as assessed through pQCT.

We observed that degradation of cartilage in the OA joints had a significant effect on vBMD distribution in the subchondral bone. In the layer adjacent to the overlying cartilage, the vBMD decreased significantly with cartilage degeneration (**Figure 5**). This could be explained by the fact that cartilage damage induced by OA can lead to increased bone remodeling as a result of changes in the loading regime. This may lead to excessive bone turnover, increased bone fraction, and decreased levels of mineralization (Grynpas et al., 1991; Fazzalari and Parkinson, 1997; Stewart et al., 1999; Cox et al., 2012; Yu et al., 2016), all leading to a decreased vBMD. However, the literature is not conclusive on the effects of OA pathology on trabecular density (Karvonen et al., 1998). A study by Dore et al. (2010) suggested that subchondral BMD could not predict cartilage loss, while other studies on OA joints claimed that there is no association between changes in OA grade and changes in BMD (Muehleman et al., 2002; Haugen et al., 2007; Abdin-Mohamed et al., 2009). Nevertheless, we observed a decreased subchondral vBMD with a pattern that

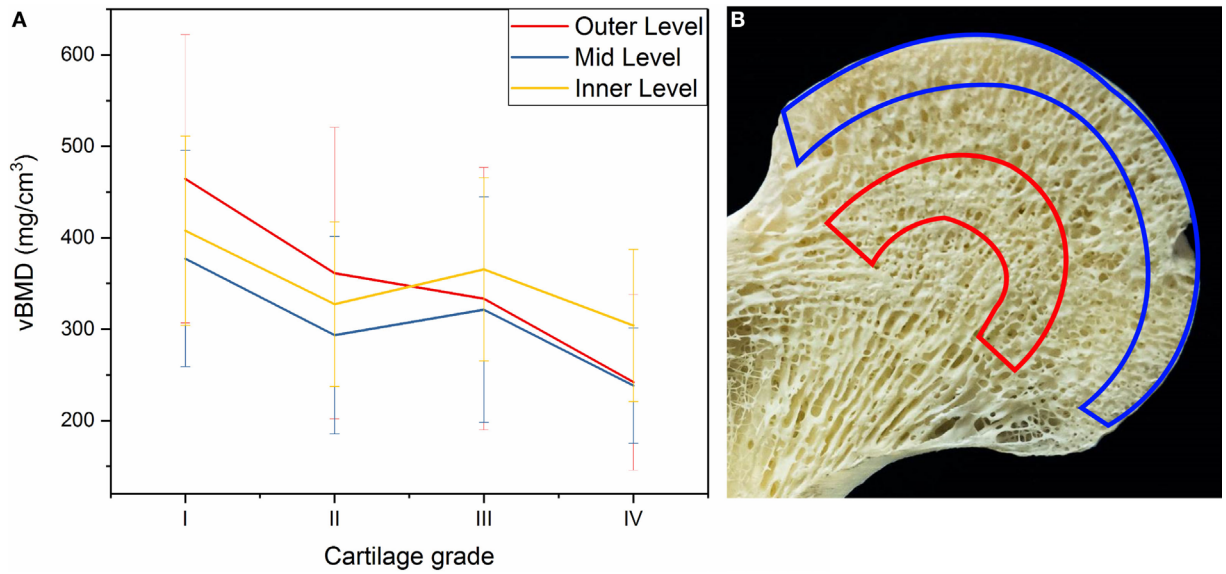

FIGURE 6 | **(A)** Changes in volumetric bone mineral density (vBMD) of OA femoral heads in outer, mid, and inner levels according to cartilage grading. **(B)** Outer and inner levels are highlighted (blue and red, respectively) in the femoral head to illustrate the density of each region.

associates with zones of damage in articular cartilage, indicating that the subchondral trabecular vBMD declines with increasing OA pathology, which was shown by the negative correlation of vBMD with Outerbridge Cartilage Scale grade as demonstrated in **Figure 4A**. This may show the potential of using pQCT for detection of early OA based on changes in vBMD; based on our results, with progression of OA, for example from grade I to grade II, a significant decrease is detectable by pQCT.

A search in the literature would hint to conflicting results regarding BMD changes with OA. While studying patients affected by OA, some researchers have discovered higher BMD in the joints, while others have not observed the same effects (Sandini et al., 2005). Sandini et al. looked at femoral BMD in subjects with OA and although they found increased bone mineral content and bone size, they did not observe higher BMD in those subjects. This was also accompanied by a faster BMD loss compared with healthy controls. Conversely, Lee et al. (2016) observed that hand and knee OA were negatively associated with the BMDs of the lumbar spine and femoral neck.

These controversies surrounding the relationship between BMD and OA may be explained by the following factors: differences in the measurement methods and differences in the measurement sites. One must note the difference between vBMD and BMD; the former is a volumetric measurement determined using QCT methods such as pQCT, while the latter is an areal measurement quantified using methods such as DXA. DXA provides a reliable evaluation of areal bone density but is incapable of distinguishing between cortical and trabecular bone (the parameter measured and discussed in this article) or take into account changes in the bone size, which may overestimate the resultant BMD, whereas pQCT can provide accurate measurements of true vBMD and can supply isolated measurement of cortical and trabecular bones (Abdin-Mohamed et al., 2009). As such, although radiographic OA of the knee is known to be connected to elevated areal BMD at the hip and spine, the vBMD of tibia was not increased in patients with knee OA (Lee et al., 2016).

Another important factor which may cause confusion when comparing BMD/vBMD data across different studies is the measurement site (i.e., systemic, distal, or local measurements). For example, Lee et al. showed that BMD loss, measured at a distant site, is associated with progressive loss of cartilage in knees with OA, confirming what was observed by Zhang et al. (2000) that again BMD loss is linked with deterioration of the joint shown by radiographic joint space narrowing. Changes in BMD with OA may differ in different joints. For example, using Raman Spectroscopy it has been shown that the subchondral bone from OA *hip* joints can have reduced mineral-to-collagen ratio (decreased vBMD), whereas subchondral bone from OA *knee* joints can have increased mineral-to-collagen ratio (increased vBMD) (Buckley et al., 2014).

The results from our study suggest that vBMD is highest in the outer layer of the trabecular bone, followed by the inner layer, and finally the mid layer as demonstrated in **Figure 5B**. The outer layer includes the cortical subchondral bone plate which may explain the highest vBMD. The fact that inner layers showed higher vBMD compared to mid layer may be explained according to the trabecular patterns observed by Wolff's Law, where the inner layer in our study coincides with the denser region of where principal compressive and tensile trabecular groups meet as shown in **Figure 6B**.

The level which experienced the most change with increasing OA grade of the cartilage was the outer level, as shown in **Figure 6A**, suggesting that the outer layer is the most affected one by the cartilage degeneration in the OA joints and the core in the femoral head was the one least affected. This is possibly

because OA pathology related changes such as cysts or microcracks occur much more on the surface than in deeper layers. In fact, two studies performed on OA patellae and tibial plateaus in different depths showed similar results and found that the least dense layer was the internal layer (Burnett et al., 2016) and deeper trabecular bone layers have decreased vBMD compared to the surface (Johnston et al., 2011).

We observed subchondral bone cysts in all of OA samples, which are consistent with other reports on OA hip (Chiba et al., 2014). These fluid-filled voids in subchondral bone, which are typically referred to as "subchondral bone cysts," are normally reported in OA patients. There are two main theories about the source of subchondral bone cysts in OA. The "synovial fluid intrusion" theory suggests that due to cracks in the osteochondral region, synovial fluid enters into subchondral bone and leads to development of these cysts; while the "bone contusion" theory proposes that the necrotic lesions in subchondral bone, generated by abnormal mechanical stress result in microcracks, edema, focal bone resorption, and subsequent cyst formation (Li et al., 2013). Our study showed that the vBMD of the subchondral bone surrounding the cysts are significantly higher than the neighboring areas, indicating possible bone remodeling as a result of cyst formation. Increased local BMD has also been previously associated with bone marrow lesions in patients with knee OA (Lo et al., 2005), showing a positive relationship between loading and BMD as the response of bone to local stresses.

Further studies in the field could increase the understanding of OA pathogenesis and facilitate the development of new and improved treatments, possibly using pQCT techniques.

CONCLUSION

The local changes in subchondral vBMD with OA were assessed in OA femoral head using pQCT. We observed a negative association between local vBMD and severity of cartilage damages, especially in outer layers of subchondral bone, which we believe is linked to the changes in subchondral bone remodeling. PQCT was able to detect significant changes in vBMD between areas of different cartilage degeneration score, which points to its potential as a technique for detection of early OA.

ETHICS STATEMENT

All procedures performed in this study involving human participants were approved by the ethical standards of NHS Health Research Authority, London—City & East Research Ethics Committee (REC reference: 15/LO/2052) and were in accordance with the 1964 Helsinki declaration and its later amendments or comparable ethical standards. Also written informed consent was obtained from all individual participants included in the study.

AUTHOR CONTRIBUTIONS

MT contributed to the experimental work and prepared the manuscript; SC and LV conducted the experimental work and contributed to drafting the manuscript; AH, ME-H, and JH collected the samples; CL designed the study and contributed to editing of the manuscript. All authors reviewed the paper critically for intellectual content and approved the final version. All authors agreed to be accountable for all aspects of the work in ensuring that questions related to the accuracy or integrity of any part of the work are appropriately investigated and resolved.

FUNDING

This work was financially supported by The Arthritis Research UK Proof of Concept Award (grant no: 21160) and Rosetrees Trust (project no: A1184).

REFERENCES

Abdin-Mohamed, M., Jameson, K., Dennison, E. M., Cooper, C., and Arden, N. K. (2009). Volumetric bone mineral density of the tibia is not increased in subjects with radiographic knee osteoarthritis. *Osteoarthr. Cartil.* 17, 174–177. doi:10.1016/j.joca.2008.06.004

Adams, J. E. (2013). Advances in bone imaging for osteoporosis. *Nat. Rev. Endocrinol.* 9, 28–42. doi:10.1038/nrendo.2012.217

Bennell, K. L., Creaby, M. W., Wrigley, T. V., and Hunter, D. J. (2008). Tibial subchondral trabecular volumetric bone density in medial knee joint osteoarthritis using peripheral quantitative computed tomography technology. *Arthritis Rheum.* 58, 2776–2785. doi:10.1002/art.23795

Buckley, K., Kerns, J. G., Parker, A. W., Goodship, A. E., and Matousek, P. (2014). Decomposition of in vivo spatially offset Raman spectroscopy data using multivariate analysis techniques. *J. Raman Spectrosc.* 45, 188–192. doi:10.1002/jrs.4434

Burnett, W., Kontulainen, S., McLennan, C., Hazel, D., Talmo, C., Hunter, D., et al. (2016). Patella bone density is lower in knee osteoarthritis patients experiencing moderate-to-severe pain at rest. *J. Musculoskelet. Neuronal. Interact.* 16, 33–39. doi:10.1016/j.joca.2012.02.326

Chiba, K., Burghardt, A. J., Osaki, M., and Majumdar, S. (2014). Three-dimensional analysis of subchondral cysts in hip osteoarthritis: an ex vivo HR-pQCT study. *Bone* 66, 140–145. doi:10.1016/j.bone.2014.06.001

Cox, L. G., van Donkelaar, C. C., van Rietbergen, B., Emans, P. J., and Ito, K. (2012). Decreased bone tissue mineralization can partly explain subchondral sclerosis observed in osteoarthritis. *Bone* 50, 1152–1161. doi:10.1016/j.bone.2012.01.024

Dore, D., Quinn, S., Ding, C., Winzenberg, T., Cicuttini, F., and Jones, G. (2010). Subchondral bone and cartilage damage: a prospective study in older adults. *Arthritis Rheum.* 62, 1967–1973. doi:10.1002/art.27467

Fazzalari, N. L., and Parkinson, I. H. (1997). Fractal properties of subchondral cancellous bone in severe osteoarthritis of the hip. *J. Bone Miner. Res.* 12, 632–640. doi:10.1359/jbmr.1997.12.4.632

Goldring, M. B., and Goldring, S. R. (2010). Articular cartilage and subchondral bone in the pathogenesis of osteoarthritis. *Ann. N. Y. Acad. Sci.* 1192, 230–237. doi:10.1111/j.1749-6632.2009.05240.x

Grynpas, M. D., Alpert, B., Katz, I., Lieberman, I., and Pritzker, K. P. H. (1991). Subchondral bone in osteoarthritis. *Calcif. Tissue Int.* 49, 20–26. doi:10.1007/BF02555898

Haugen, I. K., Slatkowsky-Christensen, B., Ørstavik, R., and Kvien, T. K. (2007). Bone mineral density in patients with hand osteoarthritis compared to population controls and patients with rheumatoid arthritis. *Ann. Rheum. Dis.* 66, 1594–1598. doi:10.1136/ard.2006.068940

Johnston, J. D., McLennan, C. E., Hunter, D. J., and Wilson, D. R. (2011). In vivo precision of a depth-specific topographic mapping technique in the CT analysis of osteoarthritic and normal proximal tibial subchondral bone density. *Skeletal Radiol.* 40, 1057–1064. doi:10.1007/s00256-010-1001-6

Karvonen, R. L., Miller, P. R., Nelson, D. A., Granda, J. L., and Fernandez-Madrid, F. (1998). Periarticular osteoporosis in osteoarthritis of the knee. *J. Rheumatol.* 25, 2187–2194.

Kay, M., and Wobbrock, J. (2017). *ARTool: Aligned Rank Transform for Nonparametric Factorial ANOVAs. Version 1.6.2*.

Lee, J. Y., Harvey, W. F., Price, L. L., Paulus, J. K., Dawson-Hughes, B., and McAlindon, T. E. (2013). Relationship of bone mineral density to progression of knee osteoarthritis. *Arthritis Rheum.* 65, 1541–1546. doi:10.1002/art.37926

Lee, K.-E., Wen, L., Yim, Y.-R., Kim, J.-E., Lee, J.-W., Park, D.-J., et al. (2016). AB0758 the relationships between bone mineral density and radiographic features of hand or knee osteoarthritis in older adults: data from the Dong-Gu study. *Ann. Rheum. Dis.* 75(Suppl. 2), 1164–1164. doi:10.1136/annrheumdis-2016-eular.1952

Li, G., Yin, J., Gao, J., Cheng, T. S., Pavlos, N. J., Zhang, C., et al. (2013). Subchondral bone in osteoarthritis: insight into risk factors and microstructural changes. *Arthritis Res. Ther.* 15, 223. doi:10.1186/ar4405

Litwic, A., Edwards, M. H., Dennison, E. M., and Cooper, C. (2013). Epidemiology and burden of osteoarthritis. *Br. Med. Bull.* 105, 185–199. doi:10.1093/bmb/lds038

Lo, G. H., Hunter, D. J., Zhang, Y., McLennan, C. E., Lavalley, M. P., Kiel, D. P., et al. (2005). Bone marrow lesions in the knee are associated with increased local bone density. *Arthritis Rheum.* 52, 2814–2821. doi:10.1002/art.21290

Madry, H., Orth, P., and Cucchiarini, M. (2016). Role of the subchondral bone in articular cartilage degeneration and repair. *J. Am. Acad. Orthop. Surg.* 24, e45–e46. doi:10.5435/jaaos-d-16-00096

Maldonado, M., and Nam, J. (2013). The role of changes in extracellular matrix of cartilage in the presence of inflammation on the pathology of osteoarthritis. *Biomed. Res. Int.* 2013, 284873. doi:10.1155/2013/284873

Martel-Pelletier, J., Boileau, C., Pelletier, J.-P., and Roughley, P. J. (2008). Cartilage in normal and osteoarthritis conditions. *Best Prac. Res. Clin. Rheumatol.* 22, 351–384. doi:10.1016/j.berh.2008.02.001

Muehleman, C., Berzins, A., Koepp, H., Eger, W., Cole, A. A., Kuettner, K. E., et al. (2002). Bone density of the human talus does not increase with the cartilage degeneration score. *Anat. Rec.* 266, 81–86. doi:10.1002/ar.10040

National Joint Registry for England, Wales and Northern Ireland. (2015). *NJR Stats-Online*. Available at: http://www.njrcentre.org.uk/njrcentre/LinkClick.aspx?fileticket=QkZM7sN-HpA%3d&portalid=0

Sandini, L., Arokoski, J. P. A., Jurvelin, J. S., and Kröger, H. (2005). Increased bone mineral content but not bone mineral density in the hip in surgically treated knee and hip osteoarthritis. *J. Rheumatol.* 32, 1951–1957.

Sepriano, A., Roman-Blas, J. A., Little, R. D., Pimentel-Santos, F., Arribas, J. M., Largo, R., et al. (2015). DXA in the assessment of subchondral bone mineral density in knee osteoarthritis – a semi-standardized protocol after systematic review. *Semin. Arthritis Rheum.* 45, 275–283. doi:10.1016/j.semarthrit.2015.06.012

Stewart, A., Black, A., Robins, S. P., and Reid, D. M. (1999). Bone density and bone turnover in patients with osteoarthritis and osteoporosis. *J. Rheumatol.* 26, 622–626.

Thomas, E., Peat, G., and Croft, P. (2014). Defining and mapping the person with osteoarthritis for population studies and public health. *Rheumatology (Oxford)* 53, 338–345. doi:10.1093/rheumatology/ket346

Wobbrock, J. O., Findlater, L., Gergle, D., and Higgins, J. J. (2011). "The aligned rank transform for nonparametric factorial analyses using only ANOVA procedures," in *Proceedings of the ACM Conference on Human Factors in Computing Systems (CHI '11)*. Vancouver, British Columbia. New York: ACM Press, 143–146.

Wright, R. W. (2014). Osteoarthritis classification scales: interobserver reliability and arthroscopic correlation. *J. Bone Joint Surg. Am.* 96, 1145–1151. doi:10.2106/jbjs.m.00929

Yu, D., Xu, J., Liu, F., Wang, X., Mao, Y., and Zhu, Z. (2016). Subchondral bone changes and the impacts on joint pain and articular cartilage degeneration in osteoarthritis. *Clin. Exp. Rheumatol.* 34, 929–934.

Zhang, Y., Hannan, M. T., Chaisson, C. E., McAlindon, T. E., Evans, S. R., Aliabadi, P., et al. (2000). Bone mineral density and risk of incident and progressive radiographic knee osteoarthritis in women: the Framingham Study. *J. Rheumatol.* 27, 1032–1037.

Conflict of Interest Statement: The authors declare that the research was conducted in the absence of any commercial or financial relationships that could be construed as a potential conflict of interest.

frontiers in Materials

ORIGINAL RESEARCH
published: 23 November 2017
doi: 10.3389/fmats.2017.00039

Combining Coherent Hard X-Ray Tomographies with Phase Retrieval to Generate Three-Dimensional Models of Forming Bone

Emely L. Bortel[1], Max Langer[2], Alexander Rack[3], Jean-Baptiste Forien[4], Georg N. Duda[4], Peter Fratzl[1] and Paul Zaslansky[5]**

[1] Department of Biomaterials, Max Planck Institute of Colloids and Interfaces, Potsdam, Germany, [2] Institut National des Sciences Appliquées de Lyon (INSA-Lyon), Université de Lyon, CREATIS, Villeurbanne, France, [3] Structure of Materials – ID19, European Synchrotron Radiation Facility, Grenoble, France, [4] Julius Wolff Institute, Charité – Universitätsmedizin Berlin, Berlin, Germany, [5] Department for Restorative and Preventive Dentistry, Charité – Universitätsmedizin Berlin, Berlin, Germany

OPEN ACCESS

Edited by:
Gianluca Tozzi,
University of Portsmouth,
United Kingdom

Reviewed by:
Enrico Dall'Ara,
University of Sheffield,
United Kingdom
Antonio DiCarlo,
CECAM–IT–SIMUL Node, Italy

***Correspondence:**
Emely L. Bortel
emely.bortel@mpikg.mpg.de;
Paul Zaslansky
paul.zaslansky@charite.de

Specialty section:
This article was submitted to Mechanics of Materials, a section of the journal Frontiers in Materials

Received: 30 August 2017
Accepted: 02 November 2017
Published: 23 November 2017

Citation:
Bortel EL, Langer M, Rack A, Forien J-B, Duda GN, Fratzl P and Zaslansky P (2017) Combining Coherent Hard X-Ray Tomographies with Phase Retrieval to Generate Three-Dimensional Models of Forming Bone. Front. Mater. 4:39. doi: 10.3389/fmats.2017.00039

Holotomography, a phase-sensitive synchrotron-based (μCT) modality, is a quantitative 3D imaging method. By exploiting partial spatial X-ray coherence, bones can be imaged volumetrically with high resolution coupled with impressive density sensitivity. This tomographic method reveals the main characteristics of the important tissue compartments in forming bones, including the rapidly changing soft tissue and the partially or fully mineralized bone regions, while revealing subtle density differences in 3D. Here, we show typical results observed within the growing femur bone midshafts of healthy mice that are 1, 3, 7, 10, and 14 days old (postpartum). Our results make use of partially coherent synchrotron radiation employing inline Fresnel propagation in multiple tomographic datasets obtained in the imaging beamline ID19 of the European Synchrotron Radiation Facility. The exquisite detail creates maps of the juxtaposed soft, partially mineralized and highly mineralized bone revealing the environment in which bone cells create and shape the matrix. This high-resolution 3D data can be used to create detailed computational models to study the dynamic processes involved in bone tissue formation and adaptation. Such data can enhance our understanding of the important biomechanical interactions directing maturation and shaping of the bone micro- and macro-geometries.

Keywords: mouse, femur, midshaft, bone formation, 3D data, holotomography

INTRODUCTION

Growing bone exhibits a complex architecture in 3D. The tissue undergoes extensive reorganization and restructuring of the initially deposited, "primitive" bone material. Consequently, these forming tissues exhibit a range of morphologies that are all "normal" albeit different. They co-exist in the growing skeleton or during healing, for example, following fracture or biomaterial implantation. Initially, after the non-mineralized osteoid matrix starts to mineralize, bone material in both formation and healing conditions appears as a highly porous structure, where mineralized and soft tissue are intermixed. Such early formed bone tissues gradually transform and rearrange into solid cortical bone that eventually takes on the appearance of the mature tissue (Miller et al., 2007; Manjubala et al., 2009; Lange et al., 2011; Preininger et al., 2011; Sharir et al., 2011;

Vetter et al., 2011; Rohrbach et al., 2013; Bortel et al., 2015). The early formed tissue morphology is thus transient and contains zones of markedly different morphologies, e.g., woven bone and lamellar bone, such that different degrees of mineralization are observed in adjacent bone sites at the same developmental timepoint. This dynamically changing partially mineralized tissue can take-on a range of different geometries, with mechanical properties that are difficult to define and measure. Detailed information about both architecture and density is thus necessary for understanding and possibly predicting bone growth and tissue repair.

Much insight into the temporal and spatial events taking place during skeletal development has come from *ex vivo* experiments, with important contributions from mouse models (e.g., Richman et al., 2001; Nowlan et al., 2010; Sharir et al., 2011). A handful of studies have focused on understanding the morphogenesis and structural changes that the initially templated bone structures undergo. For the long bones in the limbs, radial growth followed by shaping appears to define the outline of the bones, adapting them into hollow tubes that sustain the future mechanical needs of animal locomotion. Ferguson et al. (2003), for example, used 2D cross-sections to study changes in the femoral bones of C57BL/6 mice. They observed a transition from a fairly round profile into an elliptical shape, a change that takes place between 7 and 8 weeks of life. Bortel et al. (2015) observed condensation occurring in the midshaft cortex within 14 days after birth. Sharir et al. (2011) examined neonatal shape formation in the C57BL/6 mice strain limbs and observed a temporary cortical asymmetric thickening with preferred zones developing mineralized struts on the periosteal side. By comparing their results to findings in a mutant mouse (mdg) strain that lacks skeletal muscle contractility, Sharir et al. (2011) proposed that intrauterine muscle forces have an important effect on the shape of the prenatal bones. Other studies support the assumption that muscle activity guides shape formation in bone development, as observed for example in mouse mutant models with targeted muscle immobilization (Nowlan et al., 2010; Sharir et al., 2013). Thus, understanding the mechanical environment and the loads and stresses appearing during tissue growth are essential for understanding healthy tissue formation as well as for predicting health or pathology during bone tissue growth.

In addition to morphological characterizations, several studies have revealed typical changes in the distribution of mineral density in normal forming bones. Price et al. (2005) performed a 2D histomorphometry study comparing bones of three different mouse strains from 1 day up to 1 year after birth, and they observed a densification of the bones within the first 4 weeks of life. Richman et al. (2001) used peripheral quantitative computed tomography to examine bones from CH3/HeJ and C57BL/6 mice aged 7–56 days. The authors found a link between morphological characteristics and peak mineral density observed in the adult animals. Higher cortical thickness and decreased marrow canal areas in postnatal and pubertal ages were found to be linked to high peak mineral density in the adult animals. Sharir et al. (2013) observed that during birth, mineral density and bone stiffness become temporarily reduced, possibly due to increased local bone resorption. It is compelling to consider this as a possible preparation process for easing parturition. In the forming tibia of Balb/c mice, Miller et al. (2007) observed that the mineral density immediately after birth is about 50% lower than the value observed in mature bones. At the same time, those authors observed that the elastic modulus only reaches approximately 14% of the mature value. Note that these authors used nanoindentation measurements, which are by now the standard method to obtain the elastic properties of such small samples. These findings indicate that there is no trivial correlation between estimates of the bone mineral density and the measured bone stiffness in the forming bone structures. Indeed, precise estimations of mineral or mass density of the (no-treated) bony tissue are demanding (Dierolf et al., 2010; Zanette et al., 2015). Furthermore, it is likely that the soft tissue has a significant effect on the overall mechanical competence of the growing bones.

A few studies employed sub-micron resolution characterization methods to study nanostructural changes that occur during murine long bone formation, revealing important changes in the mineral particle morphology and arrangement (Fratzl et al., 1991; Lange et al., 2011; Mahamid et al., 2011). A transformation toward longer and thinner nanoparticles in the bone (at length scales of less than 100 nm) appears to accompany a change in the orientation of the long axis of the mineral particles at the nanometer length scale, as they take-on a preferential arrangement parallel to the long bone axis. These structural changes take place at the same time that average tissue mineral density increases with intermixed zones of low mineral content "filling in" the gaps (Price et al., 2005; Sharir et al., 2011; Bortel et al., 2015). Following these structural changes, a rigid mature bone structure emerges, capable of sustaining loads and fulfilling locomotion and related mechanical needs, but at the same time capable of adapting to external mechanical loads (Willie et al., 2013).

The last decade has seen the study of bone structure and function benefit immensely from the incorporation of 3D imaging methods, in particular by microcomputed tomography (μCT). A variety of commercially available μCT instruments have emerged that are able to produce high fidelity virtual models (tomography data) of bone morphology with details of structures deep down into the sub-micron length scale. At the same time, large-scale X-ray facilities worldwide (Beamlines within synchrotron radiation storage rings) have been advancing both X-ray source technology and detection quality continuously increasing both resolution and flux. The high flux and use of narrow-bandwidth illumination has led to high density spatial resolution, well suited to measure small variations in mineral densities in bones (Salomé et al., 1999; Nuzzo et al., 2002). More recently, nanoCT has emerged as a method for measuring density distribution at the sub-micron length scale by making use of phase contrast effects that take place when partially coherent X-ray beams propagate through an object (Guigay, 1977; Momose and Fukuda, 1995; Snigirev et al., 1995). While phase contrast imaging is long known to be very sensitive to small density objects in the beam (Cloetens et al., 1999b), quantification of the X-ray interaction with the material is not straightforward, requiring integration of results from multiple

different measurements to resolve ambiguities. This is needed because not all structural features are recorded in a single tomographic dataset due to missing spatial frequencies in the projected radiographic images (known as missing frequencies in the Fresnel propagation transfer function) (Zabler et al., 2005). Consequently, several (at least two) projection images have to be captured per tomographic rotation angle, using measurements obtained at different sample-to-detector distances (Langer et al., 2010a; Langer and Peyrin, 2016). Experience has shown that four different measurements or more are optimal to obtain high quality reconstructions. Several algorithms have been developed to extract the phase shift and quantitatively reconstruct the 3D refractive index. This spatial information can then be converted into mass-density distributions by simple scaling (Paganin et al., 2002; Langer et al., 2010a,b, 2012a; Langer and Peyrin, 2016). The imaging and reconstruction approach known as holotomography (Cloetens et al., 1999a) exhibits high sensitivity to low absorbing material, e.g., soft tissue, because it is very sensitive to small changes in structure and/or composition. Thus, despite the increased experimental and computation complexity as compared with laboratory-based (μCT), holotomography has significant potential for revealing the 3D distribution of juxtaposed low and high mineralized structures of bone tissue.

Holotomography has been used in a handful of studies on bone. In 2009, Komlev et al. (2009) described the application of pseudo-holotomography to study bone implant integration in a mouse model. The authors reported high-resolution characterization of the implant-site morphology while visualizing vessel growth in the engineered implant. Giuliani et al. (2013) evaluated the quality of repaired defects in human mandibles 3 years after implantation of stem cell seeded scaffolds. Using a combination of histology and holotomography, the authors characterized the artificial bone scaffold as well as the infused vessels showing that the experimental bone defect was filled with highly vascularized compact bone rather than with physiologically spongy bone. Exploiting projection geometries and nanoCT, holotomography was successfully used in bone to analyze spatial variations in mineralization at the micrometer length scale (in and around osteocyte cell lacunae) (Hesse et al., 2015) and collagen-fibril orientation variations (Varga et al., 2013). More recently, nanoCT-based holotomography was used as a basis for mechanical modeling of stresses and strains around osteocyte cells in bone (Varga et al., 2015). For a review of these X-ray methods and related experimental considerations, see (Langer and Peyrin, 2016).

In this work, we demonstrate how holotomography can be used for the quantification and reproduction of the substantial morphology and mineralization changes that take place during bone tissue genesis, in normal growing mouse bone. Our proof-of-concept results demonstrate the exquisite amount of structural and compositional detail that can be extracted from the growing bone tissue at micrometer resolution. The spatially well-resolved mass-density distributions help us identify the variations in arrangement and distribution of the intricate soft tissue as well as a range of mineral densities in the forming hard tissue. Such data forms an important step toward creating reliable computer-generated 3D models at high resolution and with extensive detail. Our work showcases the richness of the available 3D high-grade histological data, obtained by employing quantitative phase-retrieved tomography with sub-micrometer resolution using partial coherence synchrotron radiation X-rays.

MATERIALS AND METHODS

Samples

Female, wild-type C57BL/6 mice were obtained following routinely discarded healthy litters maintained at the Max Planck Institute of Molecular Genetics, Berlin, Germany. Breeding, housing, and euthanasia were performed according to state legal regulations, not for any specific animal experiment, in accordance with the German animal protection law (TierSchg, § 7(2)). An ethics approval was not required as per national regulations and institutional guidelines. The left femora ($n = 1$/age) were dissected from carcasses of mice aged 1, 3, 7, 10, and 14 days after birth. The outer soft tissues (skin and muscles) were partially removed ensuring the bones remained intact, and all samples were fixed and stored in 70 wt% ethanol at 4°C. Tests were conducted to ensure that dehydration in ethanol did not affect the hard tissue architecture, as shown in calibration and reproducibility experiments comparing the bone dimensions before and after dehydration (Bortel, 2015). For μCT imaging, each sample was maintained in an ethanol atmosphere, mounted within small polypropylene cylindrical vials.

Holotomography Measurements

The midsection of each femur was scanned at the long micro tomography beamline ID19 of the European Synchrotron Radiation Facility (Grenoble, France). Samples were imaged with a high flux monoenergetic beam of 26 keV using an effective pixel size of 0.647 μm. Multiple scans of 3999 images were recorded for each sample, with an exposure time of 100 ms. Five sample-to-detector distances (d1 = 10 mm, d2 = 16 mm, d3 = 33 mm, d4 = 84 mm, and d5 = 101 mm) were used to maximize phase contrast in preparation for computation phase retrieval into 3D reconstructed holotomography datasets (Zabler et al., 2005). The energy chosen was sufficiently high to circumvent visible radiation degradation of the sample (e.g., bubble and soft tissue motion), due to exceptionally low absorption. A 1 mm diamond and 1.4 mm Al filter was used for this setup. The detector was a custom-made indirect system consisting of a 10x/0.3NA Olympus objective combined with a thin-single crystal scintillator and a pco.edge sCMOS camera (Douissard et al., 2012).

Data Processing: Phase Retrieval and Tomographic Reconstruction

Series of five-phase contrast-enhanced tomographic datasets recorded for each sample were used to reconstruct the 3D mass-density distribution $\varphi(x, y, z)$ in each bone. This was achieved by combining reconstruction of the phase shifts $\varphi_\theta(r,s)$ induced by the sample at each projection angle and in each scan, using a computation step termed—*phase retrieval*—which was followed by conventional filtered backprojection *tomography reconstruction*. The different computationally intensive data

processing steps yield the 3D distributions of the refractive index coefficient $\Psi(x,y,z)$, which can be readily converted into mass-density distributions (Langer et al., 2012a). Phase retrieval was performed using an algorithm employing a mixed approach (Langer et al., 2010a) where phase retrieval of the different zones uses a multi-material "prior" based on a conventional absorption scan. A full description of the method is beyond the scope of this paper but relies on a linearization of the intensity of the Fresnel transform, basically numerically accounting for the Fresnel propagation induced during imaging at increased sample-to-detector distances. In this way, it is possible to approximate the underlying physical processes of absorption and scattering of the X-rays by the sample, following propagation of the transmitted beam toward the detector. These lead to phase shifts observed in the images as "phase contrast" radiographs. As described elsewhere (e.g., Langer and Peyrin, 2016), transformation of the phase contrast-enhanced images at each angle uses filtering-based algorithms that are robust against strong absorption effects and relatively large propagation distances. Estimation of the phase shift at every point on each projection angle incorporates multiple propagation distances into phase-retrieved synthetically produced projections. The main inconvenience of this approach is that in addition to requiring images obtained at multiple distances, the phase retrieval relies on using an attenuation projection "reference" image (i.e., an image at the sample-detector contact plane), which is needed at each projection angle to uniquely determine the X-ray phase shifts across the projection. Due to poor contrast for low spatial frequency features in the radiographs, phase retrieval computations often suffer from noise in the low spatial frequency range. This can be addressed by using "a priori" knowledge of the sample interactions with the X-rays to "regularize" and constrain the estimated reconstructed phase shifts in each projection. For the mouse bone scans reported here, we used a multi-material "prior," considering the sample to be composed of bone and soft tissue; Thus, the phase shift at each point on every radiograph was back-calculated by assuming that the interactions of the X-rays with the tissue through which they propagate are limited to one of two ratios between the attenuation index β and the refractive index decrement δ. In practice, this is implemented by first reconstructing the attenuation scan (using public-domain available code, e.g., PyHST2, Mirone et al., 2014), yielding 3D maps of attenuation index β (x, y, z). This data is then used to assign ratios of the δ/β based on approximate composition and known (tabulated) values of this ratio. Thus, reconstruction of the phase shift at each point for each projection Ψ is obtained by taking the known tabulated δ/β ratio for mineralized bone ($\delta/\beta = 429.9$) in zones identified by the threshold maps, and assuming all other regions contain soft tissue ($\delta/\beta = 1857$). This map is then multiplied with the attenuation tomogram, yielding a prior estimate δ (x, y, z) of the refractive index decrement in 3D. Estimates of the phase at each angle $\varphi_{0,0}$ are then generated by forward projection of δ_0 (x, y, z). Finally, the phase is retrieved at each projection angle by linear least squares minimization using assumptions of the mixed approach and the generated "prior." The resulting phase maps are used for reconstruction of 3D maps of the refractive index coefficient ω (x, y, z) and converted into mass density (Langer et al., 2012a) by using the scaling relation

$$\rho\,(\mathrm{g/cm^3}) = -\frac{10\omega\,(\mathrm{1/cm})}{1.3\lambda\,(\mathrm{Å})2\pi} \approx -\frac{\omega}{390},$$

where $\lambda = 0.4769$ Å is the wavelength of the beam.

Tomographic Image Processing and Three-Dimensional Analyses

Image processing was performed using ImageJ (NIH, USA, V 1.48f) and CTVox (BrukerCT, Kontich, Belgium). Histogram analysis was used to identify the background (air) offset in the density data (Hesse et al., 2015) such that the density of air surrounding the tissues was adjusted to $\rho = 0$ g/cm^3. Peaks in the gray value of the main bone components (soft tissue, low density bone and high density bone) were used to produce 3D datasets containing only bone/tissue densities based on conventional thresholding (see e.g., Bortel et al., 2015). 3D renderings of the data were produced with CTVox (Bruker-microCT, Kontich, Belgium) using color and transparency in the transfer functions to depict the different tissue densities.

Histology

Representative samples of each mouse age were fixed in 100% ethanol and subsequently demineralized for 14 days in EDTA. After embedding in paraffin, 4 µm thin cross-sectional slices of the midshaft were produced using a rotational microtome. Movat's Pentachrome was used to stain the slices. Histological slices were imaged with an Axioskop 2 microscope (Carl Zeiss Microscopy GmbH, Germany).

RESULTS

Holotomography provides exquisite details of both hard and soft tissue in the growing bones. **Figure 1** demonstrates the visibility of details seen in cross sections of a 10 day sample obtained with holotomography (left) as compared with similar-resolution

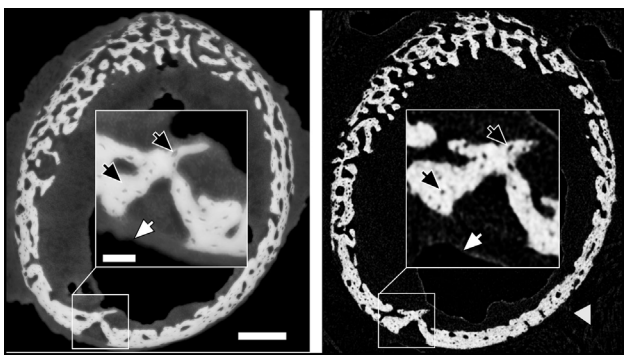

FIGURE 1 | Comparison of similar cross-sections in a 10-day sample imaged by holotomography (left) and a laboratory source CT (right). The gray arrow head highlights gauze, which supports the bone during the lab CT scan. The scale bar equals to 200 µm. The inset shows a high magnification (scale bar = 50 µm) to highlight the differences in feature visibility between the methods. Dark arrows pinpoint osteocyte lacunae, and white arrows hint to the transition between soft tissue and air.

laboratory CT (right, Skyscan 1172, 60 keV). Note the markedly different contrasts easing differentiation between the sample and the surrounding air (black). In the lab CT image, the gray values of air, soft tissue and supporting gauze (gray arrow head) cannot be differentiated. Holotomography provides good visibility while reproducing the small structures in the bone, including bone spicules and osteocyte lacunae (black arrows) that are difficult to resolve with the conventional lab CT.

The reconstructed data reveals that the growing limb midshaft contains an intricate mixture of highly mineralized nodes, embedded in a 3D scaffold of structured soft tissue exhibiting substantial changes as the tissue matures. Examples of the extensive amount of detail available are shown in **Figure 2** where typical cross-sections and histograms of the reconstructed density data are provided. Brighter shades of gray represent higher mass density, invariably zones of mineral density in our bone samples. The soft tissue is clearly distinguishable from both the surrounding air (black) and the higher density (bright) bone and may therefore be easily separated and identified in the 3D data. The cross-sections **Figure 2A** reveal extensive changes in the morphology of the bones in the first days after birth. Whereas at days 1 and 3, porous scaffolds consisting of loosely connected mineralize struts are seen, continuous growth leads toward a continuously mineralized thin outer cortex/ring of the bone midshaft appearing uniform but containing numerous cell lacunae, by 14 days. In addition to notable closing of the many pores, zones of high and low mineral density are clearly discernible. The inset figures in **Figure 2B** show that within the forming bone tissue, density varies considerably and that low and high mineral density zones are juxtaposed. White and dark arrows highlight example regions of differently mineralized bone that are difficult to separate in 3D by using other tomographic methods. The distributions of mass densities for entire sections of the growing femur mid diaphyses are plotted in **Figure 2C**. Values below a density of 0.5 g/cm^3 are truncated for improved clarity. A prominent peak identified as the soft tissue peak (s) is seen with density values in the range between 1.1 and 1.4 g/cm^3 in the different ages. For the very young animals a small peak presumably corresponding to cartilage (c) can also be seen. At higher densities, exceeding mass densities of ~1.6 g/cm^3, a peak corresponding to bone emerges and grows with increasing age. To better interpret the information content related to both soft tissue and mineralized tissue, **Figure 2D** presents a magnified section of each histogram, corresponding to the soft tissue (s) and the bone (b) regions. To facilitate comparability, the data are scaled to present the soft tissue and bone peaks, respectively. A shoulder in the soft tissue peak (marked with v) appears with a slightly higher density than the main peak except in day 3, where the shoulder has a slightly lower density. The bone peaks are clearly distinguishable from the soft tissue. We identify a bone peak in the mass-density range between 1.7 and 2.0 g/cm^3 with a noticeable increasing trend from 3 days on. The bone peak at day 1 is similar to the peak observed at day 14. Small shoulders in this peak are produced by islands of high mineral density within the bone (marked with *), possibly mineralized cartilage.

The uniformity of the densities of both the soft tissue and bone in the different cross-sectional slices along each femur midshaft axis are demonstrated by stacked histograms plotted in **Figure 3**. **Figure 3A** demonstrates how individual histograms may be stacked to represent the soft tissue and bone density information along the bone employing a pseudo-3D representation. The color histogram highlights the counts to better visualize the peak (soft tissue and bone) heights. The position of the soft tissue peak (s) and the bone peak (b) appears to be remarkably constant along the bone axis as shown by the plots in **Figure 3B**. While differences can be seen between different aged bones, only minor differences can be seen at different heights along the midshaft in the distributions of soft tissue and bone within the 1-, 3-, 7-, 10-, and 14-day samples. Some minor fluctuations in the peak positions are observed in the 7-day sample.

Figure 4 provides 3D renderings of the data surveyed in **Figure 2**, providing insight into the nature of the microstructural data in 3D. **Figure 4A** shows the complete gray value distribution, including the clearly distinguishable background (black) the soft tissue and the bone (different shades of gray) contributions within the reconstructed volume. The cutout in **Figure 4B** displayed by the dashed lines reveal the extensive details resolved within the internal structures. The exposed inner corner of the 3D cutout is magnified to provide a close-up in to the data demonstrating the available information content in the 3D datasets. The different tissues are clearly identifiable, showing the intimate spatial relationship between the bone embedded within the soft tissue. In the data obtained from a 1-day-old animal, a black arrow highlights to bone regions with greater mass density. Very thin structures are visible in the 1-day sample, marked by a gray arrowhead. Presumably, these structures transform into solid tissue during later stages of bone growth (Bortel et al., 2015). In the older samples, arrowheads highlight osteocyte lacunae that are also clearly identifiable in 3D.

The different tissues can be identified based on known values of mass density. We broadly identify air, soft tissue moderately mineralized tissue and highly mineralized tissue, as displayed graphically in pseudo-3D renderings given in **Figure 5**. Here, blue represents the soft tissue, green is assigned to the mineralized bone, and red highlights high density islands within the bone, presumably mineralized cartilage. Similar cutouts as those used in **Figure 4** reveal what the encasing soft tissue masks. For all ages, substantial amounts of soft tissue (blue) surround the forming bone material. The 3D distribution of mineralized material changes from the loosely connected foamy structures observed in the younger ages (1–7 days) into a condensed bone cortex, sandwiched between inner and outer soft tissue layers. The magnified cutouts graphically reveal the different tissues, especially the embedded high density islands (possibly mineralized cartilage) that seem to be completely encapsulated within the "normal" growing bone.

Examples of separated tissues potentially ready for meshing and incorporation into finite element (FE models) are shown in **Figure 6**. In this representation, only the two mineral densities of bone are shown in **Figure 6A**. The mineralized snapshots reveal a quantitative transition from a highly porous scaffold consisting of loosely mineralized struts in the young ages into a mature solid ring seen in the samples obtained from 14 day animals. To appreciate the intricate detail, views with increasing magnification are shown in **Figures 6B,C**. It can be seen that the bone local morphology changes extensively with ongoing maturation, accompanied by a

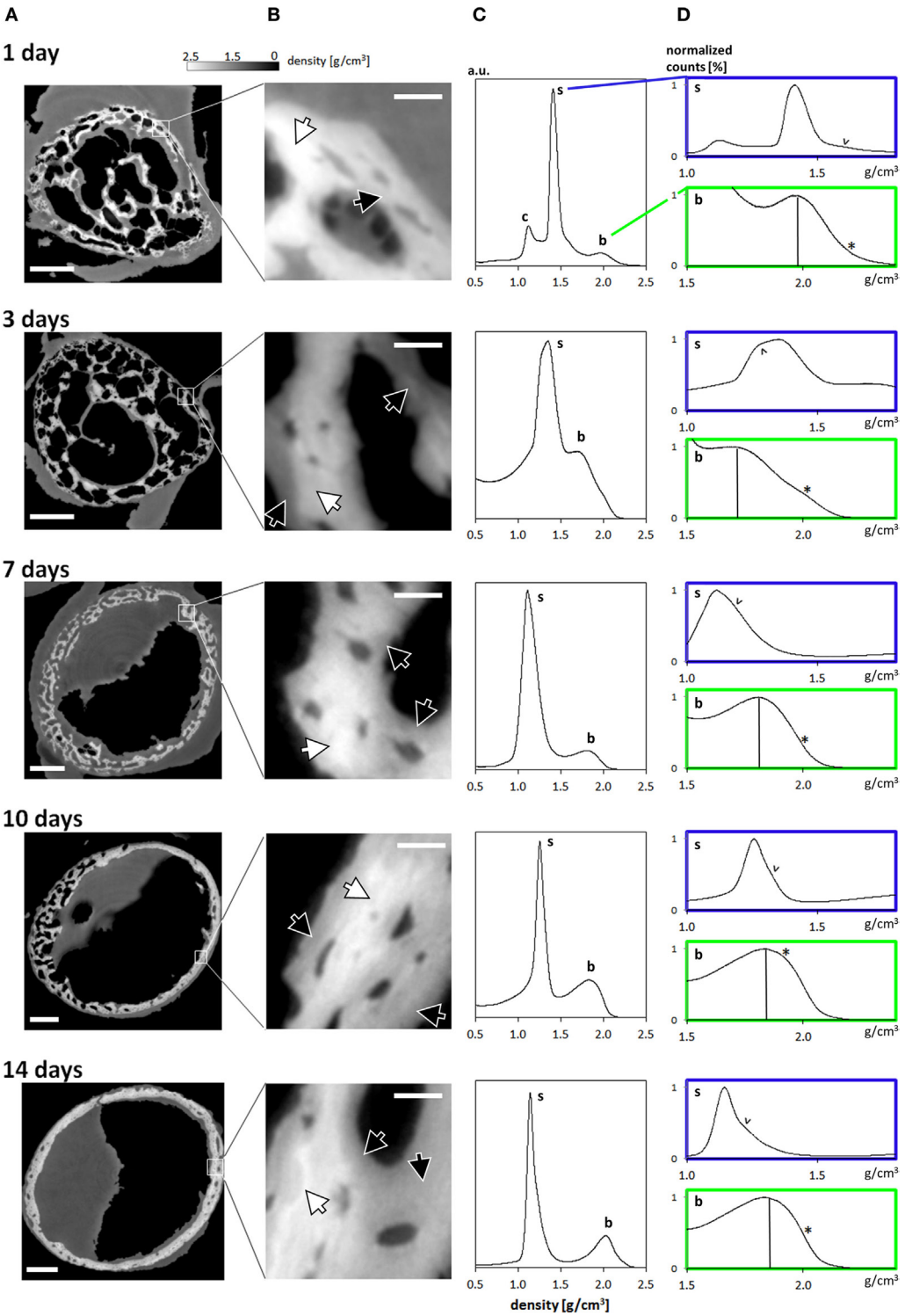

FIGURE 2 | **(A)** Typical cross-sections through femur midshafts of 1, 3, 7, 10, and 14 days old mouse bones (scale bar = 200 μm). The gray values are scaled to mass density (g/cm³). **(B)** Insets show higher magnifications of the developing bone (scale bar = 20 μm). For clarity, the contrast is enhanced. White arrows highlight regions of highly mineralized bone, and black arrows point to low mineral regions. **(C)** Mass-density histograms of typical 3D datasets (more than 10^9 values per scan) exhibiting a prominent peak of the soft tissue, a range of intermediate densities, and a shoulder depicting highly mineralized bone. **(D)** Magnified regions in each histogram in **(B)** limited to the soft tissue (s) and the bone peak (b). Within the soft tissue comprises different densities [marked by arrowheads (v)] owing to the extended holotomography density sensitivity. Vertical lines in the bone panels mark the position of the bone peak. Note the presence of substantial amounts of high mineral density bone (indicated by *).

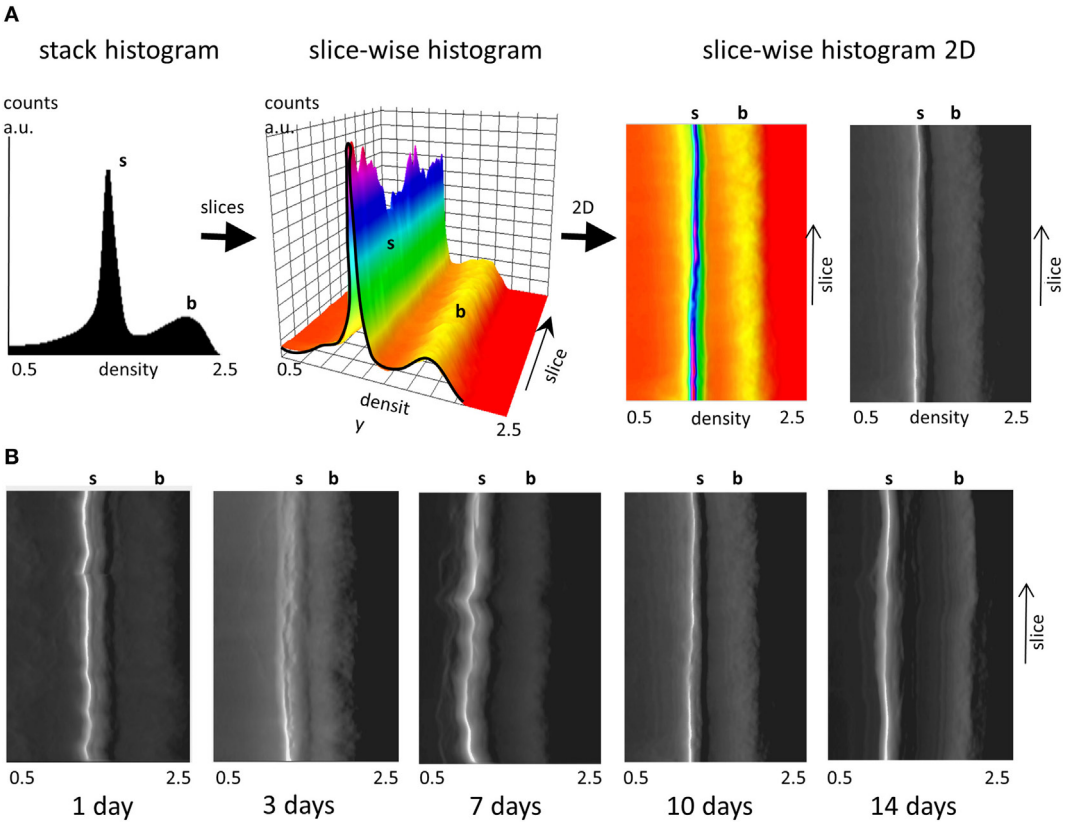

FIGURE 3 | Slice-wise density distributions along the femur midshaft axis. **(A)** Transformation of a stack histogram (left) to a pseudo-3D plot of all histograms (middle) along the different slices in femur midshaft axis. The color histogram highlights the counts. When the plot is viewed from above, (right) and converted into grayscale the plot highlights the location of the soft tissue (white) and the bone peak (transition from dark gray to black). Densities between 0.5 and 2.5 g/cm^3 are presented and the soft tissue and bone peak positions are highlighted (s, b). **(B)** Projected pseudo-3D slice-wise histograms of data stacks from 1-, 3-, 7-, 10-, and 14-day samples.

redistribution of high density regions located within the lower density bone. **Figure 7** gives an example of a histological slice of a 14-day-old paraffin embedded mouse femur stained with Movat's Pentachrome. Mineralized material is stained in yellow and can clearly be distinguished from the surrounding soft tissues such as the bone marrow (shades of blue) and muscle (red). In the enlarged inset, the different bone types that are present can be nicely distinguished from each other. Here, lamellar bone is located on the periosteal region (white arrows) whereas woven bone is found on the endosteal side (black arrow). Osteocyte lacunae can also be seen (gray arrowhead).

DISCUSSION

In this study, we demonstrate how large data in mutually aligned phase contrast-enhanced tomography datasets, processed by holotomography, reveals exquisite 3D quantitative histological-grade data in developing mouse bones. Using this approach, a large range of local gradients in density of juxtaposed soft and highly mineralized tissues are resolved down to micrometer resolution. By imaging a series of samples with increasing ages after birth we observe a host of different microstructures that are typical for the very different, normal stages of tissue formation. The complex, time-consuming sequence of acquisition and processing, currently still demanding technically, has immense potential to reveal impressive subtle structural detail in the intricate, dynamically changing forming bone tissue.

Our data reveal that in the young forming mouse bones, a mere 2–3 days are sufficient for the tissue to exhibit major transformations in the morphology of the mineralized structures. The initial formed femur bones are cylindrical scaffolds that are made of tiny discontinuous mineralized struts, clearly discernable on days 1 and 3 after birth, in 3D. These bony scaffolds increase in diameter and transform into solid mineralized tubes forming the long bone midshaft (**Figures 5** and **6**). The mineralized bony spicules are removed while new larger structures emerge through concerted actions of osteocytes and osteoblasts (see, e.g., Sharir et al., 2013), while the entire bone expands and enlarges. The high-resolution data shown here allows extraction of local morphological details down to the fundamental tissue ingredients including bony spicules and bone cell (osteocyte) lacunae.

In addition to the remarkable details revealed, the physical property of interest resulting from use of holotomography is a quantitative 3D distribution of mass density, which can be related to, but must be distinguished from mineral density. This paves the way to separating the complex tissue in 3D into the

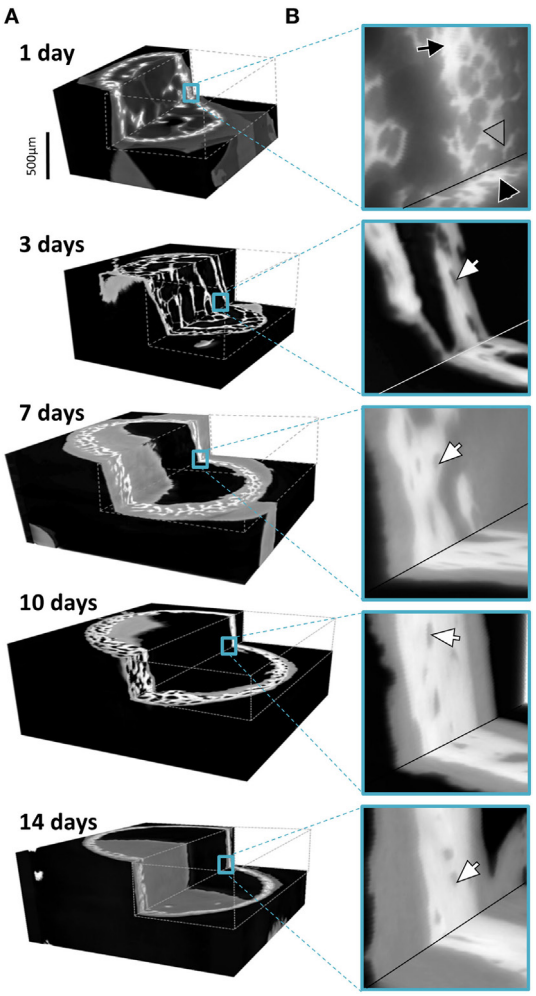

FIGURE 4 | **(A)** Graphic representations of typical 3D datasets with cutouts to reveal the holotomography calculated mass-density distributions including bone and soft tissues in the developing limb structures. Note that the growing bones were scanned in air, here colorized in black, with an approximate mass density of 0, clearly distinguishable in 3D from the soft and hard tissues. **(B)** Insets hint to the distribution of fine details in the gray values associated with both bone and the formative soft tissues. In the 1 day data, a black arrow pinpoints bone regions with high density and very thin structures are marked by a gray arrowhead. In the older samples, arrowheads highlight osteocyte lacunae.

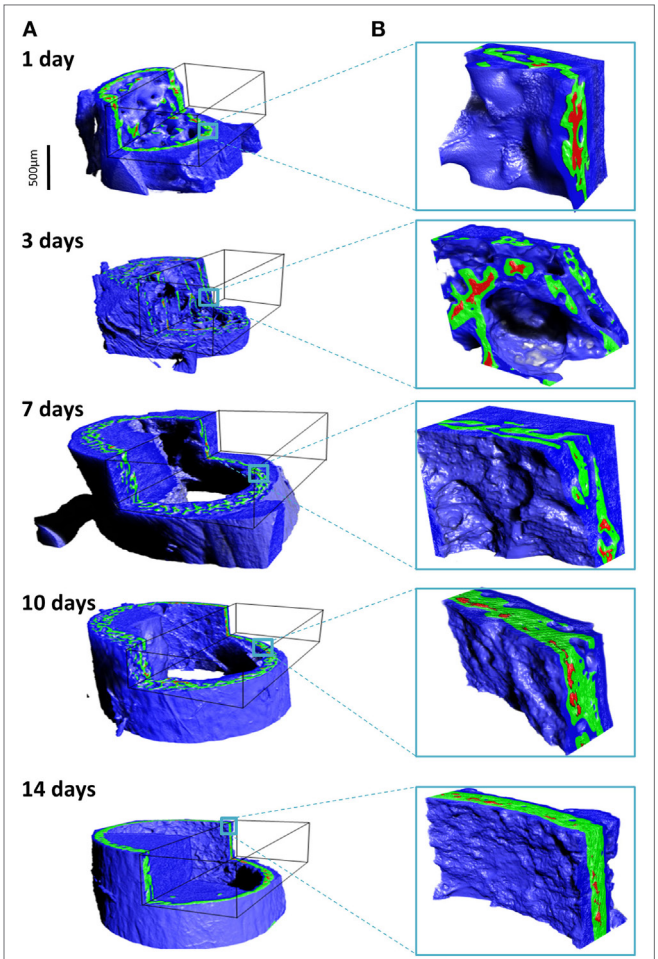

FIGURE 5 | Density assignment and 3D mapping of the soft and hard tissues in the forming mouse femur in 3D. **(A)** The soft tissue colorized in blue surrounds and comes into intimate contact with mineralized bone, colorized in green. Islands of high mineral density exceeding 1.9 g/cm^3 are shown in red, better observed in the high-magnification insets in **(B)**.

components of interest, as shown in **Figure 5**. When examining the gray value distribution of the data, the soft tissue peak exhibits density values spanning 1.1–1.4 g/cm^3 for all ages. These values are slightly higher than published values for soft (skeletal) tissue (1.0–1.06 g/cm^3) (itis, 2017; NIST, 2017) and cartilage (1.1 g/cm^3) (itis, 2017). The higher values observed in some regions of the tissue may be due to higher concentrations of mineral precursor phases in the soft tissue, prior to bone tissue mineralization, similar to observations by other methods reported for forming bone tissue (Golub, 2009; Lange et al., 2011; Langer et al., 2012b). The bone peak becomes more prominent in histograms of bones with increasing age and reveals a high density component, presumably mineralized cartilage (Vanleene et al., 2008; Bach-Gansmo et al., 2013; Shipov et al., 2013), much of which is later replaced with more mature but less mineral-dense bone material. The data shown here make it possible to map the subtle yet important density variation in 3D, measurements that are almost impossible to perform by conventional µCT (see **Figure 1**).

In this work we present examples of the distribution of bone morphologies and density variations in newly formed long bones of mice. A similar approach may be used to study bone tissue growth and maturation in adult animals, during healing. Indeed, much remains unknown about the similarities and differences in the 3D bone tissue dynamics when comparing bone growth/genesis and fracture and tissue healing, e.g., in response to implantation of biomaterials. Density and the different tissue distributions in 3D presented here may help reveal the similarities and differences in bone tissue formation in these different scenarios. In recent years, a handful of studies have used holotomography and other methods in order to evaluate new biodegradable materials and treatment for healing large bone defects (Mastrogiacomo et al., 2005, 2007; Papadimitropoulos et al., 2007; Langer et al., 2010b;

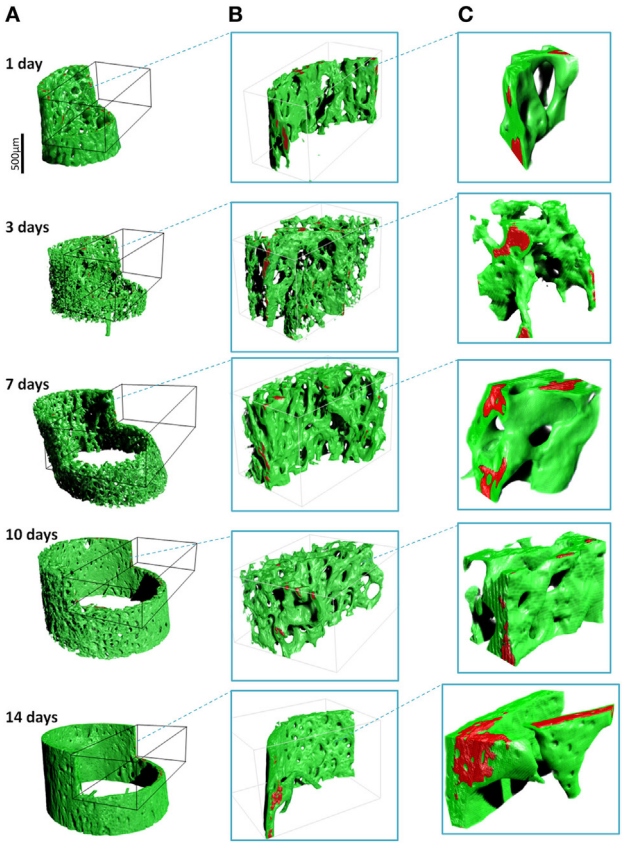

FIGURE 6 | 3D renderings of the bone (green) and high-density zones (red) with increasing magnifications (**(A)**, **(B)** and **(C)**). The high mass density (exceeding 1.9 g/cm^3) is always found within regions of lower density. Note the drastic architectural changes from 1 to 14 days, changing from a foamy network to a solid cortical tube.

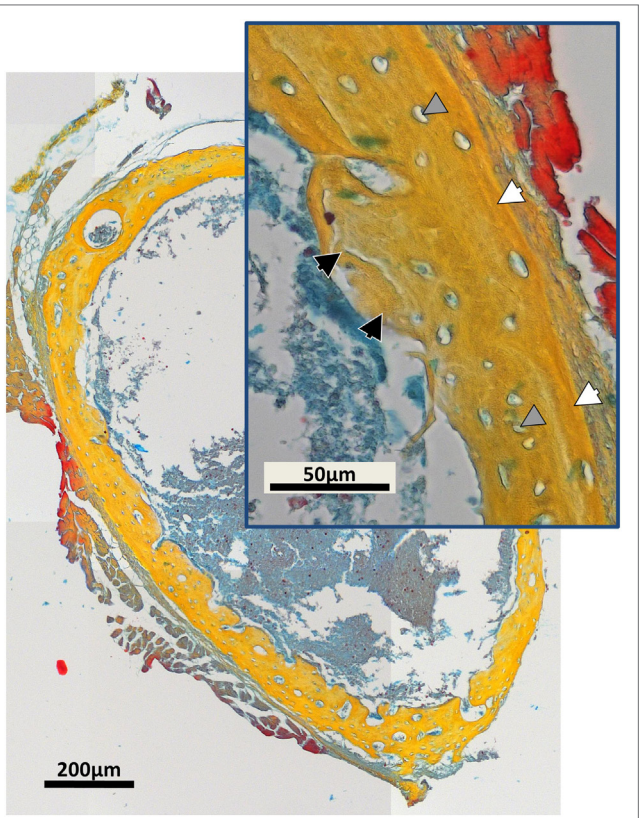

FIGURE 7 | Movat's Pentachrome stained typical histological cross-section of a paraffin-embedded 14-day-old mouse femur mid-diaphysis. Mineralized material is stained in yellow and can be clearly distinguished from the muscles (red) and the bone marrow (shades of blue). The inset shows a magnified region of the bone cortex. Regions of woven bone (black arrows) are seen on the endosteal surface, and lamellar bone (white arrows) is located on the periosteal region. Osteocyte lacunae can be detected (gray arrowheads).

Ruggiu et al., 2014). Porous 3D scaffolds consisting of tricalcium phosphates (e.g., skalite) and/or hydroxyapatites seeded with different osteogenic cells were observed to promote bone formation during resorption. Newly formed bone was identified with holotomography used to quantify formed/resorbed volumes and to characterize the resulting 3D morphologies (Mastrogiacomo et al., 2005, 2007; Papadimitropoulos et al., 2007; Langer et al., 2010b; Ruggiu et al., 2014).

Growing bone in the process of mineralization contains significant non-mineralized regions. The main benefit of measuring each bone samples using five different sample-detector distances is that the quantitative density estimates provide excellent density resolution as well as impressive feature visibility. Different tissue ingredients such as soft tissue and mineralized bone morphology can clearly be separated and quantified in 3D. As seen by comparison between bones of animals with increasing ages, there is a vast amount of soft tissue that completely enwraps the mineralized compartments of the bones.

The resulting data, although challenging in terms of computational requirements, is of a size that can be further processed by available multi-processor desktop workstations, paving the way to designing computer simulations of growing and maturing bone tissues. The mechanical interactions taking place in this environment, and any mechanical stimulation leading to bone (re)modeling and structural adaptation are practically impossible to measure mechanically, and hence there is huge significance for making use of data such as presented here for producing detailed, realistic high-resolution finite element models that can faithfully reproduce and help predict changes in the micro-anatomy of the mineralizing tissue. With our detailed 3D bone/soft tissue distribution data, it becomes possible to perform virtual mechanical loading experiments, providing previously unavailable snapshots of the state of strain and stress in the tissue as it is loaded, which may be helpful for predicting the mechanical feedback related to tissue growth and adaptation. This will open up the way for future computational simulation studies of growth, healing or pathology development/treatment in bone. Such simulations might allow to separate the effects of biological signaling from the purely mechanical (strain/deformation) stimuli, which will help researchers understand the roles of physical versus chemical interactions down to the length scale of cells (e.g., by examining different "remodeling rules"; Dunlop et al., 2009; Vetter et al., 2012). This may even eventually circumvent the need to perform

some of the lengthy, expensive live animal experiments, designed to study structure function relations in mechanically responsive tissues such as bone. Detailed finite element models (e.g., Varga et al., 2015) will help fill in the gaps needed to first understand and later predict tissue growth and anabolic response in the days and weeks following surgical intervention. As shown by Langer et al. (2010b), holotomography clearly resolves low-calcified pre-bone structures undergoing degradation in bone scaffold samples. Often, information on the local tissue density, readily available by holotomography, can be used as a proxy for predicting local tissue stiffness (Razi et al., 2015) important for producing realistic models of growing and forming bone tissue.

It is important to acknowledge that although within computation reach, a single final reconstructed dataset for each of the samples shown here exceeds 25 GB in size, and the intricate 3D structures that can be resolved in this data require careful processing to provide reliable 3D finite element meshes to be able to be used in realistic simulations. Bearing in mind that the final reconstruction is based on significant amounts of raw data (five scans of 4,000 images) as well as intermediate temporary files, an estimated 250 GB data and storage must be planned for each sample, which is to be considered for studies planned to include many time points or multiple measurements. Holotomography is thus yet another member of the "large data" problems requiring attention in scientific research.

As demonstrated, our holotomography data contains an abundance of spatially resolved, high-resolution data that is of high relevance for investigating growing bone morphology and structural dynamics.

AUTHOR CONTRIBUTIONS

The experiments were planned by PF, GD, and PZ and performed by EB, JF, AR, and PZ. Data analysis and manuscript preparation were primarily done by EB, ML, and PZ. The interpretation of the data as well as manuscript development was performed by all authors equally.

ACKNOWLEDGMENTS

We acknowledge the European Synchrotron Radiation Facility for the provision of synchrotron radiation facility beamline ID19. We thank Prof. Dr. Stefan Mundlos for support. EB thanks the Max Planck Institute and the Berlin-Brandenburg School for Regenerative Therapies for PhD and Post-Doc funding, made possible by DFG funding through the BSRT GSC 203.

REFERENCES

Bach-Gansmo, F. L., Irvine, S. C., Brüel, A., Thomsen, J. S., and Birkedal, H. (2013). Calcified cartilage islands in rat cortical bone. *Calcif. Tissue Int.* 92, 330. doi:10.1007/s00223-012-9682-6

Bortel, E. L. (2015). *Maturation of Murine Long Bones: A High Resolution Micro-Computed Tomography Study. Dissertation*. Technische Universität Berlin, Berlin, Germany.

Bortel, E. L., Duda, G. N., Mundlos, S., Willie, B. M., Fratzl, P., and Zaslansky, P. (2015). Long bone maturation is driven by pore closing: a quantitative tomography investigation of structural formation in young C57BL/6 mice. *Acta Biomater.* 22, 92–102. doi:10.1016/j.actbio.2015.03.027

Cloetens, P., Ludwig, W., and Baruchel, J. (1999a). Holotomography: quantitative phase tomography with micrometer resolution using hard synchrotron radiation x rays. *Appl. Phys. Lett.* 75, 2912. doi:10.1063/1.125225

Cloetens, P., Ludwig, W., Baruchel, J., Guigay, J. P., Pernot-Rejmánková, P., Schlenker, M., et al. (1999b). Hard x-ray phase imaging using simple propagation of a coherent synchrotron radiation beam. *J. Phys. D Appl. Phys.* 32, A145. doi:10.1088/0022-3727/32/10A/330

Dierolf, M., Menzel, A., Thibault, P., Schneider, P., Kewish, C. M., Wepf, R., et al. (2010). Ptychographic X-ray computed tomography at the nanoscale. *Nature* 467, 436–439. doi:10.1038/nature09419

Douissard, P. A., Cecilia, A., Rochet, X., Chapel, X., Martin, T., van de Kamp, T., et al. (2012). A versatile indirect detector design for hard x-ray microimaging. *J Instrum* 7, P09016. doi:10.1088/1748-0221/7/09/P09016

Dunlop, J. W. C., Hartmann, M. A., Brechet, Y. J., Fratzl, P., and Weinkamer, R. (2009). New suggestion for the mechanical control of bone remodeling. *Calcif. Tissue Int.* 85, 45–54. doi:10.1007/s00223-009-9242-x

Ferguson, V. L., Ayers, R. A., Bateman, T. A., and Simske, S. J. (2003). Bone development and age-related bone loss in male C57BL/6J mice. *Bone* 33, 387–398. doi:10.1016/S8756-3282(03)00199-6

Fratzl, P., Fratzl-Zelman, N., Klaushofer, K., Vogl, G., and Koller, K. (1991). Nucleation and growth of mineral crystals in bone studied by small-angle X-ray scattering. *Calcif Tissue Int.* 48, 407–413. doi:10.1007/BF02556454

Giuliani, A., Manescu, A., Langer, M., Rustichelli, F., Desiderio, V., Paino, F., et al. (2013). Three years after transplants in human mandibles, histological and in-line holotomography revealed that stem cells regenerated a compact rather than a spongy bone: biological and clinical implications. *Stem Cells Transl. Med.* 2, 316–324. doi:10.5966/sctm.2012-0136

Golub, E. E. (2009). Role of matrix vesicles in biomineralization. *Biochim. Biophys. Acta* 1790, 1592–1598. doi:10.1016/j.bbagen.2009.09.006

Guigay, J. P. (1977). Fourier transformation of Fresnel diffraction patterns and in-line holograms. *Optik* 46, 121–125.

Hesse, B., Varga, P., Langer, M., Pacureanu, A., Schrof, S., Männicke, N., et al. (2015). Canalicular network morphology is the major determinant of the spatial distribution of mass density in human bone tissue: evidence by means of synchrotron radiation phase-contrast nano-CT. *J. Bone Miner. Res.* 30, 346–356. doi:10.1002/jbmr.2324

itis. (2017). Available at: https://www.itis.ethz.ch/virtual-population/tissue-properties/database/density/

Komlev, V. S., Mastrogiacomo, M., Peyrin, F., Cancedda, R., and Rustichelli, F. (2009). X-ray synchrotron radiation pseudo-holotomography as a new imaging technique to investigate angio- and microvasculogenesis with no usage of contrast agents. *Tissue Eng. Part C Methods* 15, 425. doi:10.1089/ten.tec.2008.0428

Lange, C., Li, C., Manjubala, I., Wagermaier, W., Kuhnisch, J., Kolanczyk, M., et al. (2011). Fetal and postnatal mouse bone tissue contains more calcium than is present in hydroxyapatite. *J. Struct. Biol.* 176, 159–167. doi:10.1016/j.jsb.2011.08.003

Langer, M., Cloetens, P., Pacureanu, A., and Peyrin, F. (2012a). X-ray in-line phase tomography of multimaterial objects. *Opt. Lett.* 37, 2151–2153. doi:10.1364/OL.37.002151

Langer, M., Pacureanu, A., Suhonen, H., Grimal, Q., Cloetens, P., and Peyrin, F. (2012b). X-ray phase nanotomography resolves the 3D human bone ultrastructure. *PLoS ONE* 7:e35691. doi:10.1371/journal.pone.0035691

Langer, M., Cloetens, P., and Peyrin, F. (2010a). Regularization of phase retrieval with phase-attenuation duality prior for 3D holotomography. *IEEE Trans. Image Process.* 19, 2428–2436. doi:10.1109/TIP.2010.2048608

Langer, M., Liu, Y., Tortelli, F., Cloetens, P., Cancedda, R., and Peyrin, F. (2010b). Regularized phase tomography enables study of mineralized and unmineralized tissue in porous bone scaffold. *J. Microsc.* 238, 230–239. doi:10.1111/j.1365-2818.2009.03345.x

Langer, M., and Peyrin, F. (2016). 3D X-ray ultra-microscopy of bone tissue. *Osteoporos. Int.* 27, 441–455. doi:10.1007/s00198-015-3257-0

Mahamid, J., Sharir, A., Gur, D., Zelzer, E., Addadi, L., and Weiner, S. (2011). Bone mineralization proceeds through intracellular calcium phosphate loaded vesicles: a cryo-electron microscopy study. *J. Struct. Biol.* 174, 527–535. doi:10.1016/j.jsb.2011.03.014

Manjubala, I., Liu, Y., Epari, D. R., Roschger, P., Schell, H., Fratzl, P., et al. (2009). Spatial and temporal variations of mechanical properties and mineral content of the external callus during bone healing. *Bone* 45, 185–192. doi:10.1016/j.bone.2009.04.249

Mastrogiacomo, M., Muraglia, A., Komlev, V., Peyrin, F., Rustichelli, F., Crovace, A., et al. (2005). Tissue engineering of bone: search for a better scaffold. *Orthod. Craniofac. Res.* 8, 277–284. doi:10.1111/j.1601-6343.2005.00350.x

Mastrogiacomo, M., Papadimitropoulos, A., Cedola, A., Peyrin, F., Giannoni, P., Pearce, S. G., et al. (2007). Engineering of bone using bone marrow stromal cells and a silicon-stabilized tricalcium phosphate bioceramic: evidence for a coupling between bone formation and scaffold resorption. *Biomaterials* 28, 1376–1384. doi:10.1016/j.biomaterials.2006.10.001

Miller, L. M., Little, W., Schirmer, A., Sheik, F., Busa, B., and Judex, S. (2007). Accretion of bone quantity and quality in the developing mouse skeleton. *J. Bone Miner. Res.* 2, 1037–1045. doi:10.1359/jbmr.070402

Mirone, A., Brun, E., Gouillart, E., Tafforeau, P., and Kieffer, J. (2014). The PyHST2 hybrid distributed code for high speed tomographic reconstruction with iterative reconstruction and a priori knowledge capabilities. *Nucl. Instrum. Methods. Phys. Res. B* 324, 41–48. doi:10.1016/j.nimb.2013.09.030

Momose, A., and Fukuda, J. (1995). Phase-contrast radiographs of non-stained rat cerebellar specimen. *Med. Phys.* 22, 375–379. doi:10.1118/1.597472

NIST. (2017). Available at: http://physics.nist.gov/PhysRefData/XrayMassCoef/tab2.html

Nowlan, N. C., Bourdon, C., Dumas, G., Tajbakhsh, S., Prendergast, P. J., and Murphy, P. (2010). Developing bones are differentially affected by compromised skeletal muscle formation. *Bone* 46, 1275–1285. doi:10.1016/j.bone.2009.11.026

Nuzzo, S., Peyrin, F., Cloetens, P., Baruchel, J., and Boivin, G. (2002). Quantification of the degree of mineralization of bone in three dimensions using synchrotron radiation microtomography. *Med. Phys.* 29, 2672–2681. doi:10.1118/1.1513161

Paganin, D., Mayo, S. C., Gureyev, T. E., Miller, P. R., and Wilkins, S. W. (2002). Simultaneous phase and amplitude extraction from a single defocused image of a homogeneous object. *J. Microsc.* 206, 33–41. doi:10.1046/j.1365-2818.2002.01010.x

Papadimitropoulos, A., Mastrogiacomo, M., Peyrin, F., Molinari, E., Komlev, V. S., Rustichelli, F., et al. (2007). Kinetics of in vivo bone deposition by bone marrow stromal cells within a resorbable porous calcium phosphate scaffold: an X-ray computed microtomography study. *Biotechnol. Bioeng.* 98, 271–281. doi:10.1002/bit.21418

Preininger, B., Checa, S., Molnar, F. L., Fratzl, P., Duda, G. N., and Raum, K. (2011). Spatial-temporal mapping of bone structural and elastic properties in a sheep model following osteotomy. *Ultrasound Med. Biol.* 37, 474–483. doi:10.1016/j.ultrasmedbio.2010.12.007

Price, C., Herman, B. C., Lufkin, T., Goldman, H. M., and Jepsen, K. J. (2005). Genetic variation in bone growth patterns defines adult mouse bone fragility. *J. Bone Miner. Res.* 20, 1983–1991. doi:10.1359/JBMR.050707

Razi, H., Birkhold, A. I., Zaslansky, P., Weinkamer, R., Duda, G. N., Willie, B. M., et al. (2015). Skeletal maturity leads to a reduction in the strain magnitudes induced within the bone: a murine tibia study. *Acta Biomater.* 13, 301–310. doi:10.1016/j.actbio.2014.11.021

Richman, C., Kutilek, S., Miyakoshi, N., Srivastava, A. K., Beamer, W. G., Donahue, L. R., et al. (2001). Postnatal and pubertal skeletal changes contribute predominantly to the differences in peak bone density between C3H/HeJ and C57BL/6J mice. *J. Bone Miner. Res.* 16, 386–397. doi:10.1359/jbmr.2001.16.2.386

Rohrbach, D., Preininger, B., Hesse, B., Gerigk, H., Perka, C., Raum, K. (2013). The early phases of bone healing can be differentiated in a rat osteotomy model by focused transverse-transmission ultrasound. *Ultrasound Med Biol* 39, 1642–53.

Ruggiu, A., Tortelli, F., Komlev, V. S., Peyrin, F., and Cancedda, R. (2014). Extracellular matrix deposition and scaffold biodegradation in an in vitro three-dimensional model of bone by X-ray computed microtomography. *J. Tissue Eng. Regen. Med.* 8, 557–565. doi:10.1002/term.1559

Salomé, M., Peyrin, F., Cloetens, P., Odet, C., Laval-Jeantet, A.-M., Baruchel, J., et al. (1999). A synchrotron radiation microtomography system for the analysis of trabecular bone samples. *Med. Phys.* 26, 2194. doi:10.1118/1.598736

Sharir, A., Milgram, J., Dubnov-Raz, G., Zelzer, E., and Shahar, R. (2013). A temporary decrease in mineral density in perinatal mouse long bones. *Bone* 52, 197–205. doi:10.1016/j.bone.2012.09.032

Sharir, A., Stern, T., Rot, C., Shahar, R., and Zelzer, E. (2011). Muscle force regulates bone shaping for optimal load-bearing capacity during embryogenesis. *Development* 138, 3247–3259. doi:10.1242/dev.063768

Shipov, A., Zaslansky, P., Riesmeier, H., Segev, G., Atkins, A., and Shahar, R. (2013). Unremodeled endochondral bone is a major architectural component of the cortical bone of the rat. *J. Struct. Biol.* 183, 132–140. doi:10.1016/j.jsb.2013.04.010

Snigirev, A., Snigireva, I., Kohn, V., Kuznetsov, S., and Schelokov, I. (1995). On the possibilities of X-ray phase contrast microimaging by coherent high-energy synchrotron radiation. *Rev. Sci. Instrum.* 66, 5486. doi:10.1063/1.1146073

Vanleene, M., Rey, C., and Ho Ba Tho, M. C. (2008). Relationships between density and Young's modulus with microporosity and physico-chemical properties of Wistar rat cortical bone from growth to senescence. *Med. Eng. Phys.* 30, 1049–1056. doi:10.1016/j.medengphy.2007.12.010

Varga, P., Hesse, B., Langer, M., Schrof, S., Männicke, S., Suhonen, H., et al. (2015). Synchrotron X-ray phase nano-tomography-based analysis of the lacunar-canalicular network morphology and its relation to the strains experienced by osteocytes in situ as predicted by case-specific finite element analysis. *Biomech. Model. Mechanobiol.* 14, 267–282. doi:10.1007/s10237-014-0601-9

Varga, P., Pacureanu, A., Langer, M., Suhonen, H., Hesse, B., Grimal, Q., et al. (2013). Investigation of the three-dimensional orientation of mineralized collagen fibrils in human lamellar bone using synchrotron X-ray phase nano-tomography. *Acta Biomater.* 9, 8118–8127. doi:10.1016/j.actbio.2013.05.015

Vetter, A., Liu, Y., Witt, F., Manjubala, I., Sander, O., Epari, D. R., et al. (2011). The mechanical heterogeneity of the hard callus influences local tissue strains during bone healing: a finite element study based on sheep experiments. *J. Biomech.* 44, 517–523. doi:10.1016/j.jbiomech.2010.09.009

Vetter, A., Witt, F., Sander, O., Duda, G. N., and Weinkamer, R. (2012). The spatio-temporal arrangement of different tissues during bone healing as a result of simple mechanobiological rules. *Biomech. Model. Mechanobiol.* 11, 147–160. doi:10.1007/s10237-011-0299-x

Willie, B. M., Birkhold, A. I., Razi, H., Thiele, T., Aido, M., Kruck, B., et al. (2013). Diminished response to in vivo mechanical loading in trabecular and not cortical bone in adulthood of female C57Bl/6 mice coincides with a reduction in deformation to load. *Bone* 55, 335–346. doi:10.1016/j.bone.2013.04.023

Zabler, S., Cloetens, P., Guigay, J. P., and Baruchel, J. (2005). Optimization of phase contrast imaging using hard x-rays. *Rev. Sci. Instrum.* 76. doi:10.1063/1.1960797

Zanette, I., Enders, B., Dierolf, M., Thibault, P., Gradl, R., Diaz, A., et al. (2015). Ptychographic X-ray nanotomography quantifies mineral distributions in human dentine. *Sci. Rep.* 5, 9210. doi:10.1038/srep09210

Conflict of Interest Statement: The authors declare that the research was performed without any commercial or financial potential conflict of interest.

frontiers in Materials

ORIGINAL RESEARCH
published: 08 November 2017
doi: 10.3389/fmats.2017.00031

Precision of Digital Volume Correlation Approaches for Strain Analysis in Bone Imaged with Micro-Computed Tomography at Different Dimensional Levels

Enrico Dall'Ara[1], Marta Peña-Fernández[2], Marco Palanca[3], Mario Giorgi[1], Luca Cristofolini[3] and Gianluca Tozzi[2]*

[1] Department of Oncology and Metabolism and INSIGNEO Institute for In Silico Medicine, University of Sheffield, Sheffield, United Kingdom, [2] Zeiss Global Centre, School of Engineering, University of Portsmouth, Portsmouth, United Kingdom, [3] School of Engineering and Architecture, Alma Mater Studiorum – Università di Bologna, Bologna, Italy

Accurate measurement of local strain in heterogeneous and anisotropic bone tissue is fundamental to understand the pathophysiology of musculoskeletal diseases, to evaluate the effect of interventions from preclinical studies, and to optimize the design and delivery of biomaterials. Digital volume correlation (DVC) can be used to measure the three-dimensional displacement and strain fields from micro-computed tomography (μCT) images of loaded specimens. However, this approach is affected by the quality of the input images, by the morphology and density of the tissue under investigation, by the correlation scheme, and by the operational parameters used in the computation. Therefore, for each application, the precision of the method should be evaluated. In this paper, we present the results collected from datasets analyzed in previous studies as well as new data from a recent experimental campaign for characterizing the relationship between the precision of two different DVC approaches and the spatial resolution of the outputs. Different bone structures scanned with laboratory source μCT or synchrotron light μCT (SRμCT) were processed in zero-strain tests to evaluate the precision of the DVC methods as a function of the subvolume size that ranged from 8 to 2,500 μm. The results confirmed that for every microstructure the precision of DVC improves for larger subvolume size, following power laws. However, for the first time, large differences in the precision of both local and global DVC approaches have been highlighted when SRμCT or *in vivo* μCT images were used instead of conventional *ex vivo* μCT. These findings suggest that *in situ* mechanical testing protocols applied in SRμCT facilities should be optimized to allow DVC analyses of localized strain measurements. Moreover, for *in vivo* μCT applications, DVC analyses should be performed only with relatively course spatial resolution for achieving a reasonable precision of the method. In conclusion, we have extensively shown that the precision of both tested DVC approaches is affected by different bone structures, different input image resolution, and different subvolume sizes. Before each specific application, DVC users should always apply a similar approach to find the best compromise between precision and spatial resolution of the measurements.

Keywords: bone, strain, digital volume correlation, deformable registration, micro-computed tomography, precision

OPEN ACCESS

Edited by:
Davide Bigoni, University of Trento, Italy

Reviewed by:
Ivan Argatov, Technische Universität Berlin, Germany
Alberto Salvadori, University of Brescia, Italy

****Correspondence:***
Enrico Dall'Ara
e.dallara@sheffield.ac.uk

Specialty section:
This article was submitted to Mechanics of Materials, a section of the journal Frontiers in Materials

Received: *25 July 2017*
Accepted: *09 October 2017*
Published: *08 November 2017*

Citation:
Dall'Ara E, Peña-Fernández M, Palanca M, Giorgi M, Cristofolini L and Tozzi G (2017) Precision of Digital Volume Correlation Approaches for Strain Analysis in Bone Imaged with Micro-Computed Tomography at Different Dimensional Levels. Front. Mater. 4:31. doi: 10.3389/fmats.2017.00031

INTRODUCTION

This paper investigates comprehensively the precision of two digital volume correlation (DVC) approaches that can be used to measure the full three-dimensional (3D) displacement and strain fields of heterogeneous materials. While these approaches have huge potential for the assessment of complex material deformation and the validation of predictions of computational models, the fact that there is no other way of measuring such properties makes the validation of their output difficult. In this article, we will focus on a natural biomaterial: bone tissue. Even though previously other studies have investigated the precision of DVC methods, in this paper for the first time we report data obtained from five datasets acquired from different bone structures, scanned with three different techniques, and analyzed with two different DVC approaches, providing the most comprehensive dataset available in the literature to date.

Bone is a complex heterogeneous, anisotropic and hierarchical material for which the separation of scales does not hold (Viceconti, 2012). Therefore, its mechanical behavior (i.e., the load at which a certain bone fails or its toughness) depends on the intrinsic properties of the material that can be measured at the micro-scale (i.e., the heterogeneous distribution of extracellular matrix within the bone, its orientation, its mineralization, etc.), which depend on the properties of the material at the nano-scale (i.e., the molecular level, where collagen fibers and mineral grains are arranged). For example, to predict when and where a bone fracture will occur, the loading conditions on the whole bone (Cristofolini et al., 2010b; Dall'Ara et al., 2013b) as well as the density distribution and microarchitecture of the bone tissue (Bouxsein, 2003) need to be accounted for. Similarly, to evaluate the effect of mechanical stimuli (Birkhold et al., 2017), aging (Razi et al., 2015), musculoskeletal pathologies (e.g., osteoporosis imbalances the bone homeostasis toward reabsorption) (Badilatti et al., 2016), or interventions to treat them (Levchuk et al., 2014), the local mechanical properties on the different bone structural units (BSUs, i.e., trabeculae or osteons) need to be accurately quantified over the whole bone. Another example is the study of the effect of biomaterials such as injectable bone cements (Danesi et al., 2016) or systems of screws and plates on the bone mechanical properties and fracture healing (Widmer Soyka et al., 2013), where the constructs need to bio-integrate with the tissue and provide mechanical integrity to the organ. This problem can be tackled by the reliable estimation of the 3D internal full-field distribution of local properties, such as displacements and strain for the considered construct in different loading conditions. However, such measurements are not trivial because standard methods such as strain gauges (Cristofolini et al., 2010a, 2013), or digital image correlation (Gustafson et al., 2017) can only provide information on the external surface. Two options are left. The local properties can be computed with specimen-specific computational models, such as the finite element (FE) approach based on clinical (Dall'Ara et al., 2012, 2013a) or preclinical high-resolution (Levchuk et al., 2014; Lu et al., 2017) images. Nevertheless, it should be noted that the models have to be rigorously validated (Anderson et al., 2007; Jones and Wilcox, 2008) for prediction of both apparent (Schileo et al., 2008; Wolfram et al., 2010; Zysset et al., 2013; Schwiedrzik et al., 2016) and local (Zauel et al., 2006; Chen et al., 2017; Costa et al., 2017; Gustafson et al., 2017) properties before their application.

The only method that currently allows for 3D measurements within the bone structure is DVC combined with *in situ* mechanical testing within a micro-computed tomography (μCT) imaging system. This method, which is based on the deformable registration (i.e., allowing the possibility of the object to deform between the two scans) of high-resolution images of the undeformed and deformed structure, has been used to study the deformation in biological tissues and biomaterials (Bay et al., 1999; Liu and Morgan, 2007; Hussein et al., 2012; Madi et al., 2013; Gillard et al., 2014; Danesi et al., 2016) and to validate FE models based on μCT (Zauel et al., 2006; Chen et al., 2017; Costa et al., 2017) or clinical CT (Jackman et al., 2016; Palanca et al., 2017b) images. For extensive review of the literature about the applications of DVC for studying bone deformation, please refer to two recent reviews (Roberts et al., 2014; Grassi et al., 2016). Nevertheless, the accuracy and precision of the DVC in measuring the displacements depend on the quality of the input images and such errors in displacements can be amplified for the strain field, once differentiated. DVC algorithms showed errors in the displacement measurements of a fraction of voxel (precision of 0.0004–0.115 voxels) (Zauel et al., 2006; Liu and Morgan, 2007; Dall'Ara et al., 2014; Roberts et al., 2014). Nevertheless, a compromise must always be accepted between the precision of the DVC measurements and the measurement spatial resolution. In fact, the larger is the subvolume size (in local DVC) or the nodal spacing (NS, in global DVC), which represents the distance between two independent measurements of displacement, the lower are the random errors associated with the measurement (Dall'Ara et al., 2014; Palanca et al., 2015). There is no single optimal solution for all cases, but an adaptation of the method for different bone structures and image resolutions is required. Moreover, considering that there is no other measurement technique that allows evaluating the 3D bone deformations within heterogeneous structures, the precision of the method is typically estimated by registering repeated scans of the same undeformed specimen ("zero-strain" condition). Other approaches have been identified to test the precision of the method in measuring non-zero deformation fields virtually imposed to the acquired images (Christen et al., 2012). However, such methods do not account for the image noise and tend to underestimate the uncertainties. Some recent studies have estimated the precision of the DVC algorithms on repeated scans of loaded structures or in relation to virtual homogeneous deformations applied to repeated scans (Palanca et al., 2017a). However, considering the novelty of these approaches, only the precision of one DVC algorithm has been assessed on one dataset, which is not enough to generalize the findings, yet.

During the last 4 years, our groups have reported the results from zero-strain tests performed on several bone structures acquired with different μCT techniques. The uncertainties of a global (BoneDVC, formally referred to as "ShIRT-FE") and of a commercial local (DaVis, LaVision, Germany) DVC method were therefore evaluated for several bone structures, at different dimensional levels. This paper is written for potential users of DVC and of DVC data, with the aim of providing an overview

of the magnitude of the errors and of their trend, for different applications. To comprehensively present the precision of two DVC approaches, the results obtained in previous studies on different bone structures and at different dimensional levels were integrated with new results obtained from high-resolution images of trabecular bone with and without biomaterials and from *in vivo* and *ex vivo* analyses of the mouse tibia.

MATERIALS AND METHODS

In this article, data collected in several previous studies have been integrated to new datasets to provide a comprehensive understanding of the relationship between the precision of two DVC approaches and their spatial resolution for different microstructure, and for different quality of the input images. In particular, the previously examined datasets consist in results from trabecular and cortical bone scanned with μCT (Dall'Ara et al., 2014; Palanca et al., 2015) and with synchrotron light μCT (SRμCT) (Palanca et al., 2017a), from vertebral bodies with and without injected biomaterial scanned with μCT (Palanca et al., 2016; Tozzi et al., 2017), and mice tibiae scanned with SRμCT (Palanca et al., 2017a). Moreover, two new datasets from SRμCT scans of trabecular bone and biomaterials and from *in vivo* and *ex vivo* μCT scans of the mouse tibia were included in this study. More details for each study are reported in **Table 1**, **Figure 1** and below.

In these studies, the precision of the DVC method was evaluated in a particular condition of zero-strain, by registering repeated scans of the same object. The parameters of the scanning procedures are reported in **Table 2**. For the different datasets a global or a local (or both), DVC approaches were used to estimate the bone strain and the precision of the methods are reported in this study in function of the chosen subvolume size. For a more detailed description of the methods and of the results for each study (effect of image processing, results on displacement, etc.), the reader should refer to the individual publications reported in **Table 1**.

In the following sub-chapters, the two DVC algorithms used in these studies will be presented, together with a brief description of the samples and scanning procedures.

TABLE 1 | Summary of the information about the studies, the results of which are reported in this manuscript for different dimensional levels, origins of the bones, volume of interest (VOI), scanning condition, and the total number of volumes of interest (VOIs) where the measurements were performed (Nr VOIs).

Reference	Level	Origin	VOI	Condition	Nr VOIs
Dall'Ara et al. (2014),	Tissue	Bovine	Trabecular	*Ex vivo*	2
Palanca et al. (2015)	Tissue	Bovine	Cortical	*Ex vivo*	1
Tozzi et al. (2017)	Tissue	Porcine	Trabecular	*Ex vivo*	5
	Tissue	Porcine	Cement	*Ex vivo*	5
	Tissue	Porcine	Trabecualar with cement	*Ex vivo*	5
	Tissue	Porcine	Trabecular and cortical	*Ex vivo*	5
Palanca et al. (2016)	Organ	Porcine	Vertebral bodies	*Ex vivo*	5
	Organ	Porcine	Vertebral bodies with cement	*Ex vivo*	5
Palanca et al. (2017a)	Tissue	Bovine	Trabecular	*Ex vivo*	6
	Tissue	Bovine	Cortical	*Ex vivo*	8
	Tissue	Murine	Proximal tibia	*Ex vivo*	8
This publication	Organ	Murine	Whole tibia	*In vivo*	7
	Organ	Murine	Whole tibia	*Ex vivo*	4
This publication	Tissue	Ovine	Trabecular with biomaterial	*Ex vivo*	4
	Tissue	Ovine	Trabecular	*Ex vivo*	1

DVC Approaches and Estimation of the Precision

Both DVC approaches used in the studies presented in this article are based on a similar principle: two high-resolution 3D input images of the same object in undeformed and deformed configurations are imported and the algorithms compute a field of displacements, which minimizes the differences between the deformed images and the registered images (undeformed images after the application of the field of displacement). The field of displacement is then differentiated into a field of strain. The main features of the two methods are briefly reported hereafter.

BoneDVC (Previously Known As ShIRT-FE)

This global DVC (Dall'Ara et al., 2014) consists in computing the displacement map by using the Sheffield Image Registration Toolkit (ShIRT) (Barber and Hose, 2005; Barber et al., 2007; Khodabakhshi et al., 2013). With BoneDVC, a grid with selectable nodal spacing (NS, or subvolume, or grid size) is superimposed to the images to be registered. The deformable registration equations are solved at the nodes of the grid to evaluate the displacement field. The procedure consists in finding the displacement functions $u(x, y, z)$, $v(x, y, z)$, and $w(x, y, z)$ that transforms the reference image $\boldsymbol{f}(x, y, z)$ into the deformed image $\boldsymbol{m}(x', y', z')$. An additional intensity displacement function $c(x, y, z)$ is included to account for potential changes in the gray levels. For small displacement, the following equation should be solved for each voxel:

$$\boldsymbol{f}-\boldsymbol{m}\approx\frac{1}{2}\left(u\left(\frac{\partial \boldsymbol{f}}{\partial x}+\frac{\partial \boldsymbol{m}}{\partial x}\right)+v\left(\frac{\partial \boldsymbol{f}}{\partial y}+\frac{\partial \boldsymbol{m}}{\partial y}\right)+w\left(\frac{\partial \boldsymbol{f}}{\partial z}+\frac{\partial \boldsymbol{m}}{\partial z}\right)-c\left(\boldsymbol{f}+\boldsymbol{m}\right)\right).$$

However, this problem is underdetermined and the algorithm solves the equations only in the nodes of the cubic grid superimposed to the images. The displacements are interpolated with a tri-linear function between the nodes. Therefore, the problem is solving the following system of equations for the coefficients $\boldsymbol{a}$ of the displacement functions:

$$\begin{cases} u=\sum_i a_{xi}\varphi_i \\ v=\sum_i a_{yi}\varphi_i \\ w=\sum_i a_{zi}\varphi_i \end{cases}.$$

To provide a smooth solution, the algorithm includes a term based on the Laplacian operator $\boldsymbol{L}$, and the coefficient λ that weights the relative importance of smoothing:

$$(\boldsymbol{f}-\boldsymbol{m})=(\boldsymbol{T}^T\boldsymbol{T}+\lambda\boldsymbol{L}^T\boldsymbol{L})\boldsymbol{a}$$

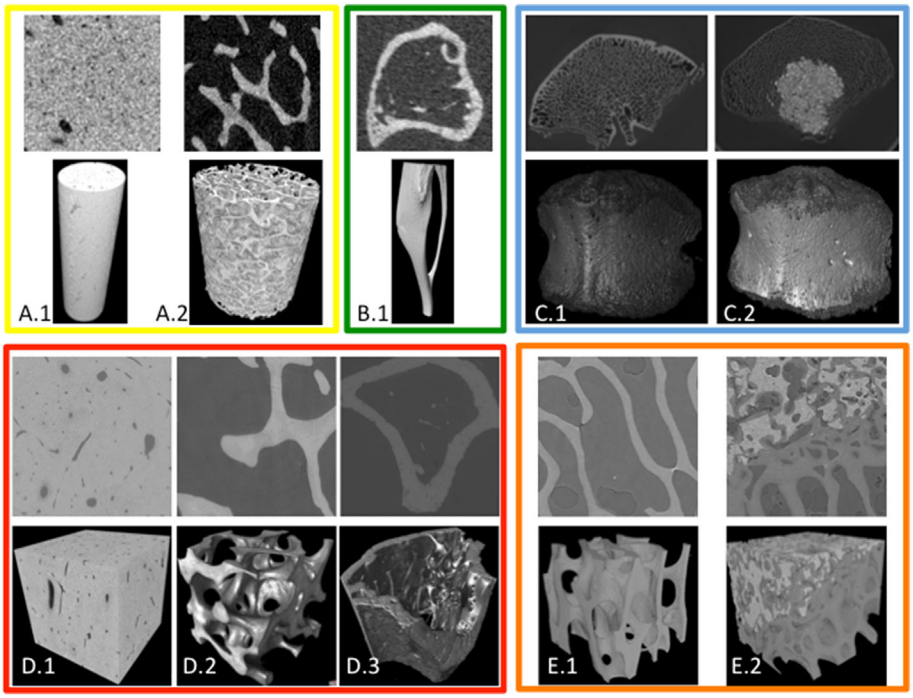

FIGURE 1 | Overview of the different image types used for the deformable registrations with BoneDVC and/or DaVis-DC. For each dataset, a typical cross-section (top) and a 3D image reconstruction (bottom) are reported. Dataset include cortical **(A.1)** and trabecular **(A.2)** bone scanned with laboratory micro-computed tomography (μCT) at 10 μm voxel size (dimension of the 2D images: 1.79 mm × 1.79 mm); mouse tibiae **(B.1)** scanned with *in vivo* μCT at 10.4 μm voxel size (dimension of the 2D image: 4.11 mm × 4.11 mm); porcine vertebrae with **(C.2)** or without **(C.1)** biomaterial scanned with μCT at 39 μm voxel size (dimension of the 2D images: 27.61 mm × 19.5 mm); cortical bone **(D.1)**, trabecular bone **(D.2)**, and proximal mouse tibia **(D.3)** scanned with synchrotron light μCT (SRμCT) at 1.6 μm voxel size (dimension of the 2D images: 1.6 mm × 1.6 mm); ovine trabecular bone with **(E.2)** and without **(E.1)** biomaterial scanned with SRμCT at 2.6 μm voxel size (dimension of the 2D images: 2.60 mm × 2.60 mm).

where $\boldsymbol{T}$ is a $K \times N$ matrix (K number of voxels in the image, and N number of nodes in the grid). $\boldsymbol{T}$ is derived from integrals of the image gradients multiplied by the basis functions of the displacements. For large displacements, the method can iterate to a correct solution. The grid is then converted into a mesh of 8-noded hexahedrons and the displacements are then imported into a FE software package (Ansys Mechanical APDL v.14.0, ANSYS, Inc., Canonsburg, PA, USA) to differentiate them into a strain field and to post-process the data efficiently.

DaVis-DC

This local approach is implemented in a commercial package (DaVis LaVision, Germany) that uses a direct correlation (DC) function to match the subvolumes (hereby referred to as DaVis-DC). With DaVis-DC, the 3D images are divided into smaller subvolumes, which are then independently correlated as a discrete function of gray levels. A piece-wise linear shape function for the reference-deformed mapping and a normalized cross-correlation function, r_{DaVis}, based on gray level gaps are used:

$$r_{\mathrm{DaVis}} = \frac{\sum_{\underline{X}(x,y,z)\in \mathrm{VOI}} f(x,y,z)g(x',y',z')}{\sqrt{\sum_{\underline{X}(x,y,z)\in \mathrm{VOI}} f(x,y,z)^2 \sum_{\underline{X}^*(x,y,z)\in \mathrm{VOI}} g(x',y',z')^2}}$$

where X (x, y, z) and X^*(x, y, z) refer to coordinates (in voxels) of a same point in the reference state and in the deformed state; f and g are the gray levels, respectively, in the reference and deformed images. A third-order spline interpolation is used. This process provides a full 3D field of displacement vectors, which describes the mapping from reference to deformed state. The displacement field is then converted into strain field using the centered finite differences scheme.

The precision of the DVC methods for displacement measurements was quantified by reporting the standard deviation of displacement along x, y, and z directions. As it was found that in a first approximation the errors affecting strains were isotropic (Palanca et al., 2015), the precision of the DVC methods was quantified by reporting the standard deviation of the strain error (SDER), computed as the standard deviation of the mean of the components of strain computed for each measurement point [referred as "precision" in Liu and Morgan (2007)]. In case more specimens were analyzed for each bone type, median and standard deviation of the SDER were computed for each sample. In case more specimens were analyzed for each bone type, median of the measurement was computed for each sample.

Datasets

μCT Scans of Bovine Trabecular and Cortical Bone (Dall'Ara et al., 2014; Palanca et al., 2015)

A trabecular bone (8 mm in diameter, 12 mm in length) and a cortical bone (3 mm in diameter and 20 mm in length) cylinders

TABLE 2 | Summary of the scanning and DVC parameters used in the different studies, the results of which are reported in this article.

Reference	Imaging technique	Scanning machine	Scanning parameters	Image voxel size (μm)	Filters	Integration time (ms)	Rotation step (°)	Subvolume BoneDVC (vox)	Subvolume DaVis-DC (vox)
Dall'Ara et al. (2014), Palanca et al. (2015)	μCT	Skyscan 1172	59 kV, 10 W 70 kV, 10 W	10.0	1.0 mm Al	1,180	0.710	5, 10, 15, 20, 25, 30, 35, 40, 45, 50	8, 10, 16, 20, 24, 28, 34, 40, 44, 52
Tozzi et al. (2017)	μCT	Nikon XTH225	88 kV, 110–115 μA	39.0	None	2,000	0.230	16, 48	16, 48
Palanca et al. (2016)	Micro-computed tomography (μCT)	Nikon XTH225	88 kV, 110–115 μA	39.0	None	2,000	0.230	16, 32, 48, 64, 80, 96, 112	16, 32, 48, 64, 80, 96, 112, 128
Palanca et al. (2017a)	Synchrotron light μCT (SRμCT)	Diamond Light Source I13-2	Polychromatic "pink" beam (5–35 keV)	1.6	0.95 mm C, 2 mm Al, 0.02 mm Ni	53	0.045	10, 15, 20, 25, 50, 75, 100, 150, 200, 250	NA
This publication	μCT	Scanco VivaCT80	55 kV, 145 μA	10.4	0.5 mm Al	200	0.240	10, 20, 30, 40, 50, 60, 70, 80, 90, 100, 110, 120, 130, 140, 150	NA
This publication	SRμCT	Diamond Light Source I13-2	Polychromatic "pink" beam (5–35 keV)	2.6	0.95 mm C, 2 mm Al, 0.06 mm steel	64	0.100	NA	16, 32, 48, 64, 80, 96, 112

were extracted from the femur of a bovine killed for alimentary purposes. In this case, ethics approval was not required as per institutional and national guidelines. Each specimen was scanned twice in saline solution with a μCT system (Skyscan 1172, Bruker, voltage: 59 kV for trabecular bone and 70 kV for cortical bone; power: 10 W; voxel size: 9.96 μm; exposure time: 1,180 ms; rotation step: 0.71; total rotation: 180°; images averages ×2; beam hardening filter: 1 mm Aluminum; height scan: 9.32 mm). After image reconstruction, a parallelepiped with square cross-section of 180 × 180 × 932 voxels was cropped in the central portion of each sample. In the trabecular specimen also a larger region 430 × 430 × 430 voxels was cropped for tests with larger subvolumes. Deformable registrations were run for different subvolume sizes with BoneDVC (5, 10, 15, 20, 25, 30, 35, 40, 45, 50 voxels) and with DaVis-DC (8, 10, 16, 20, 24, 28, 34, 40, 44, 52 voxels).

μCT Scans of Natural and Augmented Porcine Vertebral Bodies (Palanca et al., 2016; Tozzi et al., 2017)

Ten thoracic vertebral bodies were extracted from spines of pigs killed for alimentary purposes. In this case, ethics approval was not required as per institutional and national guidelines. A sample of five vertebrae was addressed for augmentation (referred as "augmented"), with acrylic vertebroplasty cement (Mendec Spine, Tecres Spa, Italy). The other five vertebrae were left untreated (referred as "natural"). The samples were scanned twice in saline solution, inside the chamber of a loading device with a μCT system (XTH225, Nikon Metrology, voltage: 88 kV; power: 10 W; voxel size: 39 μm; exposure time: 2,000 ms; rotation step: 0.23°; total rotation: 360°). Deformable registrations were run for different subvolume sizes (16, 32, 48, 64, 80, 96, 112, 128 voxels) with BoneDVC and DaVis-DC on a parallelepiped of 300 × 300 × 432 voxels cropped inside each vertebral body with and without the augmentation (VOI-1). Moreover, the image of each augmented specimen was cropped in other four VOIs of 152 × 152 × 432 voxels including fully cement-augmented trabecular bone (VOI-2); interface between augmented and non-augmented trabecular bone (VOI-3); trabecular bone (VOI-4), and regions containing both trabecular and cortical bone, with surrounding saline solution (VOI-5). The smaller VOIs were analyzed with BoneDVC and DaVis-DC with subvolume sizes of 16 and 48 voxels.

μCT Scans of Mice Tibiae *In Vivo* and *Ex Vivo* (This Study)

Eleven mouse (C57BL/6J, female, 22 weeks old) tibiae were scanned *in vivo* (seven) or *ex vivo* (four). The images from the seven tibiae scanned *in vivo* were collected from a previous study where mice were anesthetized during scanning (Lu et al., 2015). All procedures were approved by the local Research Ethics Committee of the University of Sheffield (Sheffield, UK). The four *ex vivo* specimens were dissected from mice of same strain, gender, and age, were isolated from the soft tissues, dehydrated and embedded in acrylic resin. Each tibia was scanned twice by using an *in vivo* μCT system (vivaCT80, Scanco Medical, Bruettisellen, Switzerland) with the following

scanning parameters: voltage of 55 keV, intensity of 145 μA, integration time of 200 ms, nominal isotropic image voxel size of 10.4 μm for a total scanning time of approximately 40 min per scan. Beam hardening artifacts were reduced by applying a third-order polynomial correction algorithm provided by the manufacturer based on scans of 1,200 mgHA/cm^3 wedge phantom. Deformable registrations were run for different subvolume sizes with BoneDVC (10, 20, 30, 40, 50, 60, 70, 80, 90, 100, 110, 120, 130, 140, 150 voxels).

Synchrotron μCT Scans of Bovine Cortical and Trabecular Bone and of Proximal Mice Tibiae (Palanca et al., 2017a)

Three tissue types were studied: cortical bones (three cylindrical specimens, 3 mm in diameter, 12 mm in length), trabecular bones cylinders (four cylindrical specimens, 8 mm in diameter, 12 mm in length) both obtained from the femur of a bovine killed for alimentary purposes; and four paired tibiae obtained from two 14-week-old female C57BL/6J mice (Harlan Laboratories, Bicester, UK). All procedures were approved by the local Research Ethics Committee of the University of Sheffield (Sheffield, UK). Each specimen was embedded in acrylic resin and was scanned twice at the Diamond-Manchester Imaging Beamline I13-2 of Diamond Light Source, UK. A filtered (950 μm C, 2 mm Al, 20 μm Ni) polychromatic "pink" beam (5–35 keV) of parallel geometry was used and the scanning parameters were: voxel size 1.6 μm; exposure time 53 ms; rotation step 0.045°; total rotation 180°. Two cubic volumes of interest (VOIs) with side length of 1,000 voxels were cropped from the middle of each cortical and trabecular specimen, and cubic VOIs were selected in the metaphysis of each murine tibia. The VOIs of the trabecular bone and of the mouse tibiae were masked, to evaluate the uncertainties only on bone tissues. Deformed registrations were run with BoneDVC with different subvolume sizes (10, 15, 20, 25, 50, 75, 100, 150, 200, 250, 300 voxels).

Synchrotron μCT Scans of Ovine Trabecular Bone with and without Biomaterials (This Study)

Four bone-biomaterial cylindrical specimens and two trabecular bone cylindrical specimen (4 mm in diameter and 8 mm in length) were extracted from ovine femoral condyles, where biomaterials were implanted after surgically creation of bone defects (Coathup et al., 2016). All procedures were carried out following Ethics approval granted by the Royal Veterinary College and in compliance with the United Kingdom Home Office regulations (Animal Scientific Procedures Act [1986]). Samples were placed in a loading stage (CT5000, Deben Ltd., UK) and immersed in saline solution. Each specimen was scanned twice at the imaging beamline I13-2 of Diamond Light Source, UK. A filtered (950 μm C, 2 mm Al, 60 μm steel) polychromatic "pink" beam (5–35 keV, weighted mean photon energy: 28.6 keV) of parallel geometry was used. Scanning parameters were chosen as following: voxel size: 2.6 μm; exposure time: 64 ms; rotation step: 0.1°; total rotation: 180°. One cubic VOI (1,000 voxels side length) was cropped from the middle of each specimen. To evaluate the uncertainties only in the mineralized tissue, masks were created by applying a non-local means filter (Buades et al., 2011), followed by image segmentation based on Huang's method (Huang and Wang, 1995). The masks were used to create the masked images (original gray levels corresponding to the bone voxels and zero values corresponding to the marrow), on which the deformable registrations (DaVis-DC) were run for different subvolume sizes (16, 32, 48, 64, 80, 96, 112 voxels).

RESULTS

The precisions of the DVC methods as a function of the used subvolume size are summarized in **Figure 2**. As expected for all bone types, the grid size and the SDER were highly correlated through power laws, for both DVC approaches ($0.858 < R^2 < 0.993$, **Table 3**).

As expected, the images with higher quality, obtained with SRμCT, provided the best results, followed by those obtained from *ex vivo* μCT and then those obtained from *in vivo* μCT. Similar trends were found for the two DVC algorithms. These regressions can be used to choose the best compromise between the spatial resolution of the measured displacement and the resulting precision in measuring strains (**Table 3**). In particular, one may fix a level of acceptable strain, and consequently identify the corresponding spatial resolution. If a threshold of 200 με is accepted (one order of magnitude lower than typical strains in bone subjected to physiological loading conditions), the corresponding spatial resolution can be found when images from SRμCT are used (at 1.6 μm for images used for BoneDVC and at 2.6 μm for images used for DaVis-DC) for cortical bone (33 μm for BoneDVC), for trabecular bone (96 μm for BoneDVC, 128 μm for DaVis-DC), as well as for trabecular bone with biomaterials (117 μm for DaVis-DC). Spatial resolutions that would allow the same errors on strains for measurements performed by using laboratory μCT images at the tissue level (voxel size between 10 and 39 μm) were in the range 490–564 μm for BoneDVC and 661–987 μm for DaVis-DC. The worst spatial resolution corresponding to the same errors of 200 με was found for measurements based on *in vivo* and *ex vivo* μCT images of the mouse tibiae (2,832 and 839 μm, respectively, both obtained with BoneDVC).

Only SRμCT-based DVC reached reasonable uncertainties for measurements performed the tissue level [for several BSUs, as trabeculae or osteons; spatial resolution for DVC displacement and strain measurements of 300 μm (Pfeiffer, 1998); from 9 to 46 με, **Table 4**] or at the single BSU level (spatial resolution for DVC displacement and strain measurements below 150 μm; from 21 to 156 με, **Table 4**).

The computation time varied for the different voxel sizes, volumes of interest (VOIs), DVC approach, and post-processing method used, as reported in **Table 5**.

DISCUSSION

The goal of this study was to compare the precision of two DVC algorithms in different applications for measuring bone strains at different dimensional levels and based on images acquired with different techniques and modalities. While in the last decade several studies reported strain distributions on non-homogeneous bone specimens obtained with DVC, this is the first article that

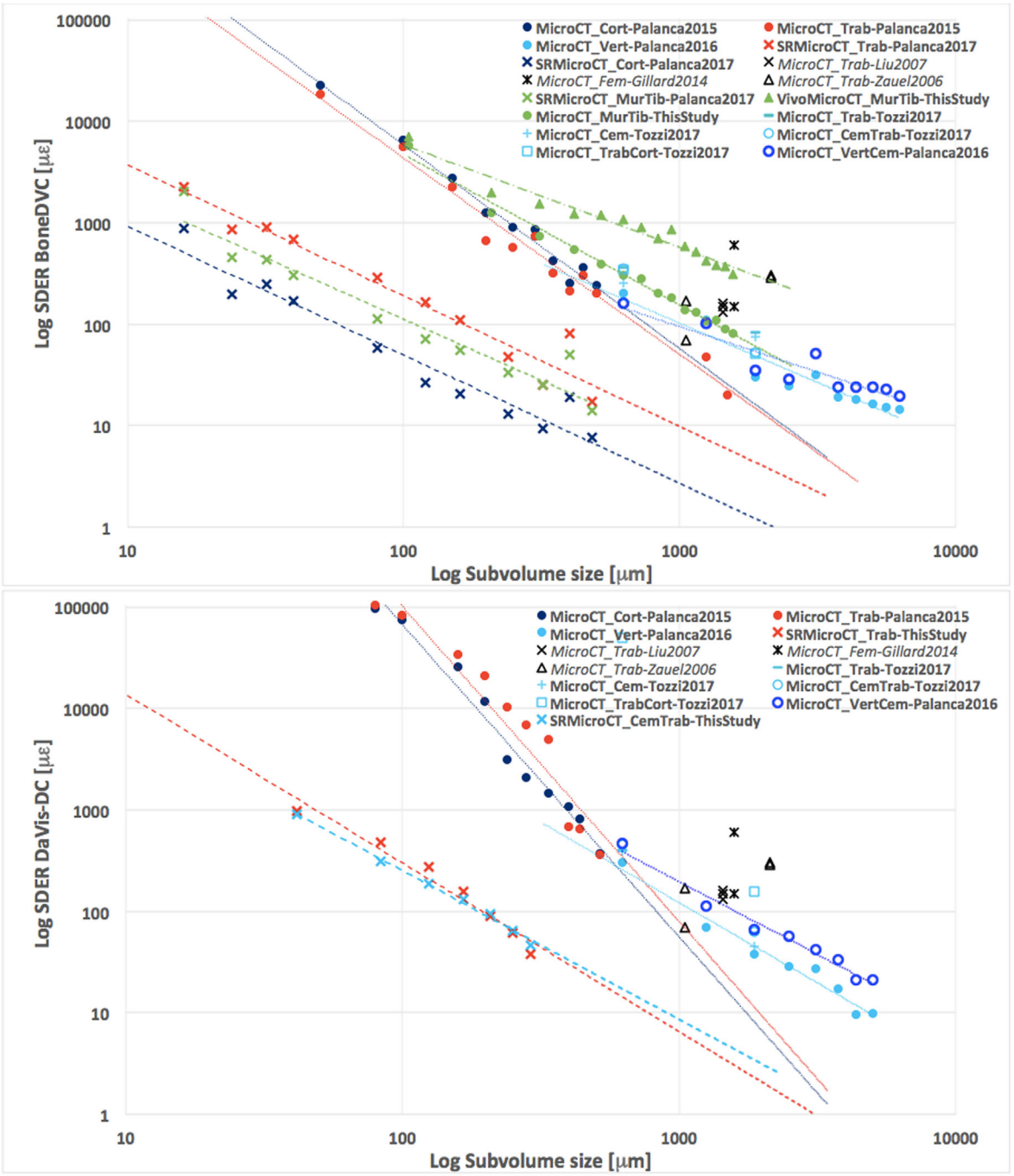

FIGURE 2 | Relationship in logarithmic scale between the standard deviation of the error (SDER; median values in case more specimens were analyzed per group) and the subvolume size for both global (BoneDVC, top) and local (DaVis-DC, bottom) DVC approaches. Dataset include cortical (MicroCT_Cort-Palanca2015) and trabecular (MicroCT_Trab-Palanca2015) bone scanned with laboratory micro-computed tomography (μCT) at 10 μm voxel size; mouse tibiae scanned with *in vivo* (VivoMicroCT_MurTib-ThisStudy) and *ex vivo* (MicroCT_MurTib-ThisStudy) settings with a μCT at 10.4 μm voxel size; porcine vertebrae with (MicroCT_VertCem-Palanca2016) or without (MicroCT_Vert-Palanca2016) biomaterial scanned with μCT at 39 μm voxel size; portions of trabecular (MicroCT_Trab-Tozzi2017), cement (MicroCT_Cem-Tozzi2017), trabecular and cement (MicroCT_CemTrab-Tozzi2017), and trabecular and cortical bone (MicroCT_TrabCort-Tozzi2017) extracted from augmented porcine vertebrae scanned with μCT at 39 μm voxel size; cortical (SRmicroCT_Cort-Palanca2017), trabecular (SRmicroCT_Trab-Palanca2017) and mouse tibia (SRmicroCT_MurTib-Palanca2017) scanned with synchrotron light μCT (SRμCT) at 1.6 μm voxel size; ovine trabecular bone with (SRmicroCT_CemTrab-ThisStudy) and without (SRmicroCT_Trab-ThisStudy) scanned with SRμCT at 2.6 μm voxel size. In order to do not overcomplicate the figure, the error bars were not reported and the interested reader should refer to the specific publications for this information. Data extracted form the literature have been also added for both graphs (MicroCT_Trab-Liu2007 for data obtained from bovine distal femur, bovine proximal tibia, rabbit distal femur, rabbit proximal tibia, rabbit vertebral body, and human vertebral body, all acquired with μCT at 36 μm voxel size, MicroCT_Trab-Zauel2006 for data obtained from human femoral and vertebral trabecular bone acquired with μCT at 35 μm voxel size; MicroCT_Fem-Gillard2014 for data obtained from porcine femoral trabecular bone acquired with μCT at 24.6 μm).

TABLE 3 | Coefficients of power law regressions (*a*, *b*) and the coefficient of determination (R^2) between the standard deviation of the error (SDER) and the "subvolume" size for the results obtained in the different studies reported in this manuscript.

$Y = a*X^b$	VOI	Condition	Digital volume correlation (DVC)	R^2	*a*	*b*	Subvolume for standard deviation of the strain error (SDER) = 200με (μm)
Dall'Ara et al. (2014), Palanca et al. (2015)	Trabecular	*Ex vivo*	BoneDVC	0.977	32874690	−1.939	490
			DaVis	0.921	164478898569	−3.106	742
	Cortical	*Ex vivo*	BoneDVC	0.983	60471448	−2.008	536
			DaVis	0.976	96263509437	−3.079	661
Palanca et al. (2016)	Vertebral bodies	*Ex vivo*	BoneDVC	0.919	335443	−1.172	564
			DaVis	0.972	6863976	−1.583	733
	Vertebral bodies with cement	*Ex vivo*	BoneDVC	0.858	46616	−0.897	436
			DaVis	0.975	3991596	−1.436	987
Palanca et al. (2017a)	Trabecular	*Ex vivo*	BoneDVC	0.941	72017	−1.289	96
	Cortical	*Ex vivo*	BoneDVC	0.938	16968	−1.266	33
	Proximal tibia	*Ex vivo*	BoneDVC	0.932	29416	−1.210	62
This publication	Whole tibia	*In vivo*	BoneDVC	0.954	613219	−1.010	2,832
	Whole tibia	*Ex vivo*	BoneDVC	0.990	4303780	−1.482	839
This publication	Trabecular with biomaterial	*Ex vivo*	DaVis	0.993	214132	−1.465	117
	Trabecular	*Ex vivo*	DaVis	0.962	641729	−1.664	128

The last column represents the calculated value of the subvolume for a SDER equal to 200 με.

provides a comprehensive understanding about how the precision of these methods (evaluated in a simple case of full-field zero-strain on repeated scans) is affected by the different tissue structures, by the input images, and by the algorithms.

The results from the different studies confirmed that the precision in the measurements of displacement of the two tested DVC approaches are in the order of a fraction of voxel, with smaller errors for the global DVC compared to the local one (**Table 4**). As expected, for all the different studies that were compared in this article, strong correlations were found between the uncertainties of the DVC-computed strains (expressed as SDER), and the spatial distance between two independent measurements. This result confirms those obtained from previous studies (Roberts et al., 2014) and extend it for different bone and bone-biomaterial structures. The equations describing such trends (**Table 3**) provide a way to choose the input parameters of the DVC according to the different applications. In particular, the elastic registrations based on higher resolution images (~1.6 μm voxel size, obtained with SRμCT) allowed achieving uncertainties of 200 με for measurement spatial resolution of 30–100 μm for all the types of microstructure considered (bovine cortical bone, bovine trabecular bone, and mouse metaphysis), allowing strain measurements within BSUs. Conversely, μCT-based DVC measurements (~10 μm voxel size) showed the same strain errors (200 με) only for larger grid size, in the order of 400–600 μm, allowing for 3D measurements performed on subvolumes including more BSUs, but still enabling to detect strain gradients over the specimens. Such measurements can be used to classify regions at high or low localized strains as for example the beginning of failure in trabecular or cortical bone. It should be noted though that the strain values in this case refer to subvolumes containing both the mineralized tissue and the marrow. When DVC is applied to μCT images acquired with lower resolution (~40 μm voxel size), reliable information about the heterogeneous strain field can be obtained only with larger subvolumes, up to 1,000 μm, which contain several BSUs. As expected, the worst case scenario among those tested was related to the *in vivo* μCT images of the mouse tibia (~10.4 μm voxel size), where the subvolume size required to obtain the same strain errors (200 με) was as large as ~2,800 μm, which is even larger than the typical diameter of the bone (~1,000 μm). It should be noted that this case represents a very extreme case where the measurement resolution is affected by several artifacts (i.e., moving artifacts and lower contrast due to the lower energy), which may considerably affect the noise in the images and disturb the deformable registration. Therefore, with the current settings, it is hard to think of using such a methodology *in vivo*, unless large deformations are applied and larger errors can be accepted (e.g., hundreds of με). This would be feasible, for example, when strain measurements are used to classify between bone strained below or above yield [7,000–10,000με (Bayraktar et al., 2004)].

The results summarized here were obtained from the best conditions studied on the different applications. For example, we noted that masking the bone tissue in non-homogeneous structures such as the trabecular bone and mouse tibia improved the precision of the DVC only if based on high-resolution SRμCT (Palanca et al., 2017a), but not on standard laboratory μCT images (Dall'Ara et al., 2014). Furthermore, for the local DVC approach, it is clear that a metric based on DC should be preferred to analyses performed after Fourier Transformation (Palanca et al., 2015). Then, the best settings were used, similar trends were found for both DVC algorithms, with the global DVC performing better in the experiments where both algorithms were tested on the same specimens for the selected dimensional level (**Tables 3** and **4**), but with slightly higher computational cost to run the registration (**Table 5**).

Both DVC approaches summarized in this paper outperform those reported in the literature for similar structures in terms

TABLE 4 | Overview of the standard deviation of the error (SDER) for the strain measurements and standard deviation for the different components of the displacement (StDev DispX, StDev DispY, and StDev DispZ) found in the different studies for a subvolume size that could be used for measurements at the tissue level (~300 μm) and at the bone structural unit (BSU) level (~150 μm).

Precision for BSU	VOI	Condition	Digital volume correlation (DVC)	Subvolume closest to 300 μm (voxels)	Physical dimension closest to 300 μm (μm)	Subvolume closest to 150 μm (voxels)	Physical dimension closest to 150 μm (μm)	SDER 300 μm (με)	StDev DispX 300 μm (μm)	StDev DispY 300 μm (μm)	StDev DispZ 150 μm (μm)	SDER 150 μm (με)	StDev DispX 150 μm (μm)	StDev DispY 150 μm (μm)	StDev DispZ 150 μm (μm)
Dall'Ara et al. (2014), Palanca et al. (2015)	Trabecular	*Ex vivo*	BoneDVC	30	299	15	149	742	0.63	0.64	0.51	2,270	1.04	1.05	0.91
			DaVis	28	279	16	159	6,865	4.33	5.22	3.86	33,957	17.66	17.33	13.06
	Cortical	*Ex vivo*	BoneDVC	30	299	15	149	849	0.70	0.67	0.61	2,781	1.45	1.43	1.28
			DaVis	28	279	16	159	2,063	2.92	2.30	3.65	25,747	14.42	11.84	19.24
Palanca et al. (2016)	Vertebral bodies	*Ex vivo*	BoneDVC	16	624	N.A.	N.A.	202	N.A.	N.A.	N.A.	N.A.	N.A.	N.A.	N.A.
			DaVis	16	624	N.A.	N.A.	302	N.A.	N.A.	N.A.	N.A.	N.A.	N.A.	N.A.
	Vertebral bodies with cement	*Ex vivo*	BoneDVC	16	624	N.A.	N.A.	160	1.22	1.27	1.13	N.A.	N.A.	N.A.	N.A.
			DaVis	16	624	N.A.	N.A.	471	1.87	1.49	2.18	N.A.	N.A.	N.A.	N.A.
Palanca et al. (2017a)	Trabecular	*Ex vivo*	BoneDVC	200	320	100	160	26	0.03	0.04	0.08	64	0.04	0.05	0.09
	Cortical	*Ex vivo*	BoneDVC	200	320	100	160	9	0.03	0.02	0.05	21	0.03	0.03	0.05
	Proximal tibia	*Ex vivo*	BoneDVC	200	320	100	160	41	0.08	0.07	0.04	55	0.08	0.07	0.05
This publication	Whole tibia	*In vivo*	BoneDVC	30	312	20	208	1,547	4.49	7.29	3.48	2,003	4.67	7.48	4.03
	Whole tibia	*Ex vivo*	BoneDVC	30	312	20	208	745	1.20	1.94	1.28	1,250	1.39	2.37	2.30
This publication	Trabecular with biomaterial	*Ex vivo*	DaVis	112	291	64	166	46	0.08	0.23	0.14	131	0.12	0.35	0.15
	Trabecular	*Ex vivo*	DaVis	112	291	64	166	38	0.21	0.24	0.18	156	0.29	0.37	0.27

of precision in the strain measurements [trabecular bone (Bay et al., 1999; Liu and Morgan, 2007; Gillard et al., 2014) and trabecular bone-cement (Zhu et al., 2016) specimens], with the exception of Zauel et al. (2006), where similar errors were found but only after substantial smoothing of the displacement field, which may hide peaks of strain in applications under realistic loading conditions.

The DVC outputs can also be used to quantitatively validate the field of local properties identified by computational models such as the FE method (Zauel et al., 2006). The typical scheme is to acquire two images of the undeformed and deformed bone structure, to apply the DVC to measure the displacement and strain fields, to generate the FE models from the underformed configuration, to impose the DVC-measured displacement field at the boundary of the FE model (Zauel et al., 2006), and to compare the experimental and computational outputs in the middle portion of the specimen (far enough from the conditions imposed at the boundary). This approach has been used to evaluate the accuracy of the models in predicting the field of displacements for trabecular bone specimens (Zauel et al., 2006; Chen et al., 2017) and vertebral bodies (Jackman et al., 2016; Costa et al., 2017). The good precision of the DVC in measuring the field of displacements (**Table 4**) allows in most cases to test the ability of the models in predicting the local displacements. However, it should be noted that the limited precision of DVC in measuring the strain field with a spatial resolution of a few tens of μm [typical size of the finite elements at the tissue level (van Rietbergen et al., 1995)], makes it impossible to accurately validate the FE predictions of strain. We have shown that this could be potentially done if high-resolution SRμCT images were used (**Figure 2**; **Table 4**) but unfortunately for such application the challenge in performing repeated imaging of the specimens under loading without inducing structural damage to the irradiated tissue remains (Barth et al., 2011).

This method for evaluating and comparing the precision of the two DVC approaches has three main limitations: (1) the precision is usually evaluated on different specimens, (2) the precision is evaluated in case of very simple strain scenario (zero-strain), and (3) different parameters for the two DVC algorithms (optimization metric, interpolation of displacements, differentiation method) were used. To overcome to the first limitation, we suggest to publish in the public domain the images used to test the DVC precision in the different publications. We started this process in previous studies (Palanca et al., 2016; Tozzi et al., 2017; Palanca et al., 2017a) and we suggest that also future publications should share the input datasets or use the published images as benchmark. The reader is encourage to look at the figshare links in the acknowledgments for the complete or partial datasets used in the presented studies and contact the corresponding author for the complete datasets. A robust solution to overcome the second limitation has not been found yet due to the intrinsic difficulty of imposing a known, non-uniform field of internal strains. One possible approach to study the precision of the DVC predictions under realistic loading condition is to register repeated scans of the structure under loading. When applied to the mouse tibia (unpublished data), this method showed similar precision as in the case of unloaded or preloaded structures, but still does

TABLE 5 | Estimated time required for the different applications split for the different parts of the procedure, from the scanning to the image pre-processing, digital volume correlation (DVC) running time, and post-processing of the results.

Computation time	VOI	Condition	DVC	VOI size (vox)	Approximate scanning time (min/specimen)	Approximate pre-processing time (min/specimen)	Approximate registration time per CPU for subvolume equal to 48, 50, or 52 voxels (min/specimen)	Approximate post-processing time (min/specimen)	Approximate total time for subvolume equal to 48, 50, or 52 (min/specimen)
Dall'Ara et al. (2014), Palanca et al. (2015)	Trabecular	*Ex vivo*	BoneDVC	180 × 180 × 932	15	30	2	5	58
			DaVis	180 × 180 × 932	15	30	1	5	55
	Cortical	*Ex vivo*	BoneDVC	180 × 180 × 932	15	30	2	5	58
			DaVis	180 × 180 × 932	15	30	1	5	55
Palanca et al. (2016)	Vertebral bodies	*Ex vivo*	BoneDVC	300 × 300 × 432	90	15	8	5	142
			DaVis	300 × 300 × 432	90	15	1	5	114
	Vertebral bodies with cement	*Ex vivo*	BoneDVC	300 × 300 × 432	90	15	8	5	142
			DaVis	300 × 300 × 432	90	15	1	5	114
Palanca et al. (2017a)	Trabecular	*Ex vivo*	BoneDVC	1,000 × 1,000 × 1,000	4	120	15	10	194
	Cortical	*Ex vivo*	BoneDVC	1,000 × 1,000 × 1,000	4	120	15	10	194
	Proximal tibia	*Ex vivo*	BoneDVC	1,000 × 1,000 × 1,000	4	120	15	10	194
This publication	Whole tibia	*In vivo*	BoneDVC	~400 × 400 × 1200	40	20	4	5	81
	Whole tibia	*Ex vivo*	BoneDVC	~100 × 400 × 1,200	40	20	4	5	81
This publication	Trabecular with biomatetial	*Ex vivo*	DaVis	1,000 × 1,000 × 1,000	2	300	2	10	320
	Trabecular	*Ex vivo*	DaVis	1,000 × 1,000 × 1,000	2	300	2	10	320

The results are reported for a subvolume size equal close to 50 voxels (48, 50, or 52 voxels according to the different applications). As the registrations have been run with different workstations, we report the approximate registration time for each CPU and for the approximate total time assuming the registrations were run with a workstation with four CPUs.

not allow measuring the accuracy of the method due to the fact that the field of displacement under loading is not known (and cannot be measured with independent measurement systems). In recent studies (Palanca et al., 2017a), we have suggested to perform analyses on repeated scans where one of them is virtually deformed with a known strain field, for estimating both accuracy and precision of the DVC methods. Nevertheless, more parameters should be accounted for during the generation of the virtually loaded images (e.g., interpolation), the application of the load (tension, compression, torsion), the load level, and their effect on the different bone structures, increasing significantly the labor, the computation, and post-processing time of the analyses. We believe that this approach should be used at least in one loading scenario and loading level until a proper standardization and benchmarking is provided. Furthermore, so far only virtually imposed affine deformations have been tested: this does not enable testing the DVC algorithms under realistic heterogeneous strain fields. Therefore, future work needs to be done to simulate a realistic loading condition, for example, imposing realistic boundary conditions and displacement (and strain) distributions derived from FE models of the constructs. To overcome the third limitation (i.e., different algorithms used for the different DVC approaches), the comparison between the two DVC methods will be further investigated for a subgroup of data, to identify which parts of the algorithms could lead to the best precision. Finally, a further limitation of this study is that some of the dataset were not processed with either one or the other DVC approach.

In conclusion in this study, we report a comprehensive analysis of the precision of two DVC methodologies for different bone structures, the microarchitecture of which has been acquired with different X-rays imaging techniques. These data can be used by the research community intending to employ DVC measurements for the estimation of the best trade-off between DVC precision in strain measurements, and the spatial resolution of independent displacement and strain measurements. The users are welcome to test new DVC approaches on the datasets shared in this and previous papers for direct comparison of the results.

ETHICS STATEMENT

All work performed on tissues collected from animals killed for alimentary purpose does not need ethic approval as per the institutional and national guidelines. All procedures performed on the mice were approved by the local Research Ethics Committee of the University of Sheffield (Sheffield, UK). The animal study from which the ovine bone specimens were extracted was performed according to the local ethical committee of the Royal National Orthopaedic Hospital.

AUTHOR CONTRIBUTIONS

All authors contributed to the collection of the data, the interpretation of the results, and/or the writing of the paper.

ACKNOWLEDGMENTS

The project was partially funded by the FP7 European program (MAMBO: PIEF-GA-2012-327357), the Engineering and Physical Sciences Research Council (Frontier Grant Multisim, EP/K03877X/1), the National Royal Society (RG130831 and RG150012), and the UK National Centre for the Replacement, Refinement and Reduction of Animals in Research (NC3Rs, grant number: NC/K000780/1). MP acknowledges the "Marco Polo" travel grant awarded by University of Bologna. The authors would like to thank the Diamond Light Source for time at the Diamond-Manchester Imaging Beamline I13-2 (under proposals: MT10315-Dall'Ara and MT14080-Tozzi), the SkeletAl (University of Sheffield), and the Zeiss Global Center (University of Portsmouth) for imaging and post-processing. We further acknowledge Prof. Hose and Prof. Barber for sharing the ShIRT scripts, Dr. Hollis (LaVision Ltd.) for assistance with DaVis software, Dr. Bodey for help with the acquisition of the Synchrotron images, and Dr. Danesi, Ms. Innocente, Mr. Morellato, and Dr. Boudiffa for help in the preparation and scanning of the samples. The whole or partial datasets used in this study can be found at the following figshare links: vertebral bodies scanned with μCT (https://doi.org/10.6084/m9.figshare.4062351.v1); vertebral bodies with bone cement scanned with μCT (https://doi.org/10.6084/m9.figshare.4308926.v2); cortical bone, trabecular bone, and mouse proximal tibia scanner with SRμCT (https://doi.org/10.15131/shef.data.4865300.v1); trabecular bone with and without biomaterial scanned with SRμCT (https://figshare.com/s/9e30505b66d77276cc9a); and mouse tibiae scanned with *in vivo* and *ex vivo* μCT (https://doi.org/10.15131/shef.data.5528104).

REFERENCES

Anderson, A. E., Ellis, B. J., and Weiss, J. A. (2007). Verification, validation and sensitivity studies in computational biomechanics. *Comput. Methods Biomech. Biomed. Engin.* 10, 171–184. doi:10.1080/10255840601160484

Badilatti, S. D., Christen, P., Parkinson, I., and Muller, R. (2016). Load-adaptive bone remodeling simulations reveal osteoporotic microstructural and mechanical changes in whole human vertebrae. *J. Biomech.* 49, 3770–3779. doi:10.1016/j.jbiomech.2016.10.002

Barber, D. C., and Hose, D. R. (2005). Automatic segmentation of medical images using image registration: diagnostic and simulation applications. *J. Med. Eng. Technol.* 29, 53–63. doi:10.1080/03091900412331289889

Barber, D. C., Oubel, E., Frangi, A. F., and Hose, D. R. (2007). Efficient computational fluid dynamics mesh generation by image registration. *Med. Image Anal.* 11, 648–662. doi:10.1016/j.media.2007.06.011

Barth, H. D., Zimmermann, E. A., Schaible, E., Tang, S. Y., Alliston, T., and Ritchie, R. O. (2011). Characterization of the effects of x-ray irradiation on the hierarchical structure and mechanical properties of human cortical bone. *Biomaterials* 32, 8892–8904. doi:10.1016/j.biomaterials.2011.08.013

Bay, B. K., Smith, T. S., Fyhrie, D. P., and Saad, M. (1999). Digital volume correlation: three-dimensional strain mapping using X-ray tomography. *Exp. Mech.* 39, 217–226. doi:10.1007/BF02323555

Bayraktar, H. H., Morgan, E. F., Niebur, G. L., Morris, G. E., Wong, E. K., and Keaveny, T. M. (2004). Comparison of the elastic and yield properties of human femoral trabecular and cortical bone tissue. *J. Biomech.* 37, 27–35. doi:10.1016/S0021-9290(03)00257-4

Birkhold, A. I., Razi, H., Duda, G. N., Checa, S., and Willie, B. M. (2017). Tomography-based quantification of regional differences in cortical bone surface remodeling and mechano-response. *Calcif. Tissue Int.* 100, 255–270. doi:10.1007/s00223-016-0217-4

Bouxsein, M. L. (2003). Bone quality: where do we go from here? *Osteoporos. Int.* 14(Suppl. 5), S118–S127. doi:10.1007/s00198-003-1489-x

Buades, A., Coll, B., and Morel, J. (2011). Non-local means denoising. *Image Process. Line* 1, 208–212. doi:10.5201/ipol.2011.bcm_nlm

Chen, Y., Dall Ara, E., Sales, E., Manda, K., Wallace, R., Pankaj, P., et al. (2017). Micro-CT based finite element models of cancellous bone predict accurately displacement once the boundary condition is well replicated: a validation study. *J. Mech. Behav. Biomed. Mater.* 65, 644–651. doi:10.1016/j.jmbbm.2016.09.014

Christen, D., Levchuk, A., Schori, S., Schneider, P., Boyd, S. K., and Muller, R. (2012). Deformable image registration and 3D strain mapping for the quantitative assessment of cortical bone microdamage. *J. Mech. Behav. Biomed. Mater.* 8, 184–193. doi:10.1016/j.jmbbm.2011.12.009

Coathup, M. J., Edwards, T. C., Samizadeh, S., Lo, W. J., and Blunn, G. W. (2016). The effect of an alginate carrier on bone formation in a hydroxyapatite scaffold. *J. Biomed. Mater. Res. Part B Appl. Biomater.* 104, 1328–1335. doi:10.1002/jbm.b.33395

Costa, M. C., Tozzi, G., Cristofolini, L., Danesi, V., Viceconti, M., and Dall'Ara, E. (2017). Micro finite element models of the vertebral body: validation of local displacement predictions. *PLoS ONE* 12:e0180151. doi:10.1371/journal.pone.0180151

Cristofolini, L., Brandolini, N., Danesi, V., Juszczyk, M. M., Erani, P., and Viceconti, M. (2013). Strain distribution in the lumbar vertebrae under different loading configurations. *Spine J.* 13, 1281–1292. doi:10.1016/j.spinee.2013.06.014

Cristofolini, L., Conti, G., Juszczyk, M., Cremonini, S., Van Sint Jan, S., and Viceconti, M. (2010a). Structural behaviour and strain distribution of the long bones of the human lower limbs. *J. Biomech.* 43, 826–835. doi:10.1016/j.jbiomech.2009.11.022

Cristofolini, L., Schileo, E., Juszczyk, M., Taddei, F., Martelli, S., and Viceconti, M. (2010b). Mechanical testing of bones: the positive synergy of finite-element models and in vitro experiments. *Philos. Trans. Series A Math. Phys. Eng. Sci.* 368, 2725–2763. doi:10.1098/rsta.2010.0046

Dall'Ara, E., Barber, D., and Viceconti, M. (2014). About the inevitable compromise between spatial resolution and accuracy of strain measurement for bone tissue: a 3D zero-strain study. *J. Biomech.* 47, 2956–2963. doi:10.1016/j.jbiomech.2014.07.019

Dall'Ara, E., Luisier, B., Schmidt, R., Kainberger, F., Zysset, P., and Pahr, D. (2013a). A nonlinear QCT-based finite element model validation study for the human femur tested in two configurations in vitro. *Bone* 52, 27–38. doi:10.1016/j.bone.2012.09.006

Dall'Ara, E., Luisier, B., Schmidt, R., Pretterklieber, M., Kainberger, F., Zysset, P., et al. (2013b). DXA predictions of human femoral mechanical properties depend on the load configuration. *Med. Eng. Phys.* 35, 1564–1572; discussion 1564. doi:10.1016/j.medengphy.2013.04.008

Dall'Ara, E., Pahr, D., Varga, P., Kainberger, F., and Zysset, P. (2012). QCT-based finite element models predict human vertebral strength in vitro significantly better than simulated DEXA. *Osteoporos. Int.* 23, 563–572. doi:10.1007/s00198-011-1568-3

Danesi, V., Tozzi, G., and Cristofolini, L. (2016). Application of digital volume correlation to study the efficacy of prophylactic vertebral augmentation. *Clin. Biomech. (Bristol, Avon)* 39, 14–24. doi:10.1016/j.clinbiomech.2016.07.010

Gillard, F., Boardman, R., Mavrogordato, M., Hollis, D., Sinclair, I., Pierron, F., et al. (2014). The application of digital volume correlation (DVC) to study the microstructural behaviour of trabecular bone during compression. *J. Mech. Behav. Biomed. Mater.* 29, 480–499. doi:10.1016/j.jmbbm.2013.09.014

Grassi, L., Vaananen, S. P., Ristinmaa, M., Jurvelin, J. S., and Isaksson, H. (2016). How accurately can subject-specific finite element models predict strains and strength of human femora? Investigation using full-field measurements. *J. Biomech.* 49, 802–806. doi:10.1016/j.jbiomech.2016.02.032

Gustafson, H. M., Cripton, P. A., Ferguson, S. J., and Helgason, B. (2017). Comparison of specimen-specific vertebral body finite element models with experimental digital image correlation measurements. *J. Mech. Behav. Biomed. Mater.* 65, 801–807. doi:10.1016/j.jmbbm.2016.10.002

Huang, L., and Wang, M. (1995). Image thresholding by minimizing the measures of fuzziness. *Pattern Recognit.* 28, 41–51. doi:10.1016/0031-3203(94)E0043-K

Hussein, A. I., Barbone, P. E., and Morgan, E. F. (2012). Digital volume correlation for study of the mechanics of whole bones. *Procedia IUTAM* 4, 116–125. doi:10.1016/j.piutam.2012.05.013

Jackman, T. M., DelMonaco, A. M., and Morgan, E. F. (2016). Accuracy of finite element analyses of CT scans in predictions of vertebral failure patterns under axial compression and anterior flexion. *J. Biomech.* 49, 267–275. doi:10.1016/j.jbiomech.2015.12.004

Jones, A. C., and Wilcox, R. K. (2008). Finite element analysis of the spine: towards a framework of verification, validation and sensitivity analysis. *Med. Eng. Phys.* 30, 1287–1304. doi:10.1016/j.medengphy.2008.09.006

Khodabakhshi, G., Walker, D., Scutt, A., Way, L., Cowie, R. M., and Hose, D. R. (2013). Measuring three-dimensional strain distribution in tendon. *J. Microsc.* 249, 195–205. doi:10.1111/jmi.12009

Levchuk, A., Zwahlen, A., Weigt, C., Lambers, F. M., Badilatti, S. D., Schulte, F. A., et al. (2014). The Clinical Biomechanics Award 2012 – presented by the European Society of Biomechanics: large scale simulations of trabecular bone adaptation to loading and treatment. *Clin. Biomech. (Bristol, Avon)* 29, 355–362. doi:10.1016/j.clinbiomech.2013.12.019

Liu, L., and Morgan, E. F. (2007). Accuracy and precision of digital volume correlation in quantifying displacements and strains in trabecular bone. *J. Biomech.* 40, 3516–3520. doi:10.1016/j.jbiomech.2007.04.019

Lu, Y., Boudiffa, M., Dall'Ara, E., Bellantuono, I., and Viceconti, M. (2015). Evaluation of in-vivo measurement errors associated with micro-computed tomography scans by means of the bone surface distance approach. *Med. Eng. Phys.* 37, 1091–1097. doi:10.1016/j.medengphy.2015.08.017

Lu, Y., Boudiffa, M., Dall'Ara, E., Liu, Y., Bellantuono, I., and Viceconti, M. (2017). Longitudinal effects of parathyroid hormone treatment on morphological, densitometric and mechanical properties of the mouse tibia. *J. Mech. Behav. Biomed. Mater.* 75, 244–251. doi:10.1016/j.jmbbm.2017.07.034

Madi, K., Tozzi, G., Zhang, Q. H., Tong, J., Cossey, A., Au, A., et al. (2013). Computation of full-field displacements in a scaffold implant using digital volume correlation and finite element analysis. *Med. Eng. Phys.* 35, 1298–1312. doi:10.1016/j.medengphy.2013.02.001

Palanca, M., Bodey, A. J., Giorgi, M., Viceconti, M., Lacroix, D., Cristofolini, L., et al. (2017a). Local displacement and strain uncertainties in different bone types by digital volume correlation of synchrotron microtomograms. *J. Biomech.* 58, 27–36. doi:10.1016/j.jbiomech.2017.04.007

Palanca, M., Cristofolini, L., Pani, M., Kinene, E., Blunn, G., Madi, K., et al. (2017b). Feasibility study for a clinical application of digital volume correlation. *Orthop. Proc.* 99-B(Suppl. 2), 18.

Palanca, M., Cristofolini, L., Dall'Ara, E., Curto, M., Innocente, F., Danesi, V., et al. (2016). Digital volume correlation can be used to estimate local strains in natural and augmented vertebrae: an organ-level study. *J. Biomech.* 49, 3882–3890. doi:10.1016/j.jbiomech.2016.10.018

Palanca, M., Tozzi, G., Cristofolini, L., Viceconti, M., and Dall'Ara, E. (2015). Three-dimensional local measurements of bone strain and displacement: comparison of three digital volume correlation approaches. *J. Biomech. Eng.* 137:071006-1–071006-14. doi:10.1115/1.4030174

Pfeiffer, S. (1998). Variability in osteon size in recent human populations. *Am. J. Phys. Anthropol.* 106, 219–227. doi:10.1002/(sici)1096-8644(199806)106:2<219:aid-ajpa8>3.0.co;2-k

Razi, H., Birkhold, A. I., Weinkamer, R., Duda, G. N., Willie, B. M., and Checa, S. (2015). Aging leads to a dysregulation in mechanically driven bone formation and resorption. *J. Bone Miner. Res.* 30, 1864–1873. doi:10.1002/jbmr.2528

Roberts, B. C., Perilli, E., and Reynolds, K. J. (2014). Application of the digital volume correlation technique for the measurement of displacement and strain fields in bone: a literature review. *J. Biomech.* 47, 923–934. doi:10.1016/j.jbiomech.2014.01.001

Schileo, E., Dall'ara, E., Taddei, F., Malandrino, A., Schotkamp, T., Baleani, M., et al. (2008). An accurate estimation of bone density improves the accuracy of subject-specific finite element models. *J. Biomech.* 41, 2483–2491. doi:10.1016/j.jbiomech.2008.05.017

Schwiedrzik, J., Gross, T., Bina, M., Pretterklieber, M., Zysset, P., and Pahr, D. (2016). Experimental validation of a nonlinear muFE model based on cohesive-frictional plasticity for trabecular bone. *Int. J. Numer. Method Biomed. Eng.* 32, e02739. doi:10.1002/cnm.2739

Tozzi, G., Dall'Ara, E., Palanca, M., Curto, M., Innocente, F., and Cristofolini, L. (2017). Strain uncertainties from two digital volume correlation approaches in prophylactically augmented vertebrae: local analysis on bone and cement-bone

microstructures. *J. Mech. Behav. Biomed. Mater.* 67, 117–126. doi:10.1016/j.jmbbm.2016.12.006

van Rietbergen, B., Weinans, H., Huiskes, R., and Odgaard, A. (1995). A new method to determine trabecular bone elastic properties and loading using micromechanical finite-element models. *J. Biomech.* 28, 69–81. doi:10.1016/0021-9290(95)80008-5

Viceconti, M. (2012). *Multiscale Modeling of the Skeletal System*. Cambridge: Cambridge University Press.

Widmer Soyka, R. P., Lopez, A., Persson, C., Cristofolini, L., and Ferguson, S. J. (2013). Numerical description and experimental validation of a rheology model for non-Newtonian fluid flow in cancellous bone. *J. Mech. Behav. Biomed. Mater.* 27, 43–53. doi:10.1016/j.jmbbm.2013.06.007

Wolfram, U., Wilke, H. J., and Zysset, P. K. (2010). Valid micro finite element models of vertebral trabecular bone can be obtained using tissue properties measured with nanoindentation under wet conditions. *J. Biomech.* 43, 1731–1737. doi:10.1016/j.jbiomech.2010.02.026

Zauel, R., Yeni, Y. N., Bay, B. K., Dong, X. N., and Fyhrie, D. P. (2006). Comparison of the linear finite element prediction of deformation and strain of human cancellous bone to 3D digital volume correlation measurements. *J. Biomech. Eng.* 128, 1–6. doi:10.1115/1.2146001

Zhu, M. L., Zhang, Q. H., Lupton, C., and Tong, J. (2016). Spatial resolution and measurement uncertainty of strains in bone and bone-cement interface using digital volume correlation. *J. Mech. Behav. Biomed. Mater.* 57, 269–279. doi:10.1016/j.jmbbm.2015.12.017

Zysset, P. K., Dall'ara, E., Varga, P., and Pahr, D. H. (2013). Finite element analysis for prediction of bone strength. *Bonekey Rep.* 2, 386. doi:10.1038/bonekey.2013.120

Conflict of Interest Statement: The authors declare that the research was conducted in the absence of any commercial or financial relationships that could be construed as a potential conflict of interest.

frontiers in Materials

ORIGINAL RESEARCH
published: 27 September 2017
doi: 10.3389/fmats.2017.00029

3D Architecture of Trabecular Bone in the Pig Mandible and Femur: Inter-Trabecular Angle Distributions

*Yehonatan Ben-Zvi[1], Natalie Reznikov[2†], Ron Shahar[3] and Steve Weiner[1]**

[1] Department of Structural Biology, Weizmann Institute of Science, Rehovot, Israel, [2] Imperial College London, London, United Kingdom, [3] Faculty of Agriculture, Food and Environment, Koret School of Veterinary Medicine, The Hebrew University of Jerusalem, Rehovot, Israel

Cancellous bone is an intricate network of interconnected trabeculae, to which analysis of network topology can be applied. The inter-trabecular angle (ITA) analysis—an analysis of network topological parameters and regularity of network-forming nodes—was previously carried out on human proximal femora and showed that trabecular bone follows two main principles: sparsity of the network connectedness (prevalence of nodes with low connectivity in the network) and maximal space spanning (angular offset of connected elements is maximal for their number and approximates the values of geometrically symmetric shapes). These observations suggest that 3D organization of trabecular bone, irrespective of size and shape of individual elements, reflects a tradeoff between minimal metabolic cost of maintenance and maximal network stability under conditions of multidirectional loading. In this study, we validate the ITA application using additional 3D structures (cork and 3D-printed metal lattices), analyze the ITA parameters in porcine proximal femora and mandibles, and carry out a spatial analysis of the most common node type in the porcine mandibular condyle. The validation shows that the ITA application reliably detects designed or evolved topological parameters. The ITA parameters of porcine trabecular bones are similar to those of human bones. We demonstrate functional adaptation in the pig mandibular condyle by showing that the planar nodes with three edges are preferentially aligned in relation to the muscle forces that are applied to the condyle. We conclude that the ITA topological parameters are remarkably conserved, but locally do adapt to applied stresses.

Keywords: trabecular bone, inter-trabecular angle, topology, anisotropy, micro-CT

OPEN ACCESS

Edited by:
Gianluca Tozzi, University of Portsmouth, United Kingdom

Reviewed by:
Peter Zioupos, Cranfield University, United Kingdom
Antonio DiCarlo, CECAM–IT–SIMUL Node, Italy

****Correspondence:***
Steve Weiner
steve.weiner@weizmann.ac.il

†These authors have contributed equally to this work.

Specialty section:
This article was submitted to Mechanics of Materials, a section of the journal Frontiers in Materials

Received: *28 June 2017*
Accepted: *11 September 2017*
Published: *27 September 2017*

Citation:
Ben-Zvi Y, Reznikov N, Shahar R and Weiner S (2017) 3D Architecture of Trabecular Bone in the Pig Mandible and Femur: Inter-Trabecular Angle Distributions. Front. Mater. 4:29. doi: 10.3389/fmats.2017.00029

INTRODUCTION

Trabecular bone (also known as cancellous or spongey bone) is a lightweight porous material that fills the interior spaces of most bones. In some cases, such as the vertebrae, it comprises almost the entire bone, as the outer compact bone shell is relatively thin. By contrast, in long bones such as the femur and humerus, cancellous bone is found mostly in the articulating ends. Much effort has been made to characterize the 3D architecture and network organization of trabecular bone, both to understand how trabecular bone functions normally and when it is compromised by pathology (Odgaard, 1997; Müller et al., 1998; Keaveny et al., 2001; Boyde, 2003; Zysset, 2003; Ryan and Krovitz, 2006; Stauber and Müller, 2007; Allen et al., 2008).

Many analytical techniques in trabecular bone research are based on histomorphometric (2D) procedures (Odgaard, 1997). The utilization of three-dimensional (3D) imaging of bone makes it possible to better characterize the architecture (Odgaard, 1997; An and Freidman, 1998; Müller, 2009; Kivell, 2016). Current micro-CT-based analyses of trabecular bone characterize its organization in terms of textural structural features within a region of interest [mean trabecular thickness (Tb.Th), mean inter-trabecular distance, bone volume-total volume ratio (BV/TV), and degree of anisotropy (DA)] (Odgaard, 1997; Bouxsein et al., 2010). BV/TV and Tb.Th parameters significantly account for the tissue stiffness and strength (Ascenzi et al., 2011). A higher DA was found to contribute to trabecular bone strength in the case of non-uniform stress by leveling out local strains (Bayraktar and Keaveny, 2004). However, a higher DA was also found in bone samples from donors who sustained a fragility fracture (Ciarelli et al., 2000). The connectivity and continuity of a trabecular network is another determinant of tissue stability (Mosekilde et al., 1987; Kinney and Ladd, 1998). It is noteworthy; however, that network connection density is a parameter independent of bone volume fraction or Tb.Th. From an ontogenetic perspective, the network connection density and the archetypal 3D plan are established early in development—around birth in humans (Roschger et al., 2001). After that the process of trabecular network coarsening continues until the stage of skeletal maturity (Ryan and Krovitz, 2006). Throughout adulthood, material texture undergoes further refinement, as seen by increased alignment of collagen fibrils and mineral crystallites along individual trabeculae (Roschger et al., 2001).

Unlike morphology, the study of forms and metric spaces of objects, topology is concerned with objects' continuity, compactness, connectedness, boundaries, etc. These are the fundamental properties of objects that do not change with deformations, transformations, and scaling (Kahn, 1975). A network is defined as a set of *nodes* connected *via* a set of *edges*. A special class of networks is "*partially connected networks,*" in which nodes are connected only to adjacent nodes (neighbors), so that the network is fully connected without the cost of maintaining the maximal possible number of edges. Saha et al. (2000) paved the way for studying trabecular bone topology—the manner in which individual elements collectively form a 3D network—by suggesting a method of uncoupling trabecular morphology from the 3D organization of the axes, or centroids, of trabeculae in a sample (edges). The topological approach itself helps explain the mechanical properties and might well determine the 3D architectural blueprint, or archetype, of trabecular bone that has been optimized throughout evolution and allows for further functional adaptation (i.e., local Tb.Th, DA, and bone volume fraction being superimposed on topological parameters such as connectedness and continuity). Network regularity and network distortion stand apart from morphology (trabecular shape and size) and topology (trabecular network continuity and connectedness). Network regularity and network distortion, Jensen et al. (1990) showed that randomization of the regular lattice/network may decrease its stability by a factor of 5 or even 10, while the density (or connectedness) of the network is preserved. Although the authors clearly indicate that a regular artificial lattice is not equivalent to trabecular bone tissue, the network topology (i.e., connectedness) and network regularity (configuration of the network nodes) must be taken into account. From the engineering perspective, Deshpande et al. (2001) illustrates that the number of connections between the network-forming nodes is crucial for the network rigidity: in a 3D network with node connectedness exceeding 12, bending deformations are eliminated and the loading of the structure becomes stretching-dominated. This is an important observation, as most natural and artificial materials are at least an order of magnitude stronger when loaded axially (in tension or compression) in comparison to bending or shear (Wainwright et al., 1976). The high connectedness of the 3D network provides its rigidity by "triangulation" of interconnected elements. A complete triangulation, however, is incompatible with the shock-absorbing properties of the structure, and the latter is often desirable in biological materials (Deshpande et al., 2001). Hence, it might be reasonable to expect that the topological plan, or blueprint, of trabecular bone incorporates 3D architectural features that optimally combine both the stability of the 3D network and its physiological compliance.

Reznikov et al. (2016) introduced a new parameter for the analysis of μCT scans of trabecular bone, namely the inter-trabecular angle (ITA). The ITA is defined as the angles between two adjacent trabeculae emanating from the same node, and the angle is calculated for each pair of trabeculae connected at a node in the entire volume of interest. This parameter is, therefore, determined for a large number of pairs (typically, in 1 cm^3 of trabecular bone tissue there are 10,000 to 40,000 ITAs).

Reznikov et al. (2016) studied different areas within the human proximal femur in adults of varying age and found remarkable similarities. First, the trabecular network is a partially connected network, which is reflected in the low connectedness of nodes. More than two-thirds of the nodes have three connecting trabeculae (three-neighbor node, 3-N), followed by one-quarter of all the nodes with four emanating trabeculae (four-neighbor node, 4-N) and about one twelfth of nodes with five connecting trabeculae (five-neighbor node, 5-N). The nodes of higher connectedness are sparse. Significantly, the proportions of 3-N, 4-N, and 5-N nodes are conserved between three areas within the proximal femur and among the individuals roughly as 12:4:1 or 10:3:1. Furthermore, the mean ITA values of nodes with three connecting trabeculae are close to 120° and nodes with 4 connecting trabeculae have a mean ITA close to 109.5°. Thus, ITA mean values are close to the angles that characterize threefold and fourfold symmetrical geometrical motifs with the maximal angular offset of the edges (Thompson, 1942). The prevalence of nodes with low connectedness and the mean ITA values typical of the maximal angular offset possibly indicate a compromise between minimizing of metabolic cost (or achieving sufficient shock dissipation) and maximizing sufficient network stability in multidirectional loading of trabecular bone tissue (Deshpande et al., 2001). Reznikov et al. (2017) have applied the ITA analysis approach to the study of functional adaptation of trabecular bone in the human calcaneus by comparing normal feet and museum specimens of feet subjected to foot binding (historical cultural practice of foot deformation). They found that while the anisotropy pattern in the calcaneus closely reflects the pattern of

loading and follows the tensile and compressive force vectors, the aforementioned ITA parameters in the calcanei of the two groups were nearly identical.

We were surprised to find that the various ITA parameters are so similar in bones that fulfill different mechanical functions and are subjected to different loading regimes. The overall objective of this study is to better understand the biological factors that influence ITA properties. To this end, we carried out this follow-up study in which we (i) tested the validity of our custom written application for ITA analysis by using engineered space-filling lattices and a natural lattice; (ii) performed ITA analysis of pig proximal femora, as well as three different areas in the pig mandible, and compared them to the previously published ITA analysis of human proximal femora; and (iii) studied the spatial distributions of 3-N nodes in different regions within the pig mandibular condyle to determine whether or not topological parameters are affected by locally varying mechanical functions.

MATERIALS AND METHODS

For details see Reznikov et al. (2016).

Materials

We analyzed selected parts of the mandible and the head of the femur (**Figure 1**) acquired from three mature 2.5-year-old domestic female pigs. The pigs were provided by Lahav C.R.O (Kibbutz Lahav, Israel). Pigs are considered to be a good non-human model for better understanding human skeletal and dental questions such as osteonecrosis of the femoral head, bone fractures, bone growth, and development, as well as for evaluating new dental implant designs (Buser et al., 1991; An and Freidman, 1998; Terheyden et al., 1999; Nkenke et al., 2003). While porcine bones in general have a denser trabecular network than human trabecular networks (Mosekilde et al., 1993), porcine bone shows similarities to human bone in terms of bone biology (modeling and remodeling), as well as bone mineral density (Mosekilde et al., 1993). The study was approved by Institutional Animal Care and Use Committee at the Weizmann Institute of Science. We also analyzed one cork specimen as an example of natural porous solid of non-animal origin that functions under different mechanical constraints and does not remodel. As examples of engineered 3D structures, we used two types of 3D-printed metal lattices. A rhombic dodecahedron honeycomb structure (here referred to as the D-lattice) in the form of a cylinder 15 mm in diameter and 15 mm in height, a strut thickness of 0.9–1.0 mm and the node connectedness was strictly configured by the design (unit cell of rhombic dodecahedron with three intersecting twofold axes) as 4-N, 6-N, and 12-N in an infinite array. This D-lattice contained about 1000 struts connected at 250 nodes, of which approximately 50% were partially truncated at the surface. The stochastic lattice (here referred to as the S-lattice) was also manufactured in a cylindrical shape of 15 mm in diameter and 15 mm in height, but contained a higher number (around 20,000) of fine connected elements of 150–250-μm thick. In the stochastic lattice, the nodes were randomly positioned in 3D and were stochastically interconnected to form a partially connected network with the average number of neighbors given as 4, as described by Ghouse et al. (2017).

Methods

The fresh porcine mandibles were cut in half at the symphyseal region using a water cooled rotary diamond saw (Buehler, IsoMet 1000 Precision saw, USA). Each hemi-mandible was sectioned further to obtain three anatomically distinct areas, namely the mandibular condyle, the angle, and the body (**Figure 1**). For specimens P1 and P2 both the right and the left hemi-mandibles were analyzed. In the case of P3, only the right hemi-mandible was analyzed (**Table 1**). The proximal part of the femur from each pig was also examined.

A cylindrical cork specimen of 5 mm in diameter was collected by trephine drilling of the outer bark layer (phloem) of a cork oak, *Quercus suber*, in the direction perpendicular to the trunk natural surface. The cork specimen was not further modified. The engineered lattices were created using computer-aided design software Rhinoceros 5.0 (McNeel Europe, Barcelona, Spain) and

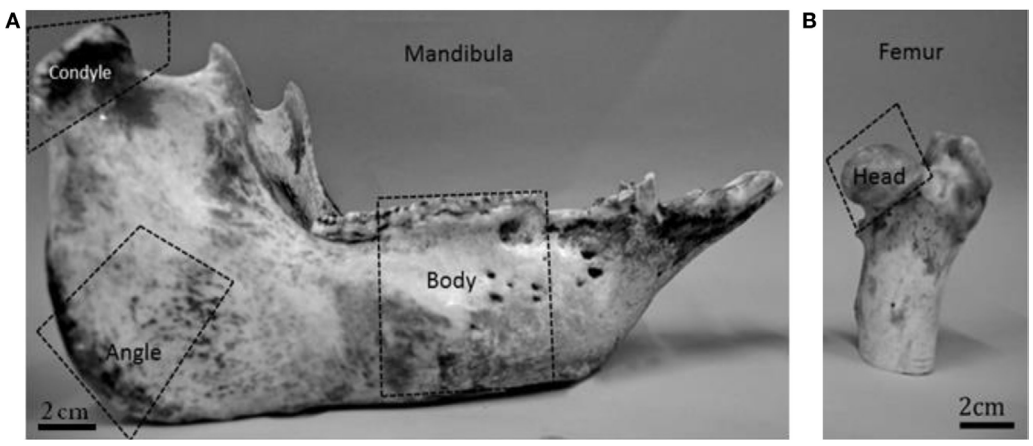

FIGURE 1 | Domestic pig mandible **(A)** and the proximal part of the pig femur **(B)**. The dotted lines indicate the areas that were selected for the analysis.

TABLE 1 | List of examined parts from each of the specimens.

Specimen P1	Mandible	Angle	Right, left
		Body	Right, left
		Condyle	Right, left
	Femoral head		Right
Specimen P2	Mandible	Angle	Right, left
		Body	Right, left
		Condyle	Right, left
	Femoral head		Left
Specimen P3	Mandible	Angle	Left
		Body	Left
		Condyle	Left
	Femoral head		Right

3D-printed using selective laser sintering of commercially pure titanium (Renishaw AM250, Renishaw Additive Manufacturing, UK) for an unrelated study.

Micro-CT Analysis

The bones were scanned using a micro-CT (Micro XCT-400, Zeiss X-ray microscopy, CA, USA) at 40 kV and 200 mA with a voxel size between 38 and 42 μm. The voxel size variability was due to minor differences in specimen sizes. For optimal resolution, the voxel size was selected in such a way that the average Tb.Th would incorporate at least five voxels. Once the scans were reconstructed, the cortical shell surrounding the trabecular interior was digitally removed in each of the selected parts (Avizo, FEI, OR, USA). In the case of the mandibular body, both the cortical shell and the teeth were removed digitally.

The cork specimen was scanned using the same set up with the voxel size of 0.8 μm for the same consideration of having each structural element resolved with at least five voxels. No artificial contrasting of the cork sample was performed. The engineered lattices were imaged using Nikon Metrology HMX ST 225 scanner (Nikon, Tring, UK), tube peak voltage 180 kV, and current 170 mA. The voxel size was the same as for bone samples, 38 μm.

Calculation of the ITA

Following the protocol described in detail by Reznikov et al. (2016), the reconstructed 3D images of all specimens were converted to a continuous networks of edges of one voxel thickness, using a skeletonization (thinning) algorithm (Fiji, Skeletonize3D plugin http://fiji.sc/Skeletonize3D) (Lee et al., 1994) (**Figure 2**). The resulting network of edges was analyzed further using the AnalyzeSkeleton plugin, Fiji, http://fiji.sc/AnalyzeSkeleton (Arganda-Carreras et al., 2010). The output of AnalyzeSkeleton is a set of vectors (hence referred to as "edges") represented by (x, y, z) coordinates of start points and end points. The junctions of three or more edges were defined as "nodes." The matrices of edge coordinates were analyzed using the ITA application in Matlab R2015b (MathWorks, USA). The application identifies the type of each node by the number of edges emanating from it and classifies the nodes into categories of 3-N, 4-N, 5-N, or more. The ITA value is calculated for each pair of connected trabeculae and the distributions of many ITA values are reported separately for each node type. Very short edges (<5 pixels for all samples or 35 pixels in the coarse D-lattice) between two closely positioned nodes were replaced by a single node because such edges were shorter than the average Tb.Th. Short edges not connected at one end, which result from the skeletonization of oddly-shaped trabeculae, were also removed following the same principle of being shorter than the average Tb.Th in pixels. The abundance of different node types and the corresponding ITA distributions were exported in Excell (Microsoft, USA) and plotted.

The ITA application for Matlab 2015b is available at the following link: http://www.weizmann.ac.il/Structural_Biology/Weiner/ita-app.

Node Planarity Analysis

The previously reported angular offset between the edges of 3-N nodes suggests that many of them are planar: it is impossible to spread three connected edges by 120° without confining them to a single plane. However, while all maximally offset 3-N nodes are planar, not all planar nodes necessarily have their edges maximally offset (for illustration as in the planar capital letter "T," compared to "Y"). Since the ITA distribution of 3-N nodes was rather broad (i.e., incorporating ITA values smaller or larger than 120°), the actual confinement of 3-N nodes to planes was analyzed. An auxiliary plane was constructed through three points on each of the three edges. Each point was located at the same unit distance from the node. We define planarity by the angle between the edges and this plane (which is the same for all three edges). We refer to a "planar" node as a 3-N node with an average angle between connecting trabeculae and the auxiliary plane of less than 4°. Non-planar nodes for this study are defined as those with an average angle of more than 20°. Next, we mapped and quantified the spatial distributions of planar and non-planar 3-N nodes in the pig mandibular condyle. We compared the number of nodes and their types per unit volume in different regions in the mandibular condyle.

Analysis of the Spatial Distributions and Orientations of the Planar and Non-Planar 3-N Nodes in the Head and Neck of the Condyle

The coordinates of the 3-N planar (within 4° of being perfectly planar) are compared to 3-N nodes that are distinctly non-planar. We, therefore, chose nodes in which the angle between the plane and the edge is greater than 20°. Each of the examined 3-N nodes (planar and non-planar) was also plotted in 3D space as a reciprocal vector perpendicular to the auxiliary plane that was used to define the planarity. Visualization of the vectors in 3D was done in Avizo (Avizo, FEI, OR, USA). The 3D volume of reciprocal vectors was anatomically aligned. In this orientation, the medial pterygoid muscle is approximately in the anterior-superior to inferior-posterior direction. A snapshot image of the vectors was recorded in this anatomical position. All images were then analyzed using the ImageJ (Fiji) fast Fourier transform (FFT) application. The FFT pattern of aligned elements creates a streak, the definition of which is proportional to the extent of alignment of these elements and the direction of which is orthogonal to that of the aligned elements. Therefore, the orientation of a well-defined streak in an FFT is reciprocal to the plot of the planarity vectors and, thus, coincides with the orientation of the planes of the 3-N nodes.

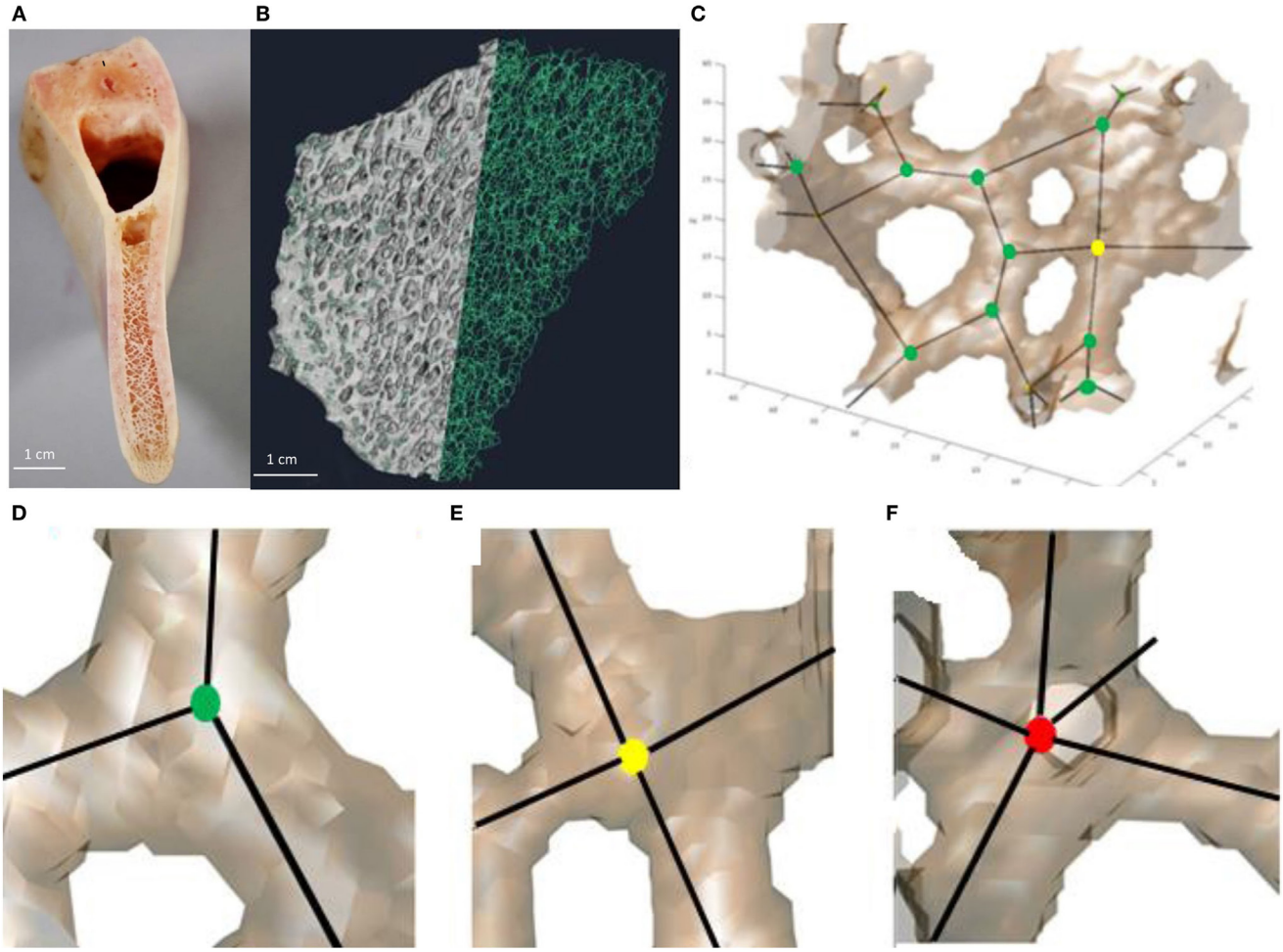

FIGURE 2 | Workflow of bone analysis using inter-trabecular angle application. **(A)** Fragment of the pig mandible that shows the trabecular interior of the mandible body. **(B)** Smaller fragment of trabecular bone in which trabeculae on the left-hand side were replaced by thin lines (edges, referred to as skeletonization). **(C)** Group of connected trabeculae with straight edges and nodes inscribed. **(D–F)** Examples of nodes with different connectedness: **(D)** 3-N node, **(E)** 4-N node, and **(F)** 5-N node.

Analysis Using the Morphometric Bone Structure Parameters

For this type of analysis the plugin BoneJ in ImageJ (Fiji) application was used (Doube et al., 2010). All examined regions of interest were of equal volume. For each volume we calculated the bone volume fraction (BV/TV), mean trabecular separation (Tb.Sp), mean Tb.Th, and DA. DA is a measure of preferential orientation of substructures in a volume http://bonej.org/anisotropy (Odgaard, 1997).

RESULTS

Validation of the ITA Application

Engineered 3D Lattices

Rhombic Dodecahedron Honeycomb Structure (D-Lattice)

The rhombic dodecahedron honeycomb structure design (**Figure 3A**) includes only even-edge nodes (such as 4-N and 6-N) by design. The odd-edge nodes are at the periphery of the specimen and are due to cropping of the infinite lattice to the cylindrical shape. The algorithm detected the mean angle of 4-N nodes as 106° (expected 109.5°) and the mean angle of 6-N nodes as 88° (expected 90°). The observed ITA distributions are sharp (**Figures 4A,B**). Some broadening of the peaks at their base results from the lattice truncation, from the minor imperfections of 3D-printing and of the skeletonization process. Analysis results show that the volume contains 246 nodes, while the expected number is 250. The expected number of intact 4-N nodes is 33% and the measured number is 39%. The expected number of intact 6-N nodes is 10% and the measured number is 13%. The number of expected truncated nodes (located at the specimen surface) is 50% and their measured number (the sum of 3-N, 5-N, and others) is 48%. **Figure 4** shows that the ITA software does calculate the most frequent angle for the 4-N and 6-N nodes very close to the designed values. Since the features identified by the ITA application are either in agreement with the design or can be fully

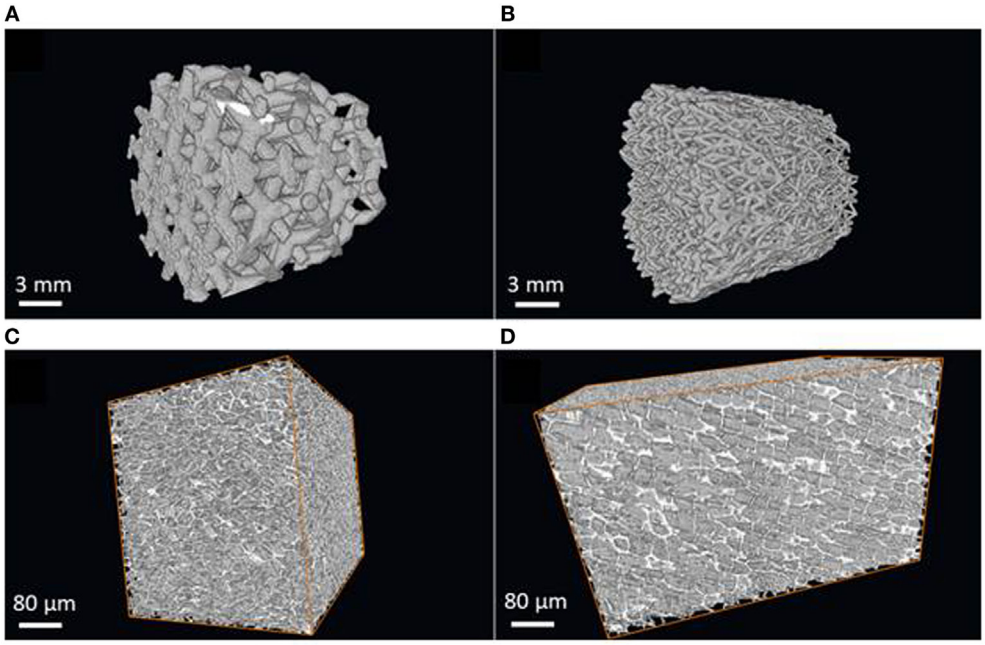

FIGURE 3 | Three-dimensional structures that were used for ITA validation, as reconstructed µCT images. **(A)** Dodecahedron-based metal lattice (D-lattice). **(B)** Stochastic metal lattice (S-lattice). **(C)** Cork viewed in the same plane as the natural surface of the tree, note hexagonal honeycomb-like structure in that projection. **(D)** Cork viewed in the radial direction. Note preferential alignment of cells in that projection.

explained by the surface cropping, we conclude that the ITA software faithfully identifies the node connectedness and correctly calculates the ITA angles. It is noteworthy that the angles detected by the application were consistently several degrees smaller than those of the *in silico* design.

Stochastic 3D Lattice (S-Lattice)

The S-lattice is shown in **Figures 3B**. As per the original design, the average network connectedness was found to be 4; the abundance of nodes declines as the number of their neighbors increases. The ratio of nodes 3-N:4-N:5-N was approximately 4:3:1, which is different from 8:3:1 typically seen in bone. Both 3-N and 4-N nodes generated bimodal ITA distributions. The peak values in these distributions suggest planar node configuration: 3-N nodes resemble the capital letters "Y" (mean angles centered around 60° and twice as abundant around 150°, that sum up to 360°); 4-N nodes resemble the capital letter "X" (equal height of two distributions centered around 60° and 120°, that in the case of four angles sum up to 360°). The angles that were previously reported for trabecular bone and formed unimodal distributions were not identified. Moreover, the presence of bimodal distributions indicates that the principle of maximal angular offset for a given number of connected elements is not observed in the S-lattice. The higher connectedness of the network and the defiance of the maximal angular offset principle may indicate that there is either no metabolic cost pressure to form a "simpler" network, and/or there are no mechanical requirements for more pronounced stress dissipation within the structure, as indeed could be expected from an artificially produced construct. We, therefore, conclude that the software is sensitive to network connectedness and differences in node configurations in 3D.

Cork

Cork is a component of the cork oak bark (*Quercus suberus*). Cork is a tough protective dead tissue, impermeable to gases and water. The honeycomb structure of cork is very fine compared to trabecular bone with an average cell wall thickness around 4–5 µm and cell size about 20–30 µm. Cork is an anisotropic structure: when viewed along the radial direction with respect to the tree trunk, a hexagonal honeycomb structure is apparent; when viewed in the tangential direction with respect to the tree trunk, the preferred radial alignment of the cell walls is clearly visible (**Figures 3C,D**). Although cork is a plant tissue with the size of its elements at least 20 times smaller than in bone, its ITA analysis demonstrates high similarity to bone 3D organization, namely the relatively low network connectedness and similar distributions of the ITA values. Although the node abundance declines with the increasing node connectedness, the trend is less pronounced than in trabecular bone, with the ratio of 5-N:4-N:3-N nodes being 6:3:1. This indicates a somewhat higher network connectedness than in trabecular bone, although lower than in the engineered stochastic lattice.

ITA Analysis of Pig Mandibles and Femora: Possibility of Adaptation at the Topological Level

Node Abundances and Proportions

Figure 5 shows the abundances of the different node types for the pig mandible samples and the pig femoral head. In general, the

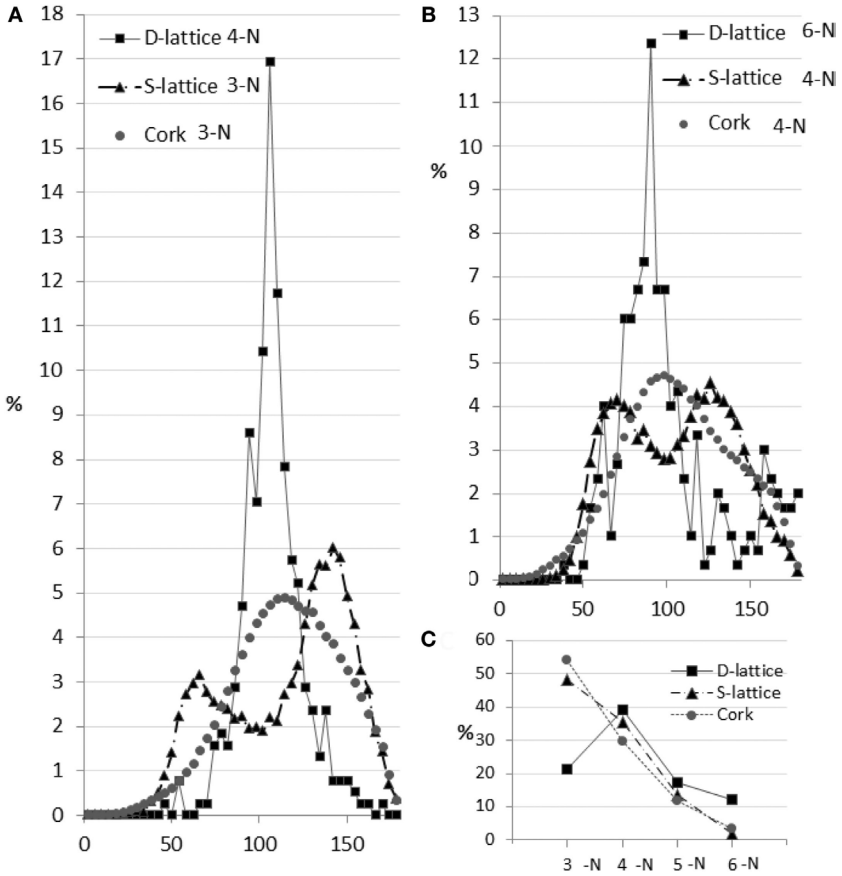

FIGURE 4 | Topological characteristics of the three examined structures. Panel **(A)** shows ITA distributions of the most abundant node (4-N in D-lattice and 3-N in S-lattice and cork). In the D-lattice, the distribution is very narrow, reflecting the fact that this is a designed configuration. In the S-lattice the ITA distribution forms two distinct peaks, one at 60° and another, twice as tall, at 150°. Since the sum of such angles is 360°, these 3-N nodes are planar, but do not possess maximal offset of the edges. In cork, the ITA distribution is unimodal, centered around 116° and, therefore, these nodes in cork approximate a planar shape. Panel **(B)** shows the ITA distributions in the second most abundant nodes for three test samples. D-lattice demonstrates a narrow peak centered as expected based on its design. Note the higher count of ITA at the large angle values (explained in the Section "Discussion"). The S-lattice has a bimodal distribution with equal counts of values around 60° and 120°, which is consistent with a planar structure with non-uniform offset of edges. The cork ITA distribution is similar to bone in shape and width and centers around 107°. That is indicative of the maximal angular offset. Panel **(C)** shows the node abundance as a function of the number of neighbors. The cork trend decays exponentially and is similar to bone; the S-lattice node abundance decays linearly; the D-lattice trend is consistent with the design and the surface cropping effects.

proportions of the 3:4:5-N nodes are similar to those reported for the human femur, such as 10:3:1.

Figure 6 shows the ITA distribution values for each of the three most abundant node types in bins of 4° for the pig samples. The abundances (in percent) of ITA values (in degrees) are plotted after normalizing to the total number of measurements, which were between about 3,000 (for the least abundant node) and about 110,000 (for the most abundant node) for each volume analyzed. Reznikov et al. (2016) estimated the errors for the 3-N, 4-N, and 5-N bins. The largest error for samples with about 3,000 nodes is around 20%. We, therefore, conclude that the ITA distributions of the different porcine samples are remarkably similar to each other, and TO TH to the human femoral heads.

We also calculated the mean ITA distribution values for all the pig samples analyzed (**Table 2**). These mean values are plotted for the different node types in **Figure 7** where they are also compared to the human femoral heads. Again the differences are small. We also note that about one-third of all the ITA values in each distribution falls within 10° on either side of the mean. In other words, ±10°, on either side of the mean values represents a third of all the values of a sample.

All the above observations clearly show that the ITA value abundances and distributions are remarkably similar when comparing the different regions within the pig mandible, the pig femoral head and the human femoral head (Reznikov et al., 2016). These ITA characteristics are, thus, conserved between two different bones and two different mammals: pigs and humans. We do, however, note that based on the validation tests that we performed this conclusion is well substantiated for rod-shaped trabeculae, but because of the inherent difficulties of obtaining reliable skeletonization products for flat objects (Stauber and Müller, 2007), this conclusion may be biased to some unknown

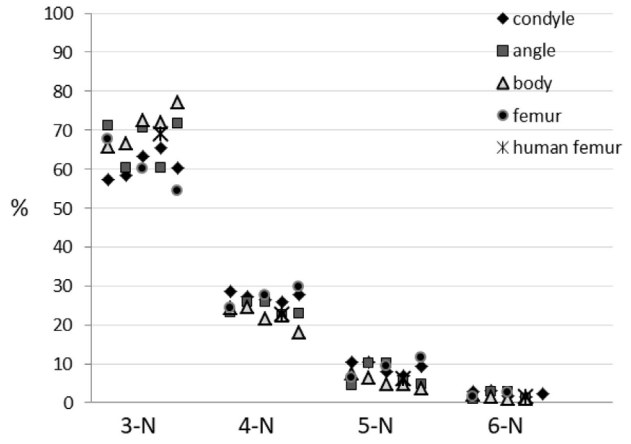

FIGURE 5 | Abundances of different nodes types in the examined areas of the pig mandibular condyle (five specimens), mandibular angle (five specimens), mandibular body (five specimens), pig proximal femur (three specimens) and human proximal femur [average of five specimens is taken from Reznikov et al. (2016)].

extent against plate-shaped trabeculae. We do, however, note that in the case of the cork sample, which is inherently platy as it consists mainly of cell walls, only about 12% of the edges were not connected and hence eliminated. Such unconnected edges mainly arise due to the skeletonization of plate-shaped elements. So we expect the bias in the bone samples after eliminating unconnected edges mainly from plates, to be less than 12%.

ITA Analysis of 3-N Nodes in the Mandibular Condylar Head and Neck

As distinct parts of the mandible are subjected to different loading patterns, we expected these differences to be reflected in the spatial distributions of the nodes within the trabecular network. We, therefore, chose to carry out a site-specific study of node spatial distributions in the condylar head and neck, as the head is subjected to strains mainly in the sagittal plane as part of the temporomandibular joint (TMJ; Liu and Herring, 2000a,b; Herring et al., 2002).

Node Distributions within the Mandibular Condyle

The head and the upper part of the neck of the condyle of specimen P1 is shown in **Figure 8**. The dotted line shows the anatomical boundary between the head and the neck (**Figure 8A**), P1 condyle showing only the outer surfaces. The nomenclature for orientation is also shown. The arrows show the directions of the prevailing principal stresses following Liu and Herring (2000a,b). Sagittal section of P1 condyle is represented in **Figures 8B**, the white dots show the 3D distribution of all the 3-N nodes (**Figures 8C**). All the nodes in the volume are projected onto one plane. This projection shows that there are more 3-N nodes closer to the articular surface of the condylar head as compared to the other areas.

In order to obtain quantitative data on the density of the nodes in different regions, we analyzed the number of nodes per unit volume in the articular portion of the condylar head and compared this value to the number of nodes in the same volume in the condylar neck. The same selected equal volumes taken from the head of the condyle and the neck were used for evaluating mean Tb.Th and separation, trabecular volume fraction and the DA. **Table 3** combines these morphometric parameters with the results of the topological analysis. It shows that the total number of nodes per unit volume in the articular portion of the condylar head is between 2.0 and 2.6 times higher than in the condylar neck. This is consistent with the visual presentation of the 3-N nodes in the condylar head and neck. As it is also visually clear, the trabecular meshwork is finer in the head than in the neck of the condyle. There are also proportionately more 4-N and 5-N nodes compared to 3-N nodes in the head compared to the neck, which is consistent with the higher network connectedness.

Alignment of Planar 3-N Nodes in the Condyle Head

We calculated the planarity of the 3-N nodes in all the pig samples analyzed here (**Figure 9**). Thirty to 35% of the 3-N nodes are within 4° of being perfectly planar. A similar observation was made for human femoral heads (Reznikov et al., 2016).

Since the condylar head of the pig mandible demonstrates a higher content of planar nodes along with the higher DA, we plotted the orientation of the planar 3-N nodes in the condyle in the same projection, as shown in **Figure 8**, which means in the direction of principal stresses. In **Figure 10**, the planes of planar 3-N nodes are shown by reciprocal vectors, perpendicular to those planes. Fast Fourier transform is generated from the image of the vectors and, also reciprocally, illustrates the co-alignment of vectors. **Figure 10** show that the vectors from the planar 3-N nodes do have a preferred orientation. The preferential orientation of the planar nodes, as revealed from the FFT, is aligned parallel to the principal directions of loading shown in **Figure 8A**.

DISCUSSION

Here, we show that the node abundances, the angular distributions, and mean ITA values in three different parts of the pig mandible and the pig proximal femur are principally similar to other previously analyzed bone samples [of the human proximal femur (Reznikov et al., 2016) and two differently loaded groups of human calcanei (Reznikov et al., 2017) in terms of node type proportions and the maximal angular offset of connected elements]. These results, therefore, clearly show that ITA values are conserved even between species from different mammalian taxonomic groups and between bones that carry out different mechanical functions. We, therefore, conclude that the topological parameters reflect functionally important aspects of trabecular bone structure.

ITA Analysis Validation

The results of the validation of ITA analysis show that for a reticulate network comprised of rod-shaped elements ("trabeculae") with known ITAs, the software accurately calculates the abundance of node types, accurately detects the mean ITA angles incorporated by design and realistically estimates the number of nodes truncated at the edges and their 3D configurations. Furthermore a stochastic reticulate structure produces

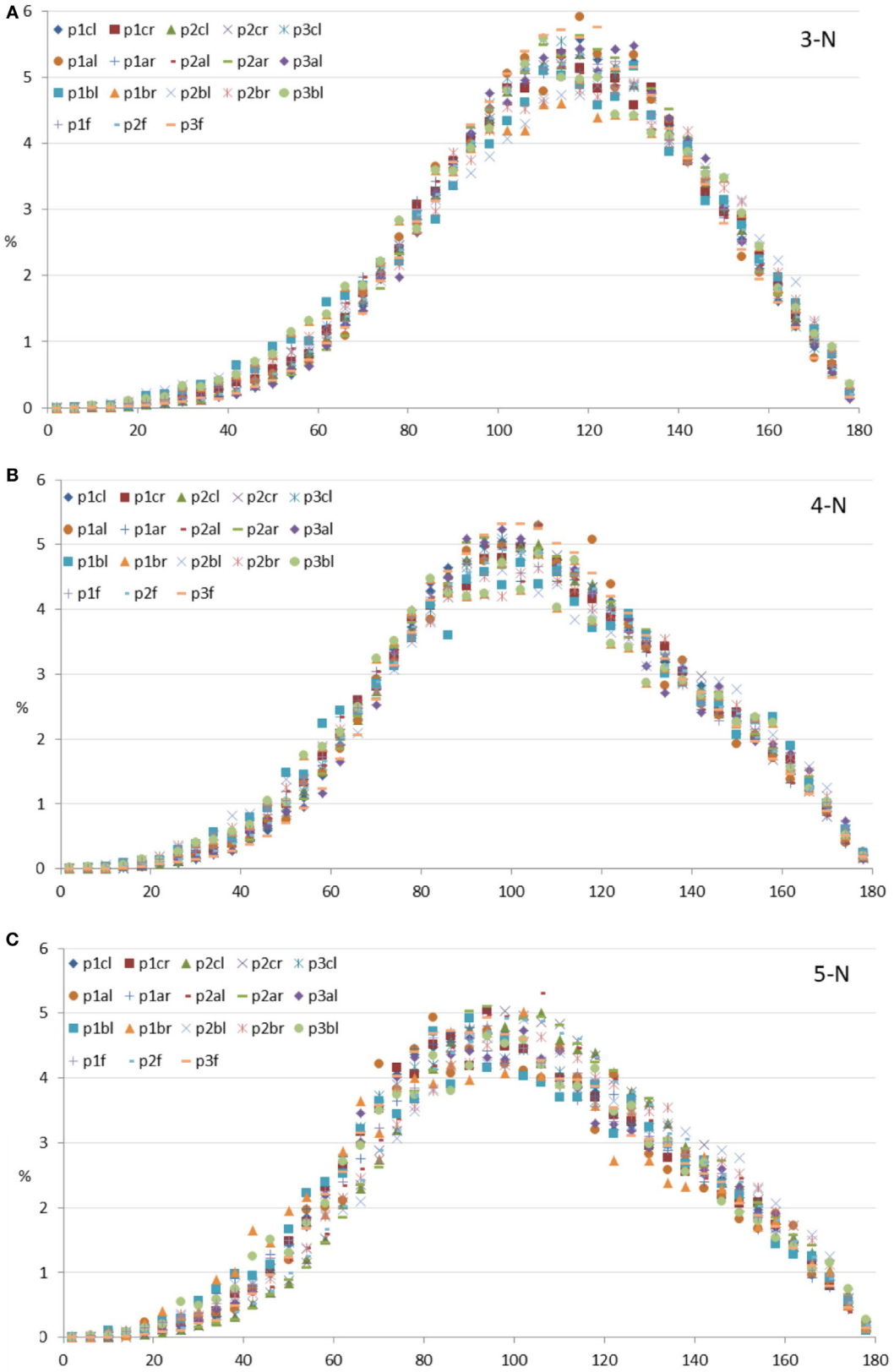

FIGURE 6 | Inter-trabecular angle (ITA) distributions of all specimens measured per node type. Frequencies of binned ITA values are given in percent of the total number measured; horizontal axes show ITA values in degrees. **(A)** 3-N nodes; **(B)** 4-N nodes; **(C)** 5-N nodes. Legends: first row, all condyles; second row, all mandibular angles; third row, all mandibular bodies; fourth row, all pig femoral heads.

distributions totally different from those reported for trabecular bone by Reznikov et al. (2016), showing that the software does not generate the same result regardless of structure.

TABLE 2 | Mean values of ITA distributions per node type, averaged for the samples measured and half width at half maximum (HWHM) of ITA distributions per node type, averaged for the samples measured.

	3-N mean	3-N HWHM	4-N mean	4-N HWHM	5-N mean	5-N HWHM
Angle	116 ± 0.5	29 ± 1.2	107 ± 0.8	31 ± 0.3	102 ± 0.5	32 ± 0.3
Body	114 ± 0.5	32 ± 1.1	105 ± 0.8	33 ± 1	102 ± 0.5	34 ± 1.3
Condyle	115 ± 0.4	28 ± 0.5	107 ± 0.5	31 ± 0.3	102 ± 0.4	32 ± 0.2
Femur	115 ± 0.6	28 ± 0.7	106 ± 0.6	30 ± 0.7	102 ± 0.6	32 ± 0.6

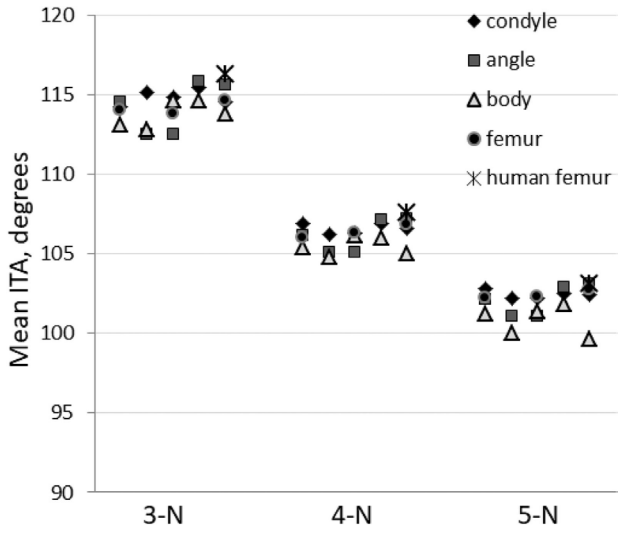

FIGURE 7 | Inter-trabecular angle mean values for the three most abundant node types. All measurements are presented: five values of porcine mandibular condyle, angle and body and three values for porcine proximal femur. Human proximal femur values are averaged (five individuals) and shown for reference (Reznikov et al., 2016).

In natural structures, as opposed to engineered structures the mean ITA values tend to be very close to angles in symmetrical geometric motifs, i.e., 120° for 3-N nodes and 109° for 4-N nodes. In these symmetrical motifs, the connecting edges are offset as far as possible from each other. In this way, the trabeculae can optimally cover 3D space with the least number of connecting elements. Together with the prevalence of simple nodes in the partially connected network, this results in an optimized combination of minimal metabolic cost of the structure and maximal stability to multidirectional loading. The width of the ITA distributions accounts for inherent irregularity of biological structures. Interestingly, both living animal tissue (bone) and dead plant tissue (cork) follow the same principles of network simplicity and maximal volume spanning, despite the different size scale of their networks. This observation stems from the fact that the ITA application analyzes topological determinants of the structure, uncoupled from their size, shape, and global orientation. Since the results obtained from the cork sample were close to the ITA parameters observed in bone, one sample of cork was deemed sufficient for validation. This observation, however, requires a thorough study of plant tissues and other similar biological lattices.

ITA and Functional Adaptation

We noticed that as the number of node neighbors increases, the ITA distributions become skewed: the 3-N distribution can be accounted for with a single Gaussian curve, as is expected from a natural continuous distribution of independent values. The distributions of 4-N and 5-N nodes, however, require a minor Gaussian curve in the region of high ITA values, for a satisfactory coefficient of determination (**Figure 11**). The contribution of the minor Gaussian curve is higher in the case of the 5-N distribution (the height of the minor peak is 25% from the height of the 4-N general distribution, and the height of the minor peak in the 5-N distribution is around 40%). A probable explanation for the presence of the minor Gaussian curves could be that the application detects not only the angles between the near branches of a node but also between remote branches in the same node of high connectivity. Indeed, in **Figures 4B**, the plot of the D-lattice demonstrates higher

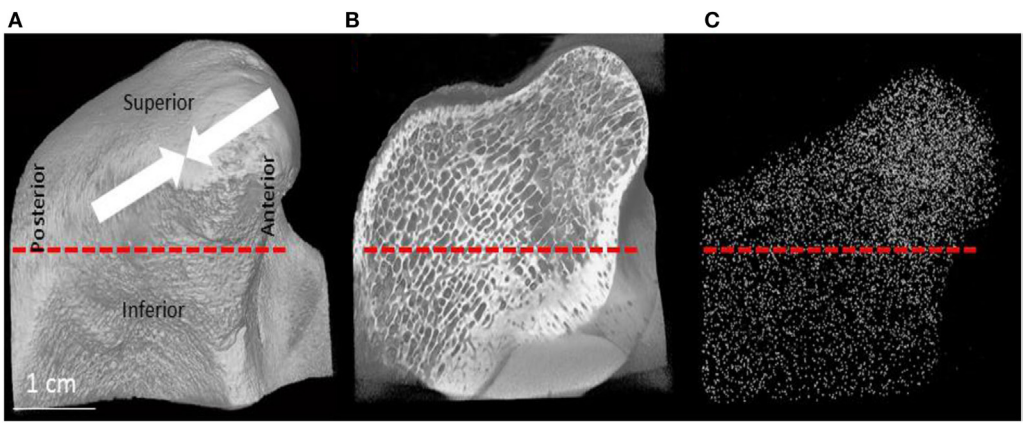

FIGURE 8 | **(A)** μCT image of the condylar head and neck of the pig. The arrows show the major compressive stress trajectories, as shown by Liu and Herring (2000a,b). **(B)** Section through the 3D μCT image of the condylar head and neck and **(C)** is a plot of the locations of all the 3-N nodes in the whole volume of the scan projected onto this plane. **(C)** Visually demonstrates that there are more 3-N nodes in the condylar head as compared to the neck.

TABLE 3 | Morphometric and topological parameters in the trabecular network of the pig mandible, condylar head (H), and neck (N), and their ratio.

Parameter	Pig 1, Left			Pig 1, Right		
	Head	**Neck**	**H/N**	**Head**	**Neck**	**H/N**
3-N, number	12,668	6,565	1.9	14,765	6,202	2.4
4-N, number	5,916	2,552	2.3	7,547	2,618	2.9
5-N, number	3,047	997	3.1	3,364	959	3.5
Total	26,708	13,204	2	31,727	12,459	2.6
3-N planar	3,445	1,839	1.9	3,989	1,611	2.5
3-N non-planar	1,632	1,251	1.3	2,062	1,069	1.9
Planar/non-planar	2.1	1.5		1.9	1.5	
Degree of anisotropy (DA)	0.8	0.5	1.6	0.8	0.5	1.6
Bone volume–total volume ratio (BV/TV)	0.4	0.5	0.8	0.5	0.5	1
Thickness (Tb.Sp), μm (SD)	380 (144)	468 (268)	0.8	387 (211)	499 (281)	0.8
Tb.Th, μm (SD)	247 (73)	468 (130)	0.5	306 (109)	413 (181)	0.7
	Pig 2, Left			**Pig 2, Right**		
	Head	**Neck**	**H/N**	**Head**	**Neck**	**H/N**
3-N, number	15,342	6,448	2.4	14,721	6,719	2.2
4-N, number	6,489	2,468	2.6	5,827	2,361	2.5
5-N, number	3,958	959	4.1	3,354	747	4.5
Total	30,464	12,539	2.4	28,727	12,333	2.3
3-N planar	3,546	1,607	2.2	3,309	1,544	2.1
3-N non-planar	1,489	1,057	1.4	1,516	962	1.6
Planar/non-planar	2.4	1.5		2.2	1.6	
DA	0.8	0.6	1.3	0.7	0.5	1.4
BV/TV	0.4	0.4	1	0.6	0.5	1.2
Tb.Sp, μm (SD)	348 (168)	420 (232)	0.8	322 (112)	402 (164)	0.8
Tb.Th, μm (sdSD)	314 (116)	357 (147)	0.9	359 (115)	470 (147)	0.8
	Pig 3, Left			**Cork**		
	Head	**Neck**	**H/N**			
3-N, number	12,453	6,256	2	88,986		
4-N, number	8,114	2,887	2.8	48,430		
5-N, number	3,452	9,55	3.6	19,119		
Total	27,940	12,833	2.2	156,535		
3-N planar	2,605	1,670	1.6	30,552		
3-N non-planar	1,316	1,065	1.2	4,435		
Planar/non-planar	1.9	1.5		6.8		
DA	0.7	0.6	1.2	0.6		
BV/TV	0.5	0.4	1.3	0.2		
Tb.Sp, μm (SD)	437 (140)	463 (160)	0.9	18 (7)		
Tb.Th, μm (SD)	316 (135)	341 (160)	0.9	3.7 (0.96)		

Number of different node types in the head and the neck present within equal sized volumes, as well as the parameters of morphometric analysis of trabecular bone.

values in the region 150–180°. This is a plot of 6-N nodes. In a 6-N node of perfect threefold symmetry all 6 edges are oriented at 90° to one another and form 12 right angles between the near edges. However, there are also 3 angles of 180° between remote edges of the same node. Nodes of three neighbors can have only three near-edge angles; 4-N nodes also can have only near-edge angles (as it has six possible pairs of near edges between which an angle can be measured). However, a 5-N node necessarily incorporates one angle between remote edges, along with nine pairs of near edges. Therefore, starting from the node complexity N-5 or higher, a bimodal ITA distribution can be expected, in which the major peak corresponds to the mean angle for pairs of near edges, and the minor peak corresponds to the angle for the only pair of remote edges. The minor peak position can be expected close to 180°. The fact that in trabecular bone ITA distribution the minor Gaussian peak is present to some extent in the 4-N ITA distribution can be possibly explained by life-long bone remodeling, when some nodes may lose one of their original branches.

The finding of highly conserved ITA properties may seem to clash with the well-established connection between trabecular bone texture and function. This connection was originally described in the work of Julius Wolff, who suggested that individual trabeculae of the proximal human femur are aligned along the principal stress directions (Wolff, 1892). Many studies examined this premise (Enlow, 1968; Bertram and Swartz, 1991; Currey, 2012), including several experimental studies that directly demonstrate this connection. Studies of trabecular bone in the knee joint of guinea fowl showed that the fine trabecular bone in the distal femur has a high degree of correspondence between the changes in joint angle and trabecular orientation (Pontzer et al., 2006). A study of the distal radius in a sheep model also supported the finding that trabecular bone adjusts and realigns

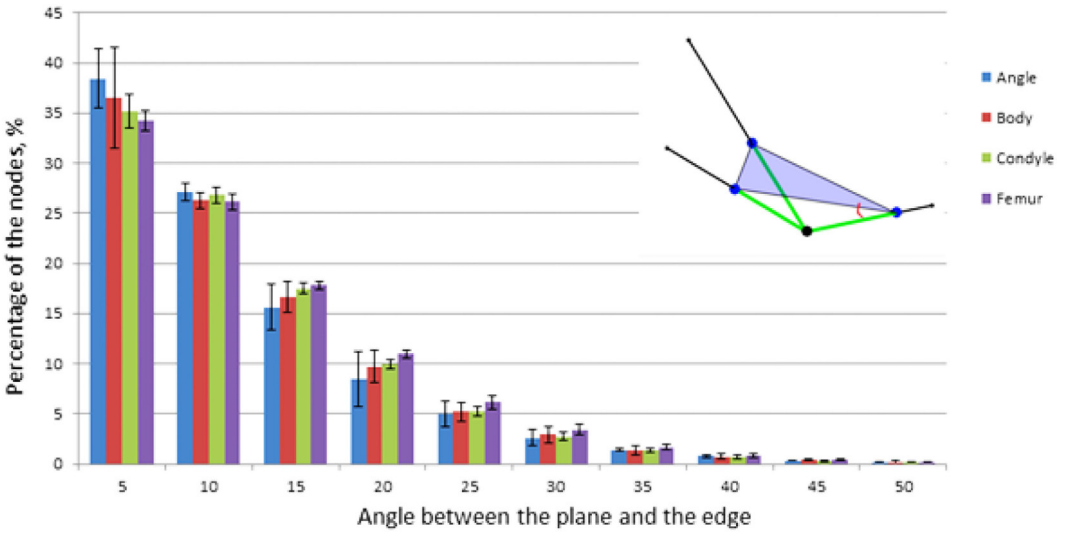

FIGURE 9 | Planarity of 3-N nodes. Percentage of nodes is plotted versus the angle between one of the edges and the plane. Insert: the measured angle, red; auxiliary plane, purple; edges, green.

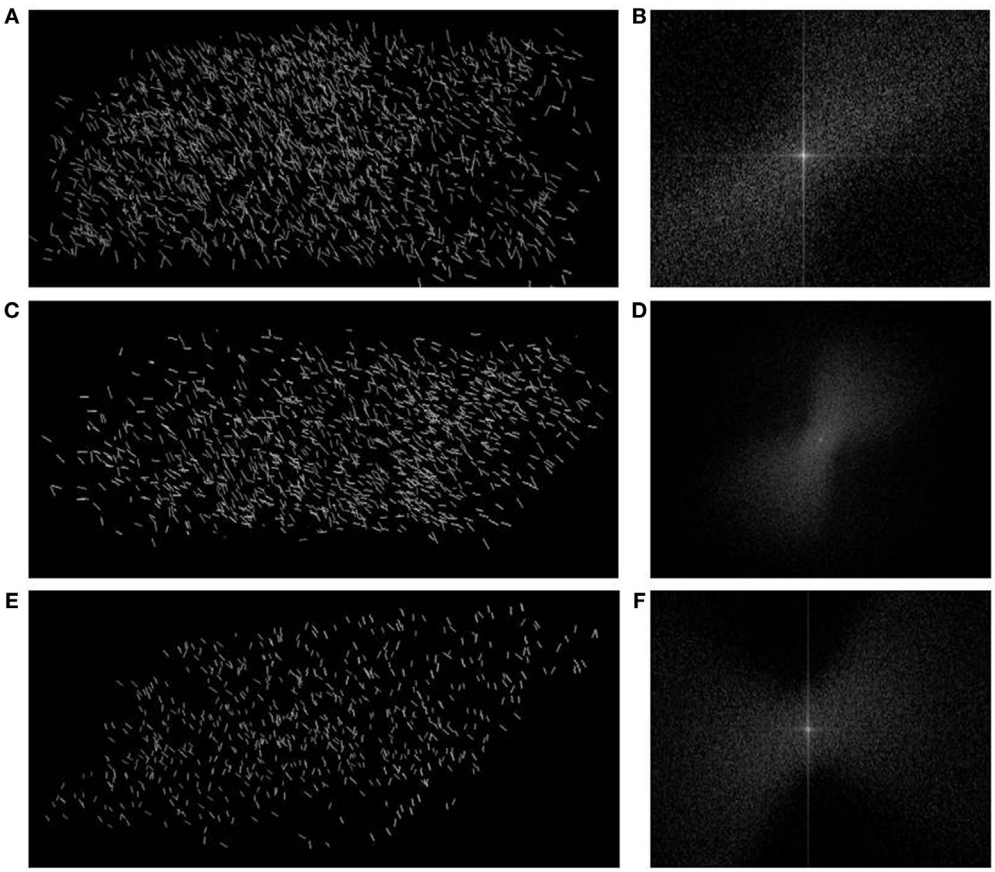

FIGURE 10 | Vector orientations of the 3-N planar nodes from specimen P1, P2, P3 represented in the right part of the figure **(A,C,E)** and the FFT analyses of images are represented in the left side **(B,D,F)**.

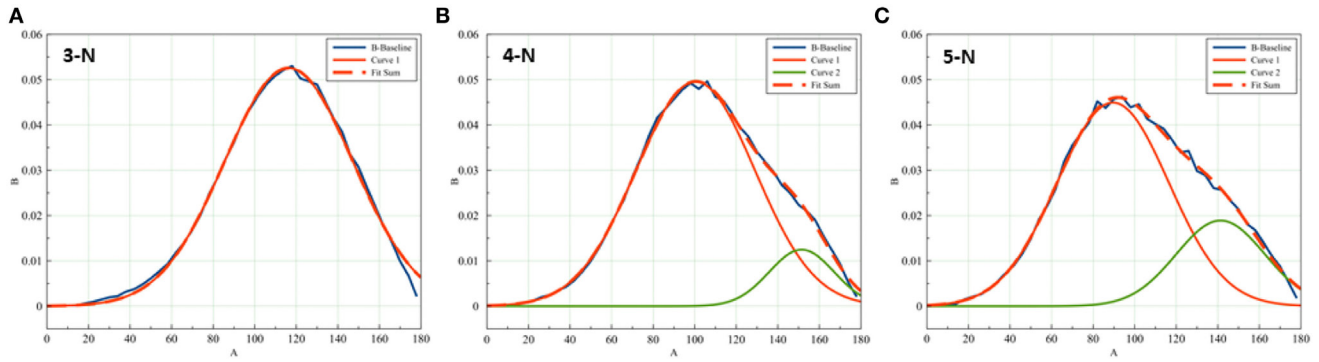

FIGURE 11 | Skewness of the ITA distribution increases with node connectedness. While **(A)** 3-N distribution can be fitted with a single Gaussian distribution, the distributions of **(B)** 4-N and **(C)** 5°-N ITA values require a minor Gaussian curve for a good fit. The minor distributions center around 150–160°.

in response to change in loading direction (Barak et al., 2011). The study of the calcaneus in normal and deformed human feet shows that consistent long-term loading results in the formation of a reproducible anisotropy pattern of trabecular bone. However, there is no real conflict between the fact that bone is capable of functional adaptation and the invariance of the ITA parameters in the analyzed samples. The difference between the traditionally analyzed morphometric parameters and the topological parameters reported here is that the ITA analysis is blind to the local thickness and form of the elements and only considers the trabecular network determinants. The universal topology of a trabecular network can be viewed as the 3D archetype on which various changes in size and shape can be superimposed. Thus, the topology observed in trabecular bone can adopt a multitude of different texture parameters such as increase in Tb.Th, without negating the principles of network simplicity and maximal spanning of the 3D space.

A detailed comparison of the nodes within the condylar head and neck did, however, reveal an alternative form of adaptation that does not involve trabecular shape, but also does not breach the topology. A higher DA was identified in all five condylar heads analyzed, in comparison with the condylar neck. Along with that the average Tb.Th and its SD are consistently lower in the condylar head, and the trabecular spacing and its SD are also lower. These observations are in accord with a finer and denser network. In addition, the total number of nodes and the proportions of 4-N and 5-N nodes were higher in the condylar head than in the condylar neck, further indicating that the fine trabecular network of the condylar head is densely connected. One way to achieve a higher DA is by network coarsening and thickening of the trabeculae that are co-oriented with the principal stress trajectories (Ryan and Krovitz, 2006). But the opposite is observed in the fine and densely connected network of the condylar head. Significantly, the ratio of planar 3-N nodes to non-planar 3-N nodes is consistently larger in the head than in the neck. Moreover, the orientation of the planes of these flat 3-N nodes was found along the physiological stress trajectory. Therefore, the higher anisotropy can be achieved by local transformation of the network elements that does not amend the general topology, but also allows retaining the scale and shape of the network elements.

The mandibular condyle is one of the components of the TMJ. The condylar head is subjected to forces in well-defined directions (Liu and Herring, 2000a,b; Herring et al., 2002; Cornish et al., 2006) as this is a paired joint that has limited freedom around the sagittal or vertical axes, and primarily allows movement around the transverse axis. Since consistent and repetitive loading of bones results in increasing their anisotropy, the structure of trabecular bone in the condylar head is expected to adapt accordingly, consistent with our results and with previous studies (Gosen, 1974; Hekneby, 1974; Teng and Herring, 1995; Kim et al., 2013). Interestingly, the higher anisotropy in the condylar head is achieved by transformation of the network motifs (preferred orientation of the planar 3-N nodes), and the fine scale of the network remains unaltered. We speculate that the biological rationale for that might be the preservation of a higher compliance of the fine trabecular tissue. Indeed, increased anisotropy combined with higher bone volume density provides the highest stiffness of trabecular bone (Maquer et al., 2015). On the other hand, it was shown that higher stiffness of trabecular bone is associated with degenerative disease of articular cartilage (Li and Aspden, 1997a,b; Hurwitz et al., 2001). We also speculate that increasing trabecular bone anisotropy by network transformation (and not by trabecular coarsening and stiffening in certain orientations) might be Nature's strategy to preserve articular cartilage from untimely wear and tear. This observation opens new insights into two important problems in bone research, namely joint degeneration (perhaps, adaptation to stereotypical loading by increased anisotropy with trabecular network coarsening, rather than co-alignment of some topological elements) and bone fragility (i.e., inability to stably cope with loads low in magnitude, but unusual in direction).

The analysis presented here certainly pertains to rod-shaped trabeculae; its validity with regard to plate-shaped trabeculae needs to be studied, as the skeletonization procedure currently used in our ITA analysis code may have some difficulties in properly identifying and separately representing plate-shaped trabeculae. Analysis results will, therefore, be more valid and mechanically significant in those instances where the majority

of the trabeculae are rod shaped, like the bodies of vertebrae (Parkinson and Fazzalari, 2013).

CONCLUSION

The ITA application reliably detects the topological characteristics of natural and artificial 3D structures.

The ITA parameters are remarkably conserved between two mammalian species and between different bones.

In the TMJ and the mandibular condyle, where conflicting requirements for higher anisotropy and finer network co-exist, the topological level of functional adaptation is preferential, as reflected by co-alignment of planar 3-N nodes.

ETHICS STATEMENT

The study was approved by Institutional Animal Care and Use Committee at the Weizmann Institute of Science.

AUTHOR CONTRIBUTIONS

Design the study—YB-Z, NR, RS, and SW. Performed the study—YB-Z. Analyzed the results—YB-Z, NR, RS, and SW. Wrote the manuscript—YB-Z, NR, RS, and SW. YB-Z and NR had equal contribution to the paper.

ACKNOWLEDGMENTS

We thank Dr. Vlad Brumfeld, Ms. Victoria Tarle, Ms. Hila Chase, and Ms. Maria Pierantoni for their invaluable help in this project. We thank Mr. Shaaz Ghouse, Imperial College London, UK, for kindly providing the 3D-printed honeycomb lattices for validation of the ITA algorithm. This research was supported by the ISRAEL SCIENCE FOUNDATION (grant numbers 29/12 and 875/15). SW holds the Dr. Walter and Dr. Trude Borchardt Professorial Chair in Structural Biology.

REFERENCES

Allen, M. R., Gineyts, E., Leeming, D. J., Burr, D. B., and Delmas, P. D. (2008). Bisphosphonates alter trabecular bone collagen cross-linking and isomerization in beagle dog vertebra. *Osteoporos. Int.* 19, 329–337. doi:10.1007/s00198-007-0533-7

An, Y. H., and Freidman, R. J. (1998). *Animal Models in Orthopaedic Research*. Boca Raton, FL: CRC Press.

Arganda-Carreras, I., Fernández-González, R., Muñoz-Barrutia, A., and Ortiz-De-Solorzano, C. (2010). 3D reconstruction of histological sections: application to mammary gland tissue. *Microsc. Res. Tech.* 73, 1019–1029. doi:10.1002/jemt.20829

Ascenzi, M.-G., Hetzer, N., Lomovtsev, A., Rude, R., Nattiv, A., and Favia, A. (2011). Variation of trabecular architecture in proximal femur of postmenopausal women. *J. Biomech.* 44, 248–256. doi:10.1016/j.jbiomech.2010.10.017

Barak, M. M., Lieberman, D. E., and Hublin, J.-J. (2011). A Wolff in sheep's clothing: trabecular bone adaptation in response to changes in joint loading orientation. *Bone* 49, 1141–1151. doi:10.1016/j.bone.2011.08.020

Bayraktar, H. H., and Keaveny, T. M. (2004). Mechanisms of uniformity of yield strains for trabecular bone. *J. Biomech.* 37, 1671–1678. doi:10.1111/j.1469-185X.1991.tb01142.x

Bertram, J. E., and Swartz, S. M. (1991). The 'law of bone transformation': a case of crying Wolff? *Biol. Rev.* 66, 245–273. doi:10.1111/j.1469-185X

Bouxsein, M. L., Boyd, S. K., Christiansen, B. A., Guldberg, R. E., Jepsen, K. J., and Müller, R. (2010). Guidelines for assessment of bone microstructure in rodents using micro-computed tomography. *J. Bone Miner. Res.* 25, 1468–1486. doi:10.1002/jbmr.141

Boyde, A. (2003). Improved digital SEM of cancellous bone: scanning direction of detection, through focus for in-focus and sample orientation. *J. Anat.* 202, 183–194. doi:10.1046/j.1469-7580.2003.00146.x

Buser, D., Schenk, R., Steinemann, S., Fiorellini, J., Fox, C., and Stich, H. (1991). Influence of surface characteristics on bone integration of titanium implants. A histomorphometric study in miniature pigs. *J. Biomed. Mater. Res.* 25, 889–902. doi:10.1002/jbm.820250708

Ciarelli, T., Fyhrie, D. P., Schaffler, M., and Goldstein, S. A. (2000). Variations in three-dimensional cancellous bone architecture of the proximal femur in female hip fractures and in controls. *J. Bone Miner. Res.* 15, 32–40. doi:10.1359/jbmr.2000.15.1.32

Cornish, R. J., Wilson, D. F., Logan, R. M., and Wiebkin, O. W. (2006). Trabecular structure of the condyle of the jaw joint in young and mature sheep: a comparative histomorphometric reference. *Arch. Oral. Biol.* 51, 29–36. doi:10.1016/j.archoralbio.2005.04.004

Currey, J. D. (2012). The structure and mechanics of bone. *J. Mater. Sci* 47, 41–54. doi:10.1007/s10853-011-5914-9

Deshpande, V., Ashby, M., and Fleck, N. (2001). Foam topology: bending versus stretching dominated architectures. *Acta Mater.* 49, 1035–1040. doi:10.1016/S1359-6454(00)00379-7

Doube, M., Kłosowski, M. M., Arganda-Carreras, I., Cordelières, F. P., Dougherty, R. P., Jackson, J. S., et al. (2010). BoneJ: free and extensible bone image analysis in ImageJ. *Bone* 47, 1076–1079. doi:10.1016/j.bone.2010.08.023

Enlow, D. H. (1968). Wolff's law and the factor of architectonic circumstance. *Am. J. Orthod.* 54, 803–822. doi:10.1016/0002-9416(68)90001-8

Ghouse, S., Babu, S., Van Arkel, R. J., Nai, K., Hooper, P. A., and Jeffers, J. (2017). The influence of laser parameters and scanning strategies on the mechanical properties of a stochastic porous material. *Mater. Design*. 131, 498–508. doi:10.1016/j.matdes.2017.06.041

Gosen, A. (1974). Mandibular leverage and occlusion. *J. Prosthet. Den.* 31, 369–376. doi:10.1016/0022-3913(74)90144-9

Hekneby, M. (1974). The load of the temporomandibular joint: physical calculations and analyses. *J. Prosthet. Den.* 31, 303–312. doi:10.1016/0022-3913(74)90201-7

Herring, S. W., Decker, J. D., Liu, Z. J., and Ma, T. (2002). Temporomandibular joint in miniature pigs: anatomy, cell replication, and relation to loading. *Anat. Rec.* 266, 152–166. doi:10.1002/ar.10049

Hurwitz, D. E., Sumner, D. R., and Block, J. A. (2001). Bone density, dynamic joint loading and joint degeneration. *Cells Tissues Organs* 169, 201–209. doi:10.1159/000047883

Jensen, K., Mosekilde, L., and Mosekilde, L. (1990). A model of vertebral trabecular bone architecture and its mechanical properties. *Bone* 11, 417–423. doi:10.1016/8756-3282(90)90137-N

Kahn, D. W. (1975). *Topology: An Introduction to the Point-Set and Algebraic Areas*. Baltimore, MD: Williams & Wilkins Co.

Keaveny, T. M., Morgan, E. F., Niebur, G. L., and Yeh, O. C. (2001). Biomechanics of trabecular bone. *Annu. Rev. Biomed. Eng.* 3, 307–333. doi:10.1146/annurev.bioeng.3.1.307

Kim, J.-E., Shin, J.-M., Oh, S.-O., Yi, W.-J., Heo, M.-S., Lee, S.-S., et al. (2013). The three-dimensional microstructure of trabecular bone: analysis of site-specific variation in the human jaw bone. *Imaging Sci. Dent.* 43, 227–233. doi:10.5624/isd.2013.43.4.227

Kinney, J., and Ladd, A. (1998). The relationship between three-dimensional connectivity and the elastic properties of trabecular bone. *J. Bone Miner. Res.* 13, 839–845. doi:10.1359/jbmr.1998.13.5.839

Kivell, T. L. (2016). A review of trabecular bone functional adaptation: what have we learned from trabecular analyses in extant hominoids and what can we apply to fossils? *J. Anat.* 228, 569–594. doi:10.1111/joa.12446

Lee, T.-C., Kashyap, R. L., and Chu, C.-N. (1994). Building skeleton models via 3-D medial surface axis thinning algorithms. *Graph. Model. Img. Process.* 56, 462–478. doi:10.1006/cgip.1994.1042

Li, B., and Aspden, R. M. (1997a). Composition and mechanical properties of cancellous bone from the femoral head of patients with osteoporosis or osteoarthritis. *J. Bone Miner. Res.* 12, 641–651. doi:10.1359/jbmr.1997.12.4.641

Li, B., and Aspden, R. M. (1997b). Mechanical and material properties of the subchondral bone plate from the femoral head of patients with osteoarthritis or osteoporosis. *Ann. Rheum. Dis.* 56, 247–254. doi:10.1136/ard.56.4.247

Liu, Z., and Herring, S. W. (2000a). Bone surface strains and internal bony pressures at the jaw joint of the miniature pig during masticatory muscle contraction. *Arch. Oral. Biol.* 45, 95–112. doi:10.1016/S0003-9969(99)00127-2

Liu, Z., and Herring, S. W. (2000b). Masticatory strains on osseous and ligamentous components of the temporomandibular joint in miniature pigs. *J. Orofac. Pain* 14, 265–278.

Maquer, G., Musy, S. N., Wandel, J., Gross, T., and Zysset, P. K. (2015). Bone volume fraction and fabric anisotropy are better determinants of trabecular bone stiffness than other morphological variables. *J. Bone Miner. Res.* 30, 1000–1008. doi:10.1002/jbmr.2437

Mosekilde, L., Mosekilde, L., and Danielsen, C. (1987). Biomechanical competence of vertebral trabecular bone in relation to ash density and age in normal individuals. *Bone* 8, 79–85. doi:10.1016/8756-3282(87)90074-3

Mosekilde, L., Weisbrode, S. E., Safron, J. A., Stills, H. F., Jankowsky, M. L., Ebert, D. C., et al. (1993). Calcium-restricted ovariectomized Sinclair S-1 minipigs: an animal model of osteopenia and trabecular plate perforation. *Bone* 14, 379–382. doi:10.1016/8756-3282(93)90167-9

Müller, R. (2009). Hierarchical microimaging of bone structure and function. *Nat. Rev. Rheumatol.* 5, 373–381. doi:10.1038/nrrheum.2009.107

Müller, R., Van Campenhout, H., Van Damme, B., Van der Perre, G., Dequeker, J., Hildebrand, T., et al. (1998). Morphometric analysis of human bone biopsies: a quantitative structural comparison of histological sections and micro-computed tomography. *Bone* 23, 59–66. doi:10.1016/S8756-3282(98)00068-4

Nkenke, E., Lehner, B., Weinzierl, K., Thams, U., Neugebauer, J., Steveling, H., et al. (2003). Bone contact, growth, and density around immediately loaded implants in the mandible of mini pigs. *Clin. Oral. Implants Res.* 14, 312–321. doi:10.1034/j.1600-0501.2003.120906.x

Odgaard, A. (1997). Three-dimensional methods for quantification of cancellous bone architecture. *Bone* 20, 315–328. doi:10.1016/S8756-3282(97)00007-0

Parkinson, I. H., and Fazzalari, N. L. (2013). "Characterisation of trabecular bone structure," in *Skeletal Aging and Osteoporosis: Biomechanics and Mechanobiology*, ed. M. J. Silva (Berlin; Heidelberg: Springer), 31–51.

Pontzer, H. L., Lieberman, D. E., Momin, E., Devlin, M. J., Polk, J. D., Hallgrimsson, B., et al. (2006). Trabecular bone in the bird knee responds with high sensitivity to changes in load orientation. *J. Exp. Biol.* 209, 57–65. doi:10.1242/jeb.01971

Reznikov, N., Chase, H., Ben Zvi, Y., Tarle, V., Singer, M., Brumfeld, V., et al. (2016). Inter-trabecular angle: a parameter of trabecular bone architecture in the human proximal femur that reveals underlying topological motifs. *Acta Biomater.* 44, 65–72. doi:10.1016/j.actbio.2016.08.040

Reznikov, N., Phillips, C., Cooke, M., Garbout, A., Ahmed, F., and Stevens, M. M. (2017). Functional adaptation of the calcaneus in historical foot binding. *J. Bone Miner. Res.* 32, 1915–1925. doi:10.1002/jbmr.3185

Roschger, P., Grabner, B., Rinnerthaler, S., Tesch, W., Kneissel, M., Berzlanovich, A., et al. (2001). Structural development of the mineralized tissue in the human L4 vertebral body. *J. Struct. Biol.* 136, 126–136. doi:10.1006/jsbi.2001.4427

Ryan, T. M., and Krovitz, G. E. (2006). Trabecular bone ontogeny in the human proximal femur. *J. Hum. Evol.* 51, 591–602. doi:10.1016/j.jhevol.2006.06.004

Saha, P. K., Gomberg, B. R., and Wehrli, F. W. (2000). Three-dimensional digital topological characterization of cancellous bone architecture. *Int. J. Imaging Syst. Technol.* 11, 81–90. doi:10.1002/(SICI)1098-1098(2000)11:1<81:AID-IMA9>3.0.CO;2-1

Stauber, M., and Müller, R. (2007). A sensitivity analysis of the volumetric spatial decomposition algorithm. *Comput. Methods Biomech. Biomed. Engin.* 10, 25–37. doi:10.1080/10255840601090053

Teng, S., and Herring, S. W. (1995). A stereological study of trabecular architecture in the mandibular condyle of the pig. *Arch. Oral. Biol.* 40, 299–310. doi:10.1016/0003-9969(94)00173-9

Terheyden, H., Jepsen, S., Möller, B., Tucker, M. M., and Rueger, D. C. (1999). Sinus floor augmentation with simultaneous placement of dental implants using a combination of deproteinized bone xenografts and recombinant human osteogenic protein-l. A histometric study in miniature pigs. *Clin. Oral. Implants Res.* 10, 510–521. doi:10.1034/j.1600-0501.1999.100609.x

Thompson, D. (1942). *On Growth and Form*. Cambridge: Cambridge University Press.

Wainwright, S. A., Biggs, W. D., Currey, J. D., and Gosline, J. M. (1976). *Mechanical Design in Organisms*. Princeton: Princeton University Press.

Wolff, J. (1892). *Das Gesetz der Transformation der Knochen*. Berlin: Verlag von August Hirschwald.

Zysset, P. K. (2003). A review of morphology-elasticity relationships in human trabecular bone: theories and experiments. *J. Biomech.* 36, 1469–1485. doi:10.1016/S0021-9290(03)00128-3

Conflict of Interest Statement: The authors declare that the research was conducted in the absence of any commercial or financial relationships that could be construed as a potential conflict of interest.

frontiers in Materials

ORIGINAL RESEARCH
published: 13 September 2017
doi: 10.3389/fmats.2017.00027

Sost Deficiency does not Alter Bone's Lacunar or Vascular Porosity in Mice

*Henry Mosey[1], Juan A. Núñez[2], Alice Goring[2], Claire E. Clarkin[2], Katherine A. Staines[3], Peter D. Lee[4], Andrew A. Pitsillides[1] and Behzad Javaheri[1]**

[1] *Skeletal Biology Group, Comparative Biomedical Sciences, The Royal Veterinary College, London, United Kingdom,* [2] *Faculty of Natural and Environmental Sciences, Biological Sciences, University of Southampton, Southampton, United Kingdom,* [3] *School of Applied Sciences, Edinburgh Napier University, Edinburgh, United Kingdom,* [4] *Manchester X-Ray Imaging Facility, University of Manchester, Manchester, United Kingdom*

SCLEROSTIN (*Sost*) is expressed predominantly in osteocytes acting as a negative regulator of bone formation. In humans, mutations in the *SOST* gene lead to skeletal overgrowth and increased bone mineral density, suggesting that SCLEROSTIN is a key regulator of bone mass. The function of SCLEROSTIN as an inhibitor of bone formation is further supported by *Sost* knockout (KO) mice which display a high bone mass with elevated bone formation. Previous studies have indicated that *Sost* exerts its effect on bone formation through Wnt-mediated regulation of osteoblast differentiation, proliferation, and activity. Recent *in vitro* studies have also suggested that SCLEROSTIN regulates angiogenesis and osteoblast-to-osteocyte transition. Despite this wealth of knowledge of the mechanisms responsible for SCLEROSTIN action, no previous studies have examined whether SCLEROSTIN regulates osteocyte and vascular configuration *in cortices of mouse tibia*. Herein, we image tibiae from *Sost* KO mice and their wild-type (WT) counterparts with high-resolution CT to examine whether lack of SCLEROSTIN influences the morphometric properties of lacunae and vascular canal porosity relating to osteocytes and vessels within cortical bone. Male Sost KO and WT mice (n = 6/group) were sacrificed at 12 weeks of age. Fixed tibiae were analyzed using microCT to examine cortical bone mass and architecture. Then, samples were imaged by using benchtop and synchrotron nano-computed tomography at the tibiofibular junction. Our data, consistent with previous studies show that, *Sost* deficiency leads to significant enhancement of bone mass by cortical thickening and bigger cross-sectional area and we find that this occurs without modifications of tibial ellipticity, a measure of bone shape. In addition, our data show that there are no significant differences in any lacunar or vascular morphometric or geometric parameters between *Sost* KO mouse tibia and WT counterparts. We, therefore, conclude that the significant increases in bone mass induced by *Sost* deficiency are not accompanied by any significant modification in the density, organization, or shape of osteocyte lacunae or vascular content within the cortical bone. These data may imply that SCLEROSTIN does not modify the frequency of osteocytogenic recruitment of osteoblasts to initiate terminal osteocytic differentiation in mice.

Keywords: *Sost*, osteocyte, vascular porosity, microCT, lacunar porosity

OPEN ACCESS

Edited by:
Gianluca Tozzi,
University of Portsmouth,
United Kingdom

Reviewed by:
Egon Perilli,
Flinders University, Australia
Himadri Shikhar Gupta,
Queen Mary University of London,
United Kingdom

****Correspondence:***
Behzad Javaheri
bjavaheri@rvc.ac.uk

Specialty section:
This article was submitted to Mechanics of Materials, a section of the journal Frontiers in Materials

Received: *17 June 2017*
Accepted: *28 August 2017*
Published: *13 September 2017*

Citation:
Mosey H, Núñez JA, Goring A, Clarkin CE, Staines KA, Lee PD, Pitsillides AA and Javaheri B (2017) Sost Deficiency does not Alter Bone's Lacunar or Vascular Porosity in Mice. Front. Mater. 4:27. doi: 10.3389/fmats.2017.00027

INTRODUCTION

Bone is a metabolically active tissue constantly adapting its structure to external mechanical stimuli, leading to changes in mass (Raab et al., 1991; Bennell et al., 2002), shape (Rubin, 1984), strength (Järvinen et al., 2003; Leppänen et al., 2008), and length (Howell, 1917; Steinberg and Trueta, 1981). The exact mechanisms for transformation of these mechanical signals into biological responses are not fully elucidated. Osteocytes, the most abundant cells within skeleton, are derived by a process termed osteocytogenesis from bone-forming osteoblasts. They reside within irregularly shaped ellipsoidal lacunar spaces (Franz-Odendaal et al., 2006) and are reported to act as strain sensors and transducers (Bonewald and Johnson, 2008; Javaheri et al., 2014). There have been a number of hypotheses put forward as to how osteocytes achieve their mechanosensory role. One, the fluid flow hypothesis, states that mechanical loading perturbs bone fluid through the lacunar-canaliculi network producing shear forces on the osteocyte cell processes (Burger and Klein-Nulend, 1999; Han et al., 2004). An alternative proposes that osteocytes are vital for efficient bone remodeling and repair of bone microdamage (Verborgt et al., 2000; Ma et al., 2008). Besides these roles, osteocytes are also reported to regulate matrix mineral homeostasis (Qing and Bonewald, 2009) through osteocytic osteolysis (Bélanger, 1969; Kerschnitzki et al., 2013).

The cellular mechanisms that regulate mechanotransduction are not fully understood, but several key pathways have been identified in osteocytes. One such pathway involves control of the canonical Wnt signaling pathway by its negative regulator (Balemans et al., 2005; Weivoda et al., 2017) SCLEROSTIN; a protein encoded by the *Sost* gene expressed predominantly by deeply embedded mature osteocytes (Balemans et al., 2001).

SCLEROSTIN and the canonical Wnt signaling pathway regulate bone mass through several mechanisms, including stem cell renewal (Reya and Clevers, 2005), stimulation of pre-osteoblast differentiation and proliferation (Kato et al., 2002), enhancement of osteoblast activity (Kato et al., 2002; Bodine et al., 2004), inhibition of osteoblast and osteocyte apoptosis (Babij et al., 2003), regulation of osteoclastogenesis (Glass et al., 2005; Holmen et al., 2005), and modulation of adaptive response to mechanical strain (Armstrong et al., 2007; Javaheri et al., 2014). In addition, previous *in vitro* studies have reported that SCLEROSTIN promotes osteocytogenesis, or osteoblast-to-osteocyte differentiation (Atkins et al., 2011), and angiogenesis in human endothelial cells *in vitro* (Oranger et al., 2017). Moreover, *Sost* deficiency leads to higher matrix mineralization and enhanced bone mass; mineralization has been reported to influence terminal osteoblast differentiation into osteocytes (Cameron et al., 1967; Prideaux et al., 2012) and angiogenesis (Choi et al., 2000; Van Wesenbeeck et al., 2002). It remains unclear whether the role of SCLEROSTIN as a negative regulator of bone mass extends, however, to controlling osteocyte lacunar organization and vascular content in bone.

Visualization of osteocytes and vascular canals is difficult in bone's highly mineralized matrix. Thus, spatial characteristics, including density, volume, and shape of osteocyte lacunae and vascular porosity have, therefore, often been used as a proxy (Qiu et al., 2003; Carter et al., 2013; Javaheri et al., 2015). This is predominantly due to the fact that 3D quantification of osteocyte and vessel density and morphology is problematic using traditional imaging techniques including confocal microscopy. More recently, nano-computed tomography (nanoCT) has been employed to attain sub-micron resolution of lacuna and vascular porosity using benchtop CT scanners that offer sub-micron scanning. We (Javaheri et al., 2015) and others (Robling and Turner, 2002; Cooper et al., 2004; Mullender et al., 2005; Skedros et al., 2005; Matsumoto et al., 2006; Vatsa et al., 2008; Schneider et al., 2009, 2010; Palacio-Mancheno et al., 2014) have previously reported that nanoCT is a useful tool to quantify osteocyte and vascular porosity in 3D. However, the gold standard for such imaging remains synchrotron-based nanoCT which provides a higher X-ray flux and lower beam hardening effect due to monochromatic beam, which in principle can improve the image quality (Pacureanu et al., 2012; Carter et al., 2013; Dong et al., 2013; Kerschnitzki et al., 2013; Mader et al., 2013; Webster et al., 2013).

To our knowledge, no previous study has investigated SCLEROSTIN's role in the 3D organization of the osteocyte and vascular networks in bone. We hypothesize that *Sost* deficiency results in altered osteoblast-to-osteocyte transition and vascular network formation as reflected by changes in lacunar properties including numbers, volume, diameter, and shape as well as vascular parameters, respectively. To address this, we employ desktop as well as synchrotron-based nanoCT analyses of lacunar and vascular contents in a *Sost*-deficient mouse model.

MATERIALS AND METHODS

Animal Model

Frozen sperm from a male *Sost* knockout (KO) mouse was purchased from the Knockout Mouse Project Repository at the University of California Davis, CA, USA. Imported sperm used to fertilize ova from C57BL/6 wild-type (WT) mice. To obtain offspring, fertilized egg was implanted into pseudopregnant female C57BL/6 mice. Offspring were bred through several generations to obtain *Sost* homozygous mice on a C57BL/6 background.

Mice were provided with standard mouse chow and water *ad libitum* throughout the study and housed up to four per cage in polypropylene cages with wood chip and paper bedding. Weaners up to 8 weeks of age were fed a standard rodent breeding diet and thereafter a standard rodent maintenance diet (Special Diet Services, South Witham, UK). All procedures performed were reviewed and approved by the ethics committee of the Royal Veterinary College (London, UK) and complied with the UK Animals (Scientific Procedures) Act 1986.

Imaging

High-Resolution Micro and NanoCT

MicroCT

Two groups of mice, male *Sost* KO and WT mice ($n = 6$/group), at 12 weeks of age were sacrificed by cervical dislocation. Right tibia from each mouse was dissected, the flesh around the bone removed and fixed in 70% EtOH. Prior to scanning, tibiae were removed from 70% EtOH and dried superficially on paper

tissue, before being wrapped in plastic "cling-film," to prevent drying during scanning, and scanned *ex vivo* using the Skyscan 1176 (Skyscan, Kontich, Belgium), with X-ray tube operated at 50 kV and 600 μA, 2,000 ms exposure time, a rotation step of 0.800°, a 1-mm aluminum filter and a voxel size of 9 μm within a field of view of 11.5 mm (width) and 7.8 mm (height). The slices were then reconstructed using NRecon 1.6.9.4 (Skyscan, Kontich, Belgium). Whole bone analysis was performed on datasets derived from CT scans using BoneJ (Doube et al., 2010) (version 1.4.0) a plugin for ImageJ (Schneider et al., 2012). Following alignment and removal of fibula from the dataset a global bone threshold of 75 Gy level was used to segment bone from non-bone in the images. To determine whether *Sost* deficiency alters cortical bone architecture, we undertook gross bone morphology analysis. The cross-sectional area (CSA), second moment of area around minor (I_{min}) and major axes (I_{max}) and mean thickness were calculated within BoneJ ("Slice Geometry"). The most proximal and the most distal 10% portions of tibial length included trabecular bone and thus were not included in the analysis.

Nano-Computed Tomography

The same tibiofibular junction of the *Sost* KO and WT mice tibiae scanned previously by micro-CT (2.2.1.1), were re-scanned using a Skyscan 1172 (Skyscan, Kontich, Belgium) X-ray microtomography as described previously (Javaheri et al., 2015). This scanner offers isotropic detail detectability down to 0.5 μm. The samples were placed in Orthodontic Wax (Kerr, CA, USA) at 200 μA, 50 kV and, 9,800 ms exposure time with a 0.25-mm aluminum filter (99.999% purity, Goodfellow, Huntington, UK), 360° at a rotation step of 0.25° and a voxel size of 0.6 μm. Scans were centered at the tibiofibular junction within a field of view of 2.3 mm (width) and 1.6 mm (height). Two-frame averaging was used to improve the signal-to-noise ratio. The scan time for each sample was approximately 7 h. Prior to reconstruction, thermal shift in projection images was corrected in NRecon 1.6.9.4 (Skyscan, Kontich, Belgium). 300 slices (0.6 μm per each slide, total 180 μm) were then reconstructed in NRecon using a ring correction factor of 15, smoothing of 1 and 35% beam hardening correction. Three 100 consecutive images from the tibiofibular junction were selected from each specimen. The images were loaded in CTAn software (Skyscan, Kontich, Belgium). The major differences between nanoCT and microCT (2.2.1.1) are the voxel size, exposure time, and angular rotation step.

Initially, foreground was segmented from background and a series of noise removal "despeckling" steps performed. Pores smaller than 13 μm^3 and larger than 1,500 μm^3 were assumed to be noise and vascular canals, respectively, and the rest were considered to be lacunae. These limits were based on a previous study using confocal microscopy indicating a size between 28 and 1,713 μm^3 for osteocytes (McCreadie et al., 2004). Previous studies used and reported these volume limits to examine lacunar and canal porosity (Tommasini et al., 2012; Carter et al., 2013; Carriero et al., 2014; Javaheri et al., 2015). Morphometric indices for lacunar and vascular canals were calculated by measuring the 3D parameters of each discreet object within the volume of interest after segmentation. These indices for lacuna included average lacunar number (N.Lc), average lacunar volume (Lc.Avg.V), total volume (Lc.Tot.V), diameter (Lc.D; calculated with the sphere-fitting method), number of lacunar pores per unit bone volume (N.Lc/Ct.BV), and number of lacunar pores per total volume (N.Lc/Tot.V). For vascular canals, number (Ca.N), total volume (Ca.Tot.V), diameter (Ca.D; calculated with the sphere-fitting method), number of vascular canals per unit bone volume (N.Ca/Ct.BV), and number of vascular canals per total volume (N.Ca/Tot.V) were measured. Shape analysis of the lacunae was conducted utilizing "Analyze Particles" function in BoneJ. Shape parameters were then computed for each ellipsoid based upon the resulting three radii. The best-fit ellipsoid provided lacuna major radius (Lc.λ1), lacuna intermediate radius (Lc.λ2), and lacuna minor radius (Lc.λ3), which correspond to the lacuna's principal axes (i.e., the eigenvalues of the inertial matrix). These values allowed calculation of the degree of lacunar elongation [$Lc.El = 1 - (Lc.\lambda2/Lc.\lambda1)$] and degree of lacunar flatness [$Lc.Fl \geq 1 - (Lc.\lambda3/Lc.\lambda2)$] (Javaheri et al., 2015). The composition of the structure was then plotted using a Flinn diagram (Flinn, 1962) showing major: intermediate axis ratio on the *y*-axis and the intermediate: minor axis ratio on the *x*-axis.

Synchrotron NanoCT

Tibiae from separate groups of male *Sost* KO and WT mice ($n = 6$/group) were fixed in 70% EtOH and were embedded in wax to prevent sample movement. Tibiofibular junctions were scanned using SR CT at the TOMCAT beamline of the Swiss Light Source at a voxel size of 0.65 μm. This scanner offers isotropic detail detectability down to 0.37 μm. For each scan projection, images were acquired over a range of 360° at a rotation step of 0.12°, a photon energy of 18.5 keV, 18 ms exposure, corrected for ring artifacts due to potential scintillator defects and reconstructed based on gridrec algorithm using graphical user interface written in Python/Jython (Marone and Stampanoni, 2012) and developed as a plugin for Fiji (Schindelin et al., 2012). Scans were centered at the tibiofibular junction (maximum outer dimension of 1.5 mm) within a field of view of 3.3 mm (width) and 1.4 mm (height). Tomographic datasets were typically acquired in 10–15 min. SR CT datasets consisted of a stack of 1,000 reconstructed CT slices, 300 of which were used for morphometric analysis as described previously (see Nano-Computed Tomography).

Statistical Analysis

Normality and homogeneity of variance were used for all comparisons between *Sost* KO and WT mice. Violations of normality and homogeneity were not observed.

For gross cortical bone morphology analysis, graphs were plotted using the programming language "R," version 3.1.3 (R Foundation for Statistical Computing, Vienna, Austria; http://www.r-project.org). For this purpose, the functions lattice and grid were used. Two-sample *t*-test was used for comparisons between *Sost* KO and WT mice. Data are presented as mean ± SEM and were considered statistically significant when $p < 0.05$.

Graphs relating to lacunar and vascular porosity data, obtained from either benchtop nanoCT or synchrotron were generated using GraphPad Prism 6 (GraphPad Software, Inc., San Diego,

CA, USA). Two-sample *t*-test was used for comparisons between *Sost* KO and WT mice. Data are presented as mean ± SEM and were considered statistically significant when $p < 0.05$.

RESULTS

Sost Deficiency Produce Gross Changes in Cortical Bone

We found that *Sost* deficiency did not alter tibial length (**Table 1**) but was a significant determinant of bone CSA (**Figure 1B**), producing higher bone CSA in *Sost* KO compared with WT mice along the entire tibia length. Furthermore, we found that *Sost* deficiency also contributed significantly to cortical thickness (**Figures 1A,B**), with *Sost* KO mice exhibiting higher thickness than WT mice. These increases in cortical thickness were accompanied by reduction in medullary cavity area (**Figure 1C**).

Our data showed that the overall effect of *Sost* deficiency on I_{min} was most pronounced distal to the mid-shaft, where significant increases in I_{min} were observed (**Figure 1D**), and that there was a lack of marked alteration in the proximal tibia. I_{max} was higher 30 and 85% along the tibia of *Sost* KO mice (**Figure 1D**). Predicted tibial resistance to torsion (J) is higher in *Sost* KO mice in two regions at ~25–35 and 70–90% of tibial length (**Figure 1E**). Moreover, we found that Sost deficiency did not modify tibial ellipticity, a measure of bone shape (**Figure 1E**).

Sost Deficiency does not Alter Lacunar and Vascular Configurations

Our data show that *Sost* deficiency leads to higher total volume (Tot.V) and bone cortical volume (Ct.BV) ($p < 0.001$; **Table 1**). Our morphometric evaluation of the cortical bone at the tibiofibular junction (**Figures 2A,B**), shows that absolute number of lacunar pores is greater in *Sost* KO than in WT bones, containing significantly greater total numbers of osteocyte lacunae (N.Lc; $p < 0.001$; **Figures 2C,D**) in images obtained from nanoCT and synchrotron. This greater lacunar number, however, was normalized to control WT mouse levels, when expressed per unit of bone volume (N.Lc/Ct.BV; **Figure 2D**) as well as total volume including bone, lacuna, and vascular canals volume (N.Lc/Tot.V; **Table 1**). The average lacunar volume (Lc.Avg.V; **Table 1**), total lacunar volume occupied by all lacunar pores (Lc.Tot.V; **Table 1**), and lacunar diameter (Lc.D; **Table 1**) were not significantly different in datasets of either imaging modalities between *Sost* KO and WT mice.

Greater absolute non-normalized N.Lc in *Sost* KO bone was also consistent with measures of greater N.Ca, in which significantly higher vascular canal number (N.Ca; $p < 0.001$; **Figures 2C,D**), were evident in *Sost* KO bones. This was also normalized to control WT mouse levels when total vascular canal number was expressed per unit bone volume (N.Ca/Ct.BV; **Figure 2D**) as well as total volume (N.Ca/Tot.V; **Table 1**). Furthermore, we found that *Sost* deficiency did not alter average volume of vascular canals (Ca.Avg.V; **Table 1**), total volume of all vascular canals (Ca.Tot.V; **Table 1**), or vascular canal diameter (Ca.D; **Table 1**). These data indicate that the *Sost* deficiency produces an elevation in bone volume but does not lead to modification in lacunar and vascular network density in bone.

Analysis of lacunar shape, using Flinn diagram (Flinn, 1962) (**Figure 2E**) showed that *Sost* deficiency does not modify osteocyte arrangement and shape. Lacunar elongation and flatness were not significantly altered in tibiofibular junction in *Sost* KO compared with WT in either imaging modalities. These data showed that *Sost* deficiency does not lead to divergence in osteocyte shape and organization in mouse tibiae.

DISCUSSION

Our data are consistent with previous studies (Krishnan et al., 2006; Li et al., 2008; Hassler et al., 2014; Suen et al., 2015; Kamiya

TABLE 1 | Porosity parameters representing lacuna and vascular porosity of male wild-type (WT) and *Sost* knockout (KO) mice at 12 weeks of age, detailing *t*-test comparisons for significant genotype effect of data obtained from nano-computed tomography (nanoCT) or synchrotron.

Morphometric parameters	WT synchrotron	KO synchrotron	*t*-Test	WT CT	KO CT	*t*-Test
Bone parameters						
Tibial length (mm)	17.39 ± 0.03	17.36 ± 0.03	NS	17.46 ± 0.04	17.23 ± 0.12	NS
Ct.BV (mm^3)	0.146 ± 0.003	0.205 ± 0.006	<0.001	0.142 ± 0.002	0.209 ± 0.001	<0.001
Tot.V (bone + canal and lacunar pores) (mm^3)	0.151 ± 0.003	0.211 ± 0.006	<0.001	0.145 ± 0.002	0.213 ± 0.001	<0.001
Vascular canal						
Ca.Avg.V (μm^3)	4,529 ± 870	3,206 ± 1,201	NS	3,418 ± 671	2,444 ± 916	NS
Ca.Tot.V (mm^3)	0.00035 ± 0.00004	0.00023 ± 0.00005	NS	0.00021 ± 0.00008	0.00028 ± 0.00002	NS
Ca.D (μm)	9.44 ± 0.81	7.93 ± 0.81	NS	8.21 ± 0.33	7.61 ± 0.24	NS
N.Ca/Tot.V (number/mm^3)	443 ± 68	605 ± 605	NS	571 ± 45	691 ± 242	NS
Lacunae						
Lc.Avg.V (μm^3)	396 ± 46	420 ± 31	NS	312 ± 19	288 ± 40	NS
Lc.Tot.V (mm^3)	0.00581 ± 0.00002	0.00659 ± 0.00004	NS	0.00377 ± 0.00002	0.00428 ± 0.00001	NS
Lc.D (μm)	3.82 ± 0.28	3.39 ± 0.14	NS	3.13 ± 0.39	2.9 ± 0.21	NS
N.Lc/Tot.V (number/mm^3)	63,189 ± 863	64,411 ± 1,240	NS	45,494 ± 4,170	42,761 ± 5,741	NS

Bone parameters included tibial length, cortical bone volume (Ct.BV), and total volume (Tot.V: volumes of bone plus lacunar and canal volumes). For vascular canals, average canal volume (Ca.Avg.V), total canal volume (Ca.Tot.V), canal diameter (Ca.D), and number of vascular canals per total volume (N.Ca/Tot.V) are shown. Morphometric measurements for lacunar pores, include average lacunar volume (Lc.Avg.V), total lacunar volume (Lc.Tot.V), lacunar diameter (Lc.D), and number of lacunar pores per total volume (N.Lc/Tot.V). WT and Sost KO tibiae scanned at the synchrotron were from a separate batch compared to micro-CT and benchtop nanoCT. Two-sample t-test was used to compare means between WT and Sost KO mice. Data represent means ± SEM with group sizes of n = 6 for WT and Sost KO mice.

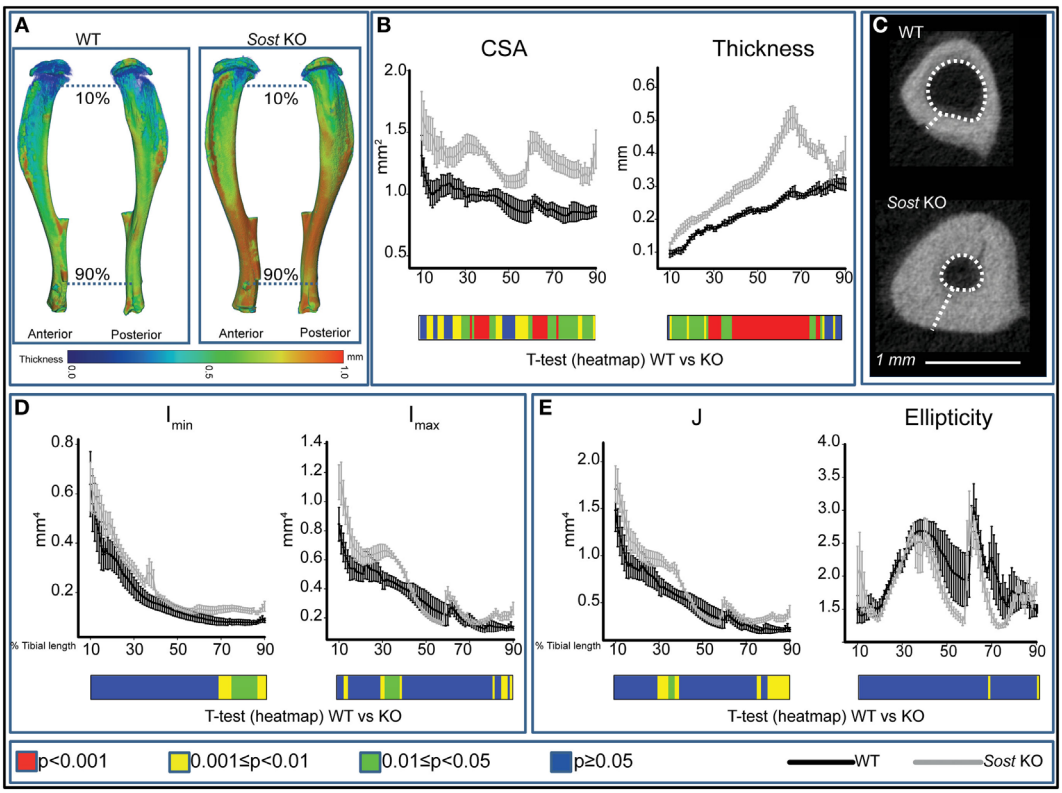

FIGURE 1 | Modification in cortical bone phenotype in *Sost* knockout (KO) (gray) mice. **(A)** Representative 3D Micro-CT color-coded images of tibial cortical bone thickness. **(B)** Bone cross-sectional area (CSA) and mean cortical thickness between 10 and 90% of total tibial length. **(C)** Gross macroscopic comparison of microCT images of cortical tibia at the tibiofibular junction for both groups demonstrating a significantly thickened tibial cortex and reduced medullary cavity in *Sost* KO compared to wild-type (WT) mice. **(D)** Minimum and maximum second moments of area (I_{min} and I_{max} respectively) and **(E)** ellipticity and J (resistance to torsion) between 10 and 90% of total tibial length of WT and *Sost* KO mice. Graphical heat map **(B,D,E)** at the bottom of each graph summarizes statistical differences at specific matched locations along the tibial length, representative of overall effect of *Sost* deficiency: red $p < 0.001$, yellow $0.001 \leq p < 0.01$, green $0.01 \leq p < 0.05$, and blue $p \geq 0.05$. Two-sample *t*-test was used to compare means between WT and *Sost* KO mice. Line graphs represent means ± SEM. Group sizes were $n = 6$ for WT and *Sost* KO mice.

et al., 2016; Qin et al., 2016; Shu et al., 2017) indicating that *Sost* deficiency leads to significant elevations of cortical bone mass. In addition, we find that these increases are not linked to significant changes in bone shape. Moreover, using two high-resolution imaging modalities, we examined whether the observed elevation of bone mass at macroscopic level in *Sost* KO mice extends to include differences in the lacunar and vascular composition of cortical bone. In particular, this focuses on the number and morphometric properties of the vascular and osteocyte lacunar cavities within the cortical bone in these mice.

We have previously used benchtop CT to study lacunar and vascular canal porosity using tibiofibular junction as a landmark (Javaheri et al., 2015). Benchtop nanoCT is essentially a micro-CT scanner with small enough focal spot, capable to be used at also sub-micrometer voxel size (0.6 μm/pixel). Herein, we have also employed synchrotron-based nanoCT imaging to compare and confirm suitability of using benchtop-based nanoCT imaging for porosity analysis. With both imaging modalities, the absolute numbers of lacunar and vascular cavities were significantly higher in *Sost* KO compared with WT mice at tibiofibular junction. This similarity suggests that data obtained from the benchtop CT are comparable, at least in terms of these parameters, to gold standard synchrotron imaging. We could not perform a paired comparison between benchtop and synchrotron nanoCT on the same specimens as bones scanned at the synchrotron were from a different batch.

Our detailed analyses reveal that there were no significant differences in shape, density or organization of lacunae or vascular canal porosity within the cortical bone of *Sost* KO mice. These data suggest that enhanced properties of bone on a macroscopic scale, specifically in terms of mass in *Sost*-deficient mice, are not reflected in significant alterations in the geometry and morphometry of lacunar and vascular porosity. The lacunar and vascular canal values per unit volume of bone obtained from both imaging modalities were similar to those reported previously (Carriero et al., 2014; Hemmatian et al., 2017). In addition, values relating to volume from both imaging modalities revealed that *Sost* deficiency does not alter average and total volume of lacunar or vascular canals. Diameter of lacunar and vascular canals were lower in KO compared with WT tibiae, but these differences did not reach levels of statistical

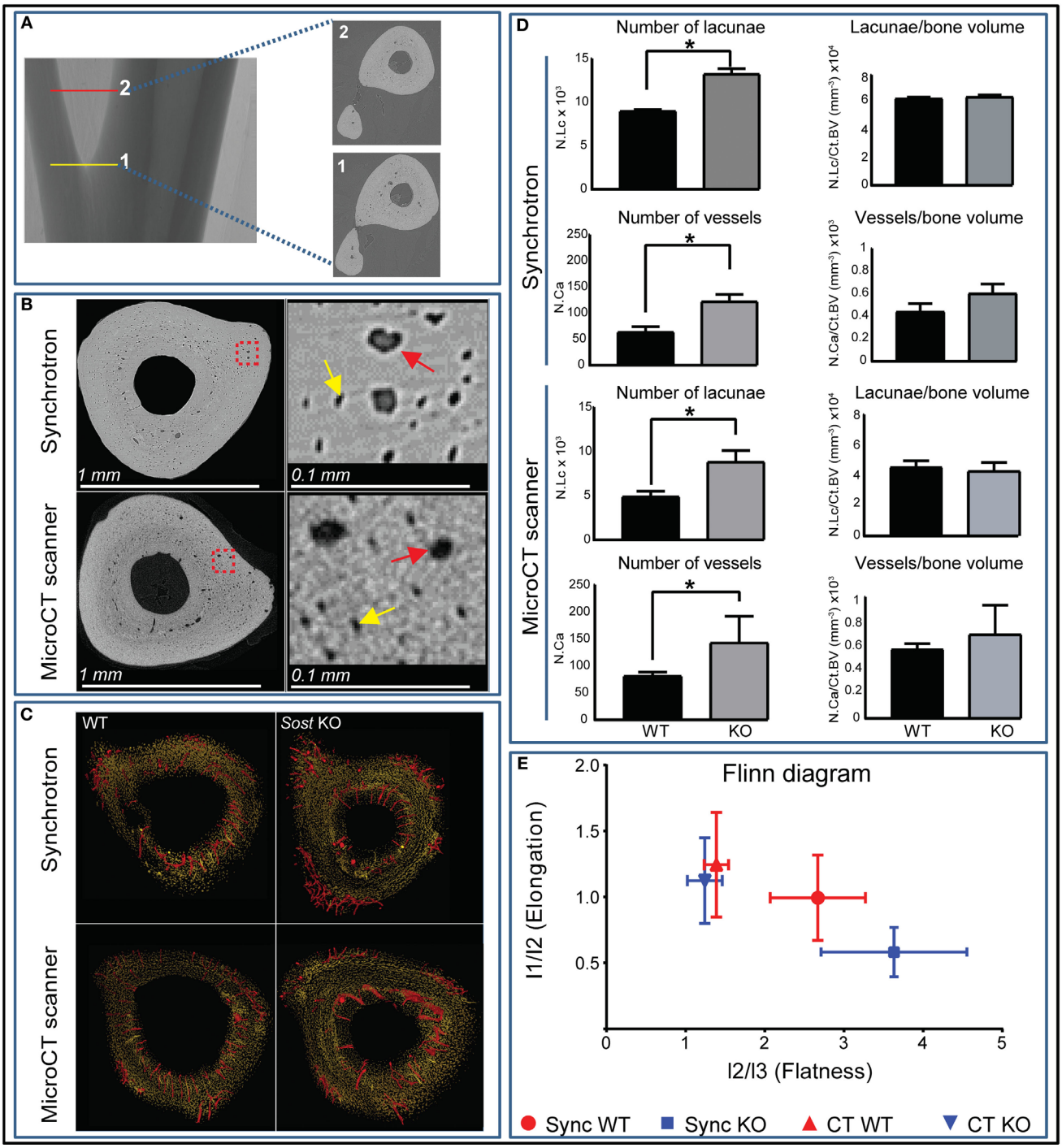

FIGURE 2 | High-resolution nano-computed tomography (nanoCT) and synchrotron-based analysis of the cortex lacunar and vascular porosity at the tibiofibular junction. **(A)** Three 100 ascending images were selected from point 1 at the tibiofibular junction to point 2 and were used for porosity analysis. **(B)** Resolving power and gross macroscopic comparison of images obtained from the nanoCT and the synchrotron. Higher magnification quadrants are also shown right side of their respective images for better appreciation. Yellow and red arrows depict selected lacunar and canal pores in both imaging modalities. **(C)** Surface representation of the lacunar (yellow) and red (vascular canal porosity) segmented from 300 consecutive images from tibiofibular junction of wild-type (WT) and *Sost* knockout (KO) mice. **(D)** Number of lacunar pores and vascular canals of WT and *Sost* KO mice at 12 weeks of age. **(E)** Flinn diagram displaying lacunar shapes in WT and *Sost* KO tibia at tibiofibular junction. The *x*-axis represents lacunar flatness which was calculated by dividing lacunar intermediate radius (l2: length of best-fit ellipsoid's intermediate radius) with lacunar minor radius (l3: length of best-fit ellipsoid's minor radius). The *y*-axis represents lacunar elongation which was calculated by dividing lacunar major radius (l1: length of best-fit ellipsoid's major radius) with lacunar intermediate radius (l2: length of best-fit ellipsoid's intermediate radius). WT and *Sost* KO tibiae scanned at the synchrotron were from a separate batch compared to micro-CT and bench top nanoCT. Two-sample *t*-test was used to compare means between WT and *Sost* KO mice. Data represent means ± SEM with group sizes of $n = 6$ for WT and *Sost* KO mice.

significance. This may explain, minor and not major increases in total volume of lacunar and canal volumes despite having significantly higher absolute number of lacunar and canal cavities. The average volume of lacunar pores was in agreement with those reported previously (Wang et al., 2005; Schneider et al., 2007; Vatsa et al., 2008; Javaheri et al., 2015; Kerckhofs et al., 2016). The average lacunar volume (~360 μm^3) we report in this manuscript is also in agreement with lacunar volume measurements reported by McCreadie et al. (2004) obtained using confocal microscopy.

Furthermore, when the absolute number of both lacunae and vessels are corrected for total and bone volume, the data become not significantly different between *Sost* KO and WT mice. This implies that the density of lacunae and vascular canals is unaffected by the action of SCLEROSTIN at least at this specific location in male mice at 12 weeks of age. These data suggest that the frequency of osteocyte recruitment from the osteogenic lineage is independent of SCLEROSTIN-mediated control, or alternatively that other factors ensure control of these recruitment processes and that there is, therefore, significant redundancy in this process. The statistically significant increases in bone mass in *Sost* KO mice implies, however, that this terminal stage of osteoblastic to osteocytic differentiation following entrapment in their own mineralized secretions (Dallas and Bonewald, 2010) occurs in a manner that is *Sost*-independent. Previous studies reported that the Wnt signaling and SCLEROSTIN regulate bone remodeling (Balemans et al., 2001; Van Wesenbeeck et al., 2003), influence pre-osteoblast differentiation and proliferation (Kato et al., 2002) and osteoblast-to-osteocyte transition *in vitro* (Atkins et al., 2011). We initially hypothesized that SCLEROSTIN influences the final stage of osteoblast differentiation in bone and expected the values related to osteocyte lacunae per unit bone volume in *Sost* KO mice to be significantly modified. As this does not appear to be the case, our data offer weight to the argument that any interaction between SCLEROSTIN and the maturation pathway occurs at an earlier stage in osteoblast cell lineage commitment. Similar arguments are also applicable to the role of SCLEROSTIN in vascular recruitment to bone. Further work should thus concentrate on identifying the exact stage or stages that are significantly influenced by the presence or absence of SCLEROSTIN.

There are several limitations to our study. The number of samples in our study are six per group and variation in our data, specifically the KO group (**Table 1** and **Figure 2D**), might have influenced our findings. In this context, it is worth noting that murine bones lack Haversian canals and that it is possible that the role of SCLEROSTIN, in species where such canals comprise a significant volume of the cortex (humans), may differ (Perilli et al., 2015). In addition, we find that canal and lacunar porosity volumes recorded by benchtop CT are smaller than those revealed by synchrotron, by 40 and 35%, respectively. It is possible that despite the similar diameter of these pores with the two CT systems, there could be some artificially broken canals and hence smaller volume measured by the benchtop CT (Palacio-Mancheno et al., 2014).

In conclusion, our data show that *Sost* deficiency in mice, despite having a significant influence on the physical and structural properties of the whole bone does not modify lacunar and vascular canal porosities. Thus, SCLEROSTIN's negative modulatory role on bone formation does not likely extend to a control over the terminal phase in osteocyte recruitment nor to any modification in bone's vascularization in mice.

ETHICS STATEMENT

This study was carried out in accordance with the recommendations and approval of ethics committee of the Royal Veterinary College (London, UK). All procedures complied with the UK Animals (Scientifc Procedures) Act 1986.

AUTHOR CONTRIBUTIONS

Conceived and designed the experiments: CC, AP, and BJ. Performed the experiments: BJ, JN, and AG. Analyzed the data: HM and BJ. Contributed reagents/materials/analysis tools: KS, CC, PL, and AP. Wrote the paper: BJ and AP.

FUNDING

This study was supported by funding from the BBSRC BB/I014608/1, Arthritis Research UK 20581, and 20039 and The Society for Endocrinology Early Career Grant.

REFERENCES

Armstrong, V. J., Muzylak, M., Sunters, A., Zaman, G., Saxon, L. K., Price, J. S., et al. (2007). Wnt/beta-catenin signaling is a component of osteoblastic bone cell early responses to load-bearing and requires estrogen receptor alpha. *J. Biol. Chem.* 282, 20715–20727. doi:10.1074/jbc.M703224200

Atkins, G. J., Rowe, P. S., Lim, H. P., Welldon, K. J., Ormsby, R., Wijenayaka, A. R., et al. (2011). Sclerostin is a locally acting regulator of late-osteoblast/preosteocyte differentiation and regulates mineralization through a MEPE-ASARM-dependent mechanism. *J. Bone Miner. Res.* 26, 1425–1436. doi:10.1002/jbmr.345

Babij, P., Zhao, W., Small, C., Kharode, Y., Yaworsky, P. J., Bouxsein, M. L., et al. (2003). High bone mass in mice expressing a mutant LRP5 gene. *J. Bone Miner. Res.* 18, 960–974. doi:10.1359/jbmr.2003.18.6.960

Balemans, W., Cleiren, E., Siebers, U., Horst, J., and Van Hul, W. (2005). A generalized skeletal hyperostosis in two siblings caused by a novel mutation in the SOST gene. *Bone* 36, 943–947. doi:10.1016/j.bone.2005.02.019

Balemans, W., Ebeling, M., Patel, N., Van Hul, E., Olson, P., Dioszegi, M., et al. (2001). Increased bone density in sclerosteosis is due to the deficiency of a novel secreted protein (SOST). *Hum. Mol. Genet.* 10, 537–543. doi:10.1093/hmg/10.5.537

Bélanger, L. F. (1969). Osteocytic osteolysis. *Calcif. Tissue Int.* 4, 1–12. doi:10.1007/BF02279101

Bennell, K. L., Khan, K. M., Warmington, S., Forwood, M. R., Coleman, B. D., Bennett, M. B., et al. (2002). Age does not influence the bone response to treadmill exercise in female rats. *Med. Sci. Sports Exerc.* 34, 1958–1965. doi:10.1097/00005768-200212000-00015

Bodine, P. V., Zhao, W., Kharode, Y. P., Bex, F. J., Lambert, A.-J., Goad, M. B., et al. (2004). The Wnt antagonist secreted frizzled-related protein-1 is a negative regulator of trabecular bone formation in adult mice. *Mol. Endocrinol.* 18, 1222–1237. doi:10.1210/me.2003-0498

Bonewald, L. F., and Johnson, M. L. (2008). Osteocytes, mechanosensing and Wnt signaling. *Bone* 42, 606–615. doi:10.1016/j.bone.2007.12.224

Burger, E. H., and Klein-Nulend, J. (1999). Mechanotransduction in bone – role of the lacuno-canalicular network. *FASEB J.* 13(Suppl.), S101–S112.

Cameron, D. A., Paschall, H. A., and Robinson, R. A. (1967). Changes in the fine structure of bone cells after the administration of parathyroid extract. *J. Cell Biol.* 33, 1–14. doi:10.1083/jcb.33.1.1

Carriero, A., Doube, M., Vogt, M., Busse, B., Zustin, J., Levchuk, A., et al. (2014). Altered lacunar and vascular porosity in osteogenesis imperfecta mouse bone as revealed by synchrotron tomography contributes to bone fragility. *Bone* 61, 116–124. doi:10.1016/j.bone.2013.12.020

Carter, Y., Thomas, C. D. L., Clement, J. G., Peele, A. G., Hannah, K., and Cooper, D. M. (2013). Variation in osteocyte lacunar morphology and density in the human femur – a synchrotron radiation micro-CT study. *Bone* 52, 126–132. doi:10.1016/j.bone.2012.09.010

Choi, I. H., Ahn, J. H., Chung, C. Y., and Cho, T. J. (2000). Vascular proliferation and blood supply during distraction osteogenesis: a scanning electron microscopic observation. *J. Orthop. Res.* 18, 698–705. doi:10.1002/jor.1100180504

Cooper, D. M., Matyas, J. R., Katzenberg, M. A., and Hallgrimsson, B. (2004). Comparison of microcomputed tomographic and microradiographic measurements of cortical bone porosity. *Calcif. Tissue Int.* 74, 437–447. doi:10.1007/s00223-003-0071-z

Dallas, S. L., and Bonewald, L. F. (2010). Dynamics of the transition from osteoblast to osteocyte. *Ann. N. Y. Acad. Sci.* 1192, 437–443. doi:10.1111/j.1749-6632.2009.05246.x

Dong, P., Pacureanu, A., Zuluaga, M. A., Olivier, C., Frouin, F., Grimal, Q., et al. (eds) (2013). "A new quantitative approach for estimating bone cell connections from nano-CT images," in *Engineering in Medicine and Biology Society (EMBC), 2013 35th Annual International Conference of the IEEE*, Osaka, Japan: (IEEE).

Doube, M., Klosowski, M. M., Arganda-Carreras, I., Cordelieres, F. P., Dougherty, R. P., Jackson, J. S., et al. (2010). BoneJ: free and extensible bone image analysis in ImageJ. *Bone* 47, 1076–1079. doi:10.1016/j.bone.2010.08.023

Flinn, D. (1962). On folding during three-dimensional progressive deformation. *Q. J. Geol. Soc.* 118, 385–428. doi:10.1144/gsjgs.118.1.0385

Franz-Odendaal, T. A., Hall, B. K., and Witten, P. E. (2006). Buried alive: how osteoblasts become osteocytes. *Dev. Dyn.* 235, 176–190. doi:10.1002/dvdy.20603

Glass, D. A. II, Bialek, P., Ahn, J. D., Starbuck, M., Patel, M. S., Clevers, H., et al. (2005). Canonical Wnt signaling in differentiated osteoblasts controls osteoclast differentiation. *Dev. Cell* 8, 751–764. doi:10.1016/j.devcel.2005.02.017

Han, Y., Cowin, S. C., Schaffler, M. B., and Weinbaum, S. (2004). Mechanotransduction and strain amplification in osteocyte cell processes. *Proc. Natl. Acad. Sci. U.S.A.* 101, 16689–16694. doi:10.1073/pnas.0407429101

Hassler, N., Roschger, A., Gamsjaeger, S., Kramer, I., Lueger, S., van Lierop, A., et al. (2014). Sclerostin deficiency is linked to altered bone composition. *J. Bone Miner. Res.* 29, 2144–2151. doi:10.1002/jbmr.2259

Hemmatian, H., Laurent, M. R., Ghazanfari, S., Vanderschueren, D., Bakker, A. D., Klein-Nulend, J., et al. (2017). Accuracy and reproducibility of mouse cortical bone microporosity as quantified by desktop microcomputed tomography. *PLoS ONE* 12:e0182996. doi:10.1371/journal.pone.0182996

Holmen, S. L., Zylstra, C. R., Mukherjee, A., Sigler, R. E., Faugere, M. C., Bouxsein, M. L., et al. (2005). Essential role of beta-catenin in postnatal bone acquisition. *J. Biol. Chem.* 280, 21162–21168. doi:10.1074/jbc.M501900200

Howell, J. (1917). An experimental study of the effect of stress and strain on bone development. *Anat. Rec.* 13, 233–252. doi:10.1002/ar.1090130502

Järvinen, T. L., Pajamäki, I., Sievänen, H., Vuohelainen, T., Tuukkanen, J., Järvinen, M., et al. (2003). Femoral neck response to exercise and subsequent deconditioning in young and adult rats. *J. Bone Miner. Res.* 18, 1292–1299. doi:10.1359/jbmr.2003.18.7.1292

Javaheri, B., Carriero, A., Staines, K. A., Chang, Y. M., Houston, D. A., Oldknow, K. J., et al. (2015). Phospho1 deficiency transiently modifies bone architecture yet produces consistent modification in osteocyte differentiation and vascular porosity with ageing. *Bone* 81, 277–291. doi:10.1016/j.bone.2015.07.035

Javaheri, B., Stern, A. R., Lara, N., Dallas, M., Zhao, H., Liu, Y., et al. (2014). Deletion of a single beta-catenin allele in osteocytes abolishes the bone anabolic response to loading. *J. Bone Miner. Res.* 29, 705–715. doi:10.1002/jbmr.2064

Kamiya, N., Shuxian, L., Yamaguchi, R., Phipps, M., Aruwajoye, O., Adapala, N. S., et al. (2016). Targeted disruption of BMP signaling through type IA receptor (BMPR1A) in osteocyte suppresses SOST and RANKL, leading to dramatic increase in bone mass, bone mineral density and mechanical strength. *Bone* 91, 53–63. doi:10.1016/j.bone.2016.07.002

Kato, M., Patel, M. S., Levasseur, R., Lobov, I., Chang, B. H., Glass, D. A. II, et al. (2002). Cbfa1-independent decrease in osteoblast proliferation, osteopenia, and persistent embryonic eye vascularization in mice deficient in Lrp5, a Wnt coreceptor. *J. Cell Biol.* 157, 303–314. doi:10.1083/jcb.200201089

Kerckhofs, G., Durand, M., Vangoitsenhoven, R., Marin, C., Van Der Schueren, B., Carmeliet, G., et al. (2016). Changes in bone macro- and microstructure in diabetic obese mice revealed by high resolution microfocus X-ray computed tomography. *Sci. Rep.* 6, 35517. doi:10.1038/srep35517

Kerschnitzki, M., Kollmannsberger, P., Burghammer, M., Duda, G. N., Weinkamer, R., Wagermaier, W., et al. (2013). Architecture of the osteocyte network correlates with bone material quality. *J. Bone Miner. Res.* 28, 1837–1845. doi:10.1002/jbmr.1927

Krishnan, V., Bryant, H. U., and Macdougald, O. A. (2006). Regulation of bone mass by Wnt signaling. *J. Clin. Invest.* 116, 1202–1209. doi:10.1172/JCI28551

Leppänen, O. V., Sievänen, H., Jokihaara, J., Pajamäki, I., Kannus, P., and Järvinen, T. L. (2008). Pathogenesis of age-related osteoporosis: impaired mechano-responsiveness of bone is not the culprit. *PLoS ONE* 3:e2540. doi:10.1371/journal.pone.0002540

Li, X., Ominsky, M. S., Niu, Q. T., Sun, N., Daugherty, B., D'Agostin, D., et al. (2008). Targeted deletion of the sclerostin gene in mice results in increased bone formation and bone strength. *J. Bone Miner. Res.* 23, 860–869. doi:10.1359/jbmr.080216

Ma, Y.-L., Dai, R.-C., Sheng, Z.-F., Jin, Y., Zhang, Y.-H., Fang, L.-N., et al. (2008). Quantitative associations between osteocyte density and biomechanics, microcrack and microstructure in OVX rats vertebral trabeculae. *J. Biomech.* 41, 1324–1332. doi:10.1016/j.jbiomech.2008.01.017

Mader, K. S., Schneider, P., Müller, R., and Stampanoni, M. (2013). A quantitative framework for the 3D characterization of the osteocyte lacunar system. *Bone* 57, 142–154. doi:10.1016/j.bone.2013.06.026

Marone, F., and Stampanoni, M. (2012). Regridding reconstruction algorithm for real-time tomographic imaging. *J. Synchrotron. Radiat.* 19, 1029–1037. doi:10.1107/S0909049512032864

Matsumoto, T., Yoshino, M., Asano, T., Uesugi, K., Todoh, M., and Tanaka, M. (2006). Monochromatic synchrotron radiation muCT reveals disuse-mediated canal network rarefaction in cortical bone of growing rat tibiae. *J. Appl. Physiol.* 100, 274–280. doi:10.1152/japplphysiol.00495.2005

McCreadie, B. R., Hollister, S. J., Schaffler, M. B., and Goldstein, S. A. (2004). Osteocyte lacuna size and shape in women with and without osteoporotic fracture. *J. Biomech.* 37, 563–572. doi:10.1016/S0021-9290(03)00287-2

Mullender, M. G., Tan, S. D., Vico, L., Alexandre, C., and Klein-Nulend, J. (2005). Differences in osteocyte density and bone histomorphometry between men and women and between healthy and osteoporotic subjects. *Calcif. Tissue Int.* 77, 291–296. doi:10.1007/s00223-005-0043-6

Oranger, A., Brunetti, G., Colaianni, G., Tamma, R., Carbone, C., Lippo, L., et al. (2017). Sclerostin stimulates angiogenesis in human endothelial cells. *Bone* 101, 26–36. doi:10.1016/j.bone.2017.03.001

Pacureanu, A., Langer, M., Boller, E., Tafforeau, P., and Peyrin, F. (2012). Nanoscale imaging of the bone cell network with synchrotron X-ray tomography: optimization of acquisition setup. *Med. Phys.* 39, 2229–2238. doi:10.1118/1.3697525

Palacio-Mancheno, P. E., Larriera, A. I., Doty, S. B., Cardoso, L., and Fritton, S. P. (2014). 3D assessment of cortical bone porosity and tissue mineral density using high-resolution microCT: effects of resolution and threshold method. *J. Bone Miner. Res.* 29, 142–150. doi:10.1002/jbmr.2012

Perilli, E., Bala, Y., Zebaze, R., Reynolds, K. J., and Seeman, E. (2015). Regional heterogeneity in the configuration of the intracortical canals of the femoral shaft. *Calcif. Tissue Int.* 97, 327–335. doi:10.1007/s00223-015-0014-5

Prideaux, M., Loveridge, N., Pitsillides, A. A., and Farquharson, C. (2012). Extracellular matrix mineralization promotes E11/gp38 glycoprotein expression and drives osteocytic differentiation. *PLoS ONE* 7:e36786. doi:10.1371/journal.pone.0036786

Qin, W., Zhao, W., Li, X., Peng, Y., Harlow, L. M., Li, J., et al. (2016). Mice with sclerostin gene deletion are resistant to the severe sublesional bone loss induced by spinal cord injury. *Osteoporos. Int.* 27, 3627–3636. doi:10.1007/s00198-016-3700-x

Qing, H., and Bonewald, L. F. (2009). Osteocyte remodeling of the perilacunar and pericanalicular matrix. *Int. J. Oral Sci.* 1, 59. doi:10.4248/ijos.09019

Qiu, S., Rao, D. S., Palnitkar, S., and Parfitt, A. M. (2003). Reduced iliac cancellous osteocyte density in patients with osteoporotic vertebral fracture. *J. Bone Miner. Res.* 18, 1657–1663. doi:10.1359/jbmr.2003.18.9.1657

Raab, D. M., Crenshaw, T. D., Kimmel, D. B., and Smith, E. L. (1991). A histomorphometric study of cortical bone activity during increased weight-bearing exercise. *J. Bone Miner. Res.* 6, 741–749. doi:10.1002/jbmr.5650060712

Reya, T., and Clevers, H. (2005). Wnt signalling in stem cells and cancer. *Nature* 434, 843–850. doi:10.1038/nature03319

Robling, A. G., and Turner, C. H. (2002). Mechanotransduction in bone: genetic effects on mechanosensitivity in mice. *Bone* 31, 562–569. doi:10.1016/S8756-3282(02)00871-2

Rubin, C. T. (1984). Skeletal strain and the functional significance of bone architecture. *Calcif. Tissue Int.* 36, S11–S18. doi:10.1007/BF02406128

Schindelin, J., Arganda-Carreras, I., Frise, E., Kaynig, V., Longair, M., Pietzsch, T., et al. (2012). Fiji: an open-source platform for biological-image analysis. *Nat. Methods* 9, 676–682. doi:10.1038/nmeth.2019

Schneider, C. A., Rasband, W. S., and Eliceiri, K. W. (2012). NIH Image to ImageJ: 25 years of image analysis. *Nat. Methods* 9, 671. doi:10.1038/nmeth.2089

Schneider, P., Krucker, T., Meyer, E., Ulmann-Schuler, A., Weber, B., Stampanoni, M., et al. (2009). Simultaneous 3D visualization and quantification of murine bone and bone vasculature using micro-computed tomography and vascular replica. *Microsc. Res. Tech.* 72, 690–701. doi:10.1002/jemt.20720

Schneider, P., Meier, M., Wepf, R., and Muller, R. (2010). Towards quantitative 3D imaging of the osteocyte lacuno-canalicular network. *Bone* 47, 848–858. doi:10.1016/j.bone.2010.07.026

Schneider, P., Stauber, M., Voide, R., Stampanoni, M., Donahue, L. R., and Müller, R. (2007). Ultrastructural properties in cortical bone vary greatly in two inbred strains of mice as assessed by synchrotron light based micro- and nano-CT. *J. Bone Miner. Res.* 22, 1557–1570. doi:10.1359/jbmr.070703

Shu, R., Ai, D., Bai, D., Song, J., Zhao, M., and Han, X. (2017). The effects of SOST on implant osseointegration in ovariectomy osteoporotic mice. *Arch. Oral Biol.* 74, 82–91. doi:10.1016/j.archoralbio.2016.11.012

Skedros, J. G., Grunander, T. R., and Hamrick, M. W. (2005). Spatial distribution of osteocyte lacunae in equine radii and third metacarpals: considerations for cellular communication, microdamage detection and metabolism. *Cells Tissues Organs* 180, 215–236. doi:10.1159/000088938

Steinberg, M. E., and Trueta, J. (1981). Effects of activity on bone growth and development in the rat. *Clin. Orthop. Relat. Res.* 156, 52–60.

Suen, P. K., Zhu, T. Y., Chow, D. H., Huang, L., Zheng, L. Z., and Qin, L. (2015). Sclerostin antibody treatment increases bone formation, bone mass, and bone strength of intact bones in adult male rats. *Sci. Rep.* 5, 15632. doi:10.1038/srep15632

Tommasini, S. M., Trinward, A., Acerbo, A. S., De Carlo, F., Miller, L. M., and Judex, S. (2012). Changes in intracortical microporosities induced by pharmaceutical treatment of osteoporosis as detected by high resolution micro-CT. *Bone* 50, 596–604. doi:10.1016/j.bone.2011.12.012

Van Wesenbeeck, L., Cleiren, E., Gram, J., Beals, R. K., Benichou, O., Scopelliti, D., et al. (2003). Six novel missense mutations in the LDL receptor-related protein 5 (LRP5) gene in different conditions with an increased bone density. *Am. J. Hum. Genet.* 72, 763–771. doi:10.1086/368277

Van Wesenbeeck, L., Odgren, P. R., MacKay, C. A., D'Angelo, M., Safadi, F. F., Popoff, S. N., et al. (2002). The osteopetrotic mutation toothless (tl) is a loss-of-function frameshift mutation in the rat Csf1 gene: evidence of a crucial role for CSF-1 in osteoclastogenesis and endochondral ossification. *Proc. Natl. Acad. Sci. U.S.A.* 99, 14303–14308. doi:10.1073/pnas.202332999

Vatsa, A., Breuls, R. G., Semeins, C. M., Salmon, P. L., Smit, T. H., and Klein-Nulend, J. (2008). Osteocyte morphology in fibula and calvaria—is there a role for mechanosensing? *Bone* 43, 452–458. doi:10.1016/j.bone.2008.01.030

Verborgt, O., Gibson, G. J., and Schaffler, M. B. (2000). Loss of osteocyte integrity in association with microdamage and bone remodeling after fatigue in vivo. *J. Bone Miner. Res.* 15, 60–67. doi:10.1359/jbmr.2000.15.1.60

Wang, L., Wang, Y., Han, Y., Henderson, S. C., Majeska, R. J., Weinbaum, S., et al. (2005). In situ measurement of solute transport in the bone lacunar-canalicular system. *Proc. Natl. Acad. Sci. U.S.A.* 102, 11911–11916. doi:10.1073/pnas.0505193102

Webster, D. J., Schneider, P., Dallas, S. L., and Müller, R. (2013). Studying osteocytes within their environment. *Bone* 54, 285–295. doi:10.1016/j.bone.2013.01.004

Weivoda, M. M., Youssef, S. J., and Oursler, M. J. (2017). Sclerostin expression and functions beyond the osteocyte. *Bone* 96, 45–50. doi:10.1016/j.bone.2016.11.024

Conflict of Interest Statement: The authors declare that the research was conducted in the absence of any commercial or financial relationships that could be construed as a potential conflict of interest.

Advantages of publishing in Frontiers

OPEN ACCESS
Articles are free to read for greatest visibility and readership

FAST PUBLICATION
Around 90 days from submission to decision

HIGH QUALITY PEER-REVIEW
Rigorous, collaborative, and constructive peer-review

TRANSPARENT PEER-REVIEW
Editors and reviewers acknowledged by name on published articles

Frontiers
Avenue du Tribunal-Fédéral 34
1005 Lausanne | Switzerland

Visit us: www.frontiersin.org
Contact us: info@frontiersin.org | +41 21 510 17 00

REPRODUCIBILITY OF RESEARCH
Support open data and methods to enhance research reproducibility

DIGITAL PUBLISHING
Articles designed for optimal readership across devices

FOLLOW US
@frontiersin

IMPACT METRICS
Advanced article metrics track visibility across digital media

EXTENSIVE PROMOTION
Marketing and promotion of impactful research

LOOP RESEARCH NETWORK
Our network increases your article's readership